frontiers | Research Topics

Design and construction of microbial cell factories for the production of fuels and chemicals

Edited by
Tian-Qiong Shi, Xiao-Jun Ji, Boyang Ji, Mingfeng Cao and Farshad Darvishi

Published in
Frontiers in Bioengineering and Biotechnology

ISSN 1664-8714
ISBN 978-2-8325-2334-6
DOI 10.3389/978-2-8325-2334-6

About Frontiers

Frontiers is more than just an open access publisher of scholarly articles: it is a pioneering approach to the world of academia, radically improving the way scholarly research is managed. The grand vision of Frontiers is a world where all people have an equal opportunity to seek, share and generate knowledge. Frontiers provides immediate and permanent online open access to all its publications, but this alone is not enough to realize our grand goals.

Frontiers journal series

The Frontiers journal series is a multi-tier and interdisciplinary set of open-access, online journals, promising a paradigm shift from the current review, selection and dissemination processes in academic publishing. All Frontiers journals are driven by researchers for researchers; therefore, they constitute a service to the scholarly community. At the same time, the *Frontiers journal series* operates on a revolutionary invention, the tiered publishing system, initially addressing specific communities of scholars, and gradually climbing up to broader public understanding, thus serving the interests of the lay society, too.

Dedication to quality

Each Frontiers article is a landmark of the highest quality, thanks to genuinely collaborative interactions between authors and review editors, who include some of the world's best academicians. Research must be certified by peers before entering a stream of knowledge that may eventually reach the public - and shape society; therefore, Frontiers only applies the most rigorous and unbiased reviews. Frontiers revolutionizes research publishing by freely delivering the most outstanding research, evaluated with no bias from both the academic and social point of view. By applying the most advanced information technologies, Frontiers is catapulting scholarly publishing into a new generation.

What are Frontiers Research Topics?

Frontiers Research Topics are very popular trademarks of the *Frontiers journals series*: they are collections of at least ten articles, all centered on a particular subject. With their unique mix of varied contributions from Original Research to Review Articles, Frontiers Research Topics unify the most influential researchers, the latest key findings and historical advances in a hot research area.

Find out more on how to host your own Frontiers Research Topic or contribute to one as an author by contacting the Frontiers editorial office: frontiersin.org/about/contact

Design and construction of microbial cell factories for the production of fuels and chemicals

Topic editors

Tian-Qiong Shi — Nanjing Normal University, China
Xiao-Jun Ji — Nanjing Tech University, China
Boyang Ji — BioInnovation Institute (BII), Denmark
Mingfeng Cao — Xiamen University, China
Farshad Darvishi — Alzahra University, Iran

Citation

Shi, T.-Q., Ji, X.-J., Ji, B., Cao, M., Darvishi, F., eds. (2023). *Design and construction of microbial cell factories for the production of fuels and chemicals*. Lausanne: Frontiers Media SA. doi: 10.3389/978-2-8325-2334-6

Table of contents

frontiers | Frontiers in Bioengineering and Biotechnology

TYPE Editorial
PUBLISHED 19 April 2023
DOI 10.3389/fbioe.2023.1198317

OPEN ACCESS

EDITED AND REVIEWED BY
Jean Marie François,
Institut Biotechnologique de Toulouse (INSA), France

*CORRESPONDENCE
Tian-Qiong Shi,
tqshi@njnu.edu.cn
Farshad Darvishi,
f.darvishi@alzahra.ac.ir,
f.darvishi@ymail.com
Mingfeng Cao,
mfcao@xmu.edu.cn
Boyang Ji,
boyangji@gmail.com
Xiao-Jun Ji,
xiaojunji@njtech.edu.cn

RECEIVED 01 April 2023
ACCEPTED 11 April 2023
PUBLISHED 19 April 2023

CITATION
Shi T-Q, Darvishi F, Cao M, Ji B and Ji X-J (2023), Editorial: Design and construction of microbial cell factories for the production of fuels and chemicals. *Front. Bioeng. Biotechnol.* 11:1198317. doi: 10.3389/fbioe.2023.1198317

Editorial: Design and construction of microbial cell factories for the production of fuels and chemicals

Tian-Qiong Shi[1]*, Farshad Darvishi[2,3]*, Mingfeng Cao[4]*, Boyang Ji[5]* and Xiao-Jun Ji[6]*

[1]School of Food Science and Pharmaceutical Engineering, Nanjing Normal University, Nanjing, China, [2]Department of Microbiology, Faculty of Biological Sciences, Alzahra University, Tehran, Iran, [3]Research Center for Applied Microbiology and Microbial Biotechnology (CAMB), Alzahra University, Tehran, Iran, [4]College of Chemistry and Chemical Engineering, Xiamen University, Fujian, China, [5]BioInnovation InstituteCopenhagen, Denmark, [6]State Key Laboratory of Materials-Oriented Chemical Engineering, College of Biotechnology and Pharmaceutical Engineering, Nanjing Tech University, Nanjing, China

KEYWORDS

microbial cell factories, fuels and chemicals, synthetic biology, design and construction, metabolic engineering

Editorial on the Research Topic
Design and construction of microbial cell factories for the production of fuels and chemicals

Green biomanufacturing refers to the advanced production of biofuels, bio-based chemicals and products using industrial biotechnology (Chi et al., 2019; Straathof et al., 2019; Lv et al., 2020; Ye et al., 2023). Microbial cell factories are the central aspect of green biomanufacturing. By introducing heterologous biosynthetic pathways and then modulating complex metabolic flux intracellularly, various fuels and chemicals can be produced in a sustainable manner from renewable carbon resource and in case of high added-value compounds such as artemisinine, they can be produced in an economically feasible manner (Gong et al., 2017; Li et al., 2018; Banner et al., 2021). Compared with chemical synthesis and plant extraction methods, microbial cell factories are not restricted by external factors such as geography, climate and expensive catalysts (Liu et al., 2021; Cho et al., 2022). At the same time, using microbial cell factories for chemical production has been paid more attention due to the inherent advantages including shorter production cycles and higher product yield compared to the previous two methods. In this Research Topic, the design and construction of microbial cell factories for the production of fuels and chemicals were extensively discussed. Ma et al. developed a hybrid system that hired both synthetic biology-based methods (Sbio) and chemical synthesis-based methods (Csyn) to synthesize clinically significant and structurally complex chanoclavine to overcome the limitations of Sbio and Csyn which could boost the production of complex natural products. The model organisms like *Saccharomyces cerevisiae*, *E. coli* and *C. glutamicum* have good potential as microbial cell factories due to their clear genetic background and powerful genetic manipulation tools (Yilmaz and Walhout, 2017). Wang et al. constructed a heterologous biosynthetic pathway in *S. cerevisiae* for mogrol production. The mogrol pathway was divided into three modules and the metabolic flux of these three modules was optimized. Finally, the mogrol titer was increased to 9.1 μg/L which was 455-fold higher than that of the original strain. Guo

et al. used *Escherichia coli* as a host cell to produce D-allulose from D-fructose via *in vivo* phosphorylation-dephosphorylation. After replacing the fructose phosphotransferase systems, blocking the carbon flux and introducing an ATP regeneration system, this engineered cell factory cultured in M9 medium with glycerol as a carbon source achieved a D-allulose titer of ≈1.59 g/L and a yield of ≈0.72 g/g on D-fructose. *C. glutamicum* is considered a promising strain for *O*-Acetylhomoserine (OAH) production. Li et al. constructed an efficient clustered regularly interspaced short palindromic repeats/dead CRISPR-associated protein 9 (CRISPR-dCas9) system to identify the key genes in central metabolism and branch pathways associated with OAH biosynthesis. 25.9 g/L OAH was obtained by the engineered strain which provides a better research basis for the industrial production of OAH in *C. glutamicum*. Apart from model organisms, several non-model organisms have also been used as cell factories for the production of high-value chemicals due to their unique advantages (Nielsen, 2019). The industrial production of iturin and fengycin relies on bacterial fermentation rather than chemical synthesis but still suffer from low yields. Wang et al. developed a systematic engineering approach to improve the antifungal activity and biosynthesis of iturin and fengycin in *Bacillus amyloliquefaciens* including increasing precursor supply of the branched-chain amino acids, disrupting sporulation to extend the stage for producing antifungal lipopeptides, blocking siderophore synthesis to enhance the availability of amino acids and fatty acids, and increasing phosphorylated Spo0A by knocking out rap protein. After combined regulation and fermentation optimization, the titer of iturin and fengycin in the final engineered strain reached 31.1 mg/L and 175.3 mg/L in a flask, and 123.5 mg/L and 1,200.8 mg/L in a bioreactor. Li et al. evaluated *Gluconobacter oxydans* ATCC9937 for the production of 2,5-diketo-D-gluconic acid (2,5-DKG) and identified the non-enzymatic browning of 2,5-DKG. After optimizing the fermentation process, the titer of 2,5-DKG increased to 50.9 g/L which provided a basis for further increases in titer of 2,5-DKG. *Yarrowia lipolytica* is an excellent chassis cell due to its ability to utilize a wide range of substrates, accumulate lipids, and resist poor industrial fermentation environment (Larroude et al., 2018; Patra et al., 2021). Zhu et al. and Liang et al. achieved efficient production of lipids and erythritol using *Yarrowia lipolytica* as the host, respectively. Their researches have contributed to a deeper understanding of the *Y. lipolytica* cell factory, laying the foundation for the production of other high-value chemicals. In summary, the selection of suitable host cells is a prerequisite for the efficient production of high-value compounds.

The development of effective strategies is also essential to obtain a robust cell factory. A variety of strategies have driven the rapid development of synthetic biology which enabled us to efficiently edit the genome of host cells to achieve precise regulation and optimization of their genetic components, synthetic pathways, and metabolic networks, and ultimately to build cell factories for the efficient production of high-value compounds (Liu et al., 2022). Ma et al. developed a transposon-mediated random deletion method that allows the random and continuous reduction of *E. coli* genome. Using this strategy, a polyhydroxybutyrate overproduction strain has been obtained with better growth, glucose utilization, protein expression, and a significant increase in electroporation efficiency. Gambacorta et al. used a combinatorial library design and a growth-coupled screening to identify an isobutanol pathway cassette capable of supporting a higher carbon flux to select for both high isobutanol and high ethanol producing strain. Conversion of cheap feedstock to value-added chemicals via green biological processes may provide an attractive approach toward carbon neutrality (Zhu et al., 2020). Methanol is favored for its abundance, low price and highly reducible properties (Wang et al., 2020). Sun et al. reprogrammed *E. coli* metabolism to improve methanol assimilation by combining rational design and adaptive laboratory evolution. Protein engineering is a promising approach to improving enzyme performance, including catalytic activity, stability, selectivity and tolerance (Yang et al., 2019; Yuan et al., 2022). Recently, Huang et al. employed a computer-aided protein design strategy to improve the catalytic efficiency and substrate specificity of the α-L-rhamnosidase from *Thermotoga petrophila* DSM 13995. The best mutant showed a catalytic efficiency increased 209-fold. With the increasing research on cell factories and the growing amount of experimental data, genome-scale metabolic models (GSMs) have been developed for network property analysis, cell phenotype prediction, metabolic engineering guidance, model-driven discovery, evolutionary process exploration, and interspecies interaction identification (Ye et al., 2022). Zhang et al. reconstructed the GEM of *Streptomyces radiopugnans* iZDZ767. The culture conditions were optimized and the potential geosmin overproduction targets were identified, the titer of geosmin reached to 581.6 ng/L. The model iZDZ767 is a powerful tool for analyzing and predicting the metabolic pathways and yields of various products in *S. radiopugnans*, which provides convenient conditions for researchers to study *S. radiopugnans* in the field of systems biology. In recent years, droplet-based microfluidics as an emerging high-throughput screening technology can generate uniformly sized, mutually independent droplets with remarkable features such as high speed, high throughput, and low cost for the screening of a variety of microorganisms, expanding the existing strain library and improving the product titer, which will pave the way for the construction of microbial cell factories (Leavell et al., 2020; Yuan et al., 2022).Zhang et al. reviewed the recent applications of droplet-based microfluidics which provides a useful quick-glance reference for anyone interested in high-throughput screening technology.

The construction of efficient microbial cell factories for the production of high-value compounds is an inevitable trend for sustainable industrial production. This Research Topic not only covers a rich diversity of microbial hosts and high-value chemicals but also introduces several promising metabolic engineering strategies. In general, numerous studies have been conducted to modify host cells to enhance product titers, including the expansion of strain libraries, optimization and regulation of biosynthetic pathways, improvement of enzyme properties, and refinement of gene editing tools. We firmly believe that the rapid development of

biotechnology will pave the way for the construction of microbial cell factories in the green biomanufacturing industry.

Author contributions

T-QS wrote the draft of the manuscript, and FD, MC, BJ, and XJJ revised the manuscript. All authors approved the final version of the submitted version.

Funding

T-QS was supported by the National Key Research and Development Program of China (No.2019YFA0904900). MC is supported by the National Natural Science Foundation of China (32271477) and the Fundamental Research Funds for the Central Universities of China (20720220012). X-JJ is supported by the National Science Fund for Excellent Young Scholars of China (21922806), and the Newton Advanced Fellowships of the Royal Society (NAF\R1\201187).

Conflict of interest

The authors declare that the research was conducted in the absence of any commercial or financial relationships that could be construed as a potential conflict of interest.

Publisher's note

References

Banner, A., Toogood, H. S., and Scrutton, N. S. (2021). Consolidated bioprocessing: Synthetic biology routes to fuels and fine chemicals. *Microorganisms* 9 (5), 1079. doi:10.3390/microorganisms9051079

Chi, H., Wang, X., Shao, Y., Qin, Y., Deng, Z., Wang, L., et al. (2019). Engineering and modification of microbial chassis for systems and synthetic biology. *Synth. Syst. Biotechnol.* 4 (1), 25–33. doi:10.1016/j.synbio.2018.12.001

Cho, J. S., Kim, G. B., Eun, H., Moon, C. W., and Lee, S. Y. (2022). Designing microbial cell factories for the production of chemicals. *JACS Au* 2 (8), 1781–1799. doi:10.1021/jacsau.2c00344

Gong, Z., Nielsen, J., and Zhou, Y. J. (2017). Engineering robustness of microbial cell factories. *Biotechnol. J.* 12 (10), 1700014. doi:10.1002/biot.201700014

Larroude, M., Rossignol, T., Nicaud, J. M., and Ledesma-Amaro, R. (2018). Synthetic biology tools for engineering *Yarrowia lipolytica*. *Biotechnol. Adv.* 36 (8), 2150–2164. doi:10.1016/j.biotechadv.2018.10.004

Leavell, M. D., Singh, A. H., and Kaufmann-Malaga, B. B. (2020). High-throughput screening for improved microbial cell factories, perspective and promise. *Curr. Opin. Biotechnol.* 62, 22–28. doi:10.1016/j.copbio.2019.07.002

Li, S., Li, Y., and Smolke, C. D. (2018). Strategies for microbial synthesis of high-value phytochemicals. *Nat. Chem.* 10 (4), 395–404. doi:10.1038/s41557-018-0013-z

Liu, H., Qi, Y., Zhou, P., Ye, C., Gao, C., Chen, X., et al. (2021). Microbial physiological engineering increases the efficiency of microbial cell factories. *Crit. Rev. Biotechnol.* 41 (3), 339–354. doi:10.1080/07388551.2020.1856770

Liu, J., Wang, X., Dai, G., Zhang, Y., and Bian, X. (2022). Microbial chassis engineering drives heterologous production of complex secondary metabolites. *Biotechnol. Adv.* 59, 107966. doi:10.1016/j.biotechadv.2022.107966

Lv, Y., Su, H., and Tan, T. (2020). Editorial for special issue on green biomanufacturing. *Synth. Syst. Biotechnol.* 5 (4), 361–362. doi:10.1016/j.synbio.2020.10.006

Nielsen, J. (2019). Yeast systems biology: Model organism and cell factory. *Biotechnol. J.* 14 (9), e1800421. doi:10.1002/biot.201800421

Patra, P., Das, M., Kundu, P., and Ghosh, A. (2021). Recent advances in systems and synthetic biology approaches for developing novel cell-factories in non-conventional yeasts. *Biotechnol. Adv.* 47, 107695. doi:10.1016/j.biotechadv.2021.107695

Straathof, A. J. J., Wahl, S. A., Benjamin, K. R., Takors, R., Wierckx, N., and Noorman, H. J. (2019). Grand research challenges for sustainable industrial biotechnology. *Trends Biotechnol.* 37 (10), 1042–1050. doi:10.1016/j.tibtech.2019.04.002

Wang, Y., Fan, L., Tuyishime, P., Zheng, P., and Sun, J. (2020). Synthetic methylotrophy: A practical solution for methanol-based biomanufacturing. *Trends Biotechnol.* 38 (6), 650–666. doi:10.1016/j.tibtech.2019.12.013

Yang, K. K., Wu, Z., and Arnold, F. H. (2019). Machine-learning-guided directed evolution for protein engineering. *Nat. Methods* 16 (8), 687–694. doi:10.1038/s41592-019-0496-6

Ye, C., Wei, X., Shi, T., Sun, X., Xu, N., Gao, C., et al. (2022). Genome-scale metabolic network models: From first-generation to next-generation. *Appl. Microbiol. Biotechnol.* 106 (13-16), 4907–4920. doi:10.1007/s00253-022-12066-y

Ye, J. W., Lin, Y. N., Yi, X. Q., Yu, Z. X., Liu, X., and Chen, G. Q. (2023). Synthetic biology of extremophiles: A new wave of biomanufacturing. *Trends Biotechnol.* 41 (3), 342–357. doi:10.1016/j.tibtech.2022.11.010

Yilmaz, L. S., and Walhout, A. J. (2017). Metabolic network modeling with model organisms. *Curr. Opin. Chem. Biol.* 36, 32–39. doi:10.1016/j.cbpa.2016.12.025

Yuan, H., Tu, R., Tong, X., Lin, Y., Zhang, Y., and Wang, Q. (2022). Ultrahigh-throughput screening of industrial enzyme-producing strains by droplet-based microfluidic system. *J. Ind. Microbiol. Biotechnol.* 49 (3), kuac007. doi:10.1093/jimb/kuac007

Zhu, T., Zhao, T., Bankefa, O. E., and Li, Y. (2020). Engineering unnatural methylotrophic cell factories for methanol-based biomanufacturing: Challenges and opportunities. *Biotechnol. Adv.* 39, 107467. doi:10.1016/j.biotechadv.2019.107467

frontiers | Frontiers in Bioengineering and Biotechnology

ORIGINAL RESEARCH
published: 27 May 2022
doi: 10.3389/fbioe.2022.919526

Construction and Optimization of the *de novo* Biosynthesis Pathway of Mogrol in *Saccharomyces Cerevisiae*

*Siyu Wang [1,2], Xianhao Xu [1,2], Xueqin Lv [1,2], Yanfeng Liu [1,2], Jianghua Li [1,2], Guocheng Du [1,2] and Long Liu [1,2] **

[1]Key Laboratory of Carbohydrate Chemistry and Biotechnology, Ministry of Education, Jiangnan University, Wuxi, China, [2]Science Center for Future Foods, Ministry of Education, Jiangnan University, Wuxi, China

Mogrol plays important roles in antihyperglycemic and antilipidemic through activating the AMP-activated protein kinase pathway. Although the synthesis pathway of mogrol in *Siraitia grosvenorii* has been clarified, few studies have focused on improving mogrol production. This study employed a modular engineerin g strategy to improve mogrol production in a yeast chassis cell. First, a *de novo* synthesis pathway of mogrol in *Saccharomyces cerevisiae* was constructed. Then, the metabolic flux of each synthetic module in mogrol metabolism was systematically optimized, including the enhancement of the precursor supply, inhibition of the sterol synthesis pathway using the Clustered Regularly Interspaced Short Palindromic Repeats Interference system (CRISPRi), and optimization of the expression and reduction system of P450 enzymes. Finally, the mogrol titer was increased to 9.1 μg/L, which was 455-fold higher than that of the original strain. The yeast strains engineered in this work can serve as the basis for creating an alternative way for mogrol production in place of extraction from *S. grosvenorii*.

Keywords: ***Siraitia grosvenorii*, Mogrol, *S. cerevisiae*, CRISPRi, Metabolic Engineering**

OPEN ACCESS

Edited by:
Xiao-Jun Ji,
Nanjing Tech University, China

Reviewed by:
Jian Zha,
Shaanxi University of Science and Technology, China
Yongjun Wei,
Zhengzhou University, China

****Correspondence:***
Long Liu
longliu@jiangnan.edu.cn

Specialty section:
This article was submitted to Synthetic Biology, a section of the journal Frontiers in Bioengineering and Biotechnology

Received: *13 April 2022*
Accepted: *26 April 2022*
Published: *27 May 2022*

Citation:
Wang S, Xu X, Lv X, Liu Y, Li J, Du G and Liu L (2022) Construction and Optimization of the de novo Biosynthesis Pathway of Mogrol in Saccharomyces Cerevisiae. Front. Bioeng. Biotechnol. 10:919526. doi: 10.3389/fbioe.2022.919526

INTRODUCTION

Mogrol, a cucurbitane-type tetracyclic triterpenoid compound, is the aglycone involved in mogroside synthesis. Mogrosides are digested into mogrol *in vivo* (Chiu et al., 2013; Wang et al., 2019). Therefore, mogrol may be the main functional unit of mogrosides to exert pharmacological effects (Liu et al., 2018). Many studies have shown that mogrol can effectively reduce blood glucose to contribute to antihyperglycemia and antilipidemia by activating AMP-activated protein kinase (Harada et al., 2016; Wang H. et al., 2020; Liang et al., 2021). Further studies have identified that it could attenuate pulmonary fibrosis, memory impairment, neuroinflammation, and apoptosis (Chen et al., 2018; Wang J. et al., 2020; Liu et al., 2021). Additionally, mogrol can also suppress leukemic cell growth by inhibiting the extracellular signal-regulated kinase 1/2 (ERK1/2) and signal transducer and activator of transcription three pathways (STAT3) implicated in leukemia carcinogenesis (Liu et al., 2015). Therefore, mogrol has a good application prospect in medicine.

Mogrosides and mogrol are extracted from *Siraitia grosvenorii* fruit, but the yield is low (0.55%–0.65%) (EFSA Panel on Food Additives and Flavourings et al., 2019). Besides, the tedious extraction process, slow growth rate, and growth process of *S. grosvenorii* are vulnerable to environmental perturbations, further limiting the large-scale production efficiency of mogrol. Therefore, it is crucial to develop another method for efficiently synthesizing mogrol. Recently, the introduction of heterologous natural product biosynthesis pathways into microbial cell factories to

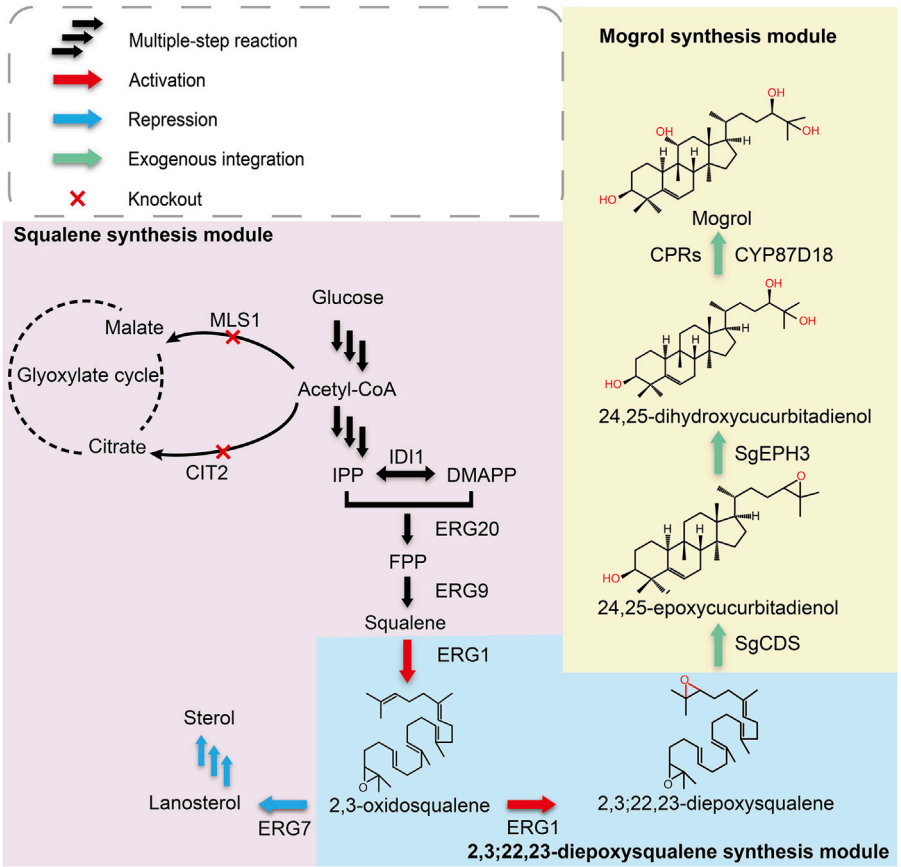

FIGURE 1 | Biosynthetic pathway for mogrol production in *S. cerevisiae*. Single arrows represent one-step conversions, whereas triple arrows represent multiple steps. Overexpressed steps are shown as red arrows, suppressed steps are shown as blue arrows, and exogenous integrated steps are shown as green arrows. Abbreviations: IPP, isopentenyl pyrophosphate; DMAPP, dimethylallyl pyrophosphate; FPP, farnesyl; IDI1, isopentenyl diphosphate isomerase; ERG20, farnesyl pyrophosphate synthetase; ERG9, squalene synthase; ERG1, squalene epoxidase; ERG7, lanosterol synthase; MLS1, malate synthase; CIT2, citrate synthase; SgCDS, cucurbitadienol synthase; SgEPH3, epoxide hydrolase; CYP87D18, cytochrome P450 enzyme.

achieve the high-efficiency synthesis of natural products is attracting the attention of researchers. The advantages of microbial synthesis of natural products include rapid growth rate, simple cell genetic manipulation, and product extraction process (Scalcinati et al., 2012; Kotopka et al., 2018; Li et al., 2018). Many natural products have been efficiently synthesized in microbial cell factories, such as protopanaxadiol (Zhao et al., 2016; Zhao et al., 2019), β-carotene (Araya et al., 2012; Bu et al., 2020), taxol (Engels et al., 2008; Ajikumar et al., 2010), and cannabinoids (Luo et al., 2019).

The biosynthesis pathway of mogrol has been extensively studied in recent years. Many studies have presumed that cucurbitadienol may be a precursor for mogrol synthesis. Therefore, a cucurbitadienol synthase gene (*SgCS*) from *S. grosvenorii* was heterologously expressed in *Saccharomyces cerevisiae*, and cucurbitadienol was detected in the fermentation broth, which realized the *de novo* biosynthesis of cucurbitadienol (Ta et al., 2012). However, the biosynthesis pathway from cucurbitadienol to mogrol has not been explored yet. Zhang et al. (2016) presumed that the enzyme CYP87D18 could catalyze the oxidation of cucurbitadienol at C-11 to generate 11-hydroxy cucurbitadienol, which could be a potential precursor to mogrol, but the following catalytic steps remained to be discovered. Therefore, researchers are committed to elucidating other pathways that could synthesize mogrol. Transcriptome and metabolomics are effective strategies to clarify the biosynthetic pathway of plant natural products (Tang et al., 2011; Dai et al., 2015). Itkin et al. (2016) screened a large number of candidate genes for mogrol biosynthesis according to the combination of genomic and transcriptomic profiling of *S. grosvenorii* and identified *SQE* (encoding squalene epoxidase), *CDS* (encoding cucurbitadienol synthase), *EPH* (encoding epoxide hydrolase), and *CYP* (encoding cytochrome P450-dependent monooxygenase) as the key genes for mogrol synthesis. Finally, Itkin et al. (2016) realized the *de novo* biosynthesis of mogrol in *S. cerevisiae* (**Figure 1**) and verified *in vitro* that UGT (glucosyltransferase) could catalyze mogrol to form mogrosides. However, the mogrol titer in their study was not quantified because it was still low.

In this study, *S. cerevisiae* was engineered as a chassis cell for mogrol biosynthesis. A modular engineering strategy was proposed to improve the synthesis efficiency of mogrol in chassis cells. A *de novo* biosynthesis pathway of mogrol was constructed in yeast by

TABLE 1 | Strains used in the study.

Strains	Characteristics	Resource
E. coli JM109	*recA*1, *endA*1, *thi, gyrA*96, *supE*44, *hsdR*17Δ (*lac-proAB*)/F' [*traD*36, *proAB*$^+$, *lacIq*, *lacZ*Δ M15]	Lab stock
S. cerevisiae CEN.PK2-1C	*MATa ura3-52 trp1-289 leu2-3,112 his3D1 MAL2-8C SUC2*	Lab stock
Y4	CEN-PK2-1C derivate, Δ*ROX1*::P_{GPD}-*tHMG1-TADH1*, inserting P_{TEF1}-*IDI*-T_{CYC1}-P_{GPD}-*tHMG1*-T_{ADH1} and P_{TEF1}-*ERG20*-T_{CYC1}-P_{PGK1}-*INO2*-T_{INO2} cassette	Lab stock
MOR001	Y4 derivate, inserting T_{ADH1}-*SgCDS-PGAL1,10-SgEPH3*-T_{CYC1} and T_{TDH3}-*CYP87D18*-$P_{GAL1,10}$-*AtCPR1*-T_{CYC1} cassette	This work
MOR002	MOR001 derivate, Δ*CIT2* Δ*MLS1*	This work
MOR003	MOR002 derivate, inserting P_{GAL1}-*dCas9*-T_{AHD1}-T_{SUP4}-sgRNA1-P_{SNR52} cassette	This work
MOR004	MOR002 derivate, inserting P_{GAL1}-*dCas9*-T_{AHD1}-T_{SUP4}-sgRNA2-P_{SNR52} cassette	This work
MOR005	MOR002 derivate, inserting P_{GAL1}-*dCas9*-T_{AHD1}-T_{SUP4}-sgRNA3-P_{SNR52} cassette	This work
MOR006	MOR002 derivate, Δ*GAL80*:: P_{TEF1}-*ERG1*-T_{CYC1}	This work
MOR007	MOR003 derivate, Δ*GAL80*:: P_{TEF1}-*ERG1*-T_{CYC1}	This work
MOR008	MOR004 derivate, Δ*GAL80*:: P_{TEF1}-*ERG1*-T_{CYC1}	This work
MOR009	MOR005 derivate, Δ*GAL80*:: P_{TEF1}-*ERG1*-T_{CYC1}	This work
MOR010	MOR008 derivate, inserting P_{TEF1}-*ERG1*-T_{CYC1} cassette	This work
MOR011	MOR010 derivate, inserting P_{TEF1}-*ERG1*-T_{CYC1} cassette	This work
MOR012	MOR004 derivate, expressing the *CYP87D18* gene via the plasmid pESC-G418	This work
MOR013	MOR010 derivate, expressing the *CYP87D18* gene via the plasmid pESC-G418	This work
MOR014	MOR010 derivate, expressing the *CYP87D18* and *AtCPR1* gene under the control of $P_{GAL1,10}$ via the plasmid pESC-G418	This work
MOR015	MOR010 derivate, expressing the *CYP87D18* and *AtCPR2* gene under the control of $P_{GAL1,10}$ via the plasmid pESC-G418	This work
MOR016	MOR010 derivate, expressing the *CYP87D18* and *CsCPR* gene under the control of $P_{GAL1,10}$ via the plasmid pESC-G418	This work
MOR017	MOR010 derivate, expressing the *CYP87D18* and *SgCPR2* gene under the control of $P_{GAL1,10}$ via the plasmid pESC-G418	This work
MOR018	MOR010 derivate, expressing the *CYP87D18* and *SrCPR1* gene under the control of $P_{GAL1,10}$ via the plasmid pESC-G418	This work
FMOR001	CEN-PK2-1C derivate, expressing the plasmid pY13-P_{ERG7}-GFP	This work
FMOR002	CEN-PK2-1C derivate, expressing the plasmid pY13-P_{ERG7}-GFP and pML104-$P_{GAL1,10}$-dCas9-mCherry-sgRNA-1	This work
FMOR003	CEN-PK2-1C derivate, expressing the plasmid pY13-P_{ERG7}-GFP and pML104-$P_{GAL1,10}$-dCas9-mCherry-sgRNA-2	This work
FMOR004	CEN-PK2-1C derivate, expressing the plasmid pY13-P_{ERG7}-GFP and pML104-$P_{GAL1,10}$-dCas9-mCherry-sgRNA-3	This work
LMOR001	CEN-PK2-1C derivate, expressing the plasmid pY15-P_{TEF1}-*SgCDS*-GFP-T_{CYC1}	This work
LMOR002	CEN-PK2-1C derivate, expressing the plasmid pY15- P_{TEF1}-*SgEPH3*-GFP-T_{CYC1}	This work
LMOR003	CEN-PK2-1C derivate, expressing the plasmid pY15- P_{TEF1}-*CYP87D18*-GFP-T_{CYC1}-P_{GAP}-mCherry-Linker-SEC12-T_{ADH1}	This work
LMOR004	CEN-PK2-1C derivate, expressing the plasmid pY15- P_{TEF1}-*AtCPR1*-GFP-T_{CYC1}-P_{GAP}-mCherry-Linker-SEC12-T_{ADH1}	This work

heterologously expressing *SgCDS*, *SgEPH3*, *CYP87D18*, and *AtCPR1* in strain Y4 (a high-yield squalene yeast constructed in our laboratory). *MLS1* (malate synthase; GenBank ID: 855606) and *CIT2* (citrate synthase; GenBank ID: 850361) were knocked out using the Clustered Regularly Interspaced Short Palindromic Repeats (CRISPRi) to enhance the precursor acetyl-CoA supply. The sterol synthesis pathway (essential for cell growth; Jordá and Puig, 2020) was repressed using CRISPRi to balance cell growth and production. The first step of the mogrol biosynthesis pathway was enhanced by overexpressing the *ERG1* gene, an important rate-limiting enzyme in the ergosterol synthesis pathway. Subsequently, cytochrome P450 reductases (CPRs) from various sources were codon-optimized and coexpressed with *CYP87D18* in the chassis cell to improve the catalysis efficiency of the last step of the mogrol biosynthesis pathway. Finally, by increasing the *CYP87D18* expression levels and paring with different CPRs, mogrol production reached 9.1 μg/L, which was 455-fold higher than that of the original strain. Overall, this study constructed a yeast platform strain for bioproduction of mogrol by systems metabolic engineering strategies.

MATERIALS AND METHODS

Chemicals and Reagents

All chemicals were purchased from Sinopharm Chemical Reagent Co., Ltd. (Shanghai, China) unless otherwise specified. Mogrol standards were purchased from Sigma-Aldrich (St. Louis, MO, United States). PrimeSTAR HS DNA polymerase used for target genes amplification was purchased from Takara (Japan). The GeneJET polymerase chain reaction (PCR) purification kit was purchased from Thermo Fisher Scientific (United States), and SanPrep Spin Column & Collection Tube used for plasmid extraction was purchased from Sangon (Shanghai, China). The primers used in this study were synthesized by Genewiz (Suzhou, China). 5-Fluoroorotic acid (5-FOA), tyrosine, histidine, leucine, and uracil were purchased from Solarbio (Beijing, China).

Strains and Medium

The strains and plasmids used in the study are listed in **Table 1**. *Escherichia coli* JM109 was used for constructing recombinant plasmids. *S. cerevisiae* Y4 was employed as the original strain, a high-yield strain of squalene constructed previously. All strains constructed in this study are listed in **Table 1**. *E. coli* was cultured in Luria–Bertani medium (10 g/L tryptone, 5 g/L yeast extract, and 10 g/L NaCl) containing 100 mg/L ampicillin at 37°C and 220 rpm, and yeast strains were cultured in YPD medium (10 g/L yeast extract, 20 g/L peptone, and 20 g/L glucose) at 30°C and 220 rpm. Yeast transformants were selected on synthetic dextrose (SD-Ura) agar plates containing 6.9 g/L yeast nitrogen base without amino acids (YNB medium), 20 g/L glucose, 0.1 g/L amino acids (L-leucine, L-tryptophan, and L-histidine), and 20 g/L agar. Dimethyl sulfoxide with 1 g/ml 5-FOA was used for the counterselection of recombinants containing the URA3

TABLE 2 | Plasmids used in the study.

Plasmids	Characteristics	Resource
pESC-Leu	Amp, LEU2, *E. coli-S. cerevisiae* shuttle vector	Lab stock
pESC-G418	pESC-LEU2 derivate, ΔP_{Leu2}-LEU2::P_{bs}-KanR-T_{tef}	Lab stock
pML104-dCas9	Amp, URA3, 2μ, P_{GAP}, dCas9, *E.coli-S. cerevisiae* shuttle vector	Lab stock
pY13	Amp, HIS3, CEN/ARS, *E. coli-S. cerevisiae* shuttle vector	
pY15	Amp, LEU2, CEN/ARS, *E. coli-S. cerevisiae* shuttle vector	
pY13-P_{ERG7}-GFP	pY13 derivate, ΔP_{TEF1}:: P_{ERG7}-GFP	This work
pML104-dCas9-mCherry	pML104-dCas9 derivate, inserting T_{CYC1}-mCherry-$P_{GAL1,10}$-dCas9 cassettes in the upstream of dCas9	This work
pML104-dCas9-mCherry-1	pML104-dCas9-mCherry derivate, P_{SNR52}-sgRNA-1 T_{SUP4}	
pML104-dCas9-mCherry-2	pML104-dCas9-mCherry derivate, P_{SNR52}-sgRNA-2 T_{SUP4}	This work
pML104-dCas9-mCherry-3	pML104-dCas9-mCherry derivate, P_{SNR52}-sgRNA-3 T_{SUP4}	This work
pESC-G418-CYP	pESC-G418 derivate, P_{GAL1}-CYP-T_{TDH3}	This work
pESC-G418-CYP-AtCPR1	pESC-G418 derivate, inserting T_{CYC1}-*AtCPR1*-*PGAL1,10*-*CYP87D18*-T_{TDH3}	This work
pESC-G418-CYP-AtCPR2	pESC-G418 derivate, inserting T_{CYC1}-*AtCPR2*-*PGAL1,10*-*CYP87D18*-T_{TDH3}	This work
pESC-G418-CYP-CsCPR	pESC-G418 derivate, inserting T_{CYC1}-*CsCPR*-*PGAL1,10*-*CYP87D18*-T_{TDH3}	This work
pESC-G418-CYP-SgCPR2	pESC-G418 derivate, inserting T_{CYC1}-Sg*CPR2*-*PGAL1,10*-*CYP87D18*-T_{TDH3}	This work
pESC-G418-CYP-SrCPR1	pESC-G418 derivate, inserting T_{CYC1}-Sr*CPR1*-*PGAL1,10*-*CYP87D18*-T_{TDH3}	This work
pY13-ERG1	pY13 derivate, inserting P_{TEF1}-*ERG1*-T_{CYC1}	This work
pY15- SgCDS-GFP	pY15 derivate, inserting P_{TEF1}-*SgCDS*-GFP-T_{CYC1}	This work
pY15- SgEPH3-GFP	pY15 derivate, inserting P_{TEF1}-*SgEPH3*-GFP-T_{CYC1}	This work
pY15-CYP87D18-GFP-mCherry- SEC12	pY15 derivate, inserting P_{TEF1}-*CYP87D18*-GFP-T_{CYC1}-P_{GAP}-mCherry-Linker-SEC12-T_{ADH1}	This work
pY15-AtCPR1-GFP-mCherry- SEC12	pY15 derivate, inserting P_{TEF1}-*AtCPR1*-GFP-T_{CYC1}-P_{GAP}-mCherry-Linker-SEC12-T_{ADH1}	This work

marker. G418 sulfate (200 mg/L; Sigma) was supplemented into the medium as required.

Yeast Transformation and Strain Construction

SgCDS, *SgEPH3*, and *CYP87D18* involved in mogrol synthesis were synthesized and codon-optimized by Genewiz. The CPRs coding *AtCPR1* (GenBank ID: 828554) and *AtCPR2* (GenBank ID: 829144) from *Arabidopsis thaliana* and *SgCPR2* (GenBank ID: AYE89265.1) from *S. grosvenorii* (Zhao et al., 2018) were synthesized and codon-optimized by Genewiz. *SrCPR1* from *Stevia* (Gold et al., 2018) was synthesized and codon-optimized by Genscript (Nanjing, China). CPRs coding *CsCPR* from *Cucumber* were provided by Prof. Sanwen Huang (Chinese Academy of Agricultural Sciences). All genetic modifications used the CRISPR-Cas9-mediated genome editing method and were performed as previously described (Gilbert et al., 2013). Genome integration loci (Reider Apel et al., 2017) and the corresponding single guide RNA (sgRNA) plasmids are listed in **Supplementary Table S1**. The target fragments were amplified using PCR, and the corresponding plasmid or *S. cerevisiae* genome was used as the template. The primers used in this experiment were synthesized by Genewiz. Overlaps (40–50 bp) of each adjacent fragment were used to implement homologous recombination in yeast. Yeast transformation was performed by the LiAc/SS carrier DNA/PEG method previously described (Gietz and Schiestl, 2007).

Plasmid Construction

A green fluorescent protein (GFP) was fused with *SgCDS*, *SgEPH3*, *CYP87D18*, and *AtCPR1*, generating plasmids pY15-SgCDS-GFP, pY15-SgEPH3-GFP, pY15-CYP87D18-GFP, and pY15-AtCPR1-GFP, respectively, to determine the localization of heterologous enzymes involved in the biosynthesis pathway of mogrol. Most plant-derived P450 enzymes are located in the endoplasmic reticulum (ER) in *S. cerevisiae* (Arendt et al., 2017). An expression cassette P_{GAP}-mCherry-Linker-SCE12-TADH1 was inserted into pY15-CYP87D18-GFP and pY15-AtCPR1-GFP, resulting in plasmids pY15-CYP87D18-GFP-mCherry-SEC12 and pY15-AtCPR1-GFP-mCherry-SEC12, respectively.

CYP and *CPR* genes, promoter $P_{GAL1,10}$, and terminators T_{TDH3} and T_{CYC1} were amplified using PCR to construct pESC-G418 series vectors, and the corresponding plasmid or *S. cerevisiae* genome was used as the template. These fragments with a 40-bp homology arm were inserted into multiple cloning sites of pESC-G418 using the Gibson Assembly® Cloning Kit (NEB). Potential sgRNA targets were predicted at http://www.rgenome.net/cas-designer/ to design specific sgRNAs for corresponding targeted genes. All plasmids used in the study are listed in **Table 2**, and the corresponding primers are listed in **Supplementary Table S2**.

Fluorescence Imaging and Analysis

Gene localization of the mogrol biosynthesis pathway was observed in strain CEN-PK2-1C. Strain CEN-PK2-1C was transformed by plasmids pY15-SgCDS-GFP, pY15-SgEPH3-GFP, pY15-CYP87D18-GFP-mCherry-SEC12, and pY15-AtCPR1-GFP-mCherry-SEC12, thereby yielding strains LMOR001, LMOR002, LMOR003 and LMOR004. These strains were streaked onto an SD-Leu plate and cultured at 30°C for 2 days. Later, a single colony was picked into a 2 ml SD-Leu medium, cultured at 30°C and 220 rpm for 24 h, and washed twice with 1× phosphate-buffered saline (0.8% NaCl, 0.02% KCl, 0.144% Na_2HPO_4, and 0.024% KH_2PO_4, pH 7.4). Subsequently, 2-μL preparations were directly plated on slides. Strain LMOR001 culture was stained with Nile red solution in acetone (1:10, v/v; 1 mg/ml; Solarbio) and incubated for 60 min in

the dark at 25°C to further confirm the specific distribution of *SgCDS*.

Fluorescence imaging was performed on a Nikon C-HGF microscope with a ×100 oil immersion objective. GFP fluorescence (excitation, 490 nm; emission, 530 nm), mCherry fluorescence (excitation, 580 nm; emission, 615 nm), and Nile red fluorescence (excitation, 561 nm; emission, 615 nm) were detected by microscopy. Image analysis was carried out on the Leica TCS SP8 software package and ImageJ (NIH).

Fluorescence Detection

The endogenous promoter of *ERG7* and the *gfp* gene were inserted into plasmid pY13 to construct plasmid pY13-P_{ERG7}-GFP. Strain CEN-PK2-1C was transformed by plasmid pY13-P_{ERG7}-GFP to yield strain FMOR001. The mCherry protein shared the bidirectional promoter $P_{GAL1,10}$ with the dcas9 protein on plasmid pML104-dCas9. The corresponding sgRNA was integrated into plasmid pML104-dCas9 to construct plasmid pML104-dCas9-mCherry-1/2/3. Strain CEN-PK2-1C was transformed by plasmids pY13-P_{ERG7}-GFP and pML104-dCas9, thereby yielding strains FMOR002, FMOR003, and FMOR004, respectively. These strains were streaked onto an SD-Ura-His (FMOR002, FMOR003 and FMOR004) or SD-His (FMOR001) plate and cultured at 30°C for 2 days. Later, a single colony was picked into a 2 ml SD-Ura-His or SD-His medium and cultured at 30°C and 220 rpm for 24 h. The 2% (v/v) seed cultures were inoculated into a 200 μL SD-Ura-His or SD-His medium in a 96-well fluorescent plate and cultured at 30°C for 72 h. Strains with plasmids pML104-dCas9 and pY13-P_{ERG7}-GFP were cultivated in the SD-Ura-His medium, and the strain with pY13-P_{ERG7}-GFP was cultivated in the SD-His medium. All strains containing plasmid pML104-dcas9 needed 2%, 4%, 6%, 8%, 10%, and 20% galactose at 0 h. GFP fluorescence (excitation, 490 nm; emission, 530 nm), mCherry fluorescence (excitation, 580 nm; emission, 615 nm), and OD600 of strains were detected using a Cytation microplate reader (BioTek). **Eq. 1** was used to calculate the repression fold of GFP fluorescence (θ) by different sgRNAs.

$$\theta = \frac{[GFP/OD]1 - [GFP/OD]0}{[GFP/OD]x - [GFP/OD]0} - 1 \quad (1)$$

where $(GFP/OD)_x$ is the relative fluorescence intensity of GFP in strain FMOR002, FMOR003 or FMOR004; $(GFP/OD)_0$ is the relative fluorescence intensity of GFP in strain MOR001 (without GFP); and $(GFP/OD)_1$ is the relative fluorescence intensity of GFP in strain FMOR001.

Heterologous Expression in Recombinant Yeast and Analysis

The strains were streaked onto a YPD solid plate and cultured at 30°C for 2 days. A single colony was picked into a 2 ml YPD medium at 30°C and 220 rpm for 24 h. The 1% (v/v) cultures were inoculated into a 250 ml flask containing 50 ml YPD medium. Strains containing plasmid pESC-G418 needed 200 mg/L G418 to add to the YPD medium. All flask fermentation results represented the mean ± standard deviation (SD) of three independent experiments.

A 1 ml fermentation culture was collected and broken by a high-pressure homogenizer (FastPrep-24 5G, United States) and extracted twice with ethyl acetate to measure the mogrol and squalene concentrations. For squalene analysis (Paramasivan and Mutturi, 2017), the samples were filtered using a 0.45 μm organic phase filtration membrane and injected into a high-performance liquid chromatography instrument (Agilent 1260 series). The column was a C18 ODS column (5 μm, 250 × 4.6 mm; Thermo Fisher Scientific), and the column temperature was 40°C. The pump flow rate was 1.6 ml/min, and the mobile phase was 100% acetonitrile. The injection volume was fixed to 10 μL. For mogrol analysis, the samples extracted with ethyl acetate were resuspended in 100 μL methanol after evaporation. Mogrol was quantified using liquid chromatography mass spectrometry (LC–MS) according to Itkin et al. (2016).

RESULTS

Construction of the *de novo* Biosynthetic Pathway of Mogrol in *S. Cerevisiae*

According to the mogrol synthetic pathway in plants, the initial step in mogrol biosynthesis is the epoxidation of 2, 3-oxidosqualene to form 2, 3; 22, 23-diepoxysqualene (the triterpenoid skeleton of mogrol). Then, 2, 3; 22, 23-diepoxysqualene is cycled into 24, 25-epoxycucurbiadienol by SgCDS. SgEPH3 catalyzes the unique hydroxylation of 24, 25-epoxycucurbiadienol to form *trans*-24, 25-dihydroxycucurbitadienol. Finally, CYP87D18 adds an oxygen atom to position C11 of 24, 25-dihydroxycucurbitadienol to form mogrol (**Figure 1**).

Therefore, to construct the *de novo* biosynthetic pathway of mogrol in *S. cerevisiae*, *SgCDS*, *SgEPH3*, and *CYP87D18* from *S. grosvenorii* and the CPR gene *AtCPR1* from *A. thaliana* were integrated into the chromosome of strain Y4 (a high-yield strain of squalene constructed previously), yielding strain MOR001. The expression of these genes was under the control of the galactose-inducible promoter $P_{GAL1,10}$. Synthetic genes were first employed as templates and then the genes were amplified to investigate the expression and distribution of SgCDS, SgEPH3, CPY87D18, and AtCPR1. Genes were integrated into plasmids, and the *gfp* gene was fused downstream of them (**Figure 2A**). These plasmids were transformed into strain MOR001, thereby yielding strains LMOR001, LMOR002, LMOR003 and LMOR004. Comparing the fluorescent images of SgCDS to the bright-field images, the green fluorescent spots showed a point-like distribution. These apparent traits showed that these spots are like lipid drops (LDs), the primary storage sites for neutral lipids in cells (Hammer and Avalos, 2017). Then, cells were stained with Nile red, a dye that can directly stain LDs (Liu et al., 2020). The spots in Nile red images exactly overlapped with the green fluorescent spots. It was concluded that SgCDS was specifically localized in LDs (**Figure 2B**), which was similar to the cycloartenol synthase from *Arabidopsis thaliana* (Milla et al., 2002) and α-amyrin synthase from *Malus* × *domestica* (Yu et al., 2020). According

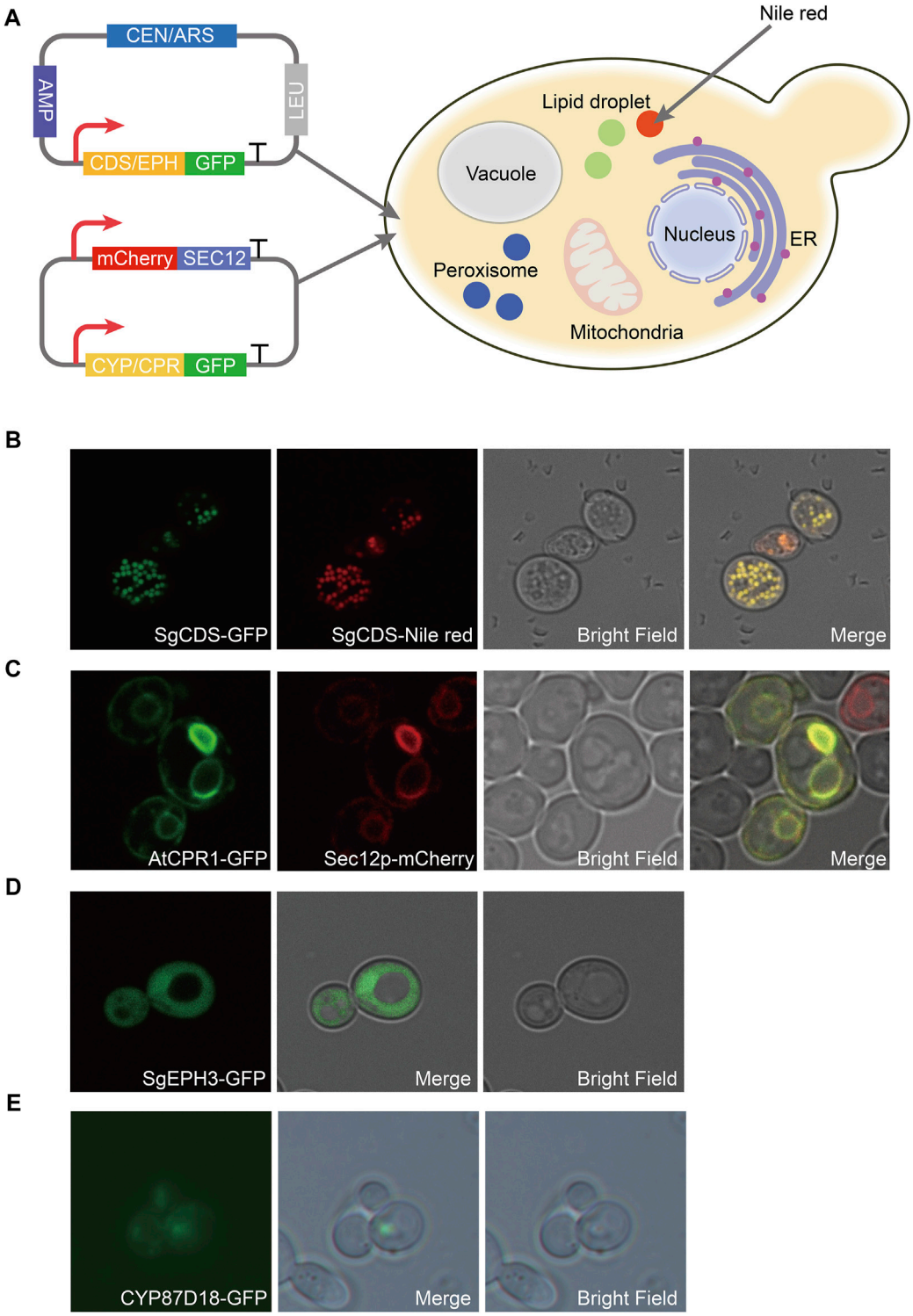

FIGURE 2 | Distribution of enzymes involved in the synthesis pathway of mogrol. (A) Construction of plasmids pY15-GFP and pY15-GFP-mCherry. SEC12 was proven to be an ER-localized protein. GFP protein was used to visualize the localization of the target protein. mCherry protein was used to specifically mark the ER, and Nile red was used to show intracellular lipophilic regions **(B–E)** Distribution analysis of *SgCDS*, *SgEPH*, *CYP87D18*, and *AtCPR1* by LSCM, respectively.

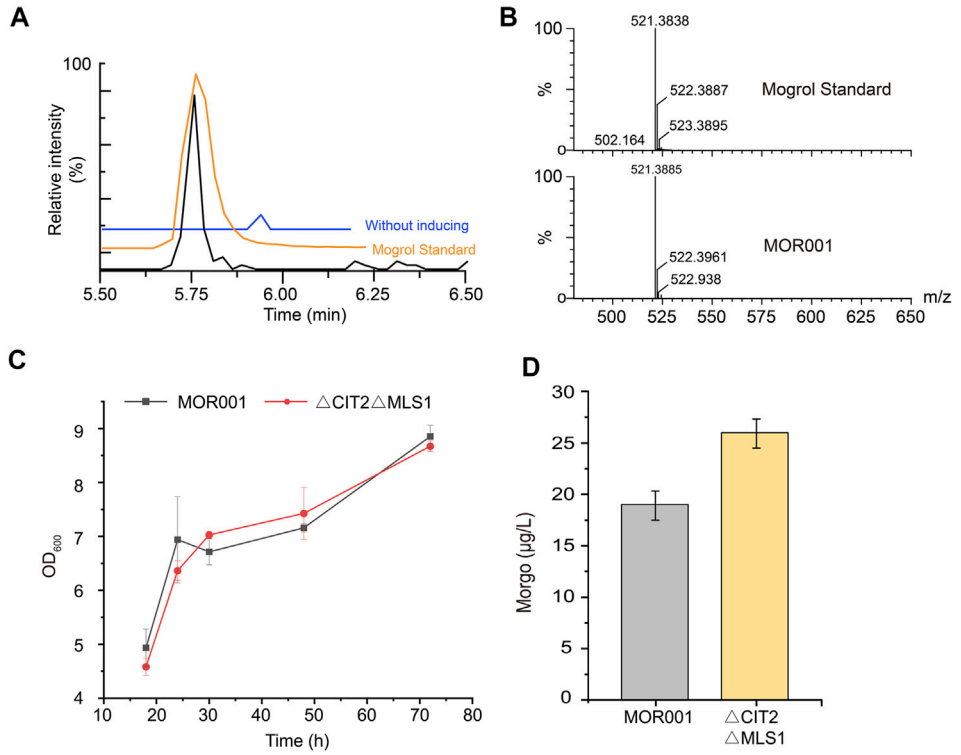

FIGURE 3 | LC–MS analysis of mogrol produced by strain MOR001. (A,B) Chromatogram analysis **(A)** and mass spectrogram analysis **(B)** of MOR001 and mogrol standard. The blue line in **(A)** represents strain MOR001 in the YPD medium without induction with galactose **(C,D)** Cell growth curves **(C)** and mogrol titer **(D)** in engineered strain MOR002, in which *MLS1* and *CIT2* genes were knocked out. Error bars represent the SD of biological triplicates (n = 3).

to the merged results of the colocalization of AtCPR1 and ER, the localization of GFP fluorescence was consistent with sec12p, suggesting that AtCPR1 was an ER-localized protein in *S. cerevisiae* (**Figure 2C**). Besides, laser scanning confocal microscopy (LSCM) analysis revealed that the GFP fluorescence of SgEPH3 filled the entire cytoplasm of *S. cerevisiae*, showing that SgEPH3 was located in the cytoplasm (**Figure 2D**). Furthermore, the GFP fluorescence of CYP87D18 was weak, indicating that the enzyme activity of CYP87D18 was a bottleneck in the biosynthesis pathway of mogrol (**Figure 2E**). These results proved that heterologous SgCDS, SgEPH3, CPY87D18 and AtCPR1 genes were successfully expressed in strain MOR001.

After strain MOR001 cultivation, a peak with a mass-to-charge ratio (m/z) value of 521.389 was detected using LC–MS in strain MOR001, in accordance with the m/z values of mogrol standard (**Figures 3A,B**). Mogrol could only be detected when the inducer galactose was added to the medium. These results demonstrated that the *de novo* biosynthetic pathway of mogrol was successfully constructed in strain MOR001. However, the mogrol titer in strain MOR001 was only 19.1 ng/L. The metabolic network was divided into three modules, including the squalene, 2, 3; 22, 23-diepoxysqualene, and mogrol synthesis modules, to synergistically regulate the metabolic network of mogrol (**Figure 1**). For the squalene synthesis module, the precursor acetyl-CoA supply was enhanced to facilitate squalene synthesis. In the cytoplasm, CIT2 and MLS1 involved in the glyoxylate pathway consumed intracellular acetyl-CoA. Therefore, *CIT2* and *MLS1* were knocked out to reduce the consumption of the precursor acetyl-CoA using the CRISPR–Cas9 system, generating strain MOR002. However, the mogrol titer in strain MOR002 only reached 25.9 ng/L, which was 1.3-fold higher than that of MOR001 (**Figure 3D**). These results indicated that the intracellular content of acetyl-CoA and squalene was sufficient to supply mogrol synthesis, which may be due to the high content of precursor squalene in the original strain Y4.

Inhibition of the Sterol Synthesis Pathway Using the CRISPRi System

In the 2, 3; 22, 23-diepoxysqualene synthesis module, Erg7p (lanosterol synthase) catalyzed the cyclization of (3*S*)-2, 3-oxidosqualene to lanosterol and further flowed into the synthesis pathway of ergosterol, one of the main components of the plasma membrane (Nes, 2011; Jordá and Puig, 2020). In general, 2,3-oxidosqualene prefers to be cyclized by ERG7 rather than oxidized into 2, 3; 22, 23-diepoxysqualene (Corey and Gross, 1967; Shan et al., 2005). Therefore, knocking out or inhibiting the activity of ERG7 is crucial for 2, 3; 22, 23-diepoxysqualene synthesis. However, directly blocking the metabolic flux to ergosterol would affect cell growth and require additional supplementation of ergosterol and Tween 80 in the medium to maintain cell growth, which was not cost-saving and conducive to industrial development (Itkin et al., 2016; Qiao et al., 2019).

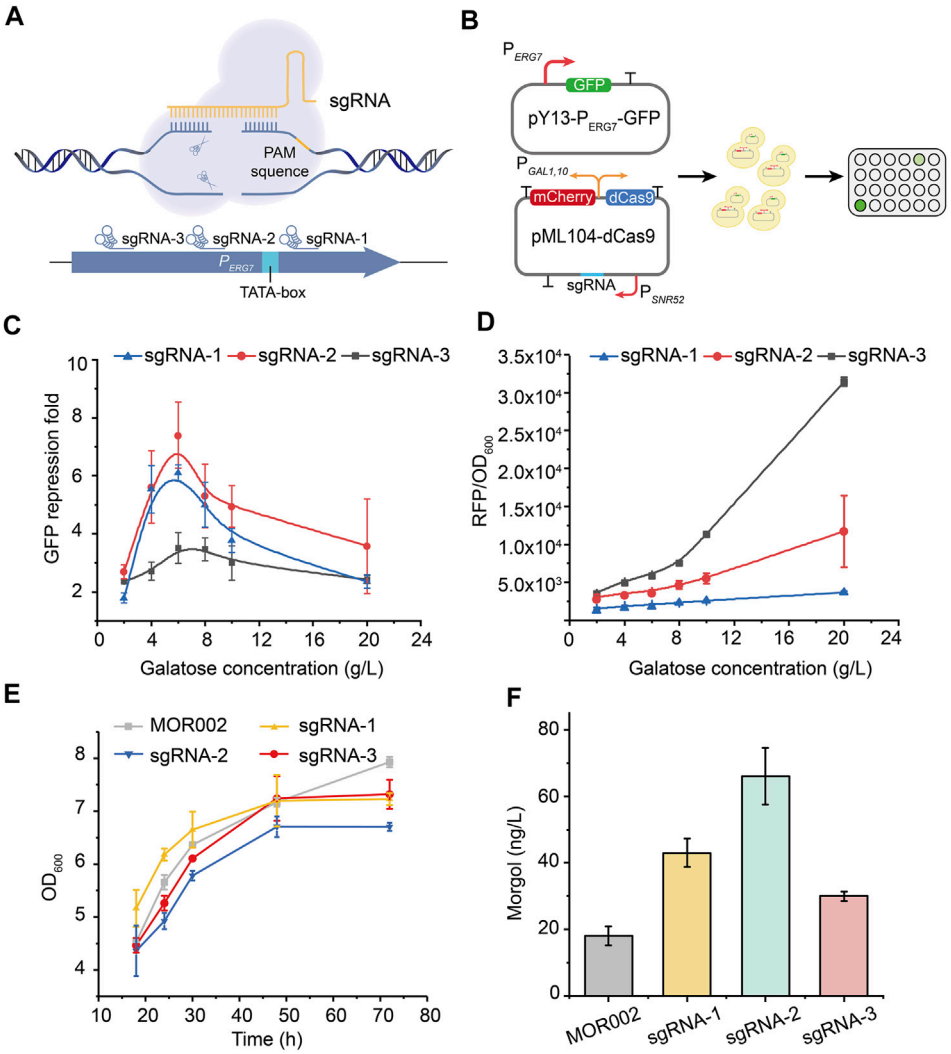

FIGURE 4 | Repression of the lanosterol biosynthesis pathway by the CRISPRi system. (A) CRISPRi was employed to repress gene expression by an inactive Cas9 protein (dCas9), which can bind to a specific sequence by sgRNA and block the elongation of RNA polymerase. sgRNAs were chosen from the endogenous *ERG7* promoter. **(B)** Construction of plasmids that characterize the feasibility of the CRISPRi system in yeast and the verification of fluorescence in a 96-well plate. **(C)** GFP fluorescence repression fold of different sgRNAs of promoter P_{ERG7}. **(D)** mCherry fluorescence intensity of dCas9 protein. **(E)** Cell growth curves of engineered strains in a 250-ml flask culture in a YPG medium **(F)** Mogrol production in engineered strains at 96 h. In **(E)** and **(F)**, sgRNA-1 represented strain MOR003, sgRNA-2 represented strain MOR004, sgRNA-3 represented strain MOR005. Error bars represent the SD of biological triplicates (n = 3).

The CRISPRi system is widely used to inhibit competing pathways in metabolic networks of various products (Gilbert et al., 2013; Jensen et al., 2017; Wu et al., 2018). Therefore, the CRISPRi system was used to inhibit *ERG7* expression, thereby redirecting the metabolic flux toward mogrol biosynthesis, enabling the decoupling of cell growth and product synthesis. First, the inhibitory targets of the CRISPRi system on the promoter of *ERG7* (P_{ERG7}) and their corresponding inhibitory effects were screened using the *gfp* reporter gene (**Figure 4A**). Control plasmid pY13-P_{ERG7}-GFP containing the reporter gene *gfp* was constructed to characterize the transcription strength of promoter P_{ERG7}. Three sgRNAs targeting different positions of the promoter P_{ERG7} were inserted into plasmid pML104-dCas9-mCherry, which contained a tandem expression cassette dCas9-mCherry under the control of galactose-inducible promoter $P_{GAL1,10}$, thereby obtaining plasmids pML104-dCas9-mCherry-1/2/3 (**Figure 4B**). The dCas9 expression level in plasmid pML104-dCas9-mCherry-1/2/3 was characterized according to the fluorescence intensity of mCherry. The control plasmid pY13-P_{ERG7}-GFP was transformed into the wild-type strain CEN-PK2-1C, yielding strain FMOR001. Plasmids pY13-P_{ERG7}-GFP and pML104-dCas9-mCherry-1/2/3 were cotransformed into the wild-type strain CEN-PK2-1C, thereby yielding strain FMOR002, FMOR003, and FMOR004 (**Figure 4B**). Finally, the fluorescence intensity of GFP and mCherry in strains FMOR001, FMOR002, FMOR003, and FMOR004 was measured. The results showed that when the inducer galactose concentration was 6 g/L, the repression fold of GFP fluorescence

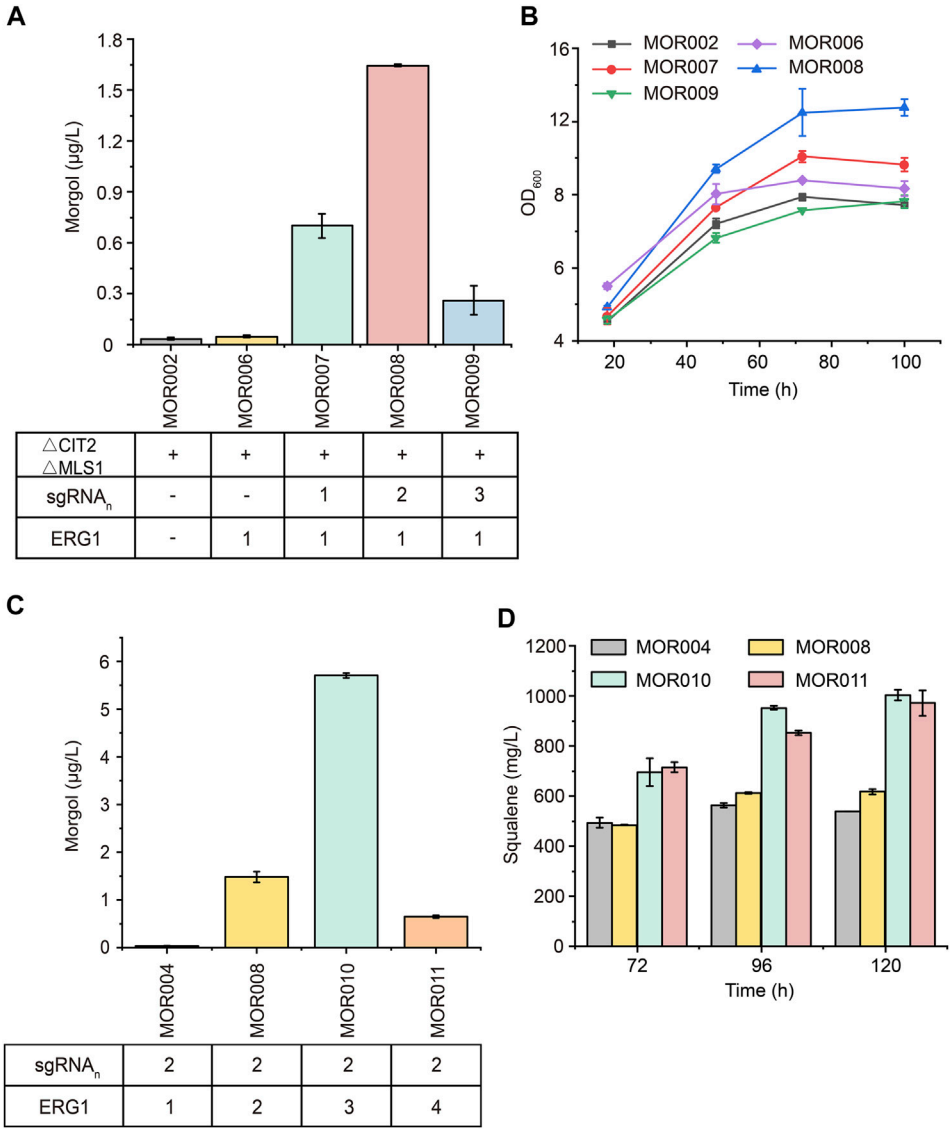

FIGURE 5 | Effects of multicopy expression of *ERG1* on mogrol. (A) Mogrol production in MOR007 to MOR009 compared to MOR002 and MOR006 **(B)** Cell growth curves of engineered strains that overexpressed *ERG1* in YPD medium. **(C,D)** Mogrol **(C)** and squalene **(D)** production after multicopy genome integration of *ERG1*. Error bars represent the SD of biological triplicates (n = 3).

(θ) in strains FMOR002, FMOR003 and FMOR004 were 6.1-, 7.4-, and 3.5-fold, respectively (**Figure 4C**, **Supplementary Figure S1**). When the galactose concentration was >6 g/L, the repression fold of GFP fluorescence (θ) by different sgRNAs was gradually decreased (**Figure 4C**). In addition, the expression level of dCas9 in strains FMOR004 was higher than FMOR002 and FMOR003, but the repression fold of GFP fluorescence (θ) in strains FMOR004 were lowest (**Figure 4D**). This result indicating that sgRNA rather than the dCas9 protein was the most essential for the efficiency of the CRISPRi system.

Subsequently, dcas9-sgRNA expression cassettes in plasmids pML104-dCas9-mCherry-1/2/3 were cloned and integrated into the genome of strain MOR002 to repress *ERG7* expression, thereby yielding strains MOR003, MOR004, and MOR005, respectively. The growth of strains MOR003, MOR004, and MOR005 was similar to strain MOR002 (**Figure 4E**), demonstrating that the CRISPRi system could inhibit *ERG7* expression without affecting cell growth. Meanwhile, the mogrol titer in strains MOR003, MOR004, and MOR005 reached 43, 66, and 30 ng/L, increased by 53%, 135%, and 7%, respectively, compared to that of MOR002 (**Figure 4F**), consistent with the GFP fluorescence repression fold of different sgRNAs.

Improving Mogrol Production by Enhancing Copies of *ERG1*

To further improve mogrol production, the metabolic flux of the mogrol synthesis module was engineered. First, the precursor 2,

3-oxidosqualene flow was "pulled" into the mogrol synthesis module rather than cell growth by overexpressing *ERG1* (squalene epoxidase), which catalyzed squalene to 2, 3-oxidosqualene and 2, 3; 22, 23-diepoxysqualene. Another copy of *ERG1* was integrated into the genome of strain MOR002, and *GAL80* (a transcriptional factor) (Pilauri et al., 2005) was simultaneously knocked out, yielding strain MOR006. LC–MS results showed that the mogrol titer in strain MOR006 reached 48 ng/L, which showed a further 240% increase than that of MOR002 (**Figure 5A**). When another copy of *ERG1* was integrated into the genome of strains MOR003, MOR004 and MOR005, the mogrol titer in the resulting strains MOR007, MOR008 and MOR009 were 13.9-, 33-, and 4.8-fold as high as that of strain MOR006, reached 670, 1600, and 230 ng/L, respectively (**Figure 5A**). These results indicated that only inhibiting the synthetic pathway of lanosterol and synergistically "pulling" the metabolic flux flow into the 2, 3; 22, 23-diepoxysqualene could maximize mogrol production. Subsequently, the copy number of *ERG1* in strain MOR008 was further increased to improve mogrol production. When the copy number of *ERG1* increased to three copies (MOR010), the mogrol titer was further increased to 5.67 μg/L. When the copy number of *ERG1* reached four copies (MOR011), the mogrol titer decreased to 0.68 μg/L (**Figure 5C**). Finally, the titer of the intermediate metabolite squalene was also measured in strains MOR004, MOR008, MOR010, and MOR011. The results showed that the squalene titer in strains MOR008, MOR010 and MOR011 at 120 h reached 617, 1002.9, and 971.4 mg/L, which was 1.1-, 1.86- and 1.81-fold higher respectively, compared to that of the strain MOR004 (**Figure 5D**). The biomass of MOR008, MOR010 and MOR011 was significantly improved compared to MOR004, which may be due to squalene being an essential precursor for cells to synthesize the plasma membrane (**Figure 5B**). These results demonstrated that *ERG1* increased mogrol production by "pulling" the metabolic flux toward the biosynthesis pathway of mogrol.

Optimization of the Expression and Reduction System of P450 Enzymes

Most plant-derived P450 enzymes (CYP) are located in the ER and are often considered as the rate-limiting enzymes in the biosynthetic pathway (Hausjell et al., 2018). They rely on CPRs to obtain electrons from NAD(P)H for subsequent catalytic reactions (Sadeghi and Gilardi, 2013). Many studies showed that different sources of CPRs may affect CYP activity, and the compatibility of native CPRs with CYPs in heterologous hosts is often not optimal (Theron et al., 2019). Hence, screening CPRs from different sources is an effective strategy to increase the activity of P450 enzymes.

Therefore, *CYP87D18* was first inserted into a high-copy plasmid pESC-G418 to test whether increasing its expression would improve mogrol production, yielding plasmid pESC-G418-CYP. Plasmid pESC-G418-CYP was transformed to MOR004 and MOR010 to construct strains MOR012 and MOR013, respectively. Compared to MOR004, *CYP87D18* expression on a multicopy plasmid significantly increased mogrol production (1.05 μg/L; **Figure 6A**). This result revealed that increasing P450 enzyme expression was beneficial to mogrol synthesis, whereas it decreased in strain MOR013 (1.64 μg/L) compared to strain MOR010 (5.67 μg/L).

Subsequently, *CYP87D18* was coexpressed in combination with five different CPRs in plasmid pESC-G418, including *AtCPR1* and *AtCPR2* from *A. thaliana*, *SgCPR2* from *S. grosvenorii* (Zhao et al., 2018), *CsCPR* from *Cucumber*, and *SrCPR1* from *Stevia* (Gold et al., 2018). The resulting plasmids were transformed into strain MOR010, thereby obtaining strains MOR014, MOR015, MOR016, MOR017, and MOR018, respectively. Fermentation data showed that the mogrol titer in strain MOR015 reached 9.1 μg/L, which was 1.6-fold higher than that of the strain MOR010. In contrast, the mogrol titer in strains MOR014 MOR016, MOR017 and MOR018 was lower than that of MOR010 (**Figure 6B**). These results demonstrated that the selection of appropriate CPR is crucial for the catalytic efficiency of CYPs in heterologous hosts. Additionally, the biomass of these strains was only 70% of MOR010 (**Figure 6C**), which may be due to the additional burden on the organism caused by that the overexpression of the second recombinant protein (Hausjell et al., 2018).

DISCUSSION

As the aglycone of mogrosides, mogrol has a significant effect on reducing blood glucose and blood lipid. However, more studies focused on the biological properties of mogrol than on its biosynthesis. Additionally, the biosynthesis pathways for mogrol from other precursors have not been explored (Li et al., 2019; Qiao et al., 2019). *S. cerevisiae* is an ideal host for the heterologous synthesis of plant-derived natural products due to its ability to express P450 enzymes located in the ER. Therefore, this study aimed to construct a yeast cell factory for efficient mogrol production. First, a *de novo* synthesis pathway for mogrol was successfully constructed in *S. cerevisiae*. Subsequently, to improve the biosynthesis efficiency of the chassis cell, the metabolic network was divided into three modules. For the squalene synthesis module, the central metabolite acetyl-CoA flow was promoted into the squalene synthesis pathway by inhibiting its flow into the glyoxylate cycle. Surprisingly, in this study, directly knocking out *CIT2* and *MLS1* involved in the glyoxylate cycle would not affect cell growth (**Figure 3C**). However, Liu et al. (2019) knocked out *CIT2* and *MLS1* in a chassis cell of β-amyrin, resulting in cell growth inhibition. This may be caused by changes in the metabolic network of cells due to the introduction of different heterologous pathways. In addition, our results indicated that the content of the precursor squalene was sufficient for the synthesis of mogrol. Compared to the squalene synthesis module, the low metabolic fluxes of the 2, 3; 22, 23-diepoxysqualene synthesis and mogrol synthesis module may be the major rate-limiting steps for the synthesis of mogrol. Therefore, we subsequently enhanced the metabolic fluxes of 2, 3; 22, 23-diepoxysqualene synthesis module and mogrol synthesis module.

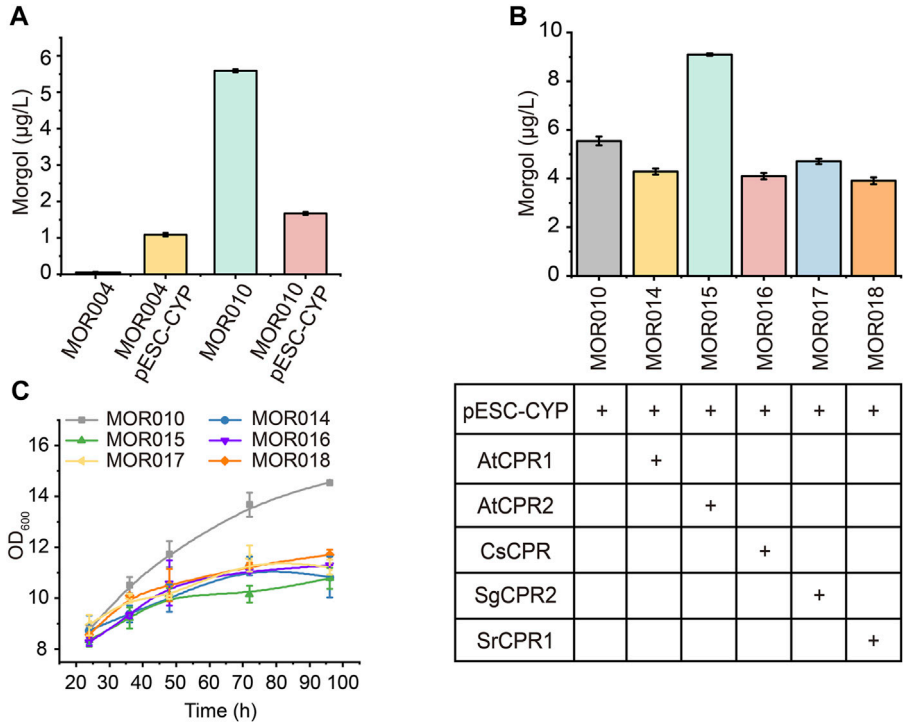

FIGURE 6 | Combined optimization of CYPs-CPRs pairing to improve mogrol production. (A) Mogrol production by overexpressing *CYP87D18* using a high-copy plasmid. **(B,C)** Mogrol production by optimizing CYPs-CPRs pairing **(B)** and cell growth curves of engineered strains **(C)** in a 250-ml flask. Error bars represent the SD of biological triplicates (n = 3).

In 2, 3; 22, 23-diepoxysqualene synthesis module, ERG1 was the only enzyme involved. ERG1 is a key rate-limiting enzyme in the sterol biosynthetic pathway. When the intracellular concentration of lanosterol is high, its activity will be feedback-inhibited, thereby maintaining the homeostasis of sterols. Therefore, reducing the intracellular sterol content is crucial for maintaining the catalytic activity of ERG1. Inhibiting *ERG7* (related to sterol synthesis pathway) expression will promote ERG1 to catalyze the synthesis of 2, 3; 22, 23-diepoxysqualene from squalene (Xu et al., 2004; Zhao et al., 2019). The traditional methods of inhibiting ERG7 expression were mainly by replacing the native P_{ERG7} promoter with an inducible promoter, such as methionine-inhibited promoter *MET3* (Baadhe et al., 2013) and a copper-inhibited promoter *CTR3* (Paddon et al., 2013; Rodriguez et al., 2016). However, adding methionine and copper ions will increase production costs, and copper ions are toxic to yeast. Therefore, the CRISPR-dCas9 system was employed to inhibit *ERG7* expression. Three sgRNAs that inhibited *ERG7* expression in different strengths were screened. sgRNA-2 had the best inhibitory effect on *ERG7* expression, probably because its target was closest to the TATA-box of P_{ERG7} (**Figure 3**). Moreover, the mogrol titer gradually increased with the inhibited effect of sgRNA. These results confirmed that reducing the metabolic flux of the sterol pathway is an effective way to increase mogrol production. More importantly, compared with other modules, the yield of mogrol was improved most obviously by adjusting this module. Furthermore, although ERG1 could catalyze the synthesis of 2, 3; 22, 23-diepoxysqualene from squalene, its activity may be low due to 2, 3; 22, 23-diepoxysqualene is not a known precursor for a metabolite in *S. cerevisiae*. Therefore, the activity of ERG1 is likely a major bottleneck for mogrol biosynthesis in *S. cerevisiae*. In future work, screening for a more efficient squalene epoxidase, or using enzyme engineering techniques to enhance the catalytic activity of ERG1, is necessary to increase the production of mogrol.

In mogrol synthesis module, the critical engineering step for mogrol overproduction was the low catalytic efficiency of P450 catalytic system. P450 enzymes are generally considered to be the rate-limiting step for triterpene synthesis (Li et al., 2021). In this study, *CYP87D18* expression in MOR001 was weak. Therefore, for the mogrol synthesis module, *CYP87D18* was expressed on the high-copy plasmid in strain MOR004, resulting in a 12-fold mogrol production. This result demonstrated that *CYP87D18* might be a rate-limiting factor for improving the mogrol titer. While overexpressing *CYP87D18* in strain MOR010, mogrol production decreased. This may be due to an imbalance of the cofactor NADPH in the cytoplasm, as Erg9p (Paramasivan and Mutturi, 2017), Erg1p (Ruckenstuhl et al., 2007) and P450 enzymes will consume NADPH for catalytic reactions. If the expression of the P450 enzyme and Erg1p increases, it may lead to an insufficient supply of intracellular NADPH. Most eukaryotic P450s are complex membrane proteins and require their redox

partner CPRs for electron transfer (Jiang et al., 2021). Besides, a suitable CYP-CPR pairing is usually beneficial for the catalytic efficiency of P450 enzymes (Chen et al., 2021). The electron transfer efficiency between them will further affect the subsequent catalytic ability of P450 enzymes. Theron et al. (2019) found that a coexpressed CPR from *Ustilago maydis* (UmCPR) with CYP53B1 resulted in a six-to seven-fold p-hydroxybenzoic acid volumetric yield than that of the endogenous CPR. Additionally, Zhu et al. (2018) introduced a novel CPR reduction system to the metabolic network of 11-oxo-β-amyrin and glycyrrhetinic acid (GA), and the 11-oxo-β-amyrin and GA titer increased by 1422- and 946.5-fold, which reached 108.1 and 18.9 mg/L, respectively. CPRs from different sources have different catalytic efficiencies for P450 enzymes, which will further affect the production synthesis. In this study, by selecting CPR from different sources, *AtCPR2* from *A. thaliana* had the highest electron transfer efficiency among the candidate CPRs, and the mogrol titer was 1.6-fold higher compared to that of MOR010. Meanwhile, we found that expressing CYP and CPRs through a high-copy plasmid resulted in a reduction of biomass. When the reaction ratio of CYP and CPR was not optimal, the excessive electron transport might lead to the release of reactive oxygen species (ROS) and cause cell damage (Zhao et al., 2017; Lin et al., 2022).

Though we significantly improved the mogrol titer by optimizing the expression of key genes of the mogrol metabolic network and improving the catalytic activity of P450 enzyme, the mogrol titer was still very low. We speculated that the activity of squalene epoxidase ERG1 and P450 enzyme might be the main rate-limiting steps that limited the synthesis of mogrol. Generally, squalene epoxidase only has the function of cyclizing squalene to form 2, 3-oxidosqualene. However, Itkin et al. (2016) found that squalene epoxidase derived from *S. grosvenorii* could further catalyze the synthesis of 2, 3; 22, 23-diepoxysqualene from 2, 3-oxidosqualene. ERG1 could perform the same function in yeast, but this catalytic step may be a side reaction because 2, 3; 22, 23-diepoxysqualene is not a known precursor for a metabolite in *S. cerevisiae*. Moreover, the enzymatic activity of P450 enzyme is the rate-limiting step that restricts the efficient synthesis of most terpenoids in *S. cerevisiae* (Hausjell et al., 2018; Jiang et al., 2021). Herein we improved the catalytic activity of P450 enzymes by paring it with a most suitable CPR, and we will carry out directed evolution of P450 enzyme to further improve the catalytic performance in the future. The titers of various hydrophobic terpenoids were improved through compartmentalizing their metabolite pathways into LDs, such as lycopene (Ma et al., 2019), α-amyrin (Yu et al., 2020), and ginsenosides (Shi et al., 2021). Therefore, compartmentalizing ERG1 and the enzymes involved in mogrol synthesis module into LDs may be an effective approach to increase the mogrol production. In summary, we achieved the bioproduction of mogrol by the engineered yeast cell factories, and the used metabolic engineering strategies may be useful for the bioproduction of the other natural products in yeast.

DATA AVAILABILITY STATEMENT

The original contributions presented in the study are included in the article/**Supplementary Material**, further inquiries can be directed to the corresponding author.

AUTHOR CONTRIBUTIONS

SW and LL conceived this project and designed the experiments. SW performed experiments. SW wrote the manuscript. XX, XL, YL, JL, GD, and LL edited the manuscript.

FUNDING

This work was financially supported by the National Natural Science Foundation of China (32021005, 32070085, 31871784), National Key Research and Development Program of China (2020YFA0908300), and the Fundamental Research Funds for the Central Universities (JUSRP52019A, JUSRP121010, JUSRP221013).

ACKNOWLEDGMENTS

We are grateful to Guanjun Tao and Tian Yang for helping us to detect mogrol by LC-MS. We would like to express our gratitude to Prof. Sanyang Li for providing the gene *CsCPR*.

SUPPLEMENTARY MATERIAL

The Supplementary Material for this article can be found online at: https://www.frontiersin.org/articles/10.3389/fbioe.2022.919526/full#supplementary-material

REFERENCES

EFSA Panel on Food Additives and FlavouringsYounes, M., Aquilina, G., Engel, K. H., Fowler, P., Frutos Fernandez, M. J., et al. (2019). Safety of Use of *Monk Fruit* Extract as a Food Additive in Different Food Categories. *EFSA. J.* 17, e05921. doi:10.2903/j.efsa.2019.5921

Ajikumar, P. K., Xiao, W.-H., Tyo, K. E. J., Wang, Y., Simeon, F., Leonard, E., et al. (2010). Isoprenoid Pathway Optimization for Taxol Precursor Overproduction in *Escherichia coli*. *Science* 330, 70–74. doi:10.1126/science.1191652

Araya-Garay, J. M., Feijoo-Siota, L., Rosa-dos-Santos, F., Veiga-Crespo, P., and Villa, T. G. (2012). Construction of New Pichia pastoris X-33 Strains for Production of Lycopene and β-carotene. *Appl. Microbiol. Biotechnol.* 93, 2483–2492. doi:10.1007/s00253-011-3764-7

Arendt, P., Miettinen, K., Pollier, J., De Rycke, R., Callewaert, N., and Goossens, A. (2017). An Endoplasmic Reticulum-Engineered Yeast Platform for Overproduction of Triterpenoids. *Metab. Eng.* 40, 165–175. doi:10.1016/j.ymben.2017.02.007

Baadhe, R. R., Mekala, N. K., Parcha, S. R., and Prameela Devi, Y. (2013). Combination ofERG9Repression and Enzyme Fusion Technology for

Improved Production of Amorphadiene inSaccharomyces Cerevisiae. *J. Anal. Methods Chem.* 2013, 1–8. doi:10.1155/2013/140469

Bu, X., Lin, J.-Y., Cheng, J., Yang, D., Duan, C.-Q., Koffas, M., et al. (2020). Engineering Endogenous ABC Transporter with Improving ATP Supply and Membrane Flexibility Enhances the Secretion of β-carotene in *Saccharomyces cerevisiae*. *Biotechnol. Biofuels.* 13, 168. doi:10.1186/s13068-020-01809-6

Chen, G., Liu, C., Meng, G., Zhang, C., Chen, F., Tang, S., et al. (2018). Neuroprotective Effect of Mogrol against Aβ1-42-Induced Memory Impairment Neuroinflammation and Apoptosis in Mice. *J. Pharm. Pharmacol.* 71, 869–877. doi:10.1111/jphp.13056

Chen, K., Liu, C., Shao, M., Xu, Z., Yang, T., and Rao, Z. (2021). Enhancing the Biotransformation Efficiency of Human CYP17A1 in *Pichia pastoris* by Co-expressing CPR and Glucose-6-Phosphate Dehydrogenase Simultaneously. *Syst Microbiol Biomanuf*. doi:10.1007/s43393-021-00063-7

Chiu, C.-H., Wang, R., Lee, C.-C., Lo, Y.-C., and Lu, T.-J. (2013). Biotransformation of Mogrosides from *Siraitia Grosvenorii* Swingle by *Saccharomyces cerevisiae*. *J. Agric. Food Chem.* 61, 7127–7134. doi:10.1021/jf402058p

Corey, E. J., and Gross, S. K. (1967). Formation of Sterols by the Action of 2,3-Oxidosqualene-Sterol Cyclase on the Factitious Substrates, 2,3,: 22,23-dioxidosqualene and 2,3-Oxido-22,23-Dihydrosqualene. *J. Am. Chem. Soc.* 89, 4561–4562. doi:10.1021/ja00993a079

Dai, L., Liu, C., Zhu, Y., Zhang, J., Men, Y., Zeng, Y., et al. (2015). Functional Characterization of Cucurbitadienol Synthase and Triterpene Glycosyltransferase Involved in Biosynthesis of Mogrosides from *Siraitia Grosvenorii*. *Plant Cell Physiol.* 56, 1172–1182. doi:10.1093/pcp/pcv043

Engels, B., Dahm, P., and Jennewein, S. (2008). Metabolic Engineering of Taxadiene Biosynthesis in Yeast as a First Step towards Taxol (Paclitaxel) Production. *Metab. Eng.* 10, 201–206. doi:10.1016/j.ymben.2008.03.001

Gietz, R. D., and Schiestl, R. H. (2007). High-efficiency Yeast Transformation Using the LiAc/SS Carrier DNA/PEG Method. *Nat. Protoc.* 2, 31–34. doi:10.1038/nprot.2007.13

Gilbert, L. A., Larson, M. H., Morsut, L., Liu, Z., Brar, G. A., Torres, S. E., et al. (2013). CRISPR-mediated Modular RNA-Guided Regulation of Transcription in Eukaryotes. *Cell* 154, 442–451. doi:10.1016/j.cell.2013.06.044

Gold, N. D., Fossati, E., Hansen, C. C., Difalco, M., Douchin, V., and Martin, V. J. J. (2018). A Combinatorial Approach to Study Cytochrome P450 Enzymes for De Novo Production of Steviol Glucosides in Baker's Yeast. *ACS Synth. Biol.* 7, 2918–2929. doi:10.1021/acssynbio.8b00470

Hammer, S. K., and Avalos, J. L. (2017). Harnessing Yeast Organelles for Metabolic Engineering. *Nat. Chem. Biol.* 13, 823–832. doi:10.1038/nchembio.2429

Harada, N., Ishihara, M., Horiuchi, H., Ito, Y., Tabata, H., Suzuki, Y. A., et al. (2016). Mogrol Derived from *Siraitia Grosvenorii* Mogrosides Suppresses 3T3-L1 Adipocyte Differentiation by Reducing cAMP-Response Element-Binding Protein Phosphorylation and Increasing AMP-Activated Protein Kinase Phosphorylation. *PLoS One* 11, e0162252. doi:10.1371/journal.pone.0162252

Hausjell, J., Halbwirth, H., and Spadiut, O. (2018). Recombinant Production of Eukaryotic Cytochrome P450s in Microbial Cell Factories. *Biosci. Rep.* 38, BSR20171290. doi:10.1042/BSR20171290

Itkin, M., Davidovich-Rikanati, R., Cohen, S., Portnoy, V., Doron-Faigenboim, A., Oren, E., et al. (2016). The Biosynthetic Pathway of the Nonsugar, High-Intensity Sweetener Mogroside V from *Siraitia Grosvenorii*. *Proc. Natl. Acad. Sci. U.S.A.* 113, e7619–e7628. doi:10.1073/pnas.1604828113

Jensen, E. D., Ferreira, R., Jakočiūnas, T., Arsovska, D., Zhang, J., Ding, L., et al. (2017). Transcriptional Reprogramming in Yeast Using dCas9 and Combinatorial gRNA Strategies. *Microb. Cell Fact.* 16, 46. doi:10.1186/s12934-017-0664-2

Jiang, L., Huang, L., Cai, J., Xu, Z., and Lian, J. (2021). Functional Expression of Eukaryotic Cytochrome P450s in Yeast. *Biotechnol. Bioeng.* 118, 1050–1065. doi:10.1002/bit.27630

Jordá, T., and Puig, S. (2020). Regulation of Ergosterol Biosynthesis in *Saccharomyces cerevisiae*. *Genes* 11, 795. doi:10.3390/genes11070795

Kotopka, B. J., Li, Y., and Smolke, C. D. (2018). Synthetic Biology Strategies toward Heterologous Phytochemical Production. *Nat. Prod. Rep.* 35, 902–920. doi:10.1039/c8np00028j

Li, S., Li, Y., and Smolke, C. D. (2018). Strategies for Microbial Synthesis of High-Value Phytochemicals. *Nat. Chem.* 10, 395–404. doi:10.1038/s41557-018-0013-z

Li, D., Ma, Y., Zhou, Y., Gou, J., Zhong, Y., Zhao, L., et al. (2019). A Structural and Data-Driven Approach to Engineering a Plant Cytochrome P450 Enzyme. *Sci. China Life Sci.* 62, 873–882. doi:10.1007/s11427-019-9538-3

Li, X., Wang, Y., Fan, Z., Wang, Y., Wang, P., Yan, X., et al. (2021). High-level Sustainable Production of the Characteristic Protopanaxatriol-type Saponins from Panax Species in Engineered *Saccharomyces cerevisiae*. *Metab. Eng.* 66, 87–97. doi:10.1016/j.ymben.2021.04.006

Liang, H., Cheng, R., Wang, J., Xie, H., Li, R., Shimizu, K., et al. (2021). Mogrol, an Aglycone of Mogrosides, Attenuates Ulcerative Colitis by Promoting AMPK Activation. *Phytomedicine* 81, 153427. doi:10.1016/j.phymed.2020.153427

Lin, N.-X., Xu, Y., and Yu, X.-W. (2022). Overview of Yeast Environmental Stress Response Pathways and the Development of Tolerant Yeasts. *Syst. Microbiol. Biomanuf.* 2, 232–245. doi:10.1007/s43393-021-00058-4

Liu, C., Dai, L., Liu, Y., Dou, D., Sun, Y., and Ma, L. (2018). Pharmacological Activities of Mogrosides. *Future Med. Chem.* 10, 845–850. doi:10.4155/fmc-2017-0255

Liu, C., Zeng, Y., Dai, L. H., Cai, T. Y., Zhu, Y. M., Dou, D. Q., et al. (2015). Mogrol Represents a Novel Leukemia Therapeutic, via ERK and STAT3 Inhibition. *Am. J. Cancer Res.* 5, 1308–1318.

Liu, H., Fan, J., Wang, C., Li, C., and Zhou, X. (2019). Enhanced β-Amyrin Synthesis in *Saccharomyces cerevisiae* by Coupling an Optimal Acetyl-CoA Supply Pathway. *J. Agric. Food Chem.* 67, 3723–3732. doi:10.1021/acs.jafc.9b00653

Liu, G.-S., Li, T., Zhou, W., Jiang, M., Tao, X.-Y., Liu, M., et al. (2020). The Yeast Peroxisome: A Dynamic Storage Depot and Subcellular Factory for Squalene Overproduction. *Metab. Eng.* 57, 151–161. doi:10.1016/j.ymben.2019.11.001

Liu, B., Yang, J., Hao, J., Xie, H., Shimizu, K., Li, R., et al. (2021). Natural Product Mogrol Attenuates Bleomycin-Induced Pulmonary Fibrosis Development through Promoting AMPK Activation. *J. Funct. Foods* 77, 104280. doi:10.1016/j.jff.2020.104280

Luo, X., Reiter, M. A., d'Espaux, L., Wong, J., Denby, C. M., Lechner, A., et al. (2019). Complete Biosynthesis of Cannabinoids and Their Unnatural Analogues in Yeast. *Nature* 567, 123–126. doi:10.1038/s41586-019-0978-9

Ma, T., Shi, B., Ye, Z., Li, X., Liu, M., Chen, Y., et al. (2019). Lipid Engineering Combined with Systematic Metabolic Engineering of *Saccharomyces cerevisiae* for High-Yield Production of Lycopene. *Metab. Eng.* 52, 134–142. doi:10.1016/j.ymben.2018.11.009

Milla, P., Viola, F., Bosso, S. O., Rocco, F., Cattel, L., Joubert, B. M., et al. (2002). Subcellular Localization of Oxidosqualene Cyclases from *Arabidopsis thaliana, Trypanosoma Cruzi*, and *Pneumocystis Carinii* Expressed in Yeast. *Lipids* 37, 1171–1176. doi:10.1007/s11745-002-1017-9

Nes, W. D. (2011). Biosynthesis of Cholesterol and Other Sterols. *Chem. Rev.* 111, 6423–6451. doi:10.1021/cr200021m

Paddon, C. J., Westfall, P. J., Pitera, D. J., Benjamin, K., Fisher, K., Mcphee, D., et al. (2013). High-level Semi-synthetic Production of the Potent Antimalarial Artemisinin. *Nature* 496, 528–532. doi:10.1038/nature12051

Paramasivan, K., and Mutturi, S. (2017). Regeneration of NADPH Coupled with HMG-CoA Reductase Activity Increases Squalene Synthesis in *Saccharomyces cerevisiae*. *J. Agric. Food Chem.* 65, 8162–8170. doi:10.1021/acs.jafc.7b02945

Pilauri, V., Bewley, M., Diep, C., and Hopper, J. (2005). Gal80 Dimerization and the Yeast *GAL* Gene Switch. *Genetics* 169, 1903–1914. doi:10.1534/genetics.104.036723

Qiao, J., Luo, Z., Cui, S., Zhao, H., Tang, Q., Mo, C., et al. (2019). Modification of Isoprene Synthesis to Enable Production of Curcurbitadienol Synthesis in *Saccharomyces cerevisiae*. *J. Ind. Microbiol. Biotechnol.* 46, 147–157. doi:10.1007/s10295-018-2116-3

Reider Apel, A., D'espaux, L., Wehrs, M., Sachs, D., Li, R. A., Tong, G. J., et al. (2017). A Cas9-Based Toolkit to Program Gene Expression in Saccharomyces Cerevisiae. *Nucleic. Acids. Res.* 45, 496–508. doi:10.1093/nar/gkw1023

Rodriguez, S., Denby, C. M., Van Vu, T., Baidoo, E. E. K., Wang, G., and Keasling, J. D. (2016). ATP Citrate Lyase Mediated Cytosolic Acetyl-CoA Biosynthesis Increases Mevalonate Production in *Saccharomyces cerevisiae*. *Microb. Cell Fact.* 15, 48. doi:10.1186/s12934-016-0447-1

Ruckenstuhl, C., Lang, S., Poschenel, A., Eidenberger, A., Baral, P. K., Kohu´t, P., et al. (2007). Characterization of Squalene Epoxidase of *Saccharomyces cerevisiae* by Applying Terbinafine-Sensitive Variants. *Antimicrob. Agents Chemother.* 51, 275–284. doi:10.1128/AAC.00988-06

Sadeghi, S. J., and Gilardi, G. (2013). Chimeric P450 Enzymes: Activity of Artificial Redox Fusions Driven by Different Reductases for Biotechnological Applications. *Biotechnol. Appl. Biochem.* 60, 102–110. doi:10.1002/bab.1086

Scalcinati, G., Knuf, C., Partow, S., Chen, Y., Maury, J., Schalk, M., et al. (2012). Dynamic Control of Gene Expression in *Saccharomyces cerevisiae* Engineered for the Production of Plant Sesquitepene α-santalene in a Fed-Batch Mode. *Metab. Eng.* 14, 91–103. doi:10.1016/j.ymben.2012.01.007

Shan, H., Segura, M. J. R., Wilson, W. K., Lodeiro, S., and Matsuda, S. P. T. (2005). Enzymatic Cyclization of Dioxidosqualene to Heterocyclic Triterpenes. *J. Am. Chem. Soc.* 127, 18008–18009. doi:10.1021/ja055822g

Shi, Y., Wang, D., Li, R., Huang, L., Dai, Z., and Zhang, X. (2021). Engineering Yeast Subcellular Compartments for Increased Production of the Lipophilic Natural Products Ginsenosides. *Metab. Eng.* 67, 104–111. doi:10.1016/j.ymben.2021.06.002

Ta, M. T., Kapterian, T. S., Fei, W., Du, X., Brown, A. J., Dawes, I. W., et al. (2012). Accumulation of Squalene is Associated with the Clustering of Lipid Droplets. *FEBS J.* 279, 4231–4244. doi:10.1111/febs.12015

Tang, Q., Ma, X., Mo, C., Wilson, I. W., Song, C., Zhao, H., et al. (2011). An Efficient Approach to Finding *Siraitia Grosvenorii* Triterpene Biosynthetic Genes by RNA-Seq and Digital Gene Expression Analysis. *BMC Genomics* 12, 343. doi:10.1186/1471-2164-12-343

Theron, C. W., Labuschagné, M., Albertyn, J., and Smit, M. S. (2019). Heterologous Coexpression of the Benzoate-para-hydroxylase CYP53B1 with Different Cytochrome P450 Reductases in Various Yeasts. *Microb. Biotechnol.* 12, 1126–1138. doi:10.1111/1751-7915.13321

Wang, H. T., Yang, J. T., Chen, K. I., Wang, T. Y., Lu, T. J., and Cheng, K. C. (2019). Hydrolyzation of Mogrosides: Immobilized β-glucosidase for Mogrosides Deglycosylation from Lo Han Kuo. *Food Sci. Nutr.* 7, 834–843. doi:10.1002/fsn3.932

Wang, H., Meng, G.-L., Zhang, C.-T., Wang, H., Hu, M., Long, Y., et al. (2020a). Mogrol Attenuates Lipopolysaccharide (LPS)-induced Memory Impairment and Neuroinflammatory Responses in Mice. *J. Asian Nat. Prod. Res.* 22, 864–878. doi:10.1080/10286020.2019.1642878

Wang, J., Liu, J., Xie, Z., Li, J., Li, J., and Hu, L. (2020b). Design, Synthesis and Biological Evaluation of Mogrol Derivatives as a Novel Class of AMPKα2β1γ1 Activators. *Bioorg. Med. Chem. Lett.* 30, 126790. doi:10.1016/j.bmcl.2019.126790

Wu, Y., Chen, T., Liu, Y., Lv, X., Li, J., Du, G., et al. (2018). CRISPRi Allows Optimal Temporal Control of N-Acetylglucosamine Bioproduction by a Dynamic Coordination of Glucose and Xylose Metabolism in *Bacillus Subtilis*. *Metab. Eng.* 49, 232–241. doi:10.1016/j.ymben.2018.08.012

Xu, R., Fazio, G. C., and Matsuda, S. P. T. (2004). On the Origins of Triterpenoid Skeletal Diversity. *Phytochemistry* 65, 261–291. doi:10.1016/j.phytochem.2003.11.014

Yu, Y., Rasool, A., Liu, H., Lv, B., Chang, P., Song, H., et al. (2020). Engineering *Saccharomyces cerevisiae* for High Yield Production of α-amyrin via Synergistic Remodeling of α-amyrin Synthase and Expanding the Storage Pool. *Metab. Eng.* 62, 72–83. doi:10.1016/j.ymben.2020.08.010

Zhang, J., Dai, L., Yang, J., Liu, C., Men, Y., Zeng, Y., et al. (2016). Oxidation of Cucurbitadienol Catalyzed by CYP87D18 in the Biosynthesis of Mogrosides fromSiraitia Grosvenorii. *Plant Cell Physiol.* 57, 1000–1007. doi:10.1093/pcp/pcw038

Zhao, F., Bai, P., Liu, T., Li, D., Zhang, X., Lu, W., et al. (2016). Optimization of a Cytochrome P450 Oxidation System for Enhancing Protopanaxadiol Production inSaccharomyces Cerevisiae. *Biotechnol. Bioeng.* 113, 1787–1795. doi:10.1002/bit.25934

Zhao, F., Du, Y., Bai, P., Liu, J., Lu, W., and Yuan, Y. (2017). Enhancing *Saccharomyces cerevisiae* Reactive Oxygen Species and Ethanol Stress Tolerance for High-Level Production of Protopanoxadiol. *Bioresour. Technol.* 227, 308–316. doi:10.1016/j.biortech.2016.12.061

Zhao, H., Wang, J., Tang, Q., Mo, C., Guo, J., Chen, T., et al. (2018). Functional Expression of Two NADPH-Cytochrome P450 Reductases from *Siraitia Grosvenorii*. *Int. J. Biol. Macromol.* 120, 1515–1524. doi:10.1016/j.ijbiomac.2018.09.128

Zhao, F., Bai, P., Nan, W., Li, D., Zhang, C., Lu, C., et al. (2019). A Modular Engineering Strategy for High-level Production of Protopanaxadiol from Ethanol by *Saccharomyces cerevisiae*. *AICHE J.* 65, 866–874. doi:10.1002/aic.16502

Zhu, M., Wang, C., Sun, W., Zhou, A., Wang, Y., Zhang, G., et al. (2018). Boosting 11-Oxo-β-Amyrin and Glycyrrhetinic Acid Synthesis in *Saccharomyces cerevisiae* via Pairing Novel Oxidation and Reduction System from Legume Plants. *Metab. Eng.* 45, 43–50. doi:10.1016/j.ymben.2017.11.009

Conflict of Interest: The authors declare that the research was conducted in the absence of any commercial or financial relationships that could be construed as a potential conflict of interest.

Publisher's Note: All claims expressed in this article are solely those of the authors and do not necessarily represent those of their affiliated organizations, or those of the publisher, the editors and the reviewers. Any product that may be evaluated in this article, or claim that may be made by its manufacturer, is not guaranteed or endorsed by the publisher.

frontiers | Frontiers in Bioengineering and Biotechnology

ORIGINAL RESEARCH
published: 21 June 2022
doi: 10.3389/fbioe.2022.926829

Computer-Aided Design of α-L-Rhamnosidase to Increase the Synthesis Efficiency of Icariside I

Jia-Jun Huang[1,2], Hao-Xuan Hu[2], Yu-Jing Lu[2,3], Ya-Dan Bao[2], Jin-Lin Zhou[2] and Mingtao Huang[1]**

[1]School of Food Science and Engineering, South China University of Technology, Guangzhou, China, [2]Golden Health Biotechnology Co., Ltd., Foshan, China, [3]School of Chemical Engineering and Light Industry, School of Biomedical and Pharmaceutical Sciences, Guangdong University of Technology, Guangzhou, China

Icariside I, the glycosylation product of icaritin, is a novel effective anti-cancer agent with immunological anti-tumor activity. However, very limited natural icariside I content hinders its direct extraction from plants. Therefore, we employed a computer-aided protein design strategy to improve the catalytic efficiency and substrate specificity of the α-L-rhamnosidase from *Thermotoga petrophila* DSM 13995, to provide a highly-efficient preparation method. Several beneficial mutants were obtained by expanding the active cavity. The catalytic efficiencies of all mutants were improved 16–200-fold compared with the wild-type TpeRha. The double-point mutant DH was the best mutant and showed the highest catalytic efficiency (k_{cat}/K_M: 193.52 s^{-1} M^{-1}) against icariin, which was a 209.76-fold increase compared with the wild-type TpeRha. Besides, the single-point mutant H570A showed higher substrate specificity than that of the wild-type TpeRha in hydrolysis of different substrates. This study provides enzyme design strategies and principles for the hydrolysis of rhamnosyl natural products.

Keywords: icariside I, icaritin, homology modeling, molecular docking, α-L-rhamnosidase

OPEN ACCESS

Edited by:
Tian-Qiong Shi,
Nanjing Normal University, China

Reviewed by:
Xiaoqing Mu,
Jiangnan University, China
Jin-Song Gong,
Jiangnan University, China

****Correspondence:***
Jin-Lin Zhou
david_zhou@goldenhealth.com.cn
Mingtao Huang
huangmt@scut.edu.cn

Specialty section:
This article was submitted to Synthetic Biology, a section of the journal Frontiers in Bioengineering and Biotechnology

Received: *23 April 2022*
Accepted: *24 May 2022*
Published: *21 June 2022*

Citation:
Huang J-J, Hu H-X, Lu Y-J, Bao Y-D, Zhou J-L and Huang M (2022) Computer-Aided Design of α-L-Rhamnosidase to Increase the Synthesis Efficiency of Icariside I. Front. Bioeng. Biotechnol. 10:926829. doi: 10.3389/fbioe.2022.926829

INTRODUCTION

Icariside I and icaritin are the main active compounds of herbal medicinal plants *Epimedium* spp. (Li et al., 1996). Icaritin (Zhu and Lou, 2005; Huang et al., 2007; Li et al., 2011) was recently approved for advanced hepatocellular carcinoma as an icaritin soft capsule. Icariside I has effective immunological anti-tumor activity (Chen et al., 2021) and may have better potential than icaritin in the treatment of certain diseases through reversion of tumor immune desertification. Both icariside I and icaritin belong to the *Epimedium* flavonoids (Ma et al., 2011), which consist of primary flavonoid glycosides, secondary flavonoid glycosides, and the aglycone. Primary flavonoid glycosides include epimedin A, epimedin B, epimedin C, icariin, etc. Sagittatoside A, sagittatoside B, icariside I, baohuoside I (icariside II), and icaritin are secondary flavonoid glycosides and the aglycone (Xu et al., 2013).

Abbreviations: 3D, three-dimensional; DH, TpeRha double-point mutant, which mutated both D506 and H570 to alanine; DK, TpeRha double-point mutant, which mutated both D506 and K579 to alanine; DHK, TpeRha triple-point mutant, which simultaneously mutated D506, H570 and K579 to alanine; HK, TpeRha double-point mutant, which mutated both H570 and K579to alanine; HPLC, high-performance liquid chromatography; IPTG, Isopropyl-β-D-thiogalactopyranoside; LB, Luria–Bertani; TB, Terrific Broth; SDS-PAGE, sodium dodecyl sulfate-polyacrylamide gel electrophoresis.

Although direct extraction is a way to obtain active chemicals from plants, the extremely low content of icaritin and icariside I in *Epimedium* spp. (lower than 0.1%) limits its large-scale preparation. Due to the complex processes, low efficiency, and environmental unfriendliness of icaritin chemical synthesis (Mu et al., 2013), preparation of icariside I and icaritin by the chemical method is greatly limited yet. Therefore, alternative methods are necessary to meet the huge demand for icariside I and icaritin. With the rapid development of biotechnology and synthetic biology, biosynthesis of icariside I and icaritin has become feasible. Recently, Wang et al. (2021) achieved *de novo* biosynthesis of icaritin. When co-culturing the 8-prenylkaempferol-producing yeast with an *Escherichia coli* strain expressing GmOMT2, the yield of icaritin reached 19.7 mg/L. Besides *de novo* synthesis, the biosynthesis of icaritin can also be carried out through a "reverse synthesis" by hydrolyzing glycosyls from epimedin C or icariin (Xie et al., 2020; Cheng et al., 2022). It was reported that both epimedin C and icariin have a rich source in the *Epimedium* spp.; epimedin C accounts for 20.8% of the total *Epimedium* flavonoids, while icariin accounts for 21.9% (Ye et al., 2007; Ma et al., 2011). It is only neccessary to use a glycoside hydrolase for a multi-step hydrolysis to generate icariside I and icaritin from epimedin C or icariin.

Glycoside hydrolases (EC 3.2.1) are a class of enzymes that hydrolyze glycosidic bonds, and they play an important role in hydrolysis and synthesis of sugars and glycoconjugates in organisms (Manzanares et al., 2007). Icariside I can be produced from epimedin C by a two-step rhamnosyl hydrolysis, or produced from icariin by a one-step rhamnosyl hydrolysis. α-L-rhamnosidase is the enzyme widely used in industry to hydrolyze rhamnosyl-based natural products, e.g., rutin, hesperidin, and naringin. Only a few studies have reported the hydrolysis of epimedin C by α-L-rhamnosidases. Moreover, most of those reported α-L-rhamnosidases, such as AnRhaE from *Aspergillus nidulans* (Lyu et al., 2019) and BtRha from *Bacteroides thetaiotaomicron* VPI-5482 (Wu et al., 2018), could only hydrolyze the outer rhamnosidic bond. The inner rhamnosidic bond of epimedin C and icariin could only be hydrolyzed by three α-L-rhamnosidases up to now, TpeRha from *T. petrophila* DSM 13995 (Xie et al., 2020), DthRha from *Dicyolomus thermophilum* DSM 3960 (Zhang et al., 2021), and Rhase-Ⅰ from *Talaromyces stollii* CLY-6 (Cheng et al., 2022). However, the catalytic efficiency of TpeRha and DthRha is insufficient, while the thermostability of Rhase-Ⅰ is poor. The weaknesses of these wild-type enzymes restrict their use in large-scale production. Improvement of these enzymes is required for industrial application in preparation of Icariside I.

Protein engineering, in the forms of directed evolution, rational protein design, computer-aided protein design (Khan et al., 2016), and machine-learning-based protein design (Saito et al., 2018; Yang et al., 2019), is currently the most powerful method for optimizing enzyme properties. Improved performances of enzymes include in catalytic efficiency (Li et al., 2019), thermal stability (Huang et al., 2021), substrate selectivity (Li et al., 2020), pH tolerance, etc. For instance, an α-L-rhamnosidase mutant with improved thermostability obtained by directed evolution and site-directed mutagenesis showed higher efficiency in hydrolyzing naringin for debittering orange juice (Li et al., 2018). The reverse hydrolysis capacity of α-L-rhamnosidase was enhanced in catalytic activity and widely pH tolerance through site-directed mutagenesis in the enzymatic active pocket (Xu et al., 2016). A double-site mutant α-L-rhamnosidase with higher thermostability was obtained by site-directed mutagenesis based on homology modeling, molecular docking, and molecular dynamic studies (Liao et al., 2019).

In this study, several α-L-rhamnosidase mutants were successfully obtained by computer-aided protein design techniques, including homology modeling and molecular docking. The design rationale was based on adjusting the steric influence of amino acids around the ligand-binding pocket (LBP) of the enzyme. These mutants showed higher hydrolysis efficiency and greater substrate specificity in conversion from icariin to icariside I. Our findings provide design principles and techniques for building α-L-rhamnosidase mutants with high catalytic efficiency and high substrate selectivity. α-L-rhamnosidase mutants identified here also pave the way for the industrial production of icariside I.

MATERIALS AND METHODS

Strains, Reagents, and Chemicals

The α-L-rhamnosidase gene of *T. petrophila* DSM 13995 (*TpeRha*, GenBank accession: ABQ47687.1) was codon-optimized, synthesized and cloned into the vector pET-28a by General Biosystems Co., Ltd. (Anhui, China). Details of strains and plasmids used in this study are listed in **Table 1**. Primers are listed in the **Supplementary Table S1**. Competent cells of *E. coli* BL31(DE3) and *E. coli* DH5α were purchased from Weidi Biotechnology Co., Ltd. (Shanghai, China). Plasmid Mini Kit I was purchased from Omega Bio-tek Inc. (Georgia, United States). The PrimeSTAR® Max DNA Polymerase, used for site-directed mutagenesis, was purchased from Takara Biomedical Technology Co., Ltd. (Dalian, China). Restriction enzymes were purchased from Thermo Fisher Scientific Co., Ltd. (Beijing, China). The HiPure Gel Pure DNA Micro Kit was acquired from Magen Co., Ltd. (Guangzhou, China). The standards epimedin C, naringin, rutin, hesperidin, naringin dihydrochalcone (NDHC), icariin, and icariside I were purchased from Shanghai yuanye Bio-Technology Co., Ltd. (Shanghai, China). The epimedin C and icariin was purchased from Tianben Bio-Engineering Co., Ltd. (Xian, China). Other general chemical reagents used in this study were obtained from standard suppliers.

Recombinant Protein Expression and Purification

The plasmid pET-28a-TpeRha was transformed into *E. coli* BL21 (DE3). The recombinant TpeRha expression strains were cultured overnight in 5 ml of Luria-Bertani (LB)

TABLE 1 | Strains and plasmids used in this study.

Strain/plasmid	Description	Source or reference
Strains		
Escherichia coli		
DH5α	F^- φ80 *lac* ZΔM15 Δ(*lac*ZYA-*arg* F) U169 *end*A1 *rec*A1 *hsd*R17(r_k^-,m_k^+) *sup*E44λ- *thi* -1 gyrA96 *rel*A1 *pho*A	Weidi Biotechnology Co., Ltd. (Shanghai, China)
BL21 (DE3)	F^- *omp*T *hsd*S_B(r_B^- m_B^-) *gal dcm*(DE3)	Weidi Biotechnology Co., Ltd. (Shanghai, China)
BL21 (DE3)/pET-28a-TpeRha	BL21(DE3) engineered strain of wild-type TpeRha	This study
BL21 (DE3)/pET-28a-E462A	BL21(DE3) engineered strain of TpeRha single-point mutant E462A	This study
*All other single-point mutant strains were constructed in this study and their descriptions were similar to mutant strain BL21 (DE3)/pET-28a-E462A, except for the different mutation site		
BL21 (DE3)/pET-28a-DH	BL21(DE3) engineered strain of TpeRha double-point mutant DH, which mutated both D506 and H570 to alanine	This study
*All other double-point mutant strains were constructed in this study and their descriptions were similar to mutant strain BL21 (DE3)/pET-28a-DH, except for the different mutation site		
BL21 (DE3)/pET-28a-DHK	BL21(DE3) engineered strain of TpeRha triple-point mutant DHK, which simultaneously mutated D506, H570 and K579 to alanine	This study
Plasmids		
pET-28a-TpeRha	Expression vector, pET-28a with the gene *TpeRha* under P_{T7} promoter	General Biosystems Co., Ltd. (Anhui, China)

medium [1% (w/v) tryptone, 0.5% (w/v) yeast extract, 1% (w/v) NaCl, pH 7.4] contained kanamycin (100 μg/ml) and then was inoculated with 1% seed solution into 100 ml fresh Terrific Broth (TB) medium [1.2% (w/v) tryptone, 2.4% (w/v) yeast extract, 0.4% (v/v) glycerol, 17 mM KH_2PO_4, 72 mM K_2HPO_4] contained kanamycin (100 μg/ml) at 37°C with mixing at 200 rpm for 2, 3 h until the optical density at 600 nm (OD_{600}) reached 0.6–0.8. Then, IPTG was added at a final concentration of 0.5 mM to induce gene expression, and the cell cultures were incubated for an additional 16 h at the same condition. The following operations were performed on ice or at 4°C unless otherwise stated. After induction, cells were harvested by centrifugation (5,000 rpm, 4°C, 10 min) and washed twice with phosphate-buffered saline (PBS) [137 mM NaCl, 2.7 mM KCl, 10 mM Na_2HPO_4, and 2 mM KH_2PO_4, pH7.4]. The precipitates were resuspended in 10 ml lysis buffer [PBS buffer (pH 7.4), 1 mM PMSF], then sonicated for 12 min in an ice bath with 25% intermittent power (4 s on, 6 s off) by Ultrasonic homogenizer SCIENTZ-IID (Ningbo Scientz Biotechnology Co., Ltd., China). The sample was centrifuged at 8,000 rpm at 4°C for 15 min to separate crude extracts and cellular debris. The crude extract was filtered through a 0.45 μm membrane and partially purified by affinity chromatography in Ni-NTA Beads 6FF agarose (Changzhou Smart-Life Sciences Biotechnology Co., Ltd., China) according to the manufacturer's instructions. The final purified protein removed imidazole and was concentrated *via* ultrafiltration (50 kDa, Millipore, Billerica, MA, United States). The purified protein was detected by sodium dodecyl sulfate-polyacrylamide gel electrophoresis (SDS-PAGE) (12%) followed by Coomassie blue staining. The concentration of protein was determined with Bradford Protein Assay Kit (Takara Biomedical Technology Co., Ltd., China).

Characterization and Kinetics of the Recombinant TpeRhas

The recombinant TpeRha optimal temperature was determined in a total reaction volume of 500 μl containing 1 mg/ml icariin and 0.05 mg/ml TpeRha in 100 mM disodium hydrogen phosphate-citrate buffer (0.2 M Na_2HPO_4 and 0.1 M citric acid, pH 4.6). The reaction was incubated under the temperature range of 55°C–90°C for 4 h.

The recombinant TpeRha optimal pH was determined in a total reaction volume of 500 μl containing 1 mg/ml icariin and 0.05 mg/ml TpeRha in 100 mM disodium hydrogen phosphate-citrate buffer with pH ranging from 4.0 to 7.0. The reactions were incubated under the temperature of 80°C for 4 h.

Reactions were terminated by adding an equal volume of dimethyl sulfoxide (DMSO) and analyzed by high-performance liquid chromatography (HPLC) [Xtimate® C18 (4.6 mm × 250 mm, 5 μm), flow rate: 1 ml/min, column temperature: 30°C, DAD detection wavelength: 270 nm, mobile phase: acetonitrile (A)–0.5% acetic acid (B). Gradient elution conditions: from A: B = 30:70 to A: B = 50:50 over 10 min, and then eluted to A: B = 85:15 for another 10 min, and finally returned to the initial condition A: B = 30:70 over 5 min, more details were shown in **Supplementary Table S2**] after filtered through a 0.45 μm membrane. The conversion rate was calculated as the product peak area/(substrate peak area + product peak area) ×100%.

The kinetic parameters of TpeRha were determined against icariin in a concentration range of 0.1–4 mg/ml under the optimal conditions *via* a proportional weighted fit using a nonlinear regression analysis program based on Michaelis-Menten enzyme kinetics. The product yield was calculated according to the F factor of the standard. All assays were carried out in triplicate.

The purifications, analytical methods, optimal conditions determination, and kinetic data determinations of mutants constructed next were performed by the same operation.

In Silico Studies and Computer-Aided Design

The three-dimension (3D) structure model of TpeRha was predicted by homology modeling *via* MODELLER software (version 10.1) (https://salilab.org/modeller/) in this study (Webb and Sali, 2016). Ranked the sequence identity of the candidate modeling templates by the build_profile module of MODELLER. The structure of α-L-rhamnosidase from *D. thermophilum* was chosen to build the homology model of TpeRha by multiple-modules of MODELLER. The stereochemical property of the 3D model was then evaluated by PROCHECK (Laskowski et al., 1993) with a Ramachandran plot in UCLA-DOE LAB - SAVES v6.0 (https://saves.mbi.ucla.edu/). TpeRha structure was then modified by adding polar hydrogens and charges by AutoDock Tools (https://autodock.scripps.edu) for molecular docking preparation.

The structure of icariin was provided from ZINC (Sterling and Irwin, 2015), a free database of commercially-available compounds for virtual screening (http://zinc15.docking.org/). Icariin structure was then energy minimized and set all its torsional bonds free by AutoDock Tools as well. Molecular docking simulation of TpeRha and icariin was performed *via* AutoDock Vina software (Trott and Olson, 2010; Eberhardt et al., 2021). The docking results were ranked according to the binding affinity between ligand and receptor. All data of results were obtained by analysis using PyMOL software (www.pymol.org). Several candidate residues were chosen for further mutation experiments and virtual mutation studies (Guex and Peitsch, 1997) (Swiss PDB Viewer, https://spdbv.unil.ch/). The docking analysis of mutants were performed by the same operation.

Site-Directed Mutagenesis

The primers for site mutation are listed in **Supplementary Table S2**. The plasmid pET-28a-TpeRha was employed as a template, whole-plasmid amplification polymerase chain reaction (PCR) was performed using PrimeSTAR® Max DNA polymerase. The PCR amplification protocol consisted of denaturation at 98°C for 3 min followed by 30 cycles of denaturation at 98°C for 10 s, annealing at 62°C for 15 s, extension at 72°C for 2 min 30 s, and a final hold for an additional 10 min at 72°C. The PCR product was purified and digested at 37°C for 1 h with *Dpn*I to remove the template plasmid and then was transformed into *E. coli* DH5α. Plasmids extracted from positive transformants were confirmed by sequencing and transformed into *E. coli* BL21 (DE3). Positive recombinant mutants were cultured as described for induction expression.

Whole-Cell Primary Screening System

The incubation system was adjusted from 100 to 20 ml, other operations of strain recovery and induction were the same as described above. After induction, cells were harvested and resuspended in PBS buffer. A reaction mixture of 1 ml disodium hydrogen phosphate-citrate buffer (pH 4.6) contained 1 mg/ml icariin and cells with a 40 mg/ml final cell concentration. The mixture was statically incubated at 55°C for 4 h to investigate the whole-cell catalysis function of cells. The reaction mixture was terminated by adding two volumes of DMSO, and then centrifuged at 12,000 rpm for 10 min. The supernatant was analyzed by HPLC. For experimental control, whole-cell catalysis by the cells carrying the empty pET-28a without gene *TpeRha* was performed at the same condition described above. The conversion rate was calculated as described above. All assays were carried out in triplicate.

Substrate Specificity Analysis

To investigate the substrate specificity of the wild-type enzyme and one of the single-point mutants, several rhamnosyl natural products (e.g., epimedin C, naringin, rutin, hesperidin, NDHC, and icariin) were used as substrates, and whole-cell catalysis experiments were performed as described above. After incubation at the optimal temperature for 4 h, two volumes of DMSO were added to terminate the reaction. All products were detected by HPLC [Xtimate® C18 (4.6 mm × 250 mm, 5 μm), flow rate: 1 ml/min, column temperature: 30°C, DAD detection wavelength: 250 nm (270 nm for icariin and icariside I), mobile phase: the conditions of each product were shown in **Supplementary Tables S2–S6**]. The specificities of the enzymes were evaluated by analyzing the conversion rate of each product by HPLC results. All assays were carried out in triplicate.

RESULTS

Three-Dimensional Predicted Model of TpeRha

To explore the relationship between the structure and function of TpeRha and then improve the catalytic efficiency for its designated substrate, a computer-aided protein design strategy was used in this study. Three-dimensional structure prediction was carried out *via* homology modeling, and substrate-enzyme binding state prediction was carried out *via* molecular docking technology. Based on the sequence alignment results of template search in homology modeling, the DtRha (Guillotin et al., 2019) from *D. thermophilum* with the highest sequence identity (48.28%) to TpeRha was selected as the template for modeling (**Supplementary Figure S1**). The predicted model was assessed by the Ramachandran plot, indicating that the model was reasonable, with 87.8% of the structure in the most favored regions, and only 0.4% of the residues in the disallowed regions (**Supplementary Figure S2**). The result verified in PROCHECK confirmed the high quality of the model. According to the DtRha structure analysis, the TpeRha structure was predicted to consist of five distinct domains, namely, domain N (1–95), domain E (96–278), domain F (307–397), catalytic domain A (398–754), and domain C (755–861) (**Figure 1A**).

Selection of Mutation Sites Based on Molecular Docking Analysis

The results of the docking simulation showed that the designated substrate icariin was bound into the catalytic pocket on the surface of TpeRha. The rhamnosyl group of icariin was precisely located in

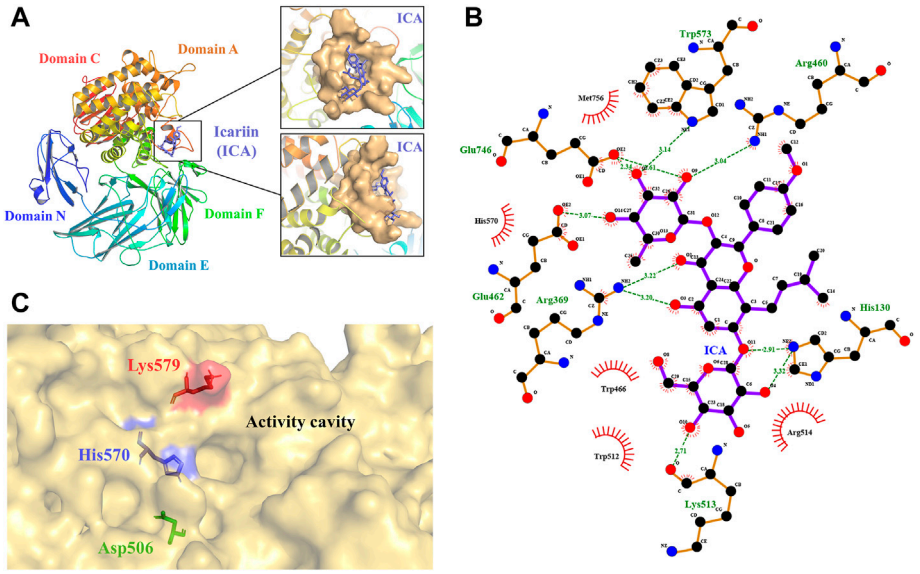

FIGURE 1 | 3D model of TpeRha and docking result of TpeRha and icariin. **(A)** The overall fold of the TpeRha model. Five distinct domains are shown in different colors (Domain N-blue, Domain E-cyan, Domain F-green, Domain A-orange, and Domain C-red). The LBP of the TpeRha is shown in the magnified area, the LBP displayed as the surface type shown in bright orange, and the ligand icariin (ICA) displayed as the sticks type shown in purple. **(B)** The receptor-ligand interactions formed between TpeRha and icariin. The hydrogen bonds (H-bonds) are shown as green dashed lines, and the bond lengths are also shown in the schematic. The names of the residues hydrogen-bonded to icariin are shown in green, and the names of nearby residues are shown in black. **(C)** Three residues were selected that could adjust the size of the active cavity based on the distribution of residues near the active pocket. The D506 at the bottom of the pocket is shown in green, the H570 at the edge of the pocket is shown in blue, and the K579 at the surface of the pocket is shown in red.

the active hole. The residues within a 5 Å distance from icariin were defined as an active pocket (**Figure 1A**), which included His130, Arg369, Asp456, Arg460, Asp461, Glu462, Trp466, Asp506, Val507, Trp512, Lys513, Arg514, Trp521, Gln 569, His 570, Trp573, Cys574, Lys579, Phe580, Glu746, Gly755, Met756, His761, and Met763. According to the analysis, the residues Glu462 and Glu746 of TpeRha might be the catalytic acid and the catalytic base respectively. Moreover, icariin also exhibited interactions with these two residues through H-bonds (**Figure 1B**). Besides, residues His130, Arg369, Arg460, Lys513, and Trp573 in the active hole were also involved in other H-bond formation (**Figure 1B**). All residues identified above were mutated to alanine to investigate their effects on enzyme activity.

The binding affinity of the docking complex TpeRha-icariin was −5.7 kcal/mol. This value implies that the binding strength of icariin to TpeRha is weak. Furthermore, the catalytic efficiency of TpeRha for the hydrolysis of icariin to icarside I might be low. Based on the analysis of the docking complex conformation, it was preliminarily speculated that the reason for the high binding affinity may be a steric hindrance from the unique core structure of icariin. In order to expand the cavity capacity of the active pocket, Asp506, His570, and Lys579 were figured out for mutating to alanine (**Figure 1C**), according to the rules including suitable residues located at the bottom of the active pocket and at the edge of the active pocket.

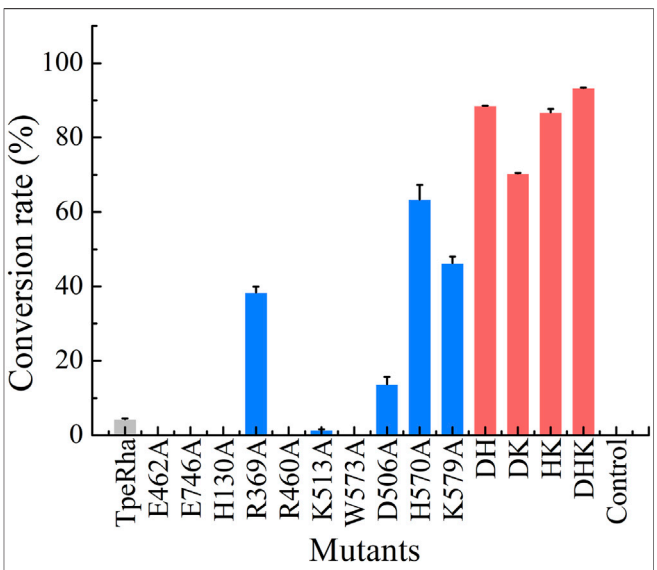

FIGURE 2 | The whole-cell catalysis screening results of mutants designed in this study are shown in three colored bars (wild-type shown in light gray, single-point mutants shown in blue, and multiple-point mutants shown in red). The conversation rate of the wild-type TpeRha was 4.33% ± 0.19%, while the control was product undetected. DHK had the highest conversion rate of 93.32% ± 0.09%.

Whole-Cell Catalysis Screening Results

Construction of mutants including E462A, E746A, H130A, R369A, R460A, K513A, W573A, D506A, H570A, and K579A was chieved *via* whole-plasmid amplification PCR. All mutants together with the wild-type TpeRha and the control strain were incubated and induced for enzyme expression. Cells were

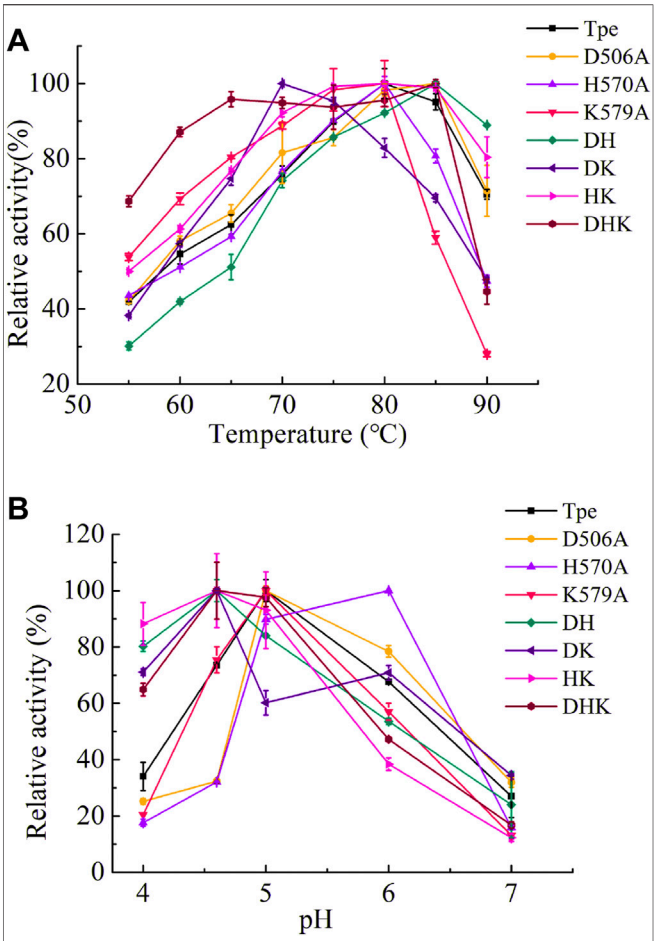

FIGURE 3 | The optimal conditions of TpeRha and mutants. **(A)** The optimal temperatures of TpeRha and mutants. **(B)** The optimal pH values of TpeRha and mutants.

collected and added to the whole-cell catalytic reaction system. The results showed that the conversion rate of icariin to icariside I by the wild-type TpeRha was 4.33% ± 0.19%, and no icariside I was detected in the control group (**Figure 2**). As expected, E462A, E746A, H130A, R460A, and W573A lost their hydrolytic activity for icariin. The activity of K513A was greatly reduced, only 1.41% ± 0.21%. Surprisingly, the activity of R369A mutant increased to 38.37% ± 1.57%, 8.86 times higher than that of the wild-type TpeRha. As for the three rational designed mutants D506A, H570A, and K579A, the activities of which were all improved compared with the wild-type TpeRha, the conversion rates reached 13.70% ± 1.93%, 63.65% ± 3.96%, and 46.29% ± 1.78%, respectively (**Figure 2**). Furthermore, combinatorial mutations of R369A, D506A, H570A, and K579A were carried out. Interestingly, the enzymatic activity was lost when Arg369 was combined with any of the other residues, while the mutual combination of the remaining three mutants resulted in better conversion rates than the corresponding single mutants. The conversion rates of the combinatorial mutants DH (D506A/H570A), DK (D506A/K579A), HK (H570A/K579A), and DHK (D506A/H570A/K579A) were 88.56% ± 0.06%, 70.38% ± 0.13%, 86.78% ± 0.90%, and 93.32% ± 0.09%, respectively (**Figure 2**).

Enzymatic Characterization of TpeRhas

The wild-type TpeRha and the beneficial mutants were purified by affinity chromatography with Ni-NTA Beads 6FF agarose, and the purified enzymes were assessed for their catalytic activities. The optimal temperature of the TpeRha was 80°C, and that of the mutants H570A, K579A, and HK were the same as the TpeRha, while the optimal temperature of D506A, DH, and DHK were 85°C (**Figure 3A**). However, the mutant DK was more suitable for catalysis at a relatively lower temperature of 70°C. Among them, the mutant DHK kept a high enzymatic activity (above 90%) in the range of 65°C to 85°C. The optimal pH of TpeRha was 5.0, and the mutants D506A and K579A had the same as TpeRha. The optimal pH of mutant H570A was 6.0, while that for DH, DK, HK, and DHK was 4.6 (**Figure 3B**). All enzymes here required an acidic condition for catalysis.

Fitting the kinetic data obtained for the wild-type TpeRha with the substrate icariin into non-linear regression yielded a V_{max} of 0.098 ± 0.054 μM/min and a K_M of 4.33 ± 3.47 μM for icariin. The detailed kinetic parameters of the TpeRha and mutants were determined using icariin as the substrate and are listed in **Table 2** (**Supplementary Figure S3**). As shown in **Table 2**, the catalytic efficiency (k_{cat}/K_M) of all mutants against icariin significantly surpassed that of the wild-type TpeRha. The k_{cat}/K_M values of single-point mutants D506A, H570A, and K579A were 16.12 times, 42.84 times, and 37.65 times higher than that of the wild-type TpeRha, respectively. Furthermore, double-point mutants exhibited more significant catalytic efficiency than that of single-point mutants. The k_{cat}/K_M values of double-point mutants DH, DK, and HK were 209.76 times, 44.30 times, and 137.69 times higher than that of the wild-type TpeRha. However, the triple-point mutant DHK did not show a superior effect to the double-point mutation but was slightly lower than that of the double-point mutant DH. The catalytic efficiency of DHK was 206.60 times higher compared with the wild-type TpeRha.

Docking Analysis of Mutants

All models of mutants were constructed *via* Swiss PDB Viewer (Guex and Peitsch, 1997). The results output by Autodock Vina included binding affinity and number of hydrogen bonds, which reflect the combinational effects of steric hindrance, flexibility, interaction force and other relevant factors. The binding affinity of the mutants and icariin complexes was lower than that of the wild-type TpeRha (**Table 3**). The docking results and schematic results of receptor-ligand interaction are shown in **Figure 4** and **Supplementary Figure S4**, respectively. As the binding affinity of these docked complexes and the hydrogen bonding force formed between the mutants and the icariin somehow reflected the difficulty of catalytic reaction, lower binding affinity indicated conformations of the mutant complexes were more stable. Therefore, the reaction was more efficient by using a mutant TpeRha. However, the interaction force between the wild-type TpeRha and icariin was the strongest, in which 10 hydrogen bonds were formed (**Figure 1B**). Decreased hydrogen bonds between the mutants and icariin might have resulted from the shortening of the side chain groups of the mutational amino acids. Although the

TABLE 2 | Kinetic parameters of the TpeRha mutants against icariin.

TpeRhas	*Vmax* (μM·min^{-1})	K_M (μM)	*kcat* (s^{-1}) (×10^{-4})	*kcat*/K_M (s^{-1}·M^{-1})
Wild-type	0.098 ± 0.054	4.33 ± 3.47	0.040	0.922569
D506A	1.906 ± 0.124	3.12 ± 0.26	0.464	14.86935
H570A	1.191 ± 0.044	0.92 ± 0.08	0.364	39.52007
K579A	1.968 ± 0.120	1.24 ± 0.09	0.431	34.73855
DH	2.505 ± 0.299	0.51 ± 0.13	0.987	193.5216
DK	1.369 ± 0.250	1.39 ± 0.45	0.568	40.86892
HK	5.564 ± 0.203	0.93 ± 0.08	1.181	127.0272
DHK	6.592 ± 0.856	1.11 ± 0.34	2.116	190.6003

TABLE 3 | Parameters affecting the docking of mutants and icariin complexes.

TpeRhas	Binding affinity (kcal/mol)	Numbers of hydrogen bonds
Wild-type	−5.7	10
D506A	−6.2	8
H570A	−7.7	5
K579A	−6.3	8
DH	−6.5	9
DK	−6.4	9
HK	−6.3	8
DHK	−7.6	5

docking complex H570A-icariin showed the lowest binding affinity (−7.7 kcal/mol) among all complexes, the interaction force between H570A and icariin was the weakest, with only five hydrogen bonds were formed (**Supplementary Figure S3C**). The complex with the least influence on hydrogen bonding force and the relatively most stable conformation was the DH-icariin complex (nine hydrogen bonds and −6.5 kcal/mol binding affinity) (**Supplementary Figure S3E**), which implied that DH was the receptor with the best binding mode for icariin in all mutants. Furthermore, this result of docking analysis was consistent with the result of the kinetic characterization that DH was the best mutant with the highest catalytic efficiency; 209.76 times higher compared with the wild-type TpeRha.

Substrate Specificity Analysis

Icariin, epimedin C, naringin, rutin, hesperidin, and NDHC were chosen for substrate specificity on the wild-type TpeRha and the single-point mutant H570A (**Supplementary Figure S5–S10**). When icariin was used as the substrate, the conversion rate of producing icariside I by the mutant H570A was higher than that of the wild-type TpeRha (**Figure 5**). Furthermore, compared with the wild-type TpeRha, the catalytic efficiencies of mutant H570A were lower when using epimedin C, naringin, hesperidin, and NDHC as substrates. The activity was basically unchanged when rutin was used as the substrate. These results indicated that the substrate specificity of mutant H570A for icariin was improved.

DISCUSSION

α-L-rhamnosidase is a specific enzyme for hydrolyzing natural products with the rhamnosyl group (Manzanares et al., 2007). This study aimed to develop an efficient α-L-rhamnosidase for hydrolyzing the rhamnosyl group of icariin to produce icariside I. TpeRha from *T. petrophila* DSM 13995 (Xie et al., 2020) is one of the enzymes that has the hydrolytic activity for icariin to icariside I. Both Rhase-I from *T. stollii* CLY-6 (Cheng et al., 2022) and DthRha from *D. thermophilum* DSM 3960 (Zhang et al., 2021) have also been reported for the hydrolysis of the rhamnosyl group. However, the 3D structure of Rhase-I is not currently available, and homology modeling cannot be performed since the enzyme with the highest protein sequence identity with Rhase-I is only at 25.20% (PDB ID: 6q2f) (Mensitieri et al., 2018). Cheng et al. (2022) used an improved deep learning-based modeling method, RoseTTAFold, to predict the Rhase-I 3D structure, and performed docking studies using the DOCK 6.9 program. According to the results of the study mentioned above, this enzyme was excluded in this study after careful evaluation, due to lack of a report on hydrolyzation of icariin to generate icariside I by its model template protein Rha-P (PDB ID: 6q2f). Rational design with undefined factors would be difficult. Fortunately, the 3D structure of DthRha can be availed from the PDB database. Interestingly, in a study of structure determination by X-ray diffraction (Guillotin et al., 2019), DthRha was not reported for its activity of hydrolyzing icariin to generate icariside I. This enzyme was later used in icaritin synthesis by Zhang et al. (2021). Therefore, TpeRha, which was first reported to have the activity of hydrolyzing icariin to generate icariside I, was selected as the target protein in this study.

During homology modeling of TpeRha, the template with the highest sequence identity (48.28%) was DthRha (PDB ID: 6i60) (Guillotin et al., 2019). By aligning the 3D structure of TpeRha obtained by homology modeling with the 3D structure of template DthRha, we figure out the active pocket of TpeRha. According previous study on DthRha, there are 11 amino acids encapsulated in rhamnose; D496, R500, E502, W506, W561, Y610, W613, E805, R806, M815, and H820. Interestingly, these corresponding amino acids were basically found in the active pocket of TpeRha, and the matching degree was as high as 90.9%. Only the amino acid H570 was different, and was considered as a key design target in this study (**Figure 6A**).

In addition to improvement of catalytic efficiency, this study also designed a mutant, H570Y, to explore whether it could maintain or change the catalytic activity of icariin after mimicking the DthRha active pocket in TpeRha. The conversion rate of icariin by mutant H570Y was 4.25 times higher than that of the wild-type, reaching 18.41% ± 2.05%, but it was still lower than that of the mutant H570A (63.65% ±

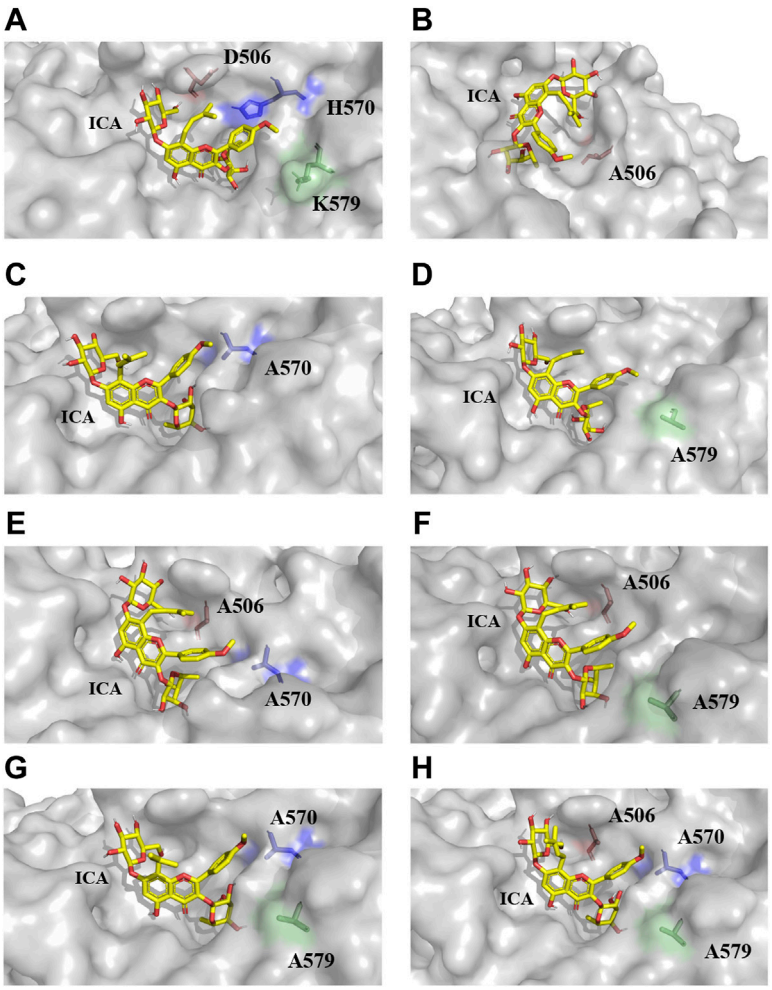

FIGURE 4 | The docking results of TpeRhas and icariin. The TpeRhas models are displayed as the surface type shown in gray, the icariin is displayed as stick type shown in yellow, the residue at position 506 is displayed as sticks type shown in salmon, the residue at position 570 is displayed as stick type shown in blue, and the residue at position 579 is displayed as stick type shown in green. **(A)** The conformation of docking complex TpeRha-icariin. **(B)** The conformation of docking complex D506A-icariin. **(C)** The conformation of docking complex H570A-icariin. **(D)** The conformation of docking complex K579A-icariin. **(E)** The conformation of docking complex DH-icariin. **(F)** The conformation of docking complex DK-icariin. **(G)** The conformation of docking complex HK-icariin. **(H)** The conformation of docking complex DHK-icariin.

3.96%). Based on these results, we proposed the hypothesis that DthRha also has the activity of hydrolyzing icariin, which was in agreement with results reported by Zhang et al. (2021).

Nine amino acids of the 10 identified key amino acids were confirmed for their importance to the function of TpeRha. No icariside I was produced in whole-cell catalysis with 9 TpeRha mutants (D456A, R460A, E462A, W466A, W521A, W573A, E746A, M756A, and H761A). The conversion rate of the mutant R747A was increased by 3.07 times (13.31% ± 0.21%). Based on the molecular docking result, R747 located at the border of the active pocket, and the distance between icariin and R747 was 6.8 Å, which was beyond generating an interaction force. Thus, R747 might not be involved in the function of locking the rhamnosyl group. After mutating arginine to alanine at the 747-site, the side chain group became shorter, and a depression was formed on the surface of the protein (**Figures 6B,C**). It was speculated that this change increased the probability of icariin binding to the active pocket, and resulted in the conversion rate improvement.

Based on the conformation structure of the docking complex TpeRha-icariin, the poor conformational stability of this complex may be due to the p-methoxybenzene ring on the core structure of icariin (**Figure 4A**). The non-rotatability of the p-methoxybenzene ring might result in a rigid steric hindrance, which hindered the rhamnose group entering the active pocket. In order to offer the rhamnosyl group of icariin easy access to the active pocket of the enzyme, potential steric hindrance was reduced on purpose. Three non-critical amino acids were rationally designed, which were located inside the enzyme (the bottom of the active pocket), at the active pocket border, and the active pocket surface,

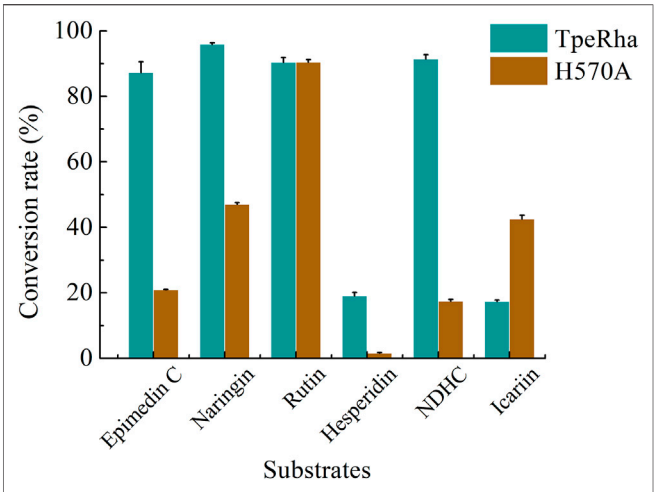

FIGURE 5 | The conversion rates of TpeRha and H570A reacted with different substrates. The conversion rates of epimedin C, naringin, hesperidin, and NDHC for TpeRha were higher than that for H570A. The conversion rates of the substrate rutin for both were comparable. The conversion rate of icariin for H570A was 2.45 times higher than that for TpeRha.

between the substrate and the enzyme. This may explain why the catalytic efficiency of the triple-point mutant DHK was less efficient than that of the double-point mutant DH (**Table 2**).

Furthermore, to the best of our knowledge, most α-L-rhamnosidases are sensitive to α-1, 2, and α-1, 6 glycosidic bonds (Manzanares et al., 2007). Only a small part of α-L-rhamnosidase has the function of cleaving the glycosidic bond α-1, while the enzymes hydrolyzing the glycosidic bond α-1 of icariin are only the three we mentioned above in this study. The reason may be that the small volume of the active cavity in the core structure hinders the rhamnosyl group connected by the glycosidic bond α-1 to the active pocket. Intentionally, in this study, the mutant H570A that only expanded the caliber of the active pocket was used to hydrolyze the rhamnosyl group of a variety of substrates, whose rhamnosyl linkages covered α-1, α-1, 2, and α-1, 6, to investigate whether changes in the size of the active pocket could affect substrate specificity. Except for icariin with glycosidic bond α-1, the conversion rates of all other substrates with glycosidic bond α-1, 2, and α-1, 6 were reduced. This implied that the enlarged caliber of the active pocket partly loosened the 'lock' of the rhamnosyl group. In

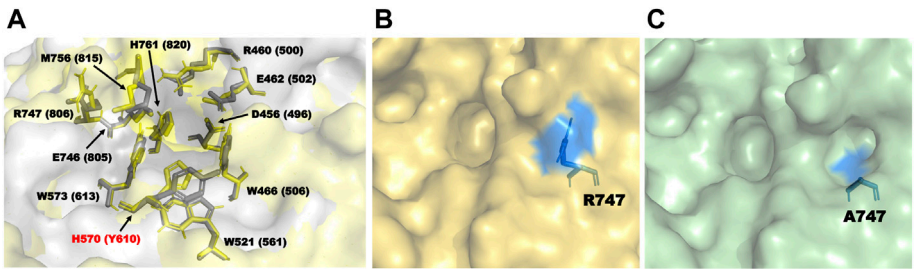

FIGURE 6 | The key residues in the TpeRha model and DtRha model. **(A)** Superimposition of active sites of TpeRha built in this study and DtRha from *D. thermophilum*. Residues are respectively colored in yellow and gray. Numbers indicate the residue from TpeRha and the corresponding residues from DtRha. The conflict residue is H570 of TpeRha and Y610 of DtRha. **(B)** The location and status of residue R747 in TpeRha. **(C)** The location and status of residue A747 in TpeRha.

respectively. D506, located inside the active pocket, was mutated to alanine to increase the depth of the active pocket. H570, located at the active pocket border, was mutated to alanine to increase the caliber of the active pocket. K579, located at the surface of the active pocket, was mutated to alanine to flatten the active pocket surface (**Figure 1C**). As expected, the catalytic efficiencies of these three mutants were improved, showing a useful strategy for improvement by increasing the caliber of the active pocket. The catalytic efficiency of H570A was 42.84 times higher than that of the wild type. This suggested that reducing the steric hindrance between the active pocket and icariin was an effective strategy to improve the catalytic efficiency of this enzyme towards icariin. The results of the protein-ligand interaction showed that the number of hydrogen bonds between the mutants and icariin was less than that between the wild-type and icariin, which suggested that the larger the active pocket of the cavity, the weaker the interaction force turn, this designed mutation improved the substrate specificity for icariin.

CONCLUSION

In conclusion, the active pocket and key residues of the TpeRha from *T. petrophila* DSM 13995 were revealed *via* computer-aided technologies, like homology modeling and molecular docking, in this study. Several efficient mutants of α-L-rhamnosidases were rationally designed for hydrolyzing the icariin to produce icariside I The double-point mutant DH was the most beneficial mutant and showed the highest catalytic efficiency (k_{cat}/K_M: 193.52 s^{-1} M^{-1}) against icariin, which was a 209.76-fold increase compared with the wild-type TpeRha. Meanwhile, a single-point mutant H570A with high substrate specificity was also obtained in this study. In addition, the strategy of adjusting the size of the active cavity led to many interesting discoveries

which explain why there are currently only three wild-type α-L-rhamnosidases that can hydrolyze icariin. This study also provides strategies and principles for designing enzymes for hydrolyzing compounds with special core structures.

DATA AVAILABILITY STATEMENT

The original contributions presented in the study are included in the article/**Supplementary Material**, further inquiries can be directed to the corresponding authors.

AUTHOR CONTRIBUTIONS

J-JH carried out the main work, collected and analyzed the data, and drafted the manuscript. H-XH participated in the research. Y-JL and Y-DB supervised the work and participated in data analysis, and revised the manuscript. J-LZ and MH participated in the conception and design of the study and finalized the manuscript. All authors read and approved the final manuscript.

FUNDING

This study was supported by the National key research and development program of China (2021YFC2100500) and Foshan Core Technology Tackling Key Project (1920001000262).

ACKNOWLEDGMENTS

We thank the support from the National key research and development program of China (2021YFC2100500) and Foshan Core Technology Tackling Key Project (1920001000262).

SUPPLEMENTARY MATERIAL

The Supplementary Material for this article can be found online at: https://www.frontiersin.org/articles/10.3389/fbioe.2022.926829/full#supplementary-material

REFERENCES

Chen, G., Cao, Z., Shi, Z., Lei, H., Chen, C., Yuan, P., et al. (2021). Microbiome Analysis Combined with Targeted Metabolomics Reveal Immunological Anti-tumor Activity of Icariside I in a Melanoma Mouse Model. *Biomed. Pharmacother.* 140, 111542. doi:10.1016/j.biopha.2021.111542

Cheng, L., Zhang, H., Cui, H., Cheng, J., Wang, W., Wei, B., et al. (2022). A Novel α-L-Rhamnosidase Renders Efficient and Clean Production of Icaritin. *J. Clean. Prod.* 341, 130903. doi:10.1016/j.jclepro.2022.130903

Eberhardt, J., Santos-Martins, D., Tillack, A. F., and Forli, S. (2021). AutoDock Vina 1.2.0: New Docking Methods, Expanded Force Field, and python Bindings. *J. Chem. Inf. Model.* 61 (8), 3891–3898. doi:10.1021/acs.jcim.1c00203

Guex, N., and Peitsch, M. C. (1997). SWISS-MODEL and the Swiss-Pdb Viewer: An Environment for Comparative Protein Modeling. *Electrophoresis* 18 (15), 2714–2723. doi:10.1002/elps.1150181505

Guillotin, L., Kim, H., Traore, Y., Moreau, P., Lafite, P., Coquoin, V., et al. (2019). Biochemical Characterization of the α-l-Rhamnosidase DtRha from Dictyoglomus Thermophilum: Application to the Selective Derhamnosylation of Natural Flavonoids. *ACS Omega* 4 (1), 1916–1922. doi:10.1021/acsomega.8b03186

Huang, X., Zhu, D., and Lou, Y. (2007). A Novel Anticancer Agent, Icaritin, Induced Cell Growth Inhibition, G1 Arrest and Mitochondrial Transmembrane Potential Drop in Human Prostate Carcinoma PC-3 Cells. *Eur. J. Pharmacol.* 564 (1-3), 26–36. doi:10.1016/j.ejphar.2007.02.039

Huang, J. J., Wei, T., Ye, Z. W., Zheng, Q. W., Jiang, B. H., Han, W. F., et al. (2021). Microbial Cell Factory of Baccatin III Preparation in *Escherichia coli* by Increasing DBAT Thermostability and *In Vivo* Acetyl-CoA Supply. *Front. Microbiol.* 12, 803490. doi:10.3389/fmicb.2021.803490

Khan, F. I., Wei, D.-Q., Gu, K.-R., Hassan, M. I., and Tabrez, S. (2016). Current Updates on Computer Aided Protein Modeling and Designing. *Int. J. Biol. Macromol.* 85, 48–62. doi:10.1016/j.ijbiomac.2015.12.072

Laskowski, R. A., MacArthur, M. W., Moss, D. S., and Thornton, J. M. (1993). PROCHECK: A Program to Check the Stereochemical Quality of Protein Structures. *J. Appl. Cryst.* 26, 283–291. doi:10.1107/s0021889892009944

Li, W.-K., Zhang, R.-Y., and Pei-Gen, X. (1996). Flavonoids from Epimedium Wanshanense. *Phytochemistry* 43 (2), 527–530. doi:10.1016/0031-9422(96)00187-2

Li, J., Liu, P., Zhang, R., Cao, L., Qian, H., Liao, J., et al. (2011). Icaritin Induces Cell Death in Activated Hepatic Stellate Cells through Mitochondrial Activated Apoptosis and Ameliorates the Development of Liver Fibrosis in Rats. *J. Ethnopharmacol.* 137 (1), 714–723. doi:10.1016/j.jep.2011.06.030

Li, L. J., Wu, Z. Y., Yu, Y., Zhang, L. J., Zhu, Y. B., Ni, H., et al. (2018). Development and Characterization of an α-l-rhamnosidase Mutant with Improved Thermostability and a Higher Efficiency for Debittering Orange Juice. *Food Chem.* 245, 1070–1078. doi:10.1016/j.foodchem.2017.11.064

Li, B.-C., Peng, B., Zhang, T., Li, Y.-Q., and Ding, G.-B. (2019). A Spectrophotometric Method for High-Throughput Screening of α-l-rhamnosidase Activity on Rutin Coupled with a β-d-glucosidase Assay. *3 Biotech.* 9 (6), 227. doi:10.1007/s13205-019-1753-1

Li, D.-D., Jiang, Y.-P., Wang, Z.-Z., Xiao, W., and Zhao, L.-G. (2020). Molecular Insights into Catalytic Specificity of α-L-rhamnosidase from Bacteroides Thetaiotaomicron by Molecular Docking and Dynamics. *Chem. Phys. Lett.* 754, 137695. doi:10.1016/j.cplett.2020.137695

Liao, H., Gong, J. Y., Yang, Y., Jiang, Z. D., Zhu, Y. B., Li, L. J., et al. (2019). Enhancement of the Thermostability of Aspergillus niger α- L -rhamnosidase Based on PoPMuSiC Algorithm. *J. Food. Biochem.* 43 (8), e12945. doi:10.1111/jfbc.12945

Lyu, Y., Zeng, W., Du, G., Chen, J., and Zhou, J. (2019). Efficient Bioconversion of Epimedin C to Icariin by a Glycosidase from *Aspergillus nidulans*. *Bioresour. Technol.* 289, 121612. doi:10.1016/j.biortech.2019.121612

Ma, H., He, X., Yang, Y., Li, M., Hao, D., and Jia, Z. (2011). The Genus *Epimedium*: An Ethnopharmacological and Phytochemical Review. *J. Ethnopharmacol.* 134 (3), 519–541. doi:10.1016/j.jep.2011.01.001

Manzanares, P., Vallés, S., Ramòn, D., and Orejas, M. (2007). "α-L-rhamnosidases: Old and New Insights," in *Industrial Emzymes*. Valencia, Spain: Springer, 117–140.

Mensitieri, F., De Lise, F., Strazzulli, A., Moracci, M., Notomista, E., Cafaro, V., et al. (2018). Structural and Functional Insights into RHA-P, a Bacterial GH106 α-L-rhamnosidase from Novosphingobium Sp. PP1Y. *Archives Biochem. Biophys.* 648, 1–11. doi:10.1016/j.abb.2018.04.013

Mu, G., Pu, W., Zhou, M., Liu, Y., Yang, H., and Wang, C. (2013). Synthesis of Icaritin. *Chin. J. Org. Chem.* 33 (6), 1298. doi:10.6023/cjoc201303016

Saito, Y., Oikawa, M., Nakazawa, H., Niide, T., Kameda, T., Tsuda, K., et al. (2018). Machine-learning-guided Mutagenesis for Directed Evolution of Fluorescent Proteins. *ACS Synth. Biol.* 7 (9), 2014–2022. doi:10.1021/acssynbio.8b00155

Sterling, T., and Irwin, J. J. (2015). ZINC 15 - Ligand Discovery for Everyone. *J. Chem. Inf. Model.* 55 (11), 2324–2337. doi:10.1021/acs.jcim.5b00559

Trott, O., and Olson, A. J. (2010). AutoDock Vina: Improving the Speed and Accuracy of Docking with a New Scoring Function, Efficient Optimization, and Multithreading. *J. Comput. Chem.* 31 (2), NA. doi:10.1002/jcc.21334

Wang, P., Li, C., Li, X., Huang, W., Wang, Y., Wang, J., et al. (2021). Complete Biosynthesis of the Potential Medicine Icaritin by Engineered *Saccharomyces cerevisiae* and *Escherichia coli*. *Sci. Bull.* 66 (18), 1906–1916. doi:10.1016/j.scib.2021.03.002

Webb, B., and Sali, A. (2016). Comparative Protein Structure Modeling Using MODELLER. *Curr. Protoc. Protein Sci.* 86, 2 9 1–2 9 37. doi:10.1002/cpps.20

Wu, T., Pei, J., Ge, L., Wang, Z., Ding, G., Xiao, W., et al. (2018). Characterization of a α-l-rhamnosidase from Bacteroides Thetaiotaomicron with High Catalytic Efficiency of Epimedin C. *Bioorg. Chem.* 81, 461–467. doi:10.1016/j.bioorg.2018.08.004

Xie, J., Zhang, S., Tong, X., Wu, T., Pei, J., and Zhao, L. (2020). Biochemical Characterization of a Novel Hyperthermophilic α-l-rhamnosidase from Thermotoga Petrophila and its Application in Production of Icaritin from Epimedin C with a Thermostable β-glucosidase. *Process Biochem.* 93, 115–124. doi:10.1016/j.procbio.2020.03.019

Xu, Y., Li, Z., Yuan, L., Zhang, X., Lu, D., Huang, H., et al. (2013). Variation of Epimedins A - C and Icariin in Ten Representative Populations of Epimedium brevicornu Maxim., and Implications for Utilization. *Chem. Biodivers.* 10, 711–721. doi:10.1002/cbdv.201100424

Xu, L., Liu, X., Yin, Z., Liu, Q., Lu, L., and Xiao, M. (2016). Site-directed Mutagenesis of α-l-rhamnosidase from Alternaria Sp. L1 to Enhance Synthesis Yield of Reverse Hydrolysis Based on Rational Design. *Appl. Microbiol. Biotechnol.* 100 (24), 10385–10394. doi:10.1007/s00253-016-7676-4

Yang, K. K., Wu, Z., and Arnold, F. H. (2019). Machine-learning-guided Directed Evolution for Protein Engineering. *Nat. Methods.* 16 (8), 687–694. doi:10.1038/s41592-019-0496-6

Ye, M., Han, J., Chen, H., Zheng, J., and Guo, D. (2007). Analysis of Phenolic Compounds in Rhubarbs Using Liquid Chromatography Coupled with Electrospray Ionization Mass Spectrometry. *J. Am. Soc. Mass Spectrom.* 18 (1), 82–91. doi:10.1016/j.jasms.2006.08.009

Zhang, S., Luo, J., Dong, Y., Wang, Z., Xiao, W., and Zhao, L. (2021). Biotransformation of the Total Flavonoid Extract of Epimedium into Icaritin by Two Thermostable Glycosidases from *Dictyoglomus Thermophilum* DSM3960. *Process Biochem.* 105, 8–18. doi:10.1016/j.procbio.2021.03.002

Zhu, D.-y., and Lou, Y.-j. (2005). Inducible Effects of Icariin, Icaritin, and Desmethylicaritin on Directional Differentiation of Embryonic Stem Cells into Cardiomyocytes *In Vitro*. *Acta Pharmacol. Sin.* 26 (4), 477–485. doi:10.1111/j.1745-7254.2005.00076.x

Conflict of Interest: J-JH, H-XH, Y-JL, Y-DB, and J-LZ were employed by Golden Health Biotechnology Co., Ltd.

The remaining author declares that the research was conducted in the absence of any commercial or financial relationships that could be construed as a potential conflict of interest.

Publisher's Note: All claims expressed in this article are solely those of the authors and do not necessarily represent those of their affiliated organizations, or those of the publisher, the editors and the reviewers. Any product that may be evaluated in this article, or claim that may be made by its manufacturer, is not guaranteed or endorsed by the publisher.

frontiers | Frontiers in Bioengineering and Biotechnology

ORIGINAL RESEARCH
published: 22 June 2022
doi: 10.3389/fbioe.2022.947469

Metabolically Engineered *Escherichia coli* for Conversion of D-Fructose to D-Allulose *via* Phosphorylation-Dephosphorylation

Qiang Guo[1†], *Chen-Yang Liu*[1†], *Ling-Jie Zheng*[1], *Shang-He Zheng*[1], *Ya-Xing Zhang*[1], *Su-Ying Zhao*[1,2], *Hui-Dong Zheng*[1,2], *Li-Hai Fan*[1,2*] *and Xiao-Cheng Lin*[1*]

[1]*Fujian Engineering Research Center of Advanced Manufacturing Technology for Fine Chemicals, College of Chemical Engineering, Fuzhou University, Fuzhou, China,* [2]*Qingyuan Innovation Laboratory, Quanzhou, China*

OPEN ACCESS

Edited by:
Xiao-Jun Ji,
Nanjing Tech University, China

Reviewed by:
Xiang Zou,
Southwest University, China
Chuang Xue,
Dalian University of Technology, China

****Correspondence:***
Li-Hai Fan
fanlh@fzu.edu.cn
Xiao-Cheng Lin
xclin@fzu.edu.cn

[†]These authors have contributed equally to this work and share first authorship

Specialty section:
This article was submitted to Synthetic Biology, a section of the journal Frontiers in Bioengineering and Biotechnology

Received: *18 May 2022*
Accepted: *07 June 2022*
Published: *22 June 2022*

Citation:
Guo Q, Liu C-Y, Zheng L-J, Zheng S-H, Zhang Y-X, Zhao S-Y, Zheng H-D, Fan L-H and Lin X-C (2022) Metabolically Engineered Escherichia coli for Conversion of D-Fructose to D-Allulose via Phosphorylation-Dephosphorylation. Front. Bioeng. Biotechnol. 10:947469. doi: 10.3389/fbioe.2022.947469

D-Allulose is an ultra-low calorie sweetener with broad market prospects. As an alternative to Izumoring, phosphorylation-dephosphorylation is a promising method for D-allulose synthesis due to its high conversion of substrate, which has been preliminarily attempted in enzymatic systems. However, *in vitro* phosphorylation-dephosphorylation requires polyphosphate as a phosphate donor and cannot completely deplete the substrate, which may limit its application in industry. Here, we designed and constructed a metabolic pathway in *Escherichia coli* for producing D-allulose from D-fructose via *in vivo* phosphorylation-dephosphorylation. PtsG-F and Mak were used to replace the fructose phosphotransferase systems (PTS) for uptake and phosphorylation of D-fructose to fructose-6-phosphate, which was then converted to D-allulose by AlsE and A6PP. The D-allulose titer reached 0.35 g/L and the yield was 0.16 g/g. Further block of the carbon flux into the Embden-Meyerhof-Parnas (EMP) pathway and introduction of an ATP regeneration system obviously improved fermentation performance, increasing the titer and yield of D-allulose to 1.23 g/L and 0.68 g/g, respectively. The *E. coli* cell factory cultured in M9 medium with glycerol as a carbon source achieved a D-allulose titer of ≈1.59 g/L and a yield of ≈0.72 g/g on D-fructose.

Keywords: D-allulose, *Escherichia coli*, fermentation, metabolic engineering, cell factory

INTRODUCTION

D-Allulose is a United States Food and Drug Administration (FDA)-approved sweetener with ultra-low calorie content and unique physiological functions (Sun et al., 2005; Mu et al., 2012; Nagata et al., 2015), thus considered as a potential alternative to sucrose and owning broad market prospects (Su et al., 2018). Currently, D-allulose is industrially produced from D-fructose through enzymatic Izumoring (Wang et al., 2020), which reversibly epimerizes D-fructose at its C-3 position using D-allulose 3-epimerase (DAE) or D-tagatose 3-epimerase (DTE) as a biocatalyst (Mu et al., 2011). The major drawback of Izumoring is the low conversion of D-fructose, only reaching around 30% at equilibrium (Kim et al., 2006; Bosshart et al., 2012; Zhang et al., 2013). Continuous removal of D-allulose from the reaction system may improve conversion efficiency, but the coupling of isomer separation

with Izumoring epimerization will definitely increase product cost (Nguyen et al., 2009; Li et al., 2018).

Recently, an *in vitro* enzymatic biosystem based on phosphorylation-dephosphorylation has been proposed for producing D-allulose from starch (Li et al., 2021). This strategy differed from Izumoring in its innovative use of epimerization between hexose monophosphates. After obtaining fructose-6-phosphate through phosphorylation and other reactions, allulose-6-phosphate epimerase (A6PE) catalyzed the reversible conversion of fructose-6-phosphate to allulose-6-phosphate, which was then dephosphorylated by allulose-6-phosphate phosphatase (A6PP) to generate D-allulose (Li et al., 2021). It is quite important that dephosphorylation was irreversible (You et al., 2017), which broke the epimerization equilibrium and drove the reactions towards target product. Although the resulting conversion ratio of D-fructose was much higher than with Izumoring, a certain amount of D-fructose would remain in products (<18%) since A6PP also exhibited a side activity on dephosphorylating fructose-6-phosphate (Li et al., 2021). Moreover, the enzymatic phosphorylation reaction in this system required expensive polyphosphate (polyP) as a phosphate donor (Shiba et al., 2000; Xiao et al., 2019), which might limit its large-scale application.

In contrast to enzymatic approach, fermentation may be a way that can fully release the application potential of phosphorylation-dephosphorylation strategy in the production of D-allulose from D-fructose, in which rational design of a microbial cell factory is the key to ensuring high fermentation performance (Lee et al., 2019; Xu et al., 2020). *Escherichia coli* is one of the most widely used bacterial hosts for cell factory development due to its clear genetic background, easy manipulation, and rapid growth (Pontrelli et al., 2018). *E. coli* can utilize D-fructose as a sole carbon source and has three routes for D-fructose uptake and phosphorylation (Aristidou et al., 1999; Kornberg, 2001), two of which are phosphoenolpyruvate (PEP): carbohydrate phosphotransferase systems (PTS). The fructose PTS (*fruA*, *fruB*) transports and concomitantly phosphorylates D-fructose to fructose-1-phosphate (Luo et al., 2014). The mannose PTS (*manXYZ*) can recognize sugars with the 3, 4, 5-D-arabino-hexose configuration (Kornberg, 2001), and the D-fructose taken up by this system appears in cells as fructose 6-phosphate (Kornberg, 1990). The fructose PTS and mannose PTS use PEP as a phosphate donor, and the resulting fructose monophosphates will be further phosphorylated to fructose-1, 6-bisphosphate before entering the central metabolic pathway (Luo et al., 2014). In addition to PTS, a mutant of glucose permease involved in the glucose PTS, which is specified by *ptsG-F*, has been found to possess the ability to transport D-fructose via facilitated diffusion (Kornberg et al., 2000). Once D-fructose is passaged, it can be phosphorylated to fructose 6-phosphate by an intracellular fructo/manno kinase (*mak*) with ATP as a phosphate donor (Miller and Raines, 2004). Therefore, the well-defined mechanisms for D-fructose transport and phosphorylation provide a prerequisite for application of phosphorylation-dephosphorylation in *E. coli*. Also, this bacterium is reported to own an endogenous allulose-6-phosphate epimerase encoded by *alsE*, whose kinetic parameters, substrate specificity and metal ion preference have been comprehensively investigated (Chan et al., 2008), suggesting that it is possible for wild-type *E. coli* to efficiently convert fructose-6-phosphate to allulose-6-phosphate.

In this work, we designed a metabolic pathway for D-allulose production from D-fructose via phosphorylation-dephosphorylation in *E. coli* JM109 (DE3) (**Figure 1**). The fructose PTS was substituted by use of *ptsG-F* and *mak*, ensuring that D-fructose could be taken up and phosphorylated to fructose-6-phosphate by cells. The *E. coli alsE* was employed to catalyze the reversible reaction from fructose-6-phosphate to allulose-6-phosphate, followed by dephosphorylation by an allulose-6-phosphate phosphatase from *Bacteroides fragilis* (Li et al., 2021). The by-product synthesis pathways and the Embden-Meyerhof-Parnas (EMP) pathway were blocked to increase the yield of product. A PEP carboxykinase (*pckA*) from *Actinobacillus succinogenes* (Singh et al., 2011), which catalyzed the formation of oxaloacetate (OAA) and ATP from PEP, CO_2, and ADP, was introduced in *E. coli* cell factory to build an ATP regeneration system, with the purpose to enhance the supply of ATP as a phosphate donor for D-fructose phosphorylation. This work is expected to provide a strategy for efficient fermentative production of D-allulose, and the research achievements will promote the application of metabolic engineering in green biomanufacturing.

MATERIALS AND METHODS

Strains and Media

The strains used in this study were listed in **Table 1**. *E. coli* Trans 10 was used for plasmid construction. *E. coli* JM109 (DE3) was employed as a host for protein expression and D-allulose production. Luria-Bertani (LB) medium was composed of 10.00 g/L NaCl, 10.00 g/L tryptone, and 5.00 g/L yeast extract. M9 minimal medium contained 0.50 g/L NaCl, 0.50 g/L NH_4Cl, 0.84 mg/L $ZnCl_2$, 44.10 mg/L $CaCl_2$ $2H_2O$, 8.30 mg/L $FeCl_3{\cdot}6H_2O$, 0.13 mg/L $CuCl_2{\cdot}2H_2O$, 0.10 mg/L $CoCl_2{\cdot}2H_2O$, 0.02 mg/L $MnCl_2{\cdot}4H_2O$, 0.25 g/L $MgSO_4{\cdot}7H_2O$, 0.10 mg/L H_3BO_3, 7.52 g/L $Na_2HPO_4{\cdot}2H_2O$, 3.00 g/L KH_2PO_4, 50.00 mg/L EDTA, 1.00 mg/L thiamin, and 1.00 mg/L biotin.

Plasmid Construction

The plasmids of pETDuet-1 (ampicillin-resistant) and pRSFDuet-1 (kanamycin-resistant) were purchased from Novagen and used to express proteins with T7 promoter. The genes of *ptsG-F* (Kornberg et al., 2000), *mak* (Gene ID 949086), *alsE* (Gene ID 948595), *a6PP* (Gene ID 66330010), and *pckA* (Singh et al., 2011) were synthesized with codon optimization by Sangon Biotech (Shanghai). Cloning of *ptsG-F* and *mak* into pETDuet-1 was carried out by use of primers *ptsG-F*-F and *ptsG-F*-R, *mak*-F and *mak*-R, respectively. The primers for cloning *alsE, a6PP,* and *pckA* into pRSFDuet-1 were *alsE*-F and *alsE*-R, *a6PP*-F and *a6PP*-R, *pckA*-F and *pckA*-R. The primers used in this study were summarized in **Table 2**. The PCR products were digested with restriction endonucleases (New England Biolabs) and then ligated into

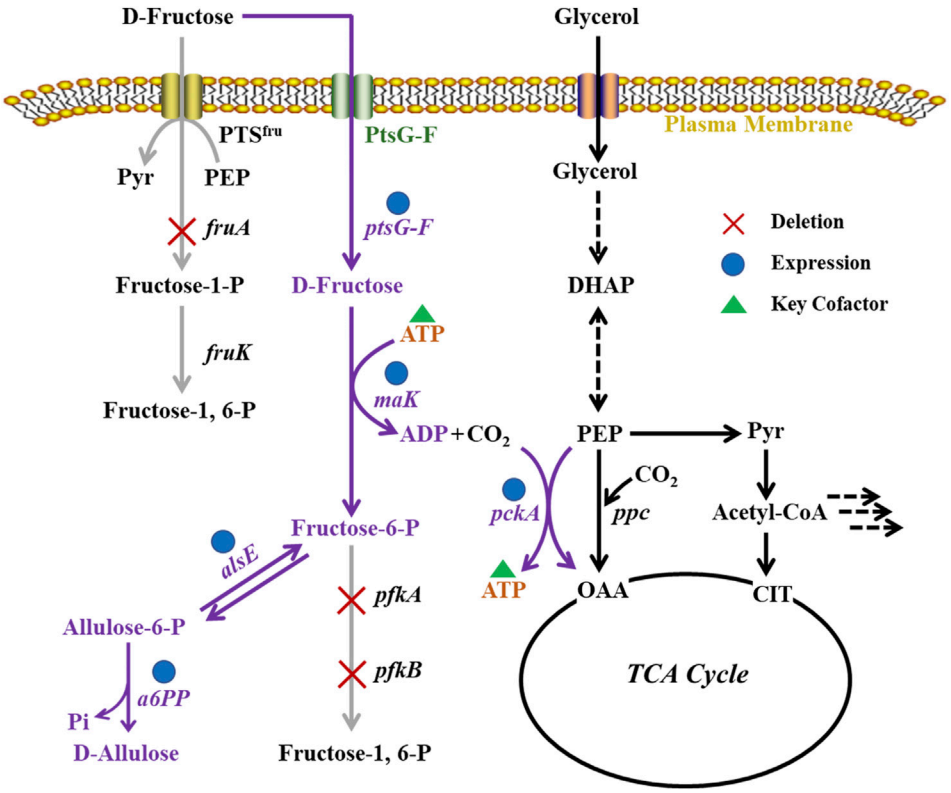

FIGURE 1 | Metabolic pathways in *E. coli* cell factory for production of D-allulose from D-fructose *via* phosphorylation-dephosphorylation.

plasmids by T4 DNA ligase (New England Biolabs). The recombinant plasmids constructed in this study were shown in **Table 1**.

Protein Expression and Enzymatic Analysis

E. coli cells were grown in 200 ml LB medium with kanamycin (50 μg/ml) at 37°C and 220 rpm. After 3 h of cultivation, we added 0.4 mM isopropyl-β-D-thiogalactoside (IPTG) to the medium to induce the expression of A6PP or AlsE for 12 h. Cells were harvested by centrifugation at 4°C and 6,000 *g* for 10 min and re-suspended in Tris-HCl buffer (pH 7.5, 50 mM), which were then broken by use of an ultrasonic cell crusher JY92-IIN (Jingxin, Shanghai). The sonication was performed on ice for 5 min (2 s pulse on and 2 s pulse off) at 50% amplitude. Cell debris was removed by centrifugation at 4°C and 6,000 *g* for 5 min. Sodium dodecyl sulfate–polyacrylamide gel electrophoresis (SDS–PAGE) was carried out using 8% polyacrylamide gels (Jinruisi Biotech, Nanjing) for analyzing the supernatant. We added the crude enzyme (20 μl, 10 mg/ml) to 1 ml Tris-HCl buffer (pH 7.5, 50 mM) containing 2.60 g/L fructose-6-phosphate, and the reaction was conducted at 37°C for 30 min for enzyme assay.

Gene Knockout

Deletion of *fruA* (Gene ID 946672), *pfkA* (Gene ID 948412), and *pfkB* (Gene ID 946230) was achieved by a λ red homologous recombination system (Datsenko and Wanner, 2000). The DNA fragments were amplified with pKD13 (kanamycin-resistant) as a template (Baba et al., 2006), and the primers were listed in **Table 2**. *E. coli* JM109 (DE3) harboring pKD46 (ampicillin-resistant) were grown in LB medium with ampicillin (100 μg/ml) at 30°C and 220 rpm, until the cell density (OD_{600}) reached ≈0.3. Then L-arabinose (4 g/L) was added to induce the expression of homologous recombinase at 37°C and 220 rpm for 1 h (Yang et al., 2018). The DNA fragments were electroporated into the L-arabinose-induced cells for gene knockout. The plasmid of pCP20 (ampicillin and chloramphenicol-resistant) was used to remove the kanamycin resistance gene in recombinant cells (Dugar et al., 2016).

Fermentation

E. coli cells were inoculated in 4 ml LB medium containing appropriate antibiotics and grown overnight at 37°C and 220 rpm. Cells were transferred to the flask with 50 ml LB medium containing appropriate antibiotics and 4.00 g/L D-fructose. Potassium phosphate (100 mM) was used to maintain the pH of the fermentation broth, and IPTG (0.4 mM) was added to induce protein expression. Air-limited fermentation was carried out in the airtight bottle with either buffered-LB medium or M9 minimal medium containing appropriate antibiotics, 2.20 g/L D-fructose, 8.00 g/L glycerol, and 0.4 mM IPTG.

TABLE 1 | The strains and plasmids used in this study.

Name	Relevant characteristics	References
Strains		
E. coli Trans 10	F$^-$ *mcr*A Δ(*mrr-hsd*RMS-*mcr*BC) φ80 *lac*ZΔM15 Δ*lac*X74 *rec*A1 *ara*Δ139 Δ(*ara-leu*)7697 *gal*U *gal*K *rps*L (Str^R) *end*A1 *nup*G	Trans gen biotech
E. coli JM109 (DE3)	*EndA1 recA1 gyr*A96 *thi hsdR17* (r_k^-, m_k^+) *relA1 sup*E44 λ$^-$ Δ(*lac-pro*AB) [F′ *tra*D36 *proAB lac*I^q Δ(*lacZ*)M15] λ(DE3)	BeNa culture collection
E. coli (*control*)	*E. coli* JM109 (DE3) harboring pRSFDuet-1	This study
E. coli (*a6PP*)	*E. coli* JM109 (DE3) harboring pRSFDuet-*a6PP*	This study
E. coli (*alsE*)	*E. coli* JM109 (DE3) harboring pRSFDuet-*alsE*	This study
E. coli (*alsE*, *a6PP*)	*E. coli* JM109 (DE3) harboring pRSFDuet-*alsE-a6PP*	This study
E. coli (*alsE*, *a6PP*, Δ*fruA*)	*E. coli* JM109 (DE3) harboring pETDuet-1 and pRSFDuet-*alsE-a6PP* with deletion of *fruA*	This study
E. coli (*alsE*, *a6PP*, *ptsG-F*, *mak*, Δ*fruA*)	*E. coli* JM109 (DE3) harboring pETDuet-*ptsG-F-mak* and pRSFDuet-*alsE-a6PP* with deletion of *fruA*	This study
E. coli (*alsE*, *a6PP*, *ptsG-F*, *mak*, Δ*fruA*, Δ*pfkA*)	*E. coli* JM109 (DE3) harboring pETDuet-*ptsG-F-mak* and pRSFDuet-*alsE-a6PP* with deletion of *fruA* and *pfkA*	This study
E. coli (*alsE*, *a6PP*, *ptsG-F*, *mak*, Δ*fruA*, Δ*pfkA*, Δ*pfkB*)	*E. coli* JM109 (DE3) harboring pETDuet-*ptsG-F-mak* and pRSFDuet-*alsE-a6PP* with deletion of *fruA*, *pfkA*, and *pfkB*	This study
E. coli (Δ*fruA*, Δ*pfkA*, Δ*pfkB*)	*E. coli* JM109 (DE3) harboring pRSFDuet-1 with deletion of *fruA*, *pfkA*, and *pfkB*	This study
E. coli (*pckA*, Δ*fruA*, Δ*pfkA*, Δ*pfkB*)	*E. coli* JM109 (DE3) harboring pRSFDuet-*pckA* with deletion of *fruA*, *pfkA*, and *pfkB*	This study
E. coli (*alsE*, *a6PP*, *ptsG-F*, *mak*, *pckA*, Δ*fruA*, Δ*pfkA*, Δ*pfkB*)	*E. coli* JM109 (DE3) harboring pETDuet-*ptsG-F-mak* and pRSFDuet-*alsE-a6PP-pckA* with deletion of *fruA*, *pfkA*, and *pfkB*	This study
Plasmids		
pRSFDuet-1	Vector for protein expression under control of T7 promoter, kan^R	Novagen
pETDuet-1	Vector for protein expression under control of T7 promoter, Amp^R	Novagen
pRSFDuet-*a6PP*	pRSFDuet-1 carrying *a6PP*	This study
pRSFDuet-*alsE*	pRSFDuet-1 carrying *alsE*	This study
pRSFDuet-*pckA*	pRSFDuet-1 carrying *pckA*	This study
pRSFDuet-*alsE-a6PP*	pRSFDuet-1 carrying *alsE* and *a6PP*	This study
pETDuet-*ptsG-F-mak*	pETDuet-1 carrying *ptsG-F*, and *mak*	This study
pRSFDuet-*alsE-a6PP-pckA*	pRSFDuet-1 carrying *alsE*, *a6PP and pckA*	This study
pKD46, pKD13, pCP20	λ red recombination system	Guo et al. (2021)

TABLE 2 | The primers used in this study.

Name	Primer sequence (5′→3′)	Description
Plasmid construction		
ptsG-F-F	CGGGATCCGATGTTTAAGAATGCATTTGCTAAC	Clone and insert *ptsG-F* into *BamH* I and *Hind* III on pETDuet-1
ptsG-F-R	CCCAAGCTTTTAGTGGTTACGGATGTACTC	
mak-F	GGAATTCCATATGGTGCGTATAGGTATCG	Clone and insert *mak* into *Nde* I and *Kpn* I on pETDuet-*ptsG-F*
mak-R	GGGGTACCTTACTCTTGTGGCCATAACCACGC	
a6PP-F	GGAATTCCATATGAAATACACCGTTTACCTGTTCG	Clone and insert *a6PP* into *Nde* I and *Kpn* I on pRSFDuet-1
a6PP-R	GGGGTACCTTACAGCGGGCAACCAGATTTATCTTC	
alsE-F	CATGCCATGGGCATGAAAATCTCCCCCTC	Clone and insert *alsE* into *Nco* I and *Hind* III on pRSFDuet-1 or pRSFDuet-*a6PP*.
alsE-R	CCCAAGCTTTTATGCTGTTTTTGCATGAG	
pckA-F	CCGCTCGAGCCTGTAGAAATAATTTTGTTTAACTTTAATAAGGAGATATACCATGAG CTTATCTGAAAG	Clone and insert *pckA* into *Xho* I and *Avr* II on pRSFDuet-1 or pRSFDuet-*a6PP-alsE*
pckA-R	CCGCCTAGGTTATAACTGTGGACCAGCC	
Gene deletion		
fruA-F	CTGACAGCAGGAGAGGCATAATGAAAACGCTGCTGATTATTGACGCTAATATTCCGG GGATCCGTCGACC	Delete *fruA*
fruA-R	GCCCTGTAACACACCTTTTATTACGCTGCTTTCGCTACTGCGTCCACTTCGTGTAGG CTGGAGCTGCTTCG	
pfkA-F	GTTCAGAGGTAGTCATGATTAAGAAAATCGGTGTGTTGACAAGCGGCGGTTGTGTAG GCTGGAGCTGCTTCG	Delete *pfkA*
pfkA-R	CGAAATCATTAATACAGTTTTTTCGCGCAGTCCAGCCAGTCACCTTTGAAATTCCGG GGATCCGTCGACC	
pfkB-F	CTGATTCGGTGCCAGACTGAAATCAGCCTATAGGAGGAAATGATGGTACGTATCTGT GTAGGCTGGAGCTGCTTCG	Delete *pfkB*
pfkB-R	GTTGGTGATGATTCCCCCAATGCTGGGGGAATGTTTTTGTTAGCGGGAAAGGATTCC GGGGATCCGTCGACC	

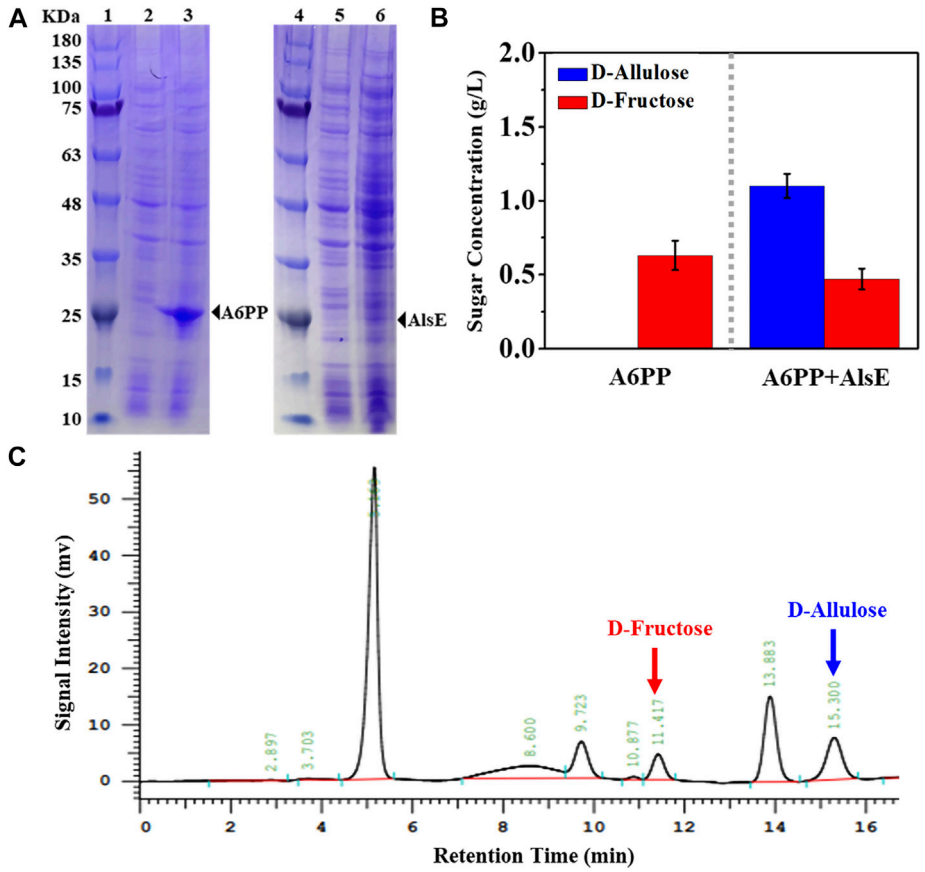

FIGURE 2 | Expression and enzyme assay of A6PP and AlsE. **(A)** SDS-PAGE analysis. Marker (lane 1 and 4), *E. coli* (*control*) (lane 2 and 5), *E. coli* (*a6PP*) (lane 3), *E. coli* (*alsE*) (lane 6). **(B)** Conversion of D-fructose to D-allulose using crude A6PP or a mixture of crude A6PP and AlsE. The reaction was carried out in Tris-HCl buffer (pH 7.5, 50 mM) containing 2.60 g/L fructose-6-phosphate at 37°C for 30 min. Error bars, *SD*, $n = 3$. **(C)** HPLC analysis for confirming the generation of D-allulose by use of A6PP and AlsE mixture.

Analytical Approach

Cell density was determined by a microplate reader (Multiskan™ FC, Thermo Scientific). The ATP in cells was measured through an ATP Content Assay Kit (BC0300, Solarbio) as previously reported (Wang et al., 2019). D-Allulose, D-fructose, and glycerol were determined using a high-performance liquid chromatograph (HPLC, HITACHI) equipped with a refractive index detector (RID) monitor. Sugar-Pak™ I Column (85°C, Waters) was used with deionized water as the mobile phase at a flow rate of 0.5 ml/min.

RESULTS AND DISCUSSION

Biosynthesis of D-Allulose Through Phosphorylation-Dephosphorylation

Wild-type *E. coli* is able to grow on D-fructose as a carbon source owing to its fructose PTS and mannose PTS (Kornberg, 2001). The D-fructose passaged *via* mannose PTS appears in cells as fructose-6-phosphate (Luo et al., 2014), which can be epimerized to allulose-6-phosphate due to the presence of allulose-6-phosphate epimerase (*alsE*) (Chan et al., 2008). Therefore, the key to establishing a phosphorylation-dephosphorylation pathway in *E. coli* for D-allulose synthesis is the introduction of an appropriate allulose-6-phosphate phosphatase for allulose-6-phosphate dephosphorylation.

We selected an allulose-6-phosphate phosphatase (*a6PP*) from *B. fragilis* since it exhibited a high activity at moderate temperatures. Expression of *a6PP* was carried out in *E. coli* JM109 (DE3), resulting in the strain *E. coli* (*a6PP*). As shown in **Figure 2A**, the SDS-PAGE results indicate that this enzyme was expressed in a soluble form with a molecular mass of ≈25 kDa. Unfortunately, it was found that *E. coli* (*a6PP*) could not produce D-allulose by fermentation even if D-fructose was supplemented in culture medium (LB), which is in good agreement with the experimental results of the *in vitro* assay (**Figure 2B**). We sonicated *E. coli* (*a6PP*) after induction and utilized the supernatant to catalyze the cascade of epimerization and dephosphorylation using fructose-6-phosphate as a substrate, and observed the absence of target product in the reaction system. Although we reconfirmed that the genome of *E. coli* JM109 (DE3) has the gene of *alsE*, its weak expression in cells might be unable to generate sufficient allulose-6-phosphate from fructose-6-phosphate. Therefore, we cloned and over-

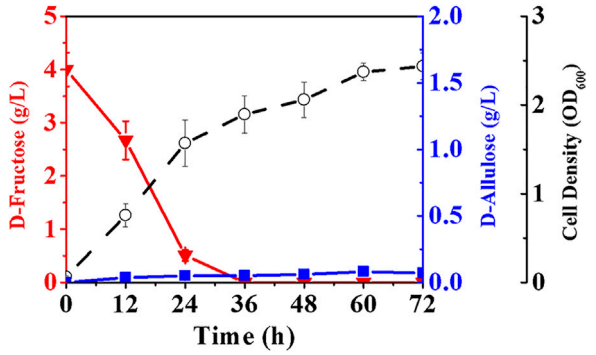

FIGURE 3 | Production of D-allulose by *E. coli* co-expressing AlsE and A6PP. *E. coli* (*alsE*, *a6PP*) was cultured in LB medium with 4.00 g/L D-fructose at 37°C. Error bars, *SD*, *n* = 3.

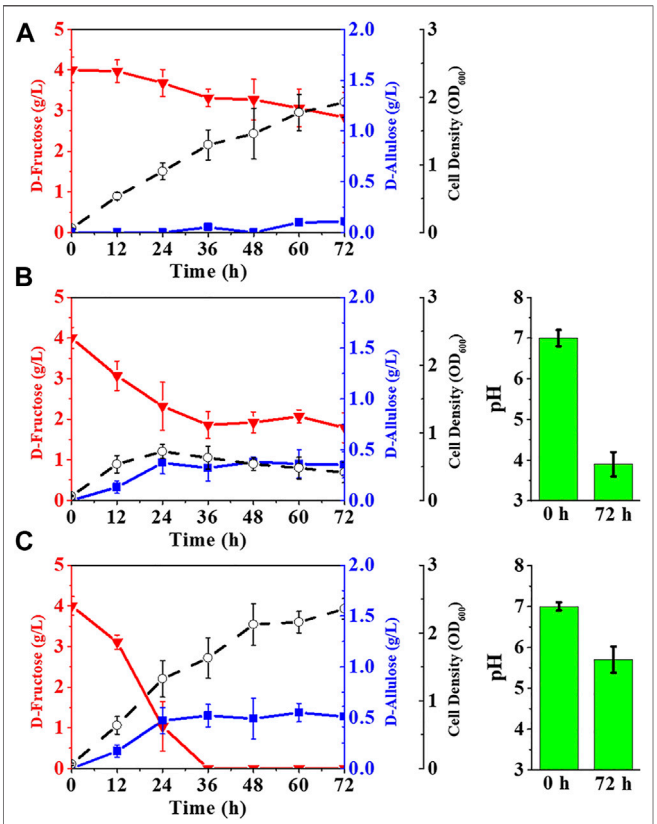

FIGURE 4 | Reprogramming of fructose transport pathways in *E. coli* to enhance D-allulose production. *E. coli* cells were cultured in LB medium with 4.00 g/L D-fructose at 37°C. **(A)** *E. coli* (*alsE*, *a6PP*, Δ*fruA*), **(B)** *E. coli* (*alsE*, *a6PP*, *ptsG-F*, *mak*, Δ*fruA*), **(C)** *E. coli* (*alsE*, *a6PP*, *ptsG-F*, *mak*, Δ*fruA*) with 100 mM potassium phosphate. Error bars, *SD*, *n* = 3.

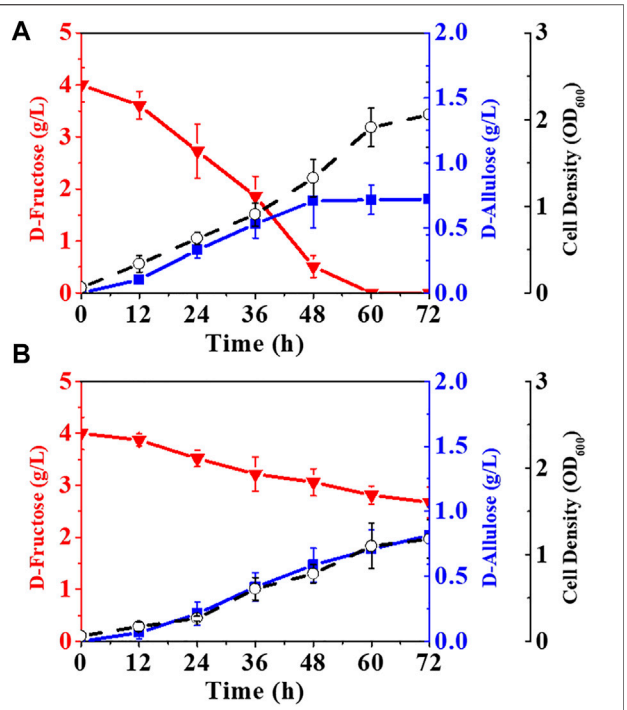

FIGURE 5 | Elimination of the pathways phosphorylating fructose-6-phosphate. *E. coli* cells were cultured in LB medium with 4.00 g/L D-fructose and 100 mM potassium phosphate at 37°C. **(A)** *E. coli* (*alsE*, *a6PP*, *ptsG-F*, *mak*, Δ*fruA*, Δ*pfkA*), **(B)** *E. coli* (*alsE*, *a6PP*, *ptsG-F*, *mak*, Δ*fruA*, Δ*pfkA*, Δ*pfkB*). Error bars, *SD*, *n* = 3.

expressed *alsE* by use of *E. coli* (*alsE*), finding the molecular mass of AlsE was close to that of A6PP, but its expression level was quite low under the same promoter and induction conditions (**Figure 2A**). When a mixed crude enzyme solution of AlsE and A6PP was tested *in vitro*, it could produce 1.10 g/L D-allulose and 0.47 g/L D-fructose from 2.60 g/L fructose-6-phosphate within 30 min (**Figures 2B,C**), which demonstrates the functionalities of AlsE and A6PP in the pathway from fructose-6-phosphate to D-allulose and confirms the presence of an activity of A6PP on fructose-6-phosphate dephosphorylation. Then we co-expressed *alsE* and *a6PP* in *E. coli* JM109 (DE3), resulting in the strain *E. coli* (*alsE*, *a6PP*). **Figure 3** shows that 0.07 g/L D-allulose could be generated when *E. coli* (*alsE*, *a6PP*) was cultured in the LB medium supplemented with 4.00 g/L D-fructose at 37°C for 60 h.

Regulation of Metabolic Pathways to Increase Cell Factory Efficiency

Although *E. coli* (*alsE*, *a6PP*) was capable of producing D-allulose from D-fructose by fermentation, the titer and yield were quite low. The fructose PTS has been reported to play a predominant role in D-fructose transport and phosphorylation in *E. coli* (Luo et al., 2014), so most of the D-fructose entering cells should be in the form of fructose-1-phosphate rather than fructose-6-phosphate. Fructose-1-phosphate is not a biosynthetic precursor for the D-allulose synthesis pathway and can only flow into the EMP pathway as a carbon source for cell growth. We thus deleted the gene of *fruA* to damage the fructose PTS in *E. coli* (*alsE*, *a6PP*). As illustrated in **Figure 4A**, the fermentation performance of *E. coli* (*alsE*, *a6PP*, Δ*fruA*) was slightly improved, with a D-allulose titer of 0.11 g/L and a yield of 0.09 g/g. However, D-fructose could not be depleted, and over

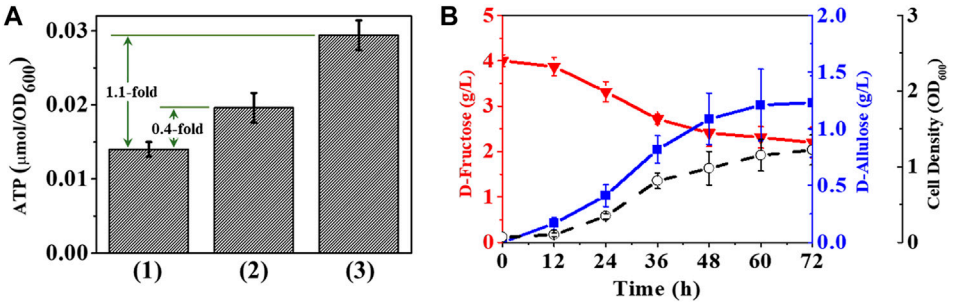

FIGURE 6 | Improvement of ATP supply in cell factory. **(A)** Intracellular ATP level, 1) *E. coli* (Δ*fruA*, Δ*pfkA*, Δ*pfkB*), 2) *E. coli* (*pckA*, Δ*fruA*, Δ*pfkA*, Δ*pfkB*), 3) *E. coli* (*pckA*, Δ*fruA*, Δ*pfkA*, Δ*pfkB*) under air-limited condition. **(B)** *E. coli* (*alsE*, *a6PP*, *ptsG-F*, *mak*, *pckA*, Δ*fruA*, Δ*pfkA*, Δ*pfkB*) cultured in buffered-LB medium with air-limitation condition at 37°C. Error bars, *SD*, *n* = 3.

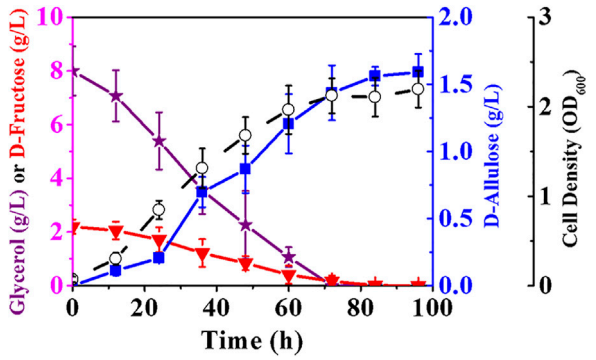

FIGURE 7 | Production of D-allulose in minimal medium with air-limited condition. *E. coli* (*alsE*, *a6PP*, *ptsG-F*, *mak*, *pckA*, Δ*fruA*, Δ*pfkA*, Δ*pfkB*) was cultured in M9 minimal medium with 2.20 g/L D-fructose and 8.00 g/L glycerol at 37°C. Error bars, *SD*, *n* = 3.

71% remained in the LB medium after 72 h. It is probable that the loss of fructose PTS severely reduced the ability of cells to take up D-fructose. We then employed the gene of *ptsG-F* to construct a facilitated diffusion passageway for D-fructose transport and the gene of *mak* for subsequent phosphorylation at its C-6 position (Kornberg et al., 2000). The D-allulose titer of *E. coli* (*alsE*, *a6PP*, *ptsG-F*, *mak*, Δ*fruA*) reached 0.35 g/L, with a product yield of 0.16 g/g (**Figure 4B**). In this case, we found an obvious deterioration in cell growth, probably due to the sharp drop in pH during fermentation, which was caused by the dephosphorylation of fructose-6-phosphate. As shown in **Figure 4C**, buffering LB medium with 100 mM potassium phosphate was able to limit this acidification to pH 5.7 after 72 h, and the D-allulose titer increased to 0.51 g/L, with depletion of 4.03 g/L D-fructose.

In *E. coli* cells, fructose-6-phosphate can also be phosphorylated into fructose-1, 6-bisphosphate by 6-phosphofructokinases (*pfkA*, *pfkB*) and utilized as a carbon source through the EMP pathway (Wang et al., 2022). Therefore, blocking the phosphorylation of fructose-6-phosphate may favor the synthesis of D-allulose. The results in **Figure 5A** show that deletion of *pfkA* in *E. coli* (*alsE*, *a6PP*, *ptsG-F*, *mak*, Δ*fruA*) increased the D-allulose titer and yield to 0.72 g/L and 0.18 g/g, respectively. When both *pfkA* and *pfkB* were knocked out (**Figure 5B**), the titer and yield were further improved, especially the product yield could reach 0.61 g/g on D-fructose, but it significantly affected cell growth, probably due to the limitation of the carbon flux into the EMP pathway. Moreover, the balance of the endogenous gene expression in *E. coli* cells might be affected after gene knockout, and a reported solution was to construct gene-inactivated libraries (Du et al., 2021; Zhu et al., 2021).

Coupling of ATP Regeneration System to Improve Cofactor Supply

Replacing the fructose PTS with *ptsG-F* and *mak* allowed D-fructose to be transported and concomitantly phosphorylated to fructose-6-phosphate, a precursor for D-allulose synthesis. Another consequence of this substitution was that the phosphate donor required for D-fructose phosphorylation changed from PEP to ATP, so the D-allulose titer of *E. coli* should be closely tied to the ability of cell factory to provide ATP. Our results show that deletion of *pfkA* and *pfkB* increased the product yield by blocking the entry of fructose-6-phosphate into the EMP pathway, but it might lead to a restriction in cellular ATP generation. To maximize D-allulose level, it is essential to develop a complementary strategy that yields ATP.

Since inactivation of fructose PTS was believed to increase the PEP pool in *E. coli* cells (Luo et al., 2014), it should be a prior consideration to utilize PEP-related reactions to enhance ATP formation. OAA is a source of four-carbon dicarboxylic acid for the tricarboxylic acid (TCA) cycle and can be formed reversibly from PEP in *E. coli* by using PEP-carboxylase (*ppc*) (Chatterjee et al., 2001; Lin et al., 2005). In contrast, the conversion of PEP to OAA in *A. succinogenes* is catalyzed by PEP-carboxykinase (*pckA*) (Singh et al., 2011), which requires ADP as a phosphate acceptor and thus facilitates ATP generation in cells. We then expressed *pckA via* T7 promoter in *E. coli* (Δ*fruA*, Δ*pfkA*, Δ*pfkB*) and measured the changes in cellular ATP content. The data in **Figure 6A** show that use of *pckA*

resulted in a 0.4-fold increase in ATP level, whereas this increase was able to rise to 1.1-fold by reducing air supply during cell cultivation, which is consistent with previous findings that PEP-carboxykinase catalyzed the reversible reaction towards the ATP-generating direction at high CO_2 concentrations (Singh et al., 2011). **Figure 6B** illustrates that the D-allulose titer and yield of *E. coli* (*alsE*, *a6PP*, *ptsG-F*, *mak*, *pckA*, Δ*fruA*, Δ*pfkA*, Δ*pfkB*) grown in buffered-LB medium with air-limitation condition reached 1.23 g/L and 0.68 g/g, respectively, as a result of increased ATP inside cells.

Production of D-Allulose in Minimal Medium With Air-Limited Condition

After achieving the construction and optimization of the cell factory pathways, we hoped to further improve the production of D-allulose through fermentation. The major problem encountered was cell growth defect caused by the block of the EMP pathway. Although LB is a nutritionally-rich medium in which yeast extract can act as a carbon source for *E. coli*, the developed cell factory did not grow well, with a cell density of less than 1.22 after 72 h (**Figure 6B**). Also, this medium has a relatively low buffering capacity that is not conducive to the cells engineered with dephosphorylation pathway, and is normally used to produce enzymes rather than synthetic chemicals due to its high cost. M9 minimal medium may be a better choice compared to LB, but the premise of using M9 in our case is to select a suitable carbon source that can be utilized by *E. coli* cells without the participation of 6-phosphofructokinases.

Theoretically, *E. coli* (*alsE*, *a6PP*, *ptsG-F*, *mak*, *pckA*, Δ*fruA*, Δ*pfkA*, Δ*pfkB*) should restore its growth on glycerol, an abundant three-carbon by-product of biodiesel industry. Glycerol can be metabolized to dihydroxyacetone phosphate (DHAP) via either fermentative or respiratory route, and the conversion of DHAP to PEP requires only the EMP pathway downstream of 6-phosphofructokinases (Chiang et al., 2020; Zhan et al., 2020). Therefore, we attempted to produce D-allulose with glycerol-containing M9 medium and air-limited condition. In order to fully exhibit the advantages of phosphorylation-dephosphorylation over Izumoring in substrate conversion ratio, the initial D-fructose concentration in medium was controlled at 2.20 g/L. The data in **Figure 7** show that glycerol was utilized by *E. coli* (*alsE*, *a6PP*, *ptsG-F*, *mak*, *pckA*, Δ*fruA*, Δ*pfkA*, Δ*pfkB*) as expected, and cell growth defect was not observed, resulting in a cell density of 2.21 after 100 h. The favorable growth conditions increased the titer of D-allulose to 1.59 g/L. It should be noted that D-fructose could be exhausted after fermentation, and most of it was used for synthesis of the target product, with a yield of 0.72 g/g.

Our achievements in this study perfectly overcome the D-fructose conversion bottleneck existing in fermentative production of D-allulose, and suggest a breakthrough in application of phosphorylation-dephosphorylation strategy in cell factories. Currently, the conversion ratio of D-fructose using Izumoring-based cell factories was only 19.6% (Guo et al., 2021). In contrast, the new synthetic route can completely consume D-fructose, which may facilitate the subsequent separation of D-allulose from culture broth. In future work, we plan to optimize the expression of allulose-6-phosphate epimerase by gene screening or tag fusion, which may greatly increase D-allulose titer while maintaining a high product yield.

DATA AVAILABILITY STATEMENT

The original contributions presented in the study are included in the article/supplementary material, further inquiries can be directed to the corresponding authors.

AUTHOR CONTRIBUTIONS

L-HF and X-CL provided research proposals and funding support. QG and C-YL organized the database and wrote the first draft of the manuscript. L-JZ, S-HZ, and Y-XZ participated in the data analysis. S-YZ and H-DZ reviewed the manuscript. All authors have made a substantial, direct, and intellectual contribution to the work and approved it for publication.

FUNDING

This study was funded by the National Natural Science Foundation of China (No. 21978014), and Quanzhou City Science and Technology Program of China (No. 2021CT006).

REFERENCES

Aristidou, A. A., San, K.-Y., and Bennett, G. N. (1999). Improvement of Biomass Yield and Recombinant Gene Expression in *Escherichia coli* by Using Fructose as the Primary Carbon Source. *Biotechnol. Prog.* 15 (1), 140–145. doi:10.1021/bp980115v

Baba, T., Ara, T., Hasegawa, M., Takai, Y., Okumura, Y., Baba, M., et al. (2006). Construction of *Escherichia coli* K-12 In-frame, Single-gene Knockout Mutants: the Keio Collection. *Mol. Syst. Biol.* 2. 2006.0008. doi:10.1038/msb4100050

Bosshart, A., Wagner, N., Bechtold, M., and Panke, S. (2012). Improving the Thermostability of D-Tagatose 3-epimerase for the Production of the Rare Sugar D-Psicose. *New Biotechnol.* 29, S199. doi:10.1016/j.nbt.2012.08.559

Chan, K. K., Fedorov, A. A., Fedorov, E. V., Almo, S. C., and Gerlt, J. A. (2008). Structural Basis for Substrate Specificity in Phosphate Binding (Beta/alpha)$_8$-Barrels: D-Allulose 6-Phosphate 3-Epimerase from *Escherichia coli* K-12. *Biochemistry* 47 (36), 9608–9617. doi:10.1021/bi800821v

Chatterjee, R., Millard, C. S., Champion, K., Clark, D. P., and Donnelly, M. I. (2001). Mutation of the *ptsG* Gene Results in Increased Production of Succinate in Fermentation of Glucose by *Escherichia coli*. *Appl. Environ. Microbiol.* 67 (1), 148–154. doi:10.1128/AEM.67.1.148-154.2001

Chiang, C.-J., Ho, Y.-J., Hu, M.-C., and Chao, Y.-P. (2020). Rewiring of Glycerol Metabolism in *Escherichia coli* for Effective Production of Recombinant Proteins. *Biotechnol. Biofuels* 13 (1), 205. doi:10.1186/s13068-020-01848-z

Datsenko, K. A., and Wanner, B. L. (2000). One-step Inactivation of Chromosomal Genes in *Escherichia coli* K-12 Using PCR Products. *Proc. Natl. Acad. Sci. U.S.A.* 97 (12), 6640–6645. doi:10.1073/pnas.120163297

Du, G., Zhu, C., Xu, M., Wang, L., Yang, S.-T., and Xue, C. (2021). Energy-efficient Butanol Production by *Clostridium Acetobutylicum* with Histidine Kinase

Knockouts to Improve Strain Tolerance and Process Robustness. *Green Chem.* 23, 2155–2168. doi:10.1039/d0gc03993d

Dugar, G., Svensson, S. L., Bischler, T., Wäldchen, S., Reinhardt, R., Sauer, M., et al. (2016). The CsrA-FliW Network Controls Polar Localization of the Dual-Function Flagellin mRNA in *Campylobacter Jejuni*. *Nat. Commun.* 7, 11667. doi:10.1038/ncomms11667

Guo, Q., Zheng, L.-J., Luo, X., Gao, X.-Q., Liu, C.-Y., Deng, L., et al. (2021). Engineering *Escherichia coli* for D-Allulose Production from D-Fructose by Fermentation. *J. Agric. Food Chem.* 69 (45), 13578–13585. doi:10.1021/acs.jafc.1c05200

Kim, H.-J., Hyun, E.-K., Kim, Y.-S., Lee, Y.-J., and Oh, D.-K. (2006). Characterization of an Agrobacterium Tumefaciens D -Psicose 3-Epimerase that Converts D -Fructose to D -Psicose. *Appl. Environ. Microbiol.* 72 (2), 981–985. doi:10.1128/AEM.72.2.981-985.2006

Kornberg, H. L. (2001). Routes for Fructose Utilization by *Escherichia coli*. *J. Mol. Microbiol. Biotechnol.* 3 (3), 355–359.

Kornberg, H. L. (1990). Fructose Transport by *Escherichia coli*. *Phil. Trans. R. Soc. Lond. B* 326 (1236), 505–513. doi:10.1098/rstb.1990.0028

Kornberg, H. L., Lambourne, L. T. M., and Sproul, A. A. (2000). Facilitated Diffusion of Fructose via the Phosphoenolpyruvate/glucose Phosphotransferase System of *Escherichia coli*. *Proc. Natl. Acad. Sci. U.S.A.* 97 (4), 1808–1812. doi:10.1073/pnas.97.4.1808

Lee, S. Y., Kim, H. U., Chae, T. U., Cho, J. S., Kim, J. W., Shin, J. H., et al. (2019). Author Correction: A Comprehensive Metabolic Map for Production of Bio-Based Chemicals. *Nat. Catal.* 2, 942–944. doi:10.1038/s41929-019-0358-8

Li, C., Lin, J., Guo, Q., Zhang, C., Du, K., Lin, H., et al. (2018). D-psicose 3-epimerase Secretory Overexpression, Immobilization, and D-Psicose Biotransformation, Separation and Crystallization. *J. Chem. Technol. Biotechnol.* 93 (2), 350–357. doi:10.1002/jctb.5360

Li, Y., Shi, T., Han, P., and You, C. (2021). Thermodynamics-driven Production of Value-Added D-Allulose from Inexpensive Starch by an *In Vitro* Enzymatic Synthetic Biosystem. *ACS Catal.* 11 (9), 5088–5099. doi:10.1021/acscatal.0c05718

Lin, H., Bennett, G. N., and San, K.-Y. (2005). Effect of Carbon Sources Differing in Oxidation State and Transport Route on Succinate Production in Metabolically Engineered *Escherichia coli*. *J. Ind. Microbiol. Biotechnol.* 32 (3), 87–93. doi:10.1007/s10295-005-0206-5

Luo, Y., Zhang, T., and Wu, H. (2014). The Transport and Mediation Mechanisms of the Common Sugars in *Escherichia coli*. *Biotechnol. Adv.* 32 (5), 905–919. doi:10.1016/j.biotechadv.2014.04.009

Miller, B. G., and Raines, R. T. (2004). Identifying Latent Enzyme Activities: Substrate Ambiguity within Modern Bacterial Sugar Kinases. *Biochemistry* 43 (21), 6387–6392. doi:10.1021/bi049424m

Mu, W., Chu, F., Xing, Q., Yu, S., Zhou, L., and Jiang, B. (2011). Cloning, Expression, and Characterization of a D-Psicose 3-epimerase from *Clostridium Cellulolyticum* H10. *J. Agric. Food Chem.* 59 (14), 7785–7792. doi:10.1021/jf201356q

Mu, W., Zhang, W., Feng, Y., Jiang, B., and Zhou, L. (2012). Recent Advances on Applications and Biotechnological Production of D-Psicose. *Appl. Microbiol. Biotechnol.* 94 (6), 1461–1467. doi:10.1007/s00253-012-4093-1

Nagata, Y., Kanasaki, A., Tamaru, S., and Tanaka, K. (2015). D-psicose, an Epimer of D-Fructose, Favorably Alters Lipid Metabolism in Sprague-Dawley Rats. *J. Agric. Food Chem.* 63 (12), 3168–3176. doi:10.1021/jf502535p

Nguyen, V. D., Le, T.-H., Kim, J.-I., Lee, J. W., and Koo, Y.-M. (2009). Separation of D-Psicose and D-Fructose Using Simulated Moving Bed Chromatography. *J. Sep. Sci.* 32 (11), 1987–1995. doi:10.1002/jssc.200800753

Pontrelli, S., Chiu, T.-Y., Lan, E. I., Chen, F. Y.-H., Chang, P., and Liao, J. C. (2018). *Escherichia coli* as a Host for Metabolic Engineering. *Metab. Eng.* 50, 16–46. doi:10.1016/j.ymben.2018.04.008

Shiba, T., Tsutsumi, K., Ishige, K., and Noguchi, T. (2000). Inorganic Polyphosphate and Polyphosphate Kinase: Their Novel Biological Functions and Applications. *Biochem. (Mosc)* 65 (3), 315–323.

Singh, A., Cher Soh, K., Hatzimanikatis, V., and Gill, R. T. (2011). Manipulating Redox and ATP Balancing for Improved Production of Succinate in *E. coli*. *Metab. Eng.* 13 (1), 76–81. doi:10.1016/j.ymben.2010.10.006

Su, L., Sun, F., Liu, Z., Zhang, K., and Wu, J. (2018). Highly Efficient Production of *Clostridium Cellulolyticum* H10 D-Psicose 3-epimerase in *Bacillus Subtilis* and Use of These Cells to Produce D-Psicose. *Microb. Cell Fact.* 17 (1), 188. doi:10.1186/s12934-018-1037-1

Sun, Y., Hayakawa, S., Ogawa, M., and Izumori, K. (2005). Evaluation of the Site Specific Protein Glycation and Antioxidant Capacity of Rare Sugar–Protein/Peptide Conjugates. *J. Agric. Food Chem.* 53 (26), 10205–10212. doi:10.1021/jf051565n

Wang, K., Wang, X., Luo, H., Wang, Y., Wang, Y., Tu, T., et al. (2022). Synergetic Fermentation of Glucose and Glycerol for High-Yield N-Acetylglucosamine Production in *Escherichia coli*. *Int. J. Mol. Sci.* 23 (2), 773. doi:10.3390/ijms23020773

Wang, Y., Carder, H. M., and Wendlandt, A. E. (2020). Synthesis of Rare Sugar Isomers through Site-Selective Epimerization. *Nature* 578 (7795), 403–408. doi:10.1038/s41586-020-1937-1

Wang, Y., Jiao, J., Zhang, S., Zheng, C., and Wu, M. (2019). RIP3 Inhibition Protects Locomotion Function through Ameliorating Mitochondrial Antioxidative Capacity after Spinal Cord Injury. *Biomed. Pharmacother.* 116, 109019. doi:10.1016/j.jhazmat.2021.12586410.1016/j.biopha.2019.109019

Xiao, Q., Niu, J., Liu, H., Liu, Y., and Zhou, X. (2019). High Conversion of D-Fructose into D-Allulose by Enzymes Coupling with an ATP Regeneration System. *Mol. Biotechnol.* 61 (6), 432–441. doi:10.1007/s12033-019-00174-6

Xu, N., Liu, Y., Jiang, H., Liu, J., and Ma, Y. (2020). Combining Protein and Metabolic Engineering to Construct Efficient Microbial Cell Factories. *Curr. Opin. Biotechnol.* 66, 27–35. doi:10.1016/j.copbio.2020.06.001

Yang, H., Lu, X., Hu, J., Chen, Y., Shen, W., and Liu, L. (2018). Boosting Secretion of Extracellular Protein by *Escherichia coli* via Cell Wall Perturbation. *Appl. Environ. Microbiol.* 84 (20), e01382–01318. doi:10.1128/AEM.01382-18

You, C., Shi, T., Li, Y., Han, P., Zhou, X., and Zhang, Y.-H. P. (2017). An *In Vitro* Synthetic Biology Platform for the Industrial Biomanufacturing of Myo-Inositol from Starch. *Biotechnol. Bioeng.* 114 (8), 1855–1864. doi:10.1002/bit.26314

Zhan, T., Chen, Q., Zhang, C., Bi, C., and Zhang, X. (2020). Constructing a Novel Biosynthetic Pathway for the Production of Glycolate from Glycerol in *Escherichia coli*. *ACS Synth. Biol.* 9 (9), 2600–2609. doi:10.1021/acssynbio.0c00404

Zhang, W., Fang, D., Xing, Q., Zhou, L., Jiang, B., and Mu, W. (2013). Characterization of a Novel Metal-dependent D-Psicose 3-epimerase from *Clostridium Scindens* 35704. *PLoS One* 8 (4), e62987. doi:10.1371/journal.pone.0062987

Zhu, C., Du, G., Zhang, J., and Xue, C. (2021). A High-efficient Strategy for Combinatorial Engineering Paralogous Gene Family: A Case Study on Histidine Kinases in *Clostridium*. *Biotechnol. Bioeng.* 118, 2770–2780. doi:10.1002/bit.27796

Conflict of Interest: The authors declare that the research was conducted in the absence of any commercial or financial relationships that could be construed as a potential conflict of interest.

Publisher's Note: All claims expressed in this article are solely those of the authors and do not necessarily represent those of their affiliated organizations, or those of the publisher, the editors and the reviewers. Any product that may be evaluated in this article, or claim that may be made by its manufacturer, is not guaranteed or endorsed by the publisher.

frontiers | Frontiers in Bioengineering and Biotechnology

ORIGINAL RESEARCH
published: 08 July 2022
doi: 10.3389/fbioe.2022.918277

Efficient Production of 2,5-Diketo-D-gluconic Acid by Reducing Browning Levels During *Gluconobacter oxydans* ATCC 9937 Fermentation

Guang Li[1,2,3,4], *Xiaoyu Shan*[1,2,3,4], *Weizhu Zeng*[1,2], *Shiqin Yu*[1,2], *Guoqiang Zhang*[1,2], *Jian Chen*[1,2] *and Jingwen Zhou*[1,2,3,4]*

[1]*Science Center for Future Foods, Jiangnan University, Wuxi, China,* [2]*Key Laboratory of Industrial Biotechnology, Ministry of Education and School of Biotechnology, Jiangnan University, Wuxi, China,* [3]*Engineering Research Center of Ministry of Education on Food Synthetic Biotechnology, Jiangnan University, Wuxi, China,* [4]*Jiangsu Province Engineering Research Center of Food Synthetic Biotechnology, Jiangnan University, Wuxi, China*

D-Glucose directly generates 2-keto-L-gulonic acid (2-KLG, precursor of vitamin C) through the 2,5-diketo-D-gluconic acid (2,5-DKG) pathway. 2,5-DKG is the main rate-limiting factor of the reaction, and there are few relevant studies on it. In this study, a more accurate quantitative method of 2,5-DKG was developed and used to screen *G. oxydans* ATCC9937 as the chassis strain for the production of 2,5-DKG. Combining the metabolite profile analysis and knockout and overexpression of production strain, the non-enzymatic browning of 2,5-DKG was identified as the main factor leading to low yield of the target compound. By optimizing the fermentation process, the fermentation time was reduced to 48 h, and 2,5-DKG production peaked at 50.9 g/L, which was 139.02% higher than in the control group. Effectively eliminating browning and reducing the degradation of 2,5-DKG will help increase the conversion of 2,5-DKG to 2-KLG, and finally, establish a one-step D-glucose to 2-KLG fermentation pathway.

Keywords: detection method, 2,5-diketo-D-gluconic acid, browning, *Gluconobacter oxydans* ATCC 9937, feed-batch

OPEN ACCESS

Edited by:
Tian-Qiong Shi,
Nanjing Normal University, China

Reviewed by:
Zhiqiang Wen,
Nanjing Normal University, China
Quanyu Zhao,
Nanjing Tech University, China

***Correspondence:**
Jingwen Zhou
zhoujw1982@jiangnan.edu.cn

Specialty section:
This article was submitted to Synthetic Biology, a section of the journal Frontiers in Bioengineering and Biotechnology

Received: *12 April 2022*
Accepted: *20 May 2022*
Published: *08 July 2022*

Citation:
Li G, Shan X, Zeng W, Yu S, Zhang G, Chen J and Zhou J (2022) Efficient Production of 2,5-Diketo-D-gluconic Acid by Reducing Browning Levels During Gluconobacter oxydans ATCC 9937 Fermentation. Front. Bioeng. Biotechnol. 10:918277. doi: 10.3389/fbioe.2022.918277

INTRODUCTION

L-Ascorbic acid has important roles in food (Cendrowski et al., 2021), medicine (Pardo-Planas et al., 2017), and health (Anitra and Silvia, 2017; Reddy et al., 2020). Recent research has also suggested it has particular functions in electron transfer (Xin et al., 2022) and microbial fuel cells (Islam et al., 2020). Currently, in industry, L-ascorbic acid is mainly synthesized by 2-keto-L-gulonic acid (2-KLG) *via* a simple chemical reaction, which uses D-sorbitol as a substrate (Cai-Yun Wang et al., 2018; Zhang et al., 2018; Zeng et al., 2020). In addition, 2-KLG can also be directly generated by 2,5-diketo-D-gluconic acid (2,5-DKG) *via* a simple reduction reaction (Sonoyama et al., 1982). 2,5-DKG is commonly and directly synthesized using D-glucose as a substrate. In addition to 2,5-DKG being the precursor of 2-KLG, recent studies reported its synthesis may also increase rare-earth element recovery in wastewater (Jindra et al., 2016; Schmitz et al., 2021). As 2,5-DKG reactions during synthesis and decomposition processes are unclear, further research in these areas may provide insights on one-step 2-KLG synthesis and environmental protection.

In *Erwinia* sp. (Sonoyama et al., 1988), *G. oxydans* (Ji and Gao, 2001), *Pseudomonas putida* (Nikel and de Lorenzo, 2018), and *Tatumella citrea* (previously known as *Erwinia citrea*) (Andreeva et al., 2011; Marin-Cevada and Fuentes-Ramirez, 2016), D-glucose is gradually oxidized to D-gluconic acid (GA), 2-keto-D-gluconic acid (2-KG), and 2,5-DKG *via* glucose dehydrogenase (GDH), D-gluconic acid dehydrogenase (GADH), and 2-keto-D-gluconic acid dehydrogenase (2-KGDH), respectively, on the cell membrane or in the periplasmic space (Kataoka et al., 2015). Then, 2,5-DKG can be transformed into 2-KLG by 2,5-DKG reductase from *Corynebacterium glutamate* (Badwar et al., 2020). Based on the reported synthesis and metabolism of 2,5-DKG, a new one-step fermentation route was established for 2-KLG production directly from D-glucose, using recombinant *Erwinia herbicola* encoding the 2,5-DKG reductase gene from *Corynebacterium* sp. (Anderson et al., 1985). As one of the cheapest carbon sources, the use of D-glucose for 2-KLG production effectively solves the disadvantages of high energy consumption, high water consumption, long cycle, and difficulty in accurate control in other pathways. However, due to uncharacterized speed-limiting factors, 2,5-DKG pathway research is still in its infancy (Panpan Wang et al., 2018).

The main speed-limiting issue with the 2,5-DKG pathway is the transformation from 2,5-DKG to 2-KLG. This reaction is mainly catalyzed by 2,5-DKG reductase; therefore, generating a highly catalytically efficient 2,5-DKG reductase could facilitate a one-step fermentation system. Previous studies have investigated different strategies to strengthen 2,5-DKG conversion to 2-KLG, and increase 2-KLG production from D-glucose *via* the 2,5-DKG pathway; however, the effect is not obvious (Scott et al., 2002; Jeudy et al., 2006; Kaswurm et al., 2013).

In addition to generate an efficient 2,5-DKG reductase, it is important to select a good chassis strain (Vivek et al., 2021), optimize 2,5-DKG production processes, and identify possible speed-limiting factors. Previous studies investigated 2,5-DKG production improvements. A mixed culture of two bacteria from soil was developed to convert 50 g/L D-glucose to 2,5-DKG, and generated a 92% conversion ratio (Sulo et al., 2001). In addition, 65.8 g/L 2,5-DKG was harvested from a 10-L bioreactor using a high-performance liquid chromatography (HPLC) method (Qazi et al., 1991). However, the fermentation time in these studies is relatively long, generally more than 120 h. According to our previous studies, due to the lack of standards and the deviation of detection methods, these research data may have large errors. Therefore, the development of a relatively accurate quantitative method monitoring 2,5-DKG changes is warranted.

In this study, we established a quantitative detection method for 2,5-DKG based on pure enzyme catalysis. Using this method, we compared 2,5-DKG production levels in five strains, with *G. oxydans* ATCC 9937 selected as the optimum strain. After analyzing *G. oxydans* ATCC 9937-mediated 2,5-DKG production from D-glucose, a putative speed-limiting factor was identified. By knocking out and overexpressing the gene encoding the putative rate-limiting enzyme, we identified browning issues, caused by prolonged fermentation times, as the main factor leading to low 2,5-DKG accumulation. While browning is irreversible, it can be slowed down by shortening fermentation times. To reduce 2,5-DKG production losses caused by browning, we accelerated strain growth and reduced fermentation times by optimizing D-glucose addition at the start of fermentation. Finally, the browning degradation of 2,5-DKG was reduced and production generated a 139.02% increase using the feeding mode. This study provides a basis for further improving the one-step fermentation of D-glucose to produce 2-KLG.

MATERIALS AND METHODS

Genes, Plasmids, and Strains

Escherichia coli BL21 (DE3) and vector pET28a were obtained from Sangon Biotech Corporation (Shanghai, China), and used to express 2,5-DKG reductase. *C. glutamicum* ATCC 13032 was purchased from the American Type Culture Collection (ATCC), and used to amplify the gene of 2,5-DKG reductase. The 2,5-DKG reductase gene from *C. glutamicum* ATCC 13032 was amplified with primer pair *dkg*-F and *dkg*-R. The pk18mobsacb vector was used to knock out *kgdSLC* gene. The plasmid pBBR1MCS-2 is used as a vector to overexpress *kgdSLC* gene.

G. oxydans ATCC 9937, *P. putida* ATCC 21813 and *C. glutamicum* ATCC 13032 were purchased from the American Type Culture Collection (ATCC); *Tatumella citrea* CICC 10802 and *T. citrea* CICC 10803 strains were obtained from the China Center of Industrial Culture Collection (Beijing, China); *P. putida* KT 2440 was preserved in our laboratory. All these strains were cultured in fermentation medium to verify their 2,5-DKG yield.

All primers are list in **Table 1**.

Media and Culture Condition

D-Gluconic acid, 2-KG, 5-keto-D-gluconic acid (5-KG), and 2-KLG were purchased from Toronto Research Chemicals INC. (Toronto, Canada). An Aminex HPX-87H liquid chromatographic column was purchased from Bio-Rad Laboratories INC. (CA, United States). Yeast extract was purchased from Oxoid (Hampshire, United Kingdom).

D-Sorbitol medium preparation: D-sorbitol (50 g/L), yeast extract (10 g/L), KH_2PO_4 (1 g/L), $MgSO_4$ (0.25 g/L), and 20 g/L agar were added to solid medium. Fermentation medium: 100 g/L D-glucose, 10 g/L yeast extract, and 0.25 g/L $MgSO_4$.

G. oxydans ATCC 9937 was grown on D-sorbitol solid medium for 20 h at 30°C, after which a single colony was transferred to liquid D-sorbitol medium and cultivated for 24 h at 30°C as seeding, and then was transferred to fermentation medium. *T. citrea* CICC10802, *T. citrea* CICC10803, *P. putida* ATCC21812, *P. putida* KT2440, and *E. coli* BL21 were activated in a solid LB medium at 30°C for 16 h and then transferred to a liquid LB medium at 30°C for 16 h, after which was transferred to fermentation medium.

Batch fermentation was performed in a 5-L fermenter (T&J-B type, J Bio-engineering Co., Ltd, Shanghai, China). The stirring speed gradually increased from 300 to 500 rpm and the

TABLE 1 | Primers used in this study.

Primers	Sequence (5′-3′)
dkg-F	CATCATCATCATCATCACATGGATCAGAAGAATAAGCTTTCGAAGTCTGA
dkg-R	GCTTCCTTTCGGGCTTTGCTAGTTCAGATCATTCGGGTGTGAACC
pET28a-F	GTGATGATGATGATGATGGCTGCTG
pET28a-R	CAAAGCCCGAAAGGAAGCTGAG
kgdC up-F	ATTCGAGCTCGGTACCCGGGCCCATTCCACAGGGACGGAG
kgdC up-R	CTTTCAGACCGAGCGCTGCC
kgdC down-F	GGCAGCGCTCGGTCTGAAAGGCCTGGATTTGGGCCAGGTT
kgdC down-R	CCTGCAGGTCGACTCTAGAGCCGTCCTTGCTTAACTGGATAT
kgdS up-F	ATTCGAGCTCGGTACCCGGGCGAGCGTCCTGTCGAATTGC
kgdS up-R	TTCCGCAACAGAGATCATTGTCATTT
kgdS down-F	CAATGATCTCTGTTGCGGAAGCTCAGTCGAGGACAGAACG
kgdS down-R	CCTGCAGGTCGACTCTAGAGGCCCCGATGGGGCAGATGGG
kgdL up-F	ATTCGAGCTCGGTACCCGGGCAACCCATTCTGGTCGAACGT
kgdL up-R	GGGTTAGTGCTCCTGACGGG
kgdL down-F	CCCGTCAGGAGCACTAACCCAGGACTGGATGCGGTCAACA
kgdL down-R	CCTGCAGGTCGACTCTAGAGTCACATTCGGCGCATACCAT
pk1-R	CCCGGGTACCGAGCTCGAAT
pk1-F	CTCTAGAGTCGACCTGCAGGCA
pBBR-*kgdSLC*-F	TCAGAAAAGGAAGAATAACAGAAATGACAATGATCTCTGTTGCGG
pBBR-*kgdSLC*-R	ACTAAAGGGAACAAAAGCTGTCAGGCCTTCGCCTTTCGGG
P7-F	ACTCACTATAGGGCGAATTGCACGATCGTCGGCAAAGTGA
P7-R	TGTTATTCTTCCTTTTCTGATCGTGACGA
pBBR-F	CAATTCGCCCTATAGTGAGTCGTATTACG
pBBR-R	CAGCTTTTGTTCCCTTTAGTGAGGGT

ventilation ratio was 1 vvm. A pH of 4.9 was automatically maintained by adding 6 mol/L NaOH.

Preparation Method of 2,5-DKG

The fermentation broth was collected and centrifuged to remove bacteria. Used HyperSep Retain-AX solid-phase extraction column (ThermoFisher Scientific, Healthpoint, United States) to remove some protein impurities and pigments in the supernatant, and then lyophilized and stored, and dissolved in water after use.

Overexpression and Purification of 2,5-DKG Reductase

E. coli BL21 (DE3) cells expressing the recombinant plasmid pET28a-Histag-2,5-DKGR were cultured at 220 rpm for 10 h at 37°C. Then, 500 μL of the culture was transferred to TB medium and grown at 220 rpm at 37°C. When the OD_{600} reached 0.8, the temperature was reduced to 20°C, 0.1 mM isopropyl β-d-1-thiogalactopyranoside was added, and incubation continued for 16 h. Then, cells were harvested by centrifugation at 8,000 *g* for 5 min. After washing twice in phosphate buffer saline (PBS), cells were disrupted using a high-pressure cell cracker, and the crude enzyme solution was clarified by centrifugation (Lei et al., 2019). The solution was purified using a protein purifier, quick-frozen in liquid nitrogen, and stored at −80°C.

Catalytic Studies on 2,5-DKG Reductase

We prepared different concentrations of 2,5-DKG. Then, added 100 μL 2,5-DKG reductase and excess NADPH, supplemented the volume to 1 ml with Tris-HCl (pH 7.0), and incubated samples at 30°C for 4 h to ensure the substrate was completely transformed to 2-KLG. (Scott et al., 2002). Then, the concentration of 2-KLG in the system was detected by HPLC. In the first reaction, a small amount of 2,5-DKG and sufficient NADPH were added, and reacted for more than 4 h to ensure that 2,5-DKG is completely converted into 2-KLG. Then, the concentration of 2,5-DKG was gradually increased, and the NADPH to be added was estimated according to the results of the first reaction, so as to ensure that the cofactor is always sufficient or excessive to ensure the complete conversion of each time.

To verify the accuracy of the standard curve, we fitted the calculated 2,5-DKG concentration to the HPLC peak area (**Figure 1B**), and the relationship between the two was determined as follows:

$$y = 160151.56x + 14403.69 \quad (1)$$

where x = the 2,5-DKG concentration and y = the peak area; therefore, the R^2 value of the relationship = 0.9924, indicating relatively high accuracy of the detection method (**Figure 1B**).

Knockout and Overexpression of *kgdSLC* Gene

The pk18mobsacb vector containing SacB system, previously developed in our laboratory, was used to edit genes in the *G. oxydans* ATCC 9937 strain (Chen et al., 2021). Using the *G. oxydans* ATCC 9937 genome as a template, primers were designed to amplify 1000 bp homologous arms upstream and downstream of the *kgdS*, *kgdL* and *kgdC* for PCR knockout (**Table 1**). Then, upstream and downstream homologous arms of the target gene were recombined using the pK18mobsacb vector to generate a recombinant plasmid. After verification, the plasmid was transformed into *G. oxydans* ATCC 9937. For more detailed procedures, please refer to our previous study (Qin et al., 2021).

Using the *G. oxydans* ATCC 9937 genome as a template, primer pair pBBR-*kgdSLC*-F and pBBR-*kgdSLC*-R were designed to amplify *kgdSLC*, primer pair P7-F and P7-R were designed to amplify promoter sequence. Then, *kgdSLC* and promoter sequence were recombined using the pBBR1MCS-2 vector to generate a recombinant. After verification, the plasmid was transformed into *G. oxydans* ATCC 9937 to overexpress *kgdSLC*.

Biomass and High-Performance Liquid Chromatography Analysis

To avoid fermentation broth interference in terms of color generation for spectrophotometric assay, bacteria were centrifuged, resuspended in an equal volume of PBS, and OD_{600} values were recorded.

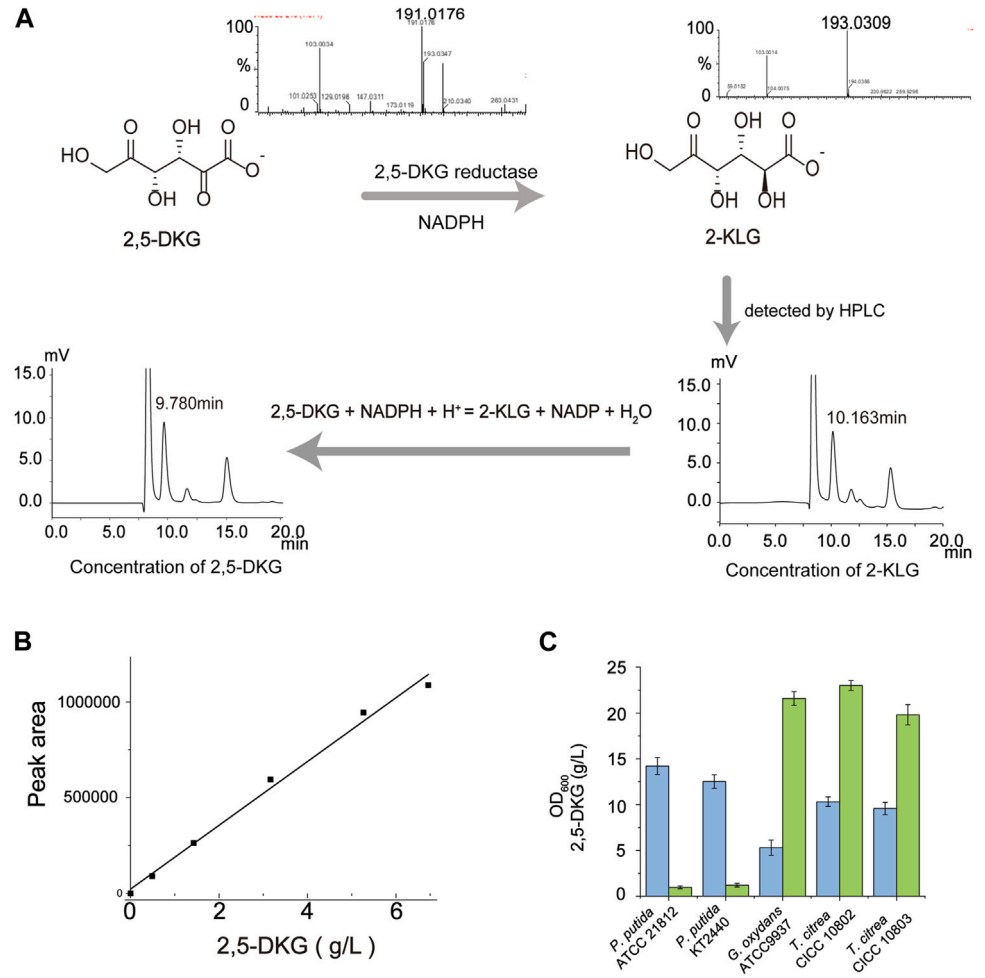

FIGURE 1 | Quantification of 2,5-DKG by indirect HPLC analysis. **(A)** The peak time of 2,5-DKG is different from that of 2-KLG in HPLC detection. Therefore, 2,5-DKG which is difficult to quantify can be transformed into 2-KLG which is easier to quantify, and the real concentration of 2,5-DKG can be calculated from the concentration of 2-KLG. **(B)** Standard 2,5-DKG curve. **(C)** Comparing 2,5-DKG production in different strains. *P. putida* ATCC 21812 (No production); *P. putida* KT 2440 (No production); *G. oxydans* ATCC 9937 (21.6 g/L); *T. citrea CICC* 10802 (23.6 g/L); and *T. citrea* CICC 10803 (19.8 g/L). Blue = OD_{600}; green = 2,5-DKG concentrations.

TABLE 2 | Detection conditions of LC-MS.

Instrument	Waters Quattro Premier XE	
Ion mode	ESI−	ESI+
Capillary	3.0 KVolts	3.5 KVolts
Cone	20/50 V	
Source block temp	100°C	
Desolvation temp	400°C	
Desolvation gas flow	700 lit/hr	
Cone gas flow	50 lit/hr	
Collision energy	6 eV	
Mass range	50–2000 m/z	
Detector	1800 V	

D-Gluconic acid, 2-KG, 2,5-DKG, and 2-KLG levels were detected and quantified by HPLC using a Shimadzu LC-20A system equipped with a refractive index detector on an Aminex HPX-87H column at 40°C in 5 mmol/L H_2SO_4 eluent (0.5 ml/min = flow rate).

2,5-DKG and 2-KLG were measured using LC-MS under the conditions of **Table 2**.

Browning Measurement by Ultraviolet Spectrophotometer

Samples were taken every 12 h to detect the content of 2,5-DKG and the degree of browning. The browning of fermentation broth was reflected by the absorbance value at 420 nm (Zhao et al., 2017; Tavares et al., 2018).

RESULT

Identifying an Optimum 2,5-DKG-Producing Strain Using Enzyme-Based Detection

The traditional host strain as a one-step fermentation pathway from D-glucose to 2-KLG has been developing slowly. Therefore,

we plan to re-screen the appropriate chassis strain and optimize its ability to produce 2,5-DKG. To obtain such a high producer of 2,5-DKG, an effective detection method of 2,5-DKG is required to be established. 2,5-DKG has no standard and lacks quantitative basis, but its oxidation product 2-KLG can be easily quantified. In this study, 2,5-DKG was transformed into 2-KLG by 2,5-DKG reductase, and the actual content of 2,5-DKG was calculated by quantitative analysis of 2-KLG. Firstly, we compared the peak time difference between 2,5-DKG and 2-KLG in HPLC. The peak time of the two were 9.35 and 10.16 min, respectively. Then, the compound 2,5-DKG was completely converted to 2-KLG under the presence of excess cofactor NADPH (**Figure 1A**); the substrate 2,5-DKG and product 2-KLG were detected by LC-MS. After the concentration of 2-KLG in the solution is detected, the actual concentration of 2,5-DKG in the solution is calculated according to 100% conversion. To verify the accuracy of this method, a standard curve was produced for the 2,5-DKG quantification based on the calculation of molar conversion (Figure B), and the results show that the detection method is reasonable.

Based on this quantitative method, five strains producing 2,5-DKG were compared (**Figure 1C**), including *G. oxydans* ATCC 9937, *T. citrea* CICC 10802, *T. citrea* CICC 10803, *P. putida* ATCC 21813, and *P. putida* KT 2440. After comparing the yield of 2,5-DKG and OD_{600} of different strains, *G. oxydans* ATCC 9937 was identified as having the highest 2,5-DKG production (4.08 g/L/OD_{600}) and was chosen as the starting strain. The strain produced 21.6 g/L 2,5-DKG from 100 g/L D-glucose, with a conversion rate of 20.7%. The conversion rate of *G. oxydans* ATCC9937 from D-glucose to 2,5-DKG is not high. In order to analyze the reasons for the low conversion rate, a detailed understanding of the whole metabolic process and conversion rate of *G. oxydans* ATCC9937 synthesizing 2,5-DKG with D-glucose as the substrate are necessary.

Metabolites in the Fermentation Process of 2,5-DKG by *G. oxydans* ATCC 9937

In *G. oxydans*, D-glucose is oxidized to GA by membrane-bound GDH, then further oxidized to 2-KG or 5-KG by GADH or glycerol dehydrogenase (Qazi et al., 1991) (**Figure 2A**). As only 2-KG is oxidized to 2,5-DKG by 2-KGDH. To find out the possible rate-limiting factors, this study verified its ability to produce 2,5-DKG. Through the detection of samples in different fermentation cycles, the product of *G. oxydans* ATCC9937 in the fermentation medium with D-glucose as the carbon source is shown in **Figure 2B**. This study did not detect 5-KG in the medium, it was speculated that the process of *G. oxydans* ATCC 9937 did not or only produce a small amount of 5-KG.

G. oxydans ATCC 9937 consumed D-glucose in the first 24 h to generate GA and low 2-KG and 2,5-DKG levels. D-gluconic acid accumulation peaked at 24 h, about 72.96 g/L, and the conversion of D-glucose to GA is about 75.5%. GA was consumed after 52 h, 2-KG peaked at 41.03 g/L at approximately 42 h, and the conversion of GA to 2-KG is about 62.8%. 2,5-DKG peaked at 21.3 g/L at approximately 60 h, and then levels of 2,5-DKG gradually decreased to 12.7 g/L at 90 h. Although the results showed that 2-KG was completely consumed in about 68 h, the conversion of 2-KG to 2,5-DKG is only 41.4% (**Figure 2C**), which is relatively low. The reason for this phenomenon may be an important rate-limiting factor for the accumulation of 2,5-DKG.

Knockout and Overexpression of *kgdSLC*

To block the synthesis of 2,5-DKG and find out other possible transformation pathways of 2-KG and optimize them, it is necessary to edit the coding gene of 2-KGDH. The gene sequence encoding 2-KGDH in *G. oxydans* ATCC9937 was found by blast. 2-KGDH contains three subunits, *kgdS*, *kgdL,* and *kgdC* (Shinagawa et al., 2014; Kataoka et al., 2015). In order to further determine that the sequence is correct, we knocked out the three subunits respectively. The result showed that, when compared with original control bacteria, all knockouts failed to convert 2-KG to 2,5-DKG. Until 156 h of fermentation, 2-KG concentrations remained at about 75.1 g/L (**Figure 3A**); the figure showed that the true conversion rate of GA to 2-KG is about 87.8%, which is much higher than the value we calculated before. No other substances were detected other than 2-KG.

In the absence of side reaction, the low efficiency of 2-KG to 2,5-DKG may also be caused by the low activity or expression of 2-KDGH. So, we used pBBR1MCS-2 plasmid to complement *kgdSLC* gene, and replaced the p7 promoter with higher strength to improve the copy number of *kgdSLC*. Then 2-KG can be transformed into 2,5-DKG again, but 2,5-DKG production did not change significantly when compared with the original control bacteria. Thus, the catalytic efficiency of 2-KGDH did not change significantly whether *kgdSLC* was overexpressed or not. The conversion rate of D-glucose to 2-KG was as high as 76.3%, while the final conversion rate to 2,5-DKG during fermentation was only 23.1%. However, the knockout and overexpression results of *kgdSLC* showed that the main rate-limiting factor of the reaction maybe is not the conversion of 2-KG. The knockout and overexpression of *kgdSLC* also brought another phenomenon; when compared with the yellowish color of the fermentation broth of control cells, the experimental group, which no longer produced 2,5-DKG, was always clear (**Figure 3B**). In control cells, with increased fermentation time, broth color gradually deepened and finally changed to dark brown, similar to soy sauce. In the earliest relevant studies, it is always mentioned that the production of 2,5-DKG is always accompanied by the color change in fermentation broth. But this color change is more like browning in Maillard reaction. It is necessary to study whether the color change is caused by the browning of 2,5-DKG or other factors.

Non-Enzymatic Browning is the Main Factor Leading to the Degradation of 2,5-DKG

The OD_{420} value of samples is usually an important index to detect the degree of browning in Maillard reaction (Paravisini and Peterson, 2019). To investigate whether the color change in fermentation broth is related to 2,5-DKG, the OD_{420} values

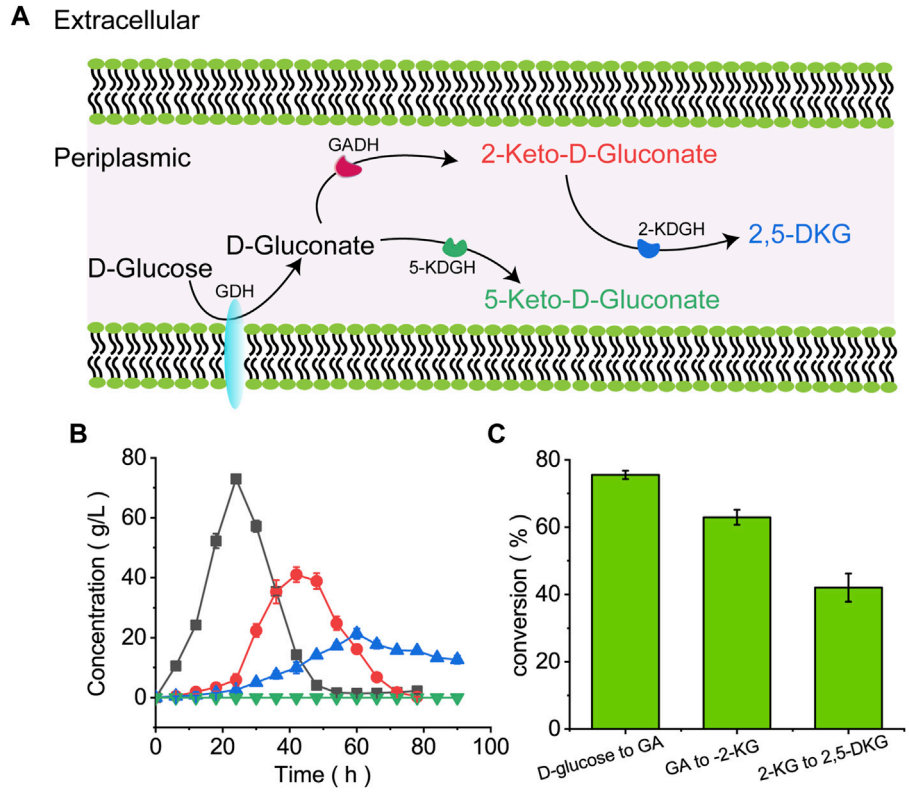

FIGURE 2 | The microbial pathway showing D-glucose conversion to 2,5-DKG. **(A)** D-Glucose conversion to 2,5-DKG in the periplasmic space; **(B)** Consumption and formation of D-gluconic acid, 2-KG, 2,5-DKG, and 5-KG by *G. oxydans* ATCC 9937. Black = D-gluconic acid levels; red = 2-KG levels; blue = 2,5-DKG levels; green = 5-KG levels. **(C)** Illusion rate of various substances.

and 2,5-DKG concentrations in fermentation broth at different periods were measured. With increased fermentation time, broth color gradually deepened, and OD_{420} values maintained an increasing trend. Also, 2,5-DKG concentrations maintained an increasing trend in the early stages, but then declined after peaking at 60 h; the concentration was only 74.52% of the maximum value after 72 h (**Figure 4A**). Then, 2,5-DKG solution was prepared with a concentration of about 15 g/L, and the same quantity of glutamine as 2,5-DKG was added. After this addition, OD_{420} absorbance values increased significantly when compared with control group (2,5-DKG solution without glutamine). After 150 h, 2,5-DKG concentrations in control group decreased by 53.9%, and in the experimental plus glutamine group, it decreased by 90.1% (**Figure 4B**). By fitting OD_{420} absorbance values of both groups with 2,5-DKG concentrations, we identified a negative correlation between OD_{420} and 2,5-DKG concentrations, but the relationship was not linear.

To further verify that browning is caused by 2,5-DKG, we added a Maillard inhibitor to destroy 2,5-DKG, and then browning will not occur again whether glutamine was added or not (**Figure 4C**). The current research results showed that the degradation of 2,5-DKG leads to the continuous deepening of the color of fermentation broth, and the main mode of degradation is non-enzymatic browning. This study tried to eliminate or inhibit the browning phenomenon of 2,5-DKG, but it did not work. 2,5-DKG continued browning and degraded with the increase in storage time unless refrigerated. Therefore, in order to reduce the browning of 2,5-DKG and improve the yield of 2,5-DKG, minimizing the fermentation time through optimization is the most feasible and efficient way.

Enhanced 2,5-DKG Production by Reducing Fermentation Period

Inappropriate fermentation conditions will inhibit the growth and metabolism of bacteria, so as to prolong the fermentation time and increase the browning degradation rate of 2,5-DKG. In order to reduce the browning rate and increase the yield of 2,5-DKG, we optimized the fermentation process. In this study, the optimization was carried out by changing the initial D-glucose concentration to reduce the growth inhibition of the strain. To find the best initial D-glucose concentration, we compared the growth curves of strains under different D-glucose concentrations, result showed that the strain grew fastest at an initial D-glucose concentration of 20 g/L (**Figure 5A**), therefore 20 g/L initial D-glucose concentration was used to optimize the subsequent fermentation process. When the initial D-glucose concentration was reduced to 20 g/L, the ability of the strain to produce 2,5-DKG was significantly accelerated, 12.3 g/L of 2,5-DKG was obtained in 16 h, and the growth of the strain was also

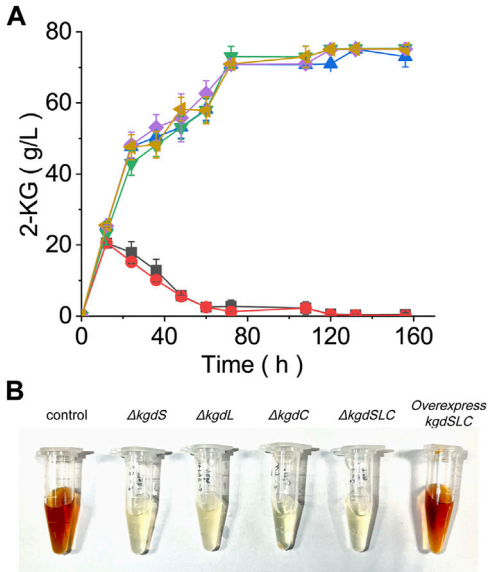

FIGURE 3 | Evaluating the fermentation performance of the *kgdSLC* knockout strain. **(A)** Changes in 2-KG concentrations in fermentation broth after *kgdSLC* knockout and overexpression. Green = *kgdL* knockout. Yellow = *kgdS* knockout. Blue = *kgdC* knockout. Purple = combined knockout. Red = Overexpressed *kgdSLC*. Black = control cells. **(B)** Broth color changes after *kgdSLC* knockout. Regardless of single or combined knockout, the broth no longer turned brown; when *kgdSLC* was overexpressed, the color of the fermentation broth turned brown.

significantly accelerated. The biomass of 16 h increased by about 56% compared with the control group (100 g/L D-glucose).

In order to further increase the yield of 2,5-DKG, after the initial D-glucose consumption of 20 g/L is completed, we continued to add D-glucose by feeding. The feeding is carried out in two ways; 1) by adding all the remaining D-glucose at one time, and 2) concentrations were maintained at 20 g/L by feeding to finally reach a concentration of 100 g/L. The results showed that the strains grew rapidly in the first 20 h of fermentation, and began to stabilize after 24 h, whether supplemented or not (feeding began at approximately 16 h). However, after reducing the initial D-glucose concentration, the growth of the strain was significantly better than that of the control group. The OD_{600} of the experimental group was approximately 1.4 times that of the control group, and the final OD_{600} of different feeding methods has little difference (**Figure 5B**). When compared with control group, 2,5-DKG production peaked after 48 h, and fermentation time had been reduced by approximately 10 h. 2,5-DKG production increased by 139.02% and 133.63%, peaking at 50.9 g/L and 49.7 g/L, in constant-rate feeding mode and single-dose feed-batch mode, respectively (**Figure 5C**). Additionally, productivity [1.06 g/(L/h)] was significantly enhanced when compared with results from a previous study (**Table 3**).

DISCUSSION

Fermentation broth containing 2,5-DKG is usually darker in color, and therefore, the detection method, which was based on NH_4OH-HCl reactions (Sulo et al., 2001), caused a large deviation due to culture broth interference. This inevitably affected the absorbance and generated higher 2,5-DKG yields. HPLC approach was relatively accurate; however, a good standard was required to generate a standard curve as 2,5-DKG standards were commercially unavailable, and product purity from self-purification is low. So, there is still a large deviation in the HPLC detection method, resulting in that the detection value of 2,5-DKG in previous studies is much greater than its real value (Qazi et al., 1991). Based on this problem, the method of pure enzyme catalysis can effectively avoid the shortcomings of no standard or insufficient purity of standard, and more accurately quantify 2,5-DKG in the reaction system.

The chassis strain *G. oxydans* ATCC9937 screened by the new quantitative method has a strong membrane dehydrogenase system (Bringer and Bott, 2016; Zou et al., 2017; Jin et al., 2019; Zhou et al., 2019; Stefanie et al., 2021), only about 10% D-glucose is phosphorylated into the pentose phosphate pathway (PPP pathway) after entering the cell and is used for oxidative function and cell growth (Krajewski et al., 2010). Most D-glucose is oxidized in its periplasmic space (Dai et al., 2022) and the final product of oxidation is 2,5-DKG. Some strains cannot completely consume D-gluconic acid, resulting in the conversion of D-gluconic acid to 2-KG becoming the rate-limiting factor, but this situation did not exist in *G. oxydans* ATCC9937, which can completely consume the D-gluconic acid and 2-KG produced in the fermentation broth, but the final 2,5-DKG is less, and the conversion from 2-KG to 2,5-DKG is low.

The conventional idea of metabolic engineering is to directly overexpress the rate-limiting enzyme to improve the yield, but this operation is not conducive to the discovery of side effects. 2-KG can be completely consumed, but the yield of its oxidized product 2,5-DKG is very low. When the cause of this situation is unclear, it is very important to first verify whether there are side reactions and convert 2-KG into other substances. To find the speed-limiting factor more accurately, this study first knocked out the possible rate-limiting factor *kgdSLC*, and then verified its overexpression. However, the knockout and overexpression results of *kgdSLC* showed that the metabolic pathway of by-products of 2-KG did not seem to exist or was very few. 2-KG is a relatively stable compound, which can exist in the fermentation broth for a long time without other degradation reactions. The powerful periplasmic dehydrogenase system of *G. oxydans* ATCC9937 can ensure the continuous and efficient reaction of D-glucose to 2,5-DKG, overexpression of *kgdSLC* by genetic engineering could not further increase the yield of 2,5-DKG. 2-KDGH is not the main rate-limiting factor of the reaction, and the main speed-limiting factor should be the degradation of 2-KG. Many studies have mentioned that 2,5-DKG is easy to degrade, but no research has proved how it is degraded. The data provided in this study showed that the main reason for the low yield of 2,5-DKG is its continuous degradation in the fermentation broth, and the main mode of degradation is browning.

Many substances will be browning during storage (Tan et al., 2020; Fatouros et al., 2021). Browning mainly includes enzymatic and non-enzymatic two pathways (Paravisini and Peterson, 2019; Pham et al., 2020). The browning of 2,5-DKG is mainly through non-enzymatic reaction. This color change was similar to L-ascorbic acid browning, which is caused by a series of complex reactions during its

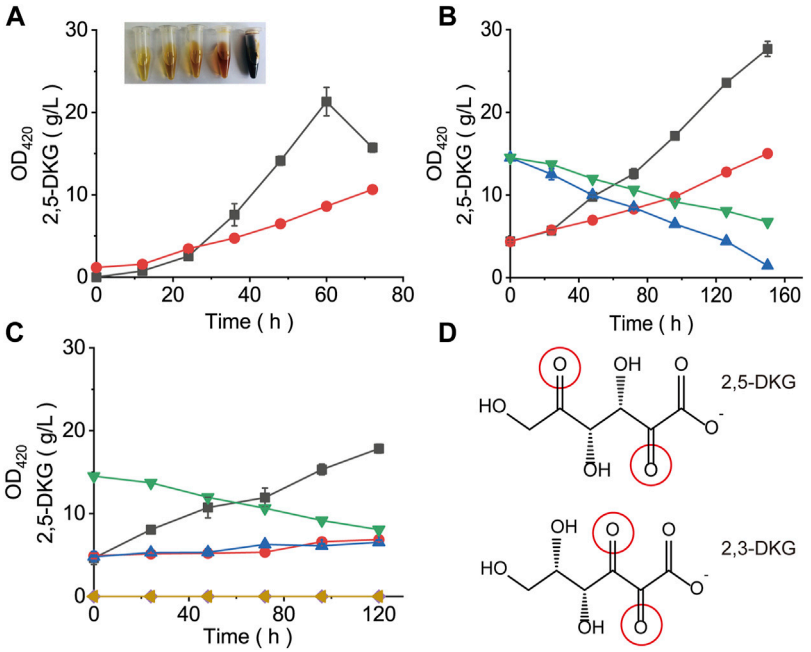

FIGURE 4 | Browning formation (absorbance at 420 nm) and the concentration of 2,5-DKG under different conditions. **(A)** Concentration of 2,5-DKG and absorbance at 420 nm in fermentation broth. Black = 2,5-DKG concentration. Red = Absorbance at 420 nm. With increased fermentation time, 2,5-DKG levels gradually decreased, and the degree of browning gradually increased. **(B)** 2,5-DKG concentration and absorbance at 420 nm in broth plus glutamine. Red = OD_{420} in control cells without glutamine. Black = OD_{420} in the experimental group plus glutamine. Green = 2,5-DKG concentration in control cells. Blue = 2,5-DKG concentration in the experiment group. **(C)** 2,5-DKG concentration and absorbance at 420 nm in broth plus browning inhibitor. Black = OD_{420} in control cells without a browning inhibitor. Blue = OD_{420} in the experimental group plus the browning inhibitor sodium sulfite. Red = OD_{420} in the experimental group plus the browning inhibitor potassium sulfite. Green = 2,5-DKG concentration in control cells. Yellow = 2,5-DKG concentration in the experiment group. **(D)** 2,5-DKG and 2,3-DKG structures.

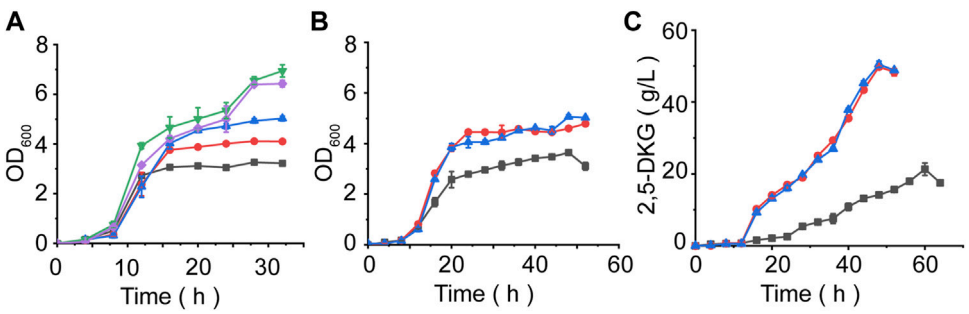

FIGURE 5 | Evaluating fermentation performances under different conditions. **(A)** *G. oxydans* ATCC9937 growth curve at different D-glucose concentrations. Black = 5 g/L D-glucose. Red = 10 g/L D-glucose. Blue = 15 g/L D-glucose. Green = 20 g/L D-glucose. Purple = 25 g/L D-glucose. **(B)** The effect of different feeding methods on OD_{600} values. **(C)** Time course of 2,5-DKG production using different feeding methods. Black = control, initial D-glucose concentration = 100 g/L. Blue: After initial glucose levels were consumed, further glucose was added in a constant-rate feeding mode. Red: Further glucose was added in a single-dose feed-batch mode after initial glucose quantities were consumed.

TABLE 3 | Comparison of productivity of 2,5-DKG in different literatures.

Substrate	Fermentation time (h)	Productivity of 2,5-DKG	Fermentation mode	Source
100 g/L glucose	120	0.55 g/L/h	Batch fermentation, 26°C	Qazi et al. (1991)
50 g/L glucose	150	0.31 g/L/h	Mixed fermentation, 30°C	Sulo et al. (2001)
25 g/L glucose + 25 g/L GA	32	0.08 g/L/h	Resting-cell system, 28°C	Ji and Gao (2001)
100 g/L glucose	60	0.36 g/L/h	Batch fermentation, 30°C	This study
20 g/L glucose	16	0.77 g/L/h	Batch fermentation, 30°C	
100 g/L glucose (20 g/L glucose + glucose feeding)	48	1.06 g/L/h	Fed-batch fermentation, 30°C	

degradation (Paravisini and Peterson, 2019), but is primarily caused by 2,3-DKG (2,3-diketo-L-gulonic acid) production (Forouhar et al., 2004). The hydration of 2,3-DKG occurs during degradation and generates colored substances (Penney and Zilva, 1945). As 2,5-DKG contained two carbonyls (**Figure 4D**), it may have had similar hydration reactions to 2,3-DKG, thereby producing colored substances. Previous studies suggested that 2,3-DKG may have similar antioxidant properties to L-ascorbic acid (Li et al., 2001). Whether 2,5-DKG is also prone to browning, due to its strong reductive capabilities, warrants further research. Therefore, using color deepening as a standard for 2,5-DKG generation is inaccurate. Thus, 2,5-DKG had no color, whereas a yellowish-brown color was caused by browning. Importantly, this browning required no specific temperature; even at 30°C, 2,5-DKG continued browning with increased content and fermentation time. Because the substances produced by browning are complex, we have not analyzed the detailed browning products for the time being, which may be targeted in subsequent studies. Moreover, the browning phenomenon was irreversible; the only way to slow down the process was to shorten fermentation times and accelerate substrate conversion to 2,5-DKG.

In previous studies, fermentation 2,5-DKG usually takes more than 120 h. However, continuous aeration and stirring during fermentation will further accelerate the browning of 2,5-DKG. Too long fermentation time leads to a large amount of browning of 2,5-DKG in the fermentation broth, resulting in very low actual purity of 2,5-DKG. Although the powerful dehydrogenase system enables to oxidize sugar alcohols in the reaction system without excessive biomass (Zhou et al., 2019; Han et al., 2021), too high initial sugar concentration will still inhibit its growth rate and corresponding enzyme activity, resulting in the increase in reaction time. By adjusting the initial D-glucose concentration in the broth, cell growth and substrate transformation efficiency were both accelerated. The time of bacterial transformation of substrate was also greatly shortened, the significant shortening of fermentation time reduced the browning rate of 2,5-DKG in the medium and greatly increased the final yield of 2,5-DKG. Browning will not only affect the accumulation of 2,5-DKG but also the dark substances produced by browning will stain the cell membrane, which will seriously affect the construction of the subsequent 2,5-DKG to 2-KLG pathway. Further research is required to analyze the main mechanisms underpinning 2,5-DKG browning, verify whether there are metabolites easy to combine with it to cause browning in the fermentation process, and further transform the metabolic pathway.

DATA AVAILABILITY STATEMENT

The original contributions presented in the study are included in the article/**Supplementary Material**; further inquiries can be directed to the corresponding author.

AUTHOR CONTRIBUTIONS

GL: methodology, investigation, formal analysis, writing—original draft. XS: investigation, writing—original draft, validation. WZ, SY, and GZ: formal analysis, writing—review and editing. JC: funding acquisition. JZ: supervision, funding acquisition, writing—review and editing.

FUNDING

This work was supported by the National Key Research and Development Program of China (2019YFA0904900) and National Natural Science Foundation of China (Key Program, 31830068).

SUPPLEMENTARY MATERIAL

The Supplementary Material for this article can be found online at: https://www.frontiersin.org/articles/10.3389/fbioe.2022.918277/full#supplementary-material

REFERENCES

Anderson, S., Marks, C. B., Lazarus, R., Miller, J., Stafford, K., Seymour, J., et al. (1985). Production of 2-Keto-L-Gulonate, an Intermediate in L-Ascorbate Synthesis, by a Genetically Modified *Erwinia Herbicola*. *Science* 230 (4722), 144–149. doi:10.1126/science.230.4722.144

Andreeva, I. G., Golubeva, L. I., Kuvaeva, T. M., Gak, E. R., Katashkina, J. I., and Mashko, S. V. (2011). Identification of *Pantoea Ananatis* Gene Encoding Membrane Pyrroloquinoline Quinone (PQQ)-dependent Glucose Dehydrogenase and pqqABCDEF Operon Essential for PQQ Biosynthesis. *FEMS. Microbiol. Lett.* 318 (1), 55–60. doi:10.1111/j.1574-6968.2011.02240.x

Anitra, C., and Silvia, M. (2017). Vitamin C and Immune Function. *Nutrients* 9 (11), 1211. doi:10.3390/nu91112111

Badwar, M. R., Bakliwal, A. A., Talele, S. G., and Jadhav, A. G. (2020). "Generation of Natural Pharmaceuticals Based on Microbial Transformation of Herbal Constituents," in *Applied Pharmaceutical Science and Microbiology: Novel Green Chemistry Methods and Natural Products*, 61–82. doi:10.1201/9781003019565-4

Bringer, S., and Bott, M. (2016). "Central Carbon Metabolism and Respiration in Gluconobacter Oxydans," in *Acetic Acid Bacteria*, 235–253. doi:10.1007/978-4-431-55933-7_11

Cendrowski, A., Królak, M., and Kalisz, S. (2021). Polyphenols, L-Ascorbic Acid, and Antioxidant Activity in Wines from Rose Fruits (Rosa Rugosa). *Molecules* 26 (9), 2561. doi:10.3390/molecules26092561

Chen, Y., Liu, L., Yu, S., Li, J., Zhou, J., and Chen, J. (2021). Identification of Gradient Promoters of *Gluconobacter Oxydans* and Their Applications in the Biosynthesis of 2-Keto-L-Gulonic Acid. *Front. Bioeng. Biotechnol.* 9, 673844. doi:10.3389/fbioe.2021.673844

Dai, L., Jiang, W., Jia, R., Zhou, X., and Xu, Y. (2022). Directional Enhancement of 2-Keto-Gluconic Acid Production from Enzymatic Hydrolysate by Acetic Acid-Mediated Bio-Oxidation with *Gluconobacter Oxydans*. *Bioresour. Technol.* 348, 126811. doi:10.1016/j.biortech.2022.126811

Fatouros, A., Einhorn-Stoll, U., Kastner, H., Drusch, S., and Kroh, L. W. (2021). Influence of the Carboxylic Function on the Degradation of D-Galacturonic Acid and its Polymers. *J. Agric. Food Chem.* 69 (32), 9376–9382. doi:10.1021/acs.jafc.1c02388

Forouhar, F., Lee, I., Benach, J., Kulkarni, K., Xiao, R., Acton, T. B., et al. (2004). A Novel NAD-Binding Protein Revealed by the Crystal Structure of 2,3-Diketo-L-

Gulonate Reductase (*YiaK*). *J. Biol. Chem.* 279 (13), 13148–13155. doi:10.1074/jbc.M313580200

Han, J., Hua, X., Zhou, X., Xu, B., Wang, H., Huang, G., et al. (2021). A Cost-Practical Cell-Recycling Process for Xylonic Acid Bioproduction from Acidic Lignocellulosic Hydrolysate with Whole-Cell Catalysis of *Gluconobacter Oxydans*. *Bioresour. Technol.* 333, 125157. doi:10.1016/j.biortech.2021.125157

Islam, J., Chilkoor, G., Jawaharraj, K., Dhiman, S. S., Sani, R., and Gadhamshetty, V. (2020). Vitamin-C-enabled Reduced Graphene Oxide Chemistry for Tuning Biofilm Phenotypes of Methylotrophs on Nickel Electrodes in Microbial Fuel Cells. *Bioresour. Technol.* 300, 122642. doi:10.1016/j.biortech.2019.122642

Jeudy, S., Monchois, V., Maza, C., Claverie, J.-M., and Abergel, C. (2006). Crystal Structure of *Escherichia coli DkgA*, a Broad-Specificity Aldo-Keto Reductase. *Proteins* 62 (1), 302–307. doi:10.1002/prot.20710

Ji, A., and Gao, P. (2001). Substrate Selectivity of *Gluconobacter Oxydans* for Production of 2,5-Diketo-D-Gluconic Acid and Synthesis of 2-Keto-L-Gulonic Acid in a Multienzyme System. *Appl. Biochem. Biotechnol.* 94 (3), 213–224. doi:10.1385/abab:94:3:213

Jin, C., Hou, W., Yao, R., Zhou, P., Zhang, H., and Bao, J. (2019). Adaptive Evolution of *Gluconobacter Oxydans* Accelerates the Conversion Rate of Non-glucose Sugars Derived from Lignocellulose Biomass. *Bioresour. Technol.* 289, 121623. doi:10.1016/j.biortech.2019.121623

Jindra, M. A., Reed, D. W., Thompson, V. S., and Daubaras, D. L. (2016). *Developing a Scalable System for Biorecovery of Critical Materials from Industrial Waste with* Gluconobacter Oxydans. Idaho Falls, ID (United States): Idaho National Lab.INL.

Kaswurm, V., Van Hecke, W., Kulbe, K. D., and Ludwig, R. (2013). Engineering of a Bi-enzymatic Reaction for Efficient Production of the Ascorbic Acid Precursor 2-Keto-L-Gulonic Acid. *Biochem. Eng. J.* 79, 104–111. doi:10.1016/j.bej.2013.07.010

Kataoka, N., Matsutani, M., Yakushi, T., and Matsushita, K. (2015). Efficient Production of 2,5-Diketo-D-Gluconate via *Heterologous* Expression of 2-ketogluconate Dehydrogenase in *Gluconobacter Japonicus*. *Appl. Environ. Microbiol.* 81 (10), 3552–3560. doi:10.1128/AEM.04176-14

Krajewski, V., Simic´, P., Mouncey, N. J., Bringer, S., Sahm, H., and Bott, M. (2010). Metabolic Engineering of *Gluconobacter Oxydans* for Improved Growth Rate and Growth Yield on Glucose by Elimination of Gluconate Formation. *Appl. Environ. Microbiol.* 76 (13), 4369–4376. doi:10.1128/AEM.03022-09

Lei, Q., Zeng, W., Zhou, J., and Du, G. (2019). Efficient Separation of Alpha-Ketoglutarate from *Yarrowia Lipolytica* WSH-Z06 Culture Broth by Converting Pyruvate to L-Tyrosine. *Bioresour. Technol.* 292, 121897. doi:10.1016/j.biortech.2019.121897

Li, M., Suzuki, E., and Kurata, T. (2001). Effects of 2,3-Diketo-L-Gulonic Acid on the Oxidation of *Yolk Lipoprotein*. *Biosci. Biotechnol. Biochem.* 65 (3), 599–604. doi:10.1271/bbb.65.599

Marin-Cevada, V., and Fuentes-Ramirez, L. E. (2016). Pink Disease, a Review of an Asymptomatic Bacterial Disease in Pineapple. *Rev. Bras. Frutic.* 38 (3), 8. doi:10.1590/0100-29452016949

Nikel, P. I., and de Lorenzo, V. (2018). Pseudomonas Putida as a Functional Chassis for Industrial Biocatalysis: from Native Biochemistry to Trans-metabolism. *Metab. Eng.* 50, 142–155. doi:10.1016/j.ymben.2018.05.005

Paravisini, L., and Peterson, D. G. (2019). Mechanisms Non-Enzymatic Browning in Orange Juice during Storage. *Food Chem.* 289, 320–327. doi:10.1016/j.foodchem.2019.03.049

Pardo-Planas, O., Prade, R. A., Müller, M., Atiyeh, H. K., and Wilkins, M. R. (2017). Prevention of Melanin Formation during Aryl Alcohol Oxidase Production under Growth-Limited Conditions Using an *Aspergillus nidulans* Cell Factory. *Bioresour. Technol.* 243, 874–882. doi:10.1016/j.biortech.2017.06.183

Penney, J. R., and Zilva, S. S. (1945). The Isolation of Barium and Calcium Diketo-L-Gulonates and the Biological Significance of 2:3-Diketo-L-Gulonic Acid. *Biochem. J.* 39 (1), 1–4. doi:10.1042/bj0390001b

Pham, H. T. T., Kityo, P., Buvé, C., Hendrickx, M. E., and Van Loey, A. M. (2020). Influence of pH and Composition on Nonenzymatic Browning of Shelf-Stable Orange Juice during Storage. *J. Agric. Food Chem.* 68 (19), 5402–5411. doi:10.1021/acs.jafc.9b07630

Qazi, G. N., Parshad, R., Verma, V., Chopra, C. L., Buse, R., Träger, M., et al. (1991). Diketo-Gluconate Fermentation by Gluconobacter Oxydans. *Enzyme. Microb. Technol.* 13 (6), 504–507. doi:10.1016/0141-0229(91)90010-8

Qin, Z., Yu, S., Liu, L., Wang, L., Chen, J., and Zhou, J. (2021). A SacB-Based System for Diverse and Multiple Genome Editing in *Gluconobacter Oxydans*. *J. Biotechnol.* 338, 31–39. doi:10.1016/j.jbiotec.2021.07.004

Reddy, R. C., Devaranavadagi, B., Yendigeri, S. M., Bagali, S., Kulkarni, R. V., and Das, K. K. (2020). Effect of L-Ascorbic Acid on Nickel-Induced Alteration of Cardiovascular Pathophysiology in *Wistar Rats*. *Biol. Trace. Elem. Res.* 195 (1), 178–186. doi:10.1007/s12011-019-01829-w

Schmitz, A. M., Pian, B., Medin, S., Reid, M. C., Wu, M., Gazel, E., et al. (2021). Generation of a *Gluconobacter Oxydans* Knockout Collection for Improved Extraction of Rare Earth Elements. *Nat. Commun.* 12 (1), 6693. doi:10.1038/s41467-021-27047-4

Scott, B., Swanson, B. A., Wu, S., Alisha, J., and Stephen, A. (2002). Alteration of the Specificity of the Cofactor-Binding Pocket of *Corynebacterium* 2,5-Diketo-D-Gluconic Acid Reductase A. *Protein. Eng.* 15 (2), 131–140. doi:10.1093/protein/15.2.131

Shinagawa, E., Matsushita, K., Adachi, O., and Ameyama, M. (2014). Purification and Characterization of 2-Keto-D-Gluconate Dehydrogenase from *Gluconobacter Melanogenus*. *Agric. Biol. Chem.* 45 (5), 1079–1085. doi:10.1080/00021369.1981.10864678

Sonoyama, T., Tani, H., Matsuda, K., Kageyama, B., Tanimoto, M., Kobayashi, K., et al. (1982). Production of 2-Keto-L-Gulonic Acid from D-Glucose by Two-Stage Fermentation. *Appl. Environ. Microbiol.* 43 (5), 1064–1069. doi:10.1128/aem.43.5.1064-1069.1982

Sonoyama, T., Yagi, S., and Kageyama, B. (1988). Facultatively Anaerobic Bacteria Showing High Productivities of 2,5-Diketo-D-Gluconate from D-Glucose. *Agric. Biol. Chem.* 52 (3), 667–674. doi:10.1271/bbb1961.52.667

Stefanie, S., Angela, K., Toshiharu, Y., Andrei, F., Tino, P., Helga, E., et al. (2021). FNR-type Regulator *GoxR* of the Obligatorily Aerobic Acetic Acid Bacterium *Gluconobacter Oxydans* Affects Expression of Genes Involved in Respiration and Redox Metabolism. *Appl. Environ. Microbiol.* 87 (11), e00195–00121. doi:10.1128/aem.00195-21

Sulo, P., Hudecová, D., Properová, A., Bašnák, I., and Sedláček, I. (2001). 2,5-Diketo- D-Gluconate Production by a Mixed Culture of Two Newly-Isolated Strains: *Flavimonas Oryzihabitans* and *Pseudomonas cepacia*. *Biotechnol. Lett.* 23 (9), 693–696. doi:10.1023/a:1010360603287

Tan, J., de Bruijn, W. J. C., van Zadelhoff, A., Lin, Z., and Vincken, J.-P. (2020). Browning of Epicatechin (EC) and Epigallocatechin (EGC) by Auto-Oxidation. *J. Agric. Food Chem.* 68 (47), 13879–13887. doi:10.1021/acs.jafc.0c05716

Tavares, W., Dong, S., Jin, W., Yang, Y., Han, K., Zha, F., et al. (2018). Effect of Different Cooking Conditions on the Profiles of Maillard Reaction Products and Nutrient Composition of Hairtail (*Thichiurus Lepturus*) Fillets. *Food Res. Int.* 103, 390–397. doi:10.1016/j.foodres.2017.10.063

Wang, C. Y., Li, Y., Gao, Z. W., Liu, L. C., Zhang, M. Y., Zhang, T. Y., et al. (2018). Establishing an Innovative Carbohydrate Metabolic Pathway for Efficient Production of 2-Keto-L-Gulonic Acid in *Ketogulonicigenium Robustum* Initiated by Intronic Promoters. *Microb. Cell. Fact.* 17 (81), 81. doi:10.1186/s12934-018-0932-9

Wang, P., Zeng, W., Xu, S., Du, G., Zhou, J., and Chen, J. (2018). Current Challenges Facing One-step Production of L-Ascorbic Acid. *Biotechnol. Adv.* 36 (7), 1882–1899. doi:10.1016/j.biotechadv.2018.07.006

Vivek, N., Hazeena, S. H., Alphy, M. P., Kumar, V., Magdouli, S., Sindhu, R., et al. (2021). Recent Advances in Microbial Biosynthesis of C3 – C5 Diols: Genetics and Process Engineering Approaches. *Bioresour. Technol.* 322, 124527. doi:10.1016/j.biortech.2020.124527

Xin, D., Blossom, B. M., Lu, X., and Felby, C. (2022). Improving Cellulases Hydrolytic Action: An Expanded Role for Electron Donors of Lytic Polysaccharide Monooxygenases in Cellulose Saccharification. *Bioresour. Technol.* 346, 126662. doi:10.1016/j.biortech.2021.126662

Zeng, W., Wang, P., Li, N., Li, J., Chen, J., and Zhou, J. (2020). Production of 2-Keto-L-Gulonic Acid by Metabolically Engineered *Escherichia coli*. *Bioresour. Technol.* 318, 124069. doi:10.1016/j.biortech.2020.124069

Zhang, Y.-h., Lin, J.-y., Bai, L., Huang, M., Chen, H.-q., Yao, S., et al. (2018). Antioxidant Capacities of *Bacillus Endophyticus* ST-1 and *Ketogulonicigenium Vulgare* 25B-1 in Vitamin C Fermentation. *Biotechnol. Biotechnol. Equip.* 32 (3), 628–637. doi:10.1080/13102818.2018.1447854

Zhao, D., Le, T. T., Larsen, L. B., Li, L., Qin, D., Su, G., et al. (2017). Effect of Glycation Derived from α-dicarbonyl Compounds on the *In Vitro* Digestibility of β-casein and

β-lactoglobulin: A Model Study with Glyoxal, Methylglyoxal and Butanedione. *Food Res. Int.* 102, 313–322. doi:10.1016/j.foodres.2017.10.002

Zhou, P., Yao, R., Zhang, H., and Bao, J. (2019). Unique Glucose Oxidation Catalysis of *Gluconobacter Oxydans* Constitutes an Efficient Cellulosic Gluconic Acid Fermentation Free of Inhibitory Compounds Disturbance. *Biotechnol. Bioeng.* 116 (9), 2191–2199. doi:10.1002/bit.27020

Zou, X., Lin, J., Mao, X., Zhao, S., and Ren, Y. (2017). Biosynthesis of L-Erythrose by Assembly of Two Key Enzymes in Gluconobacter Oxydans. *J. Agric. Food Chem.* 65 (35), 7721–7725. doi:10.1021/acs.jafc.7b02201

Conflict of Interest: The authors declare that the research was conducted in the absence of any commercial or financial relationships that could be construed as a potential conflict of interest.

Publisher's Note: All claims expressed in this article are solely those of the authors and do not necessarily represent those of their affiliated organizations, or those of the publisher, the editors, and the reviewers. Any product that may be evaluated in this article, or claim that may be made by its manufacturer, is not guaranteed or endorsed by the publisher.

frontiers | Frontiers in Bioengineering and Biotechnology

TYPE Original Research
PUBLISHED 29 August 2022
DOI 10.3389/fbioe.2022.978211

OPEN ACCESS

EDITED BY
Farshad Darvishi,
Alzahra University, Iran

REVIEWED BY
Kouhei Mizuno,
Kitakyushu College, Japan
Zheng-Jun Li,
Beijing University of Chemical Technology, China

*CORRESPONDENCE
Xuemei Lu,
luxuemei@sdu.edu.cn
Qingsheng Qi,
qiqingsheng@sdu.edu.cn

SPECIALTY SECTION
This article was submitted to Synthetic Biology,
a section of the journal
Frontiers in Bioengineering and Biotechnology

RECEIVED 25 June 2022
ACCEPTED 08 August 2022
PUBLISHED 29 August 2022

CITATION
Ma S, Su T, Liu J, Wang Q, Liang Q, Lu X and Qi Q (2022), Random genome reduction coupled with polyhydroxybutyrate biosynthesis to facilitate its accumulation in Escherichia coli.
Front. Bioeng. Biotechnol. 10:978211.
doi: 10.3389/fbioe.2022.978211

Random genome reduction coupled with polyhydroxybutyrate biosynthesis to facilitate its accumulation in *Escherichia coli*

Shuai Ma, Tianyuan Su, Jinming Liu, Qian Wang, Quanfeng Liang, Xuemei Lu* and Qingsheng Qi*

State Key Laboratory of Microbial Technology, Shandong University, Qingdao, China

Genome reduction has been emerged as a powerful tool to construct ideal chassis for synthetic biology. Random genome reduction couple genomic deletion with growth and has the potential to construct optimum genome for a given environment. Recently, we developed a transposon-mediated random deletion (TMRD) method that allows the random and continuous reduction of *Escherichia coli* genome. Here, to prove its ability in constructing optimal cell factories, we coupled polyhydroxybutyrate (PHB) accumulation with random genome reduction and proceeded to reduce the *E. coli* genome. Five mutants showed high biomass and PHB yields were selected from 18 candidates after ten rounds of genome reduction. And eight or nine genomic fragments (totally 230.1–270.0 Kb) were deleted in their genomes, encompassing 4.95%–5.82% of the parental MG1655 genome. Most mutants displayed better growth, glucose utilization, protein expression, and significant increase of electroporation efficiency compared with MG1655. The PHB content and concentration enhanced up to 13.3%–37.2% and 60.2%–102.9% when batch fermentation was performed in M9-glucose medium using the five mutants. Particularly, in mutant H16, lacking 5.28% of its genome, the increase of biomass and PHB concentration were more than 50% and 100% compared with MG1655, respectively. This work expands the strategy for creating streamlined chassis to improve the production of high value-added products.

KEYWORDS

random genome reduction, polyhydroxybutyrate, glucose utilization, growth, *E. coli*

Introduction

As for engineered microbes cultured in stable laboratory conditions, many genomic regions are considered redundant, e.g., stress response genes, insertion sequence elements, transposons, and so forth, and may even increase mutagenesis and cause the burden on cellular growth and metabolism (Kurokawa and Ying, 2020). Synthetic biologists have

been devoting to designing and modifying microorganisms to function as cell factories in which harbored a streamlined genome for full functionality and a metabolic network able to more effectively synthesize the desired products (Chi et al., 2019).

Genome reduction has been developed as a feasible strategy to obtain streamlined chassis for enhanced production of high value-added products. In many bacteria, moderate genome reduction by removing multiple dispensable genomic regions has been proved to be able to optimize metabolic pathways, enhance the heterologous protein productivity, and improve the growth and physiological performance (Kolisnychenko et al., 2002; Posfai et al., 2006; Mizoguchi et al., 2008; Komatsu et al., 2010; Wang et al., 2018; Liang et al., 2020; Qiao et al., 2020; Zhang et al., 2020). For instance, the MDS (multiple-deletion series) strains, lacking 8.11%–14.3% of genome sequences (including mobile elements, virulence genes, and so forth) in *Escherichia coli* MG1655, showed some favorable properties, normal growth, increased electroporation efficiency and protein expression level (Kolisnychenko et al., 2002; Posfai et al., 2006). *E. coli* MGF-01 lost 22% of the original genomic sequence and achieved a 2.4-fold increase in L-threonine production (Mizoguchi et al., 2008). After removal of 16.8%–18.5% of the original genome sequences (the large left subtelomeric region), a series of genome-minimized *Streptomyces avermitilis* strains were obtained in which higher heterologous expression of three secondary metabolites, streptomycin, cephamycin C and pladienolide were achieved while leaving growth and primary metabolism unaffected (Komatsu et al., 2010). Deletion of the genomic islands, phage-related genes, and some other nonessential genomic regions (accounting for 1.2%–4.12% of the total genome sizes) facilitated the transformation efficiency, heterologous protein expression, and polyhydroxyalkanoate production in *Pseudomonas putida* (Wang et al., 2018; Liang et al., 2020). The increase of multi-stress tolerance and nisin immunity was achieved in *Lactococcus lactis* when deleting 19.7-kb of prophage-related fragments (Qiao et al., 2020). The growth and surfactin production of *Bacillus amyloliquefaciens* was increased by deleting ~4.18% of genome sequences (Zhang et al., 2020). The DT (deletions of transposons) series genome-reduced *Schlegelella brevitalea* mutants were rationally constructed by sequential deletions 0.3%–4.9% of its genome, including forty-four transposases, two prophage-like regions, and seven genomic islands, and showed better growth characteristics with alleviated cell autolysis, and improved yields of six proteobacterial natural products (Liu et al., 2021).

Common methods to construct genome-simplified chassis were based on rational design and analysis of the essential DNA elements, followed by the targeted deletion of large dispensable DNA fragments *via* seamless genome deletion method (Choe et al., 2016). The limitation of rational design strategy is the difficulty to judge the necessity of targeted regions and systematic investigate the interrelation of genome deletion and phenotype due to incomplete knowledge of complex genome function and interactions. That result in decreased growth, perturbations of the physiological properties, and unstable productivity of recombinant protein or desired products in genome-reduced strains obtained by rational design (Iwadate et al., 2011; Li et al., 2016; Tsuchiya et al., 2018). To overcome this limitation, researchers have proposed random genome reduction strategies (Suzuki et al., 2008; Vernyik et al., 2020; Shaw et al., 2021)that can couple genomic deletion with cellular growth, generate favorable deletion combinations in genome, and screen cells with fitness in different environment. To date, some random genome reduction methods have been completed to the proof-of-concept stage, but they are not efficient enough to construct desired chassis cells for application (Suzuki et al., 2008; Vernyik et al., 2020; Shaw et al., 2021). In previous study, we developed a random and continuous genome reduction method, named as "transposon-mediated random deletion (TMRD)," which enables the reduction of *E. coli* genome by random deletion accompanied by simultaneous enrichment of the cells with environment fitness (Ma et al., 2022). We have proved the feasibility of this method and completed five rounds of genome reduction using *E. coli* MG1655 in rich LB medium (Ma et al., 2022), but it remains unclear that whether other appropriate conditions can be employed to create optimal cell factories for different application purposes.

Polyhydroxybutyrate (PHB) are a class of biopolymers that can be accumulated in microorganism cells under unfavorable growth conditions as both an energy and carbon store (Li et al., 2020). The PHB competent cells can be easily screened by Nile red staining as the legible red colonies are produced when PHB are combined with Nile red dye (Li et al., 2020). Here, we combined the PHB biosynthesis with random deletion and aimed at investigating whether improved PHB accumulation by engineered *E. coli* can be accomplished by random genome reduction. To this end, we continued to reduce the *E. coli* MG1655 genome *via* TMRD method while screening the PHB competent cells by Nile red assay. The mutants with high PHB accumulation were chosen to determine the genomic deletions, growth features, glucose utilization, transformation efficiency, protein expression level, and PHB accumulation compared with the original strain.

Materials and methods

Bacterial strains, culture medium, and reagents

All strains used in this study were shown in Table 1. The *E. coli* K-12 strain DH5α was used as the host strain for molecular cloning and manipulation of plasmids. The parental *E. coli*

TABLE 1 Strains and plasmids used in this work.

Strains	Genotypes	Source
E. coli DH5α	Strain K-12, F⁻ *end*A1 thi-1 *gln*V4 4*rel*A1 *rec*A1 *deo*R *gyr*A96 *nup*G *φ80dlac*ZΔM15 Δ(*lac*ZYA-*arg*F) U169 *hsd*R17 (rk^-, mk^+) λ^-	Invitrogen
E. coli MG1655	F- lambda- *ilv*G- *rfb*-50 *rph*-1	Invitrogen
H2	Mutants. Random deletion of ~270 Kb from MG1655	In this study
H5	Mutants. Random deletion of ~230 Kb from MG1655	In this study
H16	Mutants. Random deletion of ~245 Kb from MG1655	In this study
H19	Mutants. Random deletion of ~261 Kb from MG1655	In this study
H20	Mutants. Random deletion of ~236 Kb from MG1655	In this study
Plasmids	Descriptions	Source
pUC19	Cloning vector, pUC origin, Ap^R	Norrander et al. (1983)
pACYAC184	Cloning vector, P15A origin, Cm^R	Rose (1988)
pKTRED	pSC101 origin, containing Redαβγ recombinase system, Spc^R	Ma et al. (2022)
pBHR68	pUC origin, *phb*CAB operon from *Ralstonia eutropha,* Ap^R	Dila et al. (1990)
pBAC11rhi	Sing-copy bacterial artificial chromosome with a 92-kb fragment insertion, Cm^R	Ma et al. (2022)
pACYC-GFP	pACYAC184 containing GFP gene	In this study
p15A-PHB	P15A origin, *phb*CAB genes from *R. eutropha,* Ap^R	In this study
pSIP*pbh*CAB	pBHR68 containing stress-induced response fragment upstream of *rpo*S gene	In this study

MG1655 was used as the control strain in all experiments. Other strains used for genome reduction were same as previous report (Ma et al., 2022).

If it was not mentioned specifically, all experiments involving in bacterial culture growth were conducted using standard LB rich medium (10 g/L tryptone, 5 g/L yeast extract, and 5 g/L NaCl). The M9 basal medium composed of (g/L): $Na_2HPO_4.12H_2O$, 17.1; KH_2PO4, 3.0; NaCl, 0.5; and NH_4Cl, 1.0, supplemented with 1 mM $MgSO_4$, 0.1 mM $CaCl_2$, and 4 mg/L vitamin B1. M9-glucose media: M9 basal medium supplemented with appropriate glucose. When appropriate, ampicillin (Ap, 100 mg/L), chloramphenicol (Cm, 25 mg/L), isopropyl β-D-1-thiogalactopyranoside (IPTG, 1 mM) were supplemented into the cultures. Agar plates were prepared by adding 1.5% (w/v) agar to the media.

The Phanta Max Super-Fidelity DNA Polymerase (Vazyme, Qingdao, China) was utilized for the standard PCR amplifications. Green *Taq* Mix (Vazyme, Qingdao, China) was employed for colony PCR confirmation. MultiF Seamless Assembly Mix (RM20523) (Abclonal, Wuhan, China) was used for DNA fragment assembly and plasmid construction. Restriction enzymes and T4 DNA ligase were purchased from Thermo Fisher Biotech (Shanghai, China).

Plasmids construction

All the plasmids and primers used in this study were list in Table 1 and Supplementary Table S1, respectively. The plasmids used for random genome reduction were same as previous study (Ma et al., 2022). p15A-PHB, a medium-copy-number plasmid expressing the *phb*CAB operon (from *Ralstonia eutropha*) (Choi and Lee, 1999) under the control of Lac promoter, were constructed by assembling two DNA fragments with 20 bp homologous bases *in vitro via* the Gibson assembly. The P15A module was amplified from pACYC184 using primers p15A-F and p15A-R. The Amp-phbCAB module was amplified from the pBHR68 (Choi and Lee, 1999) plasmid using primers PHB-F and Ap-R. The stress-induced region fragment was amplificated using a pair of primers SIP-F/SIP-R with *E. coli* genome as template. The PCR product was digested with *Xba* I and *Bam*H I and subcloned into vector pBHR68 (Choi and Lee, 1999) in replacement of Lac promoter segment and resulted in plasmid pSIP*phb*CAB. To construct the pACYC-GFP, the module J23104-gfp was synthesized by Tsingke Biotech (Beijing, China) and then assembled into the linearized plasmid pACYC184 cut by *Xba* I and *Sac* I.

Random genome reduction for polyhydroxybutyrate accumulation

The genome reduction for PHB accumulation began with the genome-reduced library in the fifth cycle (R5) and followed the method of Ma et al. (2022) with minor modification. In detail, the cells from R5 library was used for the preparation of electrocompetent cells. Approximately 100 ng of plasmid (p15A-PHB) was electroporated into 50 μl of electrocompetent cells and spread onto LB agar plates with appropriate antibiotics. After incubation at 37°C overnight, all Ap^R colonies were collected and used as the starting library of genome reduction. Next, the random genome reduction was performed *via* TMRD

method. To select the PHB competent cells, in each cycle, after inducing the generation of genomic deletions, the cells were spreading onto the M9-glucose agar plates supplemented with appropriate Nile red dye (Sigma, St. Louis, Mo United States) to give a final concentration of 2 mM; and then the plates were incubated at 37°C for 48 h to allow the color reaction to develop. Based on the color difference, the redder colonies that incurred genomic deletions were picked with the naked eye and used as the starting library for the next new cycle.

Deletion efficiency, positions, and lengths analysis

Deletion efficiency was defined as the percentage of colonies loss of transposons against the total number of colonies analyzed and was measured following the previous method (Ma et al., 2022). The accumulative deletions in the genomes of the five selective mutants were identified by whole-genome sequencing and further verified *via* polymerase chain reaction (PCR) using genomic DNA as the template. The precise positions and lengths of the deletions in genome, and the base composition at junctions after repair of genome double-strands breaks, were confirmed by *Sanger* sequencing (Tsingke, Beijing, China). All PCR amplifications were performed using genomic DNA of the original *E. coli* MG1655 as the control.

Whole-genome sequencing and analysis were performed by GENEWIZ Biotech (Suzhou, China) using the Illumina NovaSeq platform. Using Cutadapt (v1.9.1) (Lindgreen, 2012) removed the sequcences of adaptors, PCR primers, content of N bases more than 10%, and bases of quality lower than 20. BWA (v0.7.17) (Li and Durbin, 2009) was employed to map clean data to the reference genome (NC_000913.3). Mapping results were processed by Picard (v2.25.7) for removal of duplication. The SNV and InDel was detected by GATK (V3.8.1) (McKenna et al., 2010) software. Annotations of single nucleotide variants (SNVs) and small insertions and deletions (InDels) were performed by Annovar (v21) (Odumpatta and Mohanapriya, 2020). The genomic structure variation was analyzed using Breakdancer (v1.1) (Chen et al., 2009) and CNVnator (v0.2.7) (Abyzov et al., 2011).

Physiological traits assessment

To determine the maximal growth rate of the five mutants, cells were cultivated on a 24-well microplate with continuous shaking on a microplate reader (Epoch 2, BioTek, Winooski, VT, United States) for 16–24 h in LB rich medium and M9 minimal medium supplemented with 10 g/L glucose. The maximal growth rate (h^{-1}) were measured and calculated as previously described (Ma et al., 2022). For the measurement of glucose utilization rate (g/L/h), overnight cultures were sub-cultured (1%, v/v) into 50 ml fresh M9 minimal medium supplemented with 10 g/L glucose, grown at 37°C, 220 rpm for 24 h. The glucose consumption (g/L) was quantified using a biosensor (SBA-40D, Biology Institute of Shandong Academy of Science, Shandong, China) (Feng et al., 2002) at the intervals of 1 or 2 h.

The preparation of electrocompetent cells and the assay of transformation efficiency were performed in accordance with the reported method (Ma et al., 2022). The transformation efficiency was defined as the number of colonies that formed on the corresponding antibiotic agar plates per microgram DNA (colony-forming units [cfu]/μg DNA). To assess the protein expression level, the genome-reduced strains carrying pACYC-GFP plasmids were cultivated on a 24-well microplate and grown at 37°C with continuous shaking for 24–48 h. The optical density (OD) at 600 nm and fluorescence intensity (FI, excitation at 485 nm and emission at 528 nm) were determined every 20 min using a Multi-Detection Microplate Reader (Synergy HT, Biotek, United States).

Polyhydroxybutyrate fermentation analysis

For PHB production, 10 ml starter cultures were grown overnight in LB medium at 37°C with shaking at 220 rpm. Starter cultures (2%, v/v) were inoculated into shaken-flasks containing 50 ml M9 minimal medium supplemented with 30 g/L glucose and 2.0 g/L yeast extract, grown at 37°C and 220 rpm for 48 h. About 1 ml of fermentation broth were collected every 6 h. The properly diluted broth was directly used to measure OD_{600} by a spectrophotometer (UNICO 2000, United States) and glucose consumption (g/L) by a biosensor. At 48 h, all the cultures were collected and centrifuged at 8,000 rpm for 15 min. Then, the cell pellets were harvested and lyophilized for 12 h to analyze the final biomass. For extraction of PHB, 1 ml chloroform, 850 μl methanol, and 150 μl sulfuric acid (98%, w/w) were added to 15–20 mg weighed cells, and then the mixture was incubated at 100°C for 1 h. Next, 1 ml H_2O was added into the mixture. After phage separation, the chloroform phase was used for gas chromatography analysis to quantify the intracellular PHB concentration (g/L) according to the method reported previously (Li et al., 2020).The biomass (g/L) was defined as the amount (dry weight) of cells per liter of culture broth. The PHB content (wt%) was defined as the percent ratio of PHB concentration to biomass.

Results

Coupled random genome reduction with polyhydroxybutyrate accumulation

TMRD generates random genomic deletion by combining Tn*5* transposition with CRISPR/Cas9 system. Initially, a

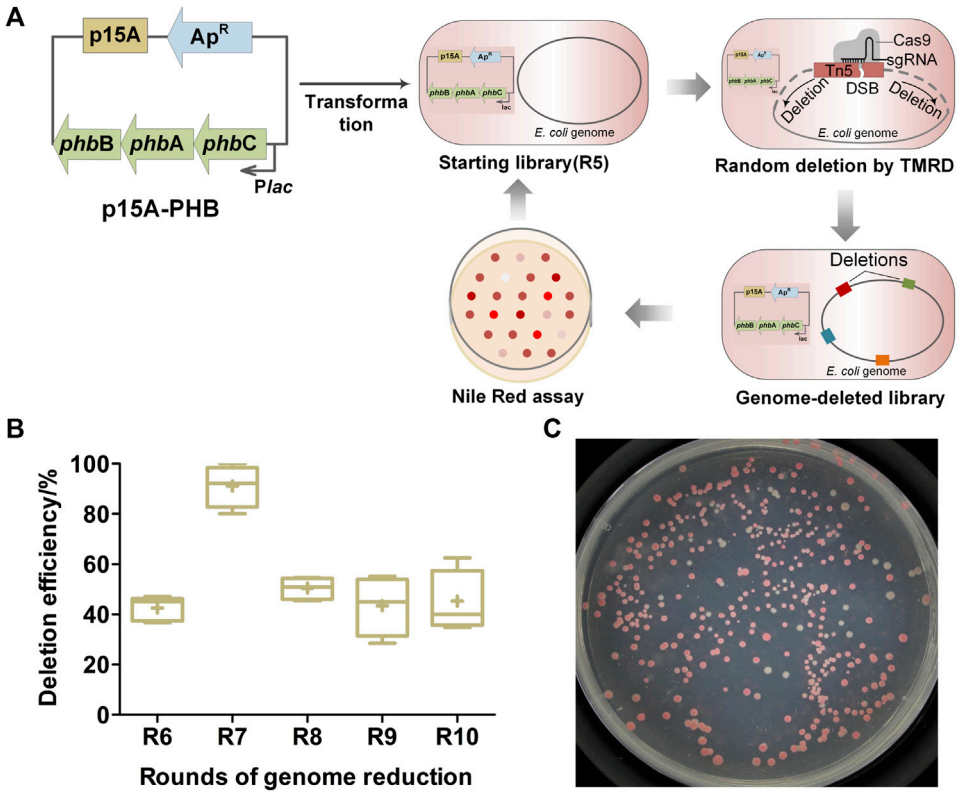

FIGURE 1
Random reduction of *E. coli* genome for PHB accumulation by transposon-mediated random deletion (TMRD) strategy. **(A)** Diagram of the coupled random genome reduction with PHB accumulation. Abbreviations: *phb*A, β-ketoacyl-CoA thiolase gene; *phb*B, acetoacetyl-CoA reductase gene; *phb*C, PHB polymerase gene; Ap^R, ampicillin resistance gene; P_{lac}, Lac promoter. DSB, double-strand break; sgRNA, sing-guide RNA. **(B)** Deletion efficiency of different TMRD cycles. Center lines show the medians. "+" represents the means. Box limits indicate the first and third quartiles. Whiskers show the maximum and minimum values. Six replicates were performed. At least 24 colonies were selected randomly in every replicate. **(C)** Screening of PHB competent cells by Nile red assay.

modified Tn5 transposon carrying the sgRNA target sequence and an antibiotic gene is randomly inserted into *E. coli* genome; then, a DSB at the insertional transposon is caused by the CRISPR/Cas9 system, followed by the DSB repair *via* the endogenous alternative end-joining mechanism accompanied by DNA fragment deletions of different sizes at random positions in the genome (Ma et al., 2022). The *in vivo* PHB biosynthesis pathway is conducted by the successive action of β-ketoacyl-CoA thiolase (PhbA), acetoacetyl-CoA reductase (PhbB), and PHB polymerase (PhbC) using acetyl-CoA (AcCoA) as the precursor (Turco et al., 2020). To couple random genome reduction with PHB accumulation, we introduced the PHB biosynthetic pathway into existing TMRD gene circuits and continued to reduce the *E. coli* genome *via* TMRD method (Figure 1A). Considering that the high-copy-number ColE1 replicon has been harnessed in TMRD circuits for genome reduction, a compatible plasmid carrying the medium-copy-number replicon (P15A origin) was selected to overexpress the three key genes involving in PHB biosynthetic pathway. Initially, the p15A-PHB was electroporated in the genome-reduced library of the fifth cycle (R5) obtained in previous study (Ma et al., 2022). Then, the further genome reduction was performed using the TMRD method with slight modification (Ma et al., 2022). In each cycle, the Nile red assay was used to screen the PHB competent cells. The redder colonies that incurred genomic deletions were selected and used as the starting library for the next cycle.

Five continuous cycles of genome reduction were accomplished using R5 as starting library. It took up about 10 days for an entire cycle, the deletion efficiencies were 40%–60% on average (Figure 1B), and approximately 100 genome-deleted cells were acquired at the end of each cycle. To screen the genome-reduced mutants with high PHB accumulation, cells from the libraries acquired at the last two rounds of reduction were spreading on M9-glucose agar plates supplemented with appropriate Nile red dye (Figure 1C), and a total of 18 darker red colonies were picked out. Then, the batch cultivation was performed to determine their PHB accumulations using

TABLE 2 The genomic deletions of the five selective mutants.

Strains	Number of deletions	Deletion events	Total sizes/bp (ratio[a])
H2	9	D1, D2, D3, D4, D5, D6, D8, D10, and D11	269,987 (5.82%)
H5	8	D1, D2, D3, D4, D5, D6, D7, and D8	229,758 (4.95%)
H16	9	D1, D2, D3, D4, D5, D6, D7, D8, and D9	244,962 (5.28%)
H19	9	D1, D2, D3, D4, D5, D6, D7, D8, and D12	260,608 (5.61%)
H20	9	D1, D2, D3, D4, D5, D6, D7, D8, and D13	236,324 (5.10%)

[a]The percentage of accumulative sizes accounts for the total length of *E. coli* MG1655 genome.

TABLE 3 Details of the deletion events in the five selective mutants.

No	Positions[a]	Sizes/bp	Number of genes	Length of (micro-) homology sequences[b]/bp	Descriptions
D1	4,506,953–4,589,174	82,222	83	0	Including ISs (IS911B, 60O, 30D, and 1F), restriction–modification system (*hsd*RSM, *mcr*BC, *mrr*)
D2	262,958–297,265	34,308	45	60	Cryptic prophage CP4-6
D3	2,457,372–2,503,630	46,259	48	1	Including cryptic prophage CPS-53
D4	4,302,186–4,321,787	19,602	23	0	—
D5	3,859,376–3,862,064	2,689	3	1	—
D6	2,102,833–2,123,824	20,992	20	9	Including IS5I
D7	3,581,911–3,583,427	1,517	2	0	—
D8	2,290,117–2,312,285	22,169	24	3	—
D9	1,196,220–1,211,423	15,204	26	11	Including cryptic prophage e14, restriction–modification system (*mcr*A)
D10	4,493,777–4,504,672	10,896	11	3	Including IS2K, IS4, cryptic prophage PR-Y
D11	4,069,828–4,100,677	30,850	29	5	—
D12	1,076,613–1,107,891	31,279	31	2	Including IS3D
D13	3,296,666–3,303,231	6,566	10	6	—

[a]Numbers correspond to the NCBI, reference genome NC_000913.3.
[b]The length of (micro-) homology sequences at the borders of genome double-strands breaks junction. IS, insertion sequence.

minimal M9 medium supplemented with glucose as sole carbon source. The 18 mutants showed different final cell dry weight, PHB contents and concentrations, with the range of 1.35–3.84 g/L, 10–25 wt% and 0.2–0.9 g/L, respectively (Supplementary Figure S1). Five of them (H2, H5, H16, H19, and H20) showed both higher final cell dry weight and PHB yields were selected for further studies (Supplementary Figure S1).

Deletion sizes and positions analysis of the mutants *via* whole-genome sequencing

Five mutants were selected from the 18 candidates in consideration of the final cell dry weight and PHB yield and subjected to whole-genome sequencing to characterize the accumulative DNA deletion fragments. The five strains were found to have been accumulated to a total number of eight or nine DNA deletion fragments; and the total length of deletions were 230.0–270.0 Kb, encompassing 4.95%–5.82% of the genomic sequence of the parental strain MG1655 (Table 2). Among the five sequenced mutants, there were 13 deletion fragments of various lengths (1.5–82.2 Kb) that randomly distributed in different positions of the *E. coli* MG1655 genome (Table 3; Supplementary Figure S2). The number of deleted genes in these fragments ranged widely from 2 to 83, including some genes encoding insertion sequence elements, cryptic prophages, and restriction–modification system, as well as many other nonessential genes (Supplementary Table S5). The borders of most deletion events showed small micro-homologous sequences (1–11 bp) or no noticeable sequence homology (Supplementary Table S2, Table 3), implying the role of intracellular alternative

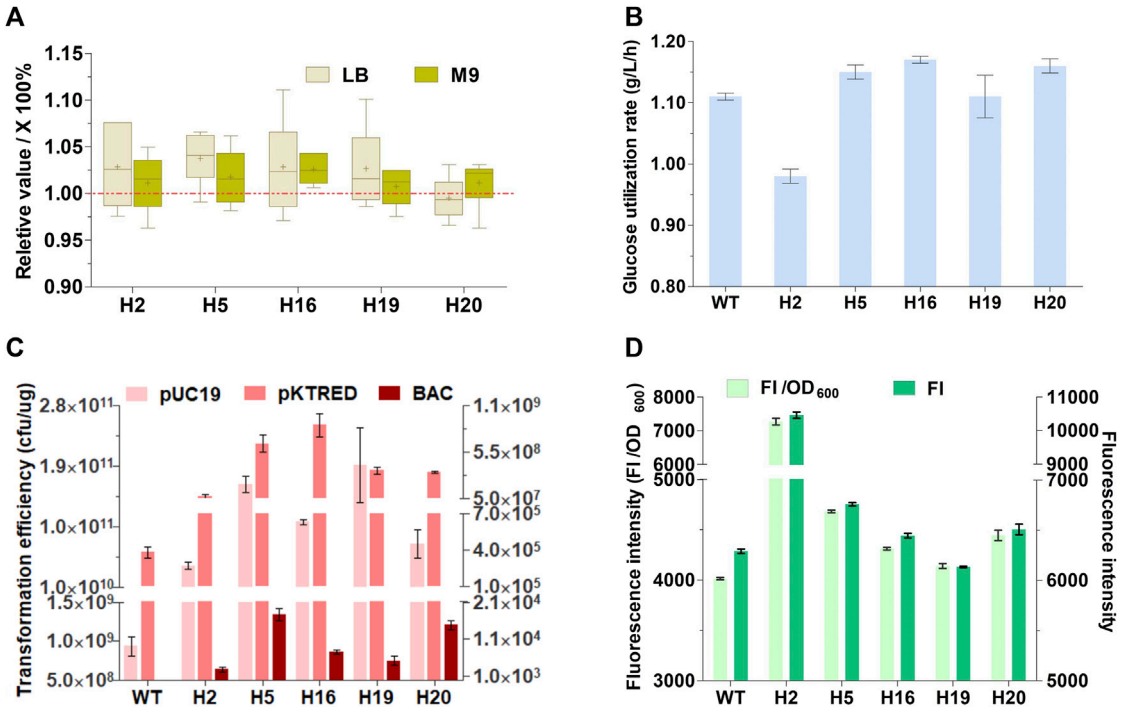

FIGURE 2
Physiological characteristics of the genome-reduced mutants. **(A)** The maximal growth rate (h^{-1}) in LB rich medium and M9 minimal medium. Data presented here are the relative growth rates compared with wild-type MG1655 (WT) that are calculated as the percentage of the growth rate of mutants against the WT. The maximal growth rate of the five genome-reduced mutants and WT were measured in LB rich medium and M9 minimal medium (The data were shown in Supplementary Table S4). For each strain, six replicates were carried out. Center lines show the medians. "+" indicate the means. Box limits indicate the first and third quartiles. Whiskers show either the maximum (or minimum) value or 1.5 times the interquartile range, whichever is smaller (or larger), and the outliers are represented by dots. **(B)** Maximal glucose utilization rate in exponential phase. **(C)** Electroporation efficiency; The absolute electroporation efficiency of the WT and the genome-deleted mutants were calculated with a small multicopy plasmids pUC19, a low-copy plasmids pKTRED, and a BAC with a 92-kb fragment insertion. The electroporation efficiency refers to the total number of transformants per microgram of DNA (colony-forming units [cfu]/μg DNA). **(D)** The relative fluorescence intensity (GFP, green fluorescent protein; FI, fluorescence intensity). Values denote mean (±s.d.) of triplicates.

end-joining mechanism (Chayot et al., 2010) in the repair of genomic double-strands breaks. In addition to genomic deletions, a few single nucleotide variants (SNVs) and small insertions and deletions (InDels) also emerged in the genomes of the five mutants (Supplementary Table S3).

Physiological characteristics of genome-reduced mutants

The growth rates and glucose utilization rates of the five selective mutants together with the wild-type MG1655 were measured (Figures 2A,B). In brief, the maximal growth rates of the five mutants approached or were higher than that of the wild-type strain both in LB rich medium and M9 minimal medium. Except for H2, all the mutants showed comparable or somewhat faster maximal glucose utilization rate in exponential phase in comparation to MG1655. These indicated that TMRD can screen suitable deletion mutants with increased cell growth and glucose utilization. An ideal chassis cell is expected to possess the excellent capacity to take up exogenous plasmids and express heterologous proteins. The electroporation efficiency of the five mutants and wild-type MG1655 was determined using a small high copy plasmid pUC19, a large plasmid pKTRED with a low-copy psc101 replicon, and a single-copy bacterial artificial chromosome with a 92-kb insertion (BAC). All mutants exhibited a significant improvement in electro-competence up to 2–4 orders of magnitude compared with the parental MG1655 (Figure 2C). The expression level of heterologous protein in the five mutants was tested using GFP as a model protein. As shown in Figure 2D, the relative fluorescence intensities of H5, H16, H19, and H20 were similar to or a little higher than that of the original strain MG1655. More significantly, H2 showed about 80% increase in the relative fluorescence intensity compared with MG1655. The results suggested that removal of some genomic regions can enhance the electroporation capacity and heterologous protein productivity.

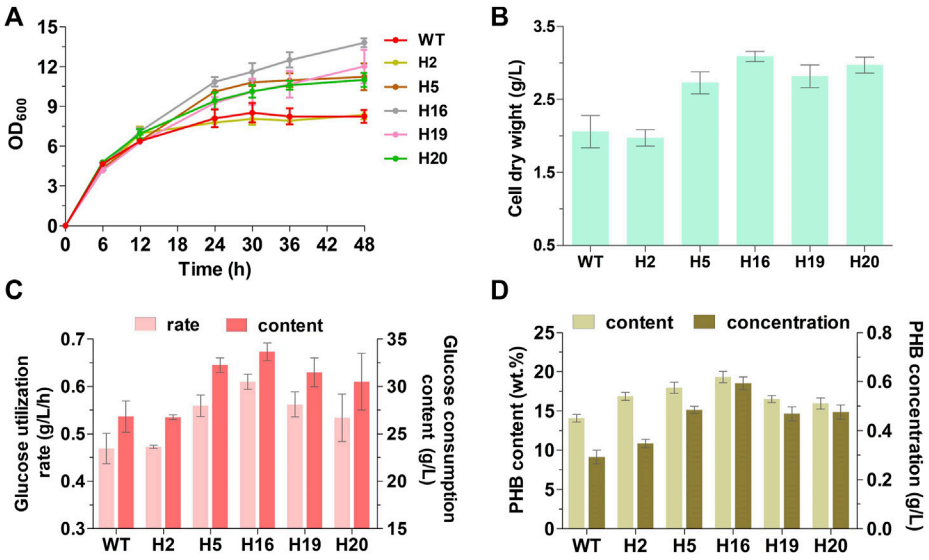

FIGURE 3
Fermentation performance of the genome-reduced mutants for PHB accumulation after 48-h cultivation. **(A)** The growth curves. Properly diluted fermentation broth was directly used for the measurement of OD_{600}, which included the cell density and intracellular PHB. **(B)** The final cell dry weight; **(C)** The glucose utilization rate and accumulative consumption content; **(D)** The PHB content (g/g cell dry weight × 100%.) and concentration. WT represents wild-type MG1655. Data are expressed as means (±s.d.) from three independent experiments.

Increased polyhydroxybutyrate accumulation in genome-reduced mutants

The intracellular PHB accumulation of the five mutants and the original strain MG1655 were compared by batch cultivation in M9 basal medium supplemented with glucose as sole carbon source, and the growth and glucose utilization of strains during the fermentation process were also measured. Apart from strain H2, all mutants had obvious advantages in growth and glucose utilization in comparation to wild-type MG1655, showing 32.5%–50.0% of increase in final cell dry weight, as well as 13.9%–30.1% and 13.7%–25.5% of improvement in glucose utilization rate and glucose consumption content, respectively (Figures 3A–C). The PHB content and concentration of the five mutants had enhanced up to 13.3%–37.2% and 60.2%–102.9%, respectively (Figure 3D). Despite that the cellular growth and glucose consumption of H2 were similar to that of MG1655, there still were certain degrees of increase in PHB content and concentration (19.7% and 18.9%, respectively) (Figure 3). Particularly, in H16, which displayed the fastest glucose utilization rate among all strains, the biomass (50.0% higher than that of MG1655 in final cell dry weight) and PHB yield (37.2% and 102.9% higher than that of MG1655 in PHB content and concentration, respectively) exhibited the most conspicuous improvement (Figure 3). Both mutants and MG1655 produced large amount of acetate (approx.17 g/L), and H2 (11.08 g/L) produced less acetate than other strains (Supplementary Figure S3). In the process of batch fermentation, low PHB yield was generated possibly because the key genes encoding PHB biosynthetic enzymes were expressed using a medium-copy plasmid and the weak Lac promoter. Hence, we utilized a high-copy replicon from pUC vectors and replaced the Lac promoter with the stress-induced system in which the PHB biosynthesis was induced under stress conditions (Kang et al., 2008). The PHB accumulation was evaluated in H16 together with wild-type MG1655 as control (Table 4). Results showed that the PHB productivity was improved about 3.3-fold (calculated as PHB concentration) by replacement of replicon and promoter both in wild-type MG1655 and H16. Compare with MG1655, the PHB content and concentration of H16 improved 53.2 % and 130.1%, reached 34.3 wt% and 2.6 g/L respectively, while still possessed obvious advantages in biomass and glucose utilization. Overall, we proved that random genome reduction has the potential to engineer *E. coli* to improve PHB accumulation.

Discussions

In this work, we combined random genome reduction with PHB biosynthesis, and succeed in randomly and continuously reducing the *E. coli* MG1655 genome *via* TMRD method accompanied by the selection of optimal mutants for PHB accumulation. Genome reduction based on rational analysis

TABLE 4 Fermentation results of H16 for PHB accumulation using high-copy-number plasmid[a].

Strains	WT	H16	[b] percentage of increase (%)
Cell dry weight (g/L)	5.01 ± 0.38	7.57 ± 0.18	51.1 ± 3.7
Glucose utilization rate (g/L/h)	0.54 ± 0.05	0.74 ± 0.01	36.1 ± 1.0
Glucose consumption (g/L)	29.0 ± 2.1	35.0 ± 0.71	20.7 ± 2.4
PHB content (wt%)	22.4 ± 3.5	34.3 ± 0.99	53.2 ± 4.4
PHB concentration (g/L)	1.13 ± 0.24	2.60 ± 0.10	130.1 ± 9.1
Acetate concentration (g/L)	18.41 ± 1.73	17.79 ± 0.69	/[c]

[a]The original strain MG1655 (WT) and mutant H16 were cultivated in M9-basal medium supplemented with 30 g/L glucose at 37°C, 220 rpm, for 48 h. The Data are expressed as means (±s.d.) from three independent experiments.
[b]The percentage of increase of H16 in cell dry weight, glucose utilization and PHB, accumulation compared with WT.
[c]Not determined.

and design has gained great progress in construction of desirable chassis for different application purposes (Sung et al., 2016; Chi et al., 2019). Owing to the inadequate understanding of genes still lacking annotation, as well as complex interactions of known genes and phenotypes, the effects of genomic deletion on cell physiology are difficult to predict and have to be tested experimentally, which is much laborious and may even cause the decay of cellular growth and performances (Ara et al., 2007; Karcagi et al., 2016; Li et al., 2016; Tsuchiya et al., 2018; Kurokawa and Ying, 2020; Liu et al., 2021). In addition, rational design method only allows the sequential removal of a single DNA fragment from a strain, and obtains one or a few genome-reduced strains in final (Posfai et al., 2006; Park et al., 2014; Liu et al., 2021). In contrast, the TMRD can randomly and continuously reduce the *E. coli* genome for a given environment, and at the same times maintained a comparable deletion rate (about 25 Kb in size per cycle every 10 days) to rational design strategy. Importantly, this method allows genomic deletions to be coupled with cellular growth, and acquire a series of genome-reduced strains with improved growth and ability to synthesize various bulk compounds.

Several random genome reduction methods based on transposition mutagenesis have been reported in some bacteria (Goryshin et al., 2003; Suzuki et al., 2008; Leprince et al., 2012; Vernyik et al., 2020; Shaw et al., 2021). Most of them have been proved the feasibility, and are inefficient to construct the chassis for industrial application (Goryshin et al., 2003; Suzuki et al., 2008; Leprince et al., 2012; Vernyik et al., 2020; Shaw et al., 2021). Our method can couple genomic deletion with PHB accumulation and demonstrated the improved accumulation of PHB by engineered *E. coli* can be achieved by random genome reduction. TMRD allows genome reduction without negatively affecting cell growth, and some genome-reduced mutants exhibited the faster glucose utilization rate, higher transformation efficiency, more biomass and PHB accumulation than that of the original strain MG1655. Importantly, the maximum increase of biomass and PHB was more than 1.5-fold and 2-fold that of original strain after batch fermentation, respectively, whatever the medium-copy plasmid or high-copy plasmid was used to express PHB pathway genes (strain H16, Table 4 and Figure 3). That suggested our method is more useful than existing random reduction methods to construct streamlined cell factory. Much effort has been done to engineer *E. coli* as an optimum chassis for PHB production with metabolic engineering strategies, and some have made great progress (Ganesh et al., 2015; Wang et al., 2019; Li et al., 2020; Boontip et al., 2021; Koh et al., 2022). The PHB productivity in this work is much lower than other researches that metabolic engineering strategies were applied to improve the PHB yields. The reason for this may be the PHB synthesis pathway is carried on a plasmid and is not directly related to genome reduction. The improved PHB accumulation possibly because the increase of cell's glucose utilization and growth. Although low PHB yield was produced in this study, at least, we provided a new insight in generation of streamlined chassis with higher chemicals and materials productivity. In future studies, combining random reduction with metabolic engineering strategy can be used to engineer *E. coli* to further improve PHB productivity.

In general, random reduction can enrich the cells with growth fitness in different environment *via* its growth-coupled genome deletion mode (Vernyik et al., 2020; Ma et al., 2022). We observed that the five mutants harbored some same deletion fragments (D1–D8, Table 2) and similar properties (enhanced glucose utilization rate, final cell density, electroporation efficiency, and PHB accumulation). That possibly are the results of environmental screening and enrichment. The growth phase (about fifteen times in LB medium and once in M9 medium per round), Nile red assay (once per round), and electroporation steps (twice

per round) incorporated in the cyclic process might act as filters to gradual screening and enrichment of the optimal deletions with fitness in the library, ultimately manifesting as the accumulation of same deletion events and the similar physiological properties of the mutants. We speculate that the increase of physiological properties (growth, glucose utilization, transformation capacity, and protein expression level) might facilitate cells to accumulate more PHB. Hence, these mutants can be easily screened *via* Nile red staining and then enriched after multiple rounds of reduction. It found that deletions of D1 (carried in all mutants) and D9 (carried in H16) contained the genes involving in restriction–modification system [*hsd*RMS (Sain, 1980), *mcr*A (Raleigh et al., 1986), *mcr*BC (Dila et al., 1990), and *mrr* (Waite-Rees et al., 1991), Table 3] that can prevent the invasion of foreign DNA elements and is a barrier to genetic manipulation in host strains (Lee et al., 2019). Since removing genes encoding the restriction–modification system greatly enhanced the transformation capacity (Wang et al., 2020), the improvement of electroporation capacity possibly because some genes that promote transformation were deleted. However, because many genes were deleted simultaneously as part of large DNA fragments, many of which are functionally unknown, and the uncertainties surrounding interactions between gene and function, it is difficult to pinpoint individual gene closely associated with the changes of physiological properties (such as, glucose utilization, growth). Moreover, the change of physiological phenotypes is more likely not caused by the deletion of an individual DNA fragment, but the combination deletion of multiple DNA segments, which make it labor-intensive to explore the causal genes. Although the relationship between genome reduction and physiological properties is hard to explain, our method has potential to obtained a series of strains with optimal genomes to produce high value-added products in the long term. In addition, the limited throughput of the final library (about 100 cells per round) decreases the diversity of deleted fragments and may cause the occurrences of repeated deletion events in different strains (Ma et al., 2022).

Conclusion

In summary, we successfully applied the TMRD approach to construct streamlined *E. coli* hosts with improved PHB accumulation. Compared with the parental MG1655, most genome-reduced strains showed significant improvements of electroporation efficiency, biomass, glucose utilization, and PHB accumulation. Our results proved that random genome reduction can be used to construct optimal microbial cell factory and provide new insights in generating controllable chassis for different application purposes.

Data availability statement

The original contributions presented in the study are included in the article/Supplementary Material, further inquiries can be directed to the corresponding authors.

Author contributions

SM and JL performed the experiments under the supervision of QQ, TS, and XL. SM collected and analyzed the data and wrote the manuscript. QQ, QW, QL, and XL reviewed and revised the manuscript. All authors read and approved the final manuscript.

Funding

This work was supported by Natural Science Foundation of China (31730003) and National Key Research and Development Program of China (2021YFC2100500).

Acknowledgments

We are grateful to Dr. Xiaoying Bian and Yongzhen Xia from State Key Laboratory of Microbial Technology, Shandong University (Qingdao, China) for their providing several of the plasmids and strains used in this study.

Conflict of interest

The authors declare that the research was conducted in the absence of any commercial or financial relationships that could be construed as a potential conflict of interest.

Publisher's note

Supplementary material

The Supplementary Material for this article can be found online at: https://www.frontiersin.org/articles/10.3389/fbioe.2022.978211/full#supplementary-material

References

Abyzov, A., Urban, A. E., Snyder, M., and Gerstein, M. (2011). CNVnator: An approach to discover, genotype, and characterize typical and atypical CNVs from family and population genome sequencing. *Genome Res.* 21, 974–984. doi:10.1101/gr.114876.110

Ara, K., Ozaki, K., Nakamura, K., Yamane, K., Sekiguchi, J., and Ogasawara, N. (2007). *Bacillus* minimum genome factory: Effective utilization of microbial genome information. *Biotechnol. Appl. Biochem.* 46, 169–178. doi:10.1042/BA20060111

Boontip, T., Waditee-Sirisattha, R., Honda, K., and Napathorn, S. C. (2021). Strategies for poly(3-hydroxybutyrate) production using a cold-shock promoter in *Escherichia coli*. *Front. Bioeng. Biotechnol.* 9, 666036. doi:10.3389/fbioe.2021.666036

Chayot, R., Montagne, B., Mazel, D., and Ricchetti, M. (2010). An end-joining repair mechanism in *Escherichia coli*. *Proc. Natl. Acad. Sci. U. S. A.* 107, 2141–2146. doi:10.1073/pnas.0906355107

Chen, K., Wallis, J. W., McLellan, M. D., Larson, D. E., Kalicki, J. M., Pohl, C. S., et al. (2009). BreakDancer: An algorithm for high-resolution mapping of genomic structural variation. *Nat. Methods* 6, 677–681. doi:10.1038/NMETH.1363

Chi, H., Wang, X., Shao, Y., Qin, Y., Deng, Z., Wang, L., et al. (2019). Engineering and modification of microbial chassis for systems and synthetic biology. *Synth. Syst. Biotechnol.* 4, 25–33. doi:10.1016/j.synbio.2018.12.001

Choe, D., Cho, S., Kim, S. C., and Cho, B. K. (2016). Minimal genome: Worthwhile or worthless efforts toward being smaller? *Biotechnol. J.* 11, 199–211. doi:10.1002/biot.201400838

Choi, J. I., and Lee, S. Y. (1999). Efficient and economical recovery of poly(3-hydroxybutyrate) from recombinant *Escherichia coli* by simple digestion with chemicals. *Biotechnol. Bioeng.* 62, 546–553. doi:10.1002/(sici)1097-0290(19990305)62:5<546::aid-bit6>3.0.co;2-0

Dila, D., Sutherland, E., Moran, L., Slatko, B., and Ea, R. (1990). Genetic and sequence organization of the *mcr*BC locus of *Escherichia coli* K-12. *J. Bacteriol.* 172, 4888–4900. doi:10.1128/jb.172.9.4888-4900.1990

Feng, D., Li, M., Zhu, S., Zhou, W., Huang, J., and Feng, D. (2002). Study on sucrose-glucoes bifunction assav of biosensor analyzer. *Food Sci.* 23, 1171002–1216630.

Ganesh, M., Senthamarai, A., Shanmughapriya, S., and Natarajaseenivasan, K. (2015). Effective production of low crystallinity poly(3-hydroxybutyrate) by recombinant *E. coli* strain JM109 using crude glycerol as sole carbon source. *Bioresour. Technol.* 192, 677–681. doi:10.1016/j.biortech.2015.06.042

Goryshin, I. Y., Naumann, T. A., Apodaca, J., and Reznikoff, W. S. (2003). Chromosomal deletion formation system based on Tn*5* double transposition: Use for making minimal genomes and essential gene analysis. *Genome Res.* 13, 644–653. doi:10.1101/gr.611403

Iwadate, Y., Honda, H., Sato, H., Hashimoto, M., and Kato, J. (2011). Oxidative stress sensitivity of engineered *Escherichia coli* cells with a reduced genome. *FEMS Microbiol. Lett.* 322, 25–33. doi:10.1111/j.1574-6968.2011.02331.x

Kang, Z., Wang, Q., Zhang, H., and Qi, Q. (2008). Construction of a stress-induced system in *Escherichia coli* for efficient polyhydroxyalkanoates production. *Appl. Microbiol. Biotechnol.* 79, 203–208. doi:10.1007/s00253-008-1428-z

Karcagi, I., Draskovits, G., Umenhoffer, K., Fekete, G., Kovacs, K., Mehi, O., et al. (2016). Indispensability of horizontally transferred genes and its impact on bacterial genome streamlining. *Mol. Biol. Evol.* 33, 1257–1269. doi:10.1093/molbev/msw009

Koh, S., Sato, M., Yamashina, K., Usukura, Y., Toyofuku, M., Nomura, N., et al. (2022). Controllable secretion of multilayer vesicles driven by microbial polymer accumulation. *Sci. Rep.* 12, 3393. doi:10.1038/s41598-022-07218-z

Kolisnychenko, V., III, G. P., Pósfai, J., Blattner, F. R., Herring, C. D., Pósfai, G., et al. (2002). Engineering a reduced *Escherichia coli* genome. *Genome Res.* 12, 640–647. doi:10.1101/gr.217202

Komatsu, M., Uchiyama, T., Omura, S., Cane, D. E., and Ikeda, H. (2010). Genome-minimized *Streptomyces* host for the heterologous expression of secondary metabolism. *Proc. Natl. Acad. Sci. U. S. A.* 107, 2646–2651. doi:10.1073/pnas.0914833107

Kurokawa, M., and Ying, B. W. (2020). Experimental challenges for reduced genomes: The cell model *Escherichia coli*. *Microorganisms* 8, 3. doi:10.3390/microorganisms8010003

Lee, J. Y. H., Carter, G. P., Pidot, S. J., Guerillot, R., Seemann, T., Goncalves da Silva, A., et al. (2019). Mining the methylome reveals extensive diversity in *Staphylococcus epidermidis* restriction modification. *mBio* 10, e02451–02419. doi:10.1128/mBio.02451-19

Leprince, A., de Lorenzo, V., Voller, P., van Passel, M. W., and Martins dos Santos, V. A. (2012). Random and cyclical deletion of large DNA segments in the genome of *Pseudomonas putida*. *Environ. Microbiol.* 14, 1444–1453. doi:10.1111/j.1462-2920.2012.02730.x

Li, H., and Durbin, R. (2009). Fast and accurate short read alignment with Burrows-Wheeler transform. *Bioinformatics* 25, 1754–1760. doi:10.1093/bioinformatics/btp324

Li, Y., Sun, Z., Xu, Y., Luan, Y., Xu, J., Liang, Q., et al. (2020). Enhancing the glucose flux of an engineered EP-Bifido pathway for high poly(hydroxybutyrate) yield production. *Front. Bioeng. Biotechnol.* 8, 517336. doi:10.3389/fbioe.2020.517336

Li, Y., Zhu, X., Zhang, X., Fu, J., Wang, Z., Chen, T., et al. (2016). Characterization of genome-reduced *Bacillus subtilis* strains and their application for the production of guanosine and thymidine. *Microb. Cell Fact.* 15, 94. doi:10.1186/s12934-016-0494-7

Liang, P., Zhang, Y., Xu, B., Zhao, Y., Liu, X., Gao, W., et al. (2020). Deletion of genomic islands in the *Pseudomonas putida* KT2440 genome can create an optimal chassis for synthetic biology applications. *Microb. Cell Fact.* 19, 70. doi:10.1186/s12934-020-01329-w

Lindgreen, S. (2012). Adapter Removal: Easy cleaning of next-generation sequencing reads. *BMC Res. Notes* 5, 337. doi:10.1186/1756-0500-5-337

Liu, J., Zhou, H., Yang, Z., Wang, X., Chen, H., Zhong, L., et al. (2021). Rational construction of genome-reduced *Burkholderiales* chassis facilitates efficient heterologous production of natural products from proteobacteria. *Nat. Commun.* 12, 4347. doi:10.1038/s41467-021-24645-0

Ma, S., Su, T., Liu, J., Lu, X., and Qi, Q. (2022). Reduction of the bacterial genome by transposon-mediated random deletion. *ACS Synth. Biol.* 11, 668–677. doi:10.1021/acssynbio.1c00353

McKenna, A., Hanna, M., Banks, E., Sivachenko, A., Cibulskis, K., Kernytsky, A., et al. (2010). The genome analysis toolkit: A mapreduce framework for analyzing next-generation DNA sequencing data. *Genome Res.* 20, 1297–1303. doi:10.1101/gr.107524.110

Mizoguchi, H., Sawano, Y., Kato, J., and Mori, H. (2008). Superpositioning of deletions promotes growth of *Escherichia coli* with a reduced genome. *DNA Res.* 15, 277–284. doi:10.1093/dnares/dsn019

Norrander, J., Kempe, T., and Messing, J. (1983). Construction of improved M13 vectors using oligodeoxynucleotide-directed mutagenesis. *Gene* 26, 101–106. doi:10.1016/0378-1119(83)90040-9

Odumpatta, R., and Mohanapriya, A. (2020). Next generation sequencing exome data analysis aids in the discovery of SNP and INDEL patterns in Parkinson's disease. *Genomics* 112, 3722–3728. doi:10.1016/j.ygeno.2020.04.025

Park, M. K., Lee, S. H., Yang, K. S., Jung, S. C., Lee, J. H., and Kim, S. C. (2014). Enhancing recombinant protein production with an *Escherichia coli* host strain lacking insertion sequences. *Appl. Microbiol. Biotechnol.* 98, 6701–6713. doi:10.1007/s00253-014-5739-y

Posfai, G., Plunkett, G., Feher, T., Frisch, D., Keil, G. M., Umenhoffer, K., et al. (2006). Emergent properties of reduced-genome *Escherichia coli*. *Science* 312, 1044–1046. doi:10.1126/science.1126439

Qiao, W., Qiao, Y., Liu, F., Zhang, Y., Li, R., Wu, Z., et al. (2020). Engineering *Lactococcus lactis* as a multi-stress tolerant biosynthetic chassis by deleting the prophage-related fragment. *Microb. Cell Fact.* 19, 225. doi:10.1186/s12934-020-01487-x

Raleigh, E. A., and Wilson, G. (1986). *Escherichia coli* K-12 restricts DNA containing 5-methylcytosine. *Proc. Natl. Acad. Sci. U. S. A.* 83, 9070–9074. doi:10.1073/pnas.83.23.9070

Rose, R. E. (1988). The nucleotide-sequence of pACYC184. *Nucleic Acids Res.* 16, 355. doi:10.1093/nar/16.1.355

Sain, B. M. N., and Murray, N. E. (1980). The *hsd* (host specificity) genes of *E. coli* K 12. *Molec. Gen. Genet.* 180, 35–46. doi:10.1007/BF00267350

Shaw, D., Miravet-Verde, S., Pinero-Lambea, C., Serrano, L., and Lluch-Senar, M. (2021). LoxTnSeq: Random transposon insertions combined with cre/lox recombination and counterselection to generate large random genome reductions. *Microb. Biotechnol.* 14, 2403–2419. doi:10.1111/1751-7915.13714

Sung, B. H., Choe, D., Kim, S. C., and Cho, B. K. (2016). Construction of a minimal genome as a chassis for synthetic biology. *Essays Biochem.* 60, 337–346. doi:10.1042/EBC20160024

Suzuki, N., Inui, M., and Yukawa, H. (2008). Random genome deletion methods applicable to prokaryotes. *Appl. Microbiol. Biotechnol.* 79, 519–526. doi:10.1007/s00253-008-1512-4

Tsuchiya, K., Cao, Y. Y., Kurokawa, M., Ashino, K., Yomo, T., and Ying, B. W. (2018). A decay effect of the growth rate associated with genome reduction in *Escherichia coli*. *BMC Microbiol.* 18, 101. doi:10.1186/s12866-018-1242-4

Turco, R., Santagata, G., Corrado, I., Pezzella, C., and Di Serio, M. (2020). *In vivo* and post-synthesis strategies to enhance the properties of PHB-based materials: A review. *Front. Bioeng. Biotechnol.* 8, 619266. doi:10.3389/fbioe.2020.619266

Vernyik, V., Karcagi, I., Timar, E., Nagy, I., Gyoerkei, A., Papp, B., et al. (2020). Exploring the fitness benefits of genome reduction in *Escherichia coli* by a selection-driven approach. *Sci. Rep.* 10, 7345. doi:10.1038/s41598-020-64074-5

Waite-Rees, P. A., Keating, C. J., Moran, L. S., Slatko, B. E., Hornstra, L. J., and Benner, J. S. (1991). Characterization and expression of the *Escherichia coli mrr* restriction system. *J. Bacteriol.* 173, 5207–5219. doi:10.1128/jb.173.16.5207-5219.1991

Wang, J., Huang, C., Guo, K., Ma, L., Meng, X., Wang, N., et al. (2020). Converting *Escherichia coli* MG1655 into a chemical overproducer through inactivating defense system against exogenous DNA. *Synth. Syst. Biotechnol.* 5, 333–342. doi:10.1016/j.synbio.2020.10.005

Wang, J., Ma, W., Wang, Y., Lin, L., Wang, T., Wang, Y., et al. (2018). Deletion of 76 genes relevant to flagella and pili formation to facilitate polyhydroxyalkanoate production in *Pseudomonas putida*. *Appl. Microbiol. Biotechnol.* 102, 10523–10539. doi:10.1007/s00253-018-9439-x

Wang, Q., Xu, J., Sun, Z., Luan, Y., Li, Y., Wang, J., et al. (2019). Engineering an *in vivo* EP-bifido pathway in *Escherichia coli* for high-yield acetyl-CoA generation with low CO_2 emission. *Metab. Eng.* 51, 79–87. doi:10.1016/j.ymben.2018.08.003

Zhang, F., Huo, K., Song, X., Quan, Y., Wang, S., Zhang, Z., et al. (2020). Engineering of a genome-reduced strain *Bacillus amyloliquefaciens* for enhancing surfactin production. *Microb. Cell Fact.* 19, 223. doi:10.1186/s12934-020-01485-z

frontiers | Frontiers in Bioengineering and Biotechnology

TYPE Original Research
PUBLISHED 07 September 2022
DOI 10.3389/fbioe.2022.961535

OPEN ACCESS

EDITED BY
Farshad Darvishi,
Alzahra University, Iran

REVIEWED BY
Rainer Borriss,
Institut für Marine Biotechnologie e.V., Germany
Jin-ho Lee,
Kyungsung University, South Korea
Dongbo Cai,
Hubei University, China

*CORRESPONDENCE
Gaofu Qi,
qigaofu@mail.hzau.edu.cn

†These authors have contributed equally to this work

SPECIALTY SECTION
This article was submitted to Synthetic Biology, a section of the journal Frontiers in Bioengineering and Biotechnology

RECEIVED 04 June 2022
ACCEPTED 17 August 2022
PUBLISHED 07 September 2022

CITATION
Wang S, Wang R, Zhao X, Ma G, Liu N, Zheng Y, Tan J and Qi G (2022), Systemically engineering Bacillus amyloliquefaciens for increasing its antifungal activity and green antifungal lipopeptides production. *Front. Bioeng. Biotechnol.* 10:961535. doi: 10.3389/fbioe.2022.961535

Systemically engineering *Bacillus amyloliquefaciens* for increasing its antifungal activity and green antifungal lipopeptides production

Susheng Wang[1†], Rui Wang[2†], Xiuyun Zhao[1†], Gaoqiang Ma[1†], Na Liu[1], Yuqing Zheng[1], Jun Tan[2] and Gaofu Qi[1*]

[1]College of Life Science and Technology, Huazhong Agricultural University, Wuhan, Hubei, China, [2]Enshi Tobacco Technology Center, Enshi City, Hubei, China

The biosynthesis of antifungal lipopeptides iturin and fengycin has attracted broad interest; however, there is a bottleneck in its low yield in wild strains. Because the key metabolic mechanisms in the lipopeptides synthesis pathway remain unclear, genetic engineering approaches are all ending up with a single or a few gene modifications. The aim of this study is to develop a systematic engineering approach to improve the antifungal activity and biosynthesis of iturin and fengycin in *Bacillus amyloliquefaciens*. First, blocking the carbon overflow metabolic pathway to increase precursor supply of the branched-chain amino acids by knockout of *bdh*, disrupting sporulation to extend the stage for producing antifungal lipopeptides by deletion of *kinA*, blocking of siderophore synthesis to enhance the availability of amino acids and fatty acids by deletion of *dhbF*, and increasing Spo0A~P by deletion of *rapA*, could improve the antifungal activity by 24%, 10%, 13% and 18%, respectively. Second, the double knockout strain Δ*bdh*Δ*kinA*, triple knockout strain Δ*bdh*Δ*kinA*Δ*dhbF* and quadruple knockout strain Δ*kinA*Δ*bdh*Δ*dhbF*Δ*rapA* could improve the antifungal activity by 38%, 44% and 53%, respectively. Finally, overexpression of *sfp* in Δ*kinA*Δ*bdh*Δ*dhbF*Δ*rapA* further increased the antifungal activity by 65%. After purifying iturin and fengycin as standards for quantitative analysis of lipopeptides, we found the iturin titer was 17.0 mg/L in the final engineered strain, which was 3.2-fold of the original strain. After fermentation optimization, the titer of iturin and fengycin reached 31.1 mg/L and 175.3 mg/L in flask, and 123.5 mg/L and 1200.8 mg/L in bioreactor. Compared to the original strain, the iturin and fengycin titer in bioreactor increased by 22.8-fold and 15.9-fold in the final engineered strain, respectively. This study may pave the way for the commercial production of green antifungal lipopeptides, and is also favorable for understanding the regulatory and biosynthetic mechanism of iturin and fengycin.

KEYWORDS

Bacillus amyloliquefaciens, metabolic engineering, lipopeptide, iturin, fengycin

Introduction

Many *Bacillus* species such as *B. amyloliquefaciens*, *B. subtilis*, *B. velezensis*, etc, are well-known bacteria for producing antifungal lipopeptides such as iturin and fengycin (Kaspar et al., 2019), which are green and broad-spectrum fungicides with potential use in developing biological pesticides (Zhao et al., 2017b), food preservatives (Kourmentza et al., 2021; Gu et al., 2022), antifungal and antitumor drugs (Lin et al., 2020; Wan et al., 2021), feed additives (Zhao et al., 2017a; Prathiviraj et al., 2021), etc. Iturin, a cyclic lipoheptapeptide that is linked to a fatty acid chain with 14–17 carbon number, has a broad-spectrum inhibitory effect on many plant pathogenic fungi. Recently, it has also been reported with anticancer activities (Wan et al., 2021). Fengycin is a cyclic antimicrobial lipopeptide consisting of a β-hydroxy fatty acid with 13–19 carbon number, which has strong wide-spectrum antifungal and antiviral activities, as well as potential anticancer activity (Gao et al., 2022). Additionally, *Bacillus* can also produce surfactin, a cyclic lipopeptide containing a fatty acid tail and a heptapeptide, as a signal molecule to trigger quorum sensing response (e.g., biofilm formation and sporulation) (Vlamakis et al., 2013; Oslizlo et al., 2014). The structure of lipopeptides is shown in Figure 1A.

Biosynthesis of iturin and fengycin has attracted significant attention in recent years (Yang et al., 2020; Wan et al., 2021). However, low fermentation yield greatly restricts their practical applications and further functional investigations (Yang et al., 2020). Moreover, there have been no reports of the chemical synthesis of iturin and fengycin. Thus, industrial production of the high-value added chemicals iturin and fengycin must rely on bacterial fermentation (Horsburgh and Moir, 1999; Gao et al., 2022). For this purpose, genetic engineering methods should be used to enhance their biosynthesis. Major concerns, however, are attributed to large genetic sequence of the operons encoding iturin (*itu*, 38-kb) and fengycin (*fen*, 30-kb) synthase (Tosato et al., 1997; Wu et al., 2007; Cheng et al., 2017; Yang et al., 2020; Wan et al., 2021). Because direct overexpression of *itu* and *fen* operons has been challenging, *Bacillus* species have been engineered to improve iturin and fengycin yield mainly through promoter exchanges of the synthase operon (Dang et al., 2019), strengthening biosynthesis of the substrates such as fatty acids (He et al., 2021; Tan et al., 2022), overexpression of genes encoding the regulators ComA, SigA, DegU, DegQ and Spo0A (Koumoutsi et al., 2007; Wang et al., 2015; Zhang et al., 2017; Klausmann et al., 2021; Sun et al., 2021), or deletion of the repressors gene such as *abrB* (Xu et al., 2020). These studies are able to efficiently increase the lipopeptides biosynthesis, and also demonstrate the importance of understanding the biosynthetic metabolism of iturin and fengycin. However, these genetic engineering methods can only result in a single or a few gene modifications, and the commercial production of antifungal lipopeptides has still not been achieved. Therefore, knowledge-based optimizations are still ongoing, and global antifungal lipopeptides biosynthesis and regulatory features still need to be explored.

For biosynthesis of lipopeptides, the first is the supply of pyruvate through the glycolytic pathway. Pyruvate can be converted to the branched-chain amino acids, which are precursors for biosynthesis of several lipopeptides such as surfactin, iturin and fengycin. However, pyruvate can also be converted to acetolactate by acetolactate synthase. Subsequently, acetolactate is decarboxylated to acetoin by acetolactate decarboxylase, then acetoin is conversed to 2,3-butanediol by 2,3-butanediol dehydrogenase (2,3-BDH) (Peng et al., 2019). The Sfp protein (4-phosphopantetheinyl transferase) plays an essential role in activation of lipopeptides synthesis by transferring the 4′-phosphopantetheinyl moiety of coenzyme A to a serine residue (Reuter et al., 1999; Wu et al., 2019). The second is lipopeptides assembly catalyzed by the iturin and fengycin synthase, which are encoded by the *itu* and *fen* operons, respectively.

There are several regulators to directly or indirectly regulate the biosynthesis of lipopeptides in *Bacillus* species. DegQ, a small regulatory protein, is positive for production of iturin (Tsuge et al., 2005). The global regulator Spo0A that can be activated to be phosphorylated by the histidine kinases such as KinA and dephosphorylated by the aspartate phosphatases RapA and Spo0E is also essential for production of lipopeptides such as iturin and fengycin (Rahman et al., 2006; Sun et al., 2021). Some regulators for biofilm formation are also involved in biosynthesis of lipopeptides. For example, SinI is negative while SinR is positive for biosynthesis of lipopeptides (Wu et al., 2019). Fur is a regulator to suppress biofilm formation in *B. subtilis* (Pi and Helmann 2017). Both ComA and SigA play a positive role in biosynthesis of lipopeptides (Zhang et al., 2017; Sun et al., 2021). However, AbrB represses the transcription of *itu* operon (Xu et al., 2020). CodY suppresses the biosynthesis of branched-chain amino acids, which are substrates for biosynthesis of lipopeptides (Fujita 2009). Spx and PerR, transcriptional regulatory proteins for redox reaction, regulate the transcription of *srf* operon for biosynthesis of surfactin (Ohsawa et al., 2006).

In our previous work, *B. amyloliquefaciens* WH1 was isolated with excellent antifungal activity from rice root (Supplementary Figure S1). Fortunately, WH1 is easy to be transformed with DNA (Zhang et al., 2022). Here, we used WH1 as an initial host to construct antifungal lipopeptides hyperproducers through system metabolic engineering strategy (Figure 1B). First, we knocked out the *bdh* gene to

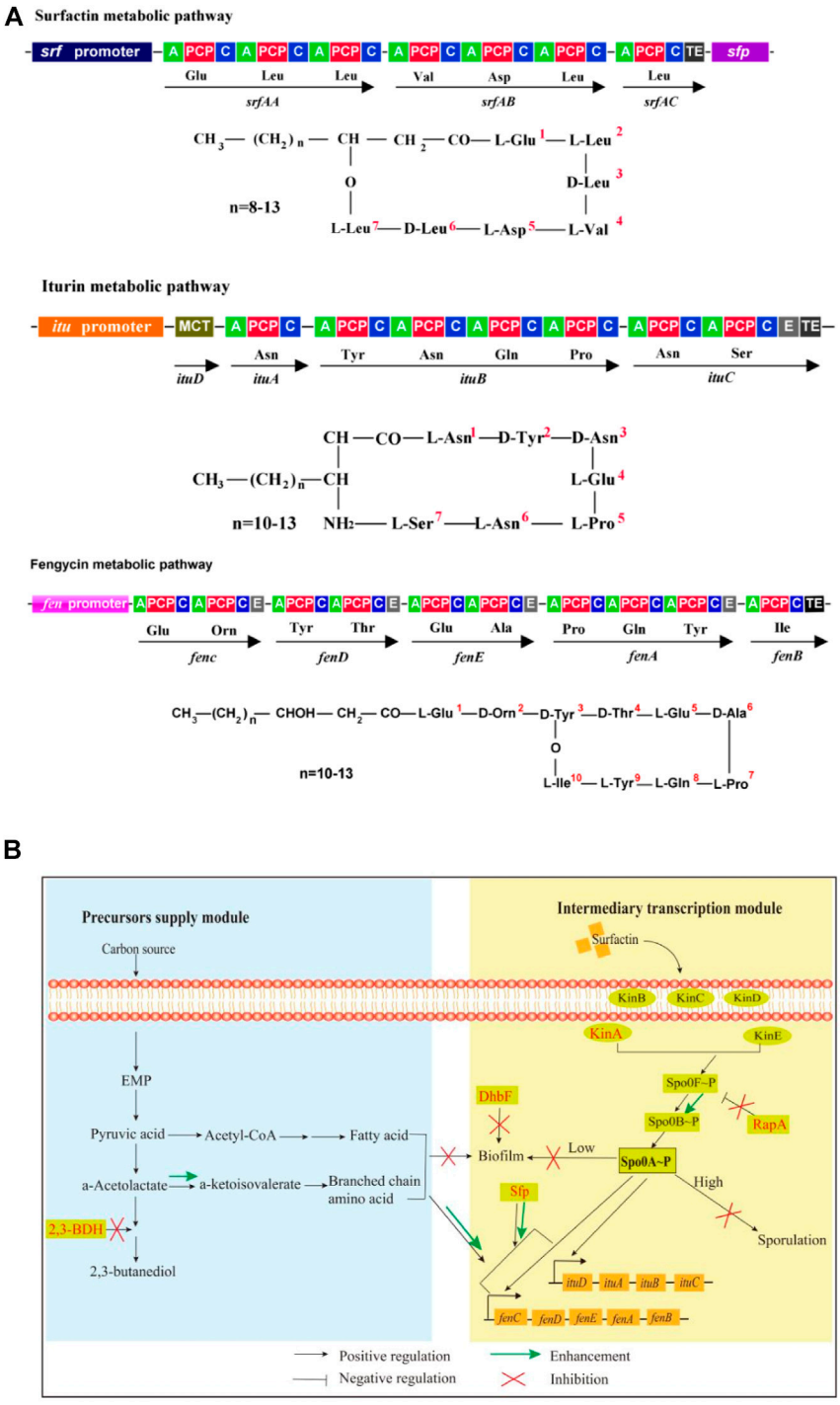

FIGURE 1
Molecular structures, biosynthesis pathways and regulator network of lipopeptides. **(A)**: Molecule structures and biosynthesis pathways of lipopeptides. In the figures, "A" means amino acid activating domain; "PCP" means peptidyl carrier protein; "C" means condensation domain; "E" means epimerization domain; "TE" means thioesterase domain; "MCT" means monocarboxylate transporter. **(B)**: Regulatory network for biosynthesis of iturin and fengycin. 2,3-BDH: 2,3-butanediol dehydrogenase; Kin A-E: histidine kinases; DhbF: biosynthesis of siderophore; Spo0A: global regulator; Spo0F and Spo0B: phosphate group transporter; RapA: aspartate phosphatase; Sfp:4-phosphopantetheinyl transferase.

block biosynthesis of 2,3-butanediol, which could improve production of precursors (branched-chain amino acids). Second, we deleted the *kinA* gene to hinder sporulation, which could extend the stage for production of antifungal lipopeptides (Rahman et al., 2006). Third, we knocked out the *dhbF* gene to disrupt siderophore production for improving biosynthesis of antifungal lipopeptides. Fourth, the gene *rapA* was deleted for maintaining the level of Spo0A~P, which was essential for biosynthesis of antifungal lipopeptides. Finally, we engineered *sfp* to strengthen the activation of precursors. This work will not only shed new light on biosynthetic and regulatory mechanisms of efficient iturin and fengycin production, but will also increase these two lipopeptides titers in *B. amyloliquefaciens*.

Materials and methods

Bacterial strains and materials

Experiments were performed with the strains listed in Table 1. Materials for DNA manipulation were purchased from Takara Bio (China). Other chemicals were of analytical grade supplied by Sinopharm Chemical Reagent (China).

Mutation of lipopeptides synthase operon

On the basis of the mutant strains Δ*ituB* and Δ*fenA* (Chen et al., 2020), we constructed the *ituB* and *fenA* double mutant strain Δ*ituB*Δ*fenA* (Table 1). The strains WH1, Δ*ituB*, Δ*fenA* and

TABLE 1 Bacterial strains used in this study.

Strains	Characteristics	Source
Fusarium oxysporum	Pathogenic fungus	Stored in this lab
Bacillus amyloliquefaciens WH1	Wild-type strain	Stored in this lab Chen et al. (2020)
Δ*ituB*	*ituB* knockout strain	Stored in this lab Chen et al. (2020)
Δ*fenA*	*fenA* knockout strain	Stored in this lab Chen et al. (2020)
Δ*ituB*Δ*fenA*	*ituB* and *fenA* double knockout strain	This study
Δ*kinA*	*kinA* knockout strain	Stored in this lab Chen et al. (2020)
Δ*bdh*	*bdh* knockout strain	This study
Δ*degS*	*degS* knockout strain	This study
Δ*tnrA*	*tnrA* knockout strain	This study
Δ*codY*	*codY* knockout strain	This study
Δ*spo0E*	*spo0E* knockout strain	This study
Δ*rapA*	*rapA* knockout strain	This study
Δ*dhbF*	*dhbF* knockout strain	This study
Δ*fur*	*fur* knockout strain	This study
Δ*abrB*	*abrB* knockout strain	This study
Δ*sinI*	*sinI* knockout strain	Stored in this lab Zhang et al. (2022)
Δ*sinR*	*sinR* knockout strain	Stored in this lab Zhang et al. (2022)
Δ*spo0A*	*spo0A* knockout strain	Stored in this lab Chen et al. (2020)
Δ*spo0A*/T2-*spo0A*	*spo0A*-complementary strain	This study
WH1/T2-*spo0A*	Overexpression of *spo0A* in WH1	This study
Δ*sfp*	*sfp* knockout strain	This study
Δ*kinA*Δ*bdh*	*kinA* and *bdh* double knockout strain	This study
Δ*sfp*/T2-*sfp*	*sfp*-complementary strain	This study
WH1/T2-*sfp*	Overexpression of *sfp* in WH1	This study
Δ*codY*Δ*kinA*	*kinA* and *codY* double knockout strain	This study
Δ*tnrA*Δ*kinA*	*kinA* and *tnrA* double knockout strain	This study
Δ*kinA*Δ*bdh*Δ*dhbF*	*kinA*, *bdh* and *dhbF* triple knockout strain	This study
Δ*kinA*Δ*bdh*Δ*dhbF*Δ*spo0E*	*kinA*, *bdh*, *dhbF* and *spo0E* quadruple knockout strain	This study
Δ*kinA*Δ*bdh*Δ*dhbF*Δ*rapA*	*kinA*, *bdh*, *dhbF* and *rapA* quadruple knockout strain	This study
Δ*kinA*Δ*bdh*Δ*rapA*Δ*dhbF*/T2-*sfp*	Overexpression of *sfp* in Δ*kinA*Δ*bdh*Δ*rapA*Δ*dhbF*	This study
Δ*kinA*Δ*bdh*Δ*rapA*Δ*dhbF*Δ*spo0A*	*kinA*, *bdh*, *dhbF*, *rapA* and *spo0A* penta knockout strain	This study
Δ*kinA*Δ*bdh*Δ*rapA*Δ*dhbF*Δ*spo0A*/T2-*spo0A*	Compensation of *spo0A* in Δ*kinA*Δ*bdh*Δ*rapA*Δ*dhbF*Δ*spo0A*	This study

Δ*ituB*Δ*fenA* were determined for the antifungal activity against *Fusarium oxysporum*. Briefly, *F. oxysporum* was inoculated on the center, and WH1, Δ*ituB*, Δ*fenA* and Δ*ituB*Δ*fenA* were inoculated on the right, left, bottom and top of the PDA (potato dextrose agar) plates, respectively. The plates were incubated at 28°C for 3 days, then the antifungal activity was observed.

Construction of knockout, complementary and overexpression strains

The genes including *bdh*, *comK*, *sigD*, *tnrA*, *codY*, *spo0E*, *rapA*, *dhbF*, *fur*, *abrB* and *sfp* were deleted by double crossover homologous recombination for constructing the single, double, triple, quadruple and penta knockout strains, respectively (Qi et al., 2014). The detailed methods to construct knockout strains were described in the Supplementary Materials.

The plasmids were constructed for expression of *spo0A* and *sfp*, respectively. Briefly, the genes *spo0A* and *sfp* with their own promoters and terminators were amplified from the genomic DNA of WH1 by PCR with the primers listed in Supplementary Table S1, cloned into the T2 plasmid joined by *BamH* I and *Xba* I restriction sites, then the constructed plasmids were used for transformation of the related hosts, respectively (Qi et al., 2014).

Determining cell growth and sporulation

The single colony of strains was used for inoculating LB medium and cultured at 37°C overnight, then 2 μl broth was transferred into 200 μl fresh LB medium in 96-well microplates for incubation at 37°C for 48 h. In this period, the growth curves were determined with an automatic growth curve analyzer (Bioscreen Cpro, OY Growth Curves, Finland). The broths were also collected for detecting sporulation via crystal violet staining after being cultured for 48 h (Chen et al., 2020). We also determined the rate of surviving cells after heat treatment. Briefly, after being cultured for 48 h, the broths were heated at 80°C for 10 min in the water bath, used for spreading LB agar plates after serial dilutions, then incubated at 37°C for 24 h. The broths without heating were used for spreading plates as control. The colony numbers were counted for calculating the rate of surviving cells after heating at 80°C for 10 min.

Detecting biofilm formation

Strains were cultured on LB agar plates, then the morphology of colonies were observed by microscope. Robust pellicles (floating biofilms) were determined in multiwell (24-well) plates (Müller et al., 2015). Briefly, 20 μL fresh broth of each strain was used for inoculating 2 ml MSgg medium in each well, then cultured at 28°C for 48 h to allow float biofilms formation. The MSgg medium contains 100 mM MOPS, 0.5% (v/v) glycerol, 0.5% (w/v) sodium glutamate, 5 mM K_2SO_4 (pH = 7), 50 μg/mL L- tryptophan, 50 μg/mL L-Phenylalanine, 2 mM $MgCl_2$, 700 μM $CaCl_2$, 50 μM $FeCl_3$, 50 μM $MnCl_2$, 2 μM thiamine and 1 μM $ZnCl_2$.

qRT-PCR

The transcription of *ywaA* and *leuA* was analyzed by qRT-PCR. Single colony of each strain was selected for inoculating LB medium and cultured at 37°C overnight, then the broth was transferred into fresh LB medium at a ratio of 1% (v/v). After incubation at 37°C for 24 h, the broth was collected for isolating mRNA with RNeasy Mini Kit (Qiagen, German). cDNA was produced by reverse transcription with 1 μg RNA, iScript Select cDNA Synthesis Kit and random oligonucleotide primers (Bio-Rad, United States). qRT-PCR was performed with cDNA, SsoAdvanced Universal SYBR Green Supermix (Bio-Rad, United States) and target-specific primers (Supplementary Table S2) in CF96 Real-Time System as following: 1 cycle of 95°C for 5 min, 40 cycles of 95°C for 10 s, 45°C for 20 s and 70°C for 30 s. All expression data were normalized to the copy number of 16S rRNA in each sample (Wen et al., 2021).

Determining antifungal activity

Strains were cultured in LB medium at 37°C and 180 rpm for 48 h. After centrifugation at 6,500 g for 10 min, the supernatant of broths were collected for determining the antifungal activity against *F. oxysporum*. Briefly, PDA plates containing the broth supernatant at a ratio of 10% (v/v) were used for culturing *F. oxysporum* at 28°C for 4 days, then the diameter of colony was determined. PDA plates without the broth supernatant were inoculated with *F. oxysporum* as control. The inhibition rate of broth supernatant was calculated by the following formula: Inhibition rate = (Colony diameter in control–Colony diameter in broth supernatant)/Colony diameter in control × 100%.

Fermentation optimization

Carbon sources, nitrogen sources, amino acids and inorganic salts in the medium were optimized for increasing antifungal activity and antifungal lipopeptides production, respectively. On the basis of medium optimization, we further studied the effect of culture conditions including temperature, initial pH, amounts of inoculation and ventilation on the antifungal activity and lipopeptides production, respectively. The detailed methods were described in Supplementary Materials.

Fermentation in bioreactor

The fermentation was batch culture with 30 L optimized medium containing 300 ml defoamer (Soybean oil) in a 50 L fermenter (GJBioTech company, Shanghai, China). Briefly, the engineered strain Δ*kinA*Δ*bdh*Δ*dhbF*Δ*rapA*/T2-*sfp* was cultured in LB medium at 37°C and 180 rpm overnight, then the broth was transferred into 400 ml fresh LB medium in 1 L—flask at a ratio of 1% (v/v). After culturing for 8 h, the fresh broth was inoculated into optimized medium at a ratio of 2% (v/v). The fermentation was performed at 37°C with an agitation speed of 180 rpm and an aeration rate of 0.5 vvm for 48 h. In this period, the broth was collected for detecting the antifungal activity, pH and biomass (OD_{600} value), respectively.

Purification and identification of antifungal lipopeptides

Antifungal lipopeptides were purified from the broth fermented in 50 L—bioreactor as described above. Briefly, 200 ml broth supernatant was adjusted to pH 2.0 with 6 M HCl for precipitating lipopeptides, then the precipitates were dissolved in 20 ml pure water and extracted by the same volume of *n*-butanol. The extracted substances were loaded into silica gel (FCP-200) column then eluted by *n*-butanol: ethanol: acetic acid: water = 30:70:5:20 (v/v) (Xing et al., 2018). The eluted fractions with iturin and fengycin were monitored by measuring the absorbance at 210 nm wavelength and the antifungal activity against *F. oxysporum*. Briefly, the fractions were dried by vacuum rotary evaporation, then the residual powers were dissolved in 2 ml pure water. After filter sterilization, 10 μl solution was loaded onto the filter paper disk with a diameter of 5 mm, then plated on the PDA plates inoculated with *F. oxysporum* to determining the antifungal activity.

The fractions with antifungal activity were further separated by HPLC (LC-100, WUFENG instruments, Shanghai, China) plus a Venusil MP C_{18} column (10 × 250 mm, 5 μm) using the mobile phase acetonitrile : 0.1% trifluoroacetic acid = 40 : 60 (v/v). The eluted fractions with iturin and fengycin were monitored by the antifungal activity against *F. oxysporum* as described above. Finally, the purified lipopeptides were identified by MALDI-TOF-MS (Li et al., 2006; Li et al., 2022).

Quantitative analysis of antifungal lipopeptides by HPLC

10 ml broth of WH1 and the engineered strain Δ*kinA*Δ*bdh*Δ*dhbF*Δ*rapA*/T2-*sfp* cultured in flask or bioreactor were centrifuged for collecting supernatants, then the pH of supernatants were adjusted to pH 2.0 for precipitating lipopeptides as above. The precipitates were dissolved in 10 ml methanol, then the supernatants were collected by centrifugation at 8,000 g for 5 min. The content of iturin and fengycin in supernatants was analyzed by HPLC (Shimadzu, Japan) equipped with a Venusil MP C_{18} column (4.6 × 250 mm, 5 μm) using the mobile phase acetonitrile: 0.1% trifluoroacetic acid = 40:60 (v/v). The purified iturin and fengycin described above were used as standards for counting the content of lipopeptides in samples.

Statistical analysis of data

All experiments are repeated in triplicates. Data between two groups were compared by a student *t*-test with a significant level of $^{*}p < 0.05$ and $^{**}p < 0.01$. Differences in multiple groups were analyzed by Analysis of Variance (ANOVA), and different letters indicate significant differences among different groups.

Results

Iturin and fengycin contributed most of antifungal activity to B. amyloliquefaciens

On the basis of Δ*ituB* and Δ*fenA*, we constructed the double knockout strain Δ*ituB*Δ*fenA*, then the antifungal activity was detected for these strains. It was found that both Δ*ituB* and Δ*fenA* showed a slightly weaker antifungal activity than the wild-type strain WH1, while the double knockout strain Δ*ituB*Δ*fenA* almost lost the antifungal activity against *F. oxysporum* (Supplementary Figure S2). These results clearly showed that iturin and fengycin contribute most of the antifungal activity to *B. amyloliquefaciens* WH1. Thereby, we used the antifungal activity to asses the antifungal lipopeptides (iturin and fengycin) production in this study.

Increasing antifungal activity by enhancement of branched-chain amino acids biosynthesis

Branched-chain amino acids are crucial component of lipopeptides such as surfactin, iturin and fengycin. Here, we deleted *bdh*, *tnrA* and *codY*, respectively, to increase the supply of branched-chain amino acids (Figures 2A,B). The result showed that deletion of *bdh* encoding 2,3-butanediol dehydrogenase led to a weaker growth than WH1, while knockout of *codY* (encoding a regulator CodY for carbon and nitrogen metabolism) or *tnrA* (encoding a regulator TnrA

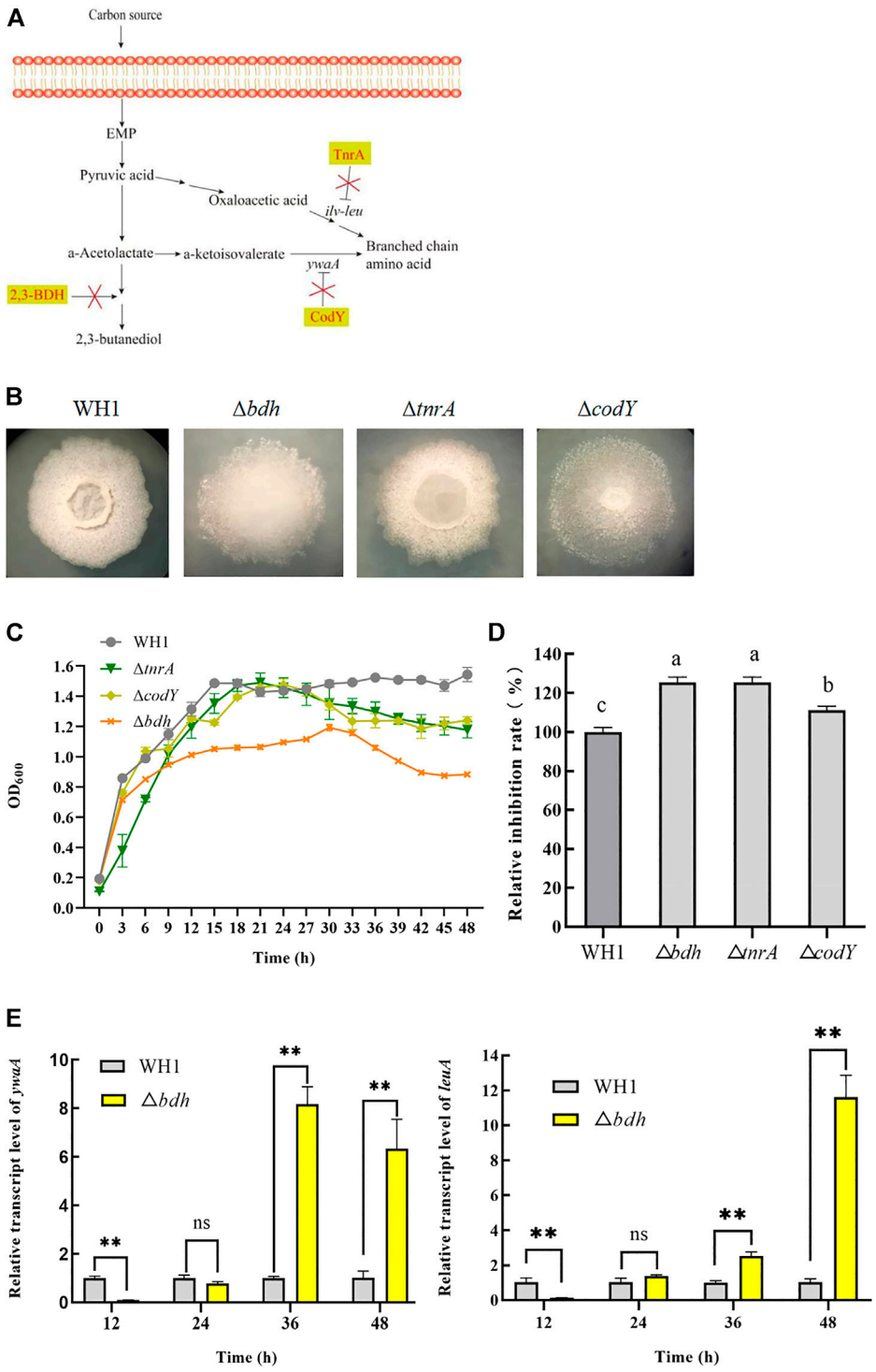

FIGURE 2
Relative inhibition rates and characteristic of knockout strains related with biosynthesis of branched-chain amino acids. **(A)**: Metabolic pathway and regulation of carbon overflow metabolism and biosynthesis of branched-chain amino acids. 2,3-BDH: 2,3-butanediol dehydrogenase; TnrA and CodY: regulators for carbon and nitrogen metabolism; *ywaA:* the aminotransferase gene; *ilv-leu*: the operon for biosynthesis of branched-chain amino acids. **(B)**: Colony morphology. **(C)**: Growth curves. **(D)**: Relative inhibition rates. **(E)**: Relative transcription level of *ywaA* and *leuA* in Δ*bdh*.

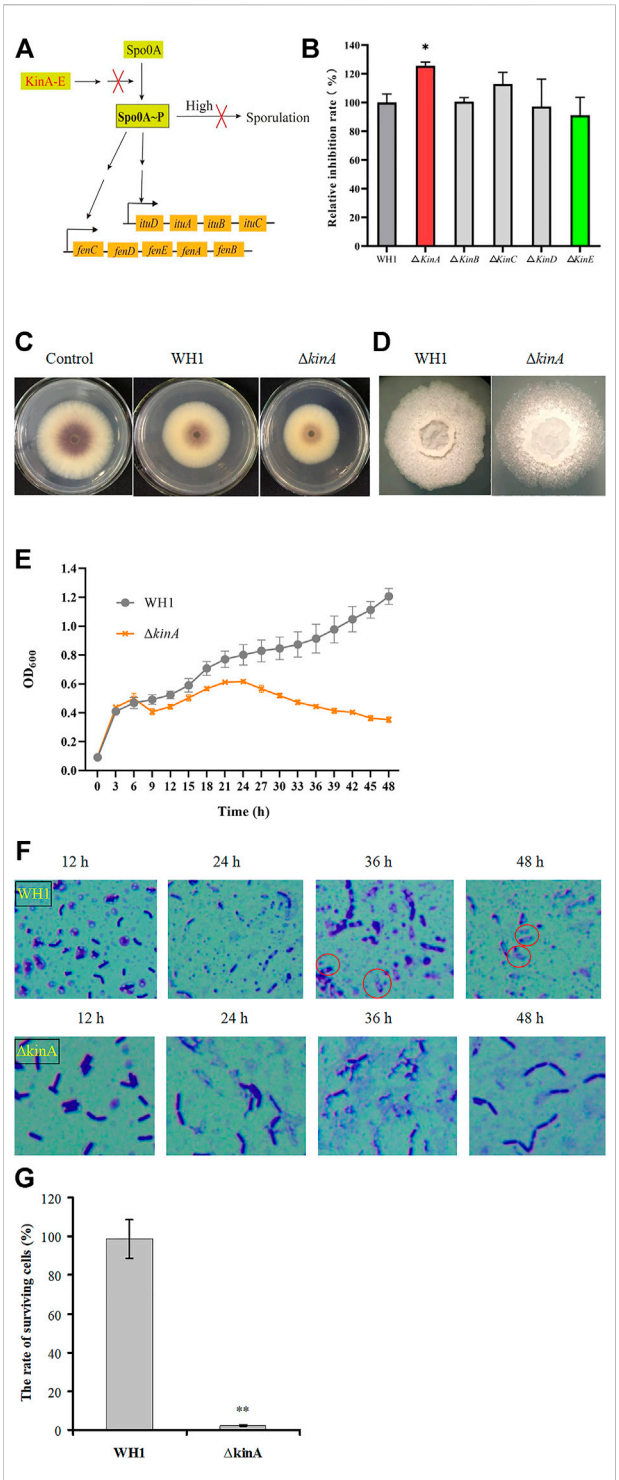

FIGURE 3
Relative inhibition rates and characteristics of the *kinA* knockout strain. **(A)**: Activation of Spo0A by Kin A-E. Arrows mean the promotion role; T-bars men the inhibition role; "High" means the high level of Spo0A~P. **(B)**: Relative inhibition rates. **(C)**: Antifungal activity determined on PDA plates. **(D)**: Colony morphology. **(E)**: Growth curves. **(F)**: Sporulation. **(G)**: The rate of surviving cells after heating.

for nitrogen metabolism) had no significant influence on the cell growth (Figure 2C).

Deletion of *bdh* resulted in an increase of antifungal activity (Figure 2D). Compared to that of WH1, the antifungal activity of Δ*bdh* was increased by 24%. The transcription of *ywaA* and *leuA*, two genes encoding key enzymes for biosynthesis of branched-chain amino acids, were both significantly up-regulated in Δ*bdh* at 36 and 48 h when compared to that of WH1 (Figure 2E). CodY and TnrA inhibit the biosynthesis of branched-chain amino acids. Consistently, deletion of *codY* and *tnrA*, respectively, resulted in an increase of antifungal activity in this study (Figure 2D). Compared to that of WH1, the antifungal activity of Δ*tnrA* was increased by 24%.

Disruption of sporulation enhanced biosynthesis of antifungal lipopeptides

Once sporulation, the biosynthesis of secondary metabolites will be remarkably reduced. In order to extend the stage for producing secondary metabolites, we deleted 5 kinase genes (*kin A* to *E*) involved in activation of Spo0A, a global regulator that is essential for triggering sporulation (Figure 3A). Deletion of *kinB*, *C*, *D* and *E* had no significant influence on the antifungal activity, respectively, but knockout of *kinA* resulted in a significant increase of antifungal activity (Figure 3B). Compared to that of WH1, the antifungal activity of Δ*kinA* was increased by 10% (Figure 3C). The colony morphology of Δ*kinA* was slightly different from WH1 (Figure 3D), but the growth of Δ*kinA* was obviously weaker than WH1 (Figure 3E). KinA is a main histidine kinase for sporulation. Consistently, deletion of *kinA* blocked the spore generation in WH1 (Figure 3F). After heating at 80 °C for 10 min, the rate of surviving cells was 98.78% for WH1, while it was only 2.33% for Δ*kinA* (Figure 3G), further confirmed that deletion of *kinA* disrupted the sporulation in WH1.

Double knockout of kinA and bdh further enhanced antifungal activity

Deletion of *bdh*, *tnrA*, *codY* and *kinA*, respectively, could increase the antifungal activity. We further constructed the double knockout stains including Δ*tnrA*Δ*kinA*, Δ*codY*ΔkinA and Δ*kinA*Δ*bdh* here (Figure 4A). The antifungal activity of Δ*tnrA*Δ*kinA* was lower than WH1, while Δ*codY*Δ*kinA* had a similar antifungal activity to WH1. However, Δ*kinA*Δ*bdh* showed a significantly higher antifungal activity than WH1 (Figure 4B). Compared to that of WH1, the antifungal activity of Δ*kinA*Δ*bdh* was increased by 38%. Due to deletion of *kinA*, the growth of double-knockout strains were all weaker than WH1 (Figure 4C).

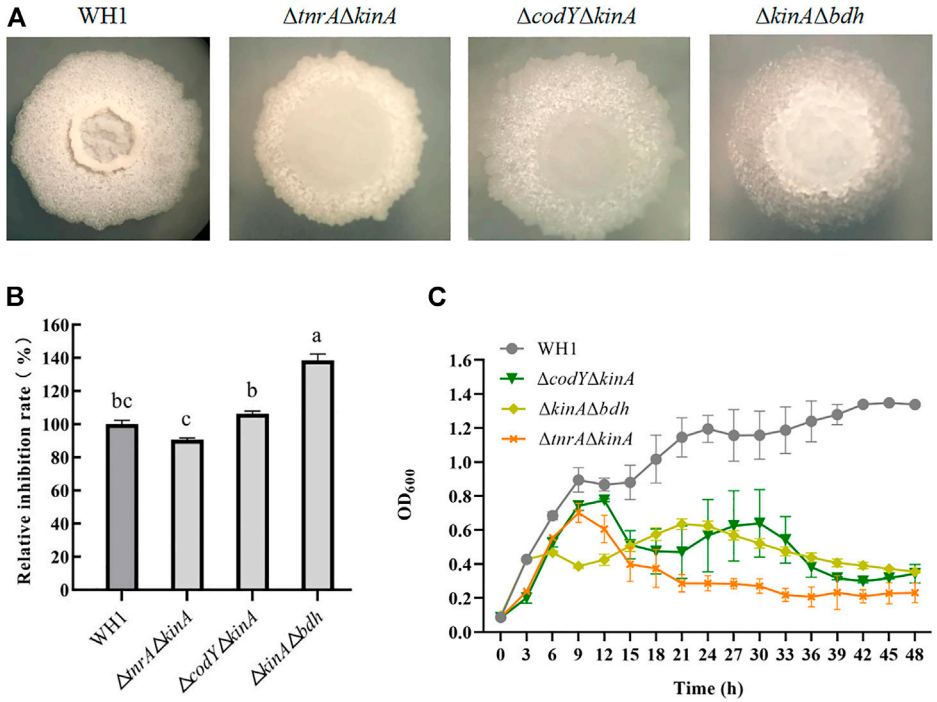

FIGURE 4
Relative inhibition rates and characteristics of double-knock strains. **(A)**: Colony morphology; **(B)**: Relative inhibition rates; **(C)**: Growth curves.

Disruption of biofilm formation strengthened antifungal activity

As illustrated in Figure 5A, we knocked out several genes related to biofilm formation such as *comK*, *sigD*, *dhbF* and *fur*, *abrB* and *sinR*, and *sinI*. Deletion of respective genes resulted in an obvious change of colony morphology (Figure 5B) and float pellicle (Figure 5C). Deletion of *dhbF*, *fur*, *abrB* and *sinR*, respectively, resulted in an obvious decrease of biofilm compared to that of WH1, while knockout of *sinI* led to a robuster float pellicle than WH1 (Figure 5C). Further analysis showed that only the antifungal activity of Δ*dhbF* (*dhbF* belonging to the *dhb* gene cluster for biosynthesis of siderophore) was increased by 13% compared to that of WH1 (Figure 5D). The growth curves showed deletion of *dhbF* had no significant influence on the cell growth (Figure 5E). Deletion of *sinI* could not improve the antifungal activity in WH1.

Triple knockout strain ΔkinAΔbdhΔdhbF with strengthened antifungal activity

For further improving the antifungal activity, we constructed the triple knockout stain Δ*kinA*Δ*bdh*Δ*dhbF* on the basis of Δ*kinA*Δ*bdh* (Figure 6A). Δ*kinA*Δ*bdh*Δ*dhbF* had a significantly higher antifungal activity than WH1 (Figure 6B). Compared to that of WH1, the antifungal activity was increased by 44% in Δ*kinA*Δ*bdh*Δ*dhbF*. Due to deletion of *kinA*, Δ*kinA*Δ*bdh*Δ*dhbF* also showed a weaker growth than WH1 (Figure 6C).

Elevation of Spo0A~P improved antifungal activity

Spo0A~P regulate biosynthesis of many secondary metabolites. Here, we deleted *spo0A* in WH1 (Figure 7B), and found the ability to produce antifungal lipopeptides was significantly reduced in Δ*spo0A* compared to WH1 (Figure 7C). As illustrated in Figure 7A, the aspartate phosphatase family RapA can indirectly dephosphorylate Spo0A~P by dephosphorylating the phosphate group transporter Spo0F~P, and the phosphatase Spo0E is able to directly dephosphorylate Spo0A~P to Spo0A. Here, both deletion of *spo0E* and *rapA* (Figure 7B) could significantly increase the antifungal activity in WH1 (Figure 7C). Except for Δ*spo0A*, the growth of Δ*spo0E* and Δ*rapA* were both similar to WH1 (Figure 7D).

Due to the importance of Spo0A for antifungal activity, we overexpressed *spo0A* in Δ*spo0A* and WH1, respectively. The results showed that compensation with *spo0A* could not restore the colony morphology (Figure 7B), but was able to

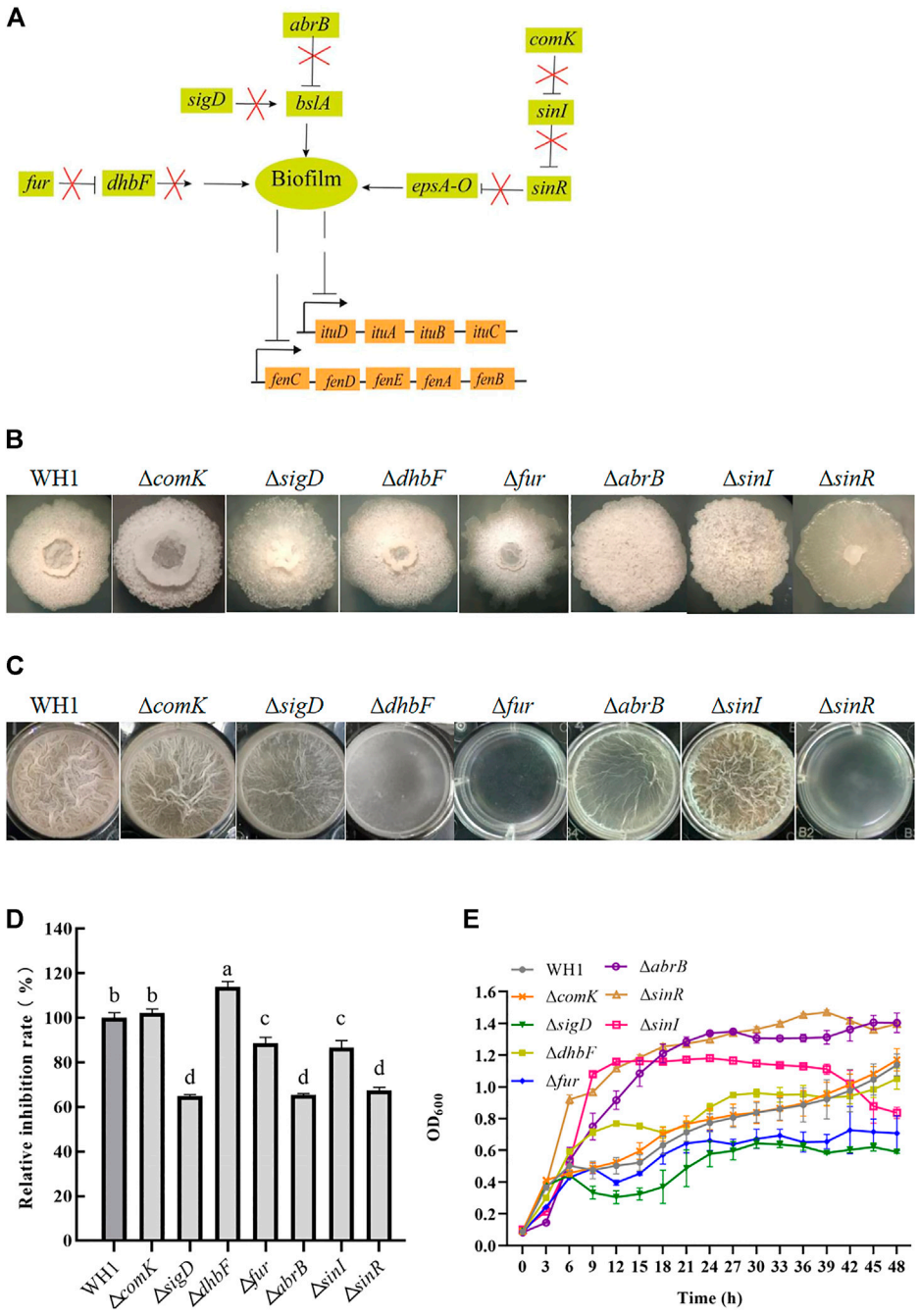

FIGURE 5
Relative inhibition rates and characteristics of knockout strains related with biofilm formation. **(A)**: Regulation of biofilm formation. The *bslA* gene encodes an extracellular protein of biofilm; the *epsA-O* operon encodes the enzymes for biosynthesizing exopolysaccharides of biofilm. ComK: competence transcription factor; SigD: sigma factor D; DhbF: enzyme for biosynthesis of siderophore; Fur: repressor of *dhb*; AbrB and SinR: regulators to suppress biofilm formation; SinI: regulator to promote biofilm formation. **(B)**: Colony morphology. **(C)**: Biofilms. **(D)**: Relative inhibition rates. **(E)**: Growth curves.

significantly increase the antifungal activity of Δ*spo0A* (Figure 7C). Also, the impaired growth of Δ*spo0A* was well restored by compensation with *spo0A* (Figure 7D). However, overexpression of *spo0A* led to a markedly different colony morphology from WH1 (Figure 7B). Moreover, overexpression of *spo0A* resulted in a decrease of antifungal activity (Figure 7C), but had no significant influence on the cell growth (Figure 7D). Accordingly, overexpression of *spo0A*

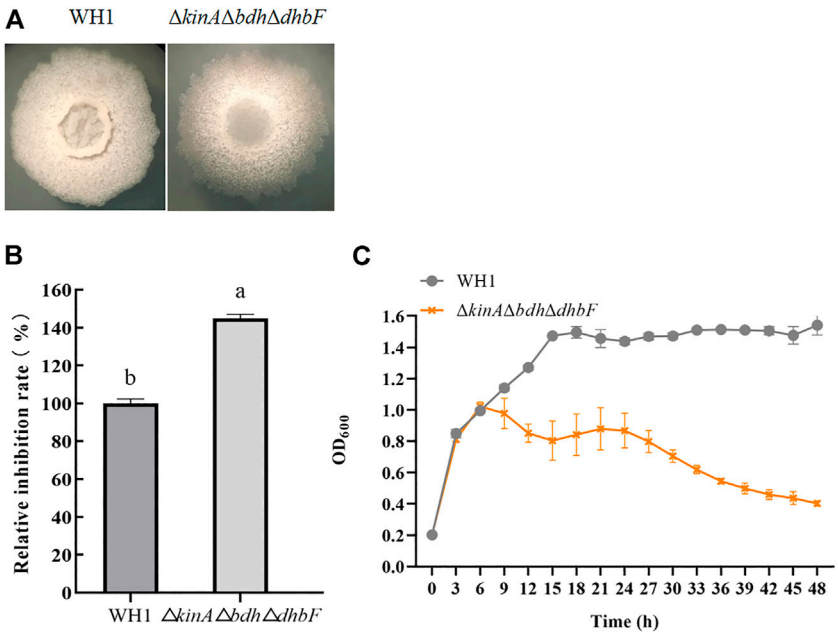

FIGURE 6
Relative inhibition rate and characteristic of Δ*kinA*Δ*bdh*Δ*dhbF*. **(A)**: Colony morphology; **(B)**: Relative inhibition rate; **(C)**: Growth curve.

for increasing lipopeptides production should be done in Δ*spo0A* rather than in WH1.

Further enhanced antifungal activity in ΔkinAΔbdhΔdhbFΔrapA

On the basis of Δ*kinA*Δ*bdh*Δ*dhbF*, we constructed the quadruple knockout strains Δ*kinA*Δ*bdh*Δ*dhbF*Δ*spo0E* and Δ*kinA*Δ*bdh*Δ*dhbF*Δ*rapA*, respectively (Figure 8A). Deletion of *spo0E* in Δ*kinA*Δ*bdh*Δ*dhbF* could not further increase the antifungal activity. Conversely, it led to a decrease of antifungal activity. However, deletion of *rapA* in Δ*kinA*Δ*bdh*Δ*dhbF* could further improve the antifungal activity (Figure 8B). Compared to that of WH1, the antifungal activity was increased by 53% in Δ*kinA*Δ*bdh*Δ*dhbF*Δ*rapA*. The growth of Δ*kinA*Δ*bdh*Δ*dhbF*Δ*spo0E* and Δ*kinA*Δ*bdh*Δ*dhbF*Δ*rapA* were both better than Δ*kinA*, Δ*kinA*Δ*bdh* and Δ*kinA*Δ*bdh*Δ*dhbF* (Figure 8C).

Overexpression of sfp increased antifungal activity

4-Phosphopantetheinyl transferase (Sfp) is essential for biosynthesis of lipopeptides. Here, deletion of *sfp* led to an obvious change of colony morphology in WH1 (Figure 9A). After deletion of *sfp*, the antifungal activity was also significantly decreased in WH1 (Figure 9B). Moreover, the growth of Δ*sfp* was impaired compared to that of WH1 (Figure 9C). Thereby, Sfp is essential for biosynthesis of antifungal lipopeptides and showing antifungal activity in *B. amyloliquefaciens*.

For further improving the antifungal activity, we overexpressed *sfp* in Δ*sfp* and WH1, respectively. Interestingly, compensation with *sfp* could not restore the colony morphology of Δ*sfp*, and overexpression of *sfp* led to a changed colony morphology in WH1 (Figure 9A). Moreover, compensation with *sfp* only restored the antifungal activity in Δ*sfp*, while overexpression of *sfp* could further improve the antifungal activity in WH1 (Figure 9B). Compared to that of WH1, the antifungal activity was increased by 12% in the overexpression strain WH1/T2-*sfp*. Compensation with *sfp* could restore the growth of Δ*sfp* (Figure 9C).

Antifungal activity was further strengthened in ΔkinAΔbdhΔdhbFΔrapA/T2-sfp

We further overexpressed *spo0A* and *sfp* in Δ*kinA*Δ*bdh*Δ*dhbF*Δ*rapA*Δ*spo0A* and Δ*kinA*Δ*bdh*Δ*dhbF*Δ*rapA*, respectively. First, we constructed the penta knockout strain Δ*kinA*Δ*bdh*Δ*dhbF*Δ*rapA*Δ*spo0A* on the basis of Δ*kinA*Δ*bdh*Δ*dhbF*Δ*rapA* (Figure 10A). Δ*kinA*Δ*bdh*Δ*dhbF*Δ*rapA*Δ*spo0A* showed a significant decease of antifungal activity due to deletion of *spo0A* (Figure 10B). Second, we transferred

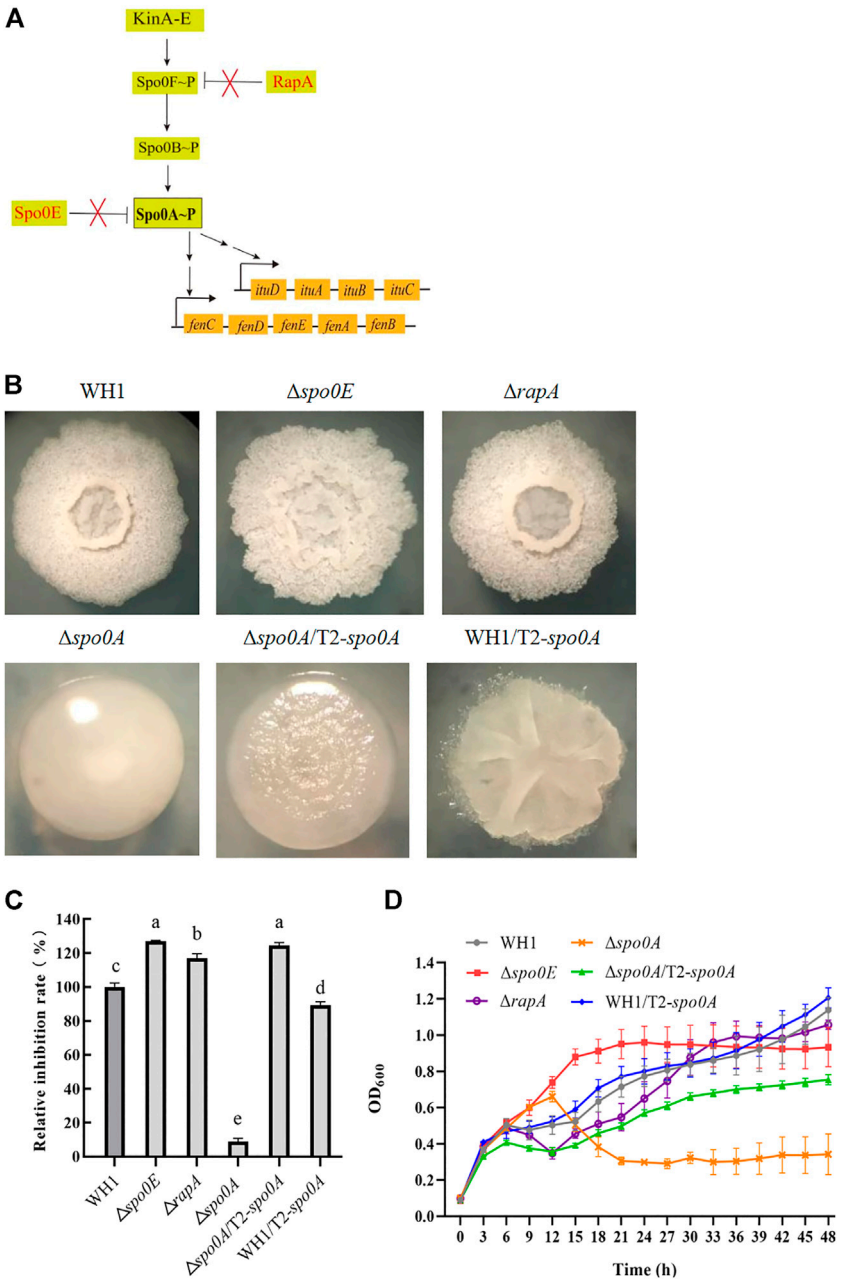

FIGURE 7
Relative inhibition rates and characteristics of engineered strains related with Spo0A phosphorylation. **(A)**: Phosphorylation and dephosphorylation of Spo0A. Spo0F and Spo0B are the phosphate group transporters. **(B)**: Colony morphology. **(C)**: Relative inhibition rates. **(D)**: Growth curves.

T2 plasmid into Δ*kinA*Δ*bdh*Δ*dhbF*Δ*rapA* as a control to rule out the possible influence induced by this plasmid (Figure 10A). The result showed the antifungal activity of Δ*kinA*Δ*bdh*Δ*dhbF*Δ*rapA*/T2 had no significant difference from the host Δ*kinA*Δ*bdh*Δ*dhbF*Δ*rapA* (Figure 10B).

Δ*kinA*Δ*bdh*Δ*dhbF*Δ*rapA*Δ*spo0A*/T2-*spo0A* and Δ*kinA*Δ*bdh*Δ*dhbF*Δ*rapA*/T2-*sfp* was constructed on the basis of Δ*kinA*Δ*bdh*Δ*dhbF*Δ*rapA*Δ*spo0A* and Δ*kinA*Δ*bdh*Δ*dhbF*Δ*rapA*, respectively (Figure 10A). Δ*kinA*Δ*bdh*Δ*dhbF*Δ*rapA*Δ*spo0A*/T2-*spo0A* had a similar antifungal activity to Δ*kinA*Δ*bdh*Δ*dhbF*Δ*rapA*Δ*spo0A*, indicating that compensation with *spo0A* could not restore the antifungal activity in this strain (Figure 10B). However, compensation with *spo0A* could partially restore the growth of Δ*kinA*Δ*bdh*Δ*dhbF*Δ*rapA*Δ*spo0A* (Figure 10C).

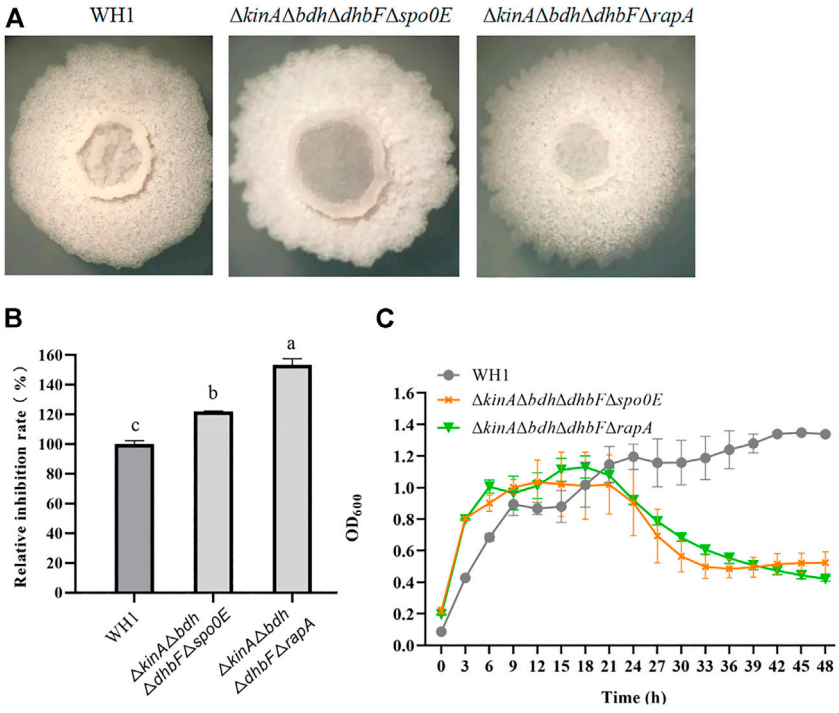

FIGURE 8
Relative inhibition rates and characteristics of quadruple knockout strains. **(A)**: Colony morphology; **(B)**: Relative inhibition rates; **(C)**: Growth curves.

Δ*kinA*Δ*bdh*Δ*dhbF*Δ*rapA*/T2-*sfp* showed a significantly higher antifungal activity than Δ*kinA*Δ*bdh*Δ*dhbF*Δ*rapA*, indicating that overexpression of *sfp* could further improve the antifungal lipopeptides production in Δ*kinA*Δ*bdh*Δ*dhbF*Δ*rapA*. Compared to that of WH1, the antifungal activity was increased by 65% in Δ*kinA*Δ*bdh*Δ*dhbF*Δ*rapA*/T2-*sfp* (Figure 10B). However, its growth was similar to Δ*kinA*Δ*bdh*Δ*dhbF*Δ*rapA*, which were both weaker than WH1 (Figure 10C).

We further verified the antifungal activity of engineered strains, including Δ*kinA*, Δ*kinA*Δ*bdh*, Δ*kinA*Δ*bdh*Δ*dhbF*, Δ*kinA*Δ*bdh*Δ*dhbF*Δ*rapA* and Δ*kinA*Δ*bdh*Δ*dhbF*Δ*rapA*/T2-*sfp*. From WH1 to Δ*kinA*Δ*bdh*Δ*dhbF*Δ*rapA*/T2-*sfp*, the antifungal activity was increased step by step. The antifungal activity was improved by 1.7-fold in the final strain Δ*kinA*Δ*bdh*Δ*dhbF*Δ*rapA*/T2-*sfp* compared to that in the original strain WH1 (Figure 10D).

Fermentation optimization significantly enhanced antifungal activity

We selected the modified Landy as an initial medium for Δ*kinA*Δ*bdh*Δ*dhbF*Δ*rapA*/T2-*sfp* to produce antifungal lipopeptides. After optimization, the final medium formula for culturing Δ*kinA*Δ*bdh*Δ*dhbF*Δ*rapA*/T2-*sfp* to produce antifungal lipopeptides contains 20 g/L glucose, 20 g/L soybean meal power, 0.5 g/L $MgSO_4 \bullet 7H_2O$, 1.0 g/L KH_2PO_4, 0.8 g/L $ZnSO_4 \bullet 7H_2O$ and 7.0 mg/L $MnSO_4 \bullet H_2O$ in 1 L water, pH 8.0. In this formula, the inhibition rate of broth achieved at 37.18%. On the basis of above medium, the fermentation conditions were also optimized, including temperature (37°C), initial pH value (8.0), inoculation rate (2%), liquid volume (100 ml medium loaded in 250 ml flask) and fermentation time (48 h). The detailed results were described in the Supplementary Materials.

Antifungal lipopeptides produced by ΔkinAΔbdhΔdhbFΔrapA/T2-sfp

We further verified the optimized fermentation medium and conditions in a 50 L- bioreactor. Δ*kinA*Δ*bdh*Δ*dhbF*Δ*rapA*/T2-*sfp* was cultured at 37°C with an agitation speed of 180 rpm and an aeration rate of 0.5 vvm. The results showed the biomass achieved at the maximum at 18 h, and the antifungal activity of broth was significantly increased from 12 h and reached the maximum at 48 h. The pH of broth was slightly decreased during the period of fermentation (Figure 11A).

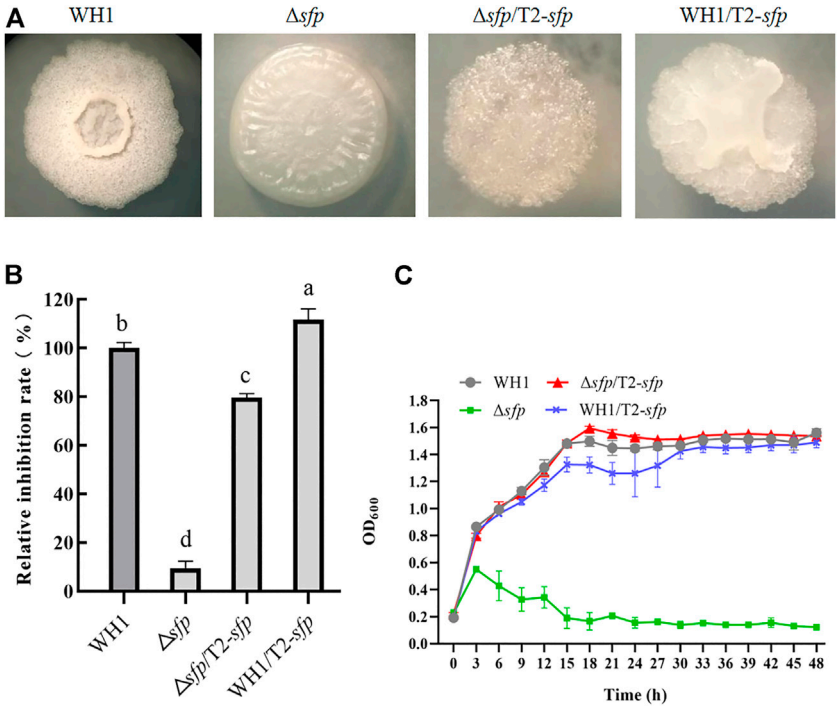

FIGURE 9
Relative inhibition rates and characteristics of engineered strains related with *sfp*. **(A)**: Colony morphology; **(B)**: Relative inhibition rates; **(C)**: Growth curves.

The broth was used for extracting the antifungal lipopeptides by *n*-butanol, then separated by silica column. After elution, two components, a and b, were collected, but only Component a showed an obvious antifungal activity (Figure 11B). Component a was further purified by HPLC with C_{18} column, and could be separated into 12 peaks. After being dried by vacuum rotary evaporation, the residual powers were dissolved in pure water to a concentration of 1 mg/L for determining antifungal activity. The results showed that P4–P12 all showed an antifungal activity against *F. oxysporum* (Figure 11C). The antifungal substances in P4–P12 were determined by LC-MS, and the results showed P4–P12 were iturin and fengycin homologues, respectively (Figure 11D). P4 was iturin A homologue with C16 fatty acid chain, and P5–P12 were fengycin A homologues with C15–C18 fatty acid chains, and fengycin B homologues with C14–C17 fatty acid chains, respectively (Table 2).

The purity of iturin and fengycin was further analyzed by HPLC with C_{18} column. P4 and P9 were detected for their purity. It was found that both P4 (Iturin A) and P9 (Fengycin A) showed a single peak after separation by HPLC (Figure 11E), suggesting these two lipopeptides were both at a high purity. Consequently, P4 and P9 were used as standards for quantitative analysis of iturin and fengycin in the broth.

Antifungal lipopeptides production was significantly increased in the engineered strain

The purified iturin A (P4) and fengycin A (P9) were used as standards for making standard curves. The content of iturin and fengycin was quantitatively determined in the broth of WH1 and Δ*kinA*Δ*bdh*Δ*dhbF*Δ*rapA*/T2-*sfp*, respectively. The results showed the antifungal activity in Δ*kinA*Δ*bdh*Δ*dhbF*Δ*rapA*/T2-*sfp* was significantly higher than WH1. Also, the antifungal activity of Δ*kinA*Δ*bdh*Δ*dhbF*Δ*rapA*/T2-*sfp* in bioreactor was significantly higher that in flask (Figure 12A). By construction of the engineered strains and fermentation optimization, the antifungal activity was increased by 2.5-fold from 18% in WH1 to 46% in Δ*kinA*Δ*bdh*Δ*dhbF*Δ*rapA*/T2-*sfp*.

In the broth of WH1, the titer of iturin and fengycin was 5.4 mg/L and 75.2 mg/L, respectively, while the titer of iturin achieved at 17.0 mg/L in Δ*kinA*Δ*bdh*Δ*dhbF*Δ*rapA*/T2-*sfp* with an increase of 3.2-fold compared to that of WH1. After fermentation optimization in flask, the titer of iturin and fengycin in Δ*kinA*Δ*bdh*Δ*dhbF*Δ*rapA*/T2-*sfp* achieved at 31.1 mg/L and 175.3 mg/L, with an approximate increase of 1.8-fold and 2.3-fold, respectively. After fermentation in 50 L bioreactor, the titer of iturin and fengycin achieved at 123.5 mg/L and 1200.8 mg/L, which further improved by 4.0-fold and 6.8-

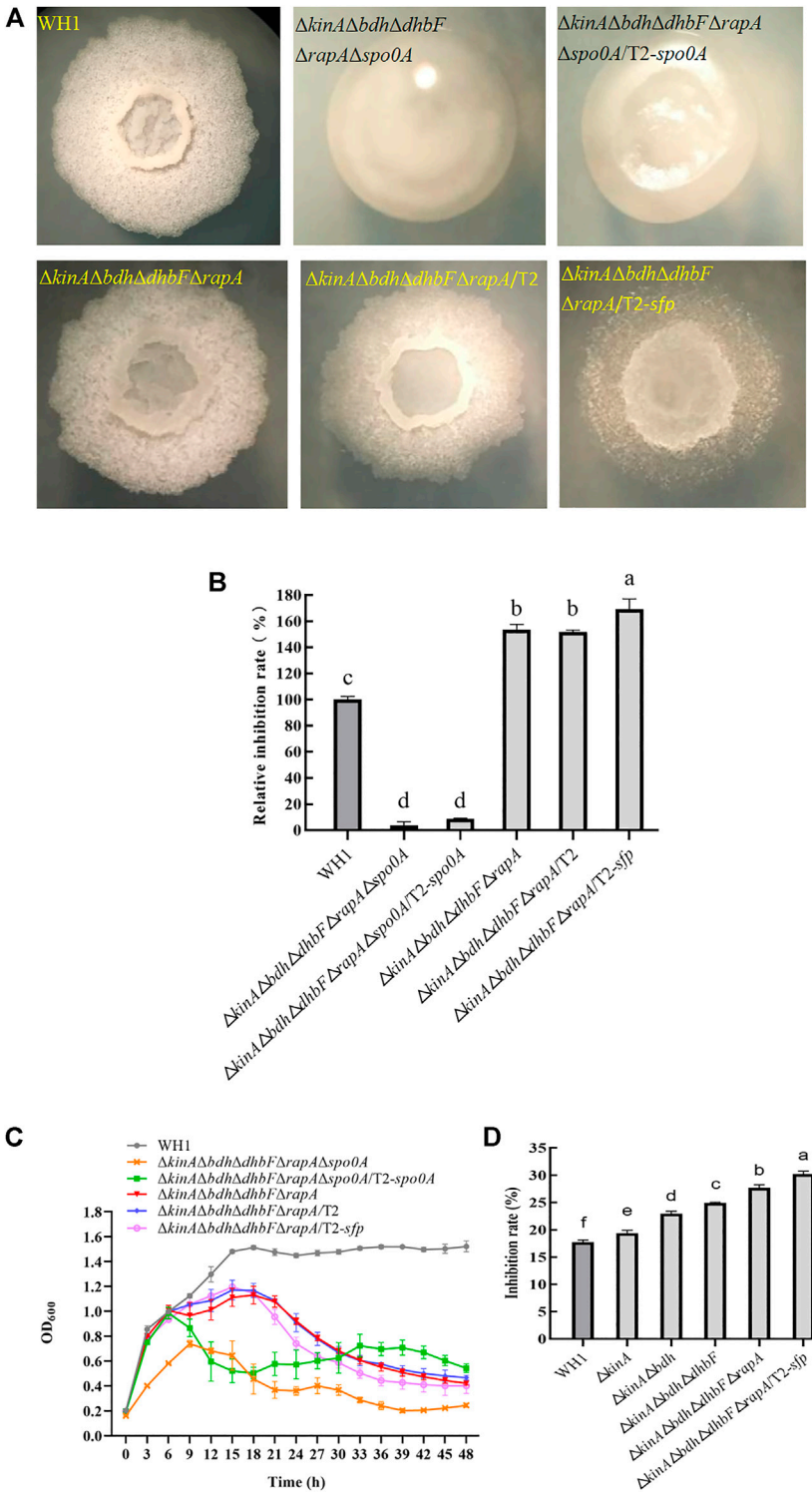

FIGURE 10
Relative inhibition rates and characteristics of Δ*kinA*Δ*bdh*Δ*dhbF*Δ*rapA*/T2-*sfp*. **(A)**: Colony morphology; **(B)**: Relative inhibition rates; **(C)**: Growth curves; **(D)**: Comparison of antifungal activity among different engineered strains (from the original strain WH1 to the final strain Δ*kinA*Δ*bdh*Δ*dhbF*Δ*rapA*/T2-*sfp*).

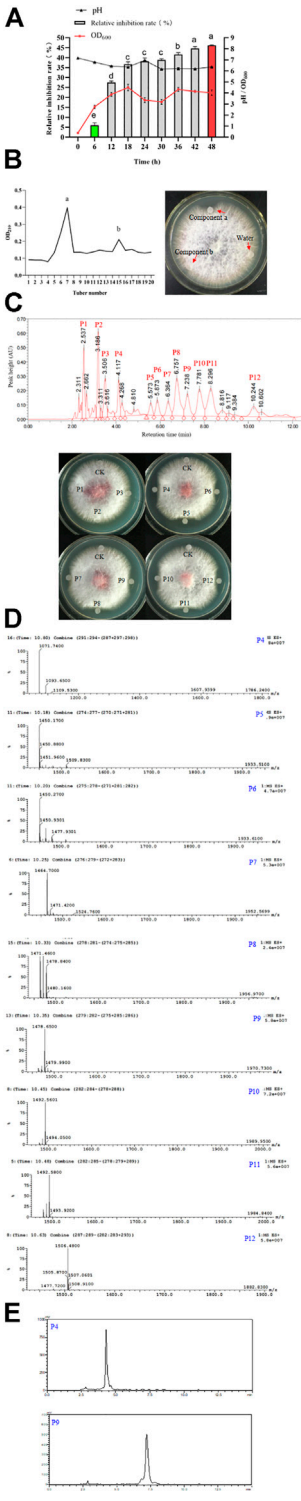

FIGURE 11
Fermentation, purification and identification of antifungal lipopeptides. **(A)**: Fermentation of antifungal lipopeptides in bioreactor. **(B)**: Separation of antifungal lipopeptides by silica gel column. Left: The extracted substances in *n*-butanol were separated by silica gel column; Right: Antifungal activity of crude lipopeptides separated by silica column. **(C)**: Purifying antifungal

(*Continued*)

TABLE 2 Characterization of lipopeptides by m/z in P4–P12.

Peak	Mass peak (m/z)	Ion type	Lipopeptide
P4	1071.74	$[M + H]^+$	C16 Iturin A
P5	1450.17	$[M + H]^+$	C15 Fengycin A
P6	1450.27	$[M + H]^+$	C15 Fengycin A
P7	1464.70	$[M + H]^+$	C16 Fengycin A
			C14 Fengycin B
P8	1471.46	$[M + Na]^+$	C15 Fengycin A
P9	1478.65	$[M + H]^+$	C17 Fengycin A
			C15 Fengycin B
P10	1492.56	$[M + H]^+$	C18 Fengycin A
			C16 Fengycin B
P11	1492.58	$[M + H]^+$	C18 Fengycin A
			C16 Fengycin B
P12	1506.48	$[M + H]^+$	C17 Fengycin B

fold, respectively (Figure 12B,C). Compared to that of WH1, the final iturin and fengycin titer of Δ*kinA*Δ*bdh*Δ*dhbF*Δ*rapA*/T2-*sfp* in bioreactor increased by 22.8-fold and 15.9-fold, respectively.

Discussion

Many *Bacillus* species can produce antifungal lipopeptides such as iturin and fengycin against fungi (Kaspar et al., 2109). Previously, we isolated a strain WH1 with excellent antifungal activity, and was characterized as *B. amyloliquefaciens*. Here, we verified that the antifungal activity was mainly attributed to iturin and fengycin, consistent with the previous reports (Farzaneh et al., 2016; Liu et al., 2020). Therefore, we used antifungal activity to asses the antifungal lipopeptides (iturin and fengycin) production in this study.

Branched-chain amino acids are crucial component of lipopeptides. In *B. subtilis*, the biosynthesis of branched-chain amino acids is suppressed by CodY (a regulator to regulate both carbon metabolism and nitrogen metabolism) and TnrA (a regulator for nitrogen metabolism) (Fujita 2009; Fu et al., 2022). Knockout of *codY* can result in an increase of biosynthesis of branched-chain amino acids such as isoleucine, valine, etc (Brinsmade et al., 2014). Consistently, deletion of *codY* also led to an increase of antifungal activity in WH1. TnrA negatively regulates the expression of *ilv-leu*

FIGURE 11 (Continued)
lipopeptides by RP-HPLC. Top: P1–P12 were the peaks with a retention time 2.537, 3.186, 3.506, 4.117, 5.573, 5.873, 6.364, 6.757, 7.238, 7.781, 8.296 and 10.244 min, respectively; Bottom: Antifungal activity of P1–P12. CK: control (water). **(D)**: Analysis of P4–P12 by mass spectrometry. **(E)**: Determination of the purity of iturin (P4) and fengycin (P9) by HPLC.

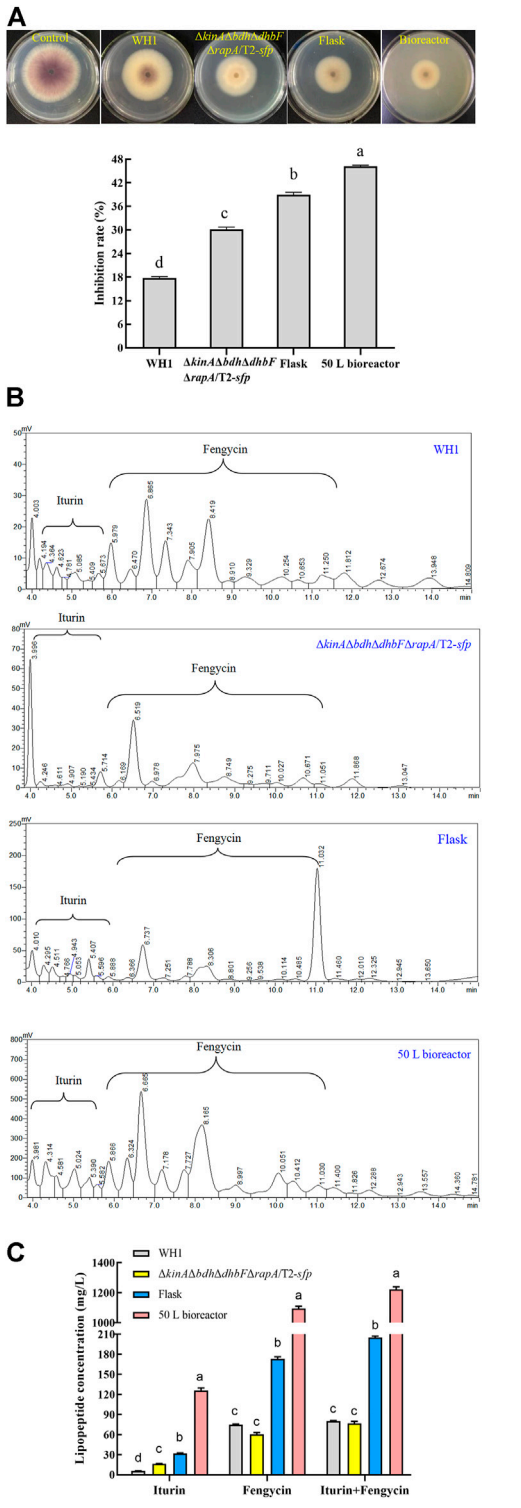

FIGURE 12
Comparison of antifungal activity and lipopeptides production between WH1 and Δ*kinA*Δ*bdh*Δ*dhbF*Δ*rapA*/T2-*sfp*. **(A)**: Antifungal activity. Top: Antifungal activity determined on PDA plates; Bottom: Inhibition rates. **(B)**: Analysis of lipopeptides in the broth by HPLC. **(C)**: Antifungal lipopeptides titer in the broth of WH1 and Δ*kinA*Δ*bdh*Δ*dhbF*Δ*rapA*/T2-*sfp*.

operon for biosynthesis of branched-chain amino acids (Tojo et al., 2005). Consistently, knockout of *tnrA* also led to a strengthening antifungal activity in WH1. For biosynthesis of lipopeptides, the pyruvate from glycolytic pathway is converted to the branched-chain amino acids, which are precursors for biosynthesis of several lipopeptides. However, pyruvate can also be sequentially converted to acetolactate, acetoin and 2,3-butanediol (Peng et al., 2019). Theoretically, deletion of the gene *bdh* encoding 2,3-butanediol dehydrogenase can increase the supply of pyruvate for biosynthesis of branched-chain amino acids. As expected, deletion of *bdh* resulted in an increase of antifungal activity here. It could be further verified by the result that the transcription of two genes *ywaA* and *leuA*, which encode key enzymes for biosynthesis of branched-chain amino acids, were both significantly up-regulated in Δ*bdh*. This might be explained by the reason that knockout of *bdh* could accumulate more pyruvate, which act as substrate to promote the expression of *ywaA* and *leuA* for biosynthesis of more branched-chain amino acids. Although Iturin A does not contain branched-chain amino acids, and fengycin contains only molecule isoleucine, surfactin contains several branched-chain amino acids. Generally, surfactin acts as a signal molecule for activation of Spo0A to form Spo0A~P via histidine kinases (López et al., 2009). We found that maintaining Spo0A~P level was favorable for increasing the antifungal lipopeptides production. Consequently, knockout of *bdh* could also increase the antifungal lipopeptides production here.

Once sporulation, the biosynthesis of secondary metabolites will be remarkably reduced in *Bacillus*. For example, the *spoIVB*-null non-spore-forming mutant of *B. subtilis* was especially efficient in producing the secondary metabolites such as surfactin (Wang et al., 2020). In order to extend the stage for producing secondary metabolites, we deleted 5 histidine kinase genes (*kin A* to *E*) involved in activation of Spo0A (a global regulator for triggering sporulation) to block sporulation, respectively (López et al., 2009). It was found that only knockout of *kinA* resulted in a significant increase of antifungal activity. In *B. subtilis*, KinA is a main histidine kinase for sporulation, and knockout of *kinA* can lead to a significant decrease of sporulation (Schultz, 2016). Consistently, deletion of *kinA* also blocked the spore generation in *B. amyloliquefaciens* WH1. We speculated that some cells were died due to the retardation for generating spores. As a result, the biomass was decreased in most of the strains with knockout of *kinA*. On the other hand, the disability to sporulate could extend the stage for producing lipopeptides.

The double knockout strains including *kinA* and one gene from *tnrA*, *codY* and *bdh* were constructed for further increasing antifungal activity. Three double knockout strains including Δ*tnrA*Δ*kinA*, Δ*codY*Δ*kinA* and Δ*bdh*Δ*kinA* were constructed, but only Δ*kinA*Δ*bdh* showed a significantly higher antifungal activity than WH1. The antifungal activity of Δ*tnrA*Δ*kinA* was lower than that of WH1, while Δ*codY*Δ*kinA* had a similar

antifungal activity compared to WH1. KinA, TnrA and CodY are all global regulators, hence double knockout of *kinA* and *tnrA* or *codY* might cause negative influence on the cellular physiological and biochemical activities. However, deletion of *bdh* only blocked the carbon overflow metabolism to produce 2,3-butanediol, so double knockout of *kinA* and *bdh* had a weaker influence than other double knockout strains.

Biofilm is considered as a suppressor of lipopeptides (e.g., surfactin) synthesis, so disruption of biofilm formation is favorable for improving lipopeptides production (Wu et al., 2019). Here, we knocked out several genes related to biofilm formation such as *comK* (She et al., 2020), *sigD* (Fan et al., 2016), *dhbF* (a gene of *dhb* operon for biosynthesis of siderophore) and *fur* (a repressor of *dhb*) (Oliveira et al., 2017; Pi and Helmann 2017), *abrB* and *sinR* (regulators to suppress biofilm formation) (Newman et al., 2013; Klausmann et al., 2021), and *sinI* (a regulator to promote biofilm formation) (López et al., 2009). Deletion of respective genes resulted in an obvious change of colony morphology and float pellicle, but only deletion of *dhbF* led to a significant increase of antifungal activity. The results ruled out the possibility that reduction of biofilm formation could generally enhance antifungal activity. The positive effect of the *dhbF* null-mutation might be due to the blocking of siderophore synthesis, which enhances the availability of amino acids and fatty acids involved in lipopeptides synthesis (Oliveira et al., 2017; Pi and Helmann 2017). On this basis, the triple knockout stain Δ*kinA*Δ*bdh*Δ*dhbF* was constructed for further improving antifungal activity.

After phosphorylation, Spo0A regulates biosynthesis of many secondary metabolites (Rahman et al., 2006; Sun et al., 2021). For example, Klausmann et al. (2021) reported that the null-mutant of *spo0A* could reduce surfactin production in *B. subtilis*. Consistently, deletion of *spo0A* led to a very significant reduction of antifungal activity in WH1. This was different from knockout of *kinA*, which resulted in a significant increase of antifungal activity by disrupting the phosphorylation of Spo0A for sporulation. In *B. subtilis*, high levels of Spo0A~P are essential for sporulation (López et al., 2009), so knockout of *kinA* only resulted in a decreased ability to phosphorylate Spo0A for sporulation, but Spo0A could still be phosphorylated via other pathways to produce lipopeptides. Due to the importance of Spo0A for antifungal activity, we overexpressed *spo0A* in Δ*spo0A* and WH1, respectively. Compensation with *spo0A* could significantly increase the antifungal activity in Δ*spo0A*, but overexpression of *spo0A* led to a decrease of antifungal activity in WH1. This result is different from the previous report that overexpression of *spo0A* could lead to an increase of iturin yield (Sun et al., 2021). This might be explained that overexpression of *spo0A* could cause interference to the expression of native *spo0A* in the wild-type strain. For this reason, overexpression of *spo0A* for increasing antifungal activity and lipopeptides production should be done in Δ*spo0A* rather than in WH1.

The aspartate phosphatase family RapA can indirectly dephosphorylate Spo0A~P by dephosphorylating the phosphate group transporter Spo0F~P (Reder et al., 2012), and the phosphatase Spo0E is able to directly dephosphorylate Spo0A~P to Spo0A (Babel et al., 2020). Deletion of *spo0E* and *rapA* could both significantly increase the antifungal activity in WH1. Thereby, Spo0A is essential for biosynthesis of antifungal lipopeptides, and maintaining a certain level of Spo0A~P is favorable for strengthening the antifungal activity in *B. amyloliquefaciens*, consistent with the previous reports that biosynthesis of fengycin and iturin is regulated by Spo0A in *B. subtilis* (Rahman et al., 2006; Zhang et al., 2016; Zhao et al., 2018). On this basis, we deleted *spo0E* and *rapA* in Δ*kinA*Δ*bdh*Δ*dhbF*, respectively, but only deletion of *rapA* could further increase the antifungal activity in Δ*kinA*Δ*bdh*Δ*dhbF*. This might be due to the reason that RapA is able to dephosphorylate several phosphorylated regulators, while Spo0E can only dephosphorylate Spo0A~P (Rahman et al., 2006; Sun et al., 2021).

4-Phosphopantetheinyl transferase (Sfp) is essential for biosynthesis of lipopeptides in *B. subtilis* (Reuter et al., 1999; Wu et al., 2019; Yang et al., 2020). After deletion of *sfp*, the antifungal activity was significantly decreased in WH1. Thus, Sfp is also essential for biosynthesis of antifungal lipopeptides and showing antifungal activity in *B. amyloliquefaciens*. This result is consistent with the previous report in *B. subtilis* (Tan et al., 2022). Consistently, overexpression of *sfp* could further increase the antifungal activity in Δ*kinA*Δ*bdh*Δ*dhbF*Δ*rapA*.

The antifungal activity was increased step by step in the engineered strains, including Δ*kinA*, Δ*kinA*Δ*bdh*, Δ*kinA*Δ*bdh*Δ*dhbF*, Δ*kinA*Δ*bdh*Δ*dhbF*Δ*rapA* and Δ*kinA*Δ*bdh*Δ*dhbF*Δ*rapA*/T2-*sfp*. Finally, the titer of iturin achieved at 17.0 mg/L in Δ*kinA*Δ*bdh*Δ*dhbF*Δ*rapA*/T2-*sfp* with an increase of 3.2-fold compared to that of WH1. After fermentation optimization, the titer of iturin and fengycin achieved at 123.5 mg/L and 1200.8 mg/L in 50 L bioreactor, respectively. Compared to that of WH1, the final iturin and fengycin titer of Δ*kinA*Δ*bdh*Δ*dhbF*Δ*rapA*/T2-*sfp* increased by 22.8-fold and 15.9-fold, respectively. Dang et al. (2019) inserted a strong promoter at the upstream of *itu* operon to increase the iturin titer to 37.35 mg/L, but it was lower than our titer (123.5 mg/L) in this study. He et al. (2021) used *B. subtilis* 168 as a surrogate for improving fengycin production by overexpression of *accA* (encoding acetyl-CoA carboxylase), *cypC* (encoding fatty acid beta-hydroxylating cytochrome P450) and *gapA* (encoding glyceraldehyde-3-phosphate dehydrogenase). As a result, the final fengycin production reached 59.87 mg/L in the engineered *B. subtilis* 168, but it was also much lower than our fengycin production (1200.8 mg/L) in this study.

In conclusion, we have systematically developed a metabolically engineered cell factory to improve the antifungal activity and increase the antifungal lipopeptides

production in *B. amyloliquefaciens*, such as blocking the carbon overflow metabolism to increase the supply of precursor branched-chain amino acids, deletion of *kinA* to disrupt sporulation for extending the stage to produce secondary metabolites, knock out of *dhbF* to hinder biosynthesis of siderophore for abolishing the competence of substrates, deletion of *rapA* to maintain an appropriate Spo0A~P level, and overexpression of *sfp* to enhance the activation of substrates. In addition, we have also systematically revealed several metabolic pathways and regulators to directly or indirectly influence the antifungal activity and biosynthesis of iturin and fengycin in *B. amyloliquefaciens*. This work may open up a new avenue for the commercial production of iturin and fengycin in *B. amyloliquefaciens*.

Data availability statement

The original contributions presented in the study are included in the article/Supplementary Material, further inquiries can be directed to the corresponding author.

Author contributions

XZ, RW and GQ designed the research. SW, GM, NL, YZ, and JT performed the experiments. SW, XZ, and GQ performed the analysis and wrote the paper.

Funding

Project 31870030 supported by National Natural Science Foundation of China.

Conflict of interest

The authors declare that the research was conducted in the absence of any commercial or financial relationships that could be construed as a potential conflict of interest.

Publisher's note

All claims expressed in this article are solely those of the authors and do not necessarily represent those of their affiliated organizations, or those of the publisher, the editors and the reviewers. Any product that may be evaluated in this article, or claim that may be made by its manufacturer, is not guaranteed or endorsed by the publisher.

Supplementary material

The Supplementary Material for this article can be found online at: https://www.frontiersin.org/articles/10.3389/fbioe.2022.961535/full#supplementary-material

References

Babel, H., Naranjo-Meneses, P., Trauth, S., Schulmeister, S., Malengo, G., Sourjik, V., et al. (2020). Ratiometric population sensing by a pump-probe signaling system in Bacillus subtilis. *Nat. Commun.* 11 (1), 1176. doi:10.1038/s41467-020-14840-w

Brinsmade, S. R., Alexander, E. L., Livny, J., Stettner, A. I., Segrè, D., Rhee, K. Y., et al. (2014). Hierarchical expression of genes controlled by the Bacillus subtilis global regulatory protein CodY. *Proc. Natl. Acad. Sci. U. S. A.* 111 (22), 8227–8232. doi:10.1073/pnas.1321308111

Chen, B., Wen, J., Zhao, X., Ding, J., and Qi, G. (2020). Surfactin: A quorum-sensing signal molecule to Relieve CCR in *Bacillus amyloliquefaciens*. *Front. Microbiol.* 11, 631. doi:10.3389/fmicb.2020.00631

Cheng, Y. C., Ke, W. J., and Liu, S. T. (2017). Regions involved in fengycin synthetases enzyme complex formation. *J. Microbiol. Immunol. Infect.* 50 (6), 755–762. doi:10.1016/j.jmii.2015.12.001

Dang, Y., Zhao, F., Liu, X., Fan, X., Huang, R., Gao, W., et al. (2019). Enhanced production of antifungal lipopeptide iturin A by Bacillus amyloliquefaciens LL3 through metabolic engineering and culture conditions optimization. *Microb. Cell Fact.* 18 (1), 68. doi:10.1186/s12934-019-1121-1

Fan, B., Li, Y. L., Mariappan, A., Becker, A., Wu, X. Q., and Borriss, R. (2016). New SigD-regulated genes identified in the rhizobacterium Bacillus amyloliquefaciens FZB42. *Biol. Open* 5 (12), 1776–1783. doi:10.1242/bio.021501

Farzaneh, M., Shi, Z. Q., Ahmadzadeh, M., Hu, L. B., and Ghassempour, A. (2016). Inhibition of the Aspergillus flavus growth and aflatoxin B1 contamination on pistachio nut by fengycin and surfactin-producing Bacillus subtilis UTBSP1. *Plant Pathol. J.* 32 (3), 209–215. doi:10.5423/PPJ.OA.11.2015.0250

Fu, Y., Guo, Q., Dong, L., Liu, X., Chen, X., Wang, P., et al. (2022). iTRAQ-based proteomic analysis of Bacillus subtilis strain NCD-2 regulated by PhoPR two-component system: A comparative analysis with transcriptomics revealed the regulation for fengycin production by branched chain amino acids. *Microbiol. Res.* 260, 127024. doi:10.1016/j.micres.2022.127024

Fujita, Y. (2009). Carbon catabolite control of the metabolic network in Bacillus subtilis. *Biosci. Biotechnol. Biochem.* 73, 245–259. doi:10.1271/bbb.80479

Gao, W., Yin, Y., Wang, P., Tan, W., He, M., and Wen, J. (2022). Production of fengycin from D-xylose through the expression and metabolic regulation of the Dahms pathway. *Appl. Microbiol. Biotechnol.* 106 (7), 2557–2567. doi:10.1007/s00253-022-11871-9

Gu, Y., Zheng, R., Sun, C., and Wu, S. (2022). Isolation, identification and characterization of two kinds of deep-sea bacterial lipopeptides against foodborne pathogens. *Front. Microbiol.* 13, 792755. doi:10.3389/fmicb.2022.792755

He, M., Wen, J., Yin, Y., and Wang, P. (2021). Metabolic engineering of *Bacillus subtilis* based on genome-scale metabolic model to promote fengycin production. *3 Biotech.* 11 (10), 448. doi:10.1007/s13205-021-02990-7

Horsburgh, M. J., and Moir, A. (1999). Sigma M, an ECF RNA polymerase sigma factor of Bacillus subtilis 168, is essential for growth and survival in high concentrations of salt. *Mol. Microbiol.* 32 (1), 41–50. doi:10.1046/j.1365-2958.1999.01323.x

Kaspar, F., Neubauer, P., and Gimpel, M. (2019). Bioactive secondary metabolites from *Bacillus subtilis*: A comprehensive review. *J. Nat. Prod.* 82, 2038–2053. doi:10.1021/acs.jnatprod.9b00110

Klausmann, P., Lilge, L., Aschern, M., Hennemann, K., Henkel, M., Hausmann, R., et al. (2021). Influence of B. subtilis 3NA mutations in spo0A and abrB on surfactin production in B. subtilis 168. *Microb. Cell Fact.* 20 (1), 188. doi:10.1186/s12934-021-01679-z

Koumoutsi, A., Chen, X. H., Vater, J., and Borriss, R. (2007). DegU and YczE positively regulate the synthesis of bacillomycin D by Bacillus amyloliquefaciens

strain FZB42. *Appl. Environ. Microbiol.* 73 (21), 6953–6964. doi:10.1128/AEM.00565-07

Kourmentza, K., Gromada, X., Michael, N., Degraeve, C., Vanier, G., Ravallec, R., et al. (2021). Antimicrobial activity of lipopeptide biosurfactants against foodborne pathogen and food spoilage microorganisms and their cytotoxicity. *Front. Microbiol.* 11, 561060. doi:10.3389/fmicb.2020.561060

Li, Q., Meng, X., Wu, X., Lin, W., Duan, C., Feng, J., et al. (2006). Purification of two antimicrobial substances produced by Bacillus subtilis strain B11 and their properties. *Agric. Sci. China* 5, 363–369. doi:10.1016/S1671-2927(06)60062-X

Li, Y., Xia, M., He, P., Yang, Q., Wu, Y., He, P., et al. (2022). Developing *Penicillium digitatum* management strategies on post-harvest citrus fruits with metabolic components and colonization of *Bacillus subtilis* L1-21. *J. Fungi (Basel).* 8 (1), 80. doi:10.3390/jof8010080

Lin, L. Z., Zheng, Q. W., Wei, T., Zhang, Z. Q., Zhao, C. F., Zhong, H., et al. (2020). Isolation and characterization of fengycins produced by *Bacillus amyloliquefaciens* JFL21 and its broad-spectrum antimicrobial potential against multidrug-resistant foodborne pathogens. *Front. Microbiol.* 11, 579621. doi:10.3389/fmicb.2020.579621

Liu, Y., Teng, K., Wang, T., Dong, E., Zhang, M., Tao, Y., et al. (2020). Antimicrobial Bacillus velezensis HC6: Production of three kinds of lipopeptides and biocontrol potential in maize. *J. Appl. Microbiol.* 128 (1), 242–254. doi:10.1111/jam.14459

López, D., Vlamakis, H., Losick, R., and Kolter, R. (2009). Paracrine signaling in a bacterium. *Genes Dev.* 23 (14), 1631–1638. doi:10.1101/gad.1813709

Müller, S., Strack, S. N., Ryan, S. E., Kearns, D. B., and Kirby, J. R. (2015). Predation by Myxococcus xanthus induces Bacillus subtilis to form spore-filled megastructures. *Appl. Environ. Microbiol.* 81, 203–210. doi:10.1128/AEM.02448-14

Newman, J. A., Rodrigues, C., and Lewis, R. J. (2013). Molecular basis of the activity of SinR protein, the master regulator of biofilm formation in Bacillus subtilis. *J. Biol. Chem.* 288 (15), 10766–10778. doi:10.1074/jbc.M113.455592

Ohsawa, T., Tsukahara, K., Sato, T., and Ogura, M. (2006). Superoxide stress decreases expression of srfA through inhibition of transcription of the comQXP quorum-sensing locus in Bacillus subtilis. *J. Biochem.* 139, 203–211. doi:10.1093/jb/mvj023

Oliveira, F., França, Â., and Cerca, N. (2017). Staphylococcus epidermidis is largely dependent on iron availability to form biofilms. *Int. J. Med. Microbiol.* 307 (8), 552–563. doi:10.1016/j.ijmm.2017.08.009

Oslizlo, A., Stefanic, P., Dogsa, I., and Mandic-Mulec, I. (2014). Private link between signal and response in Bacillus subtilis quorum sensing. *Proc. Natl. Acad. Sci. U. S. A.* 111 (4), 1586–1591. doi:10.1073/pnas.1316283111

Peng, G., Zhao, X., Li, Y., Wang, R., Huang, Y., and Qi, G. (2019). Engineering Bacillus velezensis with high production of acetoin primes strong induced systemic resistance in *Arabidopsis thaliana*. *Microbiol. Res.* 227, 126297. doi:10.1016/j.micres.2019.126297

Pi, H. L., and Helmann, J. D. (2017). Sequential induction of Fur-regulated genes in response to iron limitation in Bacillus subtilis. *Proc. Natl. Acad. Sci. U. S. A.* 114 (48), 12785–12790. doi:10.1073/pnas.1713008114

Prathiviraj, R., Rajeev, R., Fernandes, H., Rathna, K., Lipton, A. N., Selvin, J., et al. (2021). A gelatinized lipopeptide diet effectively modulates immune response, disease resistance and gut microbiome in Penaeus vannamei challenged with Vibrio parahaemolyticus. *Fish. Shellfish Immunol.* 112, 92–107. doi:10.1016/j.fsi.2021.02.018

Qi, G., Kang, Y., Li, L., Xiao, A., Zhang, S., Wen, Z., et al. (2014). Deletion of meso-2, 3-butanediol dehydrogenase gene budC for enhanced D-2, 3-butanediol production in Bacillus licheniformis. *Biotechnol. Biofuels* 7 (1), 16. doi:10.1186/1754-6834-7-16

Rahman, M. S., Ano, T., and Shoda, M. (2006). Second stage production of iturin A by induced germination of Bacillus subtilis RB14. *J. Biotechnol.* 125, 513–515. doi:10.1016/j.jbiotec.2006.03.016

Reder, A., Albrecht, D., Gerth, U., and Hecker, M. (2012). Cross-talk between the general stress response and sporulation initiation in Bacillus subtilis - the σ(B) promoter of spo0E represents an AND-gate. *Environ. Microbiol.* 14, 2741–2756. doi:10.1111/j.1462-2920.2012.02755.x

Reuter, K., Mofid, M. R., Marahiel, M. A., and Ficner, R. (1999). Crystal structure of the surfactin synthetase-activating enzyme sfp: A prototype of the 4′-phosphopantetheinyl transferase superfamily. *EMBO J.* 18, 6823–6831. doi:10.1093/emboj/18.23.6823

Schultz, D. (2016). Coordination of cell decisions and promotion of phenotypic diversity in B. subtilis via pulsed behavior of the phosphorelay. *Bioessays* 38 (5), 440–445. doi:10.1002/bies.201500199

She, Q., Hunter, E., Qin, Y., Nicolau, S., Zalis, E. A., Wang, H., et al. (2020). Negative interplay between biofilm formation and competence in the environmental strains of *Bacillus subtilis*. *mSystems* 5 (5), e00539-20. doi:10.1128/mSystems.00539-20

Sun, J., Liu, Y., Lin, F., Lu, Z., and Lu, Y. (2021). CodY, ComA, DegU and Spo0A controlling lipopeptides biosynthesis in Bacillus amyloliquefaciens fmbJ. *J. Appl. Microbiol.* 131 (3), 1289–1304. doi:10.1111/jam.15007

Tan, W., Yin, Y., and Wen, J. (2022). Increasing fengycin production by strengthening the fatty acid synthesis pathway and optimizing fermentation conditions. *Biochem. Eng. J.* 177, 108235. doi:10.1016/j.bej.2021.108235

Tojo, S., Satomura, T., Morisaki, K., Deutscher, J., Hirooka, K., and Fujita, Y. (2005). Elaborate transcription regulation of the Bacillus subtilis ilv-leu operon involved in the biosynthesis of branched-chain amino acids through global regulators of CcpA, CodY and TnrA. *Mol. Microbiol.* 56 (6), 1560–1573. doi:10.1111/j.1365-2958.2005.04635.x

Tosato, V., Albertini, A. M., Zotti, M., Sonda, S., and Bruschi, C. V. (1997). Sequence completion, identification and definition of the fengycin operon in Bacillus subtilis 168. *Microbiology* 143, 3443–3450. doi:10.1099/00221287-143-11-3443

Tsuge, K., Inoue, S., Ano, T., Itaya, M., and Shoda, M. (2005). Horizontal transfer of iturin A operon, itu, to Bacillus subtilis 168 and conversion into an iturin A producer. *Antimicrob. Agents Chemother.* 49 (11), 4641–4648. doi:10.1128/AAC.49.11.4641-4648.2005

Vlamakis, H., Chai, Y., Beauregard, P., Losick, R., and Kolter, R. (2013). Sticking together: Building a biofilm the Bacillus subtilis way. *Nat. Rev. Microbiol.* 11, 157–168. doi:10.1038/nrmicro2960

Wan, C., Fan, X., Lou, Z., Wang, H., Olatunde, A., and Rengasamy, K. (2021). Iturin: Cyclic lipopeptide with multifunction biological potential. *Crit. Rev. Food Sci. Nutr.* 13, 1–13. doi:10.1080/10408398.2021.1922355

Wang, M., Yu, H., Li, X., and Shen, Z. (2020). Single-gene regulated non-spore-forming Bacillus subtilis: Construction, transcriptome responses, and applications for producing enzymes and surfactin. *Metab. Eng.* 62, 235–248. doi:10.1016/j.ymben.2020.08.008

Wang, P., Guo, Q., Ma, Y., Li, S., Lu, X., Zhang, X., et al. (2015). DegQ regulates the production of fengycins and biofilm formation of the biocontrol agent Bacillus subtilis NCD-2. *Microbiol. Res.* 178, 42–50. doi:10.1016/j.micres.2015.06.006

Wen, J., Zhao, X., Si, F., and Qi, G. (2021). Surfactin, a quorum sensing signal molecule, globally affects the carbon metabolism in Bacillus amyloliquefaciens. *Metab. Eng. Commun.* 12, e00174. doi:10.1016/j.mec.2021.e00174

Wu, C. Y., Chen, C. L., Lee, Y. H., Cheng, Y. C., Wu, Y. C., Shu, H. Y., et al. (2007). Nonribosomal synthesis of fengycin on an enzyme complex formed by fengycin synthetases. *J. Biol. Chem.* 282 (8), 5608–5616. doi:10.1074/jbc.M609726200

Wu, Q., Zhi, Y., and Xu, Y. (2019). Systematically engineering the biosynthesis of a green biosurfactant surfactin by Bacillus subtilis 168. *Metab. Eng.* 52, 87–97. doi:10.1016/j.ymben.2018.11.004

Xing, X., Zhao, X., Ding, J., Liu, D., and Qi, G. (2018). Enteric-coated insulin microparticles delivered by lipopeptides of iturin and surfactin. *Drug Deliv. (Lond).* 25 (1), 23–34. doi:10.1080/10717544.2017.1413443

Xu, Y., Cai, D., Zhang, H., Gao, L., Yang, Y., Gao, J., et al. (2020). Enhanced production of iturin A in Bacillus amyloliquefaciens by genetic engineering and medium optimization. *Process Biochem.* 90, 50–57. doi:10.1016/j.procbio.2019.11.017

Yang, R., Lei, S., Xu, X., Jin, H., Sun, H., Zhao, X., et al. (2020). Key elements and regulation strategies of NRPSs for biosynthesis of lipopeptides by Bacillus. *Appl. Microbiol. Biotechnol.* 104 (19), 8077–8087. doi:10.1007/s00253-020-10801-x

Zhang, W. J., Guo, P., Liu, M., Yang, B. L., Wang, J. H., and Jiang, J. (2016). Isolation, identification, and optimal cultivation of a marine bacterium antagonistic to Magnaporthe grisea. *Genet. Mol. Res.* 15 (2), gmr8646. doi:10.4238/gmr.15028646

Zhang, Y., Qi, J., Wang, Y., Wen, J., Zhao, X., and Qi, G. (2022). Comparative study of the role of surfactin-triggered signalling in biofilm formation among different Bacillus species. *Microbiol. Res.* 254, 126920. doi:10.1016/j.micres.2021.126920

Zhang, Z., Ding, Z. T., Zhong, J., Zhou, J. Y., Shu, D., Luo, D., et al. (2017). Improvement of iturin A production in Bacillus subtilis ZK0 by overexpression of the comA and sigA genes. *Lett. Appl. Microbiol.* 64 (6), 452–458. doi:10.1111/lam.12739

Zhao, H., Shao, D., Jiang, C., Shi, J., Li, Q., Huang, Q., et al. (2017a). Biological activity of lipopeptides from Bacillus. *Appl. Microbiol. Biotechnol.* 101 (15), 5951–5960. doi:10.1007/s00253-017-8396-0

Zhao, J., Zhang, C., and Lu, Z. (2018). Differential proteomics research of Bacillus amyloliquefaciens and its genome-shuffled saltant for improving fengycin production. *Braz. J. Microbiol.* 49 (1), 166–177. doi:10.1016/j.bjm.2018.04.010

Zhao, X., Zhou, Z., and Han, Y. (2017b). Antifungal effects of lipopeptide produced by *Bacillus amyloliquefaciens* BH072. *Adv. Biosci. Biotechnol.* 8, 295–310. doi:10.4236/abb.2017.89022

frontiers | Frontiers in Bioengineering and Biotechnology

TYPE Original Research
PUBLISHED 14 September 2022
DOI 10.3389/fbioe.2022.978686

OPEN ACCESS

EDITED BY
Mingfeng Cao,
Xiamen University, China

REVIEWED BY
Jian-Zhong Liu,
Sun Yat-sen University, China
Zheng-Jun Li,
Beijing University of Chemical Technology, China
Guang Zhao,
Shandong University, China

*CORRESPONDENCE
Shiqin Yu,
shiqin.yu@jiangnan.edu.cn

SPECIALTY SECTION
This article was submitted to Synthetic Biology,
a section of the journal
Frontiers in Bioengineering and Biotechnology

RECEIVED 26 June 2022
ACCEPTED 26 August 2022
PUBLISHED 14 September 2022

CITATION
Li N, Shan X, Zhou J and Yu S (2022), Identification of key genes through the constructed CRISPR-dcas9 to facilitate the efficient production of O-acetylhomoserine in Corynebacterium glutamicum.
Front. Bioeng. Biotechnol. 10:978686.
doi: 10.3389/fbioe.2022.978686

Identification of key genes through the constructed CRISPR-dcas9 to facilitate the efficient production of O-acetylhomoserine in *Corynebacterium glutamicum*

Ning Li[1,2,3], Xiaoyu Shan[1,2], Jingwen Zhou[1,2,4,5] and Shiqin Yu[1,2]*

[1]Science Center for Future Foods, Jiangnan University, Wuxi, China, [2]National Engineering Research Center of Cereal Fermentation and Food Biomanufacturing, Jiangnan University, Wuxi, China, [3]School of Food Science and Technology, Jiangnan University, Wuxi, China, [4]Engineering Research Center of Ministry of Education on Food Synthetic Biotechnology, Jiangnan University, Wuxi, China, [5]Jiangsu Province Engineering Research Center of Food Synthetic Biotechnology, Jiangnan University, Wuxi, China

O-Acetylhomoserine (OAH) is an important platform chemical for the synthesis of L-methamidophos and L-methionine. It has been produced efficiently in *Corynebacterium glutamicum*. However, a wider range of key factors had not been identified, limiting further increases in OAH production. This study successfully identified some limiting factors and regulated them to improve OAH titer. Firstly, an efficient clustered regularly interspaced short palindromic repeats/dead CRISPR associated protein 9 (CRISPR-dCas9) system was constructed and used to identify the key genes in central metabolism and branch pathways associated with OAH biosynthesis. Then, the *gltA* gene involved in TCA cycle was identified as the most critical gene. A sequential promoter $P_{NCgl2698}$, which showed different transcriptional intensity in different strain growth periods, was used to control the expression of *gltA* gene, resulting in OAH production of 7.0 g/L at 48 h. Finally, the OAH titer of the engineered strain reached 25.9 g/L at 72 h in a 5-L bioreactor. These results show that the identification and regulation of key genes are critical for OAH biosynthesis, which would provide a better research basis for the industrial production of OAH in *C. glutamicum*.

KEYWORDS

Corynebacterium glutamicum*, L-homoserine, O-acetylhomoserine, CRISPR, *gltA

1 Introduction

O-Acetylhomoserine (OAH) is an important platform compound for the synthesis of useful chemicals, such as L-methamidophos and L-methionine. The biosynthesis of OAH requires not only L-homoserine and acetyl-CoA, but also an amount of energy and reducing power. Its entire biosynthesis process involves glucose transport, glycolysis pathway, pentose phosphate pathway (PPP), tricarboxylic acid (TCA) cycle and L-aspartate metabolic pathway (Li N. et al., 2021). The TCA cycle generates NADH and ATP for OAH biosynthesis and consumes a large amount of acetyl-CoA that required for L-homoserine acetylation (Krebs, 1970). The PPP provides a large amount of NADPH for OAH biosynthesis (Wang et al., 2016). Phosphoenolpyruvate and pyruvate produced by glycolysis are precursors of L-aspartic acid biosynthesis (Piao et al., 2019) and there are many pathways to consume L-aspartic acid and acetyl-CoA (Yin et al., 2012; Milke et al., 2019; Sagong et al., 2022). Currently, regulating the expression of genes related to the L-aspartate metabolic pathway and strengthening the biosynthesis of acetyl-CoA are the main strategies to improve the production of OAH in *Corynebacterium glutamicum* and *Escherichia coli* (Wei et al., 2019; Li et al., 2022). However, these cannot further improve the titer and yield of OAH, especially in *C. glutamicum*.

Pathway design and optimization are important for the construction of high-yield strains of target products (Choi et al., 2019; Li, et al., 2020b). With the maturity of gene expression, knockout and other technologies, researchers can quickly carry out a series of modifications on chassis cells to produce new bio-based chemicals (Wei et al., 2021; Kim et al., 2022). Especially, some strategies have been applied to optimize the biosynthetic pathway composed of a large number of genes or reprogram gene expression to control complex metabolic pathways, such as the application of a multidimensional heuristic process to achieve high astaxanthin production in *E. coli* (Zhang et al., 2018), and genomic iterative substitution of large synthetic DNA fragments in *C. glutamicum* (Ye et al., 2022). As a robust industrial microorganism, the gene available regulation technology in *C. glutamicum* has been continuously created and improved, and a variety of strategies have been gradually applied (Zhang et al., 2019; Du et al., 2021). However, in addition to regulating the L-aspartate metabolic pathway, the lack of research on other pathways such as glucose transport, glycolysis and TCA cycle has hampered the strain improvement in the accumulation of OAH. Previous studies found that identifying the limiting factors of OAH biosynthesis by overexpression and knockout of a single gene in *C. glutamicum* was a very time- and labor-consuming method (Li et al., 2022), and thereby the application of a more

TABLE 1 Strains used in this study.

Strain	Description	Source
E. coli JM109	Plasmid amplification	Invitrogen
C. glutamicum ATCC 13032	Wild-type	ATCC
Cg17	13,032 derivative, Δ*NCgl1021*::P_{tuf}-*cas9*::P_{prp}-*recET*, Δ*mcbR*, Δ*metD*, Δ*thrB*, Δ*NCgl2360*::P_{sod}-$thrA^{S345F}$, Δ*NCgl2688*::$P_{NCgl1676}$-$metX^{r}$_*Lm*, Δ*metY*, Δ*pck*::P_{sod}-*aspC*, P_{sod}-pyc^{PA458S}, P_{sod}-$lysC^{T311I}$, P_{sod}-*asd*, P_{sod}-hom^{V59A}, P_{sod}-*brnFE*, icd^{M1V}, $dapA^{M1V}$	Li et al. (2022)
Cg17-3	Cg-17 harboring pEC-$thrA^{S345F}$-$P_{NCgl1676}$-$metX^{r}$	Li et al. (2022)
Cg18	D10A and H840A of Cas9 in Cg17	This study
Cg18-(T)	Cg18 harboring pXM-sgRNAi-*mCherry*(T) and pNCgl1676-*mCherry*	This study
Cg18-null(T)	Cg18 harboring pXM-sgRNAi-Null and pNCgl1676-*mCherry*	This study
Cg18-1	D10A and H840A of Cas9 in Cg17-3	This study
Cg18-1 (null)	Cg18-1 harboring pXM-sgRNAi-Null	This study
Cg18-1(X)	Cg18-1 harboring pXM-sgRNAi-X	This study
Cg19-Δ*gapA*	Δ*gapA* in the strain Cg17	This study
Cg19-Δ*gltA*	Δ*gltA* in the strain Cg17	This study
Cg20	Δ*aspA*::P_{tuf}-*aspB_Pa* in the strain Cg17	This study
Cg20-1	Cg-20 harboring pEC-$thrA^{S345F}$-$P_{NCgl1676}$-$metX^{r}$	This study
Cg20-2	Δ*aspA*::P_{tuf}-*aspB_Pa* in the strain Cg17-3	This study
Cg21	Δ*aspA*::P_{tuf}-*aspB_Pa*, Δ*gltA* in the strain Cg17	This study
Cg21-1	Cg21 harboring pXMJ19 and pEC-XK99E	This study
Cg21-2	Cg21 harboring pXMJ19 and pEC-$thrA^{S345F}$-$P_{NCgl1676}$-$metX^{r}$	This study
Cg21-3	Cg21 harboring pXM-*aspB*_Pa and pEC-$thrA^{S345F}$-$P_{NCgl1676}$-$metX^{r}$	This study
Cg22	Δ*aspA*::P_{tuf}-*aspB_Pa*, Δ*gltA*::$P_{NCgl2698}$-*gltA* in the strain Cg17	This study
Cg22-1	Cg22 harboring pEC-$thrA^{S345F}$-$P_{NCgl1676}$-$metX^{r}$	This study
Cg23-1	Δ*Cas9*, Δ*recET* in the strain Cg22-1	This study

TABLE 2 Plasmids used in this study.

Plasmid	Description	Source
pEC-XK99E	IPTG-inducible P_{trc} promoter, Km^r	Kirchner and Tauch, (2003)
pXMJ19	IPTG-inducible P_{tac} promoter, Cm^r	Jakoby et al. (1999)
pK18mobsacB	Suicide vector, Km^r	Schafer et al. (1994)
pEC-*thrA*^{S345F}-$P_{NCgl1676}$-*metX*^{r}	pEC-XK99E carrying *thrA*^{S345F} and *metX*^{r}, *metX*^{r} under the control of $P_{NCgl1676}$ promoter	Li et al. (2022)
pK18-dCas9-D10A	Mutate the 10th amino acid site (aspartate to alanine) of Cas9	This study
pK18-dCas9-H840A	Mutate the 840th amino acid site (histidine to alanine) of Cas9	This study
pP_{trc}sgRNA-dCas9	Mutate the 10th amino acid site (aspartate to alanine) of Cas9	This study
pP_{H36}sgRNA-dCas9	Mutate the 840th amino acid site (histidine to alanine) of Cas9	This study
p$P_{trc}P_{H36}$sgRNA-dCas9	Mutate the 10th (aspartate to alanine) and 840th amino acid site (histidine to alanine) of Cas9	This study
pNCgl1676-*mCherry*	The plasmid carrying the *mCherry* gene under the control of the promoter $P_{NCgl1676}$	Li, et al. (2020a)
pXM-sgRNAi-*mCherry*(T)	Expression of sgRNA localized to the template chain of *mCherry* gene	This study
pXM-sgRNAi-Null	Expression of sgRNA without localization site	This study
pXM-sgRNAi-X	Expression of sgRNA localized to X gene	This study
pK18-P_{tuf}-aspB_Pa	Integrated expression of *aspB* gene from *Pseudomonas aeruginosa*	This study
pK18-gltA-QC	Deletion of *gltA* gene	This study
pK18-$P_{NCgl2698}$-gltA	Replace native promoter with promoter $P_{NCgl2698}$ of *gltA* gene	This study
p$P_{trc}P_{H36}$sgRNA-recET-cas9	Inactivation of *recET* and *cas9* genes	This study

efficient way to quickly identify the limiting step of OAH biosynthesis would be very significant.

As an efficient and accurate genome editing tool, the clustered regularly interspaced short palindromic repeats/CRISPR associated protein 9 (CRISPR-Cas9) system has been widely used in microbial metabolic engineering (Li C. et al., 2021; Qin et al., 2021; Shi et al., 2022). The functional Cas9-sgRNA complex has a high lethal rate and is unfriendly for identifying growth essential genes in prokaryotes. Therefore, two inactive mutations D10A and H840A were introduced into the RuvC1 and HNH nuclease domains of Cas9 to form dead Cas9 (dCas9), which lost its cleavage activity but still had DNA binding ability (Larson et al., 2013). This method had been widely used in many microorganisms, including *Saccharomyces cerevisiae*, *E. coli* and *C. glutamicum*. For *C. glutamicum*, previous researchers used one plasmid for dCas9 protein expression and the other plasmid for sgRNA expression to realize the application of CRISPR interference (CRISPRi) (Cleto et al., 2016; Zhang et al., 2016; Park et al., 2018). These systems consumed all two available plasmids in *C. glutamicum* (Yoon and Woo, 2018; Gauttam et al., 2019; Park et al., 2019). However, some key genes also need to be expressed by plasmids for construction of target strains. Therefore, to make CRISPRi system more widely used in *C. glutamicum*, it is necessary to construct a system using less plasmids.

In this study, to systematically identify the key genes for efficient biosynthesis of OAH in *C. glutamicum*, two sites of *cas9* gene in the genome were mutated to form dCas9 protein, based on the CRISPR-Cas9 system constructed in our previous study (Li N. et al., 2021). Taking glucose transport, glycolysis pathway, PPP and TCA cycle as the targets, the CRISPR-dCas9 system was used to inhibit the expression of related genes. It was found that the genes related to glucose transport, glycolysis and TCA cycle had a significant impact on the OAH accumulation. Finally, the sequential promoter was used to regulate *gltA* gene, which improved the OAH titer and provided some useful information for the efficient biosynthesis of OAH in *C. glutamicum*.

2 Materials and methods

2.1 Strains and plasmids

The *C. glutamicum* ATCC 13032 variants were used for the biosynthesis of target products. *E. coli* JM109 was used for plasmid construction. The plasmid pEC-XK99E and pXMJ19 were used for gene expression, pXMJ19ts was used for sgRNA expression, pK18mobsacB was used for genome editing. Details are listed in Tables 1, 2.

2.2 Strains culture

The strains culture conditions were described as our previous study (Li et al., 2022). For the shake flask culture, the engineered *C. glutamicum* strains were precultured in seed medium, cultured in fermentation medium with 4% inoculum. The fermentation medium was supplemented with 5 g/L acetate at 24 and 36 h, respectively. All strains were grown at 30°C and 220 rpm in

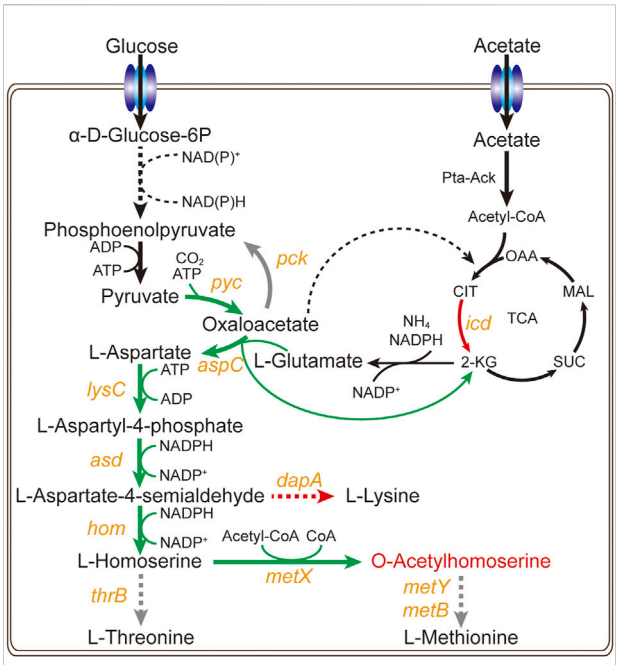

FIGURE 1
Metabolic engineering strategy for construction of the OAH-producing strains. Yellow italics represent genes. The black arrows represent the unmodified pathways, the grey arrows represent the knockout pathways, the green arrows represent the up-regulated pathways, the red arrows represent the down-regulated pathways.

shaking incubators. For a 5-L bioreactor culture, the strain was precultured in the seed medium, cultured in the fermentation medium with 10% inoculum. The pH was adjusted to 6.0 with 50% ammonia. Through ventilation and stirring speed, the dissolved oxygen (DO) was maintained at about 25%. For *E. coli*, the working concentration of kanamycin was 50 mg/L and that of chloramphenicol was 25 mg/L. For *C. glutamicum*, the working concentration of kanamycin was 15 mg/L and that of chloramphenicol was 7.5 mg/L.

2.3 Construction of Cas9 inactivated variant and genome editing plasmids

The plasmids pK18-dCas9-D10A and pK18-dCas9-H840A were used to mutate the 10th amino acid site from aspartate to alanine and 840th amino acid site from histidine to alanine of Cas9 through the sucrose lethal method (Tan et al., 2012). The plasmids pP_{trc}sgRNA-dCas9 and pP_{H36}sgRNA-dCas9 were also used to mutate the two sites through the CRISPR-Cas9 system. The plasmid $pP_{trc}P_{H36}$sgRNA-dCas9 was used to mutate the two sites simultaneously through the CRISPR-Cas9 system. The primers are listed in Supplementary Table S1.

2.4 Construction of sgRNA expression plasmids

To inhibit the expression of candidate genes using the CRISPR-dCas9 system, a series of sgRNA expression plasmids were constructed. The primers are listed in Supplementary Table S2. The DNA fragment $P_{glyA}2$ was amplified by polymerase chain reaction (PCR) with *C. glutamicum* ATCC 13032 genome as template and $P_{glyA}2$-F/$P_{glyA}2$-R as primers. The DNA fragments X-sgRNA-BIRI were amplified with plasmid pHAsgRNA as template and X-sgRNA-F/BIRI2-R as primers, respectively (Li N. et al., 2021). The plasmid pXMJ19 was digested with DNA restriction enzyme *Apa* I and *BamH* I to generate DNA fragment pXMJ19-AB. The DNA fragments, including pXMJ19-AB, $P_{glyA}2$ and X-sgRNA-BIRI, were then assembled by Gibson assembly to generate the plasmids pXM-sgRNAi-X corresponding to each candidate gene X.

2.5 Real-time quantitative PCR

Like the fermentation culture, the strains were cultured in the fermentation medium. After 24 h, the strains were collected and washed briefly by diethylpyrocarbonate-treated water (without RNase), then quickly cooled with liquid nitrogen. The RNA extraction kit, cDNA transcription kit and SYBR Premix Ex Taq II were purchased from TaKaRa (Dalian, China). The qPCR was performed on a LightCycler 480 II Real-time PCR instrument (Roche Applied Science, Mannheim, Germany). The 16s rDNA was the served as the house-keeping gene. The $2^{-\Delta\Delta Ct}$ method was used to determine the relative expression levels of genes (Chen et al., 2022). The primers are listed in Supplementary Table S3.

2.6 Delete the *cas9* and *recET* genes in the genome

To delete the *cas9* and *recET* genes, the donor DNA in the plasmid $pP_{trc}P_{H36}$sgRNA-dCas9 was replaced by DNA fragment cas9-recET to generate plasmid $pP_{trc}P_{H36}$sgRNA-recET-cas9. For the donor DNA, the upstream DNA fragment of plasmid $pP_{trc}P_{H36}$sgRNA-recET-cas9 was the same as that of plasmid $pP_{trc}P_{H36}$sgRNA-dCas9. The downstream DNA fragment was amplified with recEC-cas9-DOWN-F/recE-Ccas9-DOWN-R as primers and the genome of strain Cg17 as the template. The plasmid $pP_{trc}P_{H36}$sgRNA-dCas9 was linearized through PCR with XXH-F/XXH-R as the primers. The primers are listed in Table S1.

2.7 The transformation methods for *C. glutamicum*

About 1 μg of plasmid was transformed into the competent *C. glutamicum* by electric shock with 1 mm shock cup and

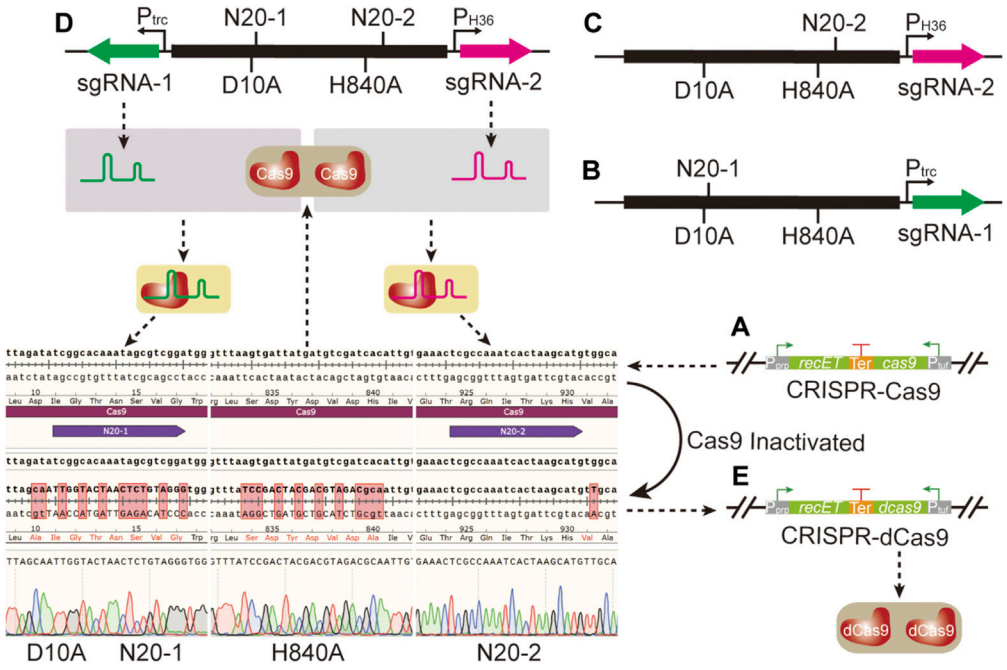

FIGURE 2
Site directed mutation of *cas9* gene through CRISPR-Cas9 system. **(A)** The CRISPR-Cas9 system. **(B)** The plasmid pP_{trc}sgRNA-dCas9; this plasmid was used to mutate the 10th amino acid site from aspartate to alanine of Cas9. **(C)** The plasmid pP_{H36}sgRNA-dCas9; this plasmid was used to mutate the 840th amino acid site from histidine to alanine of Cas9. **(D)** The plasmid $pP_{trc}P_{H36}$sgRNA-dCas9; this plasmid was used to mutate the 10th amino acid site from aspartate to alanine and 840th amino acid site from histidine to alanine of Cas9 simultaneously. **(E)** The CRISPR-dCas9 system.

1800 V voltage. The strains transferred to the LBHIS medium and incubated at 46°C for 6 min, then incubated at 30°C for 1–3 h. Next, the strains were cultured on the LBHIS plate containing the corresponding antibiotics at 30°C for 3 days. The positive transformants were verified by colony PCR with the corresponding primers. For the sucrose lethal method, the positive transformants with appropriate dilution were cultured on the LBHIS plate containing 100 g/L of sucrose at 30°C for 3 days. Finally, the following positive transformants were verified by colony PCR with the corresponding primers.

2.8 Analytical methods

2.8.1 Detection of fluorescence intensity and cell concentration

The optical density (OD_{600}) and intensity of fluorescent strains were measured with a Synergy H1 Hybrid Multi-Mode Reader (BioTek Instruments, Winooski, VT). For red fluorescence determination, the emission wavelength was 587 nm and the excitation wavelength was 610 nm.

2.8.2 Determination of biomass

The fermentation broth was diluted appropriately with 0.1 M HCl to dissolve the remaining $CaCO_3$ and the OD_{600} was determined by a Biophotometer D30 (Eppendorf AG, Hamburg).

2.8.3 Determination of glucose and acetic acid concentrations

The concentration of glucose and acetic acid in fermentation broth were determined by high performance liquid chromatography (HPLC) with a refractive-index detector and Aminex HPX-87H column (Bio-Rad, Richmond, CA).

2.8.4 Determination of amino acid concentration

After centrifugation, the supernatant of the fermentation broth was diluted with 0.4 M trichloroacetic acid, then saved at 4°C for more than 4 h. The pretreatment samples were centrifuged at 4°C for 10 min to take the supernatant, then diluted with 0.1 M acetic acid and filtered with a 0.22 μm membrane filter. The concentration of amino acids was determined after precolumn derivatization (Piao et al., 2019).

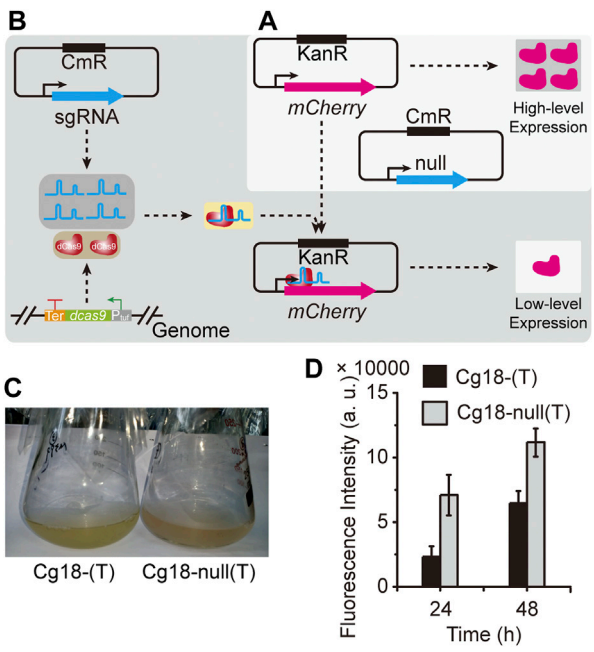

FIGURE 3
Evaluation of the CRISPR-dCas9 system. The gene inhibition ability of CRISPR-dCas9 system was evaluated through the expression intensity of mCherry protein. **(A)** The high-level expression of *mCherry* gene. **(B)** The CRISPR-dCas9 system was used to inhibit *mCherry* gene expression. **(C)** The strains with *mCherry* gene expression plasmids; the strain Cg18-(T) harbored pXM-sgRNAi-*mCherry*(T) and pNCgl1676-*mCherry*; the strain Cg18-null(T) harbored pXM-sgRNAi-Null and pNCgl1676-*mCherry*. **(D)** The Fluorescence intensity of the strains harboring *mCherry* gene expression plasmids. Error bars are standard deviation of triplicate experiments.

3 Results and discussions

3.1 Construction of an O-acetylhomoserine-producing strain

The bacterium *C. glutamicum* ATCC 13032 cannot naturally accumulate L-homoserine and O-acetylhomoserine. As in our previous studies (Li et al., 2020c; Li N. et al., 2021), the strong promoter P_{sod} was used to enhance the expression of key genes in L-homoserine biosynthesis pathway, including *pyc*, *lysC*, *asd*, hom, and *brnFE* (a nonspecific transporter component). The *aspC* gene and $thrA^{S345F}$ gene from *E. coli* was then introduced into the genome, and the expression of *icd* and *dapA* genes was downregulated through replacing the start codon ATG with GTG. The key genes of competition and degradation pathways including *mcbR*, *thrB*, *metB*, and *metY* were knocked out to obtain a L-homoserine-producing strain. The exogenous L-homoserine acetyltransferase variant $MetX^r$ from *Leptospira meyeri* was introduced to obtain an engineered strain Cg17 (Figure 1), which accumulated 0.98 g/L of OAH after 48 h.

To drain pyruvate flow to the L-aspartate biosynthesis pathway, reduce the use of pyruvate for the acetyl-CoA biosynthesis and promote the OAH accumulation, the expression of bifunctional L-aspartokinase and L-homoserine dehydrogenase ($ThrA^{S345F}$) from *E. coli* and $MetX^r$ were enhanced through the plasmid pEC-XK99E to generate strain Cg17-3 (Li et al., 2022). With the addition of 5 g/L acetate at 24 and 36 h, the resulting strain Cg17-3 produced 5.2 g/L of OAH at 48 h. Although the *C. glutamicum* achieved efficient OAH biosynthesis, few of the limiting factors of OAH biosynthesis were identified. Therefore, to further improve the OAH accumulation, expanding the identification range of key genes was a very worthwhile work.

3.2 Construction and evaluation of CRISPR-dCas9 in *C. glutamicum*

To construct a CRISPR-dCas9 system, two mutation sites D10A and H840A were introduced into the *cas9* gene that had been integrated into the genome in our previous studies (Figure 2A) (Li N. et al., 2021). The conventional genome editing method based on SacB was selected to mutate the two sites of Cas9 through two iterative editing. However, the whole process was time- and labor-consuming due to the required two edits, which made the rapid switching from CRISPR-Cas9 system to CRISPR-dCas9 system impossible. To facilitate the application of CRISPR-dCas9 in subsequent studies, CRISPR-Cas9 system was used to mutate Cas9. Two N20 (N20-1 and N20-2) located in distinct positions on *cas9* gene were designed, generating sgRNA-1 and sgRNA-2. Two sgRNA coding sequences were inserted into pXMJ19ts respectively, together with donor DNA containing two mutation sites to obtain pP_{trc}sgRNA-dCas9 and pP_{H36}sgRNA-dCas9 (Figures 2B,C). When the two plasmids were transformed into strain Cg17 respectively, only one site mutation could be achieved. Therefore, two sgRNA expression frames were inserted into pXMJ19ts simultaneously, together with donor DNA containing two mutation sites to obtain plasmid $pP_{trc}P_{H36}$sgRNA-dCas9 (Figure 2D). After the plasmid was transformed into strain Cg17, the strain Cg18 with two mutation sites was obtained (Figure 2E), which achieved the rapid switching from CRISPR-Cas9 to CRISPR-dCas9 as shown in Figure 2.

To evaluate the CRISPR-dCas9 system constructed above, the expression plasmid pNCgl1676-*mCherry* containing *mCherry* gene and pXM-sgRNAi-*mCherry*(T) containing sgRNA targeting the template chain of *mCherry* gene were transformed into Cg18, generating the strain Cg18-(T). The strain Cg18-null(T) containing pNCgl1676-*mCherry* and pXM-sgRNAi-Null without localization site was used as the control. As shown in Figure 3, CRISPR-dCas9 system had a strong inhibitory effect on *mCherry* gene expression at 24 and 48 h. The fluorescence intensity of strain Cg18-(T) was 67.6 and 36.6% of Cg18-null(T), respectively.

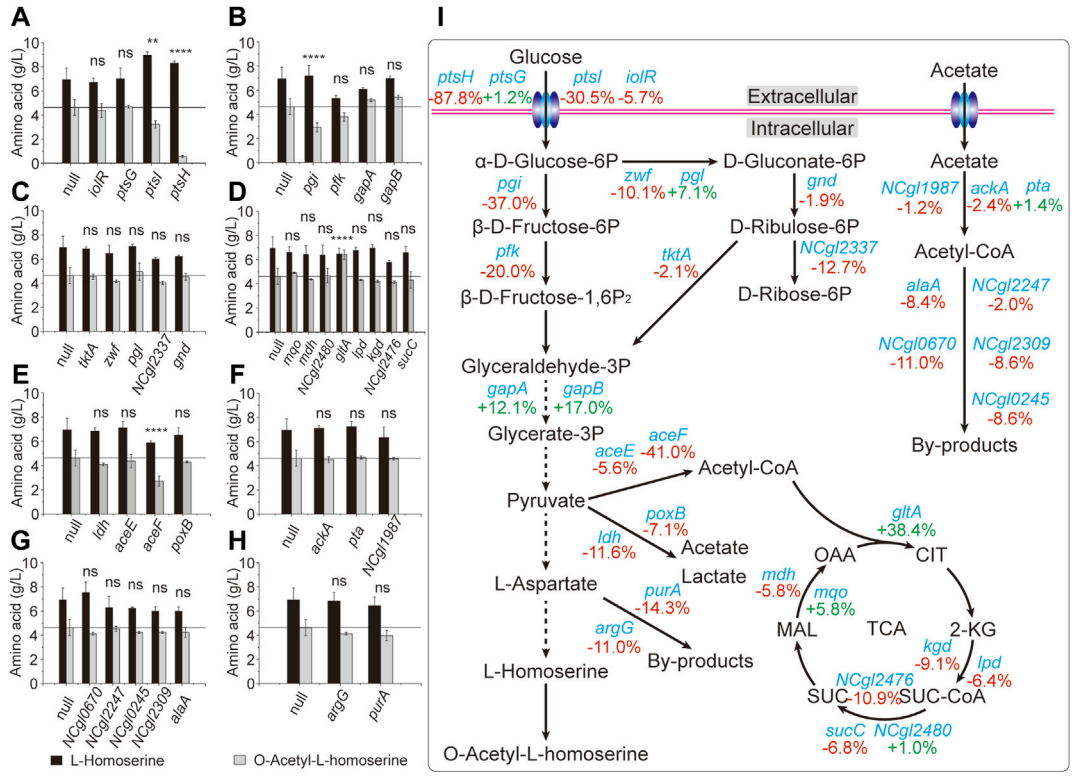

FIGURE 4
Identification of the key genes through the CRISPR-dCas9 system. The results of inhibition of different genes. **(A)** The genes of glucose transport. **(B)** The genes of glycolytic pathway. **(C)** The genes of pentose phosphate pathway. **(D)** The genes of TCA cycle. **(E)** The genes of pyruvate catabolism. **(F)** The genes of acetate acylation. **(G)** The genes of acetyl-CoA utilization. **(H)** The genes of L-aspartic acid degradation and metabolism. **(I)** The overall schematic diagram. Error bars are standard deviation of triplicate experiments. Statistical significance was determined with 95% confidence (ns > 0.05, *p < 0.05, **p < 0.005, ***p < 0.0005, ****p < 0.0001).

For *C. glutamicum*, it is very difficult and time-consuming to identify the key genes by classical gene knockout or overexpression (Yang et al., 2016). The CRISPRi can inhibit gene expression without destroying the genome. In previous studies, the CRISPR-dCas9 system had been constructed and applied in *C. glutamicum*. However, dead *cas9* (*dcas9*) gene and sgRNA consumed two antibiotic resistant plasmids pEC-XK99E and pXMJ19, resulting in no plasmid for the overexpression of other genes (Cleto et al., 2016). Therefore, Zhang et al. introduced *dcas9* gene and sgRNA expression frames into one plasmid and another plasmid can be used to express other target genes (Zhang et al., 2016). However, like Cas9, high level expression of dCas9 would also have an adverse effect on the growth of *C. glutamicum*. Some studies found that dCas9-sgRNA targeting the template chain had no obvious inhibitory effect on the gene expression (Larson et al., 2013), while some studies showed a strong inhibitory effect (Bikard et al., 2013). For *C. glutamicum*, dCas9-sgRNA had a strong inhibitory effect on gene expression whether targeted the template or non-template chains (Cleto et al., 2016; Zhang et al., 2016). In this study, the dCas9-sgRNA targeted the template chain of the *mCherry* gene, resulting in the down-regulation of *mCherry* expression. These indicated that this CRISPR-dCas9 system using a single plasmid had a strong ability to inhibit gene expression.

3.3 Application of CRISPR-dCas9 for identification of the key genes

The main pathways involved in the OAH biosynthesis include glucose transport, glycolysis, PPP, TCA cycle and L-aspartate metabolic pathway (Li et al., 2017). However, many related studies have only focused on the L-aspartate metabolic pathway, which made the metabolic engineering to construct a more efficient OAH-producing strain less targeted (Jin and Bao, 2021). Therefore, the rapid identification of the limiting steps in the OAH biosynthesis was of great significance for subsequent metabolic engineering. Some important candidate genes from these related pathways were selected (Goettl et al., 2021; Krahn et al., 2021), including *ptsG*, *ptsH*, *ptsI*, *iolR* of glucose transport; *pgi*, *pfk*, *gapA*, *gapB* of glycolytic pathway; *zwf*, *tktA*, *pgl*, *gnd*, *NCgl2337* of the PPP; *gltA*, *mdh*, *mqo*, *kgd*, *lpd*,

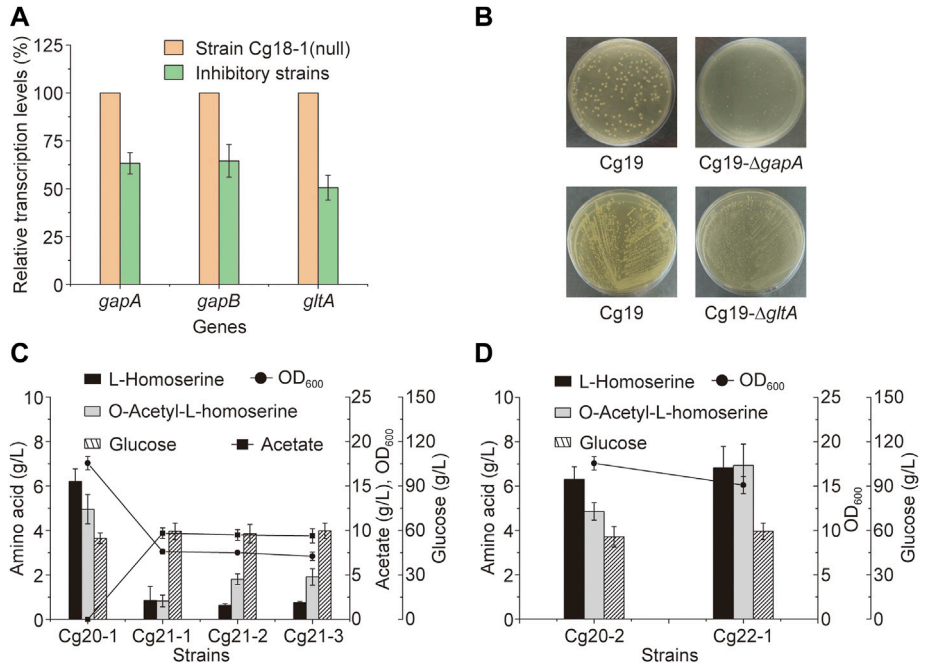

FIGURE 5
Metabolic engineering of the key genes. **(A)** The transcriptional levels of *gapA*, *gapB* and *gltA* genes under the inhibition of the CRISPR-dCas9 system, the control strain was strain Cg18-1 (null). **(B)** The growth state of the strains on the plates after knockout of *gapA* or *gltA* genes at 72 h. **(C)** The OAH titer after the knockout of *gltA* gene and the heterologous expression of a NADH dependent aspartate aminotransferase. **(D)** The OAH titer after the expression of *gltA* gene under the control of $P_{NCgl2698}$ promoter. Error bars are standard deviation of triplicate experiments.

sucC, *NCgl2476*, *NCgl2480* of the TCA cycle; *aceE*, *aceF*, *ldh*, *poxB* of pyruvate catabolism; *ackA*, *pta*, *NCgl1987* of acetate acylation; *alaA*, *NCgl2247*, *NCgl0670*, *NCgl2309*, *NCgl0245* of acetyl-CoA utilization and *purA*, *argG* of L-aspartic acid degradation and metabolism. To identify the relationship between these candidate genes and OAH biosynthesis, N20 sequences located in these candidate genes were designed to generate respective sgRNA expression plasmids. Like the strain Cg17, the *cas9* gene of the OAH-producing strain Cg17-3 was mutated to generate strain Cg18-1. The sgRNA expression plasmids were transformed into strain Cg18-1 to obtain strains Cg18-1(X), respectively. The strain Cg18-1 (null) containing pXM-sgRNAi-Null without localization site was used as the control strain. As shown in Figure 4, the OAH titer decreased after the expression of many genes was inhibited. Some of them increased the OAH titer, including *gltA* (38.4%), *gapA* (12.1%) and *gapB* (17.0%) (Figures 4B,D). However, only the OAH titer after *gltA* gene inhibition was significant. The results showed that the transcription levels of *gapA*, *gapB* and *gltA* genes of the inhibitory strains at 24 h were 63.2, 64.5, and 50.5% of those non-inhibitory strains, respectively (Figure 5A).

C. glutamicum contains two glyceraldehyde-3-phosphate dehydrogenases, including GapA and GapB. GapA is dependent on NADH, and GapB is dependent on NADPH (Takeno et al., 2016). For the OAH biosynthesis, excessive NADH would be generated and a large amount of NADPH would be consumed. We speculated that the inhibition of *gapA* and *gapB* genes by CRISPR-dCas9 may interfere the biosynthesis of NADH and NADPH. However, when the *gapA* gene of strain Cg17 was knocked out to generate strain Cg19-Δ*gapA*, which grew very slowly on the screening medium (Figure 5B), and cannot be used for subsequent metabolic engineering (Takeno et al., 2010). After the *gapB* gene was knocked out, the growth of engineered strain was not affected, but the OAH production did not change. More detailed reasons need to be further explored. Unlike the *gapA* and *gapB* genes, the expression level of *gltA* gene determines the TCA cycle rate and L-homoserine acetylation rate, the flow of acetyl-CoA into the TCA cycle is a key node of OAH accumulation. After the *gltA* gene, which encodes citrate synthase, was inhibited, the OAH titer increased to 6.4 g/L, which was the best among all the gene inhibitions, and the *gltA* gene should be a key candidate gene for the further regulation.

3.4 The expression of *gltA* gene under the control of conditional promoter

Down-regulation of *gltA* gene expression through the CRISPR-dCas9 system can enhance the OAH accumulation. Therefore, the *gltA* gene of strain Cg17 was knocked out, and

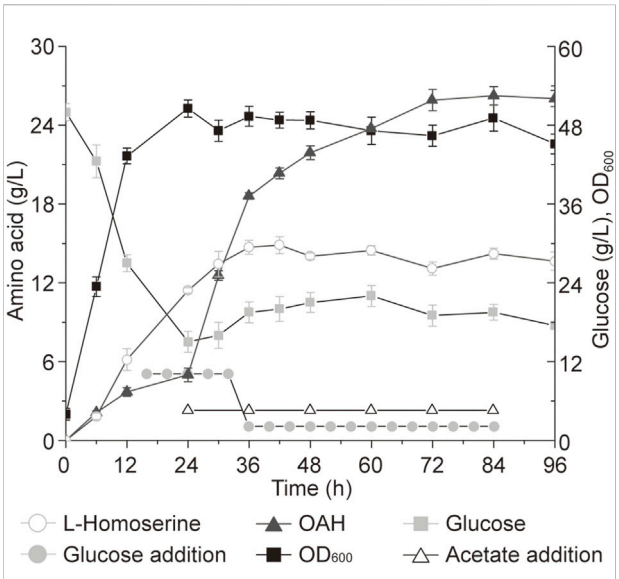

FIGURE 6
The titer of OAH in 5-L bioreactor. In a dissolved oxygen (DO) at 25% and pH 6.0, OAH can be biosynthesized quickly with glucose addition in a 5-L bioreactor. Error bars are standard deviation of triplicate experiments.

the mutant strain Cg19-Δ*gltA* was generated. However, the Cg19-Δ*gltA* showed poor growth, which made it impossible to conduct subsequent metabolic engineering (Figure 5B). It was speculated that the knockout of *gltA* gene cannot provide adequate α-ketoglutarate used for L-glutamate biosynthesis (Li X. et al., 2021), resulting in the inefficient conversion of oxaloacetate to L-aspartate using glutamate as an ammonia donor and the slow metabolic rate of the L-lysine biosynthesis pathway (Jeong et al., 2019). Meso-2,6-diaminoheptanedioate, one intermediate metabolite of L-lysine biosynthesis, was the precursor of peptidoglycan biosynthesis and the insufficient supply of peptidoglycan would lead to slow strain growth (Sgobba et al., 2018).

To enhance the cell growth, a NADH dependent aspartate aminotransferase, encoded by *aspB* gene from *Pseudomonas aeruginosa* (Wu et al., 2018), was expressed in the genome of strain Cg17 to generate Cg20. The strain Cg20 relieved the over-dependence of transamination on L-glutamate. Indeed, the growth of strain Cg21 (the strain Cg20 with *gltA* gene inactivation) was greatly restored. Then, three plasmid combinations including pXMJ19 and pEC-XK99E, pXMJ19 and pEC-$thrA^{S345F}$-$P_{NCgl1676}$-$metX^r$, pXM-*aspB*_Pa and pEC-$thrA^{S345F}$-$P_{NCgl1676}$-$metX^r$ were transformed into strain Cg21, resulting in strains Cg21-1, Cg21-2 and Cg21-3, respectively. As shown in Figure 5C, when the *gltA* gene was knocked out, all the biomass, L-homoserine titers (0.86 g/L, 0.63 g/L, and 0.75 g/L) and OAH titers (0.83 g/L, 1.81 g/L, and 1.91 g/L) decreased sharply, and acetic acid was barely consumed.

The strain needs a large amount of NADH, ATP and some important metabolites through TCA cycle for the biosynthesis of primary metabolism to meet the strain growth, the *gltA* gene inactivation has a very adverse impact on the strain (Xu et al., 2018). Therefore, a strong *gltA* gene expression level is required in the early stage of cell growth. The previous study showed that the transcriptional intensity of promoter $P_{NCgl2698}$ reduced from 75 to 8% of the constitutive strong promoter P_{tuf} after entering the stable growth period (Ma et al., 2018). It was used to replace the native promoter to regulate the expression of *gltA* gene in Cg20, generating strain Cg22. Then, the plasmid pEC-$thrA^{S345F}$-$P_{NCgl1676}$-$metX^r$ was introduced into Cg22 to generate strain Cg22-1. Taking strain Cg20-2 as the control, which was obtained from Cg17-3 with the integrated expression of the *aspB_Pa* gene, the OAH titer increased by 45.8% to 7.0 g/L (Figure 5D). Besides, the growth of strain Cg22-1 was restored compared to strain Cg21-3. Therefore, using $P_{NCgl2698}$ to control the expression of *gltA* gene could enhance the OAH accumulation, but did not have a significant impact on the growth of bacteria. The results showed that further optimization of *gltA* gene expression could enhance OAH biosynthesis.

3.5 The production of OAH in a 5-L bioreactor

The continuous and stable supply of substrate and pH control has a great impact on the production capacity, but these are difficult to achieve in a shake flask (Tan et al., 2019). Therefore, a 5-L bioreactor was used to further explore the production potential of high-performance strains. Before that, the *cas9* and *recET* genes in the genome of strain Cg22-1 were inactivated using the plasmid $pP_{trc}P_{H36}$sgRNA-recET-cas9 through the CRISPR-Cas9 system to obtain strain Cg23-1. According to previous studies, the addition of acetate was key for the efficient biosynthesis of OAH in *C. glutamicum* (Li et al., 2022). As shown in Figure 6, to make more acetyl-CoA produced from acetic acid for OAH biosynthesis, 5 g/L of acetic acid was added every 12 h starting from 24 h. At the same time, when the total consumption concentration of glucose reached 100 g/L, 500 g/L glucose was used to maintain the glucose concentration at 10–20 g/L. After the total glucose consumption exceeded 100 g/L, the mixture of 500 g/L glucose and 120 g/L ammonium sulfate was used to maintain the glucose concentration at 10–20 g/L. Finally, the OAH titer of strain Cg23-1 reached 25.9 g/L at 72 h, which was about 48.9% higher than the previous study (Li et al., 2022). This is the highest OAH titer in *C. glutamicum*, which proves that it has great potential.

4 Conclusions

Based on previous work, the OAH concentration increased to 5.2 g/L through the enhancement of the OAH

biosynthesis pathway genes and acetate supplementation in *C. glutamicum*. Then, the rapid switching from CRISPR-Cas9 to CRISPR-dCas9 was achieved through the previously constructed CRISPR-Cas9 system. Using the CRISPR-dCas9 system, the *gltA* gene was identified as the key factor affecting the OAH accumulation. The *gltA* gene expression was controlled by the sequential promoter $P_{NCgl2698}$, resulting in the increase of OAH accumulation. Finally, the OAH titer of the engineered strain reached 25.9 g/L at 72 h in a 5-L bioreactor. This was the highest OAH titer in *C. glutamicum* and would provide a good reference for the industrial production of OAH.

Data availability statement

The original contributions presented in the study are included in the article/Supplementary Material, further inquiries can be directed to the corresponding author.

Author contributions

NL: Conceptualization, Data curation, Formal analysis, Experimental design and setup, Funding acquisition, Writing—original draft. XS: Investigation, Experimental design and setup. JZ: Conceptualization, Data curation, Management and Supervision, Resources, Writing—review and editing. SY: Data curation, Writing—review and editing, Funding acquisition.

Funding

This work was supported by the National Key Research and Development Program of China (2021YFC2100700), the National Natural Science Foundation of China (22108098), and the Jiangsu Postdoctoral Research Funding Program (2021K171B).

Conflict of interest

The authors declare that the research was conducted in the absence of any commercial or financial relationships that could be construed as a potential conflict of interest.

Publisher's note

All claims expressed in this article are solely those of the authors and do not necessarily represent those of their affiliated organizations, or those of the publisher, the editors and the reviewers. Any product that may be evaluated in this article, or claim that may be made by its manufacturer, is not guaranteed or endorsed by the publisher.

Supplementary material

The Supplementary Material for this article can be found online at: https://www.frontiersin.org/articles/10.3389/fbioe.2022.978686/full#supplementary-material

References

Bikard, D., Jiang, W., Samai, P., Hochschild, A., Zhang, F., and Marraffini, L. A. (2013). Programmable repression and activation of bacterial gene expression using an engineered CRISPR-Cas system. *Nucleic Acids Res.* 41 (15), 7429–7437. doi:10.1093/nar/gkt520

Chen, Y., Zeng, W., Ma, W., Ma, W., and Zhou, J. (2022). Chromatin regulators Ahc1p and Eaf3p positively influence nitrogen metabolism in *Saccharomyces cerevisiae*. *Front. Microbiol.* 13, 883934. doi:10.3389/fmicb.2022.883934

Choi, K. R., Jang, W. D., Yang, D., Cho, J. S., Park, D., and Lee, S. Y. (2019). Systems metabolic engineering strategies: Integrating systems and synthetic biology with metabolic engineering. *Trends Biotechnol.* 37 (8), 817–837. doi:10.1016/j.tibtech.2019.01.003

Cleto, S., Jensen, J. V., Wendisch, V. F., and Lu, T. K. (2016). *Corynebacterium glutamicum* metabolic engineering with CRISPR interference (CRISPRi). *ACS Synth. Biol.* 5 (5), 375–385. doi:10.1021/acssynbio.5b00216

Du, Y., Cheng, F., Wang, M., Xu, C., and Yu, H. (2021). Indirect pathway metabolic engineering strategies for enhanced biosynthesis of hyaluronic acid in engineered *Corynebacterium glutamicum*. *Front. Bioeng. Biotechnol.* 9, 768490. doi:10.3389/fbioe.2021.768490

Gauttam, R., Seibold, G. M., Mueller, P., Weil, T., Weiss, T., Handrick, R., et al. (2019). A simple dual-inducible CRISPR interference system for multiple gene targeting in *Corynebacterium glutamicum*. *Plasmid* 103, 25–35. doi:10.1016/j.plasmid.2019.04.001

Goettl, V. L., Schmitt, I., Braun, K., Peters-Wendisch, P., Wendisch, V. F., and Henke, N. A. (2021). CRISPRi-library-guided target identification for engineering carotenoid production by *Corynebacterium glutamicum*. *Microorganisms* 9 (4), 670. doi:10.3390/microorganisms9040670

Jakoby, M., Ngouoto-Nkili, C. E., and Burkovski, A. (1999). Construction and application of new *Corynebacterium glutamicum* vectors. *Biotechnol. Tech.*, 13(6), 437–441. doi:10.1023/A:1008968419217

Jeong, S. Y., Jin, H., and Chang, J. H. (2019). Crystal structure of L-aspartate aminotransferase from *Schizosaccharomyces pombe*. *Plos One* 14 (8), e0221975. doi:10.1371/journal.pone.0221975

Jin, C., and Bao, J. (2021). Lysine production by dry biorefining of wheat straw and cofermentation of *Corynebacterium glutamicum*. *J. Agric. Food Chem.* 69 (6), 1900–1906. doi:10.1021/acs.jafc.0c07902

Kim, M., Jeong, D. W., Oh, J. W., Jeong, H. J., Ko, Y. J., Park, S. E., et al. (2022). Efficient synthesis of food-derived antioxidant l-ergothioneine by engineered *Corynebacterium glutamicum*. *J. Agric. Food Chem.* 70 (5), 1516–1524. doi:10.1021/acs.jafc.1c07541

Kirchner, O., and Tauch, A. (2003). Tools for genetic engineering in the amino acid-producing bacterium *Corynebacterium glutamicum*. *J. Biotechnol.* 104 (1-3), 287–299. doi:10.1016/s0168-1656(03)00148-2

Krahn, I., Bonder, D., Torregrosa-Barragan, L., Stoppel, D., Krause, J. P., Rosenfeldt, N., et al. (2021). Evolving a new efficient mode of fructose utilization for improved bioproduction in *Corynebacterium glutamicum*. *Front. Bioeng. Biotechnol.* 9, 669093. doi:10.3389/fbioe.2021.669093

Krebs, H. A. (1970). The history of the tricarboxylic acid cycle. *Perspect. Biol. Med.* 14 (1), 154–172. doi:10.1353/pbm.1970.0001

Larson, M. H., Gilbert, L. A., Wang, X. W., Lim, W. A., Weissman, J. S., and Qi, L. S. (2013). CRISPR interference (CRISPRi) for sequence-specific control of gene expression. *Nat. Protoc.* 8 (11), 2180–2196. doi:10.1038/nprot.2013.132

Li, C., Zhou, J., Rao, S., Du, G., and Liu, S. (2021). Visualized multigene editing system for *Aspergillus niger*. *ACS Synth. Biol.* 10 (10), 2607–2616. doi:10.1021/acssynbio.1c00231

Li, N., Wang, M., Yu, S., and Zhou, J. (2021). Optimization of CRISPR-Cas9 through promoter replacement and efficient production of L-homoserine in *Corynebacterium glutamicum*. *Biotechnol. J.* 16 (8), e2100093. doi:10.1002/biot.202100093

Li, N., Xu, S., Du, G. C., Chen, J., and Zhou, J. W. (2020c). Efficient production of L-homoserine in *Corynebacterium glutamicum* ATCC 13032 by redistribution of metabolic flux. *Biochem. Eng. J.* 161, 107665. doi:10.1016/j.bej.2020.107665

Li, N., Zeng, W., Xu, S., and Zhou, J. (2020a). Obtaining a series of native gradient promoter-5'-UTR sequences in *Corynebacterium glutamicum* ATCC 13032. *Microb. Cell Fact.* 19 (1), 120. doi:10.1186/s12934-020-01376-3

Li, N., Zeng, W., Xu, S., and Zhou, J. (2020b). Toward fine-tuned metabolic networks in industrial microorganisms. *Synth. Syst. Biotechnol.* 5 (2), 81–91. doi:10.1016/j.synbio.2020.05.002

Li, N., Zeng, W., Zhou, J., and Xu, S. (2022). O-Acetyl-L-homoserine production enhanced by pathway strengthening and acetate supplementation in *Corynebacterium glutamicum*. *Biotechnol. Biofuels Bioprod.* 15 (1), 27. doi:10.1186/s13068-022-02114-0

Li, X., Bao, T., Osire, T., Qiao, Z., Liu, J., Zhang, X., et al. (2021). MarR-type transcription factor RosR regulates glutamate metabolism network and promotes accumulation of L-glutamate in *Corynebacterium glutamicum* G01. *Bioresour. Technol.* 342, 125945. doi:10.1016/j.biortech.2021.125945

Li, Y. J., Wei, H. B., Wang, T., Xu, Q. Y., Zhang, C. L., Fan, X. G., et al. (2017). Current status on metabolic engineering for the production of L-aspartate family amino acids and derivatives. *Bioresour. Technol.* 245, 1588–1602. doi:10.1016/j.biortech.2017.05.145

Ma, Y., Cui, Y., Du, L., Liu, X., Xie, X., and Chen, N. (2018). Identification and application of a growth-regulated promoter for improving L-valine production in *Corynebacterium glutamicum*. *Microb. Cell Fact.* 17 (1), 185–194. doi:10.1186/s12934-018-1031-7

Milke, L., Kallscheuer, N., Kappelmann, J., and Marienhagen, J. (2019). Tailoring *Corynebacterium glutamicum* towards increased malonyl-CoA availability for efficient synthesis of the plant pentaketide noreugenin. *Microb. Cell Fact.* 18 (1), 71–82. doi:10.1186/s12934-019-1117-x

Park, J., Shin, H., Lee, S. M., Um, Y., and Woo, H. M. (2018). RNA-guided single/double gene repressions in *Corynebacterium glutamicum* using an efficient CRISPR interference and its application to industrial strain. *Microb. Cell Fact.* 17 (1), 4. doi:10.1186/s12934-017-0843-1

Park, J., Yu, B. J., Cho, J. I., and Woo, H. M. (2019). Heterologous production of squalene from glucose in engineered *Corynebacterium glutamicum* using multiplex CRISPR interference and high-throughput fermentation. *J. Agric. Food Chem.* 67 (1), 308–319. doi:10.1021/acs.jafc.8b05818

Piao, X., Wang, L., Lin, B., Chen, H., Liu, W., and Tao, Y. (2019). Metabolic engineering of *Escherichia coli* for production of L-aspartate and its derivative beta-alanine with high stoichiometric yield. *Metab. Eng.* 54, 244–254. doi:10.1016/j.ymben.2019.04.012

Qin, Z., Yang, Y., Yu, S., Liu, L., Chen, Y., Chen, J., et al. (2021). Repurposing the endogenous type I-E CRISPR/Cas system for gene repression in *Gluconobacter oxydans* WSH-003. *ACS Synth. Biol.* 10 (1), 84–93. doi:10.1021/acssynbio.0c00456

Sagong, H. Y., Lee, D., Kim, I. K., and Kim, K. J. (2022). Rational engineering of homoserine O-succinyltransferase from *Escherichia coli* for reduced feedback inhibition by methionine. *J. Agric. Food Chem.* 70 (5), 1571–1578. doi:10.1021/acs.jafc.1c07211

Schafer, A., Tauch, A., Jager, W., Kalinowski, J., Thierbach, G., and Puhler, A. (1994). Small mobilizable multi-purpose cloning vectors derived from the *Escherichia coli* plasmids pK18 and pK19: Selection of defined deletions in the chromosome of *Corynebacterium glutamicum*. *Gene* 145 (1), 69–73. doi:10.1016/0378-1119(94)90324-7

Sgobba, E., Stumpf, A. K., Vortmann, M., Jagmann, N., Krehenbrink, M., Dirks-Hofmeister, M. E., et al. (2018). Synthetic *Escherichia coli-Corynebacterium glutamicum* consortia for L-lysine production from starch and sucrose. *Bioresour. Technol.* 260, 302–310. doi:10.1016/j.biortech.2018.03.113

Shi, Y., Zhang, L., Zhang, M., Chu, J., Xia, Y., Yang, H., et al. (2022). A CRISPR-Cas9 system-mediated genetic disruption and multi-fragment assembly in *Starmerella bombicola*. *ACS Synth. Biol.* 11, 1497–1509. doi:10.1021/acssynbio.1c00582

Takeno, S., Hori, K., Ohtani, S., Mimura, A., Mitsuhashi, S., and Ikeda, M. (2016). L-Lysine production independent of the oxidative pentose phosphate pathway by *Corynebacterium glutamicum* with the *Streptococcus mutans gapN* gene. *Metab. Eng.* 37, 1–10. doi:10.1016/j.ymben.2016.03.007

Takeno, S., Murata, R., Kobayashi, R., Mitsuhashi, S., and Ikeda, M. (2010). Engineering of *Corynebacterium glutamicum* with an NADPH-generating glycolytic pathway for L-lysine production. *Appl. Environ. Microbiol.* 76 (21), 7154–7160. doi:10.1128/aem.01464-10

Tan, R., Lyu, Y., Zeng, W., and Zhou, J. (2019). Enhancing scleroglucan production by *Sclerotium rolfsii* WSH-G01 through a pH-shift strategy based on kinetic analysis. *Bioresour. Technol.* 293, 122098. doi:10.1016/j.biortech.2019.122098

Tan, Y. Z., Xu, D. Q., Li, Y., and Wang, X. Y. (2012). Construction of a novel *sacB*-based system for marker-free gene deletion in *Corynebacterium glutamicum*. *Plasmid* 67 (1), 44–52. doi:10.1016/j.plasmid.2011.11.001

Wang, Z. H., Chan, S. H. J., Sudarsan, S., Blank, L. M., Jensen, P. R., and Solem, C. (2016). Elucidation of the regulatory role of the fructose operon reveals a novel target for enhancing the NADPH supply in *Corynebacterium glutamicum*. *Metab. Eng.* 38, 344–357. doi:10.1016/j.ymben.2016.08.004

Wei, L., Wang, Q., Xu, N., Cheng, J., Zhou, W., Han, G., et al. (2019). Combining protein and metabolic engineering strategies for high-level production of O-acetylhomoserine in *Escherichia coli*. *ACS Synth. Biol.* 8 (5), 1153–1167. doi:10.1021/acssynbio.9b00042

Wei, L., Zhao, J., Wang, Y., Gao, J., Du, M., Zhang, Y., et al. (2021). Engineering of *Corynebacterium glutamicum* for high-level γ-aminobutyric acid production from glycerol by dynamic metabolic control. *Metab. Eng.* 69, 134–146. doi:10.1016/j.ymben.2021.11.010

Wu, W., Zhang, Y., Liu, D., and Chen, Z. (2018). Efficient mining of natural NADH-utilizing dehydrogenases enables systematic cofactor engineering of lysine synthesis pathway of *Corynebacterium glutamicum*. *Metab. Eng.* 52, 77–86. doi:10.1016/j.ymben.2018.11.006

Xu, J. Z., Wu, Z. H., Gao, S. J., and Zhang, W. (2018). Rational modification of tricarboxylic acid cycle for improving L-lysine production in *Corynebacterium glutamicum*. *Microb. Cell Fact.* 17 (1-13), 105–117. doi:10.1186/s12934-018-0958-z

Yang, J., Zhu, Y., Men, Y., Sun, S., Zeng, Y., Zhang, Y., et al. (2016). Pathway construction in *Corynebacterium glutamicum* and strain engineering to produce rare sugars from glycerol. *J. Agric. Food Chem.* 64 (50), 9497–9505. doi:10.1021/acs.jafc.6b03423

Ye, Y., Zhong, M., Zhang, Z., Chen, T., Shen, Y., Lin, Z., et al. (2022). Genomic iterative replacements of large synthetic DNA fragments in *Corynebacterium glutamicum*. *ACS Synth. Biol.* 11 (4), 1588–1599. doi:10.1021/acssynbio.1c00644

Yin, L. H., Hu, X. Q., Xu, D. Q., Ning, J. F., Chen, J., and Wang, X. Y. (2012). Co-expression of feedback-resistant threonine dehydratase and acetohydroxy acid synthase increase L-isoleucine production in *Corynebacterium glutamicum*. *Metab. Eng.* 14 (5), 542–550. doi:10.1016/j.ymben.2012.06.002

Yoon, J., and Woo, H. M. (2018). CRISPR interference-mediated metabolic engineering of *Corynebacterium glutamicum* for homo-butyrate production. *Biotechnol. Bioeng.* 115 (8), 2067–2074. doi:10.1002/bit.26720

Zhang, B., Liu, Z. Q., Liu, C., and Zheng, Y. G. (2016). Application of CRISPRi in *Corynebacterium glutamicum* for shikimic acid production. *Biotechnol. Lett.* 38 (12), 2153–2161. doi:10.1007/s10529-016-2207-z

Zhang, C., Seow, V. Y., Chen, X., and Too, H. P. (2018). Multidimensional heuristic process for high-yield production of astaxanthin and fragrance molecules in *Escherichia coli*. *Nat. Commun.* 9 (1), 1858. doi:10.1038/s41467-018-04211-x

Zhang, X., Lai, L., Xu, G., Zhang, X., Shi, J., Koffas, M. A. G., et al. (2019). Rewiring the central metabolic pathway for high-yield l-serine production in *Corynebacterium glutamicum* by using glucose. *Biotechnol. J.* 14 (6), e1800497–1800505. doi:10.1002/biot.201800497

frontiers | Frontiers in Bioengineering and Biotechnology

TYPE Original Research
PUBLISHED 02 December 2022
DOI 10.3389/fbioe.2022.1080024

OPEN ACCESS

EDITED BY
Farshad Darvishi,
Alzahra University, Iran

REVIEWED BY
David T Stuart,
University of Alberta, Canada
Eun Joong Oh,
Purdue University, United States
Taek Soon Lee,
Berkeley Lab (DOE), United States

*CORRESPONDENCE
Brian F. Pfleger,
pfleger@engr.wisc.edu

†These authors have contributed equally to this work and share first authorship

SPECIALTY SECTION
This article was submitted to Synthetic Biology, a section of the journal Frontiers in Bioengineering and Biotechnology

RECEIVED 25 October 2022
ACCEPTED 17 November 2022
PUBLISHED 02 December 2022

CITATION
Gambacorta FV, Dietrich JJ, Baerwald JJ, Brown SJ, Su Y and Pfleger BF (2022), Combinatorial library design for improving isobutanol production in *Saccharomyces cerevisiae*. *Front. Bioeng. Biotechnol.* 10:1080024. doi: 10.3389/fbioe.2022.1080024

Combinatorial library design for improving isobutanol production in *Saccharomyces cerevisiae*

Francesca V. Gambacorta[1,2†], Joshua J. Dietrich[1,2†], Justin J. Baerwald[2], Stephanie J. Brown[2], Yun Su[2] and Brian F. Pfleger[1,2*]

[1]DOE Great Lakes Bioenergy Research Center, University of Wisconsin-Madison, Madison, WI, United States, [2]Department of Chemical and Biological Engineering, University of Wisconsin-Madison, Madison, WI, United States

Saccharomyces cerevisiae is the dominant fermentative producer of ethanol in industry and a preferred host for production of other biofuels. That said, rewiring the metabolism of *S. cerevisiae* to produce other fermentation products, such as isobutanol, remains an academic challenge. Many studies report aerobic production of isobutanol, but ethanol remains a substantial by-product under these conditions due to the Crabtree effect. These studies indicate that the native isobutanol pathway is incapable of carrying sufficient flux to displace ethanol. In this report, we screened a combinatorial library of pathway enzymes to identify an isobutanol pathway cassette capable of supporting the growth of a non-ethanol producing *S. cerevisiae*. We began by identifying a diverse set of isobutanol pathway enzyme homologs and combined each open reading frame with varied-strength promoters in a combinatorial, pooled fashion. We applied a growth-coupled screen where a functional isobutanol pathway restored NAD^+ regeneration during glucose catabolism that is otherwise repressed *via* the Crabtree effect. Using this screen, we isolated a cassette consisting of a mosaic of bacterial and cytosol-localized fungal enzymes that conferred under aerobic conditions the ability to produce 364 mg/L isobutanol (8.8% of the theoretical maximum yield). We next shifted the cofactor usage of the isolated ketol-acid reductoisomerase enzyme in the cassette from NADPH to NADH-preferring to improve redox balance. The approach used herein isolated isobutanol producing strains that approach the best in the literature without producing substantial ethanol titers. Still, the best isolated cassette was insufficient to support anaerobic growth in the absence of ethanol fermentation - indicating the presence of further fundamental gaps in our understanding of yeast fermentation.

KEYWORDS

yeast, isobutanol, metabolic engineering, combinatorial library, *Saccharomayces cerevisiae*

Introduction

There is growing demand for more sustainable and environmentally responsible energy carriers, particularly in the transportation sector. Liquid organic molecules remain the preferred transportation fuel because of their high energy density and the ease with which they can be transported. The drawbacks of ethanol, the dominant first-generation biofuel, have been well documented (Peralta-Yahya et al., 2012). Relative to gasoline, ethanol has a significantly lower energy density, is more corrosive, and absorbs more moisture, greatly limiting the extent to which it can be used (Roussos et al., 2019). Ethanol however is a fermentation product that can be efficiently produced from sugars anaerobically by many industrialized microbes. The situation has motivated development of next-generation biofuels that have superior chemical properties and can be synthesized at near maximum theoretical yields. Isobutanol is one such molecule that has been targeted by academic and industrial researchers. Isobutanol is a branched-chain, four-carbon alcohol with a higher energy density and lower hygroscopicity than ethanol (Roussos et al., 2019). Isobutanol can be used as a fuel in internal combustion engines and oligomerized into higher molecular weight hydrocarbons to serve as jet and diesel fuels (Buijs et al., 2013). Isobutanol can be produced biologically from two pyruvate molecules through five enzymatic reactions catalyzed by: acetolactate synthase (ALS), ketol-acid reductoisomerase (KARI), dihydroxyacid dehydratase (DHAD), α-ketoacid decarboxylase (KDC), and alcohol dehydrogenase (ADH) (Figure 1A). The yeast *Saccharomyces cerevisiae* natively possesses each of these enzymes, and wild-type strains may produce up to ~50 mg/L of isobutanol (Longo et al., 1992). This natural ability of *S. cerevisiae* to produce isobutanol, together with its robust genetic toolkit, fast growth rate, and tolerance to a variety of stressors present in industrial fermentations have made it a popular host for metabolic engineering efforts to improve isobutanol production (Gambacorta et al., 2020).

Although there have been numerous efforts to engineer *S. cerevisiae* for isobutanol production, the titers, rates, and yields achieved by academic researchers remain below the threshold for

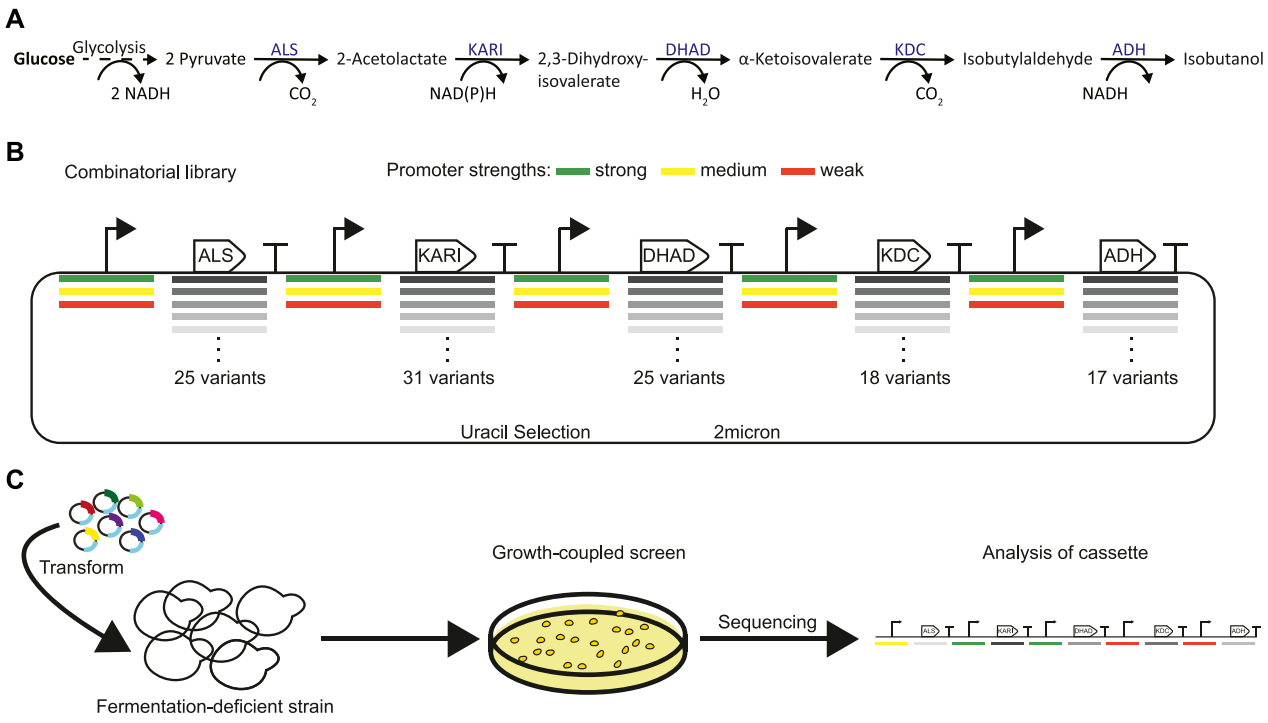

FIGURE 1
Strategy for identifying a highly active isobutanol pathway cassette. **(A)** Shows the 5 key enzymes responsible for isobutanol production from pyruvate: acetolactate synthase (ALS), ketol-acid reductoisomerase (KARI), dihydroxyacid dehydratase (DHAD), α-ketoacid decarboxylase (KDC), and alcohol dehydrogenase (ADH). **(B)** Combinatorial isobutanol pathway library design. There are 25 ALS homologs, 31 KARI homologs, 25 DHAD homologs, 18 KDC homologs, and 17 ADH homologs; each homolog is expressed with either a strong (green), medium (yellow), or weak (red) strength promoter in a high-copy (2μ) plasmid containing *URA3* as a selectable marker. **(C)** Shows the growth-coupled screening strategy for identifying highly active isobutanol pathway cassettes. The expression library is transformed into a fermentation-deficient strain (Pdc-null). Then cells that contain a functional isobutanol pathway cassette can grow due to the regeneration of NAD^+ *via* the ADH and/or the KARI enzyme. High producers can then be sequenced to identify the enzyme homologs and promoters in the cassette.

industrial feasibility. To date, the highest *S. cerevisiae* isobutanol yield reported in academic literature is only 14% of the maximum theoretical yield (Wess et al., 2019), far short of the 95% yield estimated for industrial viability (Cai et al., 2018). This low yield is due to the fact that isobutanol production in *S. cerevisiae* is overpowered by native pyruvate-to-ethanol flux. Efforts to eliminate ethanol production by deleting either the complete set of three pyruvate decarboxylase enzymes (*PDC1*, *PDC5*, and *PDC6*) or the set of six alcohol dehydrogenases (*ADH1*, *ADH2*, *ADH3*, *ADH4*, *ADH5*, and *SFA1*) have proven challenging since strains lacking these enzymes experience severe physiological defects (Flikweert et al., 1996; de Smidt et al., 2012). Strains lacking pyruvate decarboxylase cannot synthesize acetyl-CoA in the cytosol and require a C2-compound (e.g. ethanol or acetate) in the medium to grow (Flikweert et al., 1996). Additionally, both PDC and ADH-lacking strains have further growth defects because ethanol production, under both aerobic and anaerobic conditions, plays an essential role in replenishing the NAD^+ cofactor required for glycolysis and cell growth.

Metabolic modeling suggests that isobutanol can theoretically replace ethanol as a product since it is redox-balanced with glycolysis (i.e. requires two reducing equivalents) (Milne et al., 2016). However, while isobutanol production is redox balanced with glycolysis, its cofactor specificity may not be. Naturally, most KARI's have a higher specificity towards NADPH, which would result in a NADPH shortage and NADH excess (Brinkmann-Chen et al., 2013). This imbalance can be overcome by supplying a means for converting glycolytic NADH into NADPH, changing the KARI cofactor specificity through protein engineering, or using a naturally NADH-dependent KARI enzyme. In addition to balancing cofactor specificity, the carbon flux through the isobutanol pathway must match the naturally high rate of glycolysis to ensure that the NAD^+ needed for glycolysis is regenerated quickly enough. A large literature base describing the biochemistry, relative activity, and engineering of each enzyme exists. However, to date, no academic group has reported a combination of enzymes that can enable anaerobic isobutanol fermentation in non-ethanol producing *S. cerevisiae*.

A powerful approach for identifying optimal combinations of enzymes and expression levels is through the building and screening of a combinatorial library of pathway cassettes, in which expression levels and/or homolog identity is varied for each enzyme in the pathway (Jeschek et al., 2017). A screen can then be used to identify strains with improved properties and the DNA cassettes that produce the desired phenotype can be subsequently determined and reverse engineered. In designing a library, it is simplest to keep the homolog identities constant and vary only the expression levels, which can be done by exchanging promoters or other control elements. Alternatively, the specific activity of each enzyme can be varied by using homologs from across the tree of life or proteins engineered/evolved to have altered properties. A combined approach increases library complexity, but it can also streamline engineering efforts by exploring diverse homologs and expression levels simultaneously. That said, to fully leverage a large library, a high-throughput screening process must exist. When screening throughput is high enough relative to the library size, it is possible to explore a library fully and have high confidence that every permutation has been sampled (Zhang et al., 2022). If screening throughput is not sufficient, it may be possible to use machine learning methods on a small subset of the library and predict cassettes that will produce the desired phenotype (Zhou et al., 2018; Zhang et al., 2020; Kumar et al., 2021).

In this study, we used bioinformatic methods to identify a diverse set of isobutanol enzyme variants. We then built a combinatorial pathway library that had diversity in both enzyme homologs and expression levels by combining the bioprospected open reading frames with varying strength promoters. By screening the combinatorial pathway library with a growth-coupled strategy, we identified a higher-flux isobutanol cassette that produced an isobutanol titer of 364 mg/L and a yield of 36 mg isobutanol/g glucose (8.8% of the theoretical maximum yield) under aerobic conditions, while not producing ethanol. In an effort to improve redox-balance, we mutated the KARI enzyme in the best cassette to change the cofactor usage from NADPH to NADH-preferring. Unfortunately, the resulting pathway could neither enable anaerobic growth nor improve isobutanol titers under micro-aerobic conditions (sealed serum vials). Our approach was successful in isolating an improved strain from a small number of tested variants. This success motivates further work to improve the transformation efficiency of Pdc^- strains and/or limit the library size such that the ideal combination of pathway enzymes can be found.

Materials and methods

Media

When culturing strains for transformation, YPGE medium was used, containing 10 g/L yeast extract, 20 g/L peptone, 3% glycerol, and 2% ethanol. After transformation of the library or individual plasmids, strains were grown on defined synthetic complete media minus uracil (SC-ura), containing 6.7 g/L yeast nitrogen base (YNB) without amino acids with ammonium sulfate, 1.52 g/L drop-out mix synthetic minus uracil and leucine, 380 mg/L leucine, and appropriate carbon sources. SCD-ura medium contained 2% glucose, SCGE-ura medium contained 3% glycerol and 2% ethanol, SCDA-ura medium contained 2% glucose and 70 mM sodium acetate, and SCDE-

ura medium contained 2% glucose and 2% ethanol. Solid media also contained 2.5% agar.

Computational methods

Sequence similarity networks were created for each of the isobutanol enzymes (ALS, KARI, DHAD, KDC, and ADH) using the Enzyme Function Initiative-Enzyme Similarity Tool (EFI-EST) (Zallot et al., 2019) and visualized using Cytoscape (Shannon et al., 2003). The input for EFI-EST were either sequences or protein family: ALS from *Lactobacillus plantarum* (Uniprot ID: A0A0G9FA99), KARI from Pfam families PF01450 and PF07991, DHAD from *S. cerevisiae* (Uniprot ID: P39522), KDC from *S. cerevisiae* (Uniprot ID: Q06408), and ADH from *S. cerevisiae* (Uniprot ID: P38113). A diverse set of variants was chosen from the resulting network by 1) gathering homologs from clusters known to contain active enzyme variants and 2) bioprospecting the network to identify diverse sequences from a variety of kingdoms/phyla (fungi, ascomycota, firmicutes, proteobacteria, and actinobacteria). A simple Hamming distance calculation was used to maximize diversity. To ensure we had a fully cytosolic compartmentalized isobutanol pathway, the sequences were run through Mitoprot (Claros and Vincens, 1996) and any predicted mitochondrial localization sequences were removed. Pairwise amino acid identity between the proteins in each grouping was found using ClustalOmega (Madeira et al., 2022). See Supplementary Data Sheet S1 for sequences and Supplementary Data Sheet S2 for percent identity matrices.

Library construction

Library construction was performed by the DOE Joint Genome Institute (JGI). In brief, codon-optimized enzyme coding sequences (CDS), promoters, and terminators were first cloned into a pENTR vector to generate the part vectors. Transcription units (promoter-gene-terminator sets) were generated by Golden Gate assembly of the part vectors. The combinatorial library (five gene isobutanol cassettes) was then assembled in a pooled fashion (one-pot) using Gibson Assembly into a high-copy vector, pCC1FOSY, a pCC1FOS-based vector with a 2μ yeast origin and *URA3*-selection (Supplementary Table S1). Specifically the one-pot mixture consisted of 116 ORFs (25 ALS homologs, 31 KARI homologs, 25 DHAD homologs, 18 KDC homologs, and 17 ADH homologs), 15 promoters (3 ALS promoters, 3 KARI promoters, 3 DHAD promoters, 3 KDC promoters, and 3 ADH promoters), and 1 terminator (1 ALS terminator, 1 KARI terminator, 1 DHAD terminator, 1 KDC terminator, and 1 ADH terminator) . This yielded 1.44 billion unique 13 kb isobutanol pathway cassettes (3*25*3*31*3*25*3*18*3*17). The pooled library DNA was sheared to an average size of 2 kb and sequenced on a PacBio Sequel II. Each read was analyzed for the presence of a promoter-gene junction and then counted towards the number of reads for the corresponding promoter-gene pair. Each of the 348 promoter-gene pairs was present, and the largest fold-change difference between promoter-gene pair abundance was 12, while most were within a much narrower distribution. PacBio sequencing also revealed a high library fidelity, with only a small fraction of reads showing incorrect sequences (Supplementary Data Sheet S3).

Library screening and genotyping

The screening strain was generated by deleting *URA3* in *S. cerevisiae* GG570 (Flikweert et al., 1996) by CRISPR/Cas9. In brief, a sgRNA sequence targeting the CDS was identified by CRISpy-pop (sgRNA = gcacacggtgtggtgggccc) and cloned into the pXIPHOS (NatMX) plasmid as described previously (Stoneman et al., 2020), resulting in plasmid pXIP-URA3-2 (Supplementary Table S1). The CRISPR/Cas9 plasmid was transformed along with a PCR product repair template of the homology flanking the targeted gene and plated on YPGE with nourseothricin. The gene deletion was confirmed by PCR of gDNA and Sanger-sequencing.

The JGI library was then electroporated into *S. cerevisiae* FVG454, GG570*ura3*Δ, as previously described (Becker and Guarente, 1991) and plated on SCDA-ura. Plates were incubated at 30°C for ~1 month. An additional transformation of the library was conducted in the same manner, but without plating. Instead, after outgrowth in rich medium, the transformed library was used to inoculate two flasks, each with 1 L of SCDA-ura. The flasks were incubated at 30°C and 250 rpm for 10 days, then a portion was plated on SCDA-ura. Together, these screens only resulted in 28 colonies that could be successfully restreaked. These 28 colonies were then further tested with fermentation experiments in 24-well plates.

For genotyping of library colonies, cells were boiled in 20 mM NaOH for 5 min, and the resulting lysate used as a PCR template for a LongAmp Taq (NEB) reaction spanning the entire isobutanol cassette. The resulting amplicon was verified to be the correct length by agarose gel and then subjected to Sanger or Nanopore sequencing.

Yeast plasmid isolation

Yeast cultures were grown in SCGE-ura for 4 days, and yeast plasmids were isolated with a Zymoprep™ Yeast Plasmid Miniprep II (Zymo Research), then transformed into TransforMax EPI300 Electrocompetent *Escherichia coli* (Lucigen). The resulting *E. coli* cells were grown overnight in

LB with the appropriate antibiotic along with CopyControl™ Induction Solution (Lucigen), and plasmids were miniprepped using a QIAprep Spin Miniprep Kit (Qiagen).

Fermentations and spot plates

Fermentation experiments were done in either 15 ml culture tubes, 50 ml rubber-stoppered serum vials, or 24-well plates. For the 24-well plate experiments, individual colonies were restreaked onto SCGE-ura plates, then the patch was used to inoculate 1 ml SCDE-ura and grown for 4 days at 30°C and 250 rpm. For culture tube and serum vial experiments, individual colonies were first used to inoculate 5 ml pre-cultures of SCGE-ura and grown aerobically for 3 days at 30°C and 250 rpm. Cultures were then washed twice with sterile water and used to inoculate either 5 ml (culture tubes) or 30 ml (serum vials) of SCD-ura + 70 mM ethanol at an optical density (OD_{600}) of 0.1. Culture tubes were then grown for 3 days, and serum vials for 13 days, at 30°C and 250 rpm before analyzing fermentation products. For spot plate experiments, saturated SCGE-ura cultures were diluted to an OD_{600} of 0.1 and 10 µl suspensions were spotted onto agar plates with the appropriate medium. For anaerobic growth, a Coy anaerobic chamber (5% H_2, 5% CO_2, and 90% N_2) was used with stir bars on a magnetic stir plate to prevent flocculation. Medium used in anaerobic experiments was degassed for >12 h prior to use.

Fermentation product analysis

After fermentations were completed, cultures were placed on ice for 10 min (if serum vials), then centrifuged at 3000 g for 5 min. Supernatant was then removed and used for further analysis. Isobutanol titer was measured *via* headspace sampling of the supernatant and analysis by GC-MS. Specifically, the equipment used included the following: an Agilent 7890A GC system (Agilent Technologies, Inc. Palo Alto, CA); a LPAL3 autosampler and sample preparation system equipped with a heated agitator/stirrer and heated headspace sampling syringe (Agilent Technologies, Inc. Palo Alto, CA); and a Pegasus 4D ToF-MS (Leco Corp., Saint Joseph, Michi- gan). Typical analysis range is 0.065 mM–8.4 mM isobutanol and uses an aliquot volume of 500 ml and 2-Methylpropyl-d9 alcohol as an internal standard. Instrument run control and conditions are set by the Chromatof (®Leco Corp.) software (version 4.72.0.0) provided with the Pegasus 4D GcxGC ToF MS system. Samples were incubated at 70°C for 5 min in the heated agitator set to 350 rpm. 0.5 ml of the headspace is then sampled by the autosampler with a 2.5 ml gastight syringe heated to 75°C and injected into the GC system. The sample was withdrawn at 100 ml/s and injected into the GC at 1,000 ml/s. The syringe was purged with nitrogen gas for 0.5 min prior to the next injection. The analytical capillary GC column was a Stabilwax-DA® (Restek, Inc. Bellefonte, PA) length 30 m, 0.25 mm ID, 0.25 mm film thickness. Helium was used as a carrier gas with a pressure corrected constant flow rate of 1 ml/min. The GC inlet was fitted with a 4 mm deactivated glass liner and held at 250°C throughout the run. The inlet split ratio was set to 50:1. The GC oven was initially set to 50°C and held for 1 min then increased to 200°C at 40°C/min and held at 200°C for 5 min. The filaments of the mass spectrometer were turned on 42.5 s after injection and 10 spectra/sec were recorded from m/z 10 to m/z 250. The MS source temp was 200°C, electron energy set to 70 eV, and the detector voltage was adjusted to approximately 50 V above the minimum voltage determined by the instrument tune check procedure. The peak area of isobutanol was measured using the extracted ion chromatogram of m/z 43 and the peak area of 2-Methylpropyl-d9 alcohol was measured from the extracted ion chromatogram of m/z 46.

End-product analytes (glucose, ethanol, pyruvate) were measured with an analytical system consisting of an Agilent 1260 Infinity HPLC system (Agilent Technologies, Inc., Palo Alto, CA) with a quaternary pump, chilled (4°C) autosampler, vacuum degasser, refractive index detector, and a Aminex HPX-87H column with a Cation-H guard column (BioRad, Inc. Hercules, CA; 300 × 7.8 mm, cat# 125–0140). Operating parameters were as follows: 0.02 N H_2SO_4 mobile phase, 0.500 ml/min flow rate, 50°C column temperature, 50°C detector temperature, 28 min run time, and a 50 µl injection volume. Instrument control, data collection and analysis/calculation are done using Chem Station V. B04.03 software (Agilent Technologies, Inc., Palo Alto, CA).

Protein expression and purification

The wild-type *Lachnospiraceae bacterium* KARI gene (denoted *LbIlvC*) and its variants were cloned into pET-28a (from EMD Biosciences) with a C-terminal 6xHis tag. The pET28-*LbIlvC* (pFVG607), pET28-*LbIlvC*^{DD} (pFVG608), and pET28-*LbIlvC*^{DDV} (pFVG609) plasmids were transformed into *E. coli* BL21(DE3) (from New England Biosciences) (Supplementary Table S1). Cultures were grown at 37°C with shaking in LB supplemented with 50 mg/L kanamycin until the OD_{600} reached 0.8. Flasks were cooled in a 16°C bath, induced with 100 μM isopropyl-β-d-thiogalactopyranoside (IPTG), and incubated overnight at 21°C. Cells were harvested by centrifugation (8,000 rpm at 4°C for 15 min) and flash frozen as pellets in liquid nitrogen. The frozen cell pellets were broken by sonication (Fisher 550 Sonic Dismembrator, amplitude = 30%, time = 10 min with 1 s on/1 s off) while on ice in Buffer A (20 mM Tris pH 7.4, 30 mM imidazole, 100 mM NaCl, 10 mM $MgCl_2$). The lysate was cleared by centrifugation (12,000 rpm at 4°C for 30 min) and filtered with a 0.4 μM filter. The proteins

were purified by immobilized metal affinity chromatography (IMAC) over 5 ml Histrap High Performance (HP) columns (Cytiva, Sweden), using an AKTA Start system. All purification steps were performed at 4°C. The proteins were eluted with a linear gradi ent from buffer A to 100% buffer B (20 mM Tris pH 7.4, 500 mM imidazole, 100 mM NaCl, 10 mM $MgCl_2$, and 1 mM DTT (added before use). Fractions containing the protein were pooled, buffer exchanged, and concentrated into Buffer C (8 mM Tris pH 7.4, 20 mM NaCl, 1 mM $MgCl_2$, and 5 wt% glycerol) using Amicon Ultra centrifugal filters. Aliquots were stored at −80°C and used within 1 month.

Kinetic assay

LbIlvC activities were assayed by monitoring NAD(P)H consumption at 340 nm on a Nanodrop with a 1 cm path length. The assay buffer contained 250 mM potassium phosphate pH 7, 1 mM DTT, 200 μM NADPH or NADH, 10 mM 2-acetolactate, 10 mM $MgCl_2$, and 1,500 nM purified enzyme. The concentrations of the purified enzymes were determined using the Nanodrop. An unpaired *t*-test was performed to determine statistical significance.

Results

Combinatorial isobutanol pathway library design

The goal of this project was to construct a combinatorial library of genes from which a strain demonstrating a high-flux isobutanol pathway could be isolated. Variability was introduced in the library on two levels: coding sequences (i.e. DNA encoding enzyme variants from a homology search) and enzyme expression (i.e. varied transcription levels from distinct, previously characterized promoters (Lee et al., 2015)). We identified homologs of each enzyme within the isobutanol pathway by the use of bioprospecting. A diverse set of variants were chosen from the EFI-EST (Zallot et al., 2019) sequence similarity map by: 1) gathering homologs from clusters known to contain active enzyme variants, and 2) bioprospecting the network to identify diverse sequences from a variety of kingdom/phyla (fungi, ascomycota, firmicutes, proteobacteria, and actinobacteria). Specifically, 25 ALS homologs (23–62% identity to *S. cerevisiae ILV2*), 31 KARI homologs (22–67% identity to *S. cerevisiae ILV5*), 25 DHAD homologs (39–63% identity to *S. cerevisiae ILV3*), 18 KDC homologs (21–34% identity to *S. cerevisiae ARO10*), and 17 ADH homologs (23–49% identity to *S. cerevisiae AHD5*) were chosen (Figure 1B, Supplementary Figure S1, Supplementary Data Sheet S2). To ensure we had an entirely cytosolic localized isobutanol pathway, all predicted mitochondrial localization sequences from Mitoprot (Claros and Vincens, 1996) were removed. Genes were codon-optimized for *S. cerevisiae*, and each homolog was expressed under control of a well-characterized strong, medium, or weak promoter. The resulting transcriptional units for each gene were then used to build the final pooled plasmid library in which each plasmid contained a gene encoding each of the five required isobutanol pathway enzymes. In total, the library could consist of 1.44 billion unique combinations (Figure 1B). The library was sized to match the typical transformation efficiency of *S. cerevisiae* laboratory strains. A portion of the pooled library was sequenced using PacBio. The resulting reads were aligned to the designed genes and each occurrence of gene, promoter, and promoter-gene pair were counted. All promoters and CDSs in the library were represented and their distribution is detailed in Supplementary Data Sheet S3. Each of the 348 promoter-gene pairs was present, and the largest fold-change difference between promoter-gene pair abundance was 12, while most were within a much narrower distribution. Overall, the sequencing results indicate that the library achieved high diversity and fidelity.

Growth-coupled library screening

The large library size necessitated the use of a high-throughput screen to find plasmids that generate a high-flux pathway to isobutanol. Lacking a high-throughput analytical pipeline or a eukaryotic biosensor that senses isobutanol directly, we opted for a growth-coupled approach (Figure 1C) where strains possessing a high-flux isobutanol pathway would grow more quickly. At the outset, we envisioned a growth selection (anaerobic) but due to technical challenges, settled for growth enrichment (aerobic). We used a *S. cerevisiae* strain designated GG570 (Flikweert et al., 1996) whose genome lacks each of the three genes encoding pyruvate decarboxylase (T2-3D::*pdc1*Δ, *pdc5*Δ, and *pdc6*Δ). This strain grows slowly on glucose aerobically in part because of the Crabtree effect (de Alteriis et al., 2018) and cannot grow on glucose anaerobically because of the lost ability to regenerate NAD^+ through ethanol fermentation. We hypothesized that high-flux isobutanol pathways would restore NAD^+ regeneration by the ADH and KARI (if NADH-dependent) reactions and improve growth rates over the base strain. To facilitate library cloning, we deleted the *URA3* gene from GG570, resulting in strain FVG454 (Table 1), which required a plasmid containing the *URA3* marker for growth on media lacking uracil.

The combinatorial isobutanol pathway library was transformed into FVG454 *via* electroporation. The resulting cells were plated onto SCDA-ura and allowed to grow anaerobically at 30°C for 1 month. The transformation resulted in 0 colonies and we hypothesized that this growth

TABLE 1 *S. cerevisiae* strains used in this study.

Strain name	Description
GG570 (Flikweert et al., 1996)	T2-3D::*pdc1*Δ, *pdc5*Δ, *pdc6*Δ
FVG454	GG570:: *ura3*Δ
sJD189	FVG454 + e.v. (pCC1FOSY)
sJD107	FVG454 + #2 cassette (p#2)
sJD195	FVG454 + #1 cassette (p#1)
sFVG612	FVG454 + #2 cassette with *LbllvC*^{DD} (pFVG605)
sFVG613	FVG454 + #2 cassette with *LbllvC*^{DDV} (pFVG606)

selection was too strict; under anaerobic conditions, cell growth is completely dependent on isobutanol production for NAD^+ regeneration as oxidative phosphorylation cannot occur anaerobically. Next, we decided to try a growth enrichment where the combinatorial isobutanol pathway library was transformed into FVG454 *via* electroporation and the resulting cells were plated onto SCDA-ura and allowed to grow aerobically at 30°C for 1 month. Under aerobic conditions, cell growth is dependent on NAD^+ regeneration through both oxidative phosphorylation and isobutanol production. From the aerobic transformation, only 28 colonies grew from the ~5×10^4 unique genotypes that were screened (estimated library coverage of 0.0035%). A comprehensive screen was not possible due the limited transformation efficiency (10^3 cfu/μg) of the screening strain and the large plasmid size of 25.3 kb. The isobutanol production of the twenty-eight colonies was tested by performing a 4-day growth experiment in SCDE-ura medium (Figure 2). Half (14/28) of the colonies

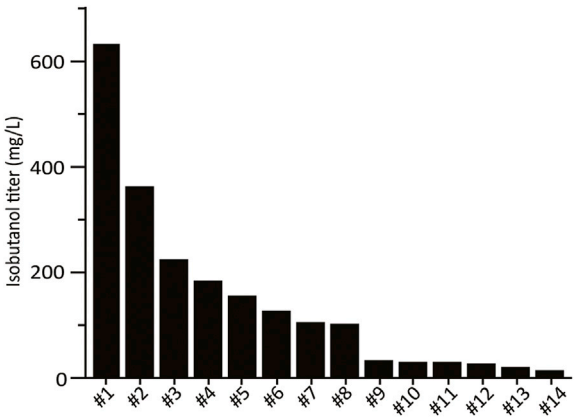

FIGURE 2
High-throughput growth-coupled screening results. Isobutanol titer from the 28 colonies isolated from the initial screen. Fermentation of one replicate for each colony was performed under aerobic conditions in 24-well plates in SCDE-ura. Isobutanol titer was measured after 4 days. Colonies for which no isobutanol was detected are not shown (14/28).

produced isobutanol and the best strain achieved an isobutanol titer of 633 mg/L, thereby validating our growth-coupled screening approach. The plasmids containing the isobutanol pathway cassettes were then isolated from the top ten producing strains. Each plasmid was sequenced with Sanger and/or Nanopore sequencing to identify the enzyme homologs and promoter strength of each gene in the cassettes (Table 2).

While our initial screening strategy demonstrated the feasibility of the growth-coupled approach to isolate high isobutanol producers, several of the isolates did not produce isobutanol. Instead, we found that many of these strains restored ethanol production, an alternative route to regenerating NAD^+. Six strains were grown in SCDA-ura medium lacking ethanol (acetate was provided as the C2 donor) so we could accurately measure ethanol production (Figure 3A). Interestingly, of the six cassettes tested, four produced significant amounts of ethanol; specifically, the highest producers were the #8 and #7 cassettes which produced 53 and 42-fold more ethanol than isobutanol, respectively (Figure 3A, Figure 3B). We hypothesized that the KDC homologs in the #8 and #7 cassettes had activity on pyruvate thus allowing the strain to regenerate NAD^+ *via* ethanol production. To test this hypothesis, we conducted a growth complementation assay by expressing the KDC homologs on a high copy vector and transforming each into the Pdc^- strain, FVG454, to observe which could restore growth on medium containing glucose. As expected, the KDC homologs in cassettes #8 (KDC07 from *Helicobacter ailurogastricus*) and #7 (KDC09 from *Enterococcus rotai*) exhibited robust growth, confirming their activity on pyruvate (Figure 3C).

To validate the isobutanol titers of our top two producing strains, designated #1 and #2, we re-transformed the isolated plasmids back into the base screening strain, FVG454, to create strains sJD195 and sJD107, respectively. The strains were cultivated aerobically (culture tube) and micro-aerobically (serum vial) at 30°C (Figure 4). sJD107 outperformed sJD195 under both micro-aerobic and aerobic conditions. Specifically, the highest producer was sJD107 under aerobic conditions which produced 364 mg/L isobutanol and had a yield of 36 mg isobutanol/g glucose which corresponds to 8.8% of the theoretical maximum yield (Figure 4A). sJD107 also performed well under micro-aerobic conditions where it produced 50 mg/L isobutanol and had a yield of 27.3 mg isobutanol/g glucose which corresponds to 6.6% of the theoretical maximum yield.

To further explore why the #1 and #2 cassettes were so successful (i.e. high isobutanol producers) we took a closer look at the homologs and expression level of the isobutanol pathway enzymes in these cassettes. The KARI promoter and the KDC homolog stood out. The gene dosage for the KARI homolog in both the #1 and #2 cassettes was high (strong promoter), while the weaker isobutanol pathway cassettes (#3, #4, #5, #7, #8, #9, and #10) had a low gene dosage (weak/medium promoter)

10.3389/fbioe.2022.1080024

TABLE 2 Homolog and expression level identification of the top 10 isobutanol producers from Figure 2 *via* Sanger and Nanopore sequencing. Green, yellow, and red boxes represent a strong, medium, or weak strength promoter, respectively (See Supplementary Data Sheet S1 for Uniprot IDs).

	ALS		KARI		DHAD		KDC		ADH	
Cassette	**Promoter**	**Homolog**	**Promoter**	**Homolog**	**Promoter**	**Homolog**	**Promoter**	**Homolog**	**Promoter**	**Homolog**
#1	P_{SAC6}	*Trichoderma gamsii*	P_{HHF2}	*Olsenella scatoligenes*	P_{RET2}	*Hypoxylon sp.*	P_{POP6}	*Dermatophilus congolensis*	P_{PAB1}	*Lactococcus lactis*
#2	P_{SAC6}	*Trichoderma gamsii*	P_{HHF2}	*Lachnospiraceae bacterium*	P_{RET2}	*Jeotgalibaca sp.*	P_{ALD6}	*Frondihabitans sp. 762G35*	P_{PAB1}	*Gluconacetobacter diazotrophicus*
#3	P_{SAC6}	*Talaromyces stipitatus*	P_{RNR2}	*Brevundimonas vesicularis*	P_{RPL18B}	*Saccharomonospora marina*	P_{TEF1}	*Enterococcus rotai*	P_{PAB1}	*Acetobacter indonesiensis*
#4	P_{HTB2}	*Brevibacterium linens*	P_{RNR2}	*Streptomyces griseorubiginosus*	P_{RPL18B}	*Acidimicrobiaceae bacterium*	P_{TEF1}	*Helicobacter ailurogastricus*	P_{TEF2}	*n.a.*
#5	P_{SAC6}	*Bifidobacterium mongoliense*	P_{RNR2}	*Slackia exigua*	P_{RPL18B}	*Arthrobacter alpinus*	P_{TEF1}	*Enterococcus rotai*	P_{RNR1}	*Tanticharoenia sakaeratensis*
#6	P_{SAC6}	*Thiohalomonas denitrificans*	P_{HHF2}	*Lactonifactor longoviformis DSM 17459*	P_{RPL18B}	*Penicillium arizonense*	P_{TEF1}	*Helicobacter ailurogastricus*	P_{PAB1}	*Arthrobacter sp. RC1.1 241*
#7	P_{SAC6}	*Oidiodendron maius*	P_{RNR2}	*Shewanella sp.*	P_{RPL18B}	*Lactococcus piscium*	P_{TEF1}	*Enterococcus rotai*	P_{RNR1}	*Tanticharoenia sakaeratensis*
#8	P_{SAC6}	*Streptomyces viridochromogenes*	P_{RNR2}	*Shewanella sp.*	P_{RPL18B}	*Methanobrevibacter smithii*	P_{TEF1}	*Helicobacter ailurogastricus*	P_{PAB1}	*Chlamydia trachomatis*
#9	P_{SAC6}	*Aspergillus nomius*	P_{HHF1}	*Clostridium populeti*	P_{THD3}	*Methanosphaera stadtmanae*	P_{TEF1}	*Enterococcus rotai*	P_{PAB1}	*Lactococcus lactis subsp. lactis (strain IL1403)*
#10	P_{PGK1}	*Talaromyces stipitatus (strain ATCC 10500)*	P_{RNR2}	*Alphaproteobacteria bacterium*	P_{THD3}	*Thiohalobacter thiocyanaticus*	P_{TEF1}	*Enterococcus rotai*	P_{PAB1}	*Arthrobacter sp. RC1.1 241*

n.a, not available; sequencing reads could not distinguish the homolog.

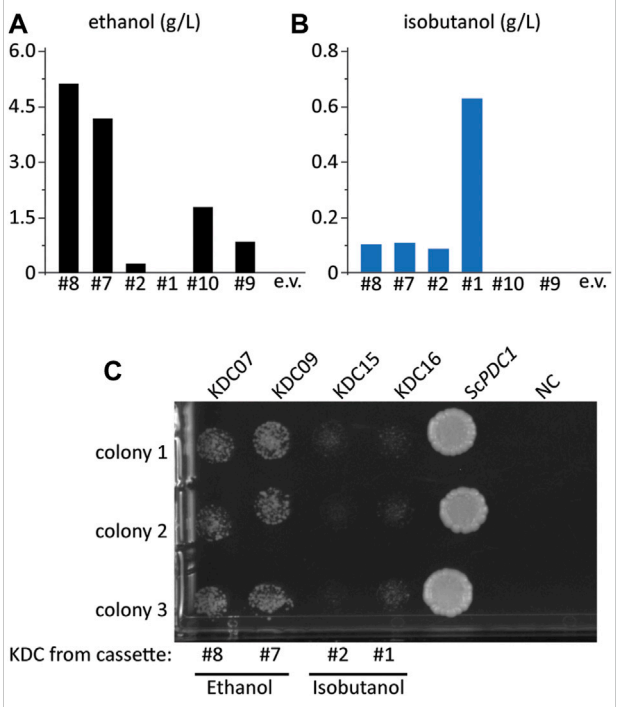

FIGURE 3
Some KDC enzymes have activity on pyruvate. **(A)** ethanol and **(B)** isobutanol titer from select colonies from the initial screen in Figure 2, FVG454 + isobutanol cassettes (p#8, p#7, p#2, p#1, p#09, p#10 or pCC1FOSY (empty vector)). Fermentation was performed under aerobic conditions with culture tubes in SCDA-ura for 4 days. **(C)** Growth complementation assay to determine which KDC homologs have activity on pyruvate. The KDC homologs from cassettes p#8, p#7, p#2, p#1 and *S. cerevisiae PDC1* (positive control) were cloned into a high copy ura-selectable vector with a strong promoter. All were transformed into the FVG454 strain along with pCC1FOSY (empty vector or NC). 10 µl cell suspensions of 1:100 diluted culture were spot plated on SCD-ura. After 4 days of growth under aerobic conditions, the plates were imaged and the strains containing KDC homologs that have activity on pyruvate grew indicating that NAD^+ was regenerated *via* ethanol production. Spot plate was done in biological triplicate.

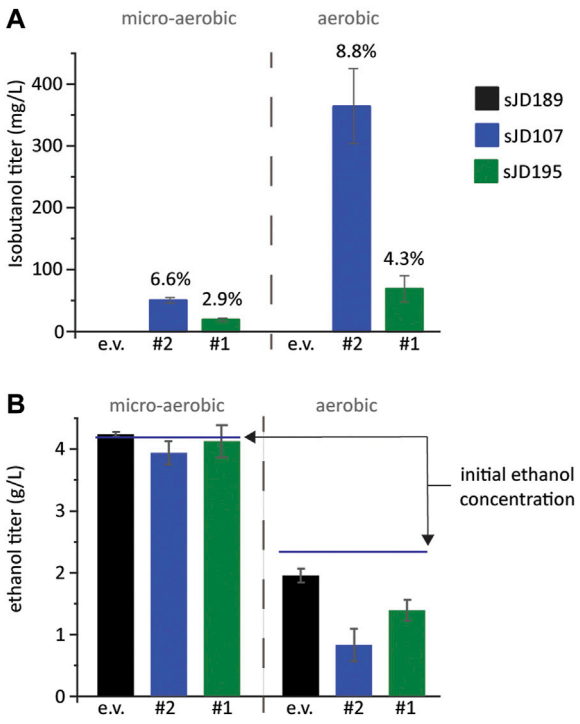

FIGURE 4
Validation of growth-coupled screening results. **(A)** Isobutanol and **(B)** ethanol titer and from the top two isobutanol-producing cassettes identified. An empty vector, the #2 cassette, and the #1 cassette plasmids were re-transformed into FVG454 resulting in strains sJD189, sJD107, and sJD195, respectively. Fermentations were performed under aerobic and micro-aerobic conditions in SCD-ura + 70 mM ethanol. Aerobic fermentations were conducted in culture tubes for 3 days while micro-aerobic fermentations were conducted in serum vials for 13 days. The percent of maximum theoretical yield achieved is shown above each bar in **(A)** and the starting concentration of ethanol is shown by a line in **(B)**. Error bars represent the standard deviation of the 3 biological replicates.

(Table 2). The strong promoter being required for KARI in our top two producers suggests that KARI is a limiting enzyme in the isobutanol pathway; this result is in agreement with previous studies in *E. coli* where KARI required the highest level of enzyme expression (Ghosh et al., 2019). Additionally, the KDC homologs in the #2 (KDC15 from *Frondihabitans sp. 762G35*) and #1 (KDC16 from *Dermatophilus congolenis*) cassettes were characterized as having minimal activity on pyruvate (Figure 3C); this is as expected since sJD107 and sJD195 produced no ethanol during fermentation in Figure 4B. Taken together, both the isobutanol pathway homologs and promoter strength are important factors for production.

Anaerobic growth unachievable after balancing NADH/NAD^+ between glycolysis and isobutanol production

We next aimed to test our best isobutanol producer, sJD107, under industrially relevant anaerobic conditions. Under these conditions, cell growth is completely dependent on isobutanol production for NAD^+ regeneration as oxidative phosphorylation cannot occur anaerobically. We hypothesized that the capacity of the strain to replenish NAD^+ by the isobutanol pathway may be limited by a redox cofactor imbalance between the engineered pathway and glycolysis; this is a result of the KARI enzyme from our #2 cassette (*Lachnospiraceae bacterium* homolog) being an NADPH-dependent enzyme. We set out to switch the cofactor preference of the *L. bacterium* KARI enzyme (*LbIlvC*) from being NADPH-dependent to NADH-dependent. The specific residues required for this switch have been previously determined and this

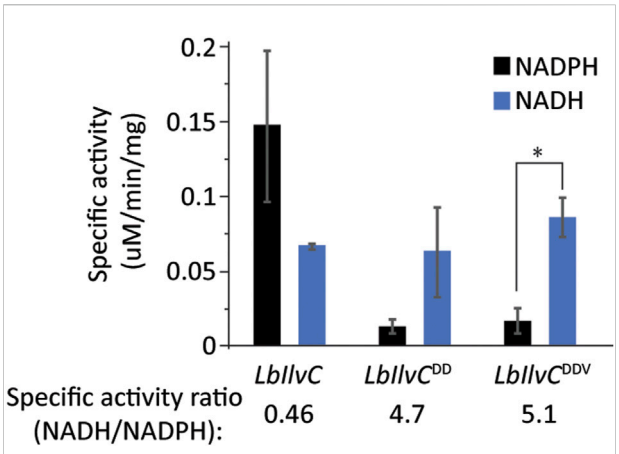

FIGURE 5
Characterization of *LbIlvC* variants. Specific activities of *LbIlvC* variants using NADPH or NADH, with 2-acetolactate as substrate in excess. All enzymes were purified prior to characterization. Each value represents the average of three independent measurements. The enzyme activities were determined in 250 mM potassium phosphate pH 7 with 1 mM DTT, 200 mM NADPH or NADH, 10 mM 2-acetolactate, and 10 mM $MgCl_2$. The concentrations of the purified enzymes were determined using a Nanodrop. The specific activity ratios of *LbIlvC* variants for NADH-to-NADPH are shown under the corresponding bars. Asterisks denote statistically significant differences by pairwise *t*-test (*, $p < 0.05$).

strategy was successful in increasing isobutanol production of a different engineered isobutanol pathway in *E. coli* (Bastian et al., 2011; Brinkmann-Chen et al., 2013). We generated two KARI variants, *LbIlvC*^{DD} (Ser53Asp, Ser55Asp) and *LbIlvC*^{DDV} (Ser53Asp, Ser55Asp, Ile87Val) and confirmed our variants exhibited a changed cofactor preference (from NADPH to NADH) by purifying the proteins and measuring the specific activity with either NADH or NADPH (Figure 5). Specifically, the *in vitro* assay consisted of monitoring the consumption of NAD(P)H over time at 340 nm when the substrate, 2-acetolactate, was in excess. The *LbIlvC*^{DD} and *LbIlvC*^{DDV} variant exhibited a ratio of NADH/NADPH activity (in U/mg) of 4.7 and 5.1 ($p < 0.05$), which is 10.3 or 11.2-fold higher than that for *LbIlvC* variant, respectively (Figure 5).

Once we validated the *LbIlvC*^{DD} and *LbIlvC*^{DDV} variants cofactor preference was switched, we cloned them into the #2 cassette in place of the original *LbIlvC* and transformed them into the FVG454 strain resulting in strains sFVG612 and sFVG613, respectively. Neither strain was able to grow anaerobically, indicating that the isobutanol pathway cassette does not support sufficient flux to rapidly replenish the NAD^+ equivalents needed for glycolysis (i.e. isobutanol production is too low to meet the cellular maintenance energy requirement).

We next asked if the *LbIlvC*^{DD} and *LbIlvC*^{DDV} variants would perform better under aerobic conditions. We aerobically cultured strains sJD189, sJD107, sFVG612, and sFVG613 for 3 days in SCD-ura + 70 mM ethanol. Strains sFVG612 and sFVG613, containing either of the NADH-dependent KARI variants, *LbIlvC*^{DD} and *LbIlvC*^{DDV}, did not outperform sJD107 with the wild-type, NADPH-dependent *LbIlvC*. Strain sJD107 produced ~280 mg/L isobutanol, which is 4.0 and 1.8-fold higher than the sFVG612 and sFVG613, respectively (Table 3). We suspect the lower isobutanol titer with the *LbIlvC*^{DD} and *LbIlvC*^{DDV} variants was due to a reduced specific activity of the KARI enzyme; the *LbIlvC*^{DD} and *LbIlvC*^{DDV} variants exhibited a ~2-fold reduction in catalytic activity (catalytic efficiency of using NADH) relative to *LbIlvC* when using NADPH (Figure 5). While sJD107 produced the highest isobutanol titer, that strain, along with all the other engineered strains, excreted significant amounts of pyruvate (0.7–1.6 g/L) indicating overflow metabolism at the pyruvate node (Table 3). Additional work is needed to enhance flux through the isobutanol pathway to prevent overflow metabolism and allow for the rapid regeneration of NAD^+ equivalents to develop a truly anaerobic isobutanol fermentative pathway for *S. cerevisiae*.

Discussion

To date, isobutanol production from a Pdc^- *S. cerevisiae* strain under anaerobic conditions has not been reported in academic literature. We hypothesize this is due to the strain's limited capacity to replenish NAD^+ through alternative fermentation pathways like isobutanol production. Here, we used a combinatorial library design and a growth-coupled screen to identify an isobutanol pathway cassette capable of supporting a higher carbon flux. Strain sJD107 which harbored our best cassette, #2, produced 364 mg/L isobutanol and had a yield of 36 mg isobutanol/g glucose under aerobic conditions which corresponds to 8.8% of the theoretical maximum yield. The #2 cassette benefited from having a KDC enzyme with minimal activity on pyruvate which minimized byproduct (ethanol) production. We then aimed to redox cofactor-balance the #2 cassette with glycolysis by changing the cofactor preference of the KARI enzyme in the #2 cassette from NADPH to NADH-preferring. However, the resulting pathway still could neither support anaerobic growth nor improve isobutanol production under aerobic conditions. While we were unable to achieve anaerobic growth, our yields micro-aerobically (serum vial cultivation) exceed previous studies; our sJD107 strain harboring the #2 cassette, achieved a yield of 27.3 mg isobutanol/g glucose which is ~3.7-fold higher than Milne et al. (Milne et al., 2016) who achieved a yield of 7.4 mg isobutanol/g glucose with a Pdc^- strain harboring a cytosolic localized pathway under micro-aerobic conditions. We hypothesize that the capacity of the isobutanol pathway must be further enhanced to achieve anaerobic growth.

TABLE 3 Fermentation products of *LbIlvC* variants. Aerobic production of strains sJD189, sJD107, sFVG612, and sFVG613. Fermentations were performed in SCD-ura + 70 mM ethanol. Isobutanol, pyruvate and ethanol titers were measured after 3 days. Standard deviation was calculated from 3 biological replicates.

Strain	Plasmid	Isobutanol (mg/L)	Pyruvate (g/L)	Ethanol (g/L)
sJD189	pCC1FOSY	0 ± 0	1.6 ± 0.2	0.3 ± 0.3
sJD107	p#2 (WT *LbIlvC*)	283.6 ± 14.8	0.7 ± 0.1	0 ± 0
sFVG612	pFVG605 (*LbIlvC*^{DD})	69.3 ± 10	0.9 ± 0	0 ± 0
sFVG613	pFVG606 (*LbIlvC*^{DDV})	154.2 ± 11.5	1.6 ± 0.2	0 ± 0

The work performed here leaves several opportunities for further improvement. First, it should be noted that our screening method can select for both high isobutanol and high ethanol producing strains so additional screening methods are required to eliminate the false-positive hits or extra care must be taken when selecting KDC homologs. Additionally, the library approach would benefit from enhanced transformation efficiency in Pdc$^-$ strains such that large libraries can be screened or working with a reduced library size so libraries could be screened in full coverage.

Data availability statement

The original contributions presented in the study are included in the article/Supplementary Material, further inquiries can be directed to the corresponding author.

Author contributions

FG and BP conceived this project. FG, BP, and JD designed experiments. FG, JD, JB, and SB performed experiments. YS aided in methodology development. FG, JD, and SB performed data analysis and visualization. FG, JD, and BP wrote and edited this manuscript.

Funding

This material is based upon work supported by the Great Lakes Bioenergy Research Center, United States Department of Energy, Office of Science, Office of Biological and Environmental Research under Award Number DE-SC0018409. Part of this work (doi:10.46936/10.25585/6000129) was conducted by the United States Department of Energy Joint Genome Institute (https://ror.org/04xm1d337), a DOE Office of Science User Facility, is supported by the Office of Science of the United States Department of Energy operated under Contract No. DE-AC02-05CH11231. JD is the recipient of a National Institutes of Health Biotechnology Training Program (NIGMS T32 GM135066).

Acknowledgments

We would like to thank Professor Chris Hittinger and Dr. Russell Wrobel for providing strain GG570 and for the generation of pXIP-URA3-2.

Conflict of interest

The authors declare that the research was conducted in the absence of any commercial or financial relationships that could be construed as a potential conflict of interest.

Publisher's note

Supplementary material

The Supplementary Material for this article can be found online at: https://www.frontiersin.org/articles/10.3389/fbioe.2022.1080024/full#supplementary-material

References

Bastian, S., Liu, X., Meyerowitz, J. T., Snow, C. D., Chen, M. M. Y. Y., and Arnold, F. H. (2011). Engineered ketol-acid reductoisomerase and alcohol dehydrogenase enable anaerobic 2-methylpropan-1-ol production at theoretical yield in *Escherichia coli*. *Metab. Eng.* 13, 345–352. doi:10.1016/j.ymben.2011.02.004

Becker, D. M., and Guarente, L. (1991). "High-efficiency transformation of yeast by electroporation," in *Methods in enzymology*. Editors C. Guthrie and G. Fink, 182–187. doi:10.1016/0076-6879(91)94015-5

Brinkmann-Chen, S., Flock, T., Cahn, J. K. B., Snow, C. D., Brustad, E. M., McIntosh, J. A., et al. (2013). General approach to reversing ketol-acid reductoisomerase cofactor dependence from NADPH to NADH. *Proc. Natl. Acad. Sci. U. S. A.* 110, 10946–10951. doi:10.1073/pnas.1306073110

Buijs, N. A., Siewers, V., and Nielsen, J. (2013). Advanced biofuel production by the yeast saccharomyces cerevisiae. *Curr. Opin. Chem. Biol.* 17, 480–488. doi:10.1016/j.cbpa.2013.03.036

Cai, H., Markham, J., Jones, S., Benavides, P. T., Dunn, J. B., Biddy, M., et al. (2018). Techno-economic analysis and life-cycle analysis of two light-duty bioblendstocks: Isobutanol and aromatic-rich hydrocarbons. *ACS Sustain. Chem. Eng.* 6, 8790–8800. doi:10.1021/acssuschemeng.8b01152

Claros, M. G., and Vincens, P. (1996). Computational method to predict mitochondrially imported proteins and their targeting sequences. *Eur. J. Biochem.* 241, 779–786. doi:10.1111/j.1432-1033.1996.00779.x

de Alteriis, E., Cartenì, F., Parascandola, P., Serpa, J., and Mazzoleni, S. (2018). Revisiting the crabtree/warburg effect in a dynamic perspective: A fitness advantage against sugar-induced cell death. *Cell Cycle* 17, 688–701. doi:10.1080/15384101.2018.1442622

de Smidt, O., du Preez, J. C., and Albertyn, J. (2012). Molecular and physiological aspects of alcohol dehydrogenases in the ethanol metabolism of *Saccharomyces cerevisiae*. *FEMS Yeast Res.* 12, 33–47. doi:10.1111/j.1567-1364.2011.00760.x

Flikweert, M. T., Van Der Zanden, L., Janssen, W. M., Steensma, H. Y., Van Dijken, J. P., and Pronk, J. T. (1996). Pyruvate decarboxylase: An indispensable enzyme for growth of *Saccharomyces cerevisiae* on glucose. *Yeast* 12, 247–257. doi:10.1002/(sici)1097-0061(19960315)12:3<247::aid-yea911>3.0.co;2-i

Gambacorta, F. V., Dietrich, J. J., Yan, Q., and Pfleger, B. F. (2020). Rewiring yeast metabolism to synthesize products beyond ethanol. *Curr. Opin. Chem. Biol.* 59, 182–192. doi:10.1016/j.cbpa.2020.08.005

Ghosh, I. N., Martien, J., Hebert, A. S., Zhang, Y., Coon, J. J., Amador-Noguez, D., et al. (2019). OptSSeq explores enzyme expression and function landscapes to maximize isobutanol production rate. *Metab. Eng.* 52, 324–340. doi:10.1016/j.ymben.2018.12.008

Jeschek, M., Gerngross, D., and Panke, S. (2017). Combinatorial pathway optimization for streamlined metabolic engineering. *Curr. Opin. Biotechnol.* 47, 142–151. doi:10.1016/j.copbio.2017.06.014

Kumar, P., Adamczyk, P. A., Zhang, X., Andrade, R. B., Romero, P. A., Ramanathan, P., et al. (2021). Active and machine learning-based approaches to rapidly enhance microbial chemical production. *Metab. Eng.* 67, 216–226. doi:10.1016/j.ymben.2021.06.009

Lee, M. E., DeLoache, W. C., Cervantes, B., and Dueber, J. E. (2015). A highly characterized yeast toolkit for modular, multipart assembly. *ACS Synth. Biol.* 4, 975–986. doi:10.1021/sb500366v

Longo, E., Velázquez, J. B., Sieiro, C., Cansado, J., Calo, P., and Villa, T. G. (1992). Production of higher alcohols, ethyl acetate, acetaldehyde and other compounds by 14*Saccharomyces cerevisiae* wine strains isolated from the same region (Salnés, N.W. Spain). *World J. Microbiol. Biotechnol.* 8, 539–541. doi:10.1007/BF01201958

Madeira, F., Pearce, M., Tivey, A. R. N., Basutkar, P., Lee, J., Edbali, O., et al. (2022). Search and sequence analysis tools services from EMBL-EBI in 2022. *Nucleic Acids Res.* 50, W276–W279. doi:10.1093/nar/gkac240

Milne, N., Wahl, S. A., van Maris, A. J. A., Pronk, J. T., and Daran, J. M. (2016). Excessive by-product formation: A key contributor to low isobutanol yields of engineered *Saccharomyces cerevisiae* strains. *Metab. Eng. Commun.* 3, 39–51. doi:10.1016/j.meteno.2016.01.002

Peralta-Yahya, P. P., Zhang, F., Del Cardayre, S. B., and Keasling, J. D. (2012). Microbial engineering for the production of advanced biofuels. *Nature* 488, 320–328. doi:10.1038/nature11478

Roussos, A., Misailidis, N., Koulouris, A., Zimbardi, F., and Petrides, D. (2019). A feasibility study of cellulosic isobutanol production—process simulation and economic analysis. *Processes* 7, 667. doi:10.3390/pr7100667

Shannon, P., Markiel, A., Ozier, O., Baliga, N. S., Wang, J. T., Ramage, D., et al. (2003). Cytoscape: A software environment for integrated models of biomolecular interaction networks. *Genome Res.* 13, 2498–2504. doi:10.1101/gr.1239303

Stoneman, H. R., Wrobel, R. L., Place, M., Graham, M., Krause, D. J., De Chiara, M., et al. (2020). CRISpy-pop: A web Tool for designing CRISPR/cas9-driven genetic modifications in diverse populations. *G3 Genes|Genomes|Genetics* 10, 4287–4294. doi:10.1534/g3.120.401498

Wess, J., Brinek, M., and Boles, E. (2019). Improving isobutanol production with the yeast *Saccharomyces cerevisiae* by successively blocking competing metabolic pathways as well as ethanol and glycerol formation. *Biotechnol. Biofuels* 12, 173. doi:10.1186/s13068-019-1486-8

Zallot, R., Oberg, N., and Gerlt, J. A. (2019). The EFI web resource for genomic enzymology tools: Leveraging protein, genome, and metagenome databases to discover novel enzymes and metabolic pathways. *Biochemistry* 58, 4169–4182. doi:10.1021/acs.biochem.9b00735

Zhang, J., Petersen, S. D., Radivojevic, T., Ramirez, A., Pérez-Manríquez, A., Abeliuk, E., et al. (2020). Combining mechanistic and machine learning models for predictive engineering and optimization of tryptophan metabolism. *Nat. Commun.* 11, 4880. doi:10.1038/s41467-020-17910-1

Zhang, Y., Cortez, J. D., Hammer, S. K., Carrasco-López, C., García Echauri, S. Á., Wiggins, J. B., et al. (2022). Biosensor for branched-chain amino acid metabolism in yeast and applications in isobutanol and isopentanol production. *Nat. Commun.* 13, 270. doi:10.1038/s41467-021-27852-x

Zhou, Y., Li, G., Dong, J., Xing, X., hui, Dai, J., and Zhang, C. (2018). MiYA, an efficient machine-learning workflow in conjunction with the YeastFab assembly strategy for combinatorial optimization of heterologous metabolic pathways in *Saccharomyces cerevisiae*. *Metab. Eng.* 47, 294–302. doi:10.1016/j.ymben.2018.03.020

frontiers | Frontiers in Bioengineering and Biotechnology

TYPE Original Research
PUBLISHED 21 December 2022
DOI 10.3389/fbioe.2022.1095464

OPEN ACCESS

EDITED BY
Tian-Qiong Shi,
Nanjing Normal University, China

REVIEWED BY
Lujing Ren,
Nanjing Tech University, China
Xing Zhang,
Nanjing Normal University, China
Hua Yuan,
Shanghai Normal University, China
Xiao Liu,
Beijing University of Chinese Medicine, China

*CORRESPONDENCE
Luoyi Wang,
wangluoyi@im.ac.cn
Shu-Shan Gao,
gaoss@tib.cas.cn
Chengsen Cui,
cuichs@tib.cas.cn

SPECIALTY SECTION
This article was submitted to Synthetic Biology, a section of the journal Frontiers in Bioengineering and Biotechnology

RECEIVED 11 November 2022
ACCEPTED 12 December 2022
PUBLISHED 21 December 2022

CITATION
Ma Y, Yan J, Yang L, Yao Y, Wang L, Gao S-S and Cui C (2022), A hybrid system for the overproduction of complex ergot alkaloid chanoclavine. *Front. Bioeng. Biotechnol.* 10:1095464. doi: 10.3389/fbioe.2022.1095464

A hybrid system for the overproduction of complex ergot alkaloid chanoclavine

Yaqing Ma[1,2,3], Juzhang Yan[2], Lujia Yang[2], Yongpeng Yao[1], Luoyi Wang[1]*, Shu-Shan Gao[2,4]* and Chengsen Cui[2,4]*

[1]CAS Key Laboratory of Microbial Physiological and Metabolic Engineering, State Key Laboratory of Microbial Resources, Institute of Microbiology, Chinese Academy of Sciences, Beijing, China, [2]Tianjin Institute of Industrial Biotechnology, Chinese Academy of Sciences, Tianjin, China, [3]University of Chinese Academy of Sciences, Beijing, China, [4]National Technology Innovation Center of Synthetic Biology, Tianjin, China

Synthetic biology-based methods (Sbio) and chemical synthesis (Csyn) are two independent approaches that are both widely used for synthesizing biomolecules. In the current study, two systems were combined for the overproduction of chanoclavine (CC), a structurally complex ergot alkaloid. The whole synthetic pathway for CC was split into three sections: enzymatic synthesis of 4-Br-Trp (4-Bromo-trptophan) using cell-lysate catalysis (CLC), chemical synthesis of prechanoclavine (PCC) from 4-Br-Trp, and overproduction CC from PCC using a whole-cell catalysis (WCC) platform. The final titer of the CC is over 3 g/L in this Sbio-Csyn hybrid system, the highest yield reported so far, to the best of our knowledge. The development of such a combined route could potentially avoid the limitations of both Sbio and Csyn systems and boost the overproduction of complex natural products.

KEYWORDS

ergot alkaloid, cell-lysate catalysis, chemical synthesis, whole-cell catalysis, Sbio-Csyn system

1 Introduction

Ergot alkaloids (EAs) are a group of highly bioactive natural products produced by a large number of filamentous fungi (Jakubczyk et al., 2014). These compounds have been intensely studied for decades, mainly due to their harmful effects on contaminated food and feeds, but also for their beneficial medicinal applications. For instants, EA compound chanoclavine (CC, Figure 1A) can stimulate dopamine receptor D2 in the mouse brain (Watanabe et al., 1987) and has been long-term used in herbal drugs (Ysrael, 2003). Furthermore, CC is the common biosynthetic intermediate for the biosynthesis of almost all EAs (Jakubczyk et al., 2015a).

The biosynthesis of CC requires three precursors: tryptophan, dimethylallyl pyrophosphate (DMAPP), and S-adenosyl methionine (SAM) (Gerhards et al., 2014; Jakubczyk et al., 2014). In the fungal cells, the shikimic acid pathway responsible for the tryptophan biosynthesis contains six enzymes (Figure 1A), whereas the mevalonate pathway for DMAPP production has seven enzymes (Figure 1A) (Zhao et al., 2013).

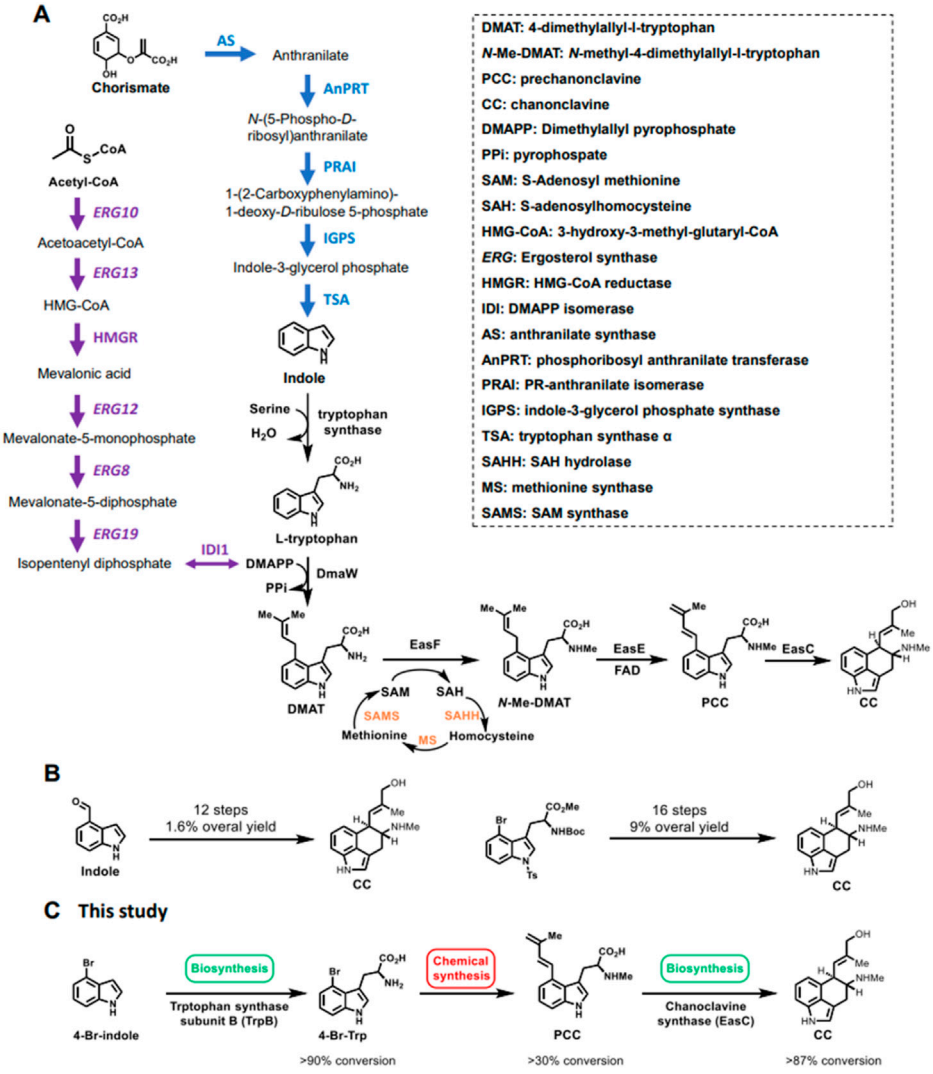

FIGURE 1
The biosynthetic pathway of chanoclavine (CC). **(A)** The biosynthetic pathway of CC in the native hosts. **(B)** Chemical synthesis of CC in the literature. **(C)** The hybrid route designed for the overproduction of CC in the current study.

Furthermore, the regeneration of SAM requires three enzymes (Figure 1A) (Parveen & Cornell, 2011). Starting from the three precursors, three prenylated-tryptophan intermediates, dimethylallyltryptophan (DMAT), *N*-methyldimethylallyltryptophan (*N*-Me-DMAT), and prechanoclavine (PCC), are generated under the successive catalysis of prenyltransferase DmaW, methyltransferase EasF, and FAD-linked oxidoreductase EasE (Gerhards et al., 2014; Jakubczyk et al., 2014). The final enzyme for converting PCC to CC remained unknown until recently when we characterized chanocalvine synthase EasC responsible for this step of oxidative cyclization (Nielsen et al., 2014; Yao et al., 2019). Overall, 20 enzymes are involved in the biosynthesis of CC in the native host (Figure 1A).

Accompanied by the complexity of the biosynthetic pathways, the construction and engineering of synthetic biology (Sbio) based methods for overproducing natural products, including microbial cell factories or cell-free systems, become increasingly difficult. As the biosynthesis of CC employed many enzymes for precursor production and tailoring modifications (Figure 1A), it led to difficulties in overproducing CC using microbial cell factories or cell-free systems. The previous production of CC in *S. cerevisiae* and *Aspergillus nidulans* reached the titers at 1.2 and 241.0 mg/L, respectively (Nielsen et al., 2014; Yao et al., 2022), which was still far from industrial application. Furthermore, our recent studies demonstrated the effort of purification of soluble EasE from *Escherichia coli*, *S. cerevisiae*, or *Trichoderma reesei* was not

successful, suggesting it was not likely to use cell-free system to overproduce CC from tryptophan. In conclusion, upgrading the current Sbio system is necessary for improving the titers of CC.

On the other hand, the chemical synthesis (Csyn) method for CC production has also been developed. CC possess complex conjugated rings with several stereocenters (Figure 1B), which led to their total synthesis being lengthy, inefficient, and not profitable (Liu & Jia, 2017). Previous research has reported two strategies for asymmetric total syntheses of CC (Kardos & Genet, 1994; Yokoyama et al., 1996), which started from complex 4-substituted indole derivatives using a 12-step and 16-step process, respectively. In addition to the shortage of expensive starting materials, these routes were inefficient for industrial applications, with 1.6% and 9% overall yield, respectively, and more research was needed to increase their efficiency.

To avoid the limitations that arise from both Csyn- and Sbio-based systems, and to take full advantage of both systems, we developed a combined system to synthesize clinically significant and structurally complex CC in this study (Figure 1C). The combined system that hired both Csyn- and Sbio-based methods could efficiently synthesize CC, with a titer of over 3 g/L and an engineering period of up to 1 week. Thus, the combined Sbio-Csyn system represents a fast, robust, and practical engineering methodology for laboratory and industrial applications.

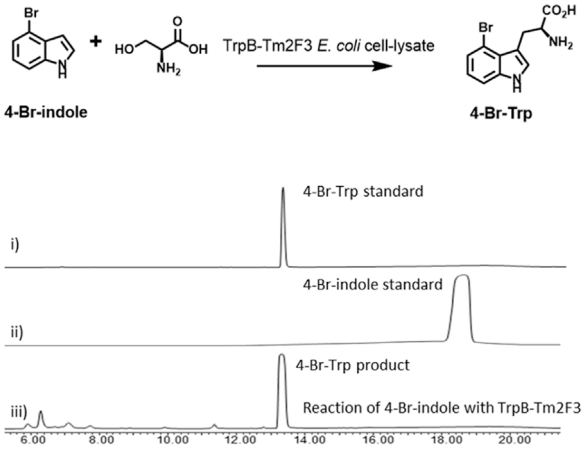

FIGURE 2
Gram-scale production of 4-Br-Trp using a cell-lysate catalysis (CLC) system: i) HPLC trace for 4-Br-Trp standard; ii) HPLC trace for 4-Br-indole standard; and iii) HPLC trace for the reaction of 4-Br-indole with TrpB-Tm2F3. Reaction conditions are 10 mM 4-Br-indole, 30 mM serine, 0.13 g/L PLP, and 100 ml cell-lysate of *E. coli* expressing TrpB-Tm2F3 extracted from 8L fermentation.

2 Materials and methods

2.1 General materials and methods

The authentic compounds prechanoclavine and agroclavine were purified and characterized, which were stored in our laboratory. All vectors and strains, including those vectors for EasC and TrpB expression, used in this study were stored in our laboratory. Electroporation was performed on A Bio-Red MicroPulser (Bio-Red 1652100, United States). The chemicals and solvents purchased and used in this study were analytical grade. All buffers and solutions were prepared with Milli-Q water. DNA sequencing and primer synthesis were done by Tsingke Biotechnologies (Beijing, China). Restriction enzymes and Q5 DNA polymerase were purchased from New England Biolabs (United States). HPLC grade acetonitrile and water were purchased from Sigma-Aldrich (St. Louis, MO, United States). A CORUI HPLC system (Chengdu, China) using C18 analytical column (Agilent Eclipse XDB-C18, 4.6 × 250 mm, 5 μm) was used to perform high performance liquid chromatography (HPLC) analysis.

2.2 Plasmid construction

The cDNAs of EasC from *Aspergillus japonicus* and Tm2F3 were synthesized for the heterologous protein expression, which were inserted into the site NdeI/XhoI of pET28a by the Gibson method to generate the corresponding plasmids. The resultant plasmids were transformed into the competent cells of *E. coli* BL21 (DE3) and plated on LB solid medium with 50 mg/ml kanamycin at 37°C overnight to get the correct transformants.

2.3 Chemical synthesis of PCC

^{1}H NMR spectra were recorded in $CDCl_3$, CD_3OD, $(CD_3)_2SO$ (400 or 600 MHz). Residual solvent peaks are used as the internal reference; the signals at 7.26 ppm are set for ^{1}H NMR spectra, taken in $CDCl_3$. Silica gel plates pre-coated on glass were used for thin-layer chromatography using UV light, or 7% ethanolic phosphomolybdic acid or potassium permanganate solution and heating as the visualizing methods. Silica gel was used for flash column chromatography with mixed CH_2Cl_2 and MeOH or ethyl acetate (EtOAc) and hexane as the eluting solvents. Yields refer to chromatographically and spectroscopically (^{1}H NMR) homogeneous materials. All reactions were performed under an oxygen-free atmosphere of nitrogen or argon, unless otherwise stated. Reagents were obtained commercially and used as received unless otherwise mentioned. Anhydrous THF, Et_2O and PhMe were freshly distilled from sodium and benzophenone ketyl and anhydrous DMA, DMF, CH_2Cl_2 and CH_3CN were freshly distilled over CaH_2, respectively, under a Ar_2 atmosphere. Room temperature is 23 °C unless otherwise stated.

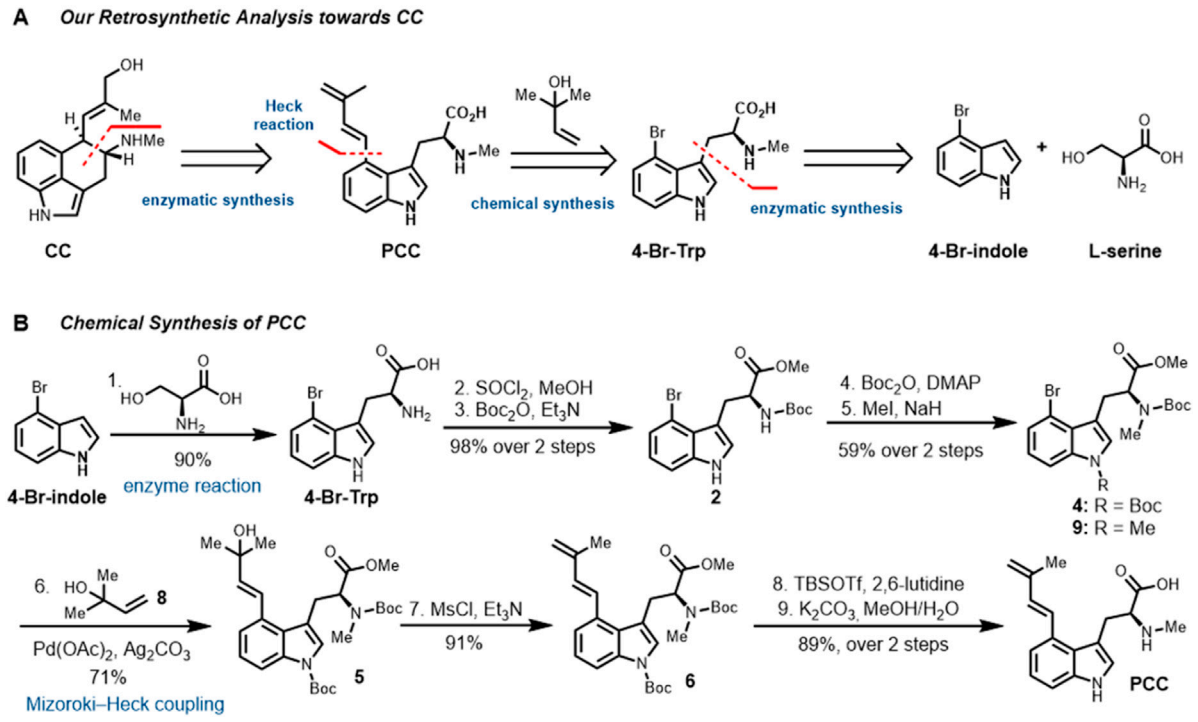

FIGURE 3
(A) Retrosynthetic bond disconnection. **(B)** Synthesis of PCC from 4-Br-Trp.

2.4 HPLC and LC-MS analysis

HPLC analysis was performed on CORUI HPLC system (Chengdu, China) using C18 columns (Agilent Eclipse XDB-C18, 4.6 × 250 mm, 5 μm) and a Photodiode Array Detector. The samples of a 10 μL injection volume were analyzed with a linear gradient method of 90%–10% H_2O (v/v, 0.1% formic acid) -acetonitrile (v/v, 0.1% formic acid) to 100% acetonitrile (v/v, 0.1% formic acid) in 10 min with a flow rate of 1.0 ml/min.

LC-MS analysis was performed on Agilent 1,100 with a mass spectrum detector (MSD) using an analytical column (Ultimate XB-C18, 2.1 × 100 mm, 3.0 μm; Welch), and the positive ion mode was used to perform the mass spectrometry. The samples of a 1.0 μL injection volume were analyzed with a linear gradient method of 90%–10% H_2O (v/v, 0.1% formic acid) -acetonitrile (v/v, 0.1% formic acid) to 100% acetonitrile (v/v, 0.1% formic acid) in 12 min with a flow rate of 0.3 ml/min.

2.5 Strain culture and biotransformation for the biosynthesis of CC

10 ml LB liquid medium containing 50 μg/ml kanamycin was inoculated with a correct transformant of EasC and cultured at 37°C and 220 rpm overnight for 12 h. The overnight culture was used a seed medium and transferred into 1L LB liquid medium and incubated at 37°C with shaking at 220 rpm to an OD_{600} of 0.6–0.8. Protein expression was induced by the addition of 10 μM isopropyl-β-D-thiogalactopyranoside (IPTG) and 5-aminolevulinic acid (5-ALA, 80 mg/L) and shaking was continued for 18 h at 16°C, 200 rpm. The bacteria were then harvested by centrifugation at 5,000 rpm for 20 min and resuspended in 50 ml sodium phosphate buffer (PBS, 50 mM, pH 7.4).

For the reaction with whole cells, different concentrations of substrate PCC and 2 eq NADPH were added to 500 μL of the above bacterial suspension, and then incubated at 30°C with shaking at 800 rpm. For the reaction with cell lysate, the bacterial suspension was firstly disrupted by ultrasonication (30 min with 5 s' on, 9 s' off cycles), then different concentrations of PCC and 2 eq NADPH were added to 500 μL of the disruption solution followed by incubating at 30°C, 800 rpm. The reactions were sampled at different times, quenched with methanol and checked for conversion with HPLC. In addition, three parallels were set for each concentration.

2.6 Enzymatic synthesis of 4-Br-Trp

Plasmid pET28a-Tm2F3 were transformed into *E. coli* BL21 (DE3) for expression the tryptophan synthase subunit B (Trp B).

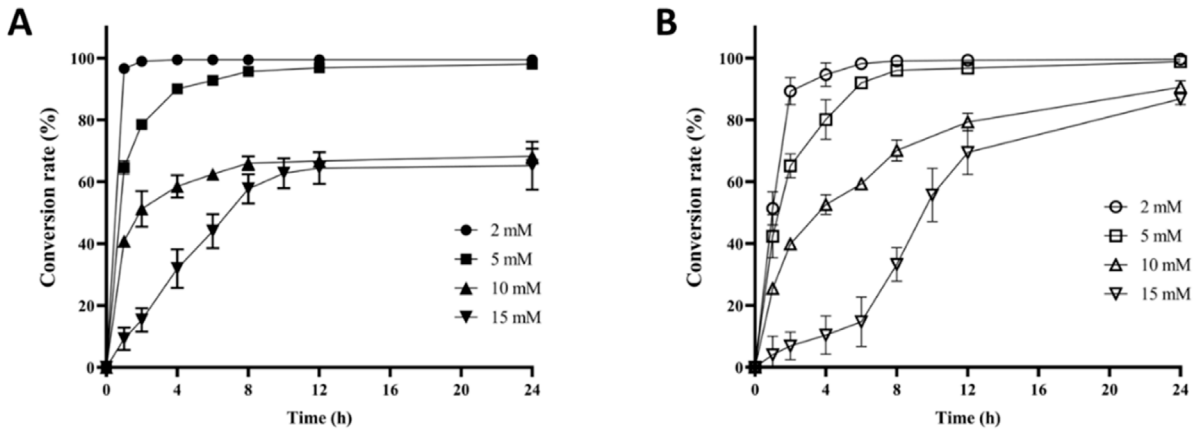

FIGURE 4
Overproduction of CC from PCC using two different methods. **(A)** The conversion rate of CC to PCC using $EasC_{aj}$ based CLC platform. **(B)** The conversion rate of CC to PCC using $EasC_{aj}$ based whole-cell catalysis (WCC) platform.

8 × 10 ml LB medium containing 50 μg/ml kanamycin was inoculated with a single colony in a shaker at 37 °C overnight. The overnight cultures were used to inoculate 8×1L LB medium and shaken at 37 °C to an OD_{600} of 0.6–0.8. Then 0.5 mM IPTG was added and induced at 16 °C for 16 h. The cells were harvested by centrifugation (5,000 rpm at 4 °C for 20 min), and the cell pallets were resuspended in 100 ml lysis buffer (100 mM PBS, pH 8.0) and disrupted by high pressure cell fragmentation apparatus (Guangzhou Juneng Biotechnology Co., LTD). To remove cellular debris, the mixture was centrifuged at 12,000 rpm for 30 min at 4°C. The supernatant was transferred into a 250 ml Erlenmeyer flask, 4-Br-indole (dissolved in DMSO) and serine were added into the reaction system. The reaction mixture was immersed in a metal bath that was pre-heated to 75°C for 24 h and then cooled to 0°C (ice bath), in which most of 4-Br-Trp precipitated. Subsequently, the reaction mixture was centrifuged at 12,000 rpm for 20 min, and the precipitate was washed with water three times and concentrated *in vacuo* to obtain 4-Br-Trp. The supernatant was subjected to the hollow fiber ultrafiltration membrane column to remove the protein, and the aqueous phase was concentrated *in vacuo* to obtain 4-Br-Trp.

3 Results

3.1 Determining the splitting point of the hybrid system

To design a combined Sbio-Csyn system, we selected PCC as the splitting point (Figure 1C). We split the whole synthetic pathway into three sections (Figure 1C): 1) enzymatic synthesis 4-Br-Trp from the cheap material 4-Br-indole using the tryptophan synthase subunit B (TrpB); 2) efficient chemical synthesis of PCC from 4-Br-Trp; and 3) overproduction of CC from PCC using the chanoclavine synthase EasC (Figure 1C). The key point of this study is to design a hybrid platform that combines the advantages of both Sbio- and Csyn-based methods to produce high-valued natural products from cheap starting materials.

3.2 Biosynthesis of 4-Br-Trp from 4-Br-indole

4-Substituted tryptophans, such as 4-Br-Trp, serve as precursors for the chemical and biological synthesis of complex structures with a wide range of medicinal applications. The enantioselective synthesis of 4-substituted tryptophan compounds is often complicated due to protection and deprotection steps. At the same time, enzymes have the potential to synthesize those products in fewer steps and with precise chemo- and stereoselectivity. A notable example is TrpB, a pyridoxal phosphate (PLP) dependent enzyme (Romney et al., 2017). TrpB is the subunit B of tryptophan synthase, which can be coupled with indole and L-serine to generate the corresponding tryptophan analogue with retention of enantiopurity (Figure 2) (Corr et al., 2016). Accordingly, the TrpB platform has the potential to provide direct access to a wide range of 4-substituted tryptophans from cheap indole analogues. Directed evolution toward TrpB isolated from *Thermotoga maritima* endows it with high activity toward non-native substrates, such as different substituted indoles. The resultant mutant Tm2F3 (P19G, I69V, K96L, P140L, N167D, L213P, T292S) is especially attractive because it shows high activity for synthesizing 4-Br-Trp directly from serine and the

corresponding 4-Br-indole (Figure 2) (Romney et al., 2017). Accordingly, TrpB-Tm2F3 mutant was used to overproduce 4-Br-Trp in the current study.

In our study, the mutant Tm2F3 was expressed in *E. coli* with a relatively high level (20 mg–30 mg/L, Supplementary Figure S1). It could be purified by heat treatment at a temperature of up to 75 °C with enhanced solubility. The cell-lysate catalysis (CLC) was applied to overproduce 4-Br-Trp, by using the cell lysate collected from the 8-L scale *E. coli* cells. Thus, enantiopure 4-Br-Trp could be synthesized by feeding the starting materials 4-Br-indole (10 mM) and serine (30 mM), and 0.01 g/L PLP to the cell lysate of *E. coli* expressing TrpB-TmF3. The overall conversion rate of CLC was below 50%, which was significantly lower than the reported rate from the literature (Romney et al., 2017). Next, we wished to see if the conversion rate could be improved by supplementing a higher concentration of cofactor PLP. Therefore, the CLC system was tested with 0.13 g/L PLP, instead of the initially used 0.01 g/L. Gratifyingly, the overall conversion rate of 4-Br-indole was improved to over 90%. Finally, 4-Br-Trp was synthesized in gram-scale with the production of 2.1 g of 4-Br-Trp (75% isolated yield) from the CLC with 8-L *E. coli* cell lysate, which provided sufficient starting material for the following chemical synthesis.

3.3 Chemical synthesis of PCC from 4-Br-Trp

Retrosynthetically (Figure 3A), the C ring of CC could be constructed from compound PCC using EasC catalyzed reaction developed in our lab ((Yao et al., 2019); Figure 1A). The polyene side chain on PCC can be installed *via* Pd-catalyzed cross-coupling reactions such as Suzuki-Miyaura, Negishi, and Mizoroki-Heck coupling reactions (Figure 3A). To consider the commercial availability of starting material, 2-methyl-3-buten-2-ol **8** was chosen as an ideal fragment for Mizoroki-Heck coupling with 4-Br-Trp, which has already been synthesized in gram-scale *via* the CLC platform using the enzyme TrpB (Figure 2).

Our synthesis started with preparing Mizoroki-Heck coupling precursor 4-Br-Trp (Figure 3B), which was synthesized from commercially available 4-Br-indole. Enzyme catalyzed reaction with L-serine under our optimized conditions to give 4-Br-Trp in 90% yield. Esterification of 4-Br-Trp with $SOCl_2$ in MeOH to obtain methyl ester in high yield. It should be noted that the esterification of 4-Br-Trp neither in Fisher condition (H_2SO_4, MeOH, reflux) nor base conditions ($NaHCO_3$ and MeI in DMF, $KHCO_3$ and MeI in MeOH, K_2CO_3 and MeI in MeCN, Cs_2CO_3 and MeI in MeOH) resulting decompose of the diene moiety. Initially, we tried to protect primary NH_2 and indole nitrogen in one sequence, but unfortunately, a low yield of **3** (not shown in Figure 3B) was isolated. Then we turn to protect them separately, which was to protect free amine first by using Boc_2O and Et_3N conditions in Devaraj's probe synthesis (Wu et al., 2014) to give a high yield of mono-protected product in 99% yield. Combining Boc_2O with DMAP successfully protected the indole nitrogen in excellent yield, followed by methylation (NaH and MeI in DMF) (Ashworth et al., 1995) at secondary amine to afford compound **4** (59%, over two steps). In the methylation step, the Boc protecting group on indole nitrogen of product **4** could be selectively removed under basic condition, subsequent methylation with MeI to give side-product **9** in about 15% yield. The structure of side-product **9** was confirmed by ^1H NMR and LCMS spectrum.

With **4** in hand, we then moved to explore the Mozoroki-Heck coupling with commercially available 2-methyl-3-buten-2-ol **8** outlined in Figure 3B. From the screening of conditions, $Pd(OAc)_2$ and Ag_2CO_3 in toluene at 90 °C was identified as the reaction condition (Xu et al., 2010), which provided the highest conversion of **4** and yield of the desired coupling product **5** (71%). In parallel with the experimental exploration, we also tried the coupling conditions with AgOAc, K_2CO_3 in DMF or K_2CO_3 in DMF/H_2O; it either provided the mass results or decomposed to the hydrolysis by-products. Notably, with $PdCl_2(PPh_3)_2$ as a catalyst system, only a trace amount of desired **5** was detected.

Having established suitable conditions to achieve our target compound, tertiary alcohol **5** was converted into the diene moiety in a mesylation and elimination; the one-pot sequence gave **6** in excellent yield (91%) (Dethe et al., 2011). Deprotection of the N-Boc protecting group under the condition of TBSOTf, followed by ester hydrolysis (K_2CO_3 in MeOH/H_2O), gave PCC in 89% yield over two steps. This synthesis can also be scaled up to multigram scale, thus providing reliable and safe access to PCC.

3.4 Overproduction of CC from PCC

With PCC in hand, we next aimed to synthesize CC by using EasC, a key enzyme that catalyzed the conversion of PCC to CC (Yao et al., 2019). To select the best ortholog of EasC, different EasC cDNAs were synthesized from *Aspergillus fumigatus*, *A. japonicus*, *Claviceps fusiformis*, *Periglandula ipomoeae*, *C. purpurea*, and *C. paspali* and introduced them into *E. coli* for protein purification (Yu et al., 2022), to evaluate their expression level. Our results indicated that EasC from *A. japonicus* ($EasC_{aj}$) showed the highest protein expression level with ~30 mg/L (Supplementary Figure S1). Accordingly, $EasC_{aj}$ was applied in the current study for the overproduction of CC from PCC.

Firstly, the overproduction of CC was performed by applying CLC or whole-cell catalysis (WCC) using *E. coli* expressing $EasC_{aj}$. According to the detected results (Figure 4), both CLC and WCC could completely transform 2 mM PCC to CC. However, the reaction rate of CLC was faster by

converting >99% PCC to CC in 2 h, while 8 h was required for complete conversion through the latter method. Based on the above study, we attempted the biosynthesis of CC using higher concentrations of PCC. As shown in Figure 4, when the concentration of PCC was 5 mM, both methods completed the >95% conversion in 8 h.

However, when the concentration of PCC was doubled into 10 mM, the study showed different final conversion rates for the two methods. The catalytic rate of CLC was faster in the first 2 hours, which converted nearly 50% PCC to CC. However, compared to the 68% final conversion of CLC method, the WCC's final conversion rate was significantly higher, with 91% conversion in 24 h' reaction. The transformation after 2 h for the CLC method became extremely slow, suggesting that rapid protein deactivation had happened. Finally, 15 mM PCC was used for the biocatalytic synthesis of CC, and final conversions of 65% and 87% (~3.34 g/L CC produced) could be obtained for CLC and WCC method, respectively. Similar to the reactions with 10 mM PCC, the CLC method showed a faster reaction rate in the first 8 h but with lower final conversion. In conclusion, based on the WCC platform using $EasC_{aj}$ expressed in *E. coli*, we were able to overproduce CC with a titer of over 3 g/L.

4 Discussion

The combined Sbio-Csyn system established in this study seems superior to either the Csyn system or the Sbio system. The low levels of protein expression, high cost of cofactors and substrates, and multiple enzymes required make the overproduction of ergot alkaloids challenging to achieve *via* Sbio system (such as microbial cell factory or cell-free system). In accordance with this, no studies about cell-free systems have been reported for CC overproduction (Figure 4). Nielsen et al. first reported the microbial synthesis of CC in *Saccharomyces cerevisiae* with a titer of ~1.2 mg/L (Nielsen et al., 2014). Later study indicated that this yeast strain with CC biosynthetic genes showed a higher final titer at low temperatures, likely due to the improved activity of the enzymes EasE and EasC (Jakubczyk et al., 2015b). Wong et al. also used yeast cells to produce CC heterologously, albeit with only detectable yield (Yan et al., 2022). The fungal platform *A. nidulans* was also applied for the biosynthesis of CC in several studies (Ryan et al., 2013; Yao et al., 2022). Ryan et al. described the production of CC by reconstituting its biosynthetic enzymes in *A. nidulans* in 2013 (Ryan et al., 2013). However, no final titer was reported. In 2022, Yao et al. used a Fungal-Yeast-Shuttle-Vector protocol to systematically refactor and engineer the CC biosynthetic pathway in *A. nidulans*, which led to a final titer of CC up to 241 mg/L (Figure 1A). In conclusion, the current protocols for the microbial synthesis of CC are not profitable for industrial production. To overcome those dilemmas, a combined Sbio-Csyn system was developed for the overproduction of CC. In the current study, the use of engineered TrpB smartly overproduced the expensive 4-Br-Trp from the cheap material 4-Br-indole in a Gram scale; through the chemical synthesis, the total synthesis of PCC from 4-Br-Trp was efficient and scalable by achieving >30% yield, and future optimization could further improve its overall yield. The final WCC platform with chanocalvine synthase EasC from *A. japonicus* led to the highest tier of CC (over 3 g/L, Figure 4) in the literature to the best of our knowledge.

Due to the abundance of minor metabolites, the isolated ergot alkaloids from ergot fermentation could be impure, leading to the industrial production of half amount of ergot alkaloid based on a field-production mode (Hanosova et al., 2015). Such difficulty could be exacerbated for those alkaloids with a low natural abundance, such as CC, typically transient intermediates in native EA-producers. Thus, developing a new mode to synthesize EAs could benefit the production of ergot-based pharmaceuticals. In this study, we developed a Sbio-Csyn hybrid system to overproduce the tricyclic CC with a titer of over 3 g/L. Our engineered systems overcame several major limitations that the current protocols for producing CC must be suffered, like strain degenerations and long growth cycles. For example, the present study of the field production for CC required months for the rye growth and harvest (Hulvova et al., 2013). In addition, *Claviceps* strains typically retained CC in its sclerotia (Hulvova et al., 2013). Instead, the *E. coli* strain for the WCC platform could secrete CC to the growth medium in our work, which would accelerate the isolation and purification of CC. Furthermore, *Claviceps* strains used for submerged fermentations suffered a degeneration process, which could reduce CC production frequently (Hulvova et al., 2013). Thus, our work will inject new power into the industrial production and medicinal application of EA-based drugs in the future. Future optimization of this combined system would improve the CC production and accelerate the industrial production of this medicinally crucial natural product. The key step in designing such a combined Sbio-Csyn system is to select a suitable splitting point between the two methods. We believe that the concept of the hybrid system could be further applied to the overproduction of more structurally complex natural products and pharmaceutical molecules, which are currently inaccessible through either the Sbio-or Csyn-based protocols.

Data availability statement

The original contributions presented in the study are included in the article/Supplementary Material, further inquiries can be directed to the corresponding authors.

Author contributions

LW, S-SG, and CC contributed to conception and design of the research project. LW and S-SG worked on synthetic biology study. CC worked on chemical synthesis study. YM worked on strain culture and biotransformation for the biosynthesis of chanoclavine. JY worked on synthesis of PCC. LY and YY worked on enzymatic synthesis of 4-bromo-trotophan. All authors contributed to manuscript revision, read, and approved the submitted version.

Funding

This study was supported by the National Key Research and Development Program of China (2019YFA0905100 and 2018YFA0901600), the National Natural Science Foundation of China (grant no. 31872614), the Youth Scientists Innovation Promotion Association of CAS (2019090) to S-SG, Innovative Cross Team project of Chinese Academy of Sciences, CAS (grant no. JCTD-2019-06), and Tianjin Synthetic Biotechnology Innovation Capacity Improvement Project (TSBICIP-CXRC-062 and TSBICIP-CXRC-069).

Conflict of interest

The authors declare that the research was conducted in the absence of any commercial or financial relationships that could be construed as a potential conflict of interest.

Publisher's note

All claims expressed in this article are solely those of the authors and do not necessarily represent those of their affiliated organizations, or those of the publisher, the editors and the reviewers. Any product that may be evaluated in this article, or claim that may be made by its manufacturer, is not guaranteed or endorsed by the publisher.

Supplementary material

The Supplementary Material for this article can be found online at: https://www.frontiersin.org/articles/10.3389/fbioe.2022.1095464/full#supplementary-material

References

Ashworth, P., Broadbelt, B., Jankowski, P., Kocienski, P., Pimm, A., and Bell, R. (1995)., 1995. Synthesis-Stuttgart, 199–206. doi:10.1055/s-1995-3870A synthesis of jaspamide based on 1, 2-metallate rearrangements of α-heteroalkenylmetal derivatives*Synthesis*2

Corr, M. J., Smith, D. R. M., and Goss, R. J. M. (2016). One-pot access to L-5, 6-dihalotryptophans and L-alknyltryptophans using tryptophan synthase. *Tetrahedron* 72 (46), 7306–7310. doi:10.1016/j.tet.2016.02.016

Dethe, D. H., Erande, R. D., and Ranjan, A. (2011). Biomimetic total syntheses of flinderoles B and C. *J. Am. Chem. Soc.* 133 (9), 2864–2867. doi:10.1021/ja1116974

Gerhards, N., Neubauer, L., Tudzynski, P., and Li, S. M. (2014). Biosynthetic pathways of ergot alkaloids. *Toxins (Basel)* 6 (12), 3281–3295. doi:10.3390/toxins6123281

Hanosova, H., Koprna, R., Valik, J., Knoppova, L., Frebort, I., Dzurova, L., et al. (2015). Improving field production of ergot alkaloids by application of gametocide on rye host plants. *N. Biotechnol.* 32 (6), 739–746. doi:10.1016/j.nbt.2015.01.008

Hulvova, H., Galuszka, P., Frebortova, J., and Frebort, I. (2013). Parasitic fungus Claviceps as a source for biotechnological production of ergot alkaloids. *Biotechnol. Adv.* 31 (1), 79–89. doi:10.1016/j.biotechadv.2012.01.005

Jakubczyk, D., Caputi, L., Hatsch, A., Nielsen, C. A., Diefenbacher, M., Klein, J., et al. (2015a). Discovery and reconstitution of the cycloclavine biosynthetic pathway--enzymatic formation of a cyclopropyl group. *Angew. Chem. Int. Ed. Engl.* 54 (17), 5117–5121. doi:10.1002/anie.201410002

Jakubczyk, D., Caputi, L., Hatsch, A., Nielsen, C. A., Diefenbacher, M., Klein, J., et al. (2015b). Discovery and reconstitution of the cycloclavine biosynthetic pathway-enzymatic formation of a cyclopropyl group. *Angew. Chem. Weinh. Bergstr Ger.* 127 (17), 5206–5210. doi:10.1002/ange.201410002

Jakubczyk, D., Cheng, J. Z., and O'Connor, S. E. (2014). Biosynthesis of the ergot alkaloids. *Nat. Prod. Rep.* 31 (10), 1328–1338. doi:10.1039/c4np00062e

Kardos, N., and Genet, J. P. (1994). Synthesis of (-)-CHANOCLAVINE-I. *Tetrahedron-Asymmetry* 5 (8), 1525–1533. doi:10.1016/0957-4166(94)80122-3

Liu, H., and Jia, Y. (2017). Ergot alkaloids: Synthetic approaches to lysergic acid and clavine alkaloids. *Nat. Prod. Rep.* 34 (4), 411–432. doi:10.1039/c6np00110f

Nielsen, C. A., Folly, C., Hatsch, A., Molt, A., Schroder, H., O'Connor, S. E., et al. (2014). The important ergot alkaloid intermediate chanoclavine-I produced in the yeast *Saccharomyces cerevisiae* by the combined action of EasC and EasE from Aspergillus japonicus. *Microb. Cell Fact.* 13, 95. doi:10.1186/s12934-014-0095-2

Parveen, N., and Cornell, K. A. (2011). Methylthioadenosine/S-adenosylhomocysteine nucleosidase, a critical enzyme for bacterial metabolism. *Mol. Microbiol.* 79 (1), 7–20. doi:10.1111/j.1365-2958.2010.07455.x

Romney, D. K., Murciano-Calles, J., Wehrmuller, J. E., and Arnold, F. H. (2017). Unlocking reactivity of TrpB: A general biocatalytic platform for synthesis of tryptophan analogues. *J. Am. Chem. Soc.* 139 (31), 10769–10776. doi:10.1021/jacs.7b05007

Ryan, K. L., Moore, C. T., and Panaccione, D. G. (2013). Partial reconstruction of the ergot alkaloid pathway by heterologous gene expression in Aspergillus nidulans. *Toxins (Basel)* 5 (2), 445–455. doi:10.3390/toxins5020445

Watanabe, H., Somei, M., Sekihara, S., Nakagawa, K., and Yamada, F. (1987). Dopamine receptor stimulating effects of chanoclavine analogues, tricyclic ergot alkaloids, in the brain. *Jpn. J. Pharmacol.* 45 (4), 501–506. doi:10.1016/s0021-5198(19)43371-4

Wu, H., Yang, J., Seckute, J., and Devaraj, N. K. (2014). *In situ* synthesis of alkenyl tetrazines for highly fluorogenic bioorthogonal live-cell imaging probes. *Angew. Chem. Int. Ed. Engl.* 53 (23), 5805–5809. doi:10.1002/anie.201400135

Xu, Z., Hu, W., Liu, Q., Zhang, L., and Jia, Y. (2010). Total synthesis of clavicipitic acid and aurantioclavine: Stereochemistry of clavicipitic acid revisited. *J. Org. Chem.* 75 (22), 7626–7635. doi:10.1021/jo101506c

Yan, J., Yin, S., Asta, M., Ritchie, R. O., Ding, J., and Yu, Q. (2022). Anomalous size effect on yield strength enabled by compositional heterogeneity in high-entropy alloy nanoparticles. *Nat. Commun.* 13 (1), 2789. doi:10.1038/s41467-022-30524-z

Yao, Y., An, C., Evans, D., Liu, W., Wang, W., Wei, G., et al. (2019). Catalase involved in oxidative cyclization of the tetracyclic ergoline of fungal ergot alkaloids. *J. Am. Chem. Soc.* 141 (44), 17517–17521. doi:10.1021/jacs.9b10217

Yao, Y., Wang, W., Shi, W., Yan, R., Zhang, J., Wei, G., et al. (2022). Overproduction of medicinal ergot alkaloids based on a fungal platform. *Metab. Eng.* 69, 198–208. doi:10.1016/j.ymben.2021.12.002

Yokoyama, Y., Kondo, K., Mitsuhashi, M., and Murakami, Y. (1996). Total synthesis of optically active chanoclavine-I. *Tetrahedron Lett.* 37 (52), 9309–9312. doi:10.1016/s0040-4039(97)82950-4

Ysrael, M. C. (2003). Tonkin herbal drug: A multidisciplinary approach to development. *Clin. Hemorheol. Microcirc.* 29 (3-4), 247–251. Available at: https://www.ncbi.nlm.nih.gov/pubmed/14724348.

Yu, Z. P., An, C., Yao, Y., Wang, C. Y., Sun, Z., Cui, C., et al. (2022). A combined strategy for the overproduction of complex ergot alkaloid agroclavine. *Synth. Syst. Biotechnol.* 7 (4), 1126–1132. doi:10.1016/j.synbio.2022.08.003

Zhao, L., Chang, W. C., Xiao, Y., Liu, H. W., and Liu, P. (2013). Methylerythritol phosphate pathway of isoprenoid biosynthesis. *Annu. Rev. Biochem.* 82, 497–530. doi:10.1146/annurev-biochem-052010-100934

frontiers | Frontiers in Bioengineering and Biotechnology

TYPE Original Research
PUBLISHED 10 January 2023
DOI 10.3389/fbioe.2022.1089639

OPEN ACCESS

EDITED BY
Tian-Qiong Shi,
Nanjing Normal University, China

REVIEWED BY
Yongjin Zhou,
Dalian Institute of Chemical Physics (CAS), China
Wenming Zhang,
Nanjing Tech University, China
Steffen N. Lindner,
Charité Universitätsmedizin Berlin, Germany

*CORRESPONDENCE
Zhen Chen,
zhenchen2013@mail.tsinghua.edu.cn

SPECIALTY SECTION
This article was submitted to Synthetic Biology, a section of the journal Frontiers in Bioengineering and Biotechnology

RECEIVED 04 November 2022
ACCEPTED 28 December 2022
PUBLISHED 10 January 2023

CITATION
Sun Q, Liu D and Chen Z (2023), Engineering and adaptive laboratory evolution of *Escherichia coli* for improving methanol utilization based on a hybrid methanol assimilation pathway. *Front. Bioeng. Biotechnol.* 10:1089639. doi: 10.3389/fbioe.2022.1089639

Engineering and adaptive laboratory evolution of *Escherichia coli* for improving methanol utilization based on a hybrid methanol assimilation pathway

Qing Sun[1], Dehua Liu[1,2,3] and Zhen Chen[1,2,3]*

[1]Key Laboratory of Industrial Biocatalysis (Ministry of Education), Department of Chemical Engineering, Tsinghua University, Beijing, China, [2]Tsinghua Innovation Center in Dongguan, Dongguan, China, [3]Center for Synthetic and Systems Biology, Tsinghua University, Beijing, China

Engineering *Escherichia coli* for efficient methanol assimilation is important for developing methanol as an emerging next-generation feedstock for industrial biotechnology. While recent attempts to engineer *E. coli* as a synthetic methylotroph have achieved great success, most of these works are based on the engineering of the prokaryotic ribulose monophosphate (RuMP) pathway. In this study, we introduced a hybrid methanol assimilation pathway which consists of prokaryotic methanol dehydrogenase (Mdh) and eukaryotic xylulose monophosphate (XuMP) pathway enzyme dihydroxyacetone synthase (Das) into *E. coli* and reprogrammed *E. coli* metabolism to improve methanol assimilation by combining rational design and adaptive laboratory evolution. By deletion and down-regulation of key genes in the TCA cycle and glycolysis to increase the flux toward the cyclic XuMP pathway, methanol consumption and the assimilation of methanol to biomass were significantly improved. Further improvements in methanol utilization and cell growth were achieved *via* adaptive laboratory evolution and a final evolved strain can grow on methanol with only 0.1 g/L yeast extract as co-substrate. ^{13}C-methanol labeling assay demonstrated significantly higher labeling in intracellular metabolites in glycolysis, TCA cycle, pentose phosphate pathway, and amino acids. Transcriptomics analysis showed that the expression of *fba*, *dhak,* and part of pentose phosphate pathway genes were highly up-regulated, suggesting that the rational engineering strategies and adaptive evolution are effective for activating the cyclic XuMP pathway. This study demonstrated the feasibility and provided new strategies to construct synthetic methylotrophy of *E. coli* based on the hybrid methanol assimilation pathway with Mdh and Das.

KEYWORDS

methanol, *Escherichia coli*, synthetic methylotrophy, xylulose monophosphate pathway, adaptive laboratory evolution

1 Introduction

Methanol is a promising non-food feedstock for the fermentation industry due to its abundance, low price, and a high degree of reduction (Wang et al., 2020b). Methanol can be produced from the greenhouse gases methane and CO_2, thus conversion of methanol to value-added chemicals *via* green biological processes may provide an attractive approach toward carbon neutrality (Zhu et al., 2020). Although natural methylotrophs such as *Methylobacterium*

extorquens (Yuan et al., 2021) and *Bacillus methanolicus* (Brito et al., 2021) have been engineered to produce several chemicals, the relatively slow cell growth, incomprehensive understanding of cellular metabolism and the lack of effective genetic engineering tools significantly hinder the systematic engineering of these organisms toward real industrial applications (Zhu et al., 2020). Alternatively, engineering of well-characterized fast-growing microbial chassis such as *Escherichia coli* as synthetic methylotrophs by introducing heterologous methanol assimilation pathways has attracted broad attention in recent years (Gregory et al., 2022; Keller et al., 2022).

Natural methylotrophs oxidize methanol to formaldehyde by different types of methanol dehydrogenase (Mdh) or alcohol oxidase (AOX), which are further assimilated *via* three main pathways, namely the ribulose monophosphate (RuMP) pathway, the serine cycle, and the xylulose monophosphate (XuMP) pathway (Zhang et al., 2017). Since the RuMP pathway is considered to be the most energy-efficient pathway (Supplementary Table S1) (Gregory et al., 2022), large efforts have been made to engineer *E. coli* (Chen et al., 2018; Keller et al., 2022) or *Corynebacterium glutamicum* (Wang et al., 2020a) to assimilate methanol by introducing heterologous NAD-dependent Mdh and the RuMP pathway enzymes 3-hexulose-6-phosphate synthase (Hps) and 6-phospho-3-hexuloisomerase (Phi). Despite great successes in heterologous expression and optimization of the RuMP pathway, it is still very challenging to convert sugar heterotrophs to efficient methylotrophs due to the poor kinetics of heterologous enzymes, metabolic imbalance of synthetic RuMP cycle (e.g., insufficient ribulose 5-phosphate generation), and toxicity of formaldehyde resulting in DNA-protein crosslinking (Chen et al., 2020). Most synthetic methylotrophs require the supplement of other sugars (e.g., glucose (Bennett et al., 2020b), gluconate (Meyer et al., 2018), xylose (Chen et al., 2018)), pyruvate (Yu and Liao, 2018) or nutrients [amino acids (Gonzalez et al., 2018)] as a co-substrate to support cell growth. Recently, Liao's group and Vorholt's group have achieved great success in engineering *E. coli* for autonomous methylotrophy *via* the RuMP pathway by combining rational design and adaptive laboratory evolution (ALE) respectively (Chen et al., 2020; Keller et al., 2022). Although both engineered strains showed a growth rate comparable with natural methylotrophs (a doubling time of ~8 h), the obtained growth rate and methanol consumption rate are still not satisfied for industrial application. Artificial one-carbon assimilation pathways, such as the reductive glycine pathway (rGlyP) (Kim et al., 2020) and the synthetic homoserine pathway (He et al., 2020), have also been proposed and experimentally verified. However, these proposed pathways still serve as proof of concept and large efforts are required to realize efficient autonomous methylotrophy. Thus, the design and engineering of efficient fast-growing synthetic methylotrophs *via* different pathways are still highly desirable for practical application.

The XuMP pathway from methylotrophic yeast is another highly efficient formaldehyde assimilation pathway (Zhu et al., 2020) while heterologous expression of the XuMP pathway in prokaryotic microorganisms has not been widely explored. The native methylotrophic yeasts such as *Pichia pastoris* can efficiently utilize methanol to obtain very high optical density. Although the energy efficiency of the natural XuMP pathway with O_2-dependent alcohol oxidase is lower than the RuMP pathway (Whitaker et al., 2015), it is possible to increase the energy efficiency by combining eukaryotic dihydroxyacetone synthase (Das) with prokaryotic NAD-dependent Mdh. The hybrid methanol assimilation pathway can generate key glycolytic intermediate glyceraldehyde 3-phosphate (GAP) with only two enzymatic steps and the energy efficiency of the pathway is equal to the RuMP pathway when fructose-6-phosphate aldolase (Fsa) and transaldolase (Tal) are used for xylulose 5-phosphate (Xu5P) generation (Supplementary Table S1). Recently, De Simone et al. demonstrated the first example of heterologous expression of Mdh and Das in *E. coli* and showed that methanol can be integrated into several intermediates in central metabolism when cells were cultured with methanol and xylose as co-substrates (De Simone et al., 2020). However, the engineered strain showed low incorporation of ^{13}C-methanol into the pentose phosphate pool and proteinogenic amino acids, indicating that the regeneration of Xu5P should be further improved to increase the efficiency of the cyclic XuMP pathway.

In this study, we attempted to increase the efficiency of the hybrid methanol assimilation pathway in *E. coli* by combining rational design and ALE. We showed that methanol consumption and the biomass yield on methanol can be increased by enforcing the metabolic flux toward the XuMP cycle. Especially, we showed that the final evolved strain can utilize methanol in the presence of a low concentration (0.1 g/L) of yeast extract and ^{13}C-methanol can be incorporated into glycolytic, pentose phosphate, and tricarboxylic acid cycle (TCA) intermediates, as well as free intracellular amino acids. Genome and transcriptome sequencing were also employed to clarify the potential reasons for improved methanol assimilation. This study demonstrated that it is possible to develop a methylotroph of *E. coli* *via* the hybrid methanol assimilation pathway with heterologous Mdh and Das.

2 Materials and methods

2.1 Bacterial strains and plasmids

All strains and plasmids used in this study are listed in Table 1. *E. coli* DH5α was used for routine cloning. The starting *E. coli* SIJ488 was derived from *E. coli* MG1655 carrying genome-integrated gene deletion machinery (Jensen et al., 2015). High-copy expression vector pTrc99a was used for the construction of the hybrid methanol assimilation pathway.

2.2 Plasmids and strains construction

To construct plasmid pTrc99a-mdh-das for the hybrid methanol assimilation pathway, *mdh* gene encoding methanol dehydrogenase from *Acinetobacter garner* and *das* gene encoding dihydroxyacetone synthase from *Pichia angusta* were codon-optimized and synthesized with a consensus RBS (AAGAAGGAGATATAC) under the control of the Trc promoter and inserted into the restriction site of EcoRI/SmaI of pTrc99a. To construct plasmid pTrc99a-mdh-das-antigapA, a fragment containing high-performing MicF M7.4 Hfq binding site (Hoynes-O'Connor and Moon, 2016) with the target binding region (TBR) of *gapA* gene was inserted into plasmid pTrc99a-mdh-das under the control of the Trc promoter. TBR sequence was designed to be complementary to the initiation codon (AUG) and extended 27 nucleotides into the coding region of *gapA*

TABLE 1 Strains and plasmids used in this study.

Strain or plasmid	Description	Sources
Plasmids		
pTrc99a	High-copy plasmid, ColE1 ori, Amp^r	Lab stock
pTrc99a-mdh-das	pTrc99a with *mdh* gene from *Acinetobacter garner* and *das* gene from *Pichia angusta*	This study
pTrc99a-mdh-das-antigapA	pTrc99a with *mdh* gene from *Acinetobacter garner*, *das* gene from *Pichia angusta*, and antisense sequence to *gapA* gene	This study
Strains		
SIJ488	*E. coli* K-12 MG1655 Tn7::para-exo-beta-gam; prha-FLP; xylSpm-IsceI	Lab stock
SIJ01	SIJ488, deletion of *frmAB* gene	This study
SIJ02	SIJ01, deletion of *pfkA* and *pfkB* genes	This study
SIJ03	SIJ02, deletion of *sucA* gene	This study
X1	SIJ488, harboring pTrc99a-mdh-das	This study
X2	SIJ01, harboring pTrc99a-mdh-das	This study
X3	SIJ02, harboring pTrc99a-mdh-das	This study
X4	SIJ03, harboring pTrc99a-mdh-das	This study
X5	SIJ03, harboring pTrc99a-mdh-das-antigapA	This study
Ev17	An isolated strain from ALE of strain X5	This study

gene. Gibson assembly was used for all plasmid construction following the standard procedure (Gibson et al., 2009).

Gene knockout in *E. coli* SIJ488 was based on the lambda Red recombineering system as described by Jensen (Jensen et al., 2015). All of the primers and synthesized gene sequences used in this study are listed in Supplementary Tables S2, S3.

2.3 Medium and culture conditions

Strains were cultivated in M9 minimal medium with 400 mM methanol, 1 g/L yeast extract, and 100 μg/mL ampicillin at 37°C and 200 rpm unless otherwise stated. The M9 minimal medium contains: $Na_2HPO_4{\cdot}12H_2O$ 17.1 g/L, KH_2PO_4 3 g/L, NH_4Cl 1 g/L, NaCl 0.5 g/L, 2 mM $MgSO_4{\cdot}7H_2O$, 0.1 mM $CaCl_2$, trace element solution 250 μL/L. The trace element solution contained $FeCl_3{\cdot}6H_2O$ 1.62 g/L, $ZnCl_2$ 0.13 g/L, $CoCl_2{\cdot}6H_2O$ 0.2 g/L, $Na_2MO_4{\cdot}2H_2O$ 0.2 g/L, $CuCl_2{\cdot}6H_2O$ 0.09 g/L, and H_3BO_3 0.05 g/L. If necessary, an amino acid mix solution was additionally added, consisting of (per liter of final culture medium): L-arginine hydrochloride, 72.5 mg; L-cystine 24.0 mg; L-histidine hydrochloride 42 mg; L-isoleucine 52.4 mg; L-leucine 52.4 mg; L-lysine hydrochloride, 126.4 mg; L-methionine,15.1 mg; L-phenylalanine, 33 mg; L-threonine, 47.6 mg; L-tryptophan, 10.2 mg; L-tyrosine, 36 mg; L-valine 46.8 mg. The expression of the hybrid methanol assimilation pathway was induced by adding 0.1 mM isopropyl β-D-1-thiogalactopyranoside (IPTG) initially.

Adaptive laboratory evolution of strain X5 was performed by serial transfers with inoculation of 2% (v/v) cultures every 2–4 days. Medium for evolution was a mixture of M9 minimal medium and Hi-Def Azure (HDA, Teknova) (Bennett et al., 2020b; Chen et al., 2020) with 400 mM methanol, 0.1 mM IPTG, and 100 μg/mL ampicillin. Strain X5 was first cultivated in the 100% HDA medium at 37°C and 200 rpm. After being cultivated to the stationary phase, the cultures were used as seed cultures to inoculate fresh medium containing 75% HDA and 25% M9 minimal medium. From passage 2 to passage 5 (liquid transfer cycles), the ratio of HDA was further reduced from 75% to 30%. From passage 6 to passage 11, cell cultures were continuously transferred in 15% HDA and 85% M9 minimal medium. Starting from passage 12, cell growth was achieved in 5% HDA and 95% M9 minimal medium, and the subsequent evolution was continued with the same medium. At passage 28, a colony was isolated and termed Ev17 strain for further studies.

2.4 Analytical methods

The cell concentration was determined at an optical density of 600 nm (OD_{600}). The percent increase of biomass caused by methanol was calculated as Eq. 1 (Gonzalez et al., 2018).

$$\frac{final\ OD_{600}\,(with\ methanol) - final\ OD_{600}\,(without\ methanol)}{final\ OD_{600}\,(without\ methanol) - initial\ OD_{600}\ of\ culture} * 100\% \quad (1)$$

Quantification of methanol concentration was carried out by using High-performance liquid chromatography (HPLC) equipped with an Aminex HPX-87H Column (300 × 7.8 mm) using 5 mM sulfuric acid as the mobile phase with a flow rate of 0.8 mL/min at 65°C. The consumption of methanol has been adjusted by subtracting the evaporation of methanol in the medium without cells. The concentration of formaldehyde was quantified by the Nash reaction (Woolston et al., 2018). 125 μL of cells supernatant was mixed with 125 μL Nash reagent (5 M ammonium acetate, 50 mM acetylacetone). The mixtures were incubated at 37°C for 1 h and measured at 412 nm. Formaldehyde standard solution needs to be prepared fresh daily and the standard curve was in the range from 0 to 100 μM.

2.5 ^{13}C labeling analysis

To carry out the ^{13}C-methanol isotopic analysis for intracellular metabolites and amino acids, cells were cultured in M9 minimal medium with 400 mM ^{13}C-methanol and 1 g/L yeast extract for 48 h and prepared according to the protocols described by Long and Antoniewicz (Long and Antoniewicz, 2019). Samples were injected into the UHPLC-Q-Orbitrap liquid chromatography-mass

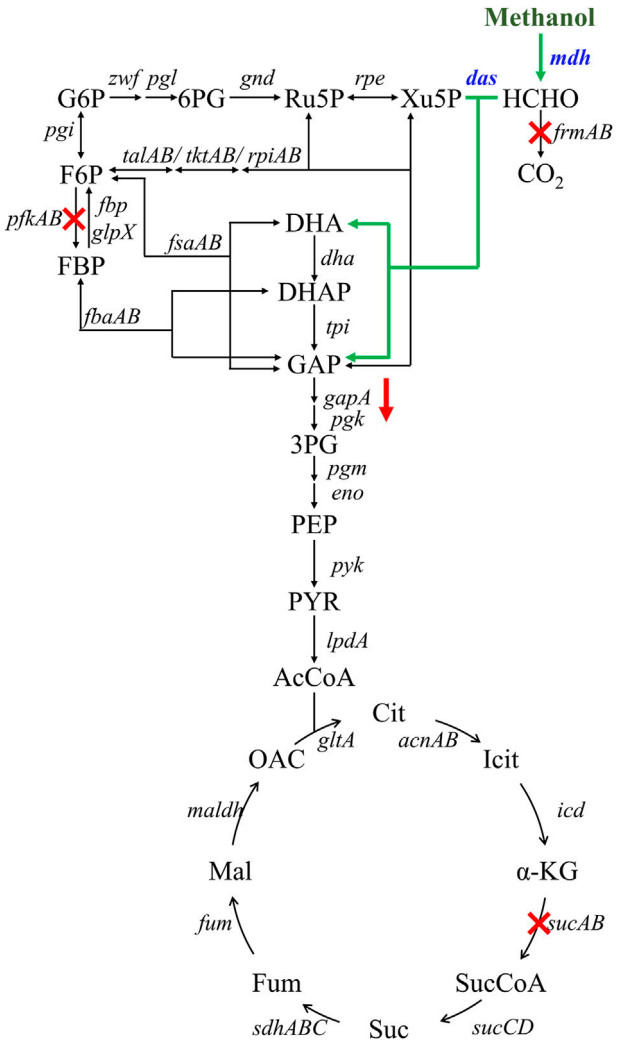

FIGURE 1
Engineering strategies for improving methanol assimilation based on a hybrid methanol assimilation pathway. The symbol "X" indicates gene deletion and the symbol "↓" indicates down-regulation of gapA gene. Abbreviations: G6P: glucose-6-phosphate; 6PG: 6-phosphogluconate; Ru5P: ribulose-5-phosphate; Xu5P: xylulose 5-phosphate; F6P: fructose-6-phosphate; FBP: fructose-1,6-diphosphate; DHA: dihydroxyacetone; DHAP: dihydroxyacetone phosphate; GAP: glyceraldehyde-3-phosphate; 3PG: glycerate-3-phosphate; PEP: phosphoenolpyruvate; PYR: pyruvate; AcCoA: acetyl-coenzyme A; Cit: citrate; Icit: isocitrate; α-KG: alpha-ketoglutarate; SucCoA: succinyl-coenzyme A; Suc: succinate; Fum: fumarate; Mal: malate; OAC: oxaloacetate.

spectrometry system (Thermo Fisher Scientific, United States). Intracellular metabolites and amino acids were separated on Waters BEH Amide Column (2.1 × 100 mm; 1.7 μm) at 35°C with solvent A (acetonitrile with 0.1% formic acid) and solvent B (deionized water with 0.1% formic acid and 10 mM ammonium acetate) as the mobile phase with a flow rate of 0.3 ml/min. The elution gradient was (% B): 0–5 min at 0%; 5–6 min at 0%–25%; 6–15 min at 25%; 15–16 min at 25%–50%; 16–25 min at 50%; 25–26 min, 0%; 26–30 min, 0%. Mass spectrometry was configured with heated electrospray ionization (HESI) and operated in both positive and negative ion modes in full MS scan mode. Isotopologue fractions (IFs) and average carbon labeling were calculated as Eqs 2, 3 (Keller et al., 2020). ^{13}C metabolic tracer analysis was obtained from three biological replicate measurements.

$$\text{Isotopologue fractions} = \frac{m_i}{\sum_{j=0}^{n} m_j} \quad (2)$$

$$\text{Average carbon labeling} = \frac{\sum_{j=0}^{n} m_j}{n^* \sum_{j=0}^{n} m_j} \quad (3)$$

Here, m_i *and* m_j are the abundance of a mass isotopologue, n is the number of carbon atoms of the metabolite.

2.6 Whole-genome sequencing and transcriptomics analysis

DNA re-sequencing and mRNA sequencing were carried out on the Illumina HiSeq instrument by Azenta (Suzhou, China). Cells were cultivated for 48 h in M9 minimal medium with 400 mM methanol and 1 g/L yeast extract. For each sample, 200 μg genomic DNA or 1 μg total RNA was used for library preparation by standard protocols. For transcriptomics analysis, HTSeq (v0.6.1p1) was employed to estimate gene expression levels from the pair-end clean data. Differential expression analysis was by the DESeq2 Bioconductor package which is a model based on the negative binomial distribution. p-value of genes were settled <.05 and $|\log_2 fold\ changes| \geq 1.5$ to detect differential expressed genes. For whole-genome sequencing, BWA (V0.7.17) was used to map clean data to reference genome. The raw datasets can be found in NCBI Bioproject database (accession number: PRJNA896773).

3 Results and discussion

3.1 Construction of the hybrid methanol assimilation pathway in *E. coli*

A hybrid methanol assimilation pathway with prokaryotic NAD-dependent Mdh and eukaryotic dihydroxyacetone synthase (Das) can convert methanol and Xu5P into glyceraldehyde 3-phosphate (GAP) and dihydroxyacetone (DHA) with the generation of NADH. DHA can be further converted into dihydroxyacetone phosphate (DHAP) by the endogenous DHA kinase of *E. coli* (Figure 1). Previously, De Simone et al. showed that a strain expressing *mdh* from *A. garner* and *das* from *P. angusta* exhibited a higher growth rate in minimal medium with methanol and xylose than that with xylose alone (De Simone et al., 2020). In that case, Xu5P was mainly derived from xylose, thus, it was not clear whether the cyclic XuMP pathway would be functional in sugar-free conditions. Thus, we first constructed the same methylotrophic module (*mdh* from *A. garner* and *das* from *P. angusta*) in plasmid pTrc99a and transformed the resulting plasmid pTrc99a-mdh-das into *E. coli* SIJ488 to generate strain X1. When cultured in M9 minimal medium with methanol and 1 g/L yeast extract, strain X1 showed 10.90 ± 0.01% higher final biomass concentration compared to that without methanol, indicating the hybrid methanol assimilation module was functional (Figure 2A). To enhance methanol assimilation, glutathione-dependent formaldehyde dehydrogenase gene (*frmA*) and S-formylglutathione hydrolase gene (*frmB*) were knocked out to reduce formaldehyde dissimilation into CO_2, generating strain X2. The methanol

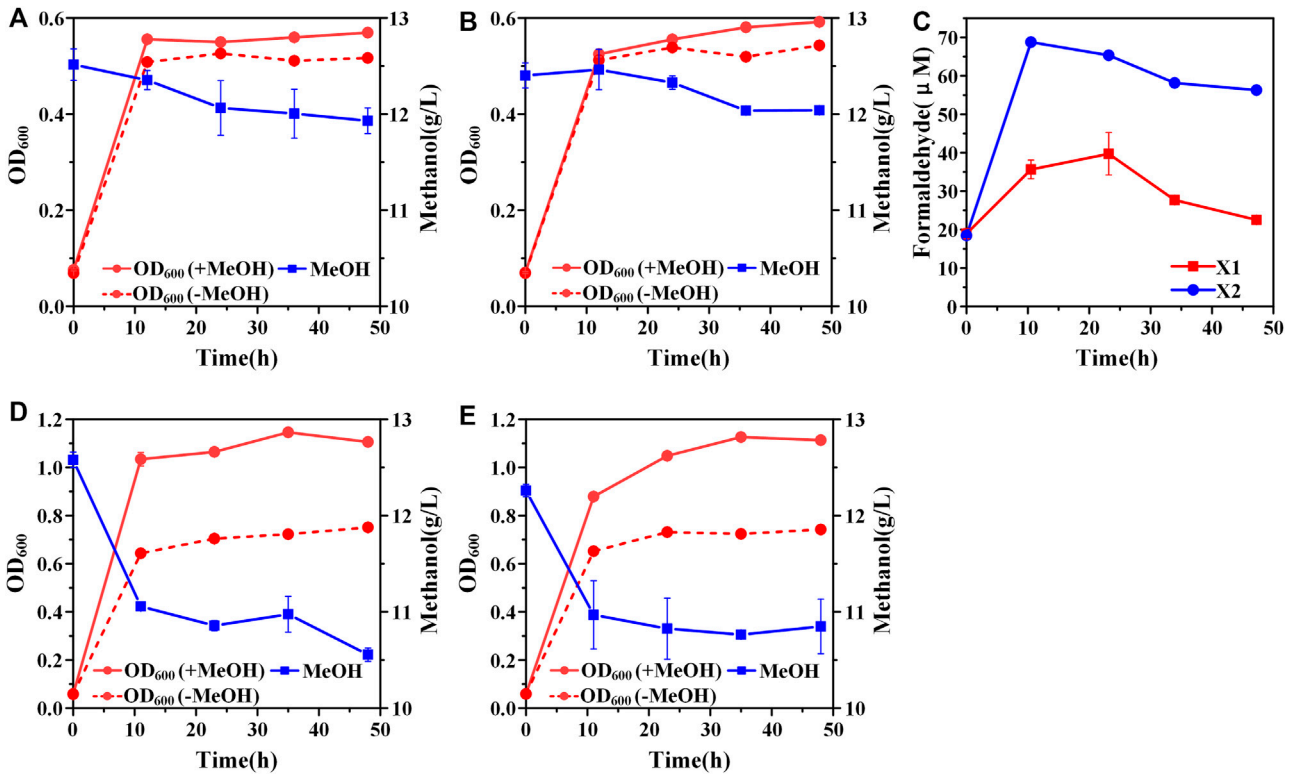

FIGURE 2
Construction of the hybrid methanol assimilation pathway. **(A)** Growth characteristics of strain X1; **(B)** Growth characteristics of strain X2; **(C)** formaldehyde accumulation. Addition of amino acids mix solution could improve cell growth and methanol consumption of both strain X1 **(D)** and strain X2 **(E)**. Error bars represent standard deviation, n = 2.

TABLE 2 Growth phenotype and methanol consumption of five strains at 48 h.

	X1	X2	X3	X4	X5	Ev17
Methanol consumed (g/L)	0.58 ± 0.03	0.36 ± 0.02	0.25 ± 0.04	0.33 ± 0.04	1.01 ± 0.26	1.63 ± 0.12
OD_{600} (+MeOH)	0.57 ± 0.01	0.59 ± 0.00	0.51 ± 0.00	0.38 ± 0.01	0.32 ± 0.00	0.71 ± 0.041
OD_{600} (−MeOH)	0.52 ± 0.01	0.54 ± 0.00	0.49 ± 0.00	0.32 ± 0.00	0.26 ± 0.01	0.40 ± 0.01
Increase of biomass caused by methanol	10.90 ± 0.00%	10.60 ± 0.01%	4.70 ± 0.01%	24.00 ± 0.00%	31.60 ± 0.01%	90.9 ± 0.01%
Methanol consumption rate ($g/L{\cdot}OD^{-1}$)	1.01 ± 0.01	0.61 ± 0.04	0.49 ± 0.00	0.86 ± 0.01	3.16 ± 0.42	2.29 ± 0.13

The percentage increase of biomass caused by methanol was calculated as Eq. 1. The data represent the means ± standard deviations (n = 2).

consumption by strain X2 and the increase of finial biomass concentration by methanol were similar to those of strain X1 (Figure 2B). When cultured with methanol, strains X1 and X2 accumulated 35.66 ± 2.43 μM and 68.78 ± 1.10 μM formaldehyde in 12 h (Figure 2C), suggesting that *mdh* from *A. garner* was successfully expressed in *E. coli*. Blocking the formaldehyde dissimilation pathway in strain X2 significantly increased formaldehyde accumulation but did not improve cell growth and methanol consumption (Table 2), suggesting an imbalance between formaldehyde formation and consumption.

Previous studies showed that the recombinant *E. coli* with Mdh and RuMP pathway cannot efficiently synthesize several amino acids (Bennett et al., 2020a). We hypothesized that the biosynthesis of some endogenous amino acids may also be limited for stains X1 and X2, which may affect cell growth and methanol consumption. When supplemented with an extra amino acid mix solution, strains X1 and X2 showed 52.1 ± 0.04% and 54.4 ± 0.05% increases of final biomass concentration by methanol respectively (Figures 2D, E). Moreover, the consumption of methanol by strains X1 and X2 was increased to 2.02 ± 0.01 g/L and 1.41 ± 0.22 g/L, which were both over 2-fold higher than those without amino acid mix solution (Figures 2D, E). The significant increase of methanol consumption and cell growth benefit by methanol confirmed that some amino acids or their intermediates cannot be efficiently synthesized in strains X1 and X2. It should be noted that the consumption of methanol by strain X2 was still lower than X1 even with the addition of amino acids mix

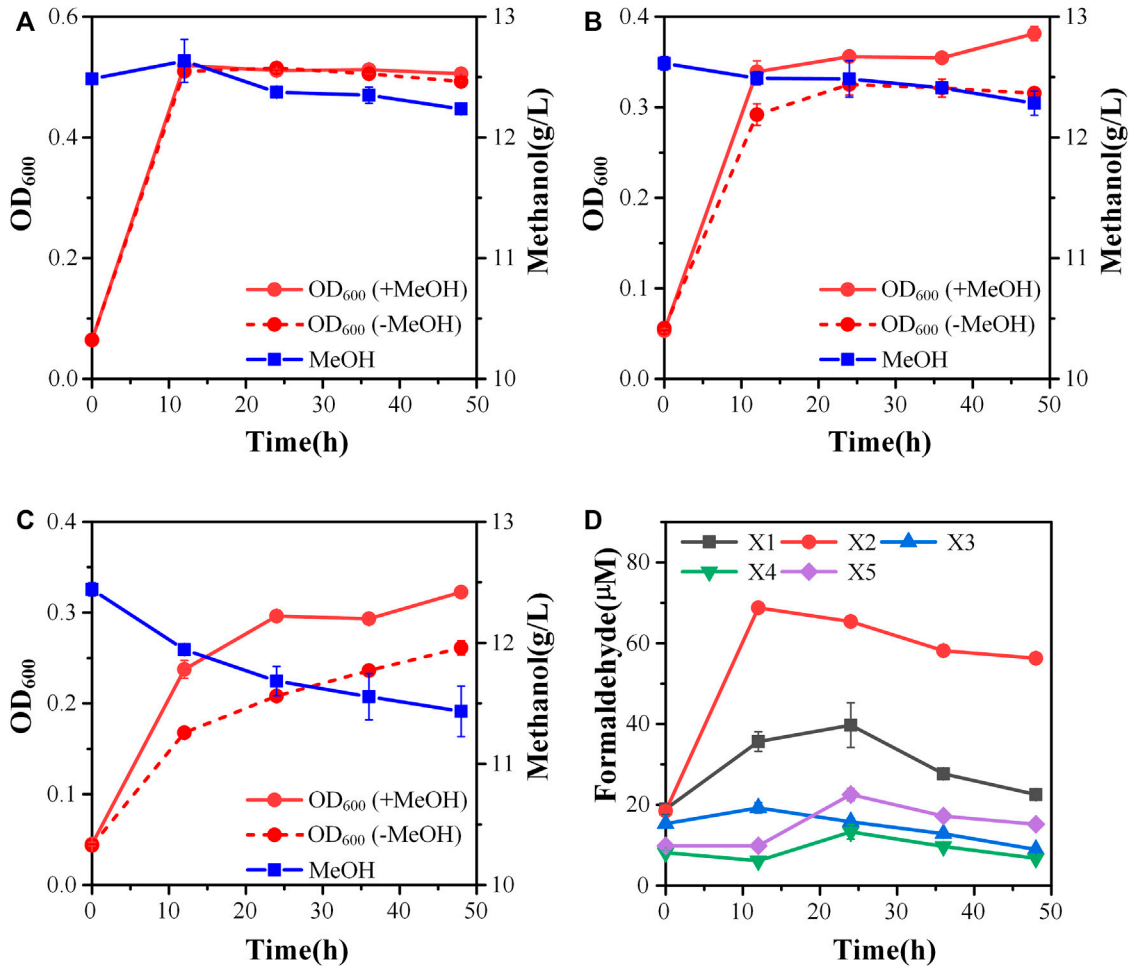

FIGURE 3
Engineering of the methylotrophic chassis to improve methanol assimilation. **(A)** Growth characteristics of strain X3; **(B)** Growth characteristics of strain X4; **(C)** Growth characteristics of strain X5; **(D)** formaldehyde accumulation. Error bars represent standard deviation, *n* = 2.

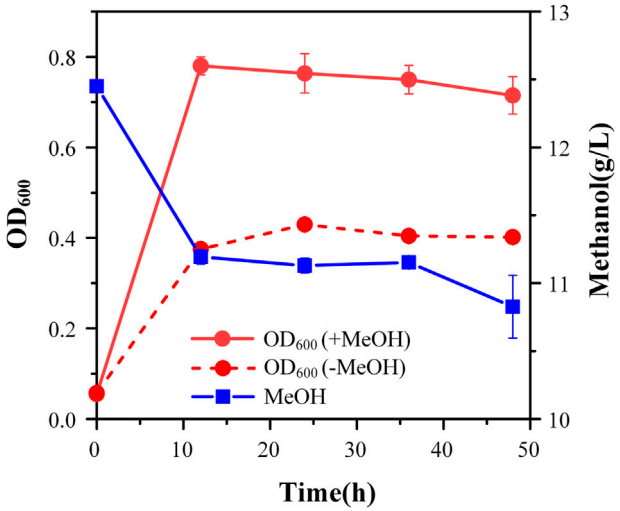

FIGURE 4
Cell growth and methanol consumption of strain Ev17. Error bars represent standard deviation, *n* = 2.

solution. We hypothesized that it was due to the cyclic XuMP pathway was not active and the regeneration of Xu5P was not sufficient for formaldehyde assimilation. Thus, we decided to further improve the efficiency of the cyclic XuMP pathway by rational optimization.

3.2 Rational design of the methylotrophic chassis

To increase the efficiency of methanol assimilation, we tried to divert the metabolic flux toward the cyclic XuMP pathway. GAP and fructose-6-phosphate (F6P) are two key metabolic nodes linking the active XuMP cycle with the glycolysis pathway and pentose phosphate pathway. Balancing the supply and consumption of GAP and F6P is highly important for the functional XuMP cycle as well as for Xu5P regeneration and biosynthesis. Phosphofructokinase is a key enzyme catalyzing the irreversible phosphorylation of F6P to fructose-1,6-bisphosphate, diverting the intracellular pool of fructose-6-phosphate to the glycolysis pathway (Figure 1). Previous studies showed that the high activity of phosphofructokinase in *E. coli* tend to destabilize the cyclic RuMP system or CO_2 assimilation cycle (Antonovsky et al.,

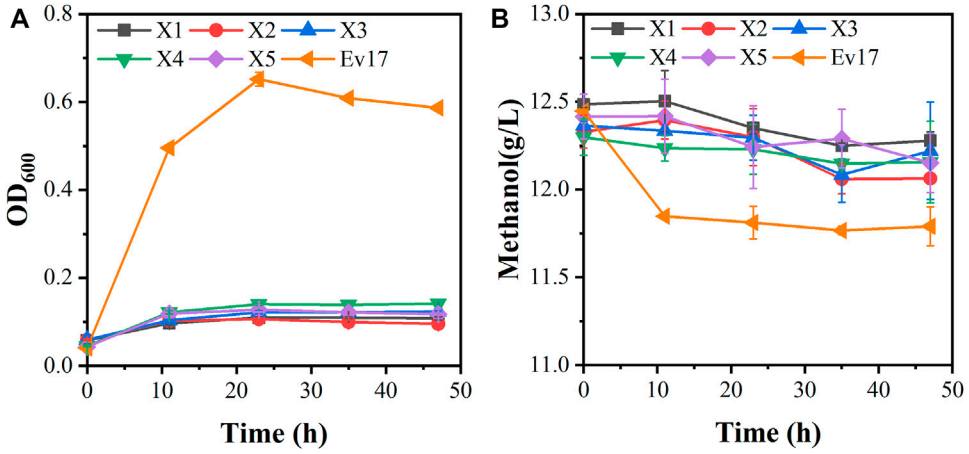

FIGURE 5
Growth characteristics of engineered strains on methanol with 0.1 g/L yeast extract. **(A)** Cell growth; **(B)** methanol consumption. Error bars represent standard deviation, n = 2.

2016; Gleizer et al., 2019). Thus, we first tried to reduce the diversion of flux away from the XuMP cycle by knocking out *pfkAB* genes encoding 6-phosphofructokinase of strain X2. The resulting strain X3 did not show improved methanol consumption or cell growth on methanol compared to strain X2 (Figure 3A), indicating that deleting *pfkAB* genes alone is not sufficient to increase methanol assimilation. However, the accumulation of formaldehyde by strain X3 was significantly reduced compared to strain X2 (Figure 3D), suggesting an improved balance of formaldehyde formation and consumption.

We then tried to further increase the supply of GAP to support the functional XuMP cycle in strain X3. For the aerobic cultivation of *E. coli* on sugars, GAP is mainly diverted to the lower glycolysis pathway and then mainly consumed *via* TCA cycle. Natural methylotrophs such as *Methylobacillus flagellatus* and *B. methanolicus* often contain an incomplete or less active TCA cycle which may be beneficial for retaining a high flux to formaldehyde assimilation pathway (e.g., RuMP pathway) and reducing NADH generation (Müller et al., 2015). NADH is a kinetic inhibitor of methanol dehydrogenase and high generation of NADH *via* the TCA cycle may disturb the redox balance and reduce methanol assimilation (Meyer et al., 2018). Reduced metabolic flux toward the TCA cycle was also observed for synthetic methylotrophs of *E. coli* (Meyer et al., 2018; Chen et al., 2020). Thus, we knocked out the *sucA* gene encoding E1 subunit of the α-ketoglutarate dehydrogenase to down-regulate the TCA cycle of strain X3, generating strain X4. Strain X4 showed a lower final cell density than strain X3, however, methanol consumption by strain X4 was increased (Figure 3B). Especially, the percent increase of biomass by methanol was increased to 24.00 ± 0.01% (Table 2), indicating that deletion of *sucA* gene to reduce the TCA cycle activity was beneficial for methanol assimilation. To further increase methanol assimilation, we set out to adjust the flux distribution at GAP node. Previous studies showed that the high activity of glyceraldehyde 3-phosphate dehydrogenase would strongly divert the metabolic flux to the glycolysis pathway, destabilizing the cyclic formaldehyde assimilation pathway (Meyer et al., 2018; Chen et al., 2020). To reduce the activity of glyceraldehyde 3-phosphate dehydrogenase, we introduced the antisense RNA to inhibit the expression of *gapA* gene of strain X4, giving strain X5. With this modification, methanol consumption by strain X5 was increased to 1.01 ± 0.26 g/L, which was over 2-fold higher than strain X4 (Figure 3C). Moreover, the percent increase of biomass by methanol was increased to 31.6 ± 0.01% (Table 2). Although strain X5 had the highest methanol consumption rate among all of the engineered strains, the low accumulation of formaldehyde during the cultivation indicated an increased formaldehyde consumption *via* the assimilation pathway (Figure 3D). Thus, reducing the activity of glyceraldehyde 3-phosphate dehydrogenase was also highly important for the functional cyclic XuMP pathway.

3.3 Adaptive laboratory evolution

Although strain X5 showed improved methanol utilization, the final cell density was still lower than strain X1. To promote cell growth of strain X5 on methanol, ALE was performed. Strain X5 was first cultivated in Hi-Def Azure (HDA) medium, a semi-minimal medium containing amino acids (Chen et al., 2020). The percent of HDA was gradually reduced and replaced by M9 minimal medium during the evolution. After 12 passages, the culture can grow on methanol with 5% HDA while strain X5 cannot grow on methanol with less than 15% HDA (Supplementary Figure S1). After 28 passages, a best growing single colony in the medium with 5% HDA was isolated and termed Ev17. When cultured in M9 minimal medium with methanol and 1 g/L yeast extract, the final cell density (OD_{600}) of strain Ev17 reached 0.71 ± 0.04 and the percent increase of biomass by methanol achieved 90.9 ± 0.01%, which was 1.8-fold higher than that of strain X5 (Figure 4). Moreover, strain Ev17 consumed 1.62 ± 0.23 g/L methanol, which was 60.4% higher than strain X5. Especially, when cultured with methanol and 0.1 g/L yeast extract, strain Ev17 achieved OD_{600} 0.65 ± 0.016 and consumed 0.66 ± 0.11 g/L methanol while other unevolved strains only showed marginal methanol consumption and cell growth (Figure 5), indicating that methanol assimilation was significantly improved by ALE.

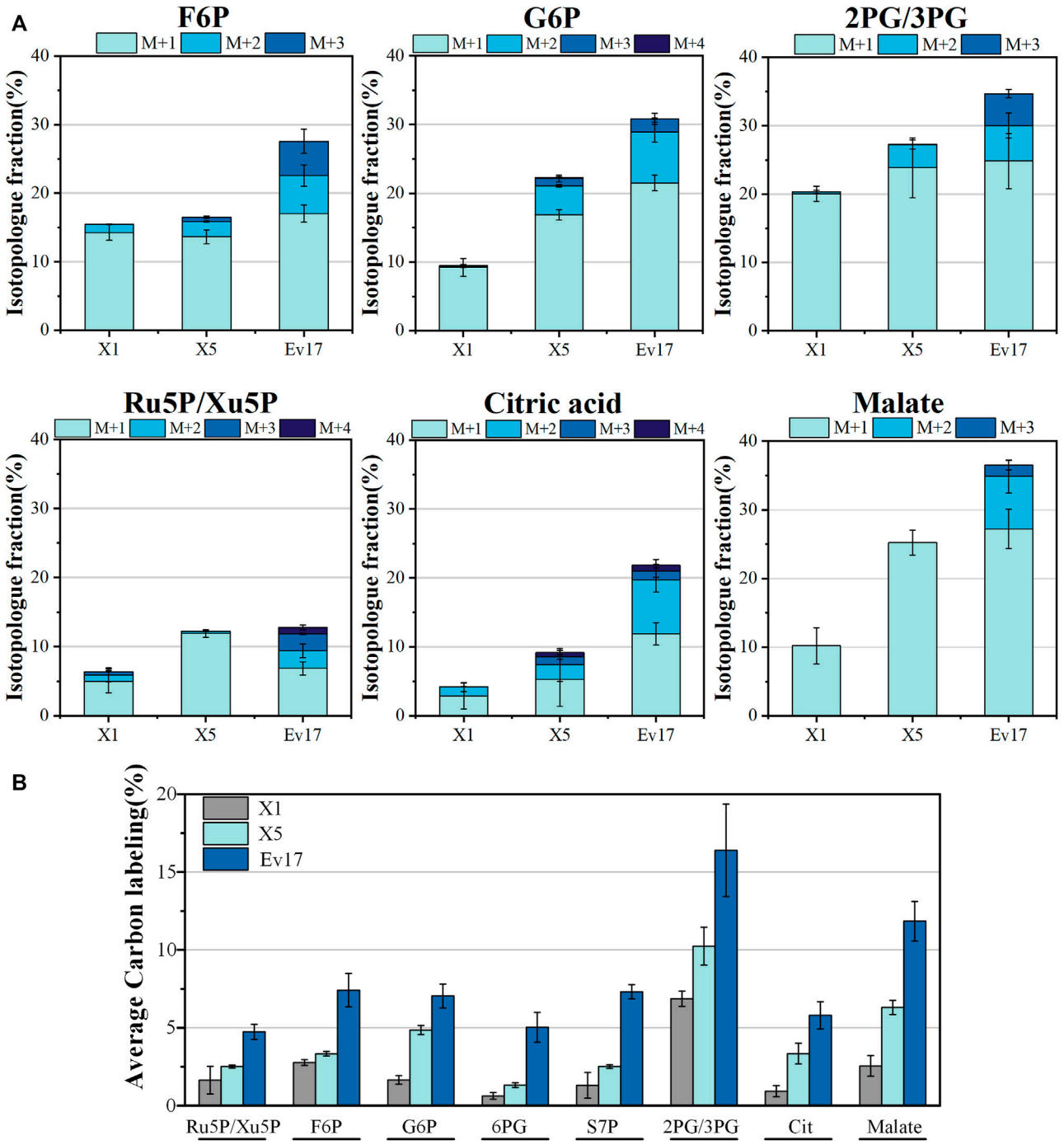

FIGURE 6
Isotopologue fraction (% ^{13}C) **(A)** and average carbon labeling of intracellular metabolites **(B)** in strain X1, X5, Ev17. Error bars represent standard deviation, *n* = 2. Abbreviations: F6P: fructose-6-phosphate; G6P: glucose-6-phosphate; 2/3PG: glycerate-3-phosphate/glycerate-2-phosphate; Ru5P/Xu5P: ribulose-5-phosphate/xylulose 5-phosphate; 6PG: 6-phosphogluconate; S7P: sedoheptulose-7-phosphate; Cit: citrate.

3.4 ^{13}C-methanol incorporation into intracellular metabolites and amino acids

To further evaluate the impact of rational design and ALE on methanol assimilation, ^{13}C-labeling analysis was performed with strains X1, X5, and Ev17. We cultured strains with ^{13}C-methanol and 1 g/L yeast extract and measured the intracellular metabolites and amino acids using liquid chromatography-mass spectrometry (Figures 6, 7). Introducing the hybrid methanol assimilation module alone in strain X1 resulted in 6.87 ± 0.48% ^{13}C-labeling of 2-phosphoglycerate/3-phosphoglycerate (2PG/3PG) and low but significant ^{13}C-labeling of several important metabolites in glycolysis, TCA cycle, and pentose phosphate pathway (Figure 6). However, most of these labeled metabolites contained only one ^{13}C atom (M1). Significant improvement of ^{13}C-labeling of all measured metabolites was observed in both strains X5 and

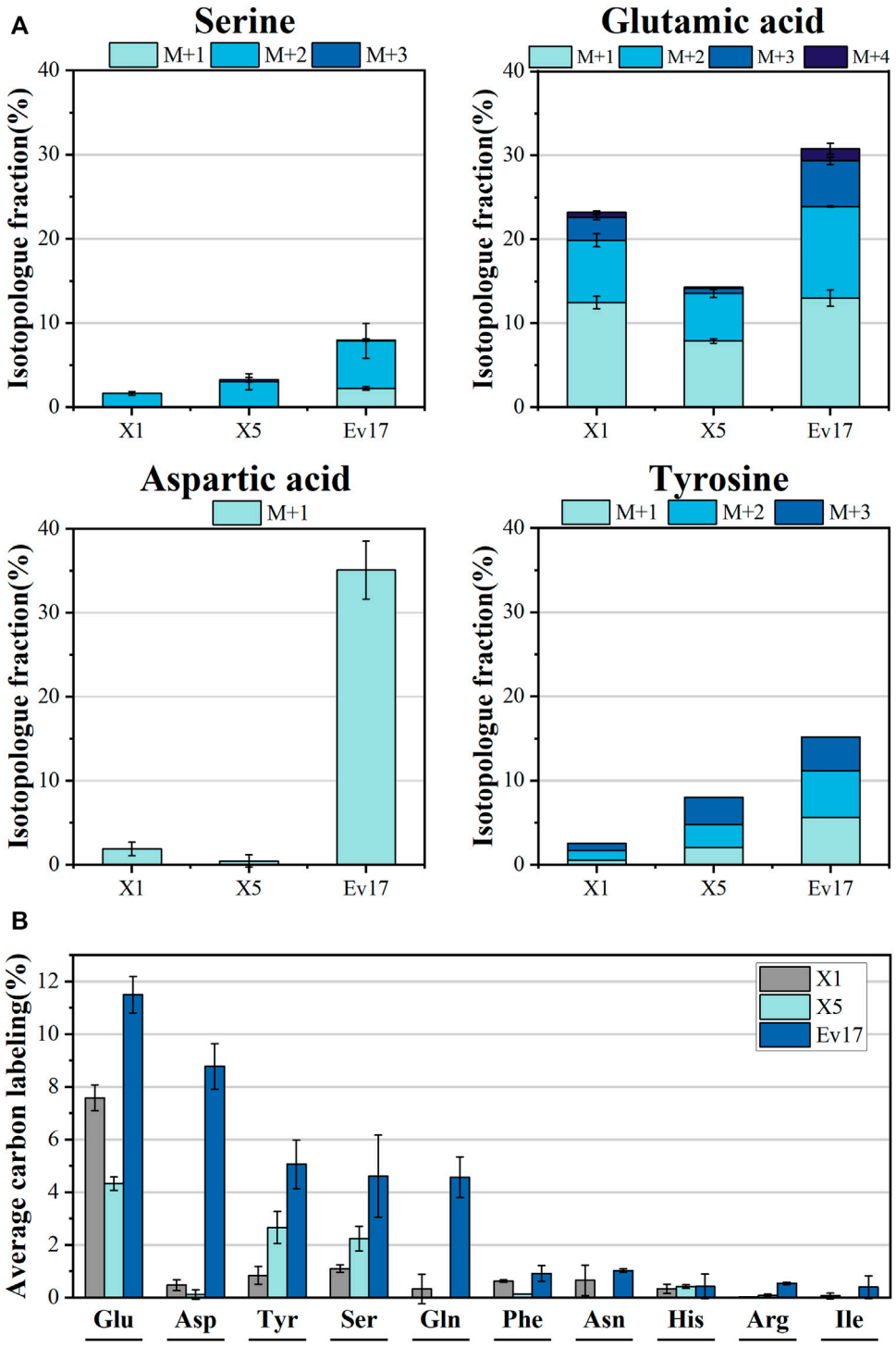

FIGURE 7
Isotopologue fraction (% ^{13}C) **(A)** and average carbon labeling **(B)** of amino acids in strain X1, X5, and Ev17. Error bars represent standard deviation, n = 2.

Ev17. For example, the average ^{13}C-labeling of 2PG/3PG in strains X5 and Ev17 was increased by 49.1% and 138.6% compared with strain X1. Especially, the increase of ^{13}C-labeling of Ru5P/Xu5P in strain X5 demonstrated the improved XuMP cycle by rational engineering. Strain X5 also exhibited the labeling of several metabolites with more than one ^{13}C atom, such as 2PG/3PG, glucose-6-phosphate (G6P) and citric acid, which were caused by XuMP cycle running more than one time. All of the measured metabolites in strain Ev17 showed higher average ^{13}C-labeling and had more than one ^{13}C atom, confirming the significant improvement of methanol assimilation *via* ALE.

To confirm that methanol was involved in biosynthetic pathways, ^{13}C-labeling analysis of intracellular amino acids was also carried out (Figure 7). Compared to strain X1, the significant

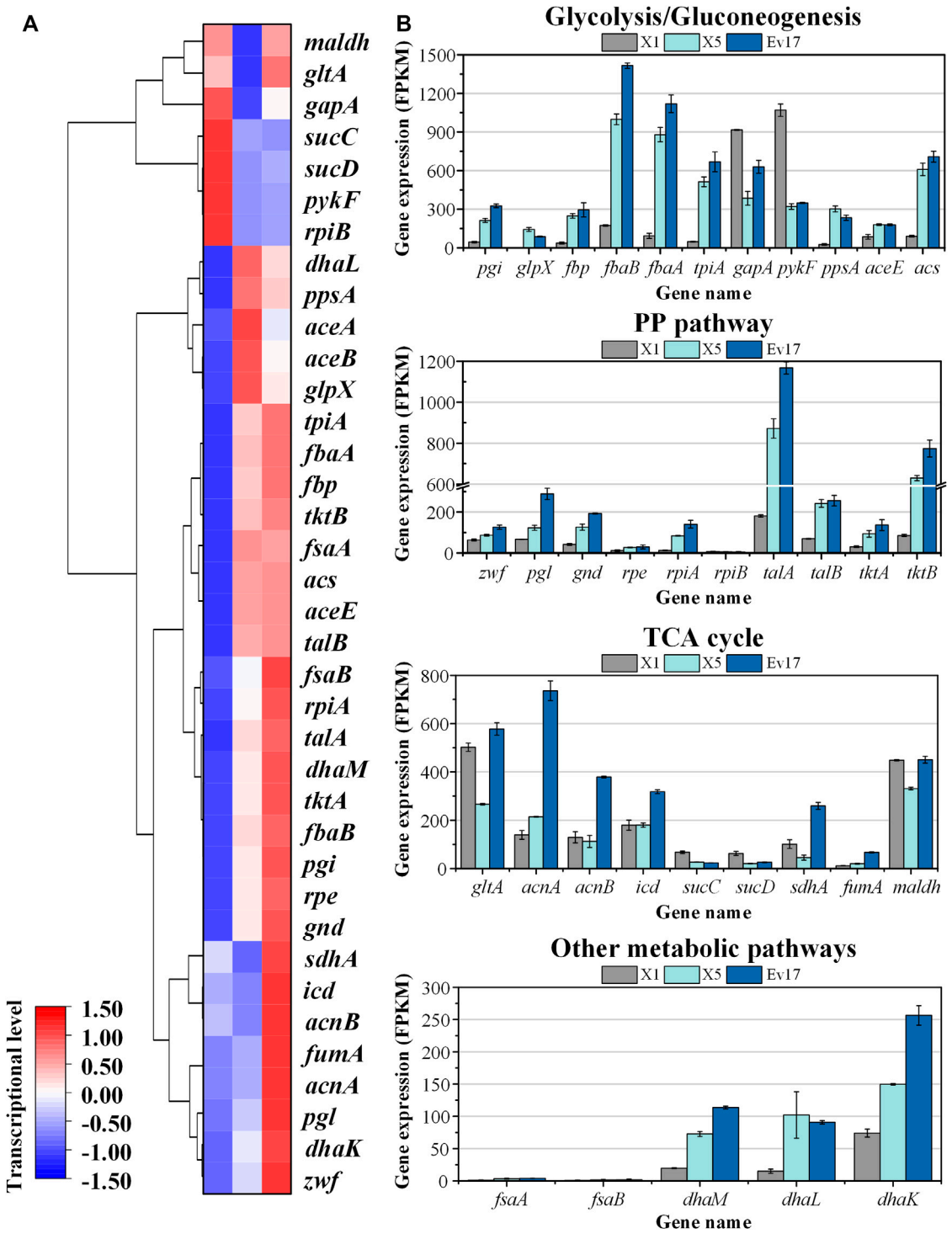

FIGURE 8
Transcriptomics analysis of strain X1, X5, and Ev17. **(A)** Heat map and hierarchical clustering of differentially expressed genes. **(B)** Gene expression of glycolysis/gluconeogenesis pathways, TCA cycle, PP pathway and other metabolic pathways of strain X1, X5, and Ev17. The transcriptional level (FPKM) has been normalized (n = 2).

increase in average labeling of glutamic acid (7.58 ± 0.50%), L-tyrosine (2.66 ± 0.61%) and L-serine (2.23 ± 0.47%) was detected in strain X5. Strain Ev17 displayed significant ^{13}C-methanol incorporation into glutamic acid (11.50 ± 0.70%), aspartic acid (8.77 ± 0.86%), tyrosine (5.06 ± 0.92%), serine (4.61 ± 1.57%), and glutamine (4.57 ± 0.77%). These improvements supported that our strategies enhanced the biosynthesis of amino acids from methanol.

3.5 Transcriptomics analysis and genome sequencing

To analyze the change of global genes expression, transcriptomics analysis of strains X1, X5, and Ev17 was further performed (Figure 8). Comparing with strain X1, most of the genes in TCA cycle, including *maldh*, *gltA*, *sucCD*, *sdhA*, were down-regulated in strain X5, indicating that deletion of *sucA* successfully reduced the activity of TCA cycle. Owing to the introduction of antisense RNA, the expression of *gapA* and *pyk* (encoding pyruvate kinase) in strain X5 were also down-regulated, demonstrating that reducing the activities of glycolysis and TCA cycle is beneficial for the higher methanol assimilation (Figure 8A). Most of genes related to DHA and GAP assimilation, such as *fbaAB* (encoding fructose-bisphosphate aldolase), *fbp* (encoding fructose-bisphosphatase), and the *dhaLMK* operon (encoding dihydroxyacetone kinase), were significantly up-regulated in strain X5 and Ev17. However, the fructose-6-phosphate aldolase (FSA) pathway encoded by *fsaAB* operon in all three strains was not transcriptionally activated (Figure 8B). These results indicated that Xu5P regeneration was successfully enhanced mainly assimilated *via* the dihydroxyacetone kinase pathway which is consistent with a previous study by (Peiro et al., 2019). Besides, the up-regulation of *talAB operon* (encoding transaldolase), *tktAB* operon (encoding transketolase) in strain X5 and Ev17 also contributed to the Xu5P regeneration (Figure 8B).

We further performed the Whole Genome Sequencing (WGS) analysis of stain Ev17. No mutations were found in the plasmid and all mutations in the genome were listed in Supplementary Table S4. Several mutations on the transcriptional regulators such as *narL*, *gntR*, and *iclR* were identified. The mutations of global transcriptional factors may play important roles in methanol metabolism and cell growth. In addition, mutations on *gltA* and *aceK* genes were also identified, which probably alter the activity of glyoxylate pathway (due to the knockout of *sucA* gene). Mutations on genes related to amino acids biosynthesis, such as *glnE* (encoding glutamine synthetase), *sdaB* (encoding serine deaminase), and *asnB* (encoding asparaginase) were also identified. The function of these mutations and their relations to methanol assimilation should be clarified in the future.

4 Conclusion

Developing a synthetic methylotrophy for C1 utilization is a big challenge for synthetic biology. In this study, we attempted to engineer a synthetic *Escherichia coli* based on a hybrid methanol assimilation pathway. The final engineered strain was successfully established by rational design and evolution and has a methanol-dependent growth phenotype with only 0.1 g/L yeast extract as co-substrate. The results showed that a combination of knocking out *pfkAB*, *sucA*, and introducing antisense RNA of *gapA* was efficient for methanol utilization. Further improvement of cell growth by ALE enabled the engineered strain to form 90.9 ± 0.01% increase of biomass by methanol and remarkable incorporation of ^{13}C-methanol into intracellular metabolites and amino acids, especially 2PG/3PG (16.39 ± 2.97%), citric acid (5.80 ± 0.87%) and glutamic acid (11.50 ± 0.70%) which were all improved over 2.5-fold than the initial strain. Notably, more than one ^{13}C atom of metabolites was detected, suggesting an effective XuMP cycle after engineering. Transcriptomics analysis demonstrated that FBA, FBP, and DAK pathways served as the key reactions for Xu5P regeneration while the FSA pathway was not transcriptionally activated. Since the of FSA variant of XuMP pathway is more energy-efficient (Supplementary Table S1), it is possible to overexpress the corresponding *fsaAB* genes to increase the pathway efficiency in the future. Further combination of rational design and ALE of strain Ev17 can be carried out in the future to develop synthetic methylotrophy that grow solely on methanol.

Data availability statement

The datasets presented in this study can be found in online repositories. The names of the repository/repositories and accession number(s) can be found in the article/Supplementary Material.

Author contributions

QS: Methodology, Investigation, Formal analysis, Data curation, Validation, Writing—original draft, preparation. DL: Supervision, Project administration. ZC: Conceptualization, Investigation, Formal analysis, Writing—review and editing, Funding acquisition, Resources, Supervision, Project administration.

Funding

This work was supported by the National Key R&D Program of China (No. 2018YFA0901500), the National Natural Science Foundation of China (Grant Nos. 21878172, 21938004, and 22078172).

Conflict of interest

The authors declare that the research was conducted in the absence of any commercial or financial relationships that could be construed as a potential conflict of interest.

Publisher's note

Supplementary material

The Supplementary Material for this article can be found online at: https://www.frontiersin.org/articles/10.3389/fbioe.2022.1089639/full#supplementary-material

References

Antonovsky, N., Gleizer, S., Noor, E., Zohar, Y., Herz, E., Barenholz, U., et al. (2016). Sugar synthesis from CO_2 in *Escherichia coli*. *Cell* 166 (1), 115–125. doi:10.1016/j.cell.2016.05.064

Bennett, R. K., Agee, A., Gerald Har, J. R., von Hagel, B., Siu, K. H., Antoniewicz, M. R., et al. (2020a). Triggering the stringent response enhances synthetic methanol utilization in *Escherichia coli*. *Metab. Eng.* 61, 1–10. doi:10.1016/j.ymben.2020.04.007

Bennett, R. K., Dillon, M., Gerald Har, J. R., Agee, A., von Hagel, B., Rohlhill, J., et al. (2020b). Engineering *Escherichia coli* for methanol-dependent growth on glucose for metabolite production. *Metab. Eng.* 60, 45–55. doi:10.1016/j.ymben.2020.03.003

Brito, L. F., Irla, M., Nærdal, I., Le, S. B., Delépine, B., Heux, S., et al. (2021). Evaluation of heterologous biosynthetic pathways for methanol-based 5-aminovalerate production by thermophilic *Bacillus methanolicus*. *Front. Bioeng. Biotechnol.* 9, 686319. doi:10.3389/fbioe.2021.686319

Chen, C. T., Chen, F. Y., Bogorad, I. W., Wu, T. Y., Zhang, R., Lee, A. S., et al. (2018). Synthetic methanol auxotrophy of *Escherichia coli* for methanol-dependent growth and production. *Metab. Eng.* 49, 257–266. doi:10.1016/j.ymben.2018.08.010

Chen, F. Y., Jung, H. W., Tsuei, C. Y., and Liao, J. C. (2020). Converting *Escherichia coli* to a synthetic methylotroph growing solely on methanol. *Cell* 182 (4), 933–946.e14. e914. doi:10.1016/j.cell.2020.07.010

De Simone, A., Vicente, C. M., Peiro, C., Gales, L., Bellvert, F., Enjalbert, B., et al. (2020). Mixing and matching methylotrophic enzymes to design a novel methanol utilization pathway in *E. coli*. *Metab. Eng.* 61, 315–325. doi:10.1016/j.ymben.2020.07.005

Gibson, D. G., Young, L., Chuang, R. Y., Venter, J. C., Hutchison, C. A., 3rd, and Smith, H. O. (2009). Enzymatic assembly of DNA molecules up to several hundred kilobases. *Nat. Methods* 6 (5), 343–345. doi:10.1038/nmeth.1318

Gleizer, S., Ben-Nissan, R., Bar-On, Y. M., Antonovsky, N., Noor, E., Zohar, Y., et al. (2019). Conversion of *Escherichia coli* to generate all biomass carbon from CO_2. *Cell* 179 (6), 1255–1263.e12. e1212. doi:10.1016/j.cell.2019.11.009

Gonzalez, J. E., Bennett, R. K., Papoutsakis, E. T., and Antoniewicz, M. R. (2018). Methanol assimilation in *Escherichia coli* is improved by co-utilization of threonine and deletion of leucine-responsive regulatory protein. *Metab. Eng.* 45, 67–74. doi:10.1016/j.ymben.2017.11.015

Gregory, G. J., Bennett, R. K., and Papoutsakis, E. T. (2022). Recent advances toward the bioconversion of methane and methanol in synthetic methylotrophs. *Metab. Eng.* 71, 99–116. doi:10.1016/j.ymben.2021.09.005

He, H., Höper, R., Dodenhöft, M., Marlière, P., and Bar-Even, A. (2020). An optimized methanol assimilation pathway relying on promiscuous formaldehyde-condensing aldolases in *E. coli*. *Metab. Eng.* 60, 1–13. doi:10.1016/j.ymben.2020.03.002

Hoynes-O'Connor, A., and Moon, T. S. (2016). Development of design rules for reliable antisense RNA behavior in *E. coli*. E. coli. *ACS Synth. Biol.* 5 (12), 1441–1454. doi:10.1021/acssynbio.6b00036

Jensen, S. I., Lennen, R. M., Herrgard, M. J., and Nielsen, A. T. (2015). Seven gene deletions in seven days: Fast generation of *Escherichia coli* strains tolerant to acetate and osmotic stress. *Sci. Rep.* 5, 17874. doi:10.1038/srep17874

Keller, P., Noor, E., Meyer, F., Reiter, M. A., Anastassov, S., Kiefer, P., et al. (2020). Methanol-dependent *Escherichia coli* strains with a complete ribulose monophosphate cycle. *Nat. Commun.* 11 (1), 5403. doi:10.1038/s41467-020-19235-5

Keller, P., Reiter, M. A., Kiefer, P., Gassler, T., Hemmerle, L., Christen, P., et al. (2022). Generation of an *Escherichia coli* strain growing on methanol via the ribulose monophosphate cycle. *Nat. Commun.* 13 (1), 5243. doi:10.1038/s41467-022-32744-9

Kim, S., Lindner, S. N., Aslan, S., Yishai, O., Wenk, S., Schann, K., et al. (2020). Growth of *E. coli* on formate and methanol via the reductive glycine pathway. *Nat. Chem. Biol.* 16 (5), 538–545. doi:10.1038/s41589-020-0473-5

Long, C. P., and Antoniewicz, M. R. (2019). High-resolution ^{13}C metabolic flux analysis. *Nat. Protoc.* 14 (10), 2856–2877. doi:10.1038/s41596-019-0204-0

Meyer, F., Keller, P., Hartl, J., Gröninger, O. G., Kiefer, P., and Vorholt, J. A. (2018). Methanol-essential growth of *Escherichia coli*. *Nat. Commun.* 9 (1), 1508. doi:10.1038/s41467-018-03937-y

Müller, J. E., Meyer, F., Litsanov, B., Kiefer, P., and Vorholt, J. A. (2015). Core pathways operating during methylotrophy of *Bacillus methanolicus* MGA3 and induction of a bacillithiol-dependent detoxification pathway upon formaldehyde stress. *Mol. Microbiol.* 98 (6), 1089–1100. doi:10.1111/mmi.13200

Peiro, C., Millard, P., de Simone, A., Cahoreau, E., Peyriga, L., Enjalbert, B., et al. (2019). Chemical and metabolic controls on dihydroxyacetone metabolism lead to suboptimal growth of *Escherichia coli*. *Appl. Environ. Microbiol.* 85 (15), e00768. doi:10.1128/aem.00768-19

Wang, Y., Fan, L., Tuyishime, P., Liu, J., Zhang, K., Gao, N., et al. (2020a). Adaptive laboratory evolution enhances methanol tolerance and conversion in engineered *Corynebacterium glutamicum*. *Commun. Biol.* 3 (1), 217. doi:10.1038/s42003-020-0954-9

Wang, Y., Fan, L., Tuyishime, P., Zheng, P., and Sun, J. (2020b). Synthetic methylotrophy: A practical solution for methanol-based biomanufacturing. *Trends Biotechnol.* 38 (6), 650–666. doi:10.1016/j.tibtech.2019.12.013

Whitaker, W. B., Sandoval, N. R., Bennett, R. K., Fast, A. G., and Papoutsakis, E. T. (2015). Synthetic methylotrophy: Engineering the production of biofuels and chemicals based on the biology of aerobic methanol utilization. *Curr. Opin. Biotechnol.* 33, 165–175. doi:10.1016/j.copbio.2015.01.007

Woolston, B. M., King, J. R., Reiter, M., Van Hove, B., and Stephanopoulos, G. (2018). Improving formaldehyde consumption drives methanol assimilation in engineered *E. coli*. *Nat. Commun.* 9 (1), 2387. doi:10.1038/s41467-018-04795-4

Yu, H., and Liao, J. C. (2018). A modified serine cycle in *Escherichia coli* coverts methanol and CO_2 to two-carbon compounds. *Nat. Commun.* 9 (1), 3992. doi:10.1038/s41467-018-06496-4

Yuan, X. J., Chen, W. J., Ma, Z. X., Yuan, Q. Q., Zhang, M., He, L., et al. (2021). Rewiring the native methanol assimilation metabolism by incorporating the heterologous ribulose monophosphate cycle into *Methylorubrum extorquens*. *Metab. Eng.* 64, 95–110. doi:10.1016/j.ymben.2021.01.009

Zhang, W., Zhang, T., Wu, S., Wu, M., Xin, F., Dong, W., et al. (2017). Guidance for engineering of synthetic methylotrophy based on methanol metabolism in methylotrophy. *RSC Adv.* 7 (7), 4083–4091. doi:10.1039/c6ra27038g

Zhu, T., Zhao, T., Bankefa, O. E., and Li, Y. (2020). Engineering unnatural methylotrophic cell factories for methanol-based biomanufacturing: Challenges and opportunities. *Biotechnol. Adv.* 39, 107467. doi:10.1016/j.biotechadv.2019.107467

frontiers | Frontiers in Bioengineering and Biotechnology

TYPE Original Research
PUBLISHED 13 January 2023
DOI 10.3389/fbioe.2023.1098116

OPEN ACCESS

EDITED BY
Boyang Ji,
BioInnovation Institute (BII), Denmark

REVIEWED BY
Dongming Xie,
University of Massachusetts Lowell, United States
Jin Hou,
Shandong University, China

*CORRESPONDENCE
Yang Gu,
guyang@nnu.edu.cn
Peng Xu,
pengxu@gtiit.edu.cn

SPECIALTY SECTION
This article was submitted to Synthetic Biology, a section of the journal Frontiers in Bioengineering and Biotechnology

RECEIVED 14 November 2022
ACCEPTED 03 January 2023
PUBLISHED 13 January 2023

CITATION
Zhu J, Gu Y, Yan Y, Ma J, Sun X and Xu P (2023), Knocking out central metabolism genes to identify new targets and alternating substrates to improve lipid synthesis in *Y. lipolytica*. *Front. Bioeng. Biotechnol.* 11:1098116. doi: 10.3389/fbioe.2023.1098116

Knocking out central metabolism genes to identify new targets and alternating substrates to improve lipid synthesis in *Y. lipolytica*

Jiang Zhu[1], Yang Gu[1,2]*, Yijing Yan[1], Jingbo Ma[2,3], Xiaoman Sun[1] and Peng Xu[2,4,5]*

[1]School of Food Science and Pharmaceutical Engineering, Nanjing Normal University, Nanjing, China, [2]Department of Chemical, Biochemical and Environmental Engineering, University of MD, Baltimore County, Baltimore, MD, United States, [3]College of Biological and Pharmaceutical Engineering, West Anhui University, Lu'an, Anhui, China, [4]Department of Chemical Engineering, Guangdong Technion-Israel Institute of Technology (GTIIT), Shantou, Guangdong, China, [5]The Wolfson Department of Chemical Engineering, Technion-Israel Institute of Technology, Haifa, Israel

Introduction: Systematic gene knockout studies may offer us novel insights on cell metabolism and physiology. Specifically, the lipid accumulation mechanism at the molecular or cellular level is yet to be determined in the oleaginous yeast *Y. lipolytica*.

Methods: Herein, we established ten engineered strains with the knockout of important genes involving in central carbon metabolism, NADPH generation, and fatty acid biosynthetic pathways.

Results: Our result showed that NADPH sources for lipogenesis include the OxPP pathway, POM cycle, and a trans-mitochondrial isocitrate-α-oxoglutarate NADPH shuttle in *Y. lipolytica*. Moreover, we found that knockout of mitochondrial NAD^+ isocitrate dehydrogenase IDH2 and overexpression of cytosolic $NADP^+$ isocitrate dehydrogenase IDP2 could facilitate lipid synthesis. Besides, we also demonstrated that acetate is a more favorable carbon source for lipid synthesis when glycolysis step is impaired, indicating the evolutionary robustness of *Y. lipolytica*.

Discussion: This systematic investigation of gene deletions and overexpression across various lipogenic pathways would help us better understand lipogenesis and engineer yeast factories to upgrade the lipid biomanufacturing platform.

KEYWORDS

***Yarrowia lipolytica*, lipogenesis, central metabolism, lipid synthesis, metabolic engineering**

1 Instruction

Currently, concerns about fossil fuel sustainability have driven researchers to develop renewable lipid-derived biofuels as an alternative (Gu et al., 2018; Lazar et al., 2018). Lipid synthesis using oleaginous yeasts, owing to their unique metabolism, can achieve high lipid titers, yields and productivity, thus creating the potential for cost-effective industrial-scale operations (Ma et al., 2020). Specifically, *Yarrowia lipolytica* is an oleaginous yeast with GRAS (generally regarded as safe) status and has several significant attributes, such as a broad substrate spectrum, relatively well-defined genome annotations, diversified genetic manipulation methods, and abundant pool size of metabolic precursors, including acetyl-CoA, malonyl-CoA, and tricarboxylic acid (TCA) cycle intermediates (Abdel-Mawgoud et al., 2018; Larroude et al., 2018; Markham and Alper, 2018). Therefore, this yeast has emerged as a

10.3389/fbioe.2023.1098116

TABLE 1 Strains and plasmids used in this study.

Names	Characteristics	References
Strains		
po1fk	Wild-type strain W29 (ATCC20460) derivate; W29 Δ*matA* Δ*xpr*2-332 Δ*axp*-2 Δ*leu*2-270 pBR platform, deletion of gene *ura* and *ku70*; po1g Δ*ura*3 Δ*ku70::loxP*	Gu et al. (2020a); Gu et al. (2020b)
po1fk_*ylPFK*	po1fk derivate; Further deletion of gene *ylPFK*; po1fk Δ*ylPFK::hygr*	This study
po1fk_*ylPYK*	po1fk derivate; Further deletion of gene *ylPYK*; po1fk Δ*ylPYK::hygr*	This study
po1fk_*ylACO1*	po1fk derivate; Further deletion of gene *ylAC O 1*; po1fk Δ*ylAC O 1::hygr*	This study
po1fk_*ylMAE1*	po1fk derivate; Further deletion of gene *ylMAE1*; po1fk Δ*ylMAE1::hygr*	This study
po1fk_*ylIDH2*	po1fk derivate; Further deletion of gene *ylIDH2*; po1fk Δ*ylIDH2::hygr*	This study
po1fk_*ylIDP2*	po1fk derivate; Further deletion of gene *ylIDP2*; po1fk Δ*ylIDP2::hygr*	This study
po1fk_*ylZWF1*	po1fk derivate; Further deletion of gene *ylZWF1*; po1fk Δ*ylZWF1::hygr*	This study
po1fk_*ylPYC1*	po1fk derivate; Further deletion of gene *ylPYC1*; po1fk Δ*ylPYC1::hygr*	This study
po1fk_*ylFAA1*	po1fk derivate; Further deletion of gene *ylFAA1*; po1fk Δ*ylFAA1::hygr*	This study
po1fk_*ylSNF1*	po1fk derivate; Further deletion of gene *ylFAA1*; po1fk Δ*ylSNF1::hygr*	This study
po1fk pYLXP'-*ylPFK*	po1fk derivate; Further expression of gene *ylPFK*	This study
po1fk pYLXP'-*ylPYK*	po1fk derivate; Further expression of gene *ylPYK*	This study
po1fk pYLXP'-*ylACO1*	po1fk derivate; Further expression of gene *ylAC O 1*	This study
po1fk pYLXP'-*ylMAE1*	po1fk derivate; Further expression of gene *ylMAE1*	This study
po1fk pYLXP'-*ylIDH2*	po1fk derivate; Further expression of gene *ylIDH2*	This study
po1fk pYLXP'-*ylIDP2*	po1fk derivate; Further expression of gene *ylIDP2*	This study
po1fk pYLXP'-*ylZWF1*	po1fk derivate; Further expression of gene *ylZWF1*	This study
po1fk pYLXP'-*ylPYC1*	po1fk derivate; Further expression of gene *ylPYC1*	This study
po1fk pYLXP'-*ylFAA1*	po1fk derivate; Further expression of gene *ylFAA1*	This study
po1fk pYLXP'-*ylSNF1*	po1fk derivate; Further expression of gene *ylFAA1*	This study
Plasmids		
pYLXP'-loxP-Hygr	pYLXP' containing the *loxP-hygr-loxP* cassette	Gu et al. (2020a); Gu et al. (2020b)
pHyloxP-*ylPFK*	pYLXP'-*loxP-hygr* containing gene *ylPFK deletion cassette*	This study
pHyloxP-*ylPYK*	pYLXP'-*loxP-hygr* containing gene *ylPYK deletion cassette*	This study
pHyloxP-*ylACO1*	pYLXP'-*loxP-hygr* containing gene *ylAC O 1 deletion cassette*	This study
pHyloxP-*ylPYC1*	pYLXP'-*loxP-hygr* containing gene *ylPYC1 deletion cassette*	This study
pHyloxP-*ylMAE1*	pYLXP'-*loxP-hygr* containing gene *ylMAE1 deletion cassette*	This study
pHyloxP-*ylIDH2*	pYLXP'-*loxP-hygr* containing gene *ylIDH2 deletion cassette*	This study
pHyloxP-*ylIDP2*	pYLXP'-*loxP-hygr* containing gene *ylIDP2 deletion cassette*	This study
pHyloxP-*ylZWF1*	pYLXP'-*loxP-hygr* containing gene *ylZWF1 deletion cassette*	This study
pHyloxP-*ylFAA1*	pYLXP'-*loxP-hygr* containing gene *ylFAA1 deletion cassette*	This study
pHyloxP-*ylSNF1*	pYLXP'-*loxP-hygr* containing gene *ylSNF1 deletion cassette*	This study
pYLXP'-*ylPFK*	pYLXP' containing gene *ylPFK expression cassette*	This study
pYLXP'-*ylPYK*	pYLXP' containing gene *ylPYK expression cassette*	This study
pYLXP'-*ylACO1*	pYLXP' containing gene *ylAC O 1 expression cassette*	This study
pYLXP'-*ylPYC1*	pYLXP' containing gene *ylPYC1 expression cassette*	This study
pYLXP'-*ylMAE1*	pYLXP' containing gene *ylMAE1 expression cassette*	This study
pYLXP'-*ylIDH2*	pYLXP' containing gene *ylIDH2 expression cassette*	This study
pYLXP'-*ylIDP2*	pYLXP' containing gene *ylIDP2 expression cassette*	This study
pYLXP'-*ylZWF1*	pYLXP' containing gene *ylZWF1 expression cassette*	This study
pYLXP'-*ylFAA1*	pYLXP' containing gene *ylFAA1 expression cassette*	This study
pYLXP'-*ylSNF1*	pYLXP' containing gene *ylSNF1 expression cassette*	This study

popular non-model organism in the lipid biomanufacturing field (Liu et al., 2015; Wong et al., 2017; Liu et al., 2019a; Yang et al., 2019).

In *Y. lipolytica*, extracellular carbon feedstock, such as glucose, is firstly internalized and converted into cytosolic pyruvate by glycolytic pathway (Qiao et al., 2017). Then, pyruvate is transported into mitochondria to synthesize mitochondrial citrate. Next, citrate is excreted to the cytoplasm by mitochondrial citrate carrier YlYhm2p (Yuzbasheva et al., 2019) and further cleaved to acetyl-CoA for lipid synthesis by cytosolic ATP-citrate lyases (Qiao et al., 2017). However, lipids are the highly reduced metabolites that need to consume the NADPHs to reduce acetyl groups (CH_3-CO-) to alkyl groups (-CH_2-CH_2-) for growing fatty acid carbon backbone (Wasylenko et al., 2015; Xu et al., 2017; Xue et al., 2017). Currently, optimizing the intracellular metabolic network of *Y. lipolytica* has become a trend to improve lipids production by metabolic engineering and synthetic biology methods (Qiao et al.,

2015; Liu et al., 2016; Xu et al., 2016; Abdel-Mawgoud et al., 2018). For example, Lazar et al. knocked out POX1-6 (peroxidase) and TGL4 (triglyceride lipase) with overexpressing GDP1 (glycerol triphosphate dehydrogenase) and DGA2 (diacylglycerol acyltransferase) in *Y. lipolytica*, improving the titer of lipids to 34 g/L (Dulermo and Nicaud, 2011). Qiao et al. optimized the supply of NADPH, which maximized the utilization of electrons from alternative NADPH pathways to increase substrate-to-lipid yields, leading to a 25% improvement over the starting strain (Qiao et al., 2017). Notwithstanding, much effort has been investigated to improve lipid accumulation, such as deletion of degradation pathways, overexpression of lipid synthesis pathways, eliminating of regulatory bottlenecks, and strengthening the supply of precursor, such as acetyl-CoA and NADPH (Groenewald et al., 2014; Silverman et al., 2016; Liu et al., 2019b). However, the influences of the important gene deficiency on lipid accumulation, such as carbon feedstock degradation and NADPH metabolism, have not been explored in *Y. lipolytica*.

Herein, we systematically investigated the influence of deleting important lipogenesis genes on lipid synthesis and cell growth, involving in carbon metabolism, NADPH metabolism, and fatty acid biosynthetic pathways. Specifically, we demonstrated that the sources of NADPH for lipogenesis include the OxPPP pathway, pyruvate-oxaloacetate-malate (POM) cycle, and isocitrate-2-oxoglutarate shuttle in *Y. lipolytica*. Moreover, the knockout of mitochondrial NAD^+ isocitrate dehydrogenase IDH2 and overexpression of cytosolic $NADP^+$ isocitrate dehydrogenase IDP2 could facilitate lipid synthesis. Besides, we also concluded that acetate is a favorable carbon source for producing lipid in *Y. lipolytica*. This study may help us better understand lipogenesis mechanisms, and the insights obtained here will guide us to engineer efficient cell factories for oleochemical production.

2 Materials and methods

2.1 Strains, plasmid, primers, and chemicals

The strain po1fk obtained in our previous work was chosen as the starting strain in this study (Gu et al., 2020a). Moreover, strains, plasmids and primers have been listed in Table1 and Supplementary Table S1, respectively. Chemicals, including methyl tridecanoic acid and triglyceryl heptadecanoic acid were purchased from Sigma-Aldrich.

2.2 Gene knockout vectors construction

The marker-free Cre-*loxP* based gene knockout method was used as previously reported (Gu et al., 2020a; Gu et al., 2020b). In this study, constructed gene knockout plasmids included pHyloxP-*ylPFK* (encoding phosphofructose kinase), pHyloxP-*ylPYK* (encoding pyruvate kinase), pHyloxP-*ylPYC1* (encoding pyruvate carboxylase), pHyloxP-*ylMAE1* (encoding malic enzyme), pHyloxP-*ylIDH2* (encoding mitochondrial isocitrate dehydrogenase), pHyloxP-*ylIDP2* (encoding cytosolic isocitrate dehydrogenase), pHyloxP-*ylFAA1* (encoding peroxisomal fatty acyl-CoA ligase), pHyloxP-*ylACO1* (encoding aconitate hydratase), and pHyloxP-*ylSNF1* (encoding AMP-activated protein kinase).

Here, we took the process of constructing the plasmid pHyloxP-*ylPFK* as an example. Firstly, the upstream and downstream sequences (both 1000 bp) of flanking gene *ylPFK* were obtained by the PCR-amplified reactions using primers ylPFK_UpF/ylPFK_UpR and ylPFK_DwF/ylPFK_DwR. Then, pYLXP'-*loxP-Hyr* containing *loxP-Hyr-loxP* cassette was digested by endonucleases *AvrII* and *SalI* to obtain *loxP-Hyr-loxP* cassette and plasmid backbone of pYLXP'-*loxP-Hyr*. Next, the upstream fragment ylPFK_Up, downstream fragments ylPFK_Dw, *loxP-Hyr-loxP* cassette and pYLXP'-*loxP-Hyr* backbone were joined by Gibson Assembly to generate the plasmid pHyloxP-*ylPFK*. The constructed plasmids were sequenced by Sangon Biotech Co., Ltd. (Shanghai, China).

2.3 The expression plasmid construction and assembly

The pYLXP', a YaliBrick plasmid, was used for gene expression (Gu et al., 2020a; Gu et al., 2020b). For example, to construct the recombinant plasmid pYLXP'-ylPFK, pYLXP' was firstly digested by *SnaBI* and *KpnI*, obtaining the linearized pYLXP'. Then, the linearized pYLXP' was ligase with the DNA fragment of gene PFK (that was obtained by the PCR-amplified reaction using primers PFK-F and PFK-R) by Gibson assembly method to generate plasmid pYLXP'-ylPFK, which was sequenced by Sangon Biotech Co., Ltd. (Shanghai, China).

2.4 Yeast transformation

The standard protocols of *Y. lipolytica* transformation have been reported (Gu et al., 2020b; Lv et al., 2020). In brief, 1-mL cells were harvested from YPD medium (yeast extract 10 g/L, peptone 20 g/L, and glucose 20 g/L) at 24 h. Then, cells were resuspended by using 105 uL transformation solution, containing 90 uL 50% PEG4000, 5 uL lithium acetate (2 M), 5 uL boiled single strand DNA (salmon sperm, denatured), and 5 uL DNA products. Next, the mixture was incubated at 39°C for 1 h before spreading on selected plates, which needed to be vortexed for 15 s every 15 min. In this study, the selected markers, including leucine and hygromycin, were used.

2.5 Shake flask cultivations

Shake flask cultivations of genetically modified *Y. lipolytica* were performed in 250 mL flasks with 25 mL fermentation medium at 220 r.p.m. and 30°C for 120 h. For this, 0.8 mL seed solution was inoculated, which was cultured in 14 mL shaking tubes under the conditions of 220 r.p.m. and 30°C for 48 h. One milliliter of fermentation broth was sampled every 24 h for OD_{600}, lipid, glucose, and acetate measurements.

Seed culture medium of CSM (the yeast complete synthetic media) contains ammonium sulfate 5.0 g/L, YNB (yeast nitrogen base without ammonium sulfate) 1.7 g/L, glucose 20.0 g/L, CSM-Leu 0.74 g/L, and L-leucine 0.20 g/L. The CSM fermentation medium (C/N = 80) contains ammonium sulfate 1.1 g/L, YNB 1.7 g/L, glucose 40.0 g/L, CSM-Leu 0.74 g/L, and L-leucine 0.20 g/L. Specifically, phosphoric buffer solution (PBS), including 0.2 M Na_2HPO_4 and 0.2 M Na_2HPO_4, with pH 6.0 was used to replace water to make CSM-Acetate fermentation medium. Besides, CSM-acetate medium (C/N = 80)

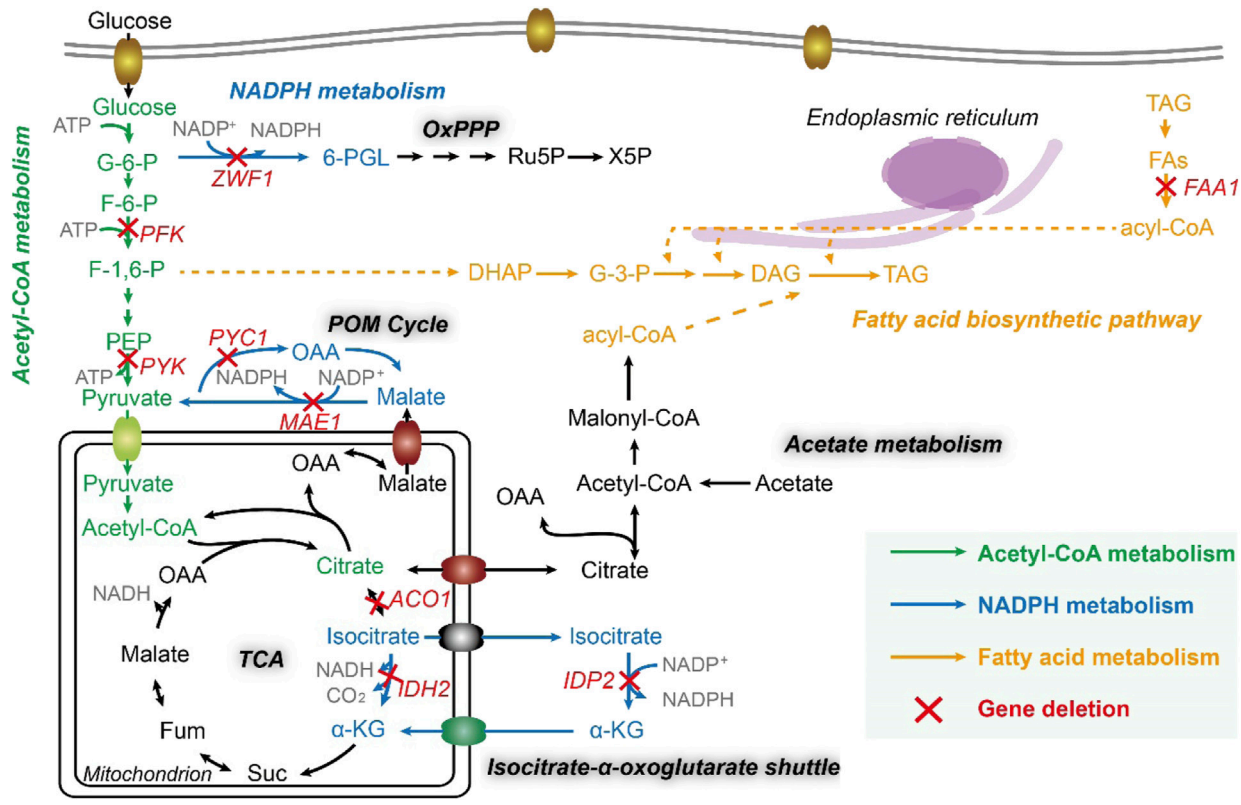

FIGURE 1
The fatty acid metabolic network of Y. lipolytica. FAA1, fatty acyl-CoA synthase; ZWF1, glucose-6-phosphate dehydrogenase; PFK, 6-phosphofructokinase; PYK, pyruvate kinase; PYC1, pyruvate carboxylase; MAE1, malic enzyme; ACO1, Aconitase; IDH2, mitochondrial isocitrate dehydrogenase; IDP2, cytosolic NADP-specific isocitrate dehydrogenase; G-6-P, Glucose-6-phosphate; F-6-P, fructose-6-phosphate; F-1,6-P, fructose-1,6-diphosphate; PEP, phosphoenolpyruvic acid; OAA, oxaloacetic acid; Fum, fumaric acid; Suc, succinyl coenzyme A; α-KG, 2-oxoglutarate; 6-PGL, 6-phosphogluconolactone; Ru5P, ribulose-5-phosphate; X5P, xylulose-5-phosphate; DHAP, dihydroxyacetone phosphate; G-3-P, glyceraldehyde-3-phosphate; DAG, diacylglycerol; TAG, triacylglycerol; FFA, free fatty acid; PL, phospholipid; Glx, glutamine; QH2, coenzyme QH2.

contains ammonium sulfate 1.1 g/L, YNB 1.7 g/L, acetate 41.0 g/L, CSM-Leu 0.74 g/L, and L-leucine 0.20 g/L.

2.6 Quantification of biomass, glucose, citrate and lipid

Cell densities were monitored by measuring the optical density at 600 nm (OD_{600}). The OD_{600} value could be converted to dry cell weight (DCW) according to Eq. 1 OD_{600} = 0.35 g/L. The concentrations of glucose and acetate were measured under a flow rate of 0.6 mL/min of the mobile phase (5 mM of H_2SO_4) at 40°C by high-performance liquid chromatography (HPLC) equipped with a HPX-87H column (Bio-Rad, Hercules, CA, United States) and a refractive index detector through Shimadzu Prominence HPLC LC-20 A. To determine lipid composition, 4 OD units of cells were directly saponified with 0.5 M sodium methoxide with vortexing at 1,200 rpm for 2 h, and then neutralized with 40 μL 98% sulfuric acid to facilitate transesterification. Next, 400 μL hexane was added to extract fatty acid methyl ester for GC analysis. Moreover, to quantitatively determine lipid titer, 100 μL of 2 g/L of tridecanoate methyl ester and 2 g/L of glyceryl trihepta-decanoate were added as internal standard at the beginning, to benchmark the transesterification and saponification efficiency, respectively. Triplicate samples were taken and results were reported as average ± standard deviations. Lipid samples were taken at 120 h of shaking incubation. The method of GC analysis is consistent with previously reported method (Xu et al., 2016).

3 Results

3.1 Selecting the important genes for investigating the lipogenesis metabolism in *Y. lipolytica*

Noticeably, cytosolic acetyl-CoA is a direct precursor for lipid synthesis (Qiao et al., 2017), which is carboxylated to malonyl-CoA, further transacetylated to malonyl-ACPs, the true precursor to extending the growing chain of fatty acids, catalyzed by fatty acid synthases (FAS1 and FAS2). Thus, in acetyl-CoA metabolism, we chose three genes for investigation, including *ylPFK* (*YALI0D16357g*, encoding 6-phosphofructokinase), *ylPYK* (*YALI0F09185g*, encoding pyruvate kinase), and *ylAC O 1* (*YALI0D09361g*, encoding aconitate hydratase), and further constructed three strain po1fk_*ylPFK*, po1fk_*ylPYK*, and po1fk_*ylACO1*.

On the other hand, acetyl groups (CH_3-CO-) originating from acetyl-CoA is reduced to alkyl groups (-CH_2-CH_2-) when growing fatty acid

10.3389/fbioe.2023.1098116

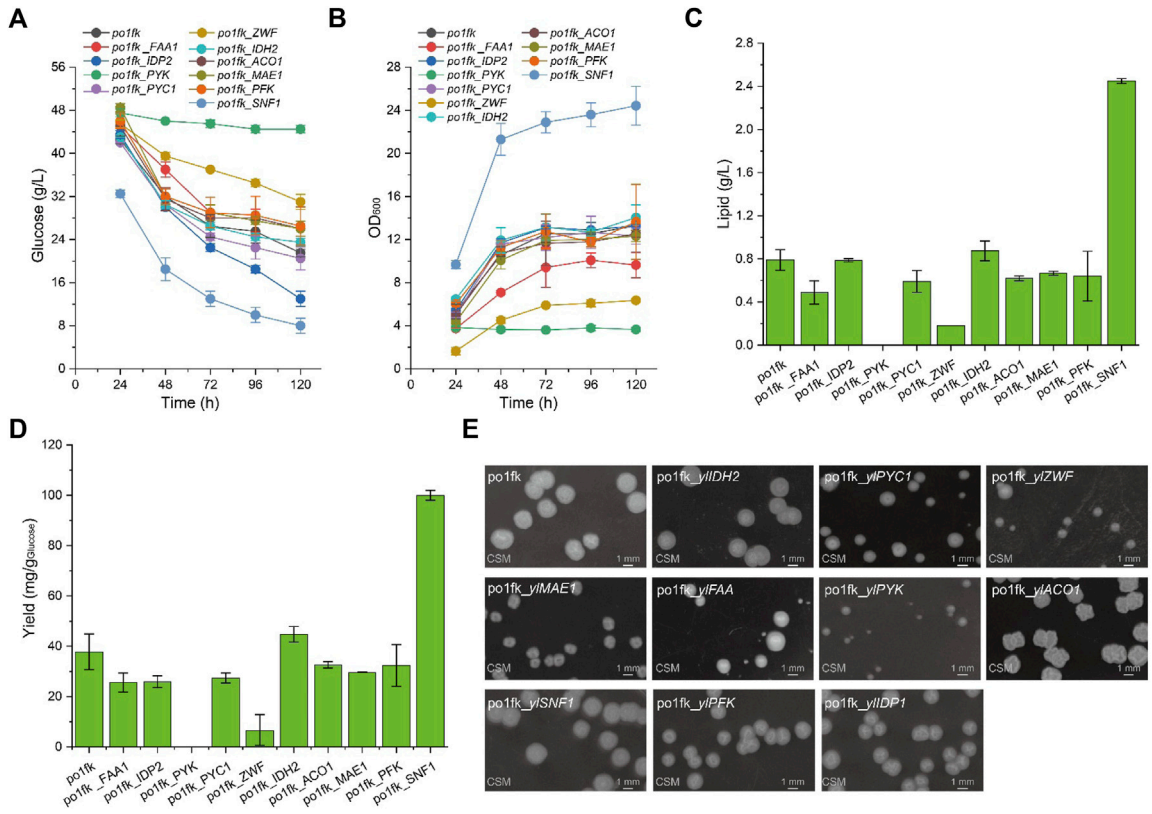

FIGURE 2
Time profiles of cell growth, glucose consumption, lipid titer and lipid yield in the CSM-leu medium and the morphology analysis of gene knockout strains. **(A)** Glucose consumption of po1fk, po1fk_ylPYK, po1fk_ylACO1, po1fk_ylPFK, po1fk_ylSNF1, po1fk_ylIDP2, po1fk_ylZWF, po1fk_ylIDH2, po1fk_ylMAE, po1fk_ylPYC1, and po1fk_ylFAA; **(B)** Cell growth of po1fk, po1fk_ylPYK, po1fk_ylACO1, po1fk_ylPFK, po1fk_ylSNF1, po1fk_ylIDP2, po1fk_ylZWF, po1fk_ylIDH2, po1fk_ylMAE, po1fk_ylPYC1, and po1fk_ylFAA; **(C)** Lipid titer of po1fk, po1fk_ylPYK, po1fk_ylACO1, po1fk_ylPFK, po1fk_ylSNF1, po1fk_ylIDP2, po1fk_ylZWF, po1fk_ylIDH2, po1fk_ylMAE, po1fk_ylPYC1, and po1fk_ylFAA; **(D)** Lipid yield of po1fk, po1fk_ylPYK, po1fk_ylACO1, po1fk_ylPFK, po1fk_ylSNF1, po1fk_ylIDP2, po1fk_ylZWF, po1fk_ylIDH2, po1fk_ylMAE, po1fk_ylPYC1, and po1fk_ylFAA; **(E)** the morphology analysis of gene knockout strains. For analyzing the morphology, cells were harvested from CSM-leu medium at 48 h and washed twice using .9% of NaCl solution. Then, cells were re-suspended and diluted to an appropriate concentration and spread on the CSM plates, cultivating at 30°C for 96 h.

carbon backbone, which needs to consume the reducing equivalent NADPH (Liu et al., 2019a). It has been reported that the sources of cytosolic NADPH include $NADP^+$-dependent isocitrate dehydrogenase, the OxPP pathway, and POM cycle (Silverman et al., 2016), related to malate dehydrogenase (encoded by gene *ylMAE1*, *YALI0E18634g*), mitochondrial isocitrate dehydrogenase (encoded by gene *ylIDH2*, *YALI0D06303g*), cytosolic isocitrate dehydrogenase (encoded by gene *ylIDP2*, *YALI0F04095g*), and glucose-6-phosphate dehydrogenase (encoded by gene *ylZWF1*, *YALI0E22649g*). Particularly, the POM cycle (Figure 1) also involves the reductive carboxylation of pyruvate to oxaloacetate by pyruvate carboxylase (encoded by gene *ylPYC1*, *YALI0C24101g*). Thus, these five genes in the NADPH metabolism were deleted to obtained strains po1fk_*ylMAE1*, po1fk_*ylIDH2*, po1fk_*ylIDP2*, po1fk_*ylZWF1*, and po1fk_*ylPYC1*, respectively. Moreover, we also investigated the influences of deleting lipogenesis gene *ylFAA1* (*YALI0D17864g*, long chain fatty acyl-CoA synthetase) on the lipid synthesis (Figure 1), which generated strain po1fk_*ylFAA1*. In addition, the regulator SNF1 (encoded by gene *YALI0D02101g*, carbon catabolite-derepressing protein kinase) was also knocked out, which is a cellular carbon metabolism regulator in *Y. lipolytica* to control the transition from growth phase to oleaginous production phase (Lazar et al., 2018), obtaining po1fk_*ylSNF1*.

3.2 Characterization of engineered *Y. lipolytica* strains under the nitrogen-limited shaking cultivation

To confirm whether cell growth and lipid levels of engineered *Y. lipolytica* strains were changed, we performed the nitrogen-limited shaking cultivation using the CSM medium (C/N = 80) to measure the lipid titers and cell growth. As a result, the maximal biomasses of strains po1fk_*ylPYC1*, po1fk_*ylACO1*, and po1fk_*ylMAE1* were slightly decreased compared with po1fk (Figure 2), and deletion of gene *ylIDP2* and *ylPFK* almost does not influence on cell growth. However, cell growth of strains po1fk_*ylPYK* and po1fk_*ylZWF* is severely inhibited. The maximum biomass of po1fk_*ylPYK* and po1fk_*ylZWF* are 72.5% and 52.2% lower than that of the control strain po1fk, respectively, reaching 3.96 and 6.47 (OD_{600}). Notably, gene *ylPYK* encodes pyruvate kinase, which converts the reaction of phosphoenolpyruvate to pyruvate in glycolysis. Therefore, deletion of gene *ylPYK* could block the metabolic flux from the glycolytic pathway to TCA cycles. On the other hand, glucose-6-phosphate dehydrogenase ZWF1 catalyzes glucose 6-phosphate to 6-phospho-glucono-1,5-lactone, providing the primary source of cytosolic NADPH in *Y. lipolytica*. It should be noted that NADPH functions as reducing equivalents to maintain cellular

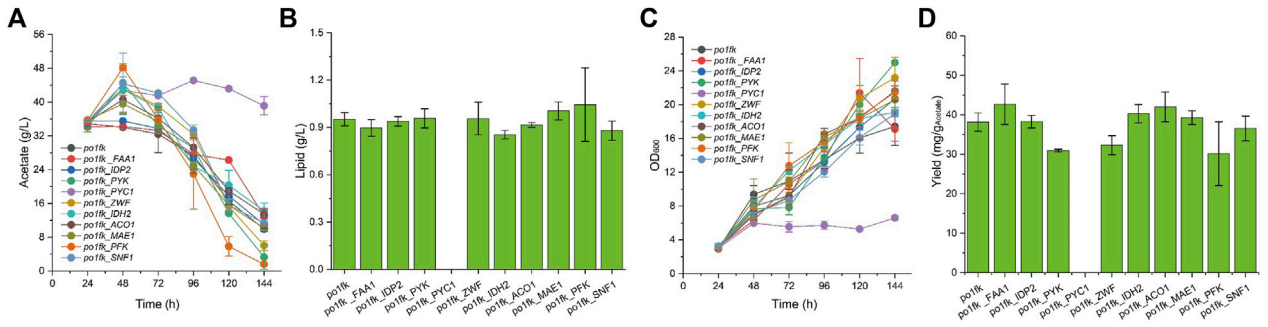

FIGURE 3
Time profiles of cell growth, acetate consumption, lipid titer and lipid yield in CSM-Acetate medium. **(A)** Glucose consumption of po1fk, po1fk_ylPYK, po1fk_ylACO1, po1fk_ylPFK, po1fk_ylSNF1, po1fk_yllDP2, po1fk_ylZWF, po1fk_yllDH2, po1fk_ylMAE, po1fk_ylPYC1, and po1fk_ylFAA; **(B)** Lipid titer of po1fk, po1fk_ylPYK, po1fk_ylACO1, po1fk_ylPFK, po1fk_ylSNF1, po1fk_yllDP2, po1fk_ylZWF, po1fk_yllDH2, po1fk_ylMAE, po1fk_ylPYC1, and po1fk_ylFAA; **(C)** Cell growth of po1fk, po1fk_ylPYK, po1fk_ylACO1, po1fk_ylPFK, po1fk_ylSNF1, po1fk_yllDP2, po1fk_ylZWF, po1fk_yllDH2, po1fk_ylMAE, po1fk_ylPYC1, and po1fk_ylFAA; **(D)** Lipid yield of po1fk, po1fk_ylPYK, po1fk_ylACO1, po1fk_ylPFK, po1fk_ylSNF1, po1fk_yllDP2, po1fk_ylZWF, po1fk_yllDH2, po1fk_ylMAE, po1fk_ylPYC1, and po1fk_ylFAA.

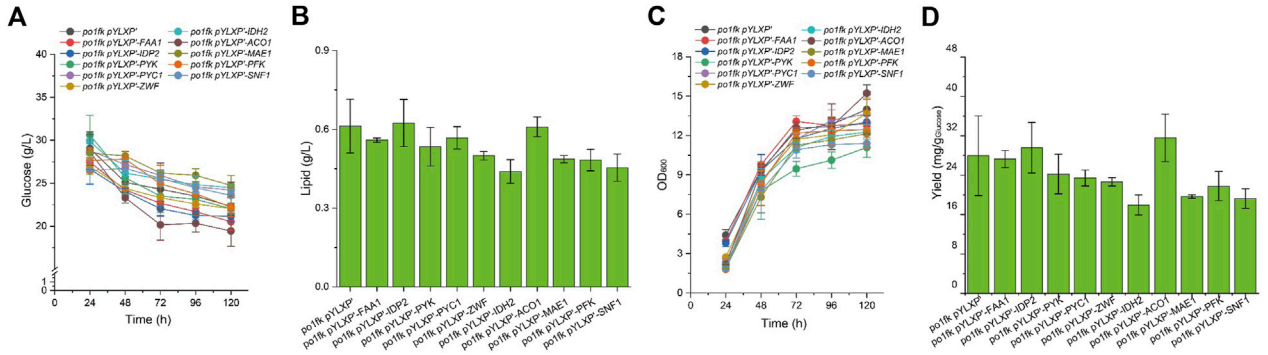

FIGURE 4
Time profiles of cell growth, glucose consumption, lipid titer and lipid yield in CSM-leu medium. **(A)** Glucose consumption of po1fk pYLXP', po1fk pYLXP'-ylPYK, po1fk pYLXP'-ylACO1, po1fk pYLXP'-ylPFK, po1fk pYLXP'-ylSNF1, po1fk pYLXP'-yllDP2, po1fk pYLXP'-ylZWF, po1fk pYLXP'-yllDH2, po1fk pYLXP'-ylMAE, po1fk pYLXP'-ylPYC1, and po1fk pYLXP'-ylFAA; **(B)** The lipid titer of po1fk pYLXP', po1fk pYLXP'-ylPYK, po1fk pYLXP'-ylACO1, po1fk pYLXP'-ylPFK, po1fk pYLXP'-ylSNF1, po1fk pYLXP'-yllDP2, po1fk pYLXP'-ylZWF, po1fk pYLXP'-yllDH2, po1fk pYLXP'-ylMAE, po1fk pYLXP'-ylPYC1, and po1fk pYLXP'-ylFAA; **(C)** Cell growth of po1fk pYLXP', po1fk pYLXP'-ylPYK, po1fk pYLXP'-ylACO1, po1fk pYLXP'-ylPFK, po1fk pYLXP'-ylSNF1, po1fk pYLXP'-yllDP2, po1fk pYLXP'-ylZWF, po1fk pYLXP'-yllDH2, po1fk pYLXP'-ylMAE, po1fk pYLXP'-ylPYC1, and po1fk pYLXP'-ylFAA; **(D)** Lipid yield of po1fk pYLXP', po1fk pYLXP'-ylPYK, po1fk pYLXP'-ylACO1, po1fk pYLXP'-ylPFK, po1fk pYLXP'-ylSNF1, po1fk pYLXP'-yllDP2, po1fk pYLXP'-ylZWF, po1fk pYLXP'-yllDH2, po1fk pYLXP'-ylMAE, po1fk pYLXP'-ylPYC1, and po1fk pYLXP'-ylFAA.

redox homeostasis and serves as important electron donors in the anabolic metabolism (Wang et al., 2017). In this study, we found that deletion of gene *ylZWF* gave a 76.9% reduction (0.18 ± 0.05 g/L with the yield of 13.01 mg/g $_{Glucose}$) in the lipid synthesis, indicating that the OxPP pathway is the primary NADPH source for lipogenesis. However, an interesting phenomenon to note is that the surface wrinkle of po1fk_*ylZWF1* is disappeared. We speculated that the reduced surface area of po1fk_*ylZWF1* colony may be attributed to the less oxygen demand for the ZWF1 deficient strain.

Moreover, the lipid titer of po1fk_*ylFAA1*, po1fk_*ylPYC1*, po1fk_*ylACO1*, and po1fk_*ylMAE1* are 0.49 ± 0.11, 0.59 ± 0.10, 0.62 ± 0.02, and 0.67 ± 0.02 g/L, decreased by 38.0%, 25.3%, 21.5%, and 15.2% relatively to po1fk (0.79 ± 0.10 g/L), respectively, suggesting that genes *ylFAA1*, *ylPYC1*, *ylAC O 1*, and *ylMAE* are necessary for the lipid synthesis in *Y. lipolytica*. However, the deletion of gene *yllDH2* increased the lipid titer, reaching .87 g/L with the yield of 44.8 mg/g $_{Glucose}$, which were 1.10-fold and 1.19-fold of that in the strain po1fk, respectively. It is incomprehensible because the mitochondrial NAD^+ isocitrate dehydrogenase IDH2 is important for TCA cycle, catalyzing isocitrate to 2-oxoglutarate. To explain this result, we performed a KEGG pathway analysis and found that the mitochondrial NAD^+ isocitrate dehydrogenases have two isoenzymes in *Y. lipolytica*, encoded by genes *YALI0E05137g* and *YALI0D06303g*, respectively. Therefore, we speculate that deletion of IDH2 downregulated the activity of mitochondrial NAD^+ isocitrate dehydrogenases, which strengthened the accumulation of citrate to promote the synthesis of lipids. Besides, the deletion of carbon catabolite repressor gene *ylSNF1* significantly increased the lipid titer, reaching 2.45 ± 0.02 g/L with the yield of 100.1 mg/g $_{Glucose}$, which was 3.10-fold and 2.65-fold of that of po1fk, respectively. This result is consistent with the previous research (Seip et al., 2013). The regulator SNF1 is involved in the transition from the growth phase to the oleaginous phase, and allows strains to accumulate lipids even in the nitrogen-abundant medium (Wang et al., 2020). However, how SNF1 regulates the lipid synthesis pathway has not been resolved (Lazar

TABLE 2 The productivity of engineering strains in the different cultivations.

Names	Productivity ($g_{Lipid}/L/g_{DCW}$)		Names	Productivity ($g_{Lipid}/L/g_{DCW}$)
	Glucose	Acetate		Glucose
po1fk	0.169	0.158	po1fk pYLXP'	0.125
po1fk_*ylPFK*	0.132	0.139	po1fk pYLXP'-*ylPFK*	0.111
po1fk_*ylPYK*	—/	0.109	po1fk pYLXP'-*ylPYK*	0.137
po1fk_*ylACO1*	0.141	0.121	po1fk pYLXP'-*ylACO1*	0.114
po1fk_*ylMAE1*	0.154	0.139	po1fk pYLXP'-*ylMAE1*	0.114
po1fk_*ylIDH2*	0.177	0.128	po1fk pYLXP'-*ylIDH2*	0.102
po1fk_*ylIDP2*	0.169	0.130	po1fk pYLXP'-*ylIDP2*	0.137
po1fk_*ylZWF1*	0.041	0.118	po1fk pYLXP'-*ylZWF1*	0.104
po1fk_*ylPYC1*	0.136	—/	po1fk pYLXP'-*ylPYC1*	0.119
po1fk_*ylFAA1*	0.144	0.150	po1fk pYLXP'-*ylFAA1*	0.124
po1fk_*ylSNF1*	0.289	0.131	po1fk pYLXP'-*ylSNF1*	0.114

et al., 2018), possibly due to the SNF1-mediated MAP kinase, which phosphorylates acetyl-CoA carboxylase and downregulates lipid synthesis. In brief summary, knocking out mitochondrial IDH2 and SNF1 will improve lipid accumulation in *Y. lipolytica* under the culture condition of using the CSM medium.

3.3 Using acetate as carbon source for lipid synthesis by engineered *Y. lipolytica* strains

The acetate uptake pathway in *Y. lipolytica* could function as an acetyl-CoA shortcut, which has been demonstrated to achieve metabolic optimality in producing polyketides (Liu et al., 2019b). Therefore, we turned to use acetate as the carbon source for lipid synthesis. Specifically, extracellular acetate is first catalyzed by acetyl-coA synthase to generate acetyl-coA, which enters into cellular metabolic pathways for maintaining cell activities. However, it should be noted that partial acetyl-CoA would pass through gluconeogenesis into the OxPP pathway to provide NADPH for fatty acid synthesis.

Noticeably, the cultivation pH will keep increasing when sodium acetate is used as a carbon source. For this, an *in situ* pH indicator (bromocresol purple) was used to track the change of cultivation pH (Liu et al., 2019a). By performing the shaking flask, we found that po1fk_*ylPYK*, po1fk_*ylZWF, and* po1fk_*ylFAA1* showed the remarkable recovery of cell growth (Figure 3) when acetate was used as sole carbon source, reaching 20.02 ± 1.18, 20.72 ± 1.56, and 21.38 ± 4.11 (the maximum biomass, OD_{600}), respectively. These results indicate that the evolutionary robustness of cells that enable them adapt to alternate carbon sources when central metabolism is compromised, and most importantly, acetate could be used as a shortcut nutrient to support cell growth. However, the cell growth of po1fk_*ylPYC1* was repressed in the CSM-acetate medium, and its maximum biomass (OD_{600}) was 5.72 ± 0.50, which could be attributed to the fact that PYC is important for cell to replenish gluconeogenesis when the cells were grown on the acetate media. The maximal lipid titer was produced by po1fk_*ylPFK*, reaching 1.04 ± 0.23 g/L, which is 1.09-fold of that of po1fk (0.95 ± 0.04 g/L). Interestingly, the lipid titer of po1fk_*ylSNF1* was close to that of po1fk using acetate as carbon source. Studies have reported that downregulation of Snf1 can activate the activity of acetyl-CoA carboxylase ACC1, which could facilitate the flux from acetyl-CoA to malonyl-CoA (Gross et al., 2019). Therefore, we speculated the increase flux from acetyl-CoA to malonyl-CoA in the engineering po1fk_*ylSNF1* strain leads to a reduction of NADPH supply and limits the synthesis of lipid under the acetate cultivation.

3.4 The effect of overexpressing the selected genes on cell growth and lipid synthesis

To further identify the potential functions of the selected genes, we overexpressed these genes under the control of strong constitutive pTEF-intron promoter by the plasmid pYLXP'. Shake flask cultivation of these engineering strains, including po1kf pYLXP'-*ylPFK*, po1kf pYLXP'-*ylPYK*, po1kf pYLXP'-*ylPYC1*, po1kf pYLXP'-*ylMAE1*, po1kf pYLXP'-*ylIDH2*, po1kf pYLXP'-*ylIDP2*, po1kf pYLXP'-*ylFAA1*, po1kf pYLXP'-*ylACO1*, and po1kf pYLXP'-*ylSNF1*, show no significant differences in cell growth (Figure 4). Further, we analyzed the lipid titer of these engineering strains. As shown in Figure 4, individual overexpression of gene *IDP2* result in a significant increase in the lipid titer, reaching 0.62 g/L with the yield of 29.58 $mg/g_{Glucose}$. In *Y. lipolytica*, gene *IDP2* encodes the cytosolic $NADP^+$ isocitrate dehydrogenase IDP2, which catalyzes the reaction of isocitrate to 2-oxoglutarate with generating one molecule of NADPH. However, the cytoplasmic TCA cycle in *Y. lipolytica* is incomplete, which lacks cytoplasmic aconitate hydratase, succinyl-CoA ligase, fumarate hydratase, etc. Thus, we speculated that has a trans-mitochondrial isocitrate-α-oxoglutarate NADPH shuttle in *Y. lipolytica*, which can be responsible for maintaining the redox homeostasis and transporting the reducing equivalent from mitochondria NADH to cytoplasm NADPH.

4 Discussions

In *Y. lipolytica*, lipogenic pathway is consisting of three parts: acetyl-CoA, NAPDH, and lipid metabolism pathways. Herein, we systematically investigated the knockout of ten important genes in these three parts, including *ylPFK*, *ylPYK*, *ylAC O 1*, *ylMAE1*, *ylIDH2*,

ylIDP2, *ylZWF1*, *ylPYC1*, *ylFAA1*, and *ylSNF1*. Noticeably, pyruvate kinase PYK plays an important role in the glycolysis pathway, which provides the precursor pyruvate for TCA. Deleting gene *ylPYK* resulted in the block of the glycolytic pathway, and thus leaded to an impaired glucose uptake, retarded cell growth and compromised lipid synthesis. Specifically, the previous effort has showed that *Y. lipolytica* possesses strong acetate utilization pathway, which is equivalent or even superior to the hexose utilization pathway (Liu et al., 2019b). Therefore, it is believable that strain po1fk_*ylPYK* showed a remarkable recovery of cell growth using acetate as the carbon source. Specifically, we deduced the overall stoichiometry of glucose or acetate conversion to lipid (Supplementary Note 1). As suggested by the stoichiometry, the yield of lipid synthesized from acetate (0.294 g/g $_{Acetate}$) is higher than that from glucose (0.271 g/g $_{Glucose}$), indicating that acetate is a dominant carbon source for lipid synthesis. As a result, strain po1fk_*ylPYK* produced 0.96 ± 0.06 g/L of lipid using acetate as the carbon source.

The glucose-6-phosphate dehydrogenase ZWF is a key enzyme that catalyzes glucose 6-phosphate to 6-phosphogluconolactone with generating NADPH. NADPH provides reducing power for synthesizing biological macromolecules (such as lipids, proteins, and glycogen) and directly affects cell growth, protein expression, and other secondary metabolites synthesis (polyketides or triterpenoids) (Xu et al., 2018). We found that deletion of PYC1 or MAE1 both decreased the synthesis of lipid, suggesting the POM cycle participates in lipogenesis for NADPH supplementation in *Y. lipolytica*. However, in the CSM-acetate medium, the cell growth of po1fk_*ylPYC1* was repressed, suggesting that the deficiency of pyruvate carboxylase PYC1 would lead to the disruption of gluconeogenesis. Moreover, it is reported that the distributions of the cellular reducing equivalent are highly compartmentalized in eukaryotes, which is attributed to the specific localization of metabolic pathways and impermeabilities of organelles membranes (Kory et al., 2020). Specifically, mitochondria are important organelles for the NADH metabolism due to its respiratory functions, the existence of electron transport chain for oxidative phosphorylation. Therefore, the dynamic balance of the reducing equivalent between mitochondria and cytoplasm are necessary for maintaining cellular redox homeostasis (Spinelli and Haigis, 2018). Our results of deletion of gene *IDH2* and overexpression of gene *IDP2* suggested the existence of a trans-mitochondrial isocitrate-α-oxoglutarate NADPH shuttle in *Y. lipolytica*. Specifically, according to the ways of NADPH supplement, we also deduced the overall stoichiometry of glucose or acetate conversion to lipid and calculated the yield of lipid (Supplementary Note 1), which could help us to understand the influences of NADPH supplement on lipid synthsis.

In addition, protein kinase ylSNF1 is a crucial regulator of glucose signal transduction, which is a negative regulator of the fatty acid biosynthesis pathway and acetyl-CoA carboxylase. It has been identified that SNF1 plays a vital role in the transition from growth to oil production in *Y. lipolytica*. Herein, deletion of genes *ylSNF1* significantly increased the lipid titer in the CSM-leu medium, reaching 2.45 ± 0.02 g/L with the yield of 100.0 mg/g $_{Glucose}$ and the productivity of 0.289 g $_{Lipid}$/L/g $_{DCW}$ (Table2), which is consistent with the previous research (Seip et al., 2013).

5 Conclusion

In this work, we established ten engineered strains with deleting the important gene involved in the central carbon, NADPH, and lipid metabolism, and systematically investigated the influence of such gene deletions on the lipid synthesis and cell growth. As a result, our study demonstrated that NADPH sources for lipogenesis include the OxPP pathway, POM cycle, and isocitrate-2-oxoglutarate shuttle in *Y. lipolytica*. Moreover, the knockout of mitochondrial isocitrate dehydrogenase IDH1 and the carbon catabolite repressor SNF1 could facilitate the lipid synthesis. Besides, acetate is a more favorable carbon source for the lipid synthesis when glycolysis step is impaired, indicating this could be alternate carbon source that reach metabolic optimality in lipid synthesis. This systematic investigation of gene deletions and overexpression across various lipogenic pathways would help us better understand lipogenesis and engineer yeast factories to upgrade the lipid biomanufacturing platform.

Data availability statement

The original contributions presented in the study are included in the article/Supplementary Material, further inquiries can be directed to the corresponding authors.

Author contributions

Author contributions YG and PX conceived and designed research. YG, JZ, YY, and JM conducted experiments. YG, JZ, XS and PX analyzed data. YG, JZ, and PX wrote the manuscript. All authors read and approved the manuscript.

Funding

This work was financially supported by the Natural Science Foundation of Jiangsu Province (BK20202002) and (BK20210572), and National Natural Science Foundation of China (22108126).

Conflict of interest

The authors declare that the research was conducted in the absence of any commercial or financial relationships that could be construed as a potential conflict of interest.

Publisher's note

Supplementary material

The Supplementary Material for this article can be found online at: https://www.frontiersin.org/articles/10.3389/fbioe.2023.1098116/full#supplementary-material

References

Abdel-Mawgoud, A. M., Markham, K. A., Palmer, C. M., Liu, N., Stephanopoulos, G., and Alper, H. S. (2018). Metabolic engineering in the host *Yarrowia lipolytica*. *Metab. Eng.* 50, 192–208. doi:10.1016/j.ymben.2018.07.016

Dulermo, T., and Nicaud, J. M. (2011). Involvement of the G3P shuttle and β-oxidation pathway in the control of TAG synthesis and lipid accumulation in *Yarrowia lipolytica*. *Metab. Eng.* 13 (5), 482–491. doi:10.1016/j.ymben.2011.05.002

Groenewald, M., Boekhout, T., Neuvéglise, C., Gaillardin, C., van Dijck, P. W., and Wyss, M. (2014). *Yarrowia lipolytica*: Safety assessment of an oleaginous yeast with a great industrial potential. *Crit. Rev. Microbiol.* 40 (3), 187–206. doi:10.3109/1040841X.2013.770386

Gross, A. S., Zimmermann, A., Pendl, T., Schroeder, S., Schoenlechner, H., Knittelfelder, O., et al. (2019). Acetyl-CoA carboxylase 1-dependent lipogenesis promotes autophagy downstream of AMPK. *J. Biol. Chem.* 294 (32), 12020–12039. doi:10.1074/jbc.RA118.007020

Gu, Y., Ma, J., Zhu, Y., Ding, X., and Xu, P. (2020a). Engineering *Yarrowia lipolytica* as a chassis for de novo synthesis of five aromatic-derived natural products and chemicals. *ACS Synth. Biol.* 9 (8), 2096–2106. doi:10.1021/acssynbio.0c00185

Gu, Y., Ma, J., Zhu, Y., and Xu, P. (2020b). Refactoring ehrlich pathway for high-yield 2-phenylethanol production in *Yarrowia lipolytica*. *ACS Synth. Biol.* 9 (3), 623–633. doi:10.1021/acssynbio.9b00468

Gu, Y., Xu, X., Wu, Y., Niu, T., Liu, Y., Li, J., et al. (2018). Advances and prospects of *Bacillus subtilis* cellular factories: From rational design to industrial applications. *Metab. Eng.* 50, 109–121. doi:10.1016/j.ymben.2018.05.006

Kory, N., Uit de Bos, J., van der Rijt, S., Jankovic, N., Güra, M., Arp, N., et al. (2020). MCART1/SLC25A51 is required for mitochondrial NAD transport. *Sci. Adv.* 6 (43), eabe5310. doi:10.1126/sciadv.abe5310

Larroude, M., Rossignol, T., Nicaud, J. M., and Ledesma-Amaro, R. (2018). Synthetic biology tools for engineering *Yarrowia lipolytica*. *Biotechnol. Adv.* 36 (8), 2150–2164. doi:10.1016/j.biotechadv.2018.10.004

Lazar, Z., Liu, N., and Stephanopoulos, G. (2018). Holistic approaches in lipid production by *Yarrowia lipolytica*. *Trends Biotechnol.* 36 (11), 1157–1170. doi:10.1016/j.tibtech.2018.06.007

Liu, H., Marsafari, M., Deng, L., and Xu, P. (2019a). Understanding lipogenesis by dynamically profiling transcriptional activity of lipogenic promoters in *Yarrowia lipolytica*. *Appl. Microbiol. Biotechnol.* 103 (7), 3167–3179. doi:10.1007/s00253-019-09664-8

Liu, H., Marsafari, M., Wang, F., Deng, L., and Xu, P. (2019b). Engineering acetyl-CoA metabolic shortcut for eco-friendly production of polyketides triacetic acid lactone in *Yarrowia lipolytica*. *Metab. Eng.* 56, 60–68. doi:10.1016/j.ymben.2019.08.017

Liu, L., Pan, A., Spofford, C., Zhou, N., and Alper, H. S. (2015). An evolutionary metabolic engineering approach for enhancing lipogenesis in *Yarrowia lipolytica*. *Metab. Eng.* 29, 36–45. doi:10.1016/j.ymben.2015.02.003

Liu, N., Qiao, K., and Stephanopoulos, G. (2016). (13)C Metabolic Flux Analysis of acetate conversion to lipids by *Yarrowia lipolytica*. *Metab. Eng.* 38, 86–97. doi:10.1016/j.ymben.2016.06.006

Lv, Y., Gu, Y., Xu, J., Zhou, J., and Xu, P. (2020). Coupling metabolic addiction with negative autoregulation to improve strain stability and pathway yield. *Metab. Eng.* 61, 79–88. doi:10.1016/j.ymben.2020.05.005

Ma, J., Gu, Y., Marsafari, M., and Xu, P. (2020). Synthetic biology, systems biology, and metabolic engineering of *Yarrowia lipolytica* toward a sustainable biorefinery platform. *J. Ind. Microbiol. Biotechnol.* 47 (9-10), 845–862. doi:10.1007/s10295-020-02290-8

Markham, K. A., and Alper, H. S. (2018). Synthetic biology expands the industrial potential of *Yarrowia lipolytica*. *Trends Biotechnol.* 36 (10), 1085–1095. doi:10.1016/j.tibtech.2018.05.004

Qiao, K., Imam Abidi, S. H., Liu, H., Zhang, H., Chakraborty, S., Watson, N., et al. (2015). Engineering lipid overproduction in the oleaginous yeast *Yarrowia lipolytica*. *Metab. Eng.* 29, 56–65. doi:10.1016/j.ymben.2015.02.005

Qiao, K., Wasylenko, T. M., Zhou, K., Xu, P., and Stephanopoulos, G. (2017). Lipid production in *Yarrowia lipolytica* is maximized by engineering cytosolic redox metabolism. *Nat. Biotechnol.* 35 (2), 173–177. doi:10.1038/nbt.3763

Seip, J., Jackson, R., He, H., Zhu, Q., and Hong, S. P. (2013). Snf1 is a regulator of lipid accumulation in *Yarrowia lipolytica*. *Appl. Environ. Microbiol.* 79 (23), 7360–7370. doi:10.1128/AEM.02079-13

Silverman, A. M., Qiao, K., Xu, P., and Stephanopoulos, G. (2016). Functional overexpression and characterization of lipogenesis-related genes in the oleaginous yeast *Yarrowia lipolytica*. *Appl. Microbiol. Biotechnol.* 100 (8), 3781–3798. doi:10.1007/s00253-016-7376-0

Spinelli, J. B., and Haigis, M. C. (2018). The multifaceted contributions of mitochondria to cellular metabolism. *Nat. Cell. Biol.* 20 (7), 745–754. doi:10.1038/s41556-018-0124-1

Wang, J., Ledesma-Amaro, R., Wei, Y., Ji, B., and Ji, X. J. (2020). Metabolic engineering for increased lipid accumulation in *Yarrowia lipolytica* - a Review. *Bioresour. Technol.* 313 (123707), 123707. doi:10.1016/j.biortech.2020.123707

Wang, M., Chen, B., Fang, Y., and Tan, T. (2017). Cofactor engineering for more efficient production of chemicals and biofuels. *Biotechnol. Adv.* 35 (8), 1032–1039. doi:10.1016/j.biotechadv.2017.09.008

Wasylenko, T. M., Ahn, W. S., and Stephanopoulos, G. (2015). The oxidative pentose phosphate pathway is the primary source of NADPH for lipid overproduction from glucose in *Yarrowia lipolytica*. *Metab. Eng.* 30, 27–39. doi:10.1016/j.ymben.2015.02.007

Wong, L., Engel, J., Jin, E., Holdridge, B., and Xu, P. (2017). YaliBricks, a versatile genetic toolkit for streamlined and rapid pathway engineering in *Yarrowia lipolytica*. *Metab. Eng. Commun.* 5, 000999–e177. doi:10.1016/j.mec.2019.e00099

Xu, J. Z., Yang, H. K., and Zhang, W. G. (2018). NADPH metabolism: A survey of its theoretical characteristics and manipulation strategies in amino acid biosynthesis. *Crit. Rev. Biotechnol.* 38 (7), 1061–1076. doi:10.1080/07388551.2018.1437387

Xu, P., Qiao, K., Ahn, W. S., and Stephanopoulos, G. (2016). Engineering *Yarrowia lipolytica* as a platform for synthesis of drop-in transportation fuels and oleochemicals. *Proc. Natl. Acad. Sci. USA.* 113 (39), 10848–10853. doi:10.1073/pnas.1607295113

Xu, P., Qiao, K., and Stephanopoulos, G. (2017). Engineering oxidative stress defense pathways to build a robust lipid production platform in *Yarrowia lipolytica*. *Biotechnol. Bioeng.* 114 (7), 1521–1530. doi:10.1002/bit.26285

Xue, J., Balamurugan, S., Li, D. W., Liu, Y. H., Zeng, H., Wang, L., et al. (2017). Glucose-6-phosphate dehydrogenase as a target for highly efficient fatty acid biosynthesis in microalgae by enhancing NADPH supply. *Metab. Eng.* 41, 212–221. doi:10.1016/j.ymben.2017.04.008

Yang, Z., Edwards, H., and Xu, P. (2019). CRISPR-Cas12a/Cpf1-assisted precise, efficient and multiplexed genome-editing in *Yarrowia lipolytica*. *Metab. Eng. Commun.* 22 (10), e00112. doi:10.1016/j.mec.2019.e00112

Yuzbasheva, E. Y., Agrimi, G., Yuzbashev, T. V., Scarcia, P., Vinogradova, E. B., Palmieri, L., et al. (2019). The mitochondrial citrate carrier in *Yarrowia lipolytica*: Its identification, characterization and functional significance for the production of citric acid. *Metab. Eng.* 54, 264–274. doi:10.1016/j.ymben.2019.05.002

frontiers | Frontiers in Bioengineering and Biotechnology

TYPE Original Research
PUBLISHED 09 February 2023
DOI 10.3389/fbioe.2023.1108653

OPEN ACCESS

EDITED BY
Xiao-Jun Ji,
Nanjing Tech University, China

REVIEWED BY
Yang Gu,
Nanjing Normal University, China
Hu-Hu Liu,
Hunan Agricultural University, China

*CORRESPONDENCE
Zongjie Dai,
daizj@tib.cas.cn

†PRESENT ADDRESS
Peixin Liang,
Ocean College of Tangshan Normal University, Tangshan, China

SPECIALTY SECTION
This article was submitted to Synthetic Biology, a section of the journal Frontiers in Bioengineering and Biotechnology

RECEIVED 26 November 2022
ACCEPTED 20 January 2023
PUBLISHED 09 February 2023

CITATION
Liang P, Li J, Wang Q and Dai Z (2023), Enhancing the thermotolerance and erythritol production of *Yarrowia lipolytica* by introducing heat-resistant devices. *Front. Bioeng. Biotechnol.* 11:1108653. doi: 10.3389/fbioe.2023.1108653

Enhancing the thermotolerance and erythritol production of *Yarrowia lipolytica* by introducing heat-resistant devices

Peixin Liang[1,2†], Jing Li[1,2,3], Qinhong Wang[1,2] and Zongjie Dai[1,2*]

[1]Tianjin Institute of Industrial Biotechnology, Chinese Academy of Sciences, Tianjin, China, [2]National Center of Technology Innovation for Synthetic Biology, Tianjin, China, [3]College of Biotechnology, Tianjin University of Science and Technology, Tianjin, China

Yarrowia lipolytica has been widely used in the food biotech-related industry, where it plays the host's role in producing erythritol. Nevertheless, a temperature of about 28°C–30°C has been estimated as the yeast's optimal growth temperature, leading to the consumption of a considerable quantity of cooling water, especially in summer, which is obligatory for fermentation. Herein is described a method for improving the thermotolerance and erythritol production efficiency at high temperatures of *Y. lipolytica*. Through screening and testing different heat resistant devices, eight refactored engineered strains showed better growth at higher temperature and the antioxidant properties of the eight engineered strains were also improved. In addition, the erythritol titer, yield and productivity of the strain FOS11-Ctt1 represented the best among the eight strains, reaching at 39.25 g/L, 0.348 g/g glucose, and 0.55 g/L/h respectively, which were increased by 156%, 86% and 161% compared with the control strain, respectively. This study provides insight into an effective heat-resistant device that could enhance the thermotolerance and erythritol production of *Y. lipolytica*, which might be considered a valued scientific reference for other resistant strains' construction.

KEYWORDS

thermotolerance, yarrowia lipolytica, erythritol, heat-resistant devices, ROS, antioxidant properties

1 Introduction

Yarrowia lipolytica has been broadly employed in the food-related industry due to its traits of the utilization of inexpensive substrates, high cell density fermentation, and biosafety, especially in the industrial production of the sugar alcohol named erythritol (Fickers et al., 2020; Abbasi et al., 2021). Sources claim that the total erythritol production value is estimated to exceed 150 million USD in 2023. This number corresponds to an increase of approximately 81 million USD compared to the recorded numbers for the year 2017 (Ross, 2018). On the other hand, a temperature of 28°C–30°C has been suggested to be the optimal temperature interval for yeast growth. Additionally, aerobic fermentation requires a large amount of oxygen, which then generates a large amount of biothermal and mechanical heat during the industrial production process (Schenk et al., 2017). Therefore, to avoid the metabolic decline and the risk of bacterial infection caused by excessive temperature (>32°C) (Costa et al., 2014), it is of extreme importance to consume large quantities of cooling water. However, the latter substantially increases the cost of erythritol's large-scale industrial production.

Recently, adaptive evolution and random mutagenesis found a broad application in tolerance engineering with the ultimate goal of creating industrial strains with superior

performance. For example, Qiu et al. identified four genes of the thiamine metabolic pathway that seem to be responsible for the thermostable phenotype of an evolutionarily adaptive mutation in the strain of *Y. lipolytica* employing transcriptomic analysis. They reported a rise in the fermentation temperature of about 3°C, reaching 33°C after overexpression of these genes in original strain (Qiu et al., 2021). Previous work successfully screened out an erythritol hyper producer in the benchtop fermenter at 35°C by combining the ARTP mutagenesis and synthetic microbial biosensor (SMB) system (Qiu et al., 2020). These semi-rational design strategies can produce strains with improved fermentation performance, but the resulting phenotypes are difficult to be transferred to new strains.

Elucidation of the thermal response and defence mechanism of the model yeast *Saccharomyces cerevisiae* has provided valuable targets for the rational breeding of thermotolerant strains. Reports suggest several target molecules have been involved in thermotolerance, including heat shock protein (Hsp), ATPase, trehalose, ubiquitin and antioxidant enzymes, whose role in heat-resistant processes for yeast species has been regarded as vital. Concerning Hsp104, it has proven essential for thermotolerance in *S. cerevisiae*. Sanchez et al. discovered an interval of 100- to 1000-fold difference, accompanied by a temperature increase of 44°C in the *Hsp104Δ* and wild-type cells' viability (Sanchez et al., 1992). Pma1 in yeast species is one of the most well-known ATPases. Authors have confirmed its pivotal impact on maintaining cells' structural integrity (Mason et al., 2014) and thermotolerance. The last discovery was based on the significant decrease in the resistance of mutant yeast in which a reduction in PMA1 expression was observed at temperatures like 50°C. The Hul5 ubiquitin ligase was also reported to account for maintaining cell fitness *via* the degradation of misfolded proteins with a short lifetime (Fang et al., 2011). Furthermore, Shahsavarani and colleagues confirmed a positive correlation between overexpression of the *S. cerevisiae* ubiquitin ligase Rsp5 and the increase of the yeast's upper limit of thermotolerance (Shahsavarani et al., 2012). When ubiquitin ligase Rsp5 was expressed in *Y. lipolytica*, the findings demonstrated a healthy growth of the engineered strain at 34°C and an efficient production of erythritol at 33°C (Wang et al., 2020).

In addition, heat-inducible genes and thermozymes are characteristic of thermophiles under high temperatures (Ahn et al., 2003; Liu et al., 2014). Ten engineered thermotolerant *S. cerevisiae* strains were constructed by transformation with heat-resistant devices with *Thermoanaerobacter tengcongensis* Hsp and ubiquitin coding genes (Liu et al., 2014). Among them, the strains overexpressing *T.te-Tte2469*, *T.te-Gros2,* and *T.te-IbpA* had increased cell concentration (above 25%) and considerably greater survival than the control cells under high temperatures. Above all, the strain overexpressing *Hsp T.te-Gros2* demonstrated a four-fold rise in cellular growth at 42°C for 72 h compared to the control cells (Gao et al., 2016). Interestingly, *Y. lipolytica* cells, overexpressing native *Hsp90,* had increased thermotolerance when cultivated at temperatures rising from 30°C to 35°C (Zhang et al., 2022). However, the genes from thermophiles have not been reported to increase the thermotolerance of *Y. lipolytica*.

The current investigation aims to develop a thermotolerant *Y. lipolytica* strain with enhanced erythritol production at 35°C. In that sense, potential thermotolerance genes with diverse functions from different thermal preference strains were screened. Based on these genes, we have studied the thermotolerance and the ability of *Y. lipolytica* cells, which were transformed with the selected genes, to withstand oxidative stress. In the meantime, we proved that these cells expressed and produced erythritol. Furthermore, based on these genes, the effects of these cells' growth and oxidative stress tolerance were investigated. This work showcases a significant improvement in thermotolerance and erythritol production of *Y. lipolytica*, which would significantly reduce energy consumption and ultimately favour the industrial production of erythritol.

2 Materials and methods

2.1 Chemical compounds and biological substances

Erythritol, 2′,7′-dichlorodihydrofluorescein diacetate (H2DCFDA, DCFH-DA) and propidium iodide solution were obtained from Solarbio (Beijing, China). New England Biolabs supplied the restriction endonucleases. KOD OneTM Master Mix -Blue- and PrimeSTAR® HS DNA Polymerase for the polymerase chain reactions (PCR) were purchased from Toyobo (Japan) or TaKaRa.

2.2 Yeast strains, culture media, and conditions

The *E. coli* and *Y. lipolytica* strains were employed here and are displayed in Supplementary Table S1. The *E. coli* cells were cultured at 37°C in LB (Jira et al., 2018) for plasmid construction. *Y. lipolytica* cells were grown at 30°C in YPD (Albers and Larsson., 2009). Where necessary, media were complemented with ampicillin (100 mg/L), nourseothricin (800 mg/L) or agarose (20 g/L). The shake-flask cultures were grown at 30°C, 35°C and 220 rpm in 100 mL of volume, containing 4 mL of fermentation medium, as previously described (Wang et al., 2020). All shake flasks were weighed before being placed into the shaker for incubation and then supplemented by adding the exact weight of sterilized water every 24 h to keep the volume unchanged.

2.3 Creation of thermotolerant gene devices and strains

Functional genes were obtained *via* PCR using the genome of *S. cerevisiae* Y-581 as templates, and others were chemically synthesized by Genewiz Inc., Suzhou, China. These genes were cloned into the pLPX-002 plasmid to give a series of plasmids. The detailed procedures of lithium acetate transformation for constructing the engineered strains are described in Holkenbrink et al. (Holkenbrink et al., 2018). Affirmative clones were verified on YPD-nourseothricin petri dishes and established by PCR detection and DNA sequencing. Information about the used primers, plasmids and engineered strains is provided in Supplementary Table S1.

2.4 Determination of cell concentration

The growth characteristics of the strains were measured under fermentation conditions. Each strain was at a primary cell density of OD_{600} = 0.1 and was grown in 100 mL of shake flasks with 4 mL of

TABLE 1 Information of the functional genes used in this study.

Categories	Functions	Genes	Sources
Stress response proteins	Proteins that can protect against heat-induced oxidative and environmental stress.	Hsf1 (SC), Skn7, Msn2 (SC), Msn4	*Saccharomyces cerevisiae*
		Msn2 (KM), Hsf1 (KM)	*Kluyveromyces marxianus*
Heat shock proteins	Proteins that can protect thermally damaged proteins and improve the thermal stability of soluble proteins, SOD and proton pumps in stressed cells.	Hsp104, Hsp12	*Saccharomyces cerevisiae*
		Hsp10	*Thermus thermophilus* HB8
		SHsp	*Pyrococcus furiosus*
		Sso2427	*Sulfolobus solfatara*
		Gros2, Ibpa, Groes	*Thermoanaerobacter tengcongensis* MB4
ATPases	ATPase can transport hydrogen against the concentration gradient through membrane-integrated glycoproteins and stabilize the intracellular pH.	Pma1, Vma2, Vma3	*Saccharomyces cerevisiae*
Ubiquitin ligases	Ubiquitin ligases play a significant role in protecting cells against acute proteotoxic stress.	Hul5, Hrd1, Rma1, San1	*Saccharomyces cerevisiae*
		Tte2469	*Thermoanaerobacter tengcongensis* MB4
Antioxidant enzymes	Antioxidant enzymes are the primary protectors against oxidative damage.	Sod1, Cta1, Ctt1, Tsa1, Ahp1, Prx1	*Saccharomyces cerevisiae*
		Bifunctional glutathione synthase gene (GCSGC)	*Streptococcus thermophilus*
Nucleic acid protectors	Nucleic acid protectors are helpful for transcriptional regulation and the establishment of new protein homeostasis.	Cspl	*Bacillus coagulans* 2–6

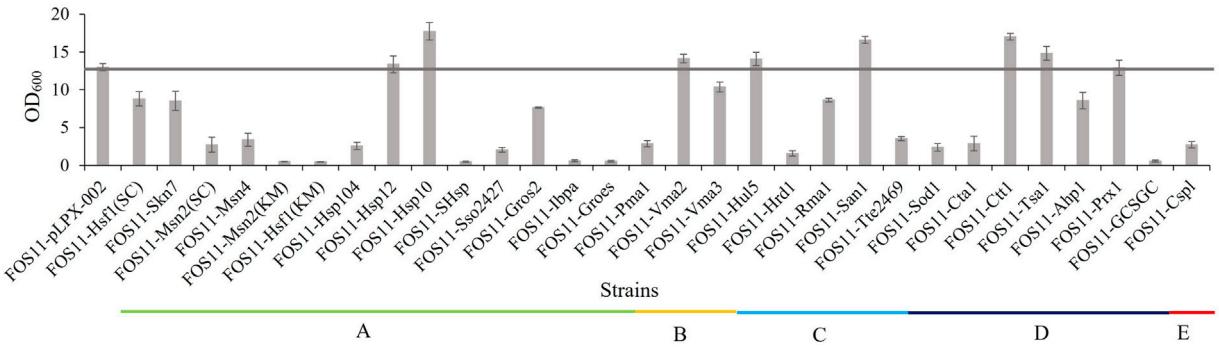

FIGURE 1
The cell density of engineered and control strains after 72 h cultured at 35°C. **(A).** Engineered strains transformed with plasmids containing different heat shock protein genes. **(B)**. Engineered strains transformed with plasmids containing different ATPase genes. **(C)**. Engineered strains transformed with plasmids containing different ubiquitin ligase genes. **(D)**. Engineered strains transformed with plasmids containing different antioxidant enzyme genes. **(E)**. Engineered strains transformed with plasmids containing different nucleic acid protector genes.

fermentation media and then cultured for 72 h at 35 C and shaking at 220 rpm. The UV-1800 spectrophotometer (Shimadzu, Kyoto, Japan) was used for cell growth optical density measurements (OD_{600}).

2.5 Measurements of oxidative stress tolerance

The ability of the cells to tolerant oxidative stress was done following the protocol by Konzock et al. (Konzock and Norbeck., 2020). H_2O_2 was applied for oxidative stress induction at 50 mM final concentration. The cells were successively diluted in 1/10 steps. Cellular drops of 5 µL were grown on YPD-nourseothricin petri dishes at 30°C. At the same time, the cells were dissolved in PBS and 5 µg/mL PI (1 mg/mL stock in water). Cells were incubated for 20 min in the dark at room temperature (Kwolek-Mirek and Zadrag., 2014)' and the cell viability based on the fluorescent dye was measured by flow cytometry (BD FACSAria III) (Qiu et al., 2021). The ROS concentration was measured following previously established procedures (Xu et al., 2017). Cells were collected and diluted to 0.3 OD_{600}. They were mixed with 5 nmol of DCFH-DA for each sample and incubated at 37°C for an hour. Fluorescence was measured at 495 nm.

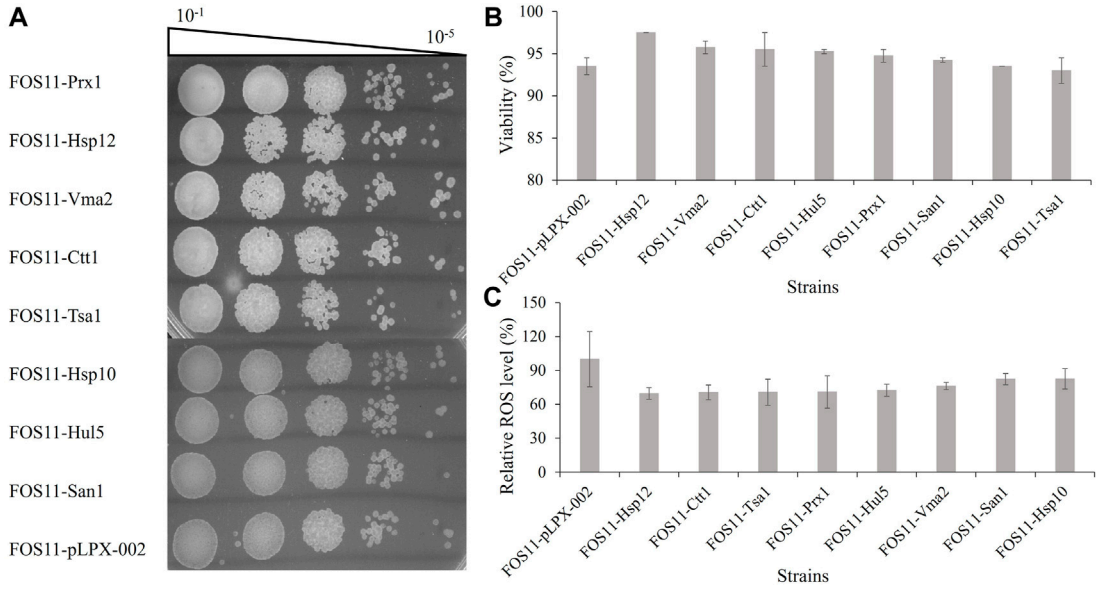

FIGURE 2
Characterization of the engineered strains treated with 50 mM H_2O_2. **(A)**. Investigation of colony forming units of the engineered and control strains by spotted plate method. **(B)**. Detection of cell viability based on the fluorescent dye of engineered and control strains by flow cytometry. **(C)**. Measurement of the intracellular ROS levels of engineered and control strains based on the fluorescent by microplate reader.

2.6 Analytical methods for erythritol and glucose measurements

Erythritol and glucose were detected by HPLC (Prominence UFLC, Shimadzu Corporation). The mobile phase was 5 μM sulfuric acid solution on an organic acid column (Aminex HPX-87H Ion Exclusion Column 300 mm × 7.8 mm; Catalog 125-0140; Bio-Rad Laboratories, Inc., United States). The entire protocol was published previously (Wang et al., 2020).

3 Results and discussion

3.1 Selection of heat-resistant genes

Improving the heat resistance of yeast strains is of great significance for reducing the energy cost required for cooling bioreactors in industrial production processes. However, thermotolerance is a complex phenotype involving various aspects of cellular physiology and metabolism (Alper et al., 2006; Liu et al., 2021). Large amounts of reactive oxygen species (ROS) are generated under higher temperatures, causing severe oxidative damage to cells, such as lipid peroxidation in cellular membranes, nucleic acid damage and increased toxicity by oxidation of proteins (Ahn et al., 2003). Several molecules have been reported to play essential roles against heat-induced oxidative stress in *S. cerevisiae* (Morano et al., 2012). Furthermore, recent data show that proteins synthesized by heat-inducible genes from different thermotolerant species, also designated as thermophiles, enhance heat resistance and thermotolerance in yeast species (Liu et al., 2014; Luan et al., 2014; Wang et al., 2015).

The high content of specific amino acids, such as Ile, Pro, Glu, Arg, and lower content of amino acids such as Cys, Ser, Thr, Asn and Asp make the heat-inducible proteins to natural proteins and valuable biological components for improving the thermotolerance of yeast (Ahn et al., 2003; Liu et al., 2014; Luan et al., 2014; Wang et al., 2015). In addition, trehalose accumulation and increased energy supply by affecting some heat-inducing genes in yeast itself (such as *TPS1* and *CDC19*) can help the strain resist heat damage (Gao et al., 2016). Furthermore, overexpression of the heat-inducing genes may contribute to maintaining cell wall integrity (Liu et al., 2014). Therefore, to improve the thermotolerance of *Y. lipolytica*, we screened and classified thirty potential heat-inducible genes which coded for stress-responsive proteins such as the Hsp family, ATPases, ubiquitin ligases, antioxidant enzymes and nucleic acid protectors from *S. cerevisiae* and different thermophilic strains such as *Thermus thermophilus* HB8, *Thermoanaerobacter tengcongensis* MB4, *Pyrococcus furiosus* and others. Information about all these genes was provided in Table 1; Supplemenetary Table S2. These stress-related genes were obtained by PCR or gene synthesis.

3.2 Screening of effective heat-resistant gene devices

Considering the possible metabolic burden on cell growth by protein expression, we selected the medium-strength promoter *EXP1p* and the low-copy plasmid pLPX-002 to construct the heat-resistant modules. The resulting plasmids were transformed into *Y. lipolytica* strain FOS11 and allowed the generation of different engineered strains for preliminary screening by detecting the optical cell density at 35°C. As shown in Figure 1, the engineered strains FOS11-Hsp12, FOS11-Vma2, FOS11-Hul5, FOS11-San1, FOS11-Tsa1, FOS11-Prx1, FOS11-Hsp10 and FOS11-Ctt1 showed better growth compared with the control strain FOS11-pLPX-002. Among them, the OD_{600} values of FOS11-San1, FOS11-Hsp10 and FOS11-Ctt1 showed 27.71%, 36.49% and 30.95% increase compared

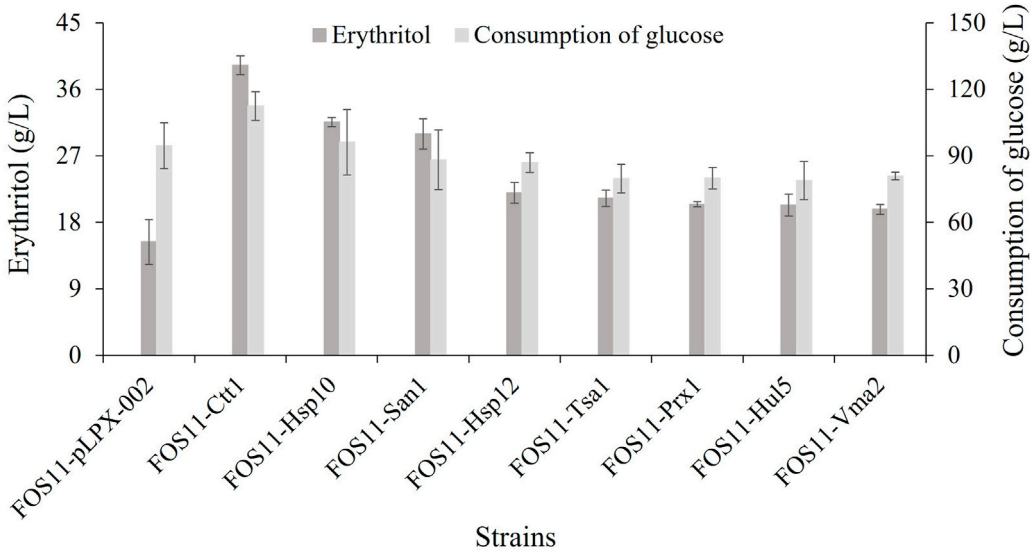

FIGURE 3
The production of erythritol and the consumption of glucose of control and engineered strains at 35°C. Data represent the mean ± SD of three biological replicates.

TABLE 2 Summary of fermentation profiles of engineered and control strains at 35°C.

Strains	Erythritol (g/L)	Q_{ery} (g/L/h)	Y_{ery} (g/g glucose)	OD_{600}
FOS11-pLPX-002	15.33 ± 3.05	0.21 ± 0.042	0.187 ± 0.02	12.99 ± 0.47
FOS11-Hsp12	22 ± 1.4	0.31 ± 0.019	0.253 ± 0.017	13.37 ± 0.13
FOS11-Hsp10	31.58 ± 0.62	0.44 ± 0.009	0.338 ± 0.064	17.73 ± 1.17
FOS11-Hul5	20.32 ± 1.48	0.28 ± 0.02	0.233 ± 0.03	14.07 ± 0.87
FOS11-San1	29.95 ± 2.04	0.42 ± 0.028	0.307 ± 0.007	16.59 ± 0.46
FOS11-Vma2	19.75 ± 0.68	0.27 ± 0.01	0.244 ± 0.008	14.13 ± 0.55
FOS11-Ctt1	39.25 ± 4.6	0.55 ± 0.064	0.348 ± 0.026	17.01 ± 0.44
FOS11-Prx1	20.43 ± 0.34	0.28 ± 0.005	0.257 ± 0.016	12.9 ± 0.99
FOS11-Tsa1	21.26 ± 1.11	0.3 ± 0.015	0.269 ± 0.037	14.82 ± 0.91

with the control strain, respectively. Except these eight modules showed a positive effect on cell growth, the rest twenty-two constructs led to worse cell growth, even almost lethality compared with the control. Still, these results suggested that introducing heat-resistant devices could improve the thermotolerance of *Y. lipolytica*, especially in the yeast transformants with *San1*, *Hsp10* and *Ctt1*.

Hsp10 (GroES) was obtained from *Thermus thermophilus,* demonstrating optimum growth at 80°C (Laksanalamai et al., 2004). Studies have shown that GroES was used firstly for structural analyses among all heat shock proteins. Then, it formed a GroESL system with GroEL (also called Hsp60, which interacted with at least approximately 250 different cytosolic protein), which potentiated the proteins in non-native conformations to fold correctly and play an essential role in improving cell heat resistance (Vabulas et al., 2010). Protein homeostasis is finely regulated by protein quality control, which allows the removal of misfolded or impaired proteins from the cells. The process is mainly driven by the ubiquitin-proteasome system in eukaryotic cells (Ibarra et al., 2016). San1, one of the ubiquitin ligases, interacts directly with mismatched substrates in the nucleus and eliminates them (Rosenbaum et al., 2011). Heat shock induces significant oxidative stress, inducing the expression of the catalase enzymes as the first and most potent response. It was reported that the cytosolic catalase T, coded by *Ctt1*, protects cells from oxidative damage caused by hydrogen peroxide (Hiltunen et al., 2003; Martins et al., 2019). The expression of *Ctt1* may help cells clear away large amounts of ROS produced at high temperatures. Taken together, these results might be why the expression of *Hsp10*, *San1* and *Ctt1* enhanced the growth of *Y. lipolytica* at 35°C.

Proteins with different functions could improve the growth of *Y. lipolytica* at 35°C, suggesting that high-temperature conditions could

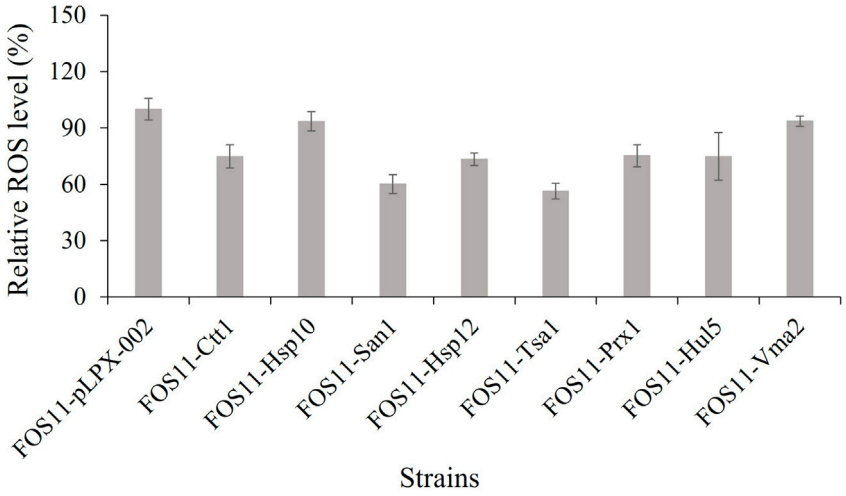

FIGURE 4
Comparison of the intracellular ROS level of engineered and control strains during fermentation at 35°C. Data represent the mean ± SD of three biological replicates.

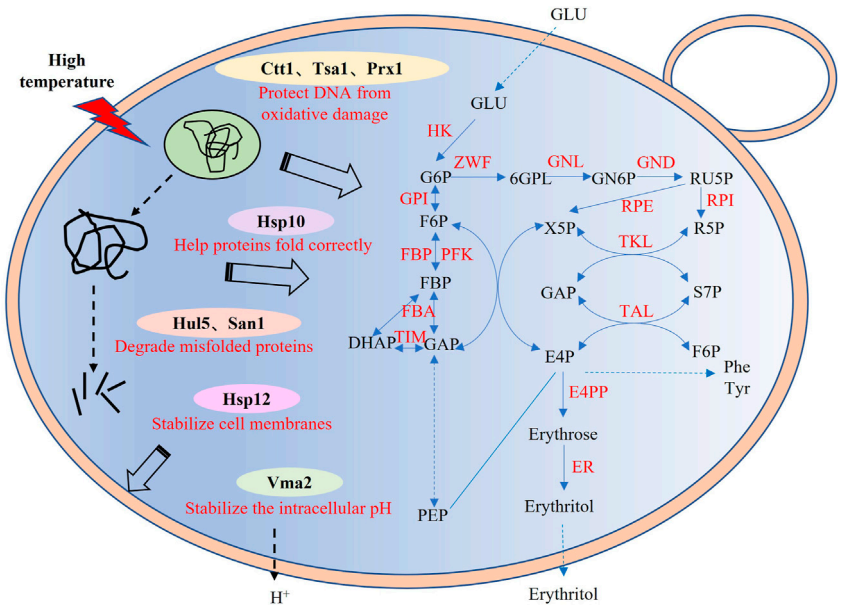

FIGURE 5
Synthetic pathway of erythritol and potential protective mechanism of heat-resistant devices. GLU, glucose; G6P, glucose-6-P; F6P, fructose-6-P; FBP, fructose-1,6-2P; DHAP, dihydroxyacetone phosphate; GAP, glyceraldehyde-P; Ru5P, ribulose-5P; X5P, xylulose-5-P; R5P, ribose-5-P; S7P, sedoheptulose-7-P; E4P, Erythrose-4-P; 6GPL, 6-P-gluconolactone; GN6P, 6-P-gluconate; PEP, phosphoenolpyruvate; HK, hexokinase; GPI, glucose-6-phosphate isomerase; FBP, fructose-1,6-bisphosphatase; PFK, 6-phosphofructokinase; RPE, ribulose-phosphate 3-epimerase; FBA, fructose-bisphosphate aldolase; TIM, triosephosphate isomerase; ZWF, glucose-6-phosphate 1-dehydrogenase; RPI, ribose 5-phosphate isomerase; GND, 6-phosphogluconate dehydrogenase; TKL, transketolase; TAL, transaldolase; GNL, 6-phosphogluconolactonase; E4PP, erythrose 4-phosphate phosphatase; XR, xylitol reductase.

induce different physiological and metabolic stress. However, in our studies, proteins with the same function resulted in little improvement or even worse growth. The possible reason may be due to the properties of the proteins themselves, such as enzyme activity and protein expression level, and the specific mechanisms involved in stress tolerance were not compatible with the growth and metabolism of host strains.

3.3 Antioxidant analysis of thermo-tolerant engineered strains

High temperature makes yeast cells accumulate a large amount of ROS, causing damage to cell growth and product biosynthesis (Gómez-Pastor et al., 2010). To further test the antioxidative effect of the eight effective heat-resistant transformant strains, we performed

antioxidant analysis on engineered strains during the exponential phase (Supplementary Figure S2) using hydrogen peroxide (H_2O_2) to generate the ROS through the spotting test. As shown in Figure 2A, there was little difference between the eight engineered strains and the control. Therefore, introducing these heat-resistant devices did not alter the reproductive capacity of the engineered strains.

Colourimetric or fluorescent methods for measuring cell viability are faster and more correct than the standard approaches as they simultaneously measure cells that can and cannot reproduce but are still viable (Kwolek-Mirek and Zadrag., 2014). Staining cells with methylene blue or propidium iodide (PI) is widely used. PI enters only diseased cells and allows assessment of cellular viability on a single-cell level. Figure 2B demonstrated the augmented cellular viability of the eight engineered strains, especially FOS11-Hsp12, in which the cell viability was improved to 97.5%, which was increased by 4.3% compared with the control strain FOS11-pLPX-002 (93.5%). Welker et al. explored the structure and heat-resistant mechanism of Hsp12 and showed that it was fully unfolded and existed as a soluble cytoplasmic protein under normal conditions. However, under heat shock conditions, it interacted with negatively charged lipids to form helical structure and inserted into the cell membrane to increase its stability, thus protecting the cells from heat damage (Welker et al., 2010). Our data showed that though the expression of *Hsp12* does not improve the engineered strain's reproductive capacity, it improved its cell viability under stress conditions. In yeast cells, negatively charged lipids, such as phospholipid inositol, are the main components of the membrane surface, accounting for about 20%–25% of the total lipid content (Welker et al., 2010). Therefore, the expression of *Hsp12* may stabilize cell membranes by regulating cell membrane fluidity at 35°C.

DCFH-DA is a commonly applied fluorometric probe for measuring oxidative stress. DCFH-DA penetrates the cells and is hydrolyzed to the DCFH carboxylate anion, thus forming dichlorofluorescein (DCF), which has fluorescence relevant to oxidation levels in the cells (Yılancıoğlu et al., 2014). To confirm whether these heat-resistant gene vehicles improved the antioxidant capacity of the studied strain, we determined ROS production by DCFH-DA. As shown in Figure 2C, the relative ROS level of all the engineered strains was considerably lesser than in control. The relative ROS level was 27.47%–30.34% lower than in the control strain FOS11-pLPX-002. The overexpression of the eight heat-resistant genes reduced the ROS levels of the strains. It made *Y. lipolytica* cells resistant to oxidative damage, which might be why the engineered strains acquired thermotolerance.

3.4 Enhanced erythritol production efficiency in thermotolerant-engineered strains

Erythritol is broadly applied in food and pharmaceuticals productions as it does not stimulate insulin production and produces fewer calories than conventional sugar (Carly et al., 2017; Janek et al., 2017). Several research teams have achieved great success in engineering *Y. lipolytica* strains capable of efficiently producing sugar alcohols (Mirończuk et al., 2017; Cheng et al., 2018; Mirończuk et al., 2019; Fickers et al., 2020). However, these yeast strains grew best at relatively low temperatures of 28°C–30°C (Gemperlein et al., 2019). Higher fermentation temperatures endangered them by inhibiting the functions of enzymes involved in PPP, which is responsible for erythritol synthesis (Fang et al., 2011). Consequently, increasing the thermotolerance of *Y. lipolytica,* even with several degrees, is of enormous advantage for effective erythritol production.

The above-discussed results showed that the heat resistance of the eight engineered strains had been improved. Because of this, we studied the erythritol production effectiveness of these engineered strains at 35°C. As shown in Figure 3; Table 2, these transformed strains had increased erythritol production compared to the control strain FOS11-pLPX-002. Significantly, the erythritol titer, yield and productivity of the strain FOS11-Ctt1 were improved to 39.25 g/L, 0.348 g/g glucose, and 0.55 g/L/h. This increased by 156%, 86% and 161%, respectively. For FOS11-San1, these parameters were equal to 29.95 g/L, 0.307 g/g glucose, and 0.42 g/L h, which was an estimated increase of 95%, 64%, and 100%, respectively. For FOS11-Hsp10, we had 31.58 g/L, 0.338 g/g glucose, and 0.44 g/L h, which increased by 106%, 81%, and 110%, respectively.

We also compared the intracellular ROS levels of the engineered and control strains at 27 h of fermentation (exponential growth phase, Supplementary Figure S2). As shown in Figure 4, the strains' relative ROS level was lower compared to the control strain. These results were consistent with previous assay data and suggested that the lower ROS level caused by the introduction of thermo-tolerant devices favoured the erythritol production of *Y. lipolytica*. We also evaluated the erythritol production capacity of the strains at 30°C. As shown in Supplementary Figure S1, there was little difference between the engineered strains and the control. This meant that the introduction of these heat-resistant devices had no effect on the erythritol production efficiency of the strain under average temperatures and further confirmed the acquired thermotolerance and enhanced erythritol production was the result of the expression of heat-resistant devices.

Previous study has shown that Wang et al. improved the thermotolerance and the erythritol productivity of *Y. lipolytica* (Wang et al., 2020). However, they only tested the ubiquitin ligase Rsp5 from *S. cerevisiae* and the engineered strain only has an efficient production of erythritol at 33°C but not 35°C. In our study, we screened and tested thirty potential thermotolerant genes with diverse functions from different thermal preference strains. The results showed that eight proteins with different functions could improve the growth and erythritol production of *Y. lipolytica* at 35°C (Figure 5). It indicated that the co-expression of these heat-resistant genes may further improve the performance of *Y. lipolytica* under high temperature conditions, especially the three genes *Ctt1*, *San1* and *Hsp10*. In conclusion, a synthetic biology-based method was used to increase the thermotolerance of *Y. lipolytica* cells and their capacity to synthesize erythritol. This study provides a new heat-resistant device for improving the thermotolerance and erythritol biosynthetic efficiency of *Y. lipolytica*, laying the foundation for building a low-energy consumption cell factory for sugar alcohols production.

Data availability statement

The original contributions presented in the study are included in the article/Supplementary Material, further inquiries can be directed to the corresponding author.

Author contributions

PL carried out the main work, collected and analyzed the data, and drafted the manuscript. JL participated in the research. QW and ZD participated in the conception and design of the study and finalized the manuscript.

Funding

This work was supported by the National Key Research and Development Program of China (2021YFA0910600), National Natural Science Foundation of China (32161133019), Hundreds of Talents Program of the Chinese Academy of Sciences (Y0J51009) and Tianjin Synthetic Biotechnology Innovation Capacity Improvement Project (TSBICIP-CXRC-002).

Conflict of interest

The authors declare that the research was conducted in the absence of any commercial or financial relationships that could be construed as a potential conflict of interest.

Publisher's note

Supplementary material

The Supplementary Material for this article can be found online at: https://www.frontiersin.org/articles/10.3389/fbioe.2023.1108653/full#supplementary-material

References

Abbasi, A. R., Liu, J., Wang, Z., Zhao, A., Ying, H., Qu, L., et al. (2021). Recent advances in producing sugar alcohols and functional sugars by engineering *Yarrowia lipolytica*. *Front. Bioeng. Biotechnol.* 9, 648382. doi:10.3389/fbioe.2021.648382

Ahn, J., Jang, H. W., Lee, H., Choi, E., Haam, S., Oh, T. K., et al. (2003). Overexpression of thermoalkalophilic lipase from *Bacillus stearothermophilus* L1 in *Saccharomyces cerevisiae*. *J. Microbiol. Biotechnol.* 13, 451–456.

Albers, E., and Larsson, C. (2009). A comparison of stress tolerance in YPD and industrial lignocellulose-based medium among industrial and laboratory yeast strains. *J. Ind. Microbiol. Biotechnol.* 36, 1085–1091. doi:10.1007/s10295-009-0592-1

Alper, H., Moxley, J., Nevoigt, E., Fink, G. R., and Stephanopoulos, G. (2006). Engineering yeast transcription machinery for improved ethanol tolerance and production. *Sci* 314, 1565–1568. doi:10.1126/science.1131969

Carly, F., Vandermies, M., Telek, S., Steels, S., Thomas, S., Nicaud, J. M., et al. (2017). Enhancing erythritol productivity in *Yarrowia lipolytica* using metabolic engineering. *Metab. Eng.* 42, 19–24. doi:10.1016/j.ymben.2017.05.002

Cheng, H., Wang, S., Bilal, M., Ge, X., Zhang, C., Fickers, P., et al. (2018). Identification, characterization of two NADPH-dependent erythrose reductases in the yeast *Yarrowia lipolytica* and improvement of erythritol productivity using metabolic engineering. *Microb. Cell Fact.* 17, 133. doi:10.1186/s12934-018-0982-z

Costa, D. A., de Souza, C. J., Costa, P. S., Rodrigues, M., dos Santos, A. F., Lopes, M. R., et al. (2014). Physiological characterization of thermotolerant yeast for cellulosic ethanol production. *Appl. Microbiol. Biotechnol.* 98, 3829–3840. doi:10.1007/s00253-014-5580-3

Fang, N. N., Ng, A. H., Measday, V., and Mayor, T. (2011). Hul5 HECT ubiquitin ligase plays a major role in the ubiquitylation and turnover of cytosolic misfolded proteins. *Nat. Cell. Biol.* 13, 1344–1352. doi:10.1038/ncb2343

Fickers, P., Cheng, H., and Sze Ki Lin, C. (2020). Sugar alcohols and organic acids synthesis in *Yarrowia lipolytica*: Where are we? *Microorganisms* 8, 574. doi:10.3390/microorganisms8040574

Gao, L., Liu, Y., Sun, H., Li, C., Zhao, Z., and Liu, G. (2016). Advances in mechanisms and modifications for rendering yeast thermotolerance. *J. Biosci. Bioeng.* 121, 599–606. doi:10.1016/j.jbiosc.2015.11.002

Gemperlein, K., Dietrich, D., Kohlstedt, M., Zipf, G., Bernauer, H. S., Wittmann, C., et al. (2019). Polyunsaturated fatty acid production by *Yarrowia lipolytica* employing designed myxobacterial PUFA synthases. *Nat. Commun.* 10, 4055. doi:10.1038/s41467-019-12025-8

Gómez-Pastor, R., Pérez-Torrado, R., Cabiscol, E., Ros, J., and Matallana, E. (2010). Reduction of oxidative cellular damage by overexpression of the thioredoxin *TRX2* gene improves yield and quality of wine yeast dry active biomass. *Microb. Cell Fact.* 12, 9. doi:10.1186/1475-2859-9-9

Hiltunen, J. K., Mursula, A. M., Rottensteiner, H., Wierenga, R. K., Kastaniotis, A. J., and Gurvitz, A. (2003). The biochemistry of peroxisomal β-oxidation in the yeast *Saccharomyces cerevisiae*. *FEMS Microbiol.* 27, 35–64. doi:10.1016/S0168-6445(03)00017-2

Holkenbrink, C., Dam, M. I., Kildegaard, K. R., Beder, J., Dahlin, J., Doménech Belda, D., et al. (2018). EasyCloneYALI: CRISPR/Cas9-eased synthetic toolbox for engineering of the yeast *Yarrowia lipolytica*. *Biotechnol. J.* 13, 1700543. doi:10.1002/biot.201700543

Ibarra, R., Sandoval, D., Fredrickson, E. K., Gardner, R. G., and Kleiger, G. (2016). The San1 ubiquitin ligase functions preferentially with ubiquitin-conjugating enzyme Ubc1 during protein quality control. *J. Biol. Chem.* 291, 18778–18790. doi:10.1074/jbc.M116.737619

Janek, T., Dobrowolski, A., Biegalska, A., and Mirończuk, A. M. (2017). Characterization of erythrose reductase from *Yarrowia lipolytica* and its influence on erythritol synthesis. *Microb. Cell Fact.* 16, 118. doi:10.1186/s12934-017-0733-6

Jira, J., Rezek, B., Kriha, V., Artemenko, A., Matolínová, I., Skakalova, V., et al. (2018). Inhibition of *E. coli* growth by nanodiamond and graphene oxide enhanced by Luria-Bertani medium. *Nanomater. (Basel).* 8, 140. doi:10.3390/nano8030140

Konzock, O., and Norbeck, J. (2020). Deletion of MHY1 abolishes hyphae formation in *Yarrowia lipolytica* without negative effects on stress tolerance. *PloS One* 15, 0231161. doi:10.1371/journal.pone.0231161

Kwolek-Mirek, M., and Zadrag-Tecza, R. (2014). Comparison of methods used for assessing the viability and vitality of yeast cells. *FEMS yeast. Res.* 14, 1068–1079. doi:10.1111/1567-1364.12202

Laksanalamai, P., Whitehead, T. A., and Robb, F. T. (2004). Minimal protein-folding systems in *hyperthermophilic archaea*. *Nat. Rev. Microbiol.* 2, 315–324. doi:10.1038/nrmicro866

Liu, Y., Lin, Y., Guo, Y., Wu, F., Zhang, Y., Qi, X., et al. (2021). Stress tolerance enhancement via SPT15 base editing in *Saccharomyces cerevisiae*. *Biotechnol. Biofuels.* 14, 155. doi:10.1186/s13068-021-02005-w

Liu, Y., Zhang, G., Sun, H., Sun, X., Jiang, N., Rasool, A., et al. (2014). Enhanced pathway efficiency of *Saccharomyces cerevisiae* by introducing thermo-tolerant devices. *Bioresour. Technol.* 170, 38–44. doi:10.1016/j.biortech.2014.07.063

Luan, G., Dong, H., Zhang, T., Lin, Z., Zhang, Y., Li, Y., et al. (2014). Engineering cellular robustness of microbes by introducing the GroESL chaperonins from extremophilic bacteria. *J. Biotechnol.* 178, 38–40. doi:10.1016/j.jbiotec.2014.03.010

Martins, D., Nguyen, D., and English, A. M. (2019). Ctt1 catalase activity potentiates antifungal azoles in the emerging opportunistic pathogen *Saccharomyces cerevisiae*. *Sci. Rep.* 9, 9185. doi:10.1038/s41598-019-45070-w

Mason, A. B., Allen, K. E., and Slayman, C. W. (2014). C-terminal truncations of the *Saccharomyces cerevisiae* PMA1 H^+-ATPase have major impacts on protein conformation, trafficking, quality control, and function. *Eukaryot. Cell.* 13, 43–52. doi:10.1128/EC.00201-13

Mirończuk, A. M., Biegalska, A., and Dobrowolski, A. (2017). Functional overexpression of genes involved in erythritol synthesis in the yeast *Yarrowia lipolytica*. *Biotechnol. Biofuels.* 10, 77. doi:10.1186/s13068-017-0772-6

Mirończuk, A. M., Kosiorowska, K. E., Biegalska, A., Rakicka-Pustułka, M., Szczepańczyk, M., and Dobrowolski, A. (2019). Heterologous overexpression of bacterial hemoglobin VHb improves erythritol biosynthesis by yeast Yarrowia lipolytica. Microbial. *Cell Factories* 18, 1–8. doi:10.1186/s12934-019-1231-9

Morano, K. A., Grant, C. M., and Moye-Rowley, W. S. (2012). The response to heat shock and oxidative stress in *Saccharomyces cerevisiae*. *Genetics* 190, 1157–1195. doi:10.1534/genetics.111.128033

Qiu, X., Gu, Y., Du, G., Zhang, J., Xu, P., and Li, J. (2021). Conferring thermotolerant phenotype to wild-type *Yarrowia lipolytica* improves cell growth and erythritol production. *Biotechnol. Bioeng.* 118, 3117–3127. doi:10.1002/bit.27835

Qiu, X., Xu, P., Zhao, X., Du, G., Zhang, J., and Li, J. (2020). Combining genetically-encoded biosensors with high throughput strain screening to maximize erythritol production in *Yarrowia lipolytica*. *Metab. Eng.* 60, 66–76. doi:10.1016/j.ymben.2020.03.006

Rosenbaum, J. C., Fredrickson, E. K., Oeser, M. L., Garrett-Engele, C. M., Locke, M. N., Richardson, L. A., et al. (2011). Disorder targets misorder in nuclear quality control degradation: A disordered ubiquitin ligase directly recognizes its misfolded substrates. *Mol. Cell.* 41, 93–106. doi:10.1016/j.molcel.2010.12.004

Ross, M. (2018). *Erythritol market size, shares-global industry revenue by top key companies*. Maharashtra: Report Hive Research.

Sanchez, Y., Taulien, J., Borkovich, K. A., and Lindquist, S. (1992). Hsp104 is required for tolerance to many forms of stress. *EMBO J.* 11, 2357–2364. doi:10.1002/j.1460-2075.1992.tb05295.x

Schenk, C., Schulz, V., Rosch, A., and von Wallbrunn, C. (2017). Less cooling energy in wine fermentation–A case study in mathematical modeling, simulation

and optimization. *Food. Bioprod. process.* 103, 131–138. doi:10.1016/J.FBP.2017.04.001

Shahsavarani, H., Sugiyama, M., Kaneko, Y., Chuenchit, B., and Harashima, S. (2012). Superior thermotolerance of *Saccharomyces cerevisiae* for efficient bioethanol fermentation can be achieved by overexpression of RSP5 ubiquitin ligase. *Biotechnol. Adv.* 30, 1289–1300. doi:10.1016/j.biotechadv.2011.09.002

Vabulas, R. M., Raychaudhuri, S., Hayer-Hartl, M., and Hartl, F. U. (2010). Protein folding in the cytoplasm and the heat shock response. *Cold Spring Harb. Perspect. Biol.* 2, 004390. doi:10.1101/cshperspect.a004390

Wang, N., Chi, P., Zou, Y., Xu, Y., Xu, S., Bilal, M., et al. (2020). Metabolic engineering of *Yarrowia lipolytica* for thermoresistance and enhanced erythritol productivity. *Biotechnol. Biofuels.* 13, 176. doi:10.1186/s13068-020-01815-8

Wang, Q., Cen, Z., and Zhao, J. (2015). The survival mechanisms of thermophiles at high temperatures: An angle of omics. *Physiol. (Bethesda)* 30, 97–106. doi:10.1152/physiol.00066.2013

Welker, S., Rudolph, B., Frenzel, E., Hagn, F., Liebisch, G., Schmitz, G., et al. (2010). Hsp12 is an intrinsically unstructured stress protein that folds upon membrane association and modulates membrane function. *Mol. Cell.* 39, 507–520. doi:10.1016/j.molcel.2010.08.001

Xu, P., Qiao, K., and Stephanopoulos, G. (2017). Engineering oxidative stress defense pathways to build a robust lipid production platform in *Yarrowia lipolytica*. *Biotechnol. Bioeng.* 114, 1521–1530. doi:10.1002/bit.26285

Yılancıoğlu, K., Cokol, M., Pastirmaci, I., Erman, B., and Çetiner, S. (2014). Oxidative stress is a mediator for increased lipid accumulation in a newly isolated *Dunaliella salina* strain. *PloS One* 9, e91957. doi:10.1371/journal.pone.0091957

Zhang, Y., Zhang, X., Xu, Y., Xu, S., Bilal, M., and Cheng, H. (2022). Engineering thermotolerant *Yarrowia lipolytica* for sustainable biosynthesis of mannitol and fructooligosaccharides. *Biochem. Eng. J.* 187, 108604. doi:10.1016/j.bej.2022.108604

frontiers | Frontiers in Bioengineering and Biotechnology

TYPE Original Research
PUBLISHED 17 February 2023
DOI 10.3389/fbioe.2023.1108412

OPEN ACCESS

EDITED BY
Mingfeng Cao,
Xiamen University, China

REVIEWED BY
Yanfeng Liu,
Jiangnan University, China
Pu Mason Xue,
Amgen, United States

*CORRESPONDENCE
Chao Ye,
chaoye09@njnu.edu.cn
He Huang,
huangh@njnu.edu.cn

†These authors have contributed equally to this work

SPECIALTY SECTION
This article was submitted to Synthetic Biology, a section of the journal Frontiers in Bioengineering and Biotechnology

RECEIVED 26 November 2022
ACCEPTED 07 February 2023
PUBLISHED 17 February 2023

CITATION
Zhang Z, Guo Q, Qian J, Ye C and Huang H (2023), Construction and application of the genome-scale metabolic model of *Streptomyces radiopugnans*. *Front. Bioeng. Biotechnol.* 11:1108412. doi: 10.3389/fbioe.2023.1108412

Construction and application of the genome-scale metabolic model of *Streptomyces radiopugnans*

Zhidong Zhang[1,2†], Qi Guo[1†], Jinyi Qian[3], Chao Ye[3*] and He Huang[1,3*]

[1]College of Biotechnology and Pharmaceutical Engineering, Nanjing Technology University, Nanjing, China, [2]Institute of Microbiology, Xinjiang Academy of Agricultural Sciences, Urumqi, China, [3]School of Food Science and Pharmaceutical Engineering, Nanjing Normal University, Nanjing, China

Geosmin is one of the most common earthy-musty odor compounds, which is mainly produced by *Streptomyces*. *Streptomyces radiopugnans* was screened in radiation-polluted soil, which has the potential to overproduce geosmin. However, due to the complex cellular metabolism and regulation mechanism, the phenotypes of *S. radiopugnans* were hard to investigate. A genome-scale metabolic model of *S. radiopugnans* named *i*ZDZ767 was constructed. Model *i*ZDZ767 involved 1,411 reactions, 1,399 metabolites, and 767 genes; its gene coverage was 14.1%. Model *i*ZDZ767 could grow on 23 carbon sources and five nitrogen sources, which achieved 82.1% and 83.3% prediction accuracy, respectively. For the essential gene prediction, the accuracy was 97.6%. According to the simulation of model *i*ZDZ767, D-glucose and urea were the best for geosmin fermentation. The culture condition optimization experiments proved that with D-glucose as the carbon source and urea as the nitrogen source (4 g/L), geosmin production could reach 581.6 ng/L. Using the OptForce algorithm, 29 genes were identified as the targets of metabolic engineering modification. With the help of model *i*ZDZ767, the phenotypes of *S. radiopugnans* could be well resolved. The key targets for geosmin overproduction could also be identified efficiently.

KEYWORDS

geosmin, *Streptomyces radiopugnans*, genome-scale metabolic model, culture condition optimization, metabolic engineering

Introduction

Geosmin (trans-1,10-dimethyl-trans-9-decalol) is an irregular sesquiterpenoid of various actinomycetes and fungi, which has a distinct earthy or musty odor (Jiang et al., 2007). Geosmin is associated with the flavors in drinking water, wine, fish, and other foodstuffs. Several microorganisms, such as most *Streptomyces* (Jiang et al., 2006; Becher et al., 2020) and several species of cyanobacteria (Jiang et al., 2006; Giglio et al., 2008), myxobacteria (Dickschat et al., 2005), and fungi (Liato and Aider, 2017) can produce geosmin. *Streptomyces radiopugnans* belongs to the genus of *Streptomyces* and has been isolated from radiation-polluted soil from the Xinjiang Province in China (Mao et al., 2007). The genome of *S. radiopugnans* was sequenced in 2016 and can be accessed from the NCBI database. However, limited by the lack of experimental data, the regulation mechanism of geosmin biosynthesis was not clear in *S. radiopugnans*.

The genome-scale metabolic model (GSMM) is a mathematical model, which presents the gene-protein-reaction relationship. GSMM has been being developed for more than 20 years, since the first published GSMM of *Haemophilus influenzae* in 1999. Over 2,000 GSMMs have been published for over 1,000 organisms (Ye et al., 2022). With the increase of experimental data, some published GSMMs are continuously being improved. Some typical organisms, such as *Escherichia coli* K12 (6 GSMMs) (Ye et al., 2022), *Saccharomyces cerevisiae* S288c (12 GSMMs) (Ye et al., 2022), and *Yarrowia lipolytica* CLIB 122 (6 GSMMs) (Loira et al., 2012; Pan and Hua, 2012; Kavscek et al., 2015; Kerkhoven et al., 2016; Wei et al., 2017; Mishra et al., 2018) have more than one GSMM. Combined with different algorithms, GSMMs have been widely applied in network properties analysis, cellular phenotype prediction, metabolic engineering guidance, model-driven discovery, evolutionary process exploration, and interspecies interaction identification (Gu et al., 2019; Jansma and El Aidy, 2021; Patra et al., 2021).

In this study, based on the genome sequence of *S. radiopugnans*, a GSMM named *i*ZDZ767 was constructed. Model *i*ZDZ767 contained 1,411 reactions, 1,399 metabolites, and 767 genes. Compared with experimental data, *i*ZDZ767 could achieve 82.1% and 83.3% accuracy for the utilization of different carbon sources and nitrogen sources. In addition, the prediction accuracy of essential genes was 97.6%, compared with the DEG database (Luo et al., 2021). Then, based on *i*ZDZ767, D-glucose and urea were identified as the most suitable carbon source and nitrogen source, respectively. The experiments proved that when urea was used as nitrogen and controlled at 4 g/L, geosmin production could reach 581.6 ng/L. Finally, 29 genes (seven upregulation, six downregulation, and 16 knockout targets) were identified as potential targets, which could improve the geosmin synthesis rate using the OptForce algorithm (Ranganathan et al., 2010). This study provides new insights that could be used to investigate the phenotype of *S. radiopugnans* and identify the metabolic engineering targets for geosmin overproduction.

Materials and methods

Strain

The *S. radiopugnans* R97^T strain was screened from the contaminated radiation-contaminated area in Xinjiang, China (Mao et al., 2007).

Genome sequence

The genome sequence of *S. radiopugnans* was downloaded from the NCBI database (https://www.ncbi.nlm.nih.gov/genome/49825?genome_assembly_id=1862392). The protein sequences of *S. radiopugnans* were downloaded from the UniProt database (https://www.uniprot.org/taxonomy/403935).

Culture medium

The fermentation medium (1 L) contained 10 g/L glucose, 4 g/L yeast tract, 4 g/L K_2HPO_4, 4 g/L KH_2PO_4, and 0.5 g/L $MgSO_4$. Before cultivation, the medium pH was adjusted to 7.2 using NH_4OH (25%, v/v).

Culture condition

For shake-flask cultivation, the *S. radiopugnans* strain was first cultured on an agar plate. Then, a single colony was selected to be cultured in 50 mL fresh medium until the OD_{600} reached a value of 0.8. Finally, the strain was transferred into a 500 mL shake-flask containing 50 mL fermentation medium and cultivated at 30°C for 240 h with shaking at 200 rpm.

Determining the growth rate and glucose consumption rate

The optical density (OD) was first measured at 600 nm with a spectrophotometer. The cell dry weight was then calculated by multiplying OD_{600} by 0.36 g/L (Supplementary Figure S1) (Fischer and Sawers, 2013). The growth curve was fitted using the Logistic function of Origin software. Finally, the cell growth rate was calculated with differential values of cell dry weight (Supplementary Figure S2). Similarly, the glucose consumption rate was also calculated using Origin software, based on the experimental data (Supplementary Figure S3).

Geosmin extraction and analysis

The extraction and analysis of geosmin were followed by (Shen et al., 2021).

Prediction of optimized fermentation conditions

The robustness analysis [(controlFlux, objFlux) = robustnessAnalysis (model, controlRxn, nPoints, plotResFlag, objRxn, objType)] program was run in MATLAB to simulate the effect of the urea uptake rate on the synthesis rate of geosmin.

Hardware and software used for model construction and analysis

Detailed information is listed in Supplementary Table S1.

Results

Model construction and characteristics analysis

To construct the genome-scale metabolic model of *S. radiopugnans*, several steps were carried out. First, ModelSEED (Henry et al., 2010) and CarveME (Machado et al., 2018) were used to construct the draft model of *S. radiopugnans*. Then, based on

TABLE 1 The characteristic of model *i*ZDZ767.

Features	*i*ZDZ767	*i*AA1259
Genome features		
Genome size	6.1 Mb	8.59 Mb
Open reading frames	5,426	8,126
***In silico* metabolic model**		
Reactions included in the model	1,411	1914
Biochemical reactions	1,268	1,510
Transport reactions	73	195
Exchange reactions	70	209
Metabolites	1,399	1,471
Genes	767	1,259
ORF coverage (%)	14.1	15.1
Network characteristics		
Number of nodes	3,577	4,645
Number of edges	8,706	11427
Avg. number of neighbors	4.872	4.920
Network diameter	13	12
Network radius	7	6
Characteristic path length	4.204	4.232
Network density	0.001	0.001
Network heterogeneity	3.415	3.789
Network centralization	0.204	0.213
Connected components	2	1

the KAAS annotation (Moriya et al., 2007) results, gaps were fixed by referring to KEGG pathway maps, manually. In addition, the biomass composition of *S. radiopugnans* was identified through literature mining, which includes proteins, RNA, DNA, lipids, cell wall, and small molecules (Supplementary Material S1). Finally, the defined model was mathematized with COBRA toolbox 3.0 (Heirendt et al., 2019). The model of *S. radiopugnans* consisted of 1,411 reactions, 1,399 metabolites, and 767 genes, and was named *i*ZDZ767 (Table 1; Supplementary Material S1). Of these reactions, 88.0% were gene associated. According to the KEGG pathway maps, these reactions can be classified into 10 subsystems. Lipid metabolism, carbohydrate metabolism, and amino acid metabolism were the most common, accounting for 25.3%, 18.1%, and 16.3%, respectively (Figure 1). The gene coverage of model *i*ZDZ767 was 14.1%, which was close to the newest model *i*AA1259 of *Streptomyces coelicolor* (15.1%) (Amara et al., 2018). Cytoscape software was used to analyze the network characteristics of model *i*ZDZ767. There were 3,577 nodes and 8,706 edges in model *i*ZDZ767.

Model verification

Based on the minimal culture medium, model *i*ZDZ767 was used to simulate whether 28 carbon sources and 6 nitrogen sources could be utilized. For carbon sources, model *i*ZDZ767 achieved 82.1% (23/28) correction. For the nitrogen sources, there was 83.3% (5/6) agreement with the experimental results, which could not grow with L-Cysteine as the sole nitrogen source (Table 2). In addition, the simulated maximum growth rate (μ_{max}) was 0.131 h^{-1}, which was only 4.4% lower than the measured growth rate (0.137 h^{-1}, Supplementary Figure S2). The essentialities of individual genes of *S. radiopugnans* were analyzed under minimal glucose medium conditions using *i*ZDZ767 by deleting each gene in turn. The genes were categorized into three classes: essential genes, partially essential genes, and non-essential genes. There were 84 genes identified as essential genes. These genes were further compared with the DEG database (Luo et al., 2021), and 97.6% of the predicted essential genes could be matched by sequence blast (identity ≥30%,

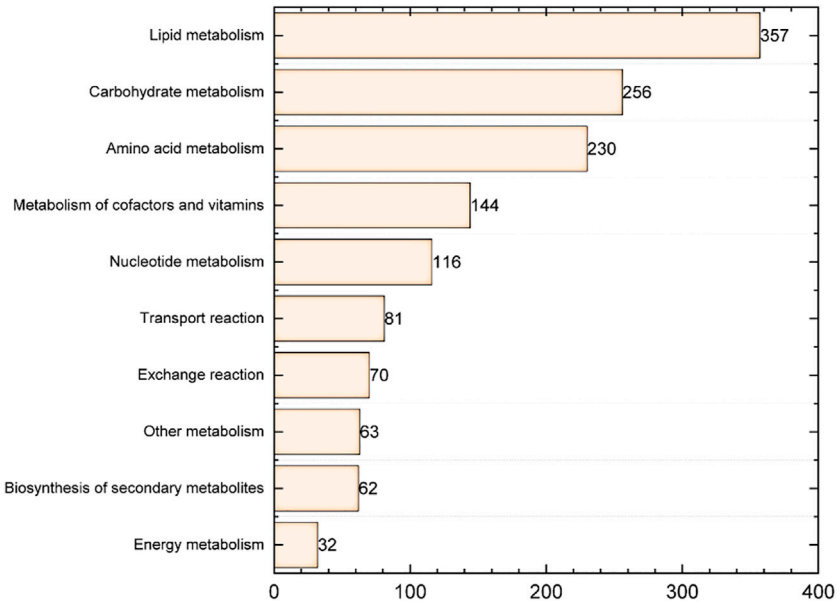

FIGURE 1
The response distribution of the metabolic subsystem in model *i*ZDZ767.

TABLE 2 The utilization of different carbon and nitrogen sources.

Characteristics	*In vivo*	*In silico*	References
Growth on sole carbon sources			
D-glucose	+	+	(Zhu et al., 2011)
D-Fructose	+	+	(Zhu et al., 2011)
Raffinose	+	+	(Zhu et al., 2011)
L-Arabinose	+	+	(Zhu et al., 2011)
Mannose	+	+	(Dhamodharan et al., 2019)
Lactose	+	+	(Dhamodharan et al., 2019)
Trehalose	+	+	(Dhamodharan et al., 2019)
Melibiose	−	+	(Dhamodharan et al., 2019)
Acetate	+	−	(Dhamodharan et al., 2019)
Inositol	−	−	(Mao et al., 2007)
Mannitol	+	+	(Mao et al., 2007)
L-Rhamnose	+	+	(Mao et al., 2007)
Sucrose	+	+	(Mao et al., 2007)
Xylitol	+	+	(Mao et al., 2007)
D-xylose	+	+	(Mao et al., 2007)
Citrate	+	+	(Mao et al., 2007)
L-Arginine	+	+	(Dhamodharan et al., 2019)
L-Alanine	+	+	(Dhamodharan et al., 2019)
L-Aspartate	+	+	(Dhamodharan et al., 2019)
Glycine	+	+	(Dhamodharan et al., 2019)
L-Histidine	−	+	(Dhamodharan et al., 2019)
L-Lysine	+	+	(Dhamodharan et al., 2019)
L-phenylalanine	+	+	(Dhamodharan et al., 2019)
L-Tryptophan	+	−	(Dhamodharan et al., 2019)
L-Methionine	+	−	(Dhamodharan et al., 2019)
L-Isoleucine	−	−	(Dhamodharan et al., 2019)
L-Valine	−	−	(Dhamodharan et al., 2019)
L-Asparagine	−	−	(Dhamodharan et al., 2019)
Growth on sole nitrogen sources			
NH_4^+	+	+	This study
KNO_3	+	+	This study
Urea	+	+	This study
L-Cysteine	+	−	(Mao et al., 2007)
L-phenylalanine	+	+	(Santhanam et al., 2012)
L-Threonine	+	+	(Santhanam et al., 2012)

e-value ≤ 1e-6, Supplementary Material S2). These results proved that model *i*ZDZ767 could predict the phenotype of *S. radiopugnans* well.

The optimization of culture condition with *i*ZDZ767

The carbon source was a key factor for cell growth and product synthesis. Using model *i*ZDZ767, the effect of different carbon sources, such as D-glucose, D-Fructose, Mannose, L-Rhamnose, and D-xylose was predicted. Of these selected carbon sources, D-glucose was the most suitable, the GPR was 2.04 mmol/gDW/h (Figure 2A). The experimental results show that when D-glucose was used as a carbon source, the yield of geosmin was 317.5 ng/L, which was higher than others (Figure 2B). Similarly, three types of nitrogen sources were used for simulation. The model predicted that when urea was used as a nitrogen source, the GPR was 3.03 mmol/gDW/h, which was 48.9% and 50.7% higher than NH_4^+ and NO_3^- (Figure 3A). Compared with the experiments, the geosmin yield was 435.1 ng/L, which agreed with the simulation (Figure 3B). In addition, a robustness analysis algorithm was used to analyze the effect of the urea uptake rate on the geosmin production rate. The simulated results showed that with the increase in the urea uptake rate, the GPR would first increase to the maximum value, then remain stable until the urea uptake rate was over 500 mmol/gDW/h. Finally, the GPR would decrease to 0, which means that the suitable urea uptake rate should be 88.38 mmol/gDW/h (Figure 3C). When we controlled the addition of urea at different levels, the experiment results proved that 4 g/L urea could achieve a maximum geosmin production of 581.6 ng/L (Figure 3D).

Identification of the potential geosmin overproduction targets with *i*ZDZ767

To identify potential targets for the improvement of geosmin production, the OptForce algorithm was used (Ranganathan et al., 2010). According to the predicted results, a total of 29 genes were identified as the targets, including seven upregulation, six downregulation, and 16 knockout targets (Supplementary Material S3). According to the function of each gene, these targets can be classified into four types: precursor accumulation, geosmin biosynthesis, by-product elimination, and energy supplement. For the geosmin synthesis pathway, the *geoA* gene, which encodes geosmin synthase, catalyzing the synthesis of geosmin from farnesyl diphosphate, should be upregulated (Shen et al., 2021). For by-product elimination, to accumulate more geosmin, the *acnA* gene (Aconitate hydratase A) should be downregulated to decrease the carbon flux of the TCA cycle (Figure 4). Similarly, the *fabD* gene [(acyl-carrier-protein) S-malonyltransferase] should also be downregulated to limit the flux of fatty acids synthesis. For energy supplements, the *nuo* gene (NADH-quinone oxidoreductase) was predicted to be knocked out so that more NADH could be supplied for geosmin synthesis.

Discussion

Geosmin is a common pollutant and is widely recognized by the public, but this is not the case when studying some biological systems and organisms. Toxicological studies have shown that a certain concentration of geosmin could inhibit the growth of *Salmonella typhimurium* and sea urchin embryos (Dionigi et al., 1993; Nakajima et al., 1996). This provides a new direction for the study of how to inhibit pathogens. At the same time, researchers have also found that geosmin has a potential effect on genotoxicity. Geosmin is only mildly toxic at extremely high concentrations, far exceeding the actual level in the environment (Silva et al., 2015). Some researchers have found that geosmin, at a concentration of 50–5000 ng/L, can increase the body length and change the growth-related genes of zebrafish (Zhou et al., 2020).

S. radiopugnans can be screened from radiation-contaminated soil and, although not widely studied, are capable of producing geosmin in large quantities. However, phenotypes of *S.*

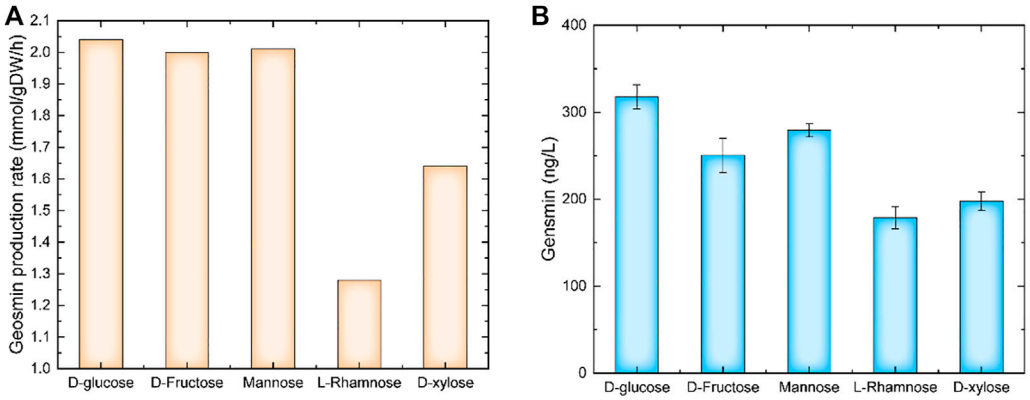

FIGURE 2
The effect of carbon sources on geosmin production. **(A)** Simulation results of different carbon sources. **(B)** Experimental results of different carbon sources.

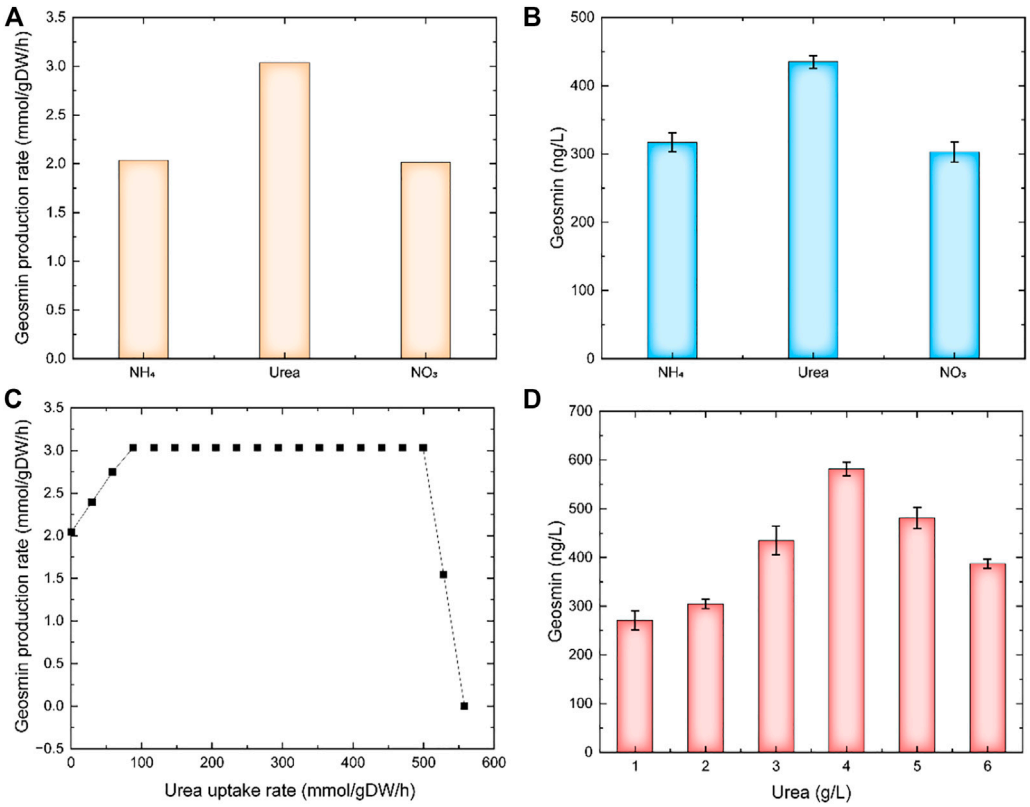

FIGURE 3
The effect of nitrogen sources on geosmin production. **(A)** simulation results of different nitrogen sources. **(B)** Experimental results of different nitrogen sources. **(C)** Robustness analysis results of urea uptake rate. **(D)** Effect of urea concentration on geosmin production.

radiopugnans are difficult to study due to their complex cellular metabolism and regulatory mechanisms. Therefore, by manually refining the first genome-scale metabolic network model (*i*ZDZ767) of *S. radiopugnans*, we analyzed the synthesis mechanism of geosmin and identified the key targets of geosmin synthesis based on the model, which provided a basis for further study of the synthesis of geosmin and the internal mechanism of *S. radiopugnans*.

Traditional model construction methods are mainly divided into automatic construction and manual construction. Among them, automatic construction automatically obtains the GSMM of the target strain or plant by uploading the genomic data to the

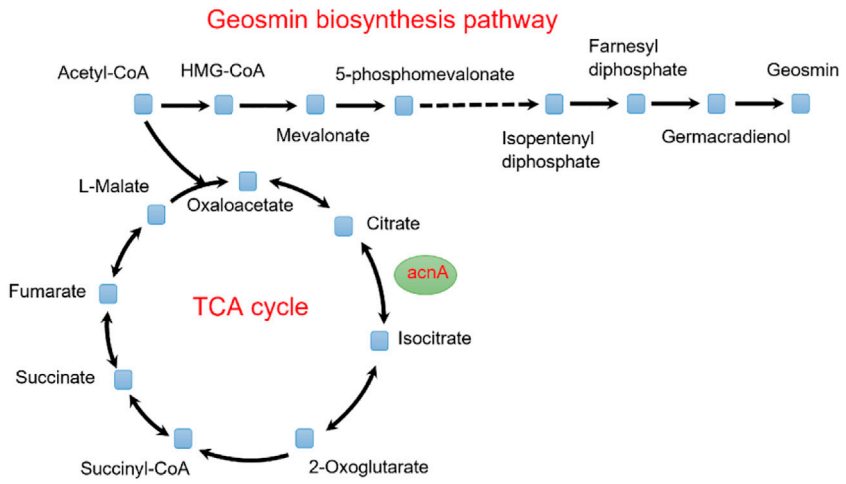

FIGURE 4
Effect of the TCA cycle on the synthesis of geosmin.

existing tools. To date, researchers have developed many tools, such as ModelSEED (Flowers et al., 2018; Seaver et al., 2021), COBRA (Dal'molin et al., 2014; King et al., 2015), and RAVEN (Wang et al., 2018), for the automatic construction of models. The advantage of this construction method is that the model can be built in a short time, but the accuracy of the model is low and its applicability is not strong. The manual construction of this method mainly depends on the results of genome annotation, combined with the metabolic pathway of KEGG, it collates information, such as the genes and metabolites of each reaction, and manually adds it to the model. Considering the problems of traditional modeling methods, we used a semi-automatic modeling method. This method integrates the first two methods, first obtaining a coarse model through the automated construction tool, then manually refining the model so that a more accurate model can be obtained. Based on the automatic construction of the ModelSEED database and CarveME (Machado et al., 2018), combined with the complete metabolic pathway in KEGG, we added the missing reaction to the model and added the known metabolic pathway of geosmin to the model and, thus, manually refined a genome-scale metabolic network model of *S. radiopugnans*. Based on model *i*ZDZ767, a series of strategies for improving geosmin were proposed. Although *S. radiopugnans* can make good use of microbial fermentation to produce geosmin, its metabolic network is complex, and the fermentation experiment period is long. It depends on repeated experiments to increase the production of geosmin, and the economic cost is high. Model *i*ZDZ767 can predict the effects of carbon and nitrogen sources on the synthesis rate of geosmin well and provide directions for optimizing the culture conditions of *S. radiopugnans*. At the same time, the model is used to analyze the algorithm to predict the key targets for improving the geosmin synthesis rate. Through the analysis of these key targets, we found that the key reactions affecting the synthesis of geosmin are mainly divided into two types. One type of reaction is related to the synthesis of geosmin itself, while the other is related to the growth and reproduction of *S. radiopugnans*. No matter which type of reaction is upregulated, downregulated, or knocked out, the synthesis of geosmin can be effectively improved. Although the effectiveness of these regulation methods has not been proven, they provide the opportunity to study geosmin production by fermentation. In summary, model *i*ZDZ767 is a powerful tool for analyzing and predicting the metabolic pathways and yields of various products in *S. radiopugnans*, which provides convenient conditions for us to study *S. radiopugnans* in the field of systems biology.

Data availability statement

Publicly available datasets were analyzed in this study. This data can be found here: https://www.uniprot.org/taxonomy/403935.

Author contributions

ZZ constructed the model and wrote this manuscript. QG analyzed data and drew figures. JQ answered the reviewers' questions. CY and HH proof-read the manuscript. All authors have read and approved the final manuscript.

Funding

This work was supported by the National Natural Science Foundation of China (32060004), the Xinjiang Academy of Agricultural Sciences Science and technology innovation key cultivation project (xjkcpy-2021002, xjkcpy-2022004), the Third Xinjiang Scientific Expedition Program (2022xjkk1200), and the "Outstanding Youth Fund" of Xinjiang Natural Science Foundation (2022D01E19).

Conflict of interest

The authors declare that the research was conducted in the absence of any commercial or financial relationships that could be construed as a potential conflict of interest.

Publisher's note

All claims expressed in this article are solely those of the authors and do not necessarily represent those of their affiliated organizations, or those of the publisher, the editors and the reviewers. Any product that may be evaluated in this article, or claim that may be made by its manufacturer, is not guaranteed or endorsed by the publisher.

Supplementary material

The Supplementary Material for this article can be found online at: https://www.frontiersin.org/articles/10.3389/fbioe.2023.1108412/full#supplementary-material

References

Amara, A., Takano, E., and Breitling, R. (2018). Development and validation of an updated computational model of *Streptomyces coelicolor* primary and secondary metabolism. *BMC Genomics* 19, 519. ARTN 519. doi:10.1186/s12864-018-4905-5

Becher, P. G., Verschut, V., Bibb, M. J., Bush, M. J., Molnar, B. P., Barane, E., et al. (2020). Developmentally regulated volatiles geosmin and 2-methylisoborneol attract a soil arthropod to *Streptomyces* bacteria promoting spore dispersal. *Nat. Microbiol.* 5 (6), 821–829. doi:10.1038/s41564-020-0697-x

Dal'molin, C. G. O., Quek, L-E., Palfreyman, R. W., and Nielsen, L. K. (2014). Plant genome-scale modeling and implementation. *Methods Mol. Biol. Clift. NJ)* 1090, 317–332. doi:10.1007/978-1-62703-688-7_19

Dhamodharan, D., Naine, S. J., Keziah, S. M., and Devi, C. S. (2019). Novel fibrinolytic protease producing *Streptomyces radiopugnans* VITSD8 from marine sponges. *Mar. Drugs* 17 (3), 164. ARTN 164. doi:10.3390/md17030164

Dickschat, J. S., Bode, H. B., Mahmud, T., Muller, R., and Schulz, S. (2005). A novel type of geosmin biosynthesis in myxobacteria. *J. Org. Chem.* 70 (13), 5174–5182. doi:10.1021/jo050449g

Dionigi, C. P., Lawlor, T. E., Mcfarland, J. E., and Johnsen, P. B. J. W. R. (1993). Evaluation of geosmin and 2-methylisoborneol on the histidine dependence of TA98 and TA100 *Salmonella typhimurium* tester strains. *Water Res.* 27 (11), 1615–1618. doi:10.1016/0043-1354(93)90125-2

Flowers, J. J., Richards, M. A., Baliga, N., Meyer, B., and Stahl, D. A. (2018). Constraint-based modelling captures the metabolic versatility of Desulfovibrio vulgaris. *Environ. Microbiol. Rep.* 10 (2), 190–201. doi:10.1111/1758-2229.12619

Giglio, S., Jiang, J. Y., Saint, C. P., Cane, D. E., and Monis, P. T. (2008). Isolation and characterization of the gene associated with geosmin production in *cyanobacteria*. *Environ. Sci. Technol.* 42 (21), 8027–8032. doi:10.1021/es801465w

Gu, C., Kim, G. B., Kim, W. J., Kim, H. U., and Lee, S. Y. (2019). Current status and applications of genome-scale metabolic models. *Genome Biol.* 20 (1), 121. doi:10.1186/s13059-019-1730-3

Heirendt, L., Arreckx, S., Pfau, T., Mendoza, S. N., Richelle, A., Heinken, A., et al. (2019). Creation and analysis of biochemical constraint-based models using the COBRA Toolbox v.3.0. *Nat. Protoc.* 14 (3), 639–702. doi:10.1038/s41596-018-0098-2

Henry, C. S., DeJongh, M., Best, A. A., Frybarger, P. M., Linsay, B., and Stevens, R. L. (2010). High-throughput generation, optimization and analysis of genome-scale metabolic models. *Nat. Biotechnol.* 28 (9), 977–982. doi:10.1038/nbt.1672

Jansma, J., and El Aidy, S. (2021). Understanding the host-microbe interactions using metabolic modeling. *Microbiome* 9 (1), 16. ARTN 16. doi:10.1186/s40168-020-00955-1

Jiang, J. Y., He, X. F., and Cane, D. E. (2007). Biosynthesis of the earthy odorant geosmin by a bifunctional *Streptomyces coelicolor* enzyme. *Nat. Chem. Biol.* 3 (11), 711–715. doi:10.1038/nchembio.2007.29

Jiang, J. Y., He, X. F., and Cane, D. E. (2006). Geosmin biosynthesis. *Streptomyces coelicolor* germacradienol/germacrene D synthase converts farnesyl diphosphate to geosmin. *J. Am. Chem. Soc.* 128 (25), 8128–8129. doi:10.1021/ja062669x

Kavscek, M., Bhutada, G., Madl, T., and Natter, K. (2015). Optimization of lipid production with a genome-scale model of *Yarrowia lipolytica*. *BMC Syst. Biol.* 9, 72. ARTN 72. doi:10.1186/s12918-015-0217-4

Kerkhoven, E. J., Pomraning, K. R., Baker, S. E., and Nielsen, J. (2016). Regulation of amino-acid metabolism controls flux to lipid accumulation in *Yarrowia lipolytica*. *NPJ Syst. Biol. Appl.* 2, 16005. ARTN 16005. doi:10.1038/npjsba.2016.5

King, Z. A., Lloyd, C. J., Feist, A. M., and Palsson, B. O. (2015). Next-generation genome-scale models for metabolic engineering. *Curr. Opin. Biotechnol.* 35, 23–29. doi:10.1016/j.copbio.2014.12.016

Liato, V., and Aider, M. (2017). Geosmin as a source of the earthy-musty smell in fruits, vegetables and water: Origins, impact on foods and water, and review of the removing techniques. *Chemosphere* 181, 9–18. doi:10.1016/j.chemosphere.2017.04.039

Loira, N., Dulermo, T., Nicaud, J. M., and Sherman, D. J. (2012). A genome-scale metabolic model of the lipid-accumulating yeast *Yarrowia lipolytica*. *BMC Syst. Biol.* 6 (1), 35. doi:10.1186/1752-0509-6-35

Luo, H., Lin, Y., Liu, T., Lai, F. L., Zhang, C. T., Gao, F., et al. (2021). DEG 15, an update of the Database of Essential Genes that includes built-in analysis tools. *Nucleic Acids Res.* 49 (D1), D677–D686. doi:10.1093/nar/gkaa917

Machado, D., Andrejev, S., Tramontano, M., and Patil, K. R. (2018). Fast automated reconstruction of genome-scale metabolic models for microbial species and communities. *Nucleic Acids Res.* 46 (15), 7542–7553. doi:10.1093/nar/gky537

Mao, J., Tang, Q. Y., Zhang, Z. D., Wang, W., Wei, D., Huang, Y., et al. (2007). *Streptomyces radiopugnans* sp nov., a radiation-resistant actinomycete isolated from radiation-polluted soil in China. *Int. J. Syst. Evol. Microbiol.* 57, 2578–2582. doi:10.1099/ijs.0.65027-0

Mishra, P., Lee, N. R., Lakshmanan, M., Kim, M., Kim, B. G., and Lee, D. Y. (2018). Genome-scale model-driven strain design for dicarboxylic acid production in *Yarrowia lipolytica*. *BMC Syst. Biol.* 12, 12. ARTN 12. doi:10.1186/s12918-018-0542-5

Moriya, Y., Itoh, M., Okuda, S., Yoshizawa, A. C., and Kanehisa, M. (2007). Kaas: An automatic genome annotation and pathway reconstruction server. *Nucleic Acids Res.* 35, W182–W185. doi:10.1093/nar/gkm321

Nakajima, M., Ogura, T., Kusama, Y., Iwabuchi, N., Imawaka, T., Araki, A., et al. (1996). Inhibitory effects of odor substances, geosmin and 2-methylisoborneol, on early development of sea urchins. *early Dev. sea urchins* 30 (10), 2508–2511. doi:10.1016/0043-1354(96)00104-2

Pan, P., and Hua, Q. (2012). Reconstruction and *in silico* analysis of metabolic network for an oleaginous yeast, *Yarrowia lipolytica*. *Plos One* 7 (12), e51535. doi:10.1371/journal.pone.0051535

Patra, P., Das, M., Kundu, P., and Ghosh, A. (2021). Recent advances in systems and synthetic biology approaches for developing novel cell-factories in non-conventional yeasts. *Biotechnol. Adv.* 47, 107695. ARTN 107695. doi:10.1016/j.biotechadv.2021.107695

Ranganathan, S., Suthers, P. F., and Maranas, C. D. (2010). OptForce: An optimization procedure for identifying all genetic manipulations leading to targeted overproductions. *PLoS Comp. Biol.* 6 (4), e1000744. ARTN e1000744. doi:10.1371/journal.pcbi.1000744

Santhanam, R., Okoro, C. K., Rong, X. Y., Huang, Y., Bull, A. T., Weon, H. Y., et al. (2012). *Streptomyces atacamensis* sp nov., isolated from an extreme hyper-arid soil of the Atacama Desert, Chile. *Int. J. Syst. Evol. Microbiol.* 62, 2680–2684. doi:10.1099/ijs.0.038463-0

Seaver, S. M. D., Liu, F., Zhang, Q. Z., Jeffryes, J., Faria, J. P., Edirisinghe, J. N., et al. (2021). The ModelSEED Biochemistry Database for the integration of metabolic annotations and the reconstruction, comparison and analysis of metabolic models for plants, fungi and microbes. *Nucleic Acids Res.* 49 (D1), D575–D588. doi:10.1093/nar/gkaa746

Shen, Q. Y., Shimizu, K., Miao, H. C., Tsukino, S., Utsumi, M., Lei, Z. F., et al. (2021). Effects of elevated nitrogen on the growth and geosmin productivity of *Dolichospermum smithii*. *Environ. Sci. Pollut. R.* 28 (1), 177–184. doi:10.1007/s11356-020-10429-4

Silva, A. F., Lehmann, M., and Dihl, R. R. (2015). Geosmin induces genomic instability in the mammalian cell microplate-based comet assay. *Environ. Sci. Pollut. Res.* 22 (21), 17244–17248. doi:10.1007/s11356-015-5381-y

Wang, H., Marcisauskas, S., Sanchez, B. J., Domenzain, I., Hermansson, D., Agren, R., et al. (2018). Raven 2.0: A versatile toolbox for metabolic network reconstruction and a case study on Streptomyces coelicolor. *Plos Comput. Biol.* 14 (10), e1006541. doi:10.1371/journal.pcbi.1006541

Wei, S. S., Jian, X. X., Chen, J., Zhang, C., and Hua, Q. (2017). Reconstruction of genome-scale metabolic model of *Yarrowia lipolytica* and its application in overproduction of triacylglycerol. *Bioresour. Bioprocess* 4, 51. ARTN 51. doi:10.1186/s40643-017-0180-6

Ye, C., Wei, X. Y., Shi, T. Q., Sun, X. M., Xu, N., Gao, C., et al. (2022). Genome-scale metabolic network models: From first-generation to next-generation. *Appl. Microbiol. Biotechnol.* 106 (13-16), 4907–4920. doi:10.1007/s00253-022-12066-y

Zhou, W. C., Wang, J. L., Zhang, J. L., Peng, C. R., Li, G. B., and Li, D. H. (2020). Environmentally relevant concentrations of geosmin affect the development, oxidative stress, apoptosis and endocrine disruption of embryo-larval zebrafish. *Sci. Total Environ.* 735, 139373. doi:10.1016/j.scitotenv.2020.139373

Zhu, H. H., Jiang, S. M., Yao, Q., Wang, Y. H., Chen, M. B., Chen, Y. L., et al. (2011). *Streptomyces fenghuangensis* sp nov., isolated from seawater. *Int. J. Syst. Evol. Microbiol.* 61, 2811–2815. doi:10.1099/ijs.0.029280-0

frontiers | Frontiers in Bioengineering and Biotechnology

TYPE Perspective
PUBLISHED 10 March 2023
DOI 10.3389/fbioe.2023.1105277

OPEN ACCESS

EDITED BY
Boyang Ji,
BioInnovation Institute (BII), Denmark

REVIEWED BY
Guoqiang Zhang,
Jiangnan University, China
Mingtao Huang,
South China University of Technology, China
Xiaowei Li,
Chalmers University of Technology, Sweden

*CORRESPONDENCE
Yuetong Wang,
wangyt@nnu.edu.cn
He Huang,
huangh@njnu.edu.cn

†These authors have contributed equally to this work

SPECIALTY SECTION
This article was submitted to Synthetic Biology, a section of the journal Frontiers in Bioengineering and Biotechnology

RECEIVED 22 November 2022
ACCEPTED 17 February 2023
PUBLISHED 10 March 2023

CITATION
Zhang Z, Guo Q, Wang Y and Huang H (2023), High-throughput screening of microbial strains in large-scale microfluidic droplets.
Front. Bioeng. Biotechnol. 11:1105277.
doi: 10.3389/fbioe.2023.1105277

High-throughput screening of microbial strains in large-scale microfluidic droplets

Zhidong Zhang[1,2,3†], Qi Guo[1,2†], Yuetong Wang[2*] and He Huang[1,2*]

[1]College of Biotechnology and Pharmaceutical Engineering, Nanjing Tech University, Nanjing, China, [2]School of Food Science and Pharmaceutical Engineering, Nanjing Normal University, Nanjing, China, [3]Institute of Applied Microbiology, Xinjiang Academy of Agricultural Sciences/ Xinjiang Laboratory of Special Environmental Microbiology, Urumqi, Xinjiang, China

The transformation of engineered microbial cells is a pivotal link in green biomanufacturing. Its distinctive research application involves genetic modification of microbial chassis to impart targeted traits and functions for effective synthesis of the desired products. Microfluidics, as an emerging complementary solution, focuses on controlling and manipulating fluid in channels at the microscopic scale. One of its subcategories is droplet-based microfluidics (DMF), which can generate discrete droplets using immiscible multiphase fluids at kHz frequencies. To date, droplet microfluidics has been successfully applied to a variety of microbes, including bacteria, yeast, and filamentous fungi, and the detection of massive metabolites of strain products, such as polypeptides, enzymes, and lipids, has been realized. In summary, we firmly believe that droplet microfluidics has evolved into a powerful technology that will pave the way for high-throughput screening of engineered microbial strains in the green biomanufacturing industry.

KEYWORDS

microfluidics, droplets, high-throughput screening, microbe, green biomanufacturing

Introduction

The continuous increase of global average atmospheric carbon dioxide has led to a serious environmental crisis, and one of the main culprits is the excessive use of fossil fuel energy. Introducing the green biomanufacturing system into traditional chemical processing, with sustainable cell factories for biofuels and commodity chemical production, has fundamentally minimized or prevented toxic pollutants and greenhouse gas emissions (Orsi et al., 2021; Yang et al., 2021). In green biomanufacturing, one pivotal link is the transformation of engineered microbial cells. Its characteristic research application involves genetic modification of microbial chassis, imparting targeted traits and functions for effective synthesis of the desired products (Guo et al., 2022). Furthermore, the rapid acquisition of target strains requires the establishment of a high-throughput screening (HTS) strategy aimed at identifying certain phenotypes such as enzyme activity and specific products yielding (Yuan et al., 2022). Currently, the most widely used screening methods employ compartmentalizing clonal populations in microtiter plate (MTP) wells, which are detected by a microplate plate reader (Böttcher et al., 2017). However, these methods commonly demand sophisticated automated instruments and time-consuming operation procedures, which limit the screening types and efficiency. Fluorescence-activated cell sorting (FACS) allows specific cell populations to be isolated from each mixture with the aid of flow cytometry. The sorting depends on cells' light-scattering or fluorescent properties,

TABLE 1 Differences of MTP, FACS, and DMF for strain screening.

Method	MTP	FACS	DMF
Detection signal	Fluorescence and absorbance	Fluorescence	Fluorescence, Raman, absorbance, and mass spectrometry.
Sensitivity	Normal	High	High
Throughput	10^6/day	10^8/h	10^8/day
References	Utharala et al. (2022)	Körfer et al. (2016)	Wang et al. (2021)

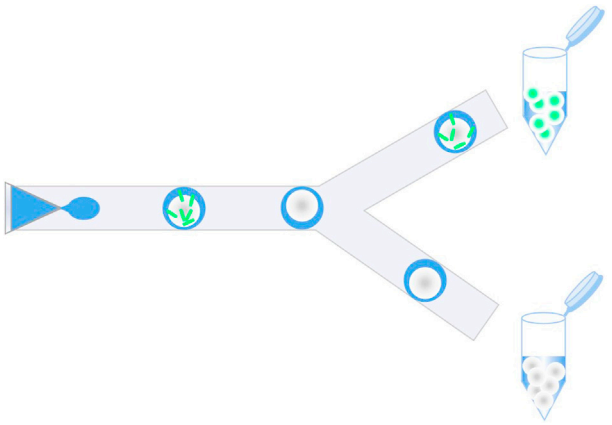

FIGURE 1
Schematic of high-throughput screening of microbial strains in microfluidic droplets, mainly including mutant library encapsulation and droplet sorting.

offering a throughput of up to 10^8 events per hour, as shown in Table 1 (Körfer et al., 2016). Standard FACS can merely capture fluorescent signals from the surface of cell membranes or intracellular products, while not from extracellular secretions.

Microfluidics, as an emerging complementary solution, focuses on controlling and manipulating fluid in channels at the microscopic scale. One of its subcategories is droplet-based microfluidics (DMF), which generates discrete droplets using immiscible multiphase fluids at kHz frequencies (Wang et al., 2021; Utharala et al., 2022). Each droplet is equivalent to a micro-reactor with a single strain encapsulated inside, thereby facilitating distinct microbial analysis without cross-contamination, as shown in Figure 1. The environment within a single droplet is similar to that of the conventional liquid medium, with sufficient oxygen supply for the growth of individual strains. DMF has revolutionized strain screening due to its ability to precisely handle fluids at length scales comparable to cells (Yuan et al., 2022). For example, a droplet-based microfluidic platform was constructed to rapidly characterize a series of native and heterologous constitutive promoters in *Streptomyces lividans 66* in droplets, and then a set of engineered promoter variants with desired strengths were efficiently screened out from two synthetic promoter libraries (Tu et al., 2021). Before sorting, strains should first be enclosed in droplets, i.e., single-cell encapsulation, kept alive for a certain period of time, and enabled by diversified operations comprising reagent injection, coalescence, lysis, splitting, sorting, *etc.* By this means, the microfluidic droplets possess a uniform and tunable size and a volume ranging from femtoliter to nanoliter, which greatly reduces reagent consumption and the corresponding cost. Therefore, it has been confirmed that droplet microfluidics provides new insights and solutions into practical application in engineered strain modification and mutant host screening. This perspective focuses on the applications of DMF in high-throughput screening of a variety of microbes, including bacteria, yeast, and filamentous fungi; this study discusses the advantages brought by large-scale droplets and presents the future trends.

Mutant generation and droplet encapsulation

The primary step for microbial strain HTS is constructing large-scale mutant libraries. The more variants available for screening, the greater the possibility of identifying extremely rare but beneficial mutations. Thus, microbial transformation usually utilizes random mutagenesis to accumulate variations with sufficient throughput, involving physical means such as ultraviolet irradiation, atmospheric and room temperature plasma (ARTP), heavy ion radiation, and other chemical mutagenesis approaches (Zeng et al., 2020). Subsequently, the mutant cells are then enclosed in individual droplets, and normal growth is maintained. Most mainstream research studies used the single emulsion system which is based on passive hydrodynamic pressure, and whose microchannel junctions can be classified into flow-focusing, cross-flow, and co-flow configurations (Wang et al., 2022). Concretely, a microbial culture medium with/without the substrate for further detection reactions contains common component similar to the dispersed aqueous phase. Then, the fluids are infused into the continuous oil phase, with favorable biocompatibility and water immiscibility, and break up into monodisperse water-in-oil (W/O) droplets when meeting at the junction. Surfactant addition to the two phases can stabilize the droplets and prevent coalescence. It is worth mentioning that the number of strains in a single droplet is not exactly one, which does not follow the Poisson distribution. High dilution can prevent the internal number from exceeding one, to a certain extent. The size of droplets can be altered by adjusting the channel geometry and the relative flow rates of the two phases. Picoliter droplets are well-suited for loading individual bacterium (~10 pL), yeast cells (300 pL), characterizing the production or consumption of their extracellular metabolites, and screening monoclonal antibodies produced by hybridoma cells (660 pL) (El Debs et al., 2012; Wang et al., 2014). For large-sized filamentous fungi with well-

developed hyphae, nanoliter-level droplets (~10 nL) are selected for encapsulation, where the strain can keep growing until droplet rupture occurs, pierced by the tip of germinated mycelium (Romero et al., 2015). The droplets' stability remarkably affects the long-term cultivation of internal strains and subsequent product detection. Nevertheless, the favorable air permeability of the typically used material for microfluidic chips, poly (dimethylsiloxane) (PDMS), can easily cause the volatilization of inner oil fluids and the destruction of the droplet state. Moreover, considering that an *in situ* culture is inconvenient for later detection and sorting, droplets are commonly transferred to centrifuge tubes or syringes for off-line culture.

Signal screening

Additionally, appropriate screening signals and reaction strategies need to be determined. Since the droplets are transparent, signals of either intracellular or extracellular products can be accurately detected without interference. Ordinary screening signals include fluorescence, absorbance, Raman spectrum, and mass spectrometry (MS), expanding the variety of strains (Markel et al., 2020). Their sources differentiate related droplet operation, including self-products, biosensors, and exogenously added reagents. The products of some microorganisms possess autofluorescence (e.g., carotenoids and riboflavin), so the absorbance and fluorescence intensity of droplets together with internal strains can be directly captured, free from additional reagents and complicated manipulation. Among several signals, the rate of fluorescence-based sorting can reach 300 droplets per second. Also, the Raman and mass spectra of the products can be measured. However, the signal intensity of the former is weak, with a long acquisition time, and the latter needs matching MS analysis, causing a low sorting throughput of approximately 200 per minute (Stucki et al., 2021). When the products lack obvious detectable characteristics, four ingredients can be integrated and co-encapsulated with strains, including fluorescent substrates for enzyme activity determination, fluorescent protein labeling, fluorescent probe coupling, and biosensors enabling sensing target products (Bouzetos et al., 2022). The principal action lies in converting the biological activity into a detectable fluorescent signal. The latest studies emphasize designing a living biosensor. Specifically, the production strain and the sensing strain, the latter of which can homogeneously respond to the former's products, are co-embedded in the droplet, and then the fluorescent signal emitted by the sensing strain can indirectly reflect the targeted content (Lim et al., 2018; Hua et al., 2022). This approach is appealing for a wide range of unexpected or difficult to genetically manipulate engineered strains.

Droplets sorting

For cases where the reaction between the substrate reagents and products occurs quickly, the strains are required to first be encapsulated in the droplet and grow for a while for metabolite secretion. After that, the reactant can be added to the droplet through coalescence or injection, fostering the resulting detection and sorting. Droplet fusion can be categorized into passive and active ways. In passive coalescence, precise control over the velocity of individual droplets is a prerequisite to help the droplets gradually approach each other and finally merge; this is achieved by designing the channel geometry. Passive methods are inefficient and error-prone, so active strategies that provide external energy input to apply local actuation, such as electrical, magnetic, thermal, and mechanical forces, are often employed in practical applications. Among them, implementing electric control to induce droplet interface destabilization to aid coalescence or injection is most common, with a throughput of thousands of droplets per second. Similarly, droplets can also be sorted passively based on physical properties, such as size, or actively by on-demand activation. For instance, under dielectrophoretic forces, droplets with strong fluorescent signals are dragged into the downstream collection channel, and the remaining droplets are distributed to the waste channel (Shang et al., 2017).

Perspective

To date, droplet microfluidics has been successfully applied to a variety of microbes, including bacteria, yeast, and filamentous fungi, and the detection of massive metabolites of strain products, such as polypeptides, enzymes, and lipids, has been realized. By virtue of droplet-based HTS, high-yielding mutants have been obtained. In addition to the expansion of microbial strains, screening signals, and reaction strategies, some innovative ideas emerged, optimized from the perspectives of chip construction, droplet conversion into hydrogel microbeads (Li et al., 2018), and the combination with double emulsion systems (Körfer et al., 2022) and FACS (Li et al., 2021). Despite the promising potential of droplet microfluidics in green biomanufacturing, there are still urgent problems to be solved. Fluorescence is currently the most dominant screening signal, but there still exists a large number of compounds that cannot be detected by fluorescence, so it is necessary to develop other high-efficiency screening signals. In addition, specific strains do not appear to be the smoothly spherical or ellipsoidal but harbor dense mycelial network, such as *Aspergillus niger*, *Streptomyces*, and *Gibberella Fujikura* (Beneyton et al., 2016; He et al., 2019). However, compared to other strains, there are two limiting factors that make the use of droplet microfluidics for filamentous fungi challenging. First, their hyphae tip can readily puncture the droplet and cause leakage of extracellular products. Furthermore, the long droplet incubation times needed for protein expression and the different individual growth rates contribute to droplet volume polydispersity post-incubation, which complicates the sorting procedure. Last but not least, droplets containing mycelium are more susceptible to high-voltage electric fields, which deform and break the droplets (Samlali et al., 2022). Therefore, diverse solutions for optimal droplet morphology and material systems need to be developed to match categories of strains. Moreover, versatile automatic devices integrating functional modules of droplet generation, cultivation, coalescence, reagent injection, and sorting are still lacking, which limits industrial upscaling. In summary, we firmly believe that droplet microfluidics has evolved into a powerful technology that will pave the way for HTS of engineered microbial strains in the green biomanufacturing industry.

Author contributions

YW provided the idea. GQ and ZZ wrote the manuscript. HH and YW revised the manuscript.

Funding

This study was supported by the National Key Research and Development Program of China (No. 2021YFF0600805 and 2021YFC2104300), the National Natural Science Foundation of China (22208167), the Natural Science Foundation of Jiangsu Province (BK20210573), the Tianjin Synthetic Biotechnology Innovation Capacity Improvement Project (TSBICIP-PTJS-003-04), and the Outstanding Youth Fund of Xinjiang Natural Science Foundation (2022D01E19).

Conflict of interest

The authors declare that the research was conducted in the absence of any commercial or financial relationships that could be construed as a potential conflict of interest.

Publisher's note

References

Beneyton, T., Wijaya, I. P., Postros, P., Najah, M., Leblond, P., Couvent, A., et al. (2016). High-throughput screening of filamentous fungi using nanoliter-range droplet-based microfluidics. *Sci. Rep.* 6, 27223. doi:10.1038/srep27223

Böttcher, D., Zägel, P., Schmidt, M., and Bornscheuer, U. T. (2017). A Microtiter Plate-based Assay to screen for active and stereoselective hydrolytic enzymes in enzyme libraries. *Methods Mol. Biol.* 1539, 197–204. doi:10.1007/978-1-4939-6691-2_11

Bouzetos, E., Ganar, K. A., Mastrobattista, E., Deshpande, S., and van der Oost, J. (2022). (R)evolution-on-a-chip. *Trends Biotechnol.* 40 (1), 60–76. doi:10.1016/j.tibtech.2021.04.009

El Debs, B., Utharala, R., Balyasnikova, I. V., Griffiths, A. D., and Merten, C. A. (2012). Functional single-cell hybridoma screening using droplet-based microfluidics. *Proc. Natl. Acad. Sci. U. S. A.* 109 (29), 11570–11575. doi:10.1073/pnas.1204514109

Guo, Q., Li, Y. W., Yan, F., Li, K., Wang, Y. T., Ye, C., et al. (2022). Dual cytoplasmic-peroxisomal engineering for high-yield production of sesquiterpene α-humulene in Yarrowia lipolytica. *Biotechnol. Bioeng.* 119 (10), 2819–2830. doi:10.1002/bit.28176

He, R., Ding, R., Heyman, J. A., Zhang, D., and Tu, R. (2019). Ultra-high-throughput picoliter-droplet microfluidics screening of the industrial cellulase-producing filamentous fungus Trichoderma reesei. *J. Ind. Microbiol. Biotechnol.* 46 (11), 1603–1610. doi:10.1007/s10295-019-02221-2

Hua, E., Zhang, Y., Yun, K., Pan, W., Liu, Y., Li, S., et al. (2022). Whole-cell biosensor and producer Co-cultivation-Based microfludic platform for screening saccharopolyspora erythraea with hyper erythromycin production. *ACS Synth. Biol.* 11 (8), 2697–2708. doi:10.1021/acssynbio.2c00102

Körfer, G., Besirlioglu, V., Davari, M. D., Martinez, R., Vojcic, L., and Schwaneberg, U. (2022). Combinatorial InVitroFlow-assisted mutagenesis (CombIMut) yields a 41-fold improved CelA2 cellulase. *Biotechnol. Bioeng.* 119 (8), 2076–2087. doi:10.1002/bit.28110

Körfer, G., Pitzler, C., Vojcic, L., Martinez, R., and Schwaneberg, U. (2016). *In vitro* flow cytometry-based screening platform for cellulase engineering. *Sci. Rep.* 6, 26128. doi:10.1038/srep26128

Li, M., Liu, H., Zhuang, S., and Goda, K. (2021). Droplet flow cytometry for single-cell analysis. *RSC Adv.* 11 (34), 20944–20960. doi:10.1039/d1ra02636d

Li, M., van Zee, M., Riche, C. T., Tofig, B., Gallaher, S. D., Merchant, S. S., et al. (2018). A gelatin microdroplet platform for high-throughput sorting of hyperproducing single-cell-derived microalgal clones. *Small* 14 (44), e1803315. doi:10.1002/smll.201803315

Lim, H. G., Jang, S., Jang, S., Seo, S. W., and Jung, G. Y. (2018). Design and optimization of genetically encoded biosensors for high-throughput screening of chemicals. *Curr. Opin. Biotechnol.* 54, 18–25. doi:10.1016/j.copbio.2018.01.011

Markel, U., Essani, K. D., Besirlioglu, V., Schiffels, J., Streit, W. R., and Schwaneberg, U. (2020). Advances in ultrahigh-throughput screening for directed enzyme evolution. *Chem. Soc. Rev.* 49 (1), 233–262. doi:10.1039/c8cs00981c

Orsi, E., Claassens, N. J., Nikel, P. I., and Lindner, S. N. (2021). Growth-coupled selection of synthetic modules to accelerate cell factory development. *Nat. Commun.* 12 (1), 5295. doi:10.1038/s41467-021-25665-6

Romero, P. A., Tran, T. M., and Abate, A. R. (2015). Dissecting enzyme function with microfluidic-based deep mutational scanning. *Proc. Natl. Acad. Sci. U. S. A.* 112 (23), 7159–7164. doi:10.1073/pnas.1422285112

Samlali, K., Alves, C. L., Jezernik, M., and Shih, S. C. C. (2022). Droplet digital microfluidic system for screening filamentous fungi based on enzymatic activity. *Microsyst. Nanoeng.* 8, 123. doi:10.1038/s41378-022-00456-1

Shang, L., Cheng, Y., and Zhao, Y. (2017). Emerging droplet microfluidics. *Chem. Rev.* 117 (12), 7964–8040. doi:10.1021/acs.chemrev.6b00848

Stucki, A., Vallapurackal, J., Ward, T. R., and Dittrich, P. S. (2021). Droplet microfluidics and directed evolution of enzymes: An intertwined journey. *Angew. Chem. Int. Ed. Engl.* 60 (46), 24368–24387. doi:10.1002/anie.202016154

Tu, R., Zhang, Y., Hua, E., Bai, L., Huang, H., Yun, K., et al. (2021). Droplet-based microfluidic platform for high-throughput screening of Streptomyces. *Commun. Biol.* 4 (1), 647. doi:10.1038/s42003-021-02186-y

Utharala, R., Grab, A., Vafaizadeh, V., Peschke, N., Ballinger, M., Turei, D., et al. (2022). A microfluidic Braille valve platform for on-demand production, combinatorial screening and sorting of chemically distinct droplets. *Nat. Protoc.* 17, 2920–2965. doi:10.1038/s41596-022-00740-4

Wang, B. L., Ghaderi, A., Zhou, H., Agresti, J., Weitz, D. A., Fink, G. R., et al. (2014). Microfluidic high-throughput culturing of single cells for selection based on extracellular metabolite production or consumption. *Nat. Biotechnol.* 32 (5), 473–478. doi:10.1038/nbt.2857

Wang, Y., Shang, L., Zhao, Y., and Sun, L. (2022). Microfluidic generation of multicomponent soft biomaterials. *Engineering* 13, 128–143. doi:10.1016/j.eng.2021.02.026

Wang, Y., Zhang, X., Shang, L., and Zhao, Y. (2021). Thriving microfluidic technology. *Sci. Bull.* 66 (1), 9–12. doi:10.1016/j.scib.2020.07.030

Yang, J., Tu, R., Yuan, H., Wang, Q., and Zhu, L. (2021). Recent advances in droplet microfluidics for enzyme and cell factory engineering. *Crit. Rev. Biotechnol.* 41 (7), 1023–1045. doi:10.1080/07388551.2021.1898326

Yuan, H., Tu, R., Tong, X., Lin, Y., Zhang, Y., and Wang, Q. (2022). Ultrahigh-throughput screening of industrial enzyme-producing strains by droplet-based microfluidic system. *J. Ind. Microbiol. Biotechnol.* 49 (3), kuac007. doi:10.1093/jimb/kuac007

Zeng, W., Guo, L., Xu, S., Chen, J., and Zhou, J. (2020). High-throughput screening technology in industrial biotechnology. *Trends Biotechnol.* 38 (8), 888–906. doi:10.1016/j.tibtech.2020.01.001

Frontiers in
Bioengineering and Biotechnology

Accelerates the development of therapies, devices, and technologies to improve our lives

A multidisciplinary journal that accelerates the development of biological therapies, devices, processes and technologies to improve our lives by bridging the gap between discoveries and their application.

Discover the latest Research Topics

See more →

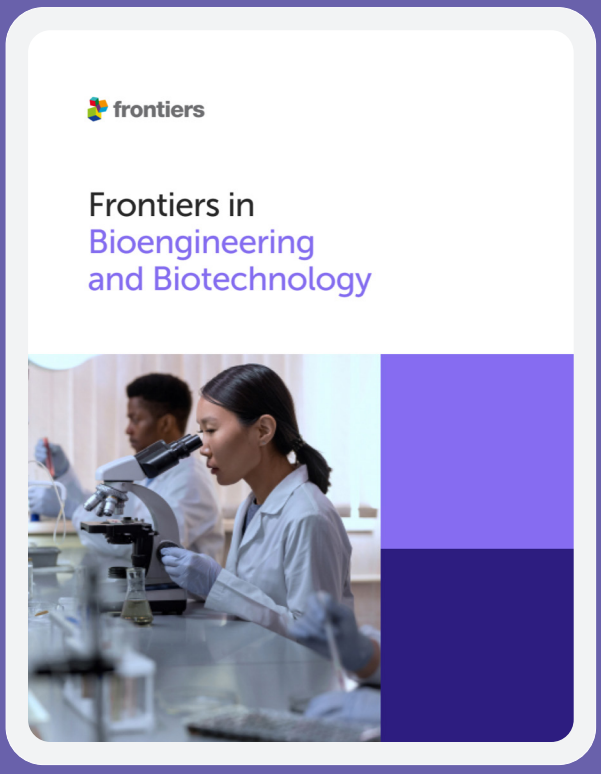

Frontiers

Avenue du Tribunal-Fédéral 34
1005 Lausanne, Switzerland
frontiersin.org

Contact us

+41 (0)21 510 17 00
frontiersin.org/about/contact